INFORMATION TO USERS

This manuscript has been reproduced from the microfilm master. UMI films the text directly from the original or copy submitted. Thus, some thesis and dissertation copies are in typewriter face, while others may be from any type of computer printer.

The quality of this reproduction is dependent upon the quality of the copy submitted. Broken or indistinct print, colored or poor quality illustrations and photographs, print bleedthrough, substandard margins, and improper alignment can adversely affect reproduction.

In the unlikely event that the author did not send UMI a complete manuscript and there are missing pages, these will be noted. Also, if unauthorized copyright material had to be removed, a note will indicate the deletion.

Oversize materials (e.g., maps, drawings, charts) are reproduced by sectioning the original, beginning at the upper left-hand corner and continuing from left to right in equal sections with small overlaps. Each original is also photographed in one exposure and is included in reduced form at the back of the book.

Photographs included in the original manuscript have been reproduced xerographically in this copy. Higher quality 6" x 9" black and white photographic prints are available for any photographs or illustrations appearing in this copy for an additional charge. Contact UMI directly to order.

Developing, coupling, and applying a gas, aerosol, transport, and radiation model to study urban and regional air pollution

Jacobson, Mark Zachary, Ph.D.

University of California, Los Angeles, 1994

UNIVERSITY OF CALIFORNIA

Los Angeles

Developing, Coupling, and Applying a Gas, Aerosol,

Transport, and Radiation Model to Study Urban and Regional

Air Pollution

A dissertation submitted in partial satisfaction of the

requirements for the degree Doctor of Philosophy in
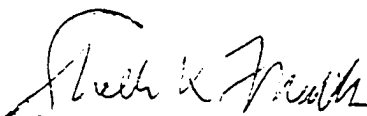
Atmospheric Sciences

by

Mark Zachary Jacobson

1994

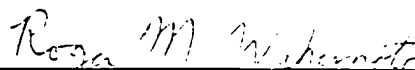(c) Copyright by

Mark Zachary Jacobson

1994

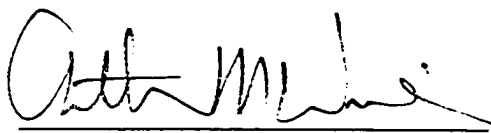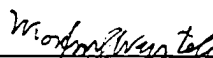The dissertation of Mark Zachary Jacobson is approved.

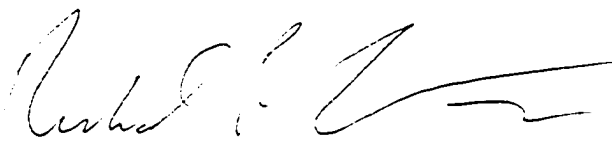Sheldon K. Friedlander

Roger M. Wakimoto

Arthur M. Winer

Morton G. Wurtele

Richard P. Turco, Committee Chair

University of California, Los Angeles

1994

ii

DEDICATION

I dedicate this thesis to the loving memory of my sister, Michelle, and to my parents,

Yvonne and William Jacobson

iii

TABLE OF CONTENTS

iv

v

LIST OF FIGURES

viii

LIST OF TABLES

ACKNOWLEDGMENTS

I extend thanks to all my thesis committee members -- Richard Turco, Sheldon Friedlander, Arthur Winer, Morton Wurtele, and Roger Wakimoto -- for their help and guidance during my tenure at UCLA. Further, I thank my advisor, Richard Turco, for allowing me the freedom to pursue the topic of research discussed here and for patiently working with me for several years. I also thank my wife, Azadeh, for loving and supporting me, for working with me on a project to study equilibrium in electrolyte solutions and for helping me learn details of thermodynamics. I further thank Rong Lu for working with me and allowing me to use his dynamics model, Brian Toon for giving advice and allowing me to use his extensive computer algorithms, Joe Cassmassi for providing valuable insight, advice and data, and Ruiyan Lin for developing map-projection graphics.

Next, I thank Robert Chatfield, Scott Elliott, Mei Shen, Sajal Kar, Eric Jensen, Bill McKie, Jeffrey Lew, Pat Hamill, Suzanne Paulson, Xuepeng Zhao, Sybil Anderson, Ziping Sun, Jingxia Zhao, John Vastano, Doug Westphal, Joe Jordan, Fabrice Cuq, Louise Lee, Bill Weibel, Joseph Spahr, and James Murakami for giving me advice on topics discussed in this work or on computing. Also, I especially thank L. V. Oliver, Michael Carr, and Rick Fort for their guidance and support during my time at UCLA. In addition, I thank Paul Allen and Bart Croes from the California Air Resources Board and Satoru Mitsutomi and Julia Lestor from the SCAQMD for providing me with data. I further thank Darrell Winner and Glen Cass for providing me with the CIT dry deposition model, advice, and literature, and thank Donald Dabdub and John Seinfeld for providing me with literature and advice. Thanks also go to my grandmother, Sylvia Jacobson, my parents, William and Yvonne Jacobson, my sister, Laura Jacobson, my parents in law, Azar and Moji Tabazadeh, my brother-in-law and his wife, Afshin and Narsis, my sister-

x

in-law, Afshan, and my friends Dave Gampell, Danny Kaplan, and Scott Mosher for all their kindness and support.

Finally, three articles were reprinted from or used with kind permission from Elsevier Science Ltd, The Boulevard, Langford Lane, Kidlington OX5 1GB, UK. These include (1) "SMVGEAR: a sparse-matrix, vectorized Gear code for atmospheric models," by M. Z. Jacobson and R. P. Turco, *Atmos. Environ.* **28A**, 273 - 284, (2) "Modeling coagulation among particles of different composition and size," by M. Z. Jacobson, R. P. Turco, E. J. Jensen, and O. B. Toon, *Atmos. Environ.* **28A**, 1327 - 1338, and (3) "GATOR: A gas, aerosol, transport, and radiation model for studying urban and regional air pollution," *Atmos. Environ.*, in review.

-

VITA

September 26, 1965	Born, Sunnyvale, California
1982	Yale Book Award Gunn Sr. High School, Palo Alto, California
1983	National Merit Scholarship Harvard National Honorary Scholarship Faculty Cup Award Gunn Sr. High School, Palo Alto, California
1985-7	NCAA-ITCA Scholar-Athlete of Year Award Stanford University Stanford, California
1986	Tennis Scholarship Stanford University Stanford, California
1988	B. S., with distinction, Civil Engineering B. A., with distinction, Economics M. S., Environmental Engineering Stanford University Stanford, California
1989	Chancellor's Fellowship University of California, Los Angeles
1991	M. S., Atmospheric Sciences University of California, Los Angeles
1992	Neiburger Teaching Award Department of Atmospheric Sciences University of California, Los Angeles
1993	Dissertation Year Fellowship University of California, Los Angeles
1994	Assistant Professorship Stanford University

xii

PUBLICATIONS

Delitsky M. L., Turco, R. P. and Jacobson M. Z. (1990) Nitrogen ion clusters in Triton's atmosphere. *Geophys. Res. Lett.* **17**, 1725-1728.

Elliott S., Turco R. P. and Jacobson M. Z. (1991) Efficient photochemical packages for coupling with multi-dimensional transport models: Initial development and tests in the middle atmosphere. UCLA Dept. of Atmospheric Sciences Internal Report.

Elliott S., Turco R. P. and Jacobson M. Z. (1992) Tests on combined projection / forward differencing integration for stiff photochemical family systems at long time step. Submitted to *Computers Chem.* **17**, 91 - 102.

Elliott S., Prueitt M. L., Jacobson M. Z., Turco R. P., Bossert J. E. and Mronz E. J. (1993) Engineering photochemical smog through convection towers. Los Alamos National Laboratory Technical Report LA-12762-MS.

Jacobson M. Z. (1990) Modeling aerosol formation, growth, and depletion in an urban airshed. In the *National Center for Intermedia Transport Research Progress Report*, EPA Agreement CR 8127771-03.

Jacobson M. Z., Turco R. P., Venkataraman C. and Friedlander S. K. (1991) Simulating spatial and temporal evolution of aerosol size distribution and composition using a 3-D air pollution model. *EOS Supplement*, Oct. 29, p. 103.

Jacobson M. Z. and Turco R. P. (1992) Chemistry, aerosol microphysics, and transport model for local and regional 3-D simulations. *EOS Supplement*, Oct. 22, p. 88.

Jacobson M. Z. and Turco R. P. (1994) SMVGEAR: A sparse-matrix, vectorized Gear code for atmospheric models. *Atmos. Environ.* **28A**, 273-284.

Jacobson M. Z., Turco R. P., Jensen E. J. and Toon O. B. (1994) Modeling coagulation among particles of different composition and size. *Atmos. Environ.* **28A**, 1327-1338.

Jacobson M. Z. and Turco R. P. (1994) Simulating condensational growth, evaporation, and coagulation of aerosols using a combined moving and stationary size grid. *Aerosol Sci. and Technol.*, in press.

Jacobson M. Z., Turco R. P. and Tabazadeh A. (1994) Simulating equilibrium within aerosols and non-equilibrium between gases and aerosols. *J. Geophys. Res.*, in review.

Jacobson M. Z., Turco R. P., Lu R. and Toon O. B. (1994) GATOR: A gas, aerosol, transport, and radiation modeling system for studying urban and regional air pollution. Regional Photochemical Measurement & Modeling Studies Abstracts Book, AWMA and *Atmos. Environ.*, in final review.

xiii

Jacobson M. Z., Turco R. P., Lu R. and Toon O. B. (1994) Simulating an air pollution episode with a gas, aerosol, transport, and radiation modeling system. *EOS Supplement*, Spring, 1994, p. 87.

Lu R., Turco R. P. and Jacobson M. Z. (1993) Modeling of elevated ozone layers over Southern California. Regional Photochemical Measurement & Modeling Studies Abstracts Book, AWMA, p. 115.

Lu R., Turco R. P. and Jacobson M. Z. (1994) Three-dimensional ozone distributions over the Los Angeles Basin. *EOS Supplement*, Spring, 1994, p. 87.

Shen M., Turco R. P., Paulson S. and Jacobson M. (1994) Role of isoprene in tropospheric photochemistry. *EOS Supplement*, Spring, 1994, p. 86.

Tabazadeh A., Turco R. P. and Jacobson M. Z. (1993) A model for heterogeneous chemical processes on stratospheric aerosols. *EOS Supplement.*, Spring, 1993

Tabazadeh A., Turco R. P. and Jacobson M. Z. (1994) A model for studying the composition and chemical effects of stratospheric aerosols. *J. Geophys. Res.*, in press.

Tabazadeh A., Turco R. P. and Jacobson M. Z. (1994) Nucleation mechanism for Type-I polar stratospheric clouds. *J. Geophys. Res.*, in press.

Tabazadeh A., Turco R. P. and Jacobson M. Z. (1994) The relationship between the physical state of stratospheric aerosols and Type I PSC formation. *EOS Supplement*, Spring, 1994, p. 99.

ABSTRACT OF THE DISSERTATION

Developing, Coupling, and Applying a Gas, Aerosol,

Transport, and Radiation Model to Study Urban and Regional

Air Pollution

by

Mark Zachary Jacobson

Doctor of Philosophy in Atmospheric Sciences

University of California, Los Angeles, 1994

Professor Richard P. Turco, Chair

This thesis discusses the development of a *g*as, *a*erosol, *t*ransport, and *r*adiation air quality model (GATOR), the coupling of GATOR to a *m*esoscale *m*eteorological and *t*racer *d*ispersion model (MMTD), and the application of the resulting GATOR / MMTD *a*ir *p*ollution *m*odeling *s*ystem (APMS) to studies of gas and aerosol pollution buildup in the Los Angeles Basin. GATOR consists of computer algorithms that simulate four groups of atmospheric processes: gas, aerosol, transport, and radiation processes. Gas processes include chemistry, emissions, gas-to-particle conversion, optical depth attenuation, and deposition. Aerosol processes include size-resolved emissions, nucleation, coagulation, condensational growth, dissolutional growth, evaporation, chemical equilibrium, aqueous chemistry, optical depth attenuation, deposition, and sedimentation. Transport processes include horizontal advection and diffusion and

xv

vertical diffusion of all gases and particles, and they require meteorological data as inputs. To drive the transport processes, the MMTD, developed by R. Lu and R. P. Turco, was coupled to GATOR. The MMTD predicts wind speed, wind direction, temperature, humidity, and pressure, among other variables. Finally, radiation processes in GATOR include spectrally-resolved scattering and absorption by gases, aerosols, fogs, and clouds, and calculation of mean intensities and heating rates. I used the GATOR / MMTD modeling system to predict pollution buildup in Los Angeles during the Southern California Air Quality Study (SCAQS) period of August 26 - 28, 1987. Among the model inputs were emissions, soil moisture, albedo, topographical, landuse, and chemical rate data. To validate the model, surface observations were compared to model predictions of gas-phase ozone, nitric oxide, nitrogen dioxide, carbon monoxide, sulfur dioxide, methane, total non-methane hydrocarbons, formaldehyde, peroxyacetylnitrate, hydrogen peroxide, nitric acid, nitrous acid, and ammonia concentrations. Observations were also compared to predictions of aerosol-phase ammonium, nitrate, sodium, chloride, sulfate, and total particulate concentrations. Finally, observations were compared to predictions of solar radiation and scattering coefficients. In sum, the GATOR / MMTD system predicted ozone to within a normalized gross error of 20 - 35% during the study period. Additional statistics and time-series plots are shown.

Chapter 1

Introduction

Gas and aerosol pollution buildup has been a problem in the Los Angeles Basin and other urban airsheds for many years. Factors leading to poor air quality include emissions of gases and particles, topography, meteorology, chemistry, and gas-to-particle conversion. Since the interactions leading to air pollution are complex, researchers have developed computer models to simulate pollution production. These models have ranged from simple box and empirical types to complex airshed models.

The motivation for the research discussed here was to create a new integrated air pollution model that educators, researchers, and regulators can ultimately use to study and reduce air pollution. With a comprehensive model, educators can teach students about pollution movement and transformations and researchers can study how physical, chemical, and dynamical processes interact to form pollutants in different regions of an airshed. Such studies can increase understanding of pollutant flow and formation in domains where topography, weather conditions, and emissions differ. Finally, regulators can use such a model to test effects of reducing or relocating emissions, to estimate concentrations of pollutants where measurements are not normally taken, and to forecast pollution episodes in specific areas. Finally, over the years, such a model can improve as computational speed, understanding of physical processes, and input data improve.

1

Simulating gas and aerosol pollution buildup requires a computer model that accounts for physical, chemical, and dynamical processes in the atmosphere. These processes include gas-phase chemistry, aqueous-phase chemistry, condensational and dissolutional growth of aerosols, aerosol and gas dry and wet deposition, aerosol coagulation, aerosol homogeneous and heterogeneous nucleation, gas and aerosol advection, diffusion, convection, and emissions, chemical equilibrium processes, and radiative transfer. Modeling also requires sufficient data, such as data for emissions, land-use, topography, albedo, soil moisture, and more.

Two groups of well-established air pollution models in use today are variations of the Urban Airshed Model (UAM) and the California Institute of Technology (CIT) model. Versions of both models appear to have branched from the same initial research (*e. g.*, Roth *et al.*, 1971, 1974; Reynolds *et al.*, 1973, 1974). The UAM has since been expanded and used in numerous studies. Scheffe and Morris (1993) detail the history of the UAM. Similarly, the CIT has co-evolved, with significant contributions from McRae (1981), McRae *et al.* (1982), Russell *et al.* (1988a,b, 1993), and Harley *et al.* (1993a,b), among others.

Here, I discuss the development of an air quality model that has been coupled to a meteorological model to form a new air pollution modeling system. While I applied the system to study photochemical smog and aerosol buildup in the Los Angeles Basin, it can be used to study pollution in other urban regions, given sufficient input data. In addition, if the air quality model is coupled to a global-scale meteorological model, the resulting system can be used to study global pollution. To validate the current modeling system for the Los Angeles Basin, I compared model predictions to observations from the Southern California Air Quality Study (SCAQS) period of August 26 - 28, 1987. These comparisons are discussed within this thesis.

2

The air pollution modeling system discussed here consists of GATOR, a gas, aerosol, transport, and radiation model (Jacobson et al., 1994a-e) and the MMTD model, a mesoscale meteorological and tracer dispersion model (Lu and Turco, 1993, 1994a,b). Thus, the system is referred to here as the GATOR / MMTD air pollution modeling system (APMS). Figure 1.1 summarizes the processes simulated in the system, and Figures 1.2 - 1.6 summarize each group of processes accounted for in GATOR and / or the MMTD. The gas processes (Figure 1.2) include chemistry, emissions, gas-to-particle conversion, optical depth attenuation, deposition, and gas transport. The aerosol processes (Figure 1.3) include size-resolved emissions, nucleation, coagulation, condensational growth, dissolutional growth, evaporation, chemical equilibrium, aqueous chemistry, optical depth attenuation, deposition, sedimentation, and aerosol transport. The MMTD (Figure 1.4) predicts winds, diffusion, pressure, temperature, and humidity, all of which are used in GATOR. The transport processes in GATOR include horizontal advection and diffusion and vertical diffusion of all gases and aerosol using predicted meteorological data from the MMTD (Figure 1.5). Finally, the radiation processes in GATOR (Figure 1.6) include optical depth calculations for determining visibility and radiative fluxes, and spatially-resolved ultraviolet, visible, and infrared radiative flux calculations for determining photodissociation and heating rates.

Table A.1 of Appendix A describes and lists the references for each of the processes simulated in the coupled GATOR / MMTD system. Similarly, Table A.2 lists each of the subroutines in the modeling system. Several algorithms in GATOR originated from the NASA Ames Tracer / Transport model (Turco et al., 1977, 1979a,b; Toon et al., 1988, 1989a,b), which has been used in a number of regional and global simulations (e. g. Turco et al., 1982; Malone et al., 1986; Toon et al., 1987, 1988, 1989a; Westphal et al., 1988, 1991; Kao et al., 1990; Jensen and Toon, 1992). To the Ames code, a gas

3

GATOR ☐ / MMTD ☒
AIR POLLUTION MODELING
SYSTEM
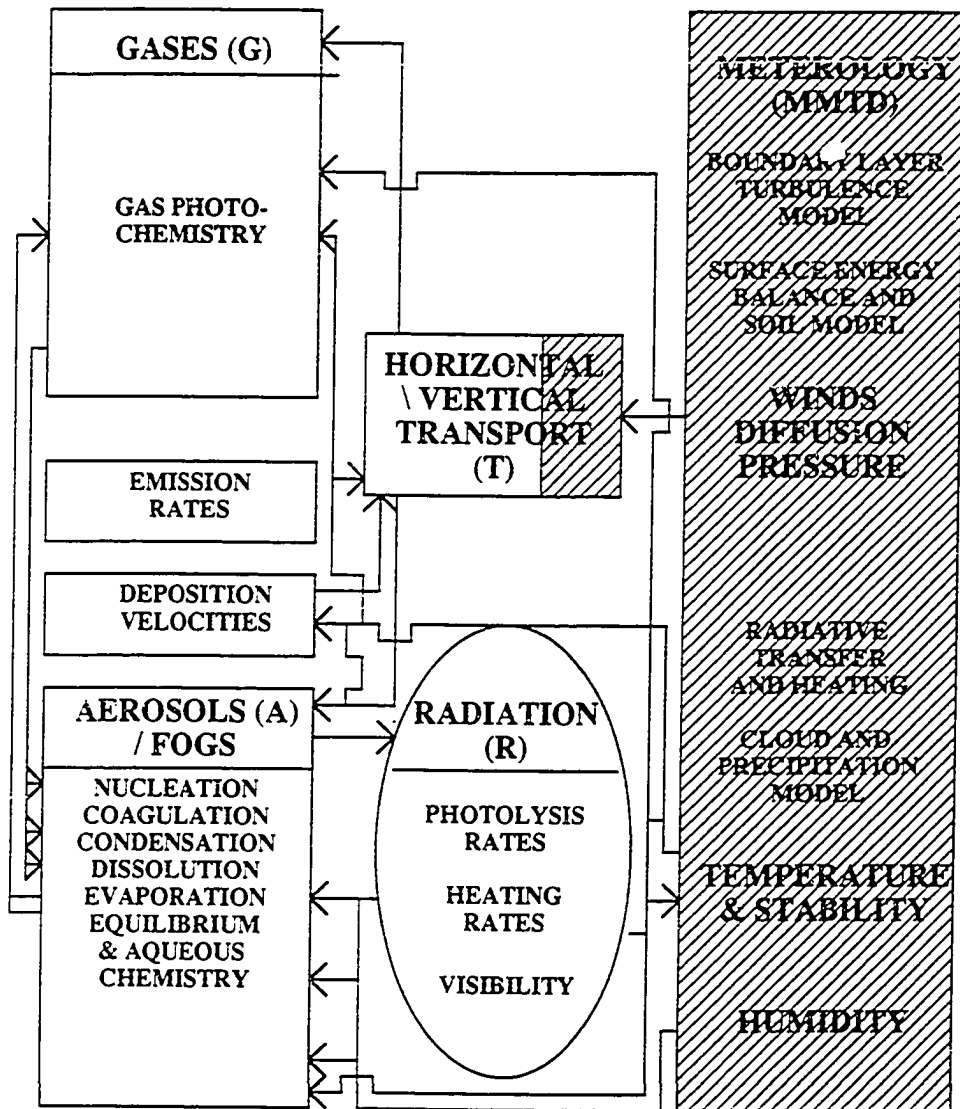
Fig. 1.1. Summary of the GATOR / MMTD air pollution modeling system and the feedbacks occurring between components of the system. For example, the MMTD feeds winds, diffusion, pressure, temperature, and humidity to GATOR and GATOR feeds heating rates back to the MMTD. The MMTD uses the heating rates to calculate part of temperature changes.

4

GAS PROCESSES

ATTENUATION OF
SUNLIGHT BY GASES

CONVECTION /
DIFFUSION OF
GASES

REMOVAL OF GASES BY
NUCLEATION OF
AEROSOLS

ADVECTION /
DIFFUSION OF GASES

GAS-PHASE
CHEMISTRY AND
PHOTOCHEMISTRY

AEROSOL

GAS-PARTICLE TRANSFER BY
CONDENSATIONAL AND DISSOLUTIONAL
GROWTH, EQUILIBRIUM PROCESSES, AND
PARTICLE EVAPORATION

RAINOUT

GAS EFFECTS ON
VISIBILITY

DRY DEPOSITON

EMISSIONS
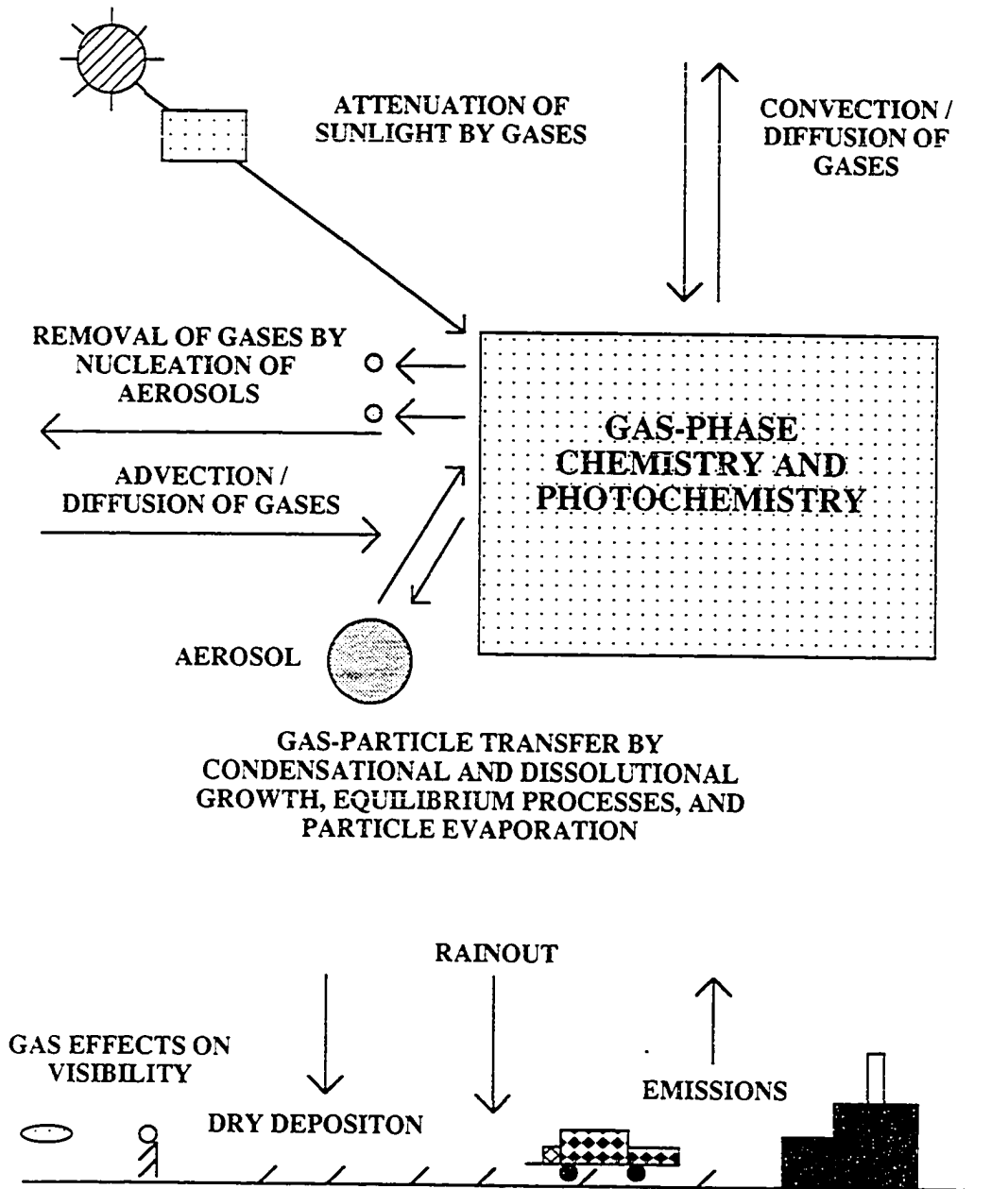
Fig. 1.2. Gas-phase processes in GATOR.

5

AEROSOL PROCESSES

CONVECTION /
DIFFUSION OF
AEROSOLS

ATTENUATION OF
SUNLIGHT BY AEROSOLS

CREATION OF ADDITIONAL
AEROSOLS BY NUCLEATION
OF GASES

GAS

ADVECTION / DIFFUSION
OF AEROSOLS

GAS

AEROSOL
CHEMICAL
EQUILIBRIUM

AQUEOUS
CHEMISTRY

GAS-PARTICLE TRANSFER BY
CONDENSATIONAL AND
DISSOLUTIONAL GROWTH,
EQUILIBRIUM PROCESSES, AND
EVAPORATION

SEDIMENTATION OF
AEROSOLS

COAGULATION
OF AEROSOLS

RAINOUT

AEROSOL
EFFECTS ON
VISIBILITY

DRY DEPOSITION OF
AEROSOLS

EMISSIONS

Fig. 1.3. Aerosol-phase processes in GATOR.

6

MESOSCALE METEOROLOGY
AND TRACER DISPERSION MODEL
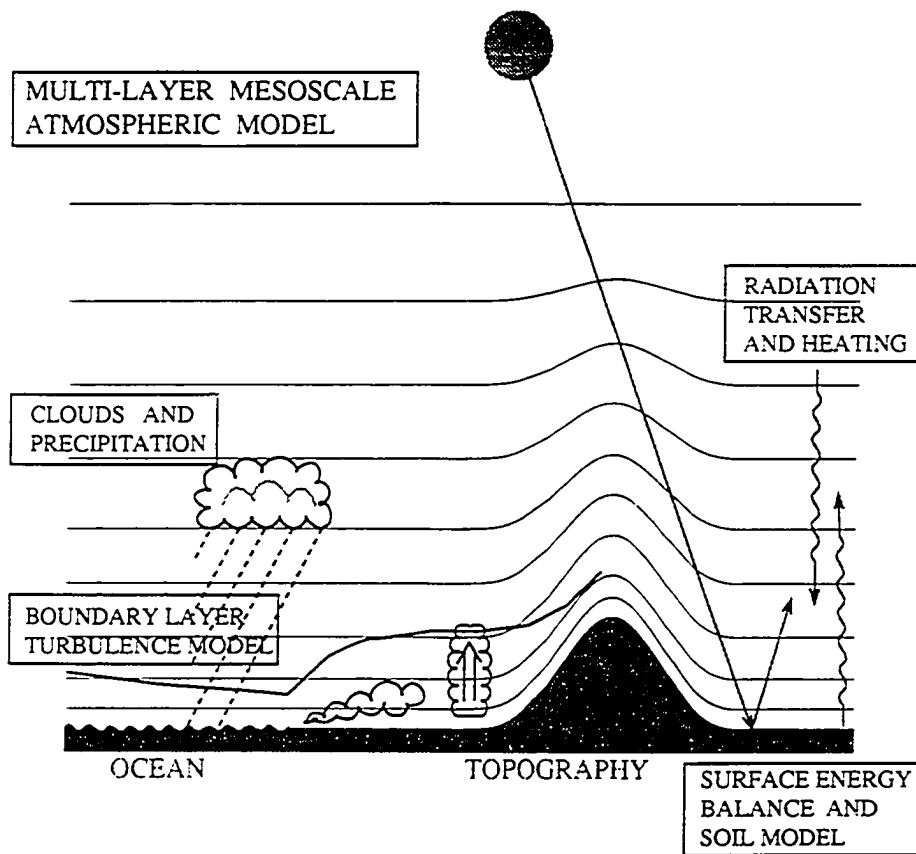
Fig. 1.4. MMTD meteorological processes (courtesy of R. Lu).

7

TRANSPORT PROCESSES

○ THE MESOSCALE METEOROLOGY AND TRACER DISPERSION MODEL
(MMTD) PREDICTS WIND SPEED AND DIRECTION, VERTICAL
DIFFUSION COEFFICIENTS, TEMPERATURE, AND HUMIDITY.
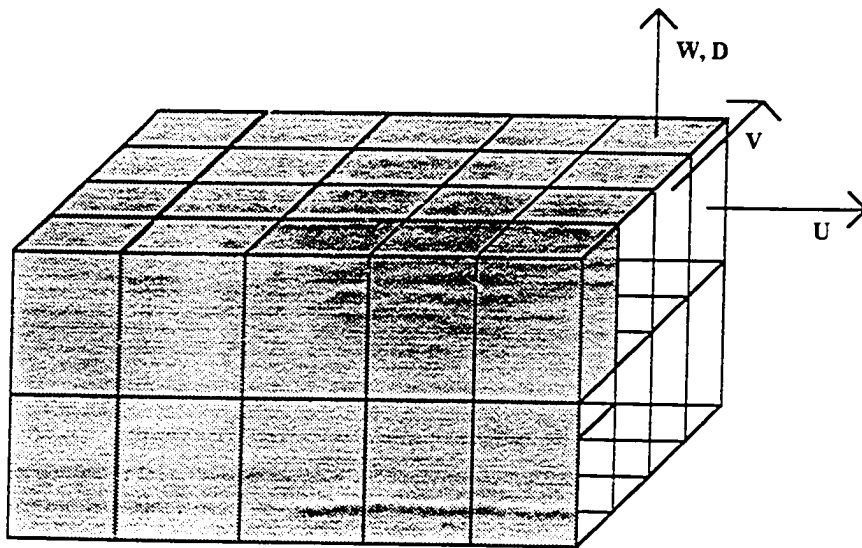
○ THE TRANSPORT ALGORITHMS MOVE GASES AND PARTICLES USING THE
PREDICTED WINDS AND DIFFUSION COEFFICIENTS FROM THE MMTD.

Fig. 1.5. GATOR / MMTD transport processes.

8

RADIATIVE PROCESSES
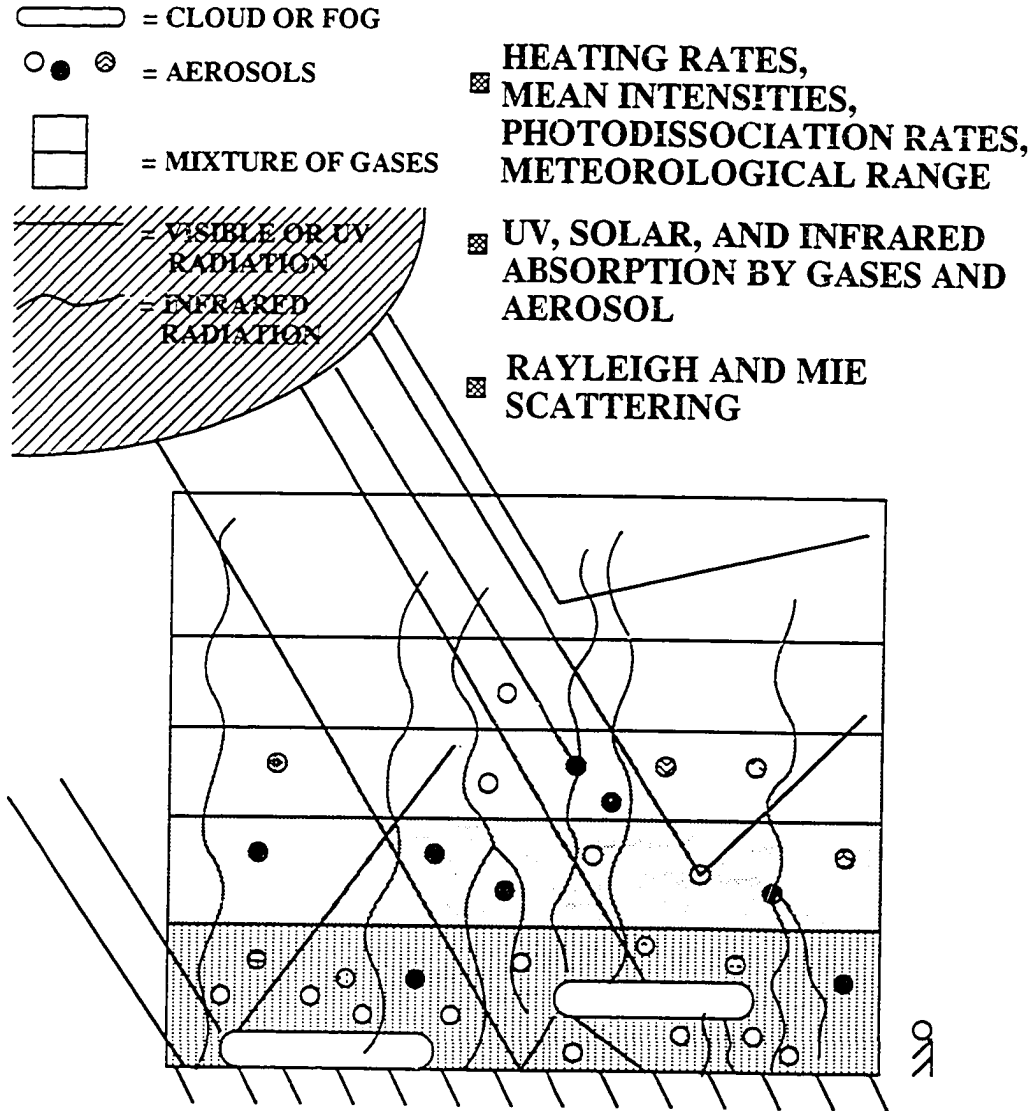
Fig. 1.6. Radiative transfer processes in GATOR.

9

chemistry algorithm and the aerosol microphysics and chemistry algorithms listed in Tables A.1 and A.2, Appendices B - E, and Chapters 5 and 6 were added for this work.

Further, to the radiation portion of the code, developed primarily by Toon et al. (1989b), the following components were added for this work: (1) spatially-resolved zenith angle calculations from the Astronomical Almanac (Nautical Almanac office, 1993), (2) visibility calculations, (3) the option of three wavelength grids for photodissociation, (4) new routines (based in part, on work by R. P. Turco) for reading in wavelength, absorption cross-section, and quantum yield data, (5) the ability to read and calculate temperature dependent absorption cross-section data, (6) index of refraction data for about 30 aerosol components, (7) a speedup of the Mie scattering routine (Toon and Ackerman, 1981) by a factor of thirty, (8) altitude-dependent mixing ratios of ozone and water to scale ozone and water column abundances above the model top, (9) the addition to total extinction of the current extinction of every photodissociating gas in the model, (10) photodissociation rates calculated at the beginning and end of a time interval so that the rates could be interpolated each time step in the chemistry solver, and (11) the coupling of heating rates to the MMTD.

Also, to the horizontal and vertical transport codes, developed primarily by Toon et al. (1988) and Turco et al. (1979a,b), the following components were added for this work: (1) four possible horizontal boundary conditions for the advection solver, (2) vectorization of the vertical transport code around the species instead of altitude dimension, (3) an emissions module, and (4) the coupling of the California Institute of Technology dry deposition model.

In addition, statistical programs to analyze model results, input routines for reading in data, and pre-processing routines for assembling input data have been added. Finally, I optimized the model for use on CRAY computers by vectorizing physical and chemical processes in the code around the grid-cell dimension.

10

Thus, the primary components remaining in GATOR from the NASA Ames model include the horizontal and vertical transport codes (Toon et al., 1988, Turco et al., 1979a,b), the two-steam solution to the radiative transfer equation (Toon et al., 1989b), and the option of using several horizontal and vertical coordinate grid systems.

Some of the contributions to GATOR described in detail here are three individual algorithms, SMVGEAR, EQUISOLV, and COAGSOLV. First, SMVGEAR (Appendix B) is a sparse-matrix, vectorized Gear code that solves stiff first-order, ordinary differential equations over large grid domains. Since all atmospheric processes can be described as a series of ordinary differential equations, SMVGEAR has wide application. Currently, SMVGEAR is used in GATOR to solve all equations for gas chemistry, aqueous chemistry, and condensational growth. Second, EQUISOLV (Appendix D) is a chemical equilibrium algorithm that predicts equilibrium vapor pressures of all dissolving gases and predicts intra-aerosol solid, liquid, and ion distributions. An advantage of EQUISOLV is that it predicts the water content of aerosols when the humidity is less the 100%, predicts the formation of solids in aerosols, and predicts the distribution of ions in non-ideal solutions. Finally, COAGSOLV (Appendix C; Turco et al., 1979a,b; Toon et al. 1988) is an algorithm that solves coagulation equations among any number of particle types, each with a different size distribution and composition.

In 1993 R. Lu and I coupled the MMTD (Lu and Turco, 1993, 1994a,b) to GATOR. The MMTD solves the primitive equations to predict wind speed, wind direction, diffusion, temperature, humidity, and pressure and enables the realistic simulation of meteorology in the Los Angeles Basin. The alternative to using a prognostic model is to use interpolated observed meteorological data. However, observed data are often unavailable, especially for regions aloft. Further, while observed data can be assimilated into a model that predicts past pollution, they cannot be assimilated into a

11

model that predicts future pollution. Since a goal was to develop a model that can predict future pollution, data assimilation was not used for this work.

In sum, advantages of the coupled GATOR / MMTD air pollution modeling system are the following: (1) all processes in the system are prognostic; (2) the system contains algorithms that simulate gas-phase, aerosol-phase, dynamical, transport, and radiative processes; (3) the system predicts temporally- and spatially- distributed gas and aerosol concentrations, aerosol compositions and size distribution, radiative heating rates and mean intensities, wind, temperature, pressure, and other meteorological parameters, (4) all gas and aerosol physical and chemical processes are mass conserving and stable; (5) feedbacks between GATOR and the MMTD are practical (*e.g.* the radiative heating rate from GATOR currently contributes to the temperature calculation in the MMTD); (6) the model grid location and size are changeable, and the vertical and horizontal grid-cell resolution is expandable and contractible; (7) several horizontal map projections and vertical grid choices are available in GATOR; (8) all processes in the system are controlled by switches in an input data file; (9) any number of gas and aerosol species and any number of gas, aqueous, and equilibrium chemical reactions can be solved for by adding them to input data files.

To validate the coupled GATOR / MMTD system, I compared simulation results to data measured during the SCAQS period of August 26 - 28, 1987. Another source of ambient data is current readings from South Coast Air Quality Management District (SCAQMD) monitoring sites. Figure 1.7, a topographical map of the basin, shows the location of most SCAQMD sites. An advantage of SCAQS data over daily measurements is that, during SCAQS, more measurements were taken than are taken daily by the SCAQMD. For example, during the summer SCAQS, upper-air soundings were taken at 15 sites, while only one sounding, at UCLA, is normally taken on a daily basis. Another advantage is that during the SCAQS period, an emissions inventory was compiled. Since

12

emissions have changed significantly since 1987 and meteorological conditions affecting emissions are often different from those that occurred during SCAQS, significant errors may arise in extrapolating August, 1987 emissions to current scenarios. Thus, because more ambient measurements are available from SCAQS and an emissions data base was gathered during that period, I chose to validate the GATOR / MMTD model against SCAQS data.

Thus, this thesis describes some of the development and application of the GATOR / MMTD air pollution modeling system. Chapter 2 describes the problem of ozone buildup in the Los Angeles Basin, Chapter 3 describes aerosol buildup and visibility problems, Chapter 4 describes the theoretical formulation and structure of the

Fig. 1.7. (next page) Topographical map of the Los Angeles Basin showing the location of most SCAQMD and other monitoring sites. The numbers are elevation, in feet and each four-letter symbol identifies a station site. The sites are Newhall (NEWL), Reseda (RESE), West Los Angeles (WSLA), Burbank (BURK), Los Angeles (CELA), Hawthorne (HAWT), Lynwood (LYNN), Pasadena (PASA), Pico Rivera (PICO), Long Beach (LGBH), Azusa (AZUS), Glendora (GLEN), Whittier (WHIT), La Habra (LAHB), Los Alamitos (LSAL), Anaheim (ANAH), Costa Mesa (CSTA), Pomona (POMA), El Toro (TORO), Upland (UPLA), Fontana (FONT), Claremont (CLAR), Norco (NORC), Riverside (RIVR), Crestline (CRES), San Bernardino (SNBO), Redlands (RDLD), Perris (PERI), Elsinore (ELSI), Hemet (HEME), and Banning (BANN). Sites referred to later but not shown are Thousand Oaks (west of Reseda), Simi Valley (north of Thousand Oaks), Long Beach City College (near Long Beach), and Oceanside (along the coast, south of Costa Mesa).

LOS ANGELES BASIN
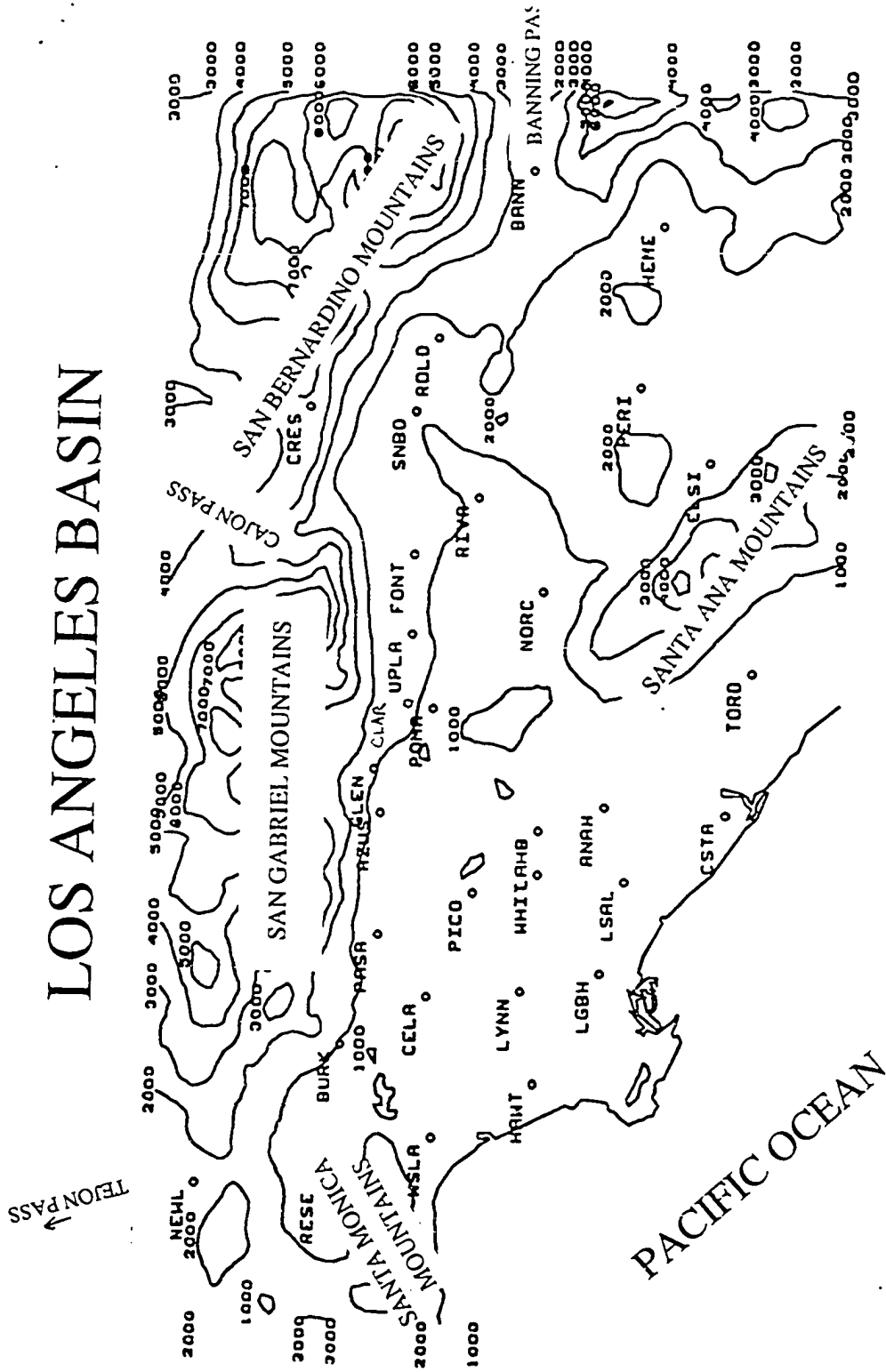
GATOR / MMTD system, Chapter 5 describes the gas-phase chemical solvers developed for GATOR, Chapter 6 discusses aerosol processes in GATOR, Chapter 7 outlines the MMTD and describes the transport processes in GATOR, Chapter 8 describes radiative processes, Chapter 9 discusses data, boundary conditions, initial conditions, and error checks, and Chapter 10 shows and analyzes model results. In addition, Appendix A lists tables describing the model, some of its components, and gas and aqueous phase chemical rate data, while Appendices B - E contain papers detailing the work in Chapters 5 and 6 more thoroughly.

.

15

Chapter 2

Ozone Buildup in the Los Angeles Basin

Los Angeles smog contains numerous constituents, both in the gas and aerosol phases. Among the constituents are ozone, carbon monoxide, oxides of nitrogen, reactive organic gases, and particulate matter. Since levels of ozone exceed federal and state standards more often than do levels of other pollutants, air quality managers focus significantly on methods of decreasing ozone concentrations. In Section 2.1, I discuss characteristics and the spatial distribution of ozone in the Los Angeles Basin. In Section 2.2, the important mechanisms of ozone production, transport, and loss are described. These mechanisms include emissions (2.2.1), meteorology (2.2.2), photochemistry (2.2.3), deposition, and loss of precursors to aerosols (2.2.4).

2.1 Characteristics and Spatial Distribution of Ozone

Ozone is colorless but exhibits an odor at ambient concentrations above about 0.02 ppmv (*e.g.* Turco, 1994). While ozone in the stratosphere protects surface life from harmful UV-B radiation, it is a pollutant in the lower troposphere. Tropospheric ozone directly affects human health in the short term by causing chest pain (observed at concentrations > 0.25 ppmv), sore throat and cough (> 0.30 ppmv), and headache (>

16

0.15 ppmv) (USEPA, 1978). Furthermore, ozone decreases lung function for those who exercise steadily for over an hour in concentrations as low as 0.30 ppmv (*ibid.*). Also, above 1 ppmv (high above ambient concentrations) ozone can temporarily narrow passages deep in the lung, increasing airway resistance and inhibiting the breathing process. Even small decreases in lung function affect those with asthma, chronic bronchitis, and emphysema. Finally, while few studies have examined the effect, ozone may accelerate the aging of lung tissue.

Also, above ambient levels of 0.1 ppmv, ozone affects animals by increasing their susceptibility to bacterial infection (*ibid.*). It also adversely affects the growth of plants, crops, and trees. Finally, ozone reacts with and deteriorates organic materials, such as rubber, textile dyes and fibers, and selected paints and coatings (*ibid.*).

Ozone is a *criteria air pollutant*, thus each state and air quality district must prepare plans to hold its concentration below the federal one-hour standard of 0.12 ppmv. California demands a tougher one-hour standard of 0.09 ppmv. In the Los Angeles Basin, ozone concentrations exceed the federal standard more frequently than in any other region of the United States (SCAQMD-SCAG, 1991). In 1990, the SCAQMD monitored ozone at 33 sites, and concentrations exceeded the California standard at least once at every site and the federal standard at least once at all but two sites. Both the Crestline site, in the San Bernardino Mountains and Glendora, at the base of the San Gabriel Mountains, recorded a national maximum of 103 days of federal ozone standard violations in 1990. Furthermore, Glendora achieved 147 and Crestline achieved 144 state standard violations. Glendora also exceeded the Stage I episode level of 0.20 ppmv 29 times, but no place in the basin exceeded 0.35 ppmv, the level for a Stage II smog alert. Crestline recorded the highest one-hour average in the basin of 0.33 ppmv. Figure 2.1 shows how frequently ozone concentrations exceeded the state standard in 1990 at different locations.

17
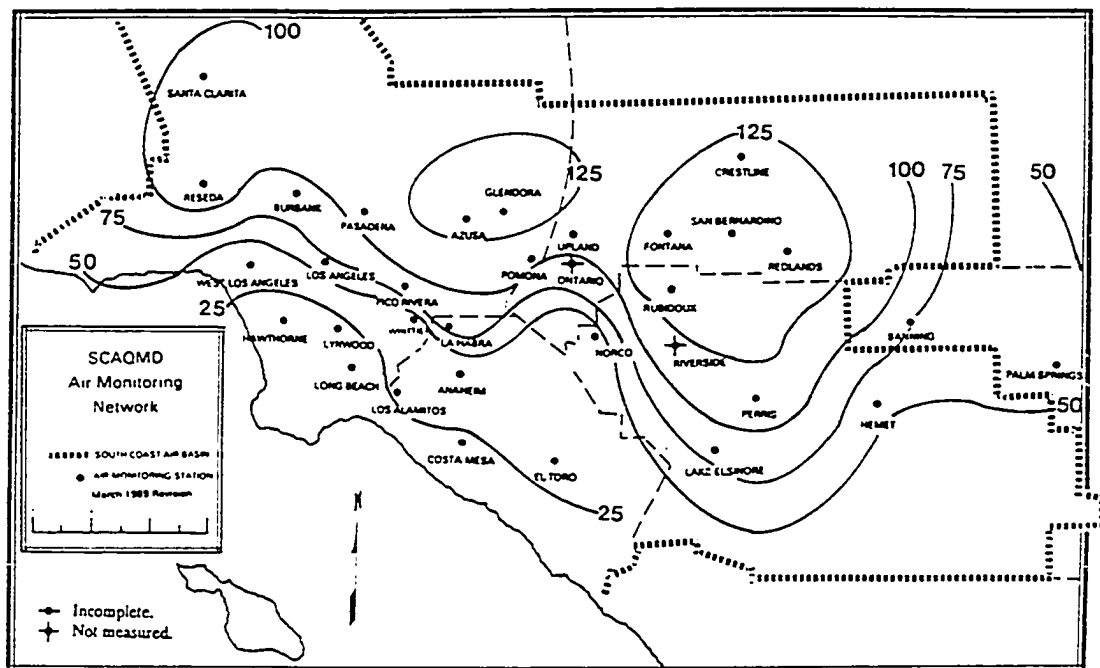
Fig. 2.1. Map showing the number of days in 1990 that the concentration of ozone exceeded the state one-hour standard of 0.09 ppmv at different locations throughout the Los Angeles Basin. Map courtesy of SCAQMD (SCAQMD, 1991).

18

In 1990 ozone concentrations in West Los Angeles exceeded the state standard 30 times, exceeded the federal standard eight times, and achieved a maximum of 0.16 ppmv. In general, coastal regions exceeded standards least frequently and the eastern San Fernando Valley, the San Gabriel Valley, and the Riverside-San Bernardino areas garnered the most violations. Outside of California, the highest number of federal standard violations for ozone was 14, which occurred in Houston, Texas.

In 1975, ozone exceeded the federal standard at least once in the basin during 53% of the days in the year, while in 1990, it exceeded the standard during 42% of the days. Furthermore, between 1979 and 1989, the number of station-hours per year that ozone exceeded the federal standard dropped from 10,561 to 4833 (Cassmassi, 1992). One reason concentrations have improved over the years is that technologies, such as the three-way catalyst for the automobile, have steadily reduced emissions. Furthermore, control strategies by the SCAQMD, the CARB, and the United States Environmental Protection Agency (EPA) have contributed to the decrease. Finally, changes in meteorology may have influenced smog concentrations.

Because ozone levels in the basin continue to routinely exceed federal and state standards, controlling ozone is necessary and required by law. Although difficult, the easiest method of controlling ozone is controlling emissions of its precursors -- reactive organic gases (ROG) and oxides of nitrogen (NO_x). In the past, many have advocated controlling one or the other. However, regulators now try to control both ROG and NO_x emissions. To determine the effect of controlling ROG and NO_x emissions and to predict occurrences of ozone episodes, regulators often use models. Such models need to be accurate because both model forecasts and emissions laws can affect the health and livelihood of many people.

19

2.2 Factors Affecting Ozone Buildup

2.2.1 Emissions of Ozone Precursors

Gas-phase ozone concentrations in Los Angeles depend on emissions of its precursors, and on the other factors mentioned earlier. Data compiled by the SCAQMD (SCAQMD, 1991) from the 1987 SCAQS emissions inventory indicate that stationary and mobile sources emitted about 1200 tons per day (tpd) of NO_x, 1375 tpd of ROG, 4988 tpd CO, and 134 tpd of SO_x into the basin during the study. ROGs and CO emission estimates from on-road hot-exhaust sources may be low by a factor of three (Harley et al., 1993a, Ingalls et al. 1989). Hot-exhaust sources in the inventory accounted for about 17% of total ROG emissions but a much large fraction of CO emissions (Harley et al., 1993a).

Stationary sources are either point or area sources. Point sources are facilities, such as refineries, power plants, and factories, with at least one emissions source. Area sources consist of groups of transient locations where emissions such as architectural coating and household spray emissions, occur. Stationary emissions, primarily from fuel combustion, waste burning, solvent use, petroleum processing, and industrial processing, accounted for about 300 tpd of NO_x (about 25% of total NO_x) and 700 tpd of ROG (about 50% of total ROG) based on the 1987 SCAQS emissions data. Mobile emissions, including from on- and off- road vehicles, accounted for the difference.

Because the population clusters on the west side of the basin, most mobile and stationary source emissions occur on the west side. For example, according to 1987 SCAQS emissions data compiled by the SCAQMD, 85% of all NO_x and 87% of all ROG emissions originated from Los Angeles and Orange counties while the remaining emissions came from Riverside and San Bernardino counties. Furthermore, many of the

20

busiest freeways in the world lie on the western side of the basin, and NO_x (and carbon monoxide) emission patterns tend to follow freeway patterns.

2.2.2 Meteorological Factors

In addition to emissions, the topography, meteorology, and location of the Los Angeles basin affect ozone concentrations. Figure 1.7 shows that, while the Pacific Ocean borders the western edge, the Santa Monica, San Gabriel, San Bernardino, and Santa Ana Mountains either surround or intersect the basin. Also, passes, such as Cajon and Banning in the San Bernardino Mountains and Tejon in the Tehachapi Mountains (not shown in Figure 1.7) provide narrow passageways for flow in and out of the basin.

A major characteristic of Los Angeles meteorology is an almost daily inversion caused by the semi-permanent Pacific high pressure system. As air sinks in the high, it warms adiabatically. Because the warmed air descends upon cooler marine air below, an inversion layer forms. The high pressure inversion is strongest in summer. In winter surface radiation inversions dominate and the mixing height (inversion base height) reaches its lowest level. In the fall and spring, mixing heights are highest since neither high pressure nor radiation inversions are so strong as in their respective peak seasons (Cassmassi, 1992).

During a particular day, the mixing height is lowest (inversion strongest) in the morning and rises as the day progresses. As the land surface heats during a day, layers of air above the surface gradually warm and become more unstable. By late afternoon, the mixing height reaches its maximum. Paradoxically, many secondary pollutants, such as ozone, reach their maximum concentration around mid-afternoon, when the mixing volume is large compared to in the morning. This is because secondary pollutants often take time to form photochemically. In the morning, when the mixing height is low, ozone is relatively scarce because, during the night, it is destroyed in many areas and not

21

produced. As shown later, ozone concentrations peak only after the photolysis rate of nitrogen dioxide (NO_2) peaks, and this occurs after mixing height begins to rise.

The stability of the high pressure inversion that inhibits clouds of vertical development enhances coastal stratus cloud formation. Stratus clouds form when westerly winds advect a warm, moist air mass from far offshore towards cooler coastal waters (Ahrens, 1991). The coastal waters cool the air mass from below to the dew point, creating a fog. As the fog moves inland, slightly warmer surface temperatures dissipate it from below, producing the stratus. If the sea breeze is strong, the stratus can extend to San Bernardino. As solar radiation intensifies during the morning, however, the stratus usually burns off entirely. One effect of the stratus is to reduce solar radiation in the morning, delaying the formation of ozone.

Another feature of the basin is the daily sea-breeze. As a day progresses, the land heats up significantly and pressure over the land decreases relative to that over the ocean. The resulting pressure gradient induces a sea breeze, which strengthens as the temperature gradient increases. The sea breeze transports the primary emissions from western to eastern and northeastern parts of the basin, and also to the San Fernando Valley. As air flows to the different mountain ranges, it either rises and flows over the mountains, rises and returns back towards the sea, or funnels directly through mountain passes. During nighttime, the land cools down faster than the ocean, reversing the pressure gradient, and causing a weak land breeze. Because the land-sea temperature gradient is strongest in the summer and weakest in winter, sea-breezes are strongest in summer (June through mid-August) and weakest in winter (December through March).

Winds tend to follow one of five major transport routes in the Los Angeles Basin (Figure 2.2 -- DeMarrais et al., 1965; Cassmassi, 1992). These include: (1) *typical* sea-breeze flow from Lennox and Long Beach, through Pasadena and Glendora in the San Gabriel Valley, then eastward to Upland, San Bernardino, Crestline, and Redlands; (2)

22

eddy flow from Santa Monica, through central Los Angeles, then northward to Burbank and Reseda in the San Fernando Valley; (3) *south route* sea breeze flow from Los Alamitos to La Habra, then eastward to Riverside, Hemet, and Perris; (4) weak Santa Ana flow from Tejon Pass southward and from Cajon and Banning passes westward, stalling in or to the east of Los Angeles because of opposition by the sea breeze, and (5) strong Santa Ana flow either stalling in West Los Angeles because of opposition by the sea-breeze or continuing to the ocean. Of these, the first route is most common and results in the consistent ozone episodes at Glendora and Crestline.

2.2.3 Photochemical Factors

Because the Los Angeles Basin is further south than most United States cities (about 34° N latitude), it receives more sunlight than most. Furthermore, because the Pacific high suppresses vertical motions of air, clouds other than stratus form infrequently. As a result, Los Angeles receives significant radiation, especially in the summer. The radiation not only draws many people into the region, increasing emissions sources, but also affects the rate of photochemical smog formation.

Ozone in photochemical smog forms when reactive hydrocarbons break down to form radicals that react with nitric oxide (NO), forming nitrogen dioxide (NO_2). The sun subsequently pholoyzes NO_2 to form ground-state atomic oxygen, $O(^3P)$, which combines with molecular oxygen in the presence of a third body to form ozone.

Six major processes break down hydrocarbons in the atmosphere -- photolysis and reaction with each the hydroxyl radical (OH·), the hydroperoxyl radical (HO₂·), ground-state atomic oxygen, the nitrate radical (NO₃·), and ozone, itself (Finlayson-Pitts and Pitts, 1986). The hydroxyl radical and atomic oxygen exist during the daytime only, because they are short-lived and require photolysis for their production. Nitrate radicals, on the other hand, break down significantly during the day because of photolysis; thus,

23
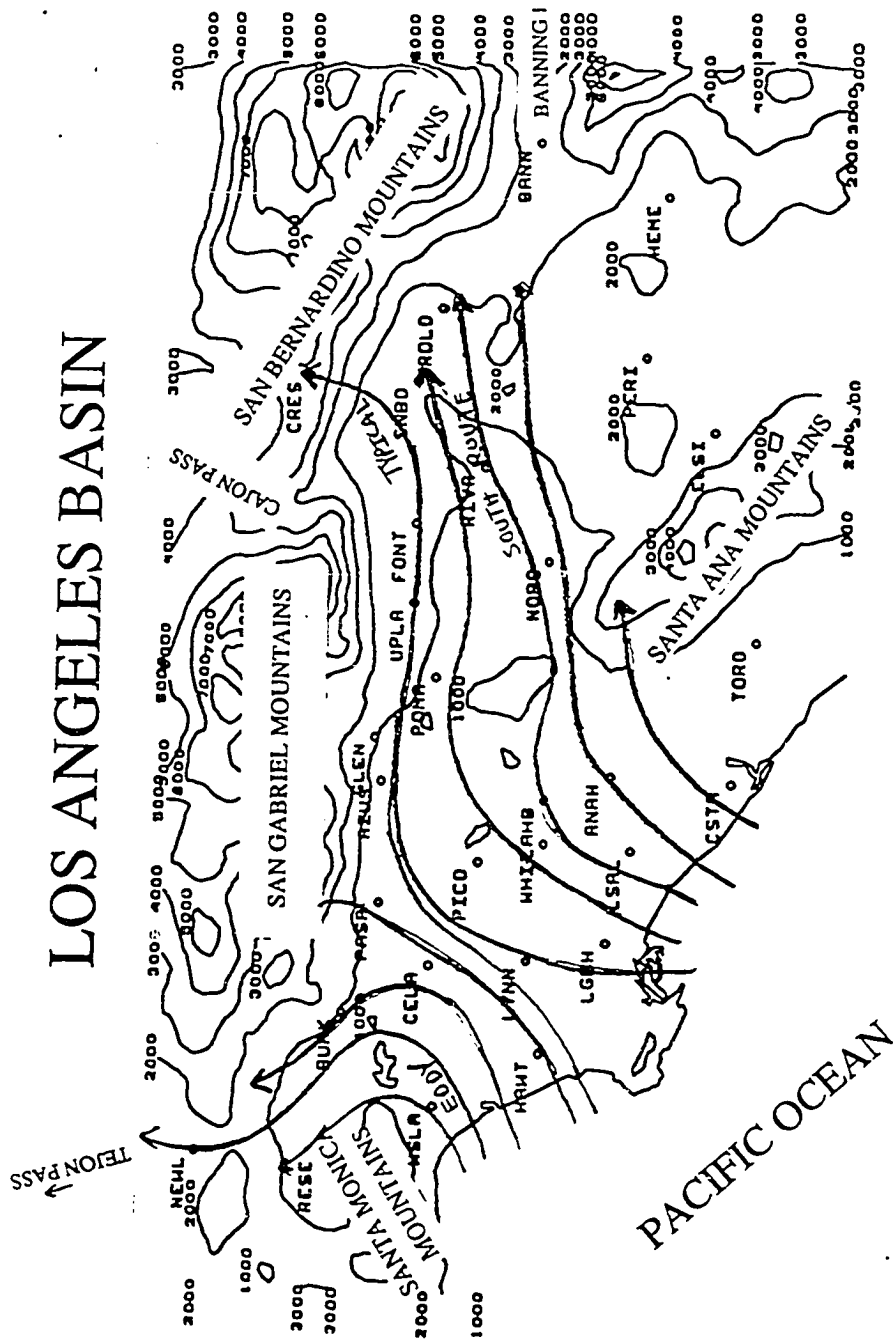
Fig. 2.2. Map demonstrating the "typical," "eddy," and "south route" sea breeze flows in the Los Angeles Basin. Courtesy of J. Cassmassi and the SCAQMD.

24

they are important mostly at night. Finally, ozone and hydroperoxyl radical concentrations can be significant during both day and night. Although hydroperoxyl is produced mainly by photolysis, two nighttime sources include peroxyacetyl nitrate (PAN) decomposition and formyl (HCO·) or alkoxy (RO·) radical reaction with molecular oxygen.

The major hydrocarbon compounds leading to ozone production in polluted air include alkanes, alkenes, alkynes, aldehydes, ketones, aromatics, and, in some locations, terpenes. Of these, photolysis breaks down aldehydes and ketones, the hydroxyl radical reacts with all seven groups during the day, the hydroperoxyl radical reacts mainly with aldehydes, atomic oxygen reacts with alkenes and terpenes during the day, the nitrate radical reacts with alkanes, alkenes, aldehydes, aromatics, and terpenes at night, and ozone breaks down primarily alkenes and terpenes (*ibid.*). Table 2.1 shows the estimated lifetime of hydrocarbons representing the different groups, against breakdown by six processes.

Table 2.1. Estimated lifetime of hydrocarbons representing alkanes, alkenes, alkynes, aldehydes, ketones, aromatics, and terpenes against photodissociation and oxidation by several species. Estimated peak concentrations and lifetimes of most species are from Finlayson-Pitts and Pitts (1986). Isoprene lifetimes were calculated from rates in the Carbon-Bond IV mechanism (Gery *et al.*, 1989) and photolysis lifetimes were calculated from the radiative transfer code described in Section 8.2 for noon of June 21 at 34° N latitude. Units are (m) = minutes, (h) = hours, (d) = days, (y) = years, and (---) = no data or insignificant loss.

Table 2.1

Hydrocarbon	photolysis	OH· 1×10^7	HO$_2$· 2×10^9	O(^3P) 8×10^4	NO$_3$· 1×10^{10}	O$_3$ 5×10^{12}
			Oxidizing species and concentration (No. cm^{-3})			
n-Butane	---	11 h	> 1000 y	18 y	29 d	> 650 y
$trans$-2-Butene	---	26 m	> 4 y	6.3 d	4 m	17 m
Acetylene	---	1.5 d	---	2.5 y	---	> 200 d
Formaldehyde	1.4 h	3.1 h	1.9 h	2.5 y	1.8 d	> 3200 y
Acetone	4.4 d	3.0 d	---	---	---	---
Toluene	---	4.5 h	---	5.6 y	33 d	> 200 d
Isoprene	---	17.4 m	---	7.9 d	5.2 m	4.6 h

Below is an example of how hydroxyl radicals and the sun attack and break down alkanes (RH) and aldehydes (RCHO) to stimulate ozone production. First, the hydroxyl radical abstracts a hydrogen atom from primary emissions of alkanes and aldehydes to produce alkyl (R·) and acyl (RCO·) radicals. The abstraction reactions are

$$RH \quad + OH· \quad ----> R· \quad + H_2O \quad (2.1)$$

and

$$RCHO \quad + OH· \quad ----> RCO· \quad + H_2O. \quad (2.2)$$
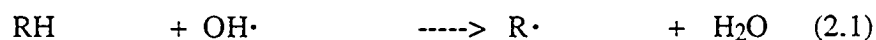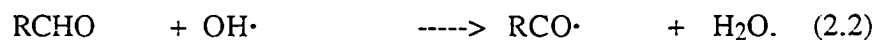
Aldehyde photolysis also produces alkyl (as well as formyl) radicals by

$$RCHO \quad + h\nu \quad ----> R· \quad + HCO·. \quad (2.3)$$

26
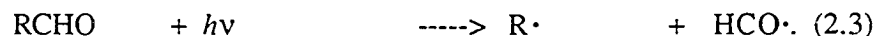
The alkyl and acyl radicals quickly combine with oxygen in the presence of a third body, which carries away the excess energy of the reaction, to form the alkylperoxy ($RO_2\cdot$) and acylperoxy ($RC(O)O_2\cdot$) radicals. These reactions are

$$R\cdot \quad + O_2 \quad \xrightarrow{M} RO_2\cdot \tag{2.4}$$

and

$$RCO\cdot \quad + O_2 \quad \xrightarrow{M} RC(O)O_2\cdot. \tag{2.5}$$
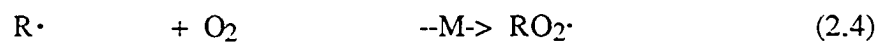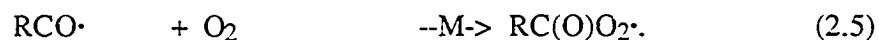
Subsequently, primary emissions of nitric oxide react with the peroxy radicals to form nitrogen dioxide, alkoxy radicals, and acyloxy radicals ($RC(O)O\cdot$) through the reactions

$$NO \quad + RO_2\cdot \quad \longrightarrow NO_2 \quad + RO\cdot \tag{2.6}$$

and

$$NO \quad + RC(O)O_2\cdot \quad \longrightarrow NO_2 \quad + RC(O)O\cdot. \tag{2.7}$$
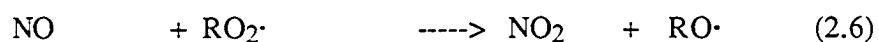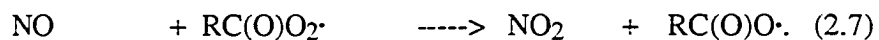
Sunlight then breaks down nitrogen dioxide to ground-state atomic oxygen and nitric oxide through

$$NO_2 \quad + h\nu \quad \longrightarrow NO \quad + O(^3P). \tag{2.8}$$
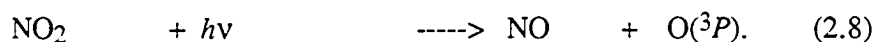
Subsequently, in the only ozone producing reaction, atomic oxygen combines with molecular oxygen in the presence of a third body, by

$$O(^3P) \quad + O_2 \quad \xrightarrow{M} O_3. \tag{2.9}$$

27
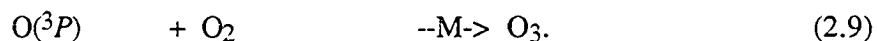
Both recombination with nitric oxide and photolysis slow the accumulation of ozone through the reactions

$$NO \quad + O_3 \quad \dashrightarrow NO_2 \quad + O_2, \quad (2.10)$$

$$O_3 \quad + h\nu \quad \dashrightarrow O_2 \quad + O(^3P), \quad (2.11)$$

and

$$O_3 \quad + h\nu \quad \dashrightarrow O_2 \quad + O(^1D). \quad (2.12)$$
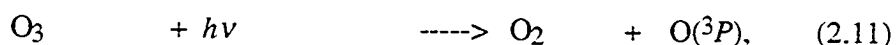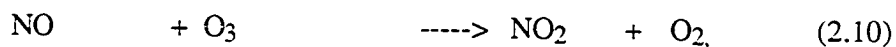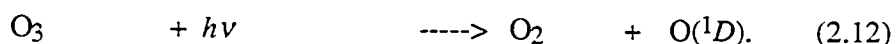
However, nitrogen dioxide from (2.10) and ground-state atomic oxygen from (2.11) reproduce ozone through (2.8) and (2.9). Also, excited atomic oxygen $(O(^1D))$ from (2.12) leads to reproduction of hydroxyl radicals by

$$O(^1D) \quad + H_2O \quad \dashrightarrow 2\ OH\cdot, \quad (2.13)$$
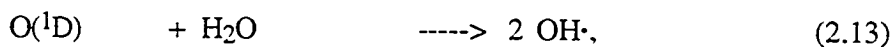
especially in the afternoon when ozone concentrations peak. Furthermore, formyl radicals, produced by aldehyde photolysis in (2.3), create mid-morning hydroperoxyl radicals, hydroxyl radicals, and nitrogen dioxide by

$$HCO\cdot \quad + O_2 \quad \dashrightarrow HO_2\cdot \quad + CO \quad (2.14)$$

and

$$NO \quad + HO_2\cdot \quad \dashrightarrow NO_2 \quad + OH\cdot. \quad (2.15)$$
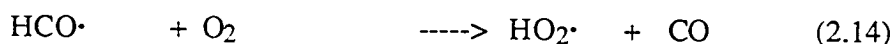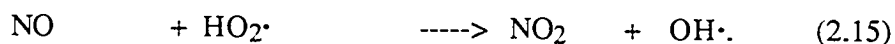
A morning source of the hydroxyl radical is photolysis of nitrous acid, which accumulates due to nighttime surface reactions and morning direct emissions. The photolysis reaction is

28

$$HONO \quad + h\nu \quad \quad ----> OH \quad + NO. \quad (2.16)$$
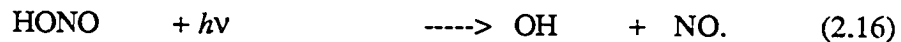
Finally, the processes that produce ozone also produce other oxidants, such as PAN, a potent eye irritant found is smog. PAN forms when nitrogen dioxide reacts with the acetylperoxy radical, which forms when the aldehyde in (2.3) is acetaldehyde. The PAN formation reaction is

$$NO_2 \quad + CH_3C(O)O_2\cdot \quad ----> CH_3C(O)ONO_2. \quad (2.17)$$
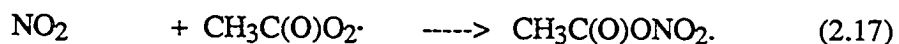
In sum, photochemical ozone production depends heavily on concentrations of NO_x, ROGs, oxidizing radicals, and on the rates of photolysis and reaction of both organic and inorganic gases. Because the Pacific high pressure system prevents the significant formation of clouds past morning, photolysis rates in the Los Angeles basin are high, especially in summer, spurring ozone formation.

The description drawn above is a simplification of a much more complex system of chemical processes occurring in the atmosphere. Table A.4 shows an actual set of reaction used here to simulate smog processes in the Los Angeles area. However, even this set of reactions does not adequately describe the thousands of interactions occurring.

2.2.4 Other Factors

Other factors that influence ozone production and loss include dry deposition and aqueous dissolution. Dry deposition is an important removal process of both gases and aerosols near the surface (*e. g.* Main and Friedlander, 1990). For example, Russell *et al.* (1993) estimated that dry deposition removes more than 50% of NO_x emitted in the Los Angeles Basin each day. The removed nitrogen is in the form of NO, NO_2, PAN,

HNO₃, NH₃, and NH₄NO₃. Dry deposition also removes ozone, itself. For example McRae and Russell (1984) estimated a deposition velocity of ozone over soil and short grass of 0.1 - 2.1 cm s^{-1} and Sehmel (1980) compiled values over several surfaces of between 0.002 and 2.0 cm s^{-1}. However, the velocity over urban areas has not been studied significantly (Russell *et al.*, 1993).

While dry deposition is important for gases near the surface, direct loss of gas-phase ozone, nitric oxide, and nitrogen dioxide to aerosols and fog, is small. In Table 2.2 the fractions of several species partitioned between the gas- and aerosol phases are estimated, for when the air contains aerosols, a fog, or clouds.

While the results shown in Table 2.2 do not include the effects of aqueous chemistry, activity coefficients, meteorology, or the significant variations in *pH* or particle distributions, they give basic insight into the removal of gases to the aqueous phase. In sum, the only gases removed significantly by aerosols are ammonia (NH₃), nitric acid (HNO₃), hydrochloric acid (HCl), and sulfuric acid (not shown since its Henry's constant is too large to be measured accurately). In addition to the four species

Table 2.2. Estimated molar fraction ($f_M = H_{eff} \times R \times T \times LWC$ -- moles of a species partitioned in the aqueous phase per mole partitioned in the gas phase) at $T = 298$ K when the liquid water content of air (LWC -- L - H₂O L^{-1} - air) is 5 x 10^{-11} for aerosols, 1 x 10^{-7} for the fog, or 5 x 10^{-7} for clouds. H is the Henry's law coefficient while K_1 and K_2 are the first and second (if applicable) dissociation constants, respectively, of each species. The overall Henry's coefficient of each species, H_{eff}, is defined in the notes, below, and activity coefficients are ignored. For simplicity, a pH = 4.3 was assumed for aerosols, fogs, and clouds although aerosols are usually much more acidic. Also, R = 0.08206 L atm mole^{-1} K^{-1}.

Table 2.2

Species	H (M atm^{-1})	K_1 (M)	K_2 (M^2)	H_{eff} (M atm^{-1})	f_M Aerosol	Fog	Cloud
O$_3$[a]	1.13×10^{-2}	—	—	1.13×10^{-2}	1.4×10^{-11}	2.8×10^{-8}	1.4×10^{-7}
NO[b]	1.90×10^{-3}	—	—	1.90×10^{-3}	2.3×10^{-12}	4.6×10^{-9}	2.3×10^{-8}
NO$_2$[c]	1.00×10^{-2}	—	—	1.00×10^{-2}	1.2×10^{-11}	2.4×10^{-8}	1.2×10^{-7}
OH[d]	2.50×10^{1}	—	—	2.50×10^{1}	3.1×10^{-8}	6.2×10^{-5}	3.1×10^{-4}
HO$_2$[d]	2.00×10^{3}	3.50×10^{-5}	—	3.40×10^{3}	4.2×10^{-6}	8.4×10^{-3}	4.2×10^{-2}
H$_2$O$_2$[e]	7.45×10^{4}	2.20×10^{-12}		7.45×10^{4}	9.1×10^{-5}	1.8×10^{-1}	9.1×10^{-1}
SO$_2$[f]	1.23×10^{0}	1.23×10^{-2}	6.61×10^{-8}	3.04×10^{2}	3.7×10^{-7}	7.4×10^{-4}	3.7×10^{-3}
NH$_3$[g]	5.76×10^{1}	1.81×10^{-5}	—	5.23×10^{6}	6.4×10^{-3}	1.3×10^{1}	6.4×10^{1}
HCl[h]	1.15×10^{0}	1.72×10^{6}	—	3.95×10^{10}	4.8×10^{1}	9.6×10^{4}	4.8×10^{5}
HONO[i]	4.90×10^{1}	5.10×10^{-4}		5.48×10^{2}	6.7×10^{-7}	1.3×10^{-3}	6.7×10^{-3}
HNO$_3$[j]	2.10×10^{5}	1.96×10^{1}	—	6.45×10^{10}	7.9×10^{1}	1.6×10^{5}	7.9×10^{5}
HO$_2$NO$_2$[k]	2.0×10^{4}			2.0×10^{4}	2.4×10^{-5}	4.8×10^{-2}	2.4×10^{-1}
CO$_2$[f]	3.39×10^{-2}	4.46×10^{-7}	4.68×10^{-11}	3.42×10^{-2}	4.2×10^{-11}	8.3×10^{-8}	4.2×10^{-7}
CH$_2$O[l]	3.46×10^{0}	6.30×10^{3}	—	2.18×10^{4}	2.7×10^{-5}	5.4×10^{-2}	2.7×10^{-1}
CH$_3$O$_2$[d]	6.00×10^{0}	—	—	6.00×10^{0}	7.3×10^{-9}	1.5×10^{-5}	7.3×10^{-5}
CH$_3$OH[m]	2.20×10^{2}			2.20×10^{2}	2.7×10^{-7}	5.4×10^{-4}	2.7×10^{-3}
HCOOH[n]	3.50×10^{3}	1.78×10^{-4}	—	1.59×10^{4}	1.9×10^{-5}	3.9×10^{-2}	1.9×10^{-1}
CH$_3$OOH[o]	2.27×10^{2}			2.27×10^{2}	2.8×10^{-7}	5.6×10^{-4}	2.8×10^{-3}
CH$_3$COOH[p]	8.80×10^{3}	1.70×10^{-5}		1.18×10^{4}	1.4×10^{-5}	2.9×10^{-2}	1.4×10^{-1}
CH$_3$C(O)OOH[o]	4.73×10^{2}			4.73×10^{2}	5.8×10^{-7}	1.2×10^{-3}	5.8×10^{-3}
PAN[q]	2.90×10^{0}	—	—	2.90×10^{0}	3.5×10^{-9}	7.1×10^{-6}	3.5×10^{-5}
CH$_3$CHO[r]	1.50×10^{1}			1.50×10^{1}	1.8×10^{-8}	3.7×10^{-5}	1.8×10^{-4}
CH$_3$COCHO[s]	3.70×10^{3}			3.70×10^{3}	4.5×10^{-6}	9.0×10^{-3}	4.5×10^{-2}
CH$_3$COCH$_3$[r]	3.00×10^{1}			3.00×10^{1}	3.7×10^{-8}	7.3×10^{-5}	3.7×10^{-4}
TOL[r]	1.51×10^{-1}			1.51×10^{-1}	1.8×10^{-10}	3.7×10^{-7}	1.8×10^{-6}
XYL[r]	1.74×10^{-1}			1.74×10^{-1}	2.1×10^{-10}	4.3×10^{-7}	2.1×10^{-6}

31

References for Henry's and dissociation coefficients and the form of H_{eff} for each species.

[a]   Kozac-Channing and Heltz (1983). $H_{eff} = H$.

[b]   Schwartz and White (1981). $H_{eff} = H$.

[c]   Schwartz (1984). $H_{eff} = H$.

[d]   Jacob (1986). $H_{eff} = H$.

[e]   Lind and Kok (1986). $H_{eff} = H \, (\, 1 + K_1 / [H^+] \,)$.

[f]   Smith and Martell (1976). $H_{eff} = H \, (\, 1 + K_1 / [H^+] + K_1 K_2 / [H^+]^2 \,)$.

[g]   Kim et al. (1993). $H_{eff} = H \, (\, 1 + K_1 [H^+] / K_w \,)$ since $NH_3(g)$ converts to $NH_4OH(l)$ and NH_4^+ in the aqueous phase.

[h]   Marsh and McElroy (1985); Kim et al. (1993). $H_{eff} = H \, (\, 1 + K_1 / [H^+] \,)$.

[i]   Schwartz and White (1981). $H_{eff} = H \, (\, 1 + K_1 / [H^+] \,)$.

[j]   Schwartz (1984). $H_{eff} = H \, (\, 1 + K_1 / [H^+] \,)$.

[k]   Park and Lee (1987). $H_{eff} = H$.

[l]   Ledbury and Blair (1925); Le Henaff (1968). $CH_2O(l)$ exists primarily as $H_2C(OH)_2$, where $CH_2O(l) + H_2O \Longleftrightarrow H_2C(OH)_2$. Thus, $H_{eff} = H \, (\, 1 + K_1 \,)$.

[m]   Snider and Dawson (1985). $H_{eff} = H$.

[n]   Latimer (1952); Martell and Smith (1977). $H_{eff} = H \, (\, 1 + K_1 / [H^+] \,)$.

[o]   Lind and Kok (1986). $H_{eff} = H$.

[p]   Weast (1986); Martell and Smith (1977). $H_{eff} = H \, (\, 1 + K_1 / [H^+] \,)$.

[q]   Lee (1984). $H_{eff} = H$.

[r]   Calvert (1984). $H_{eff} = H$.

[s]   Betterton and Hoffman (1988). $H_{eff} = H$.

removed by aerosols, fogs remove a fair fraction of hydrogen peroxide (H_2O_2), peroxynitric acid (HO_2NO_2), hydroperoxy radical (HO_2), formaldehyde (CH_2O), formic acid ($HCOOH$), and acetic acid (CH_3COOH). Clouds remove some methylglyoxal (CH_3COCHO) as well as the species removed by aerosols and fogs. Further, if the effects of aqueous chemistry are included, then SO_2, OH, HO_2, H_2O_2 and other species will be removed much faster than the table indicates. Finally, while f_M for carbon dioxide is low, the gas-phase concentration of CO_2 is high enough to force a modest amount of CO_2 into the aqueous phase.

An interesting result from Table 2.2 is that neither aerosols, fogs, nor clouds remove much ozone, nitric oxide, nitrogen dioxide, PAN, toluene, or xylene. However, oxidation products of toluene and xylene form nitro-cresol, which has a sufficiently low vapor pressure to condense onto aerosols. In addition, cyclopentene and cyclohexene,

32

photo-oxidize to produce glutaric acid and adipic acid, respectively, which also readily condense (Pilinis and Seinfeld, 1988) Further, toluene, xylene, alkylbenzenes, biogenic hydrocarbons, alkanes and alkenes oxidize to form additional condensable products (Pandis *et al.*, 1992).

Thus, aerosols, clouds, and fog remove some organic ozone precursors from the gas phase. However, if a fog evaporates, dissolved species return to the gas phase unless they dry or wet deposit to the ground or react chemically within the aerosol. While aerosol removal of ozone precursors may be important, another effect aerosols, fogs, and clouds have on ozone concentration is to decrease optical depth. The lower the optical depth in the atmosphere, the less the solar intensity and the slower the rate of ozone production.

In sum, emissions, meteorology, topography, location, chemistry, aerosols, and fog affect the mixing ratio of ozone in the Los Angeles Basin. Next, I discuss factors affecting aerosol buildup and visibility degradation.

Chapter 3

Particle Buildup and Visibility Degradation

Corresponding to gas-phase pollution buildup in the Los Angeles basin is aerosol production. Studying particles is important because those between 0.1 and 1.0 μm diameter penetrate to the deepest parts of human lungs and all particles serve as sites in or on which chemical reactions take place. Further, particles impede visibility, especially when the relative humidity is high. Major particle components are water, elemental carbon, organic carbon, sulfate, nitrate, ammonium, sodium, chloride, dust, metals, and more. In this chapter, I discuss the characteristics and sources of particles in the Los Angeles Basin (Section 3.1), focusing on ambient concentrations (3.1.1), primary emissions (3.1.2), and secondary production (3.1.3). Finally, visibility degradation is discussed in Section 3.2.

34

3.1 Characteristics and Sources of Particles

3.1.1 Locations of Particle Buildup

Particle concentrations in the Los Angeles Basin typically exceed state and federal standards. The California standard for suspended PM_{10} (particulate matter smaller than 10 μm in diameter) is a 24-hour average of 50 μg m^{-3} or an annual geometric mean of 30 μg m^{-3}. The federal standard, on the other hand, is a 24-hour average of 150 μg m^{-3} or an annual arithmetic mean of 50 μg m^{-3}. In 1990, each of the 18 SCAQMD stations that monitored PM_{10} registered at least one state standard exceedence (SCAQMD, 1991). Figure 3.1 shows a map indicating where particulate matter in the basin accumulated in 1991. The figure indicates that concentrations tended to build up in Rubidoux. In fact, in 1990, Rubidoux reported an annual geometric mean of 67 μg m^{-3} (*ibid.*) Other locations, such as Indio and Fontana, reported the highest 24-hour average PM_{10} concentrations of 520 and 475 μg m^{-3}, respectively. These values, however, resulted from high winds kicking up soil and dust (*ibid.*)

Particles in the Los Angeles Basin contain a combination of inorganic and organic compounds. For example, Schuetzle *et al.* (1975) reported sulfates, nitrates, chloride, sodium, iron, lead, zinc, bromine, and several organic species present in aerosols. Russell and Cass (1984) also reported that the major ionic constituents of aerosols in the Los Angeles Basin were nitrate, sulfate, ammonium, sodium, calcium magnesium, potassium, chloride, and probably carbonate. Further, Lyons *et al.* (1993) measured iron, lead, manganese, zinc copper, and nickel and Venkataraman *et al.* (1994a,b) measured elemental carbon and several polycyclic aromatic hydrocarbons in ambient particles.

35
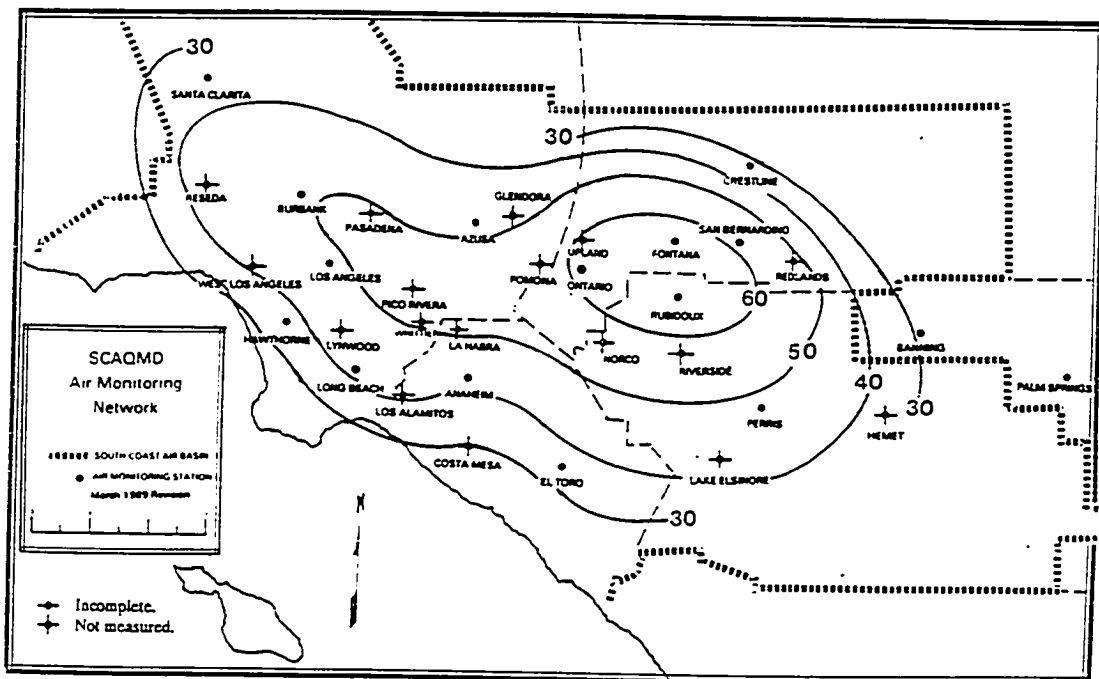
Fig. 3.1. Map showing the annual geometric mean concentration (μg m^{-3}) of PM$_{10}$ at different locations in the Los Angeles Basin. The state standard to compare against is 30 μg m^{-3}. Map courtesy of SCAQMD (SCAQMD, 1991).

36

In addition, particles contain numerous other components. For example, as discussed in Section 2.2.4, the gases that most likely dissolve into water-containing aerosols, fogs, and / or clouds are NH_3, HNO_3, HCl, H_2SO_4, SO_2, OH, H_2O_2, HO_2, HO_2NO_2, CH_2O, $HCOOH$, CH_3COOH, CH_3COCHO, and CO_2, and the major condensing organic species are byproducts of toluene, xylene, alkylbenzene, alkane, alkene, and biogenic hydrocarbon oxidation. Thus, these are the most likely secondary components present in aerosols.

Particle distributions in the atmosphere can often be described with a trimodal distribution consisting of a nucleation, accumulation, and coarse particle mode (Whitby, 1978). The *nucleation mode* (mean diameter $(D_p) < 0.1$ μm) usually contains either homogeneously or heterogeneously nucleated particles. Typically, hot vapors from combustion nucleate quickly. If small particles are present already, heterogeneous nucleation will be favored over homogeneous nucleation (Section 6.2). Once particles nucleate, they grow by condensation and dissolution. Further, particles coagulate to larger sizes. Secondary growth and coagulation move particles into the *accumulation mode*, where diameters are typically between 0.1 - 2 μm. Such particles are often lost by rainout and washout, but are generally too light to sediment out significantly. Particles in the nuclei and accumulation modes, together, are known as *fine particles*.

The coarse mode consists of particles larger than about 2 μm diameter. These particles originate from wind blown dust, sea spray, volcanos, plant particle emissions, and other sources (Whitby, 1978). Further, they are generally heavy enough to sediment out. In sum, the emissions sources and deposition sinks of fine particles are generally different from those of coarse particles. In fact fine particles usually do not grow by condensation much larger than 1 μm (*ibid.*), indicating that coarse mode particles originate primarily from emissions.

37

The size distributions of several individual components in atmospheric aerosols have been measured. For example, Hering and Friedlander (1982) observed that the mass median diameter of particles containing sulfate was about 0.20 μm on dry days (relative humidity 17 - 68%) and 0.54 μm on moist days (r. h. 26 - 100%). Also, Noll *et al.* (1990) found that the average mass median diameter of coarse-mode particles containing sulfate was about 12.3 μm and those containing nitrate was about 8.1 μm. Further, the relative mass of sulfate in the coarse mode was about five times smaller than the mass of nitrate. Further, Mylonas *et al.* (1991) found that the distribution of organonitrates in ambient aerosols was typically bimodal. In one set of measurements, they found particles in the two size ranges of 0.05 - 0.075 μm and 0.12 - 0.26 μm, and in the second set of measurements they found particles in the two ranges of 0.075 - 0.12 μm and 0.5 - 1.0 μm in size.

Similarly, Lyons *et al.* (1993) observed uni-, bi-, and trimodal distributions for trace metals in the basin. For example, iron distributions were unimodal (2 - 4 μm), lead distributions were trimodal (< 0.1 μm, 0.5 - 1.0 μm, and 2 - 4 μm), manganese distributions were trimodal, zinc, copper, and nickel distributions varied. Finally, Venkataraman and Friedlander (1994b) found that ambient PAH and elemental carbon size distributions were bimodal, with sizes of 0.05 - 0.12 μm and 0.5 - 1.0 μm, in the two modes, respectively.

In the cases above, the bimodal fine-particle distributions can be explained. For example, the smaller mode usually results from newly emitted combustion particles and the larger mode results from secondary particle growth onto older emissions (*e.g.* Venkataraman and Friedlander, 1994b). Also, when the relative humidity is high, all modes generally shift to larger sizes because water condenses significantly onto electrolyte-containing particles. Further, in the case of sulfur, particle growth occurs most probably by dissolution and subsequent liquid-phase oxidation of SO_2 rather than by gas-

phase oxidation of SO_2 and condensation of sulfuric acid (Hering and Friedlander, 1982). In addition, the presence of metals in coarse particles appears to result primarily from emissions of soil dust (Lyons et al., 1993).

Finally, sodium and chloride appear mostly in large sea-spray particles. For example, Kritz and Rancher (1980) measured the size distribution of particles containing NaCl, over the ocean, and the geometric mean volume diameter of the distribution of these particles was about 6.9 μm. However, HNO_3 tends to dissolve in coarse-mode particles, displacing HCl to the gas-phase. Aqueous HNO_3 buildup is slightly favored over aqueous HCl buildup because hydrochloric acid is more volatile than nitric acid (e.g. Table 2.2). Thus, during competition for available cations, NO_3^- will force Cl^- to aqueous HCl and then to the gas phase.

Similarly, in a competition between aqueous sulfuric and nitric acids, sulfuric acid pressures nitric acid into the gas phase because HNO_3 is more volatile than H_2SO_4. Thus, because H_2SO_4 forms within or condenses upon accumulation-mode particles more readily than it does upon coarse-mode particles, sulfuric acid forces nitric acid away from the accumulation mode and towards the coarse mode. Sulfuric acid favors the accumulation mode since this mode usually contains more surface area (Table 3.1) and more liquid water than do other modes. Sulfuric acid accumulates in such particles by directly condensing on their surfaces or forming from aqueous oxidation of sulfur dioxide in the bulk liquid.

Table 3.1. Average continental particle number, surface area, and volume in each of three size modes. Also shown are the geometric standard deviation (σ_g) and the geometric number ($\overline{D}_N$), surface area ($\overline{D}_S$), and volume ($\overline{D}_V$) diameters of each mode. Section 9.2 defines some of the parameters in more detail. Data from Whitby (1978).

39

Table 3.1

| | <------------------------- Mode -------------------------> | | |
Parameter	Nuclei	Accumulation	Coarse Particle
σ_g	1.7	2.03	2.15
Number (No. cm^{-3})	7.7 x 10^4	1.3 x 10^4	4.2
$\overline{D}_N$ (μm)	0.013	0.069	0.97
Surface (μm^2 cm^{-3})	74	535	41
$\overline{D}_S$ (μm)	0.023	0.19	3.1
Volume (μm^3 cm^{-3})	0.33	22	29
$\overline{D}_V$ (μm)	0.031	0.31	5.7

A lesser reason nitric acid grows more readily on coarse- over accumulation-mode particles is because of the Kelvin effect, which increases the equilibrium vapor pressure over smaller particles. Since nitric acid is somewhat volatile, the Kelvin effect reduces the difference between the partial and equilibrium vapor pressures of nitric acid over small drops. However, since sulfuric acid is involatile (its equilibrium vapor pressure is low), the Kelvin effect has negligible influence on the difference between the partial and equilibrium vapor pressures of sulfuric acid over small drops. Thus, sulfuric acid can grow on particles of almost any size but nitric acid tends to grow on particles of relatively little curvature. Next, I expand upon the processes that influence aerosol concentration and composition -- emissions and gas-to-particle conversion.

3.1.2 Primary Emissions

The California Air Resources Board has compiled an extensive aerosol emissions inventory. Among the data are emissions of particulate matter in four size regimes: < 1

40

μm, 1 - 2.5 μm, 2.5 - 10 μm, and > 10 μm diameter. Table 3.2 shows the magnitude of such emissions for different species.

Table 3.2. Emissions of different aerosol components (kg day^{-1}) as a function of aerosols size. The 'all sizes' column is a sum over the four size regimes to the left of it. Aerosol data were summed from tapes, provided by Allen and Wagner (1993). The component 'other' identifies oxygen, nitrogen, hydrogen, water and additional components not included in the aerosol analysis (P. Allen, *pers. comm.*). Thus, for example, the oxygen atoms in oxides of silicon, aluminum, and iron are included as 'other'.

Table 3.2

Substance	< 1 μm	1-2.5 μm	2.5-10 μm	> 10 μm	all sizes	Total %
	<----------------------------Particle Size--------------------------->					
other	147,884	86,431	380,221	712,049	1,326,585	53.167
silicon	37,312	37,086	183,641	166,527	424,566	17.015
organic carbon	28,462	9,363	69,967	58,111	165,903	6.649
aluminum	14,550	14,644	67,991	58,216	155,401	6.228
iron	7090	7,189	37,210	38,947	90,436	3.624
calcium	5,587	5,511	32,619	34,028	77,745	3.116
sulfates	45,922	894	3,998	3,122	53,936	2.162
potassium	7,364	3,586	16,266	18,989	46,205	1.852
elemen. carbon	28,467	1,095	7,247	7,429	44,238	1.773
unknown	9,919	6,745	11,110	11,903	39,677	1.590
chloride	11,318	814	4,535	4,796	21,463	0.860
titanium	1,048	877	4,241	4,716	10,882	0.436
sulfur	618	573	3,216	2,129	6,536	0.262
carbonate ion	306	162	2,514	1,879	4,861	0.195
sodium	569	233	2080	1916	4,798	0.192
manganese	899	521	1,511	1,824	4,755	0.191
phosphorous	130	286	1,660	1,148	3,224	0.129
nitrates	1,237	147	935	782	3,101	0.124
zinc	226	154	729	674	1,783	0.071
lead	173	156	758	653	1,740	0.070
barium	79	88	544	856	1,567	0.063
ammonium	841	51	120	136	1,148	0.046
strontium	25	42	308	364	739	0.030
vanadium	94	66	274	280	714	0.029
copper	132	60	203	208	603	0.024

41

cobalt	127	52	158	212	549	0.022
nickel	130	48	132	158	468	0.019
chromium	87	26	158	176	447	0.018
rubidium	11	12	91	100	214	0.009
zirconium	6	10	80	110	206	0.008
lanthanum	26	7	52	65	150	0.006
bromine	68	5	30	24	127	0.005
arsenic	26	3	10	19	58	0.002
cadmium	9	2	23	16	50	0.002
antimony	5	3	15	23	46	0.002
yttrium	2	3	17	22	44	0.002
tin	6	7	15	14	42	0.002
indium	5	1	11	12	29	0.001
mercury	2	1	11	13	27	0.001
molybdenum	3	1	7	9	20	<0.001
silver	5	2	6	6	19	<0.001
palladium	3	1	5	10	19	<0.001
selenium	3	0	1	2	6	<0.001
gallium	0	0	5	0	5	<0.001
totals	350,776	176,958	834,725	1,132,673	2,495,132	100.00
% of total	14.06	7.09	33.45	45.40	100.00	

Table 3.2 shows that particulate emissions of sub 10-micron particles were about 1,362 tons per day (tpd) and that emissions of all-sized particles were about 2,495 tpd. Similar data prepared by the SCAQMD (SCAQMD, 1991) indicate that about 51% of PM_{10} emissions originated in Los Angeles County, 18% originated in Riverside County, 17% originated in Orange County, and 14% originated in San Bernardino County. Further, about 91% of such emissions originated from area sources, 5% originated from on-road mobile source, 3% came from point sources, and 2% came from other mobile sources (ibid.) Some of the largest individual sources of PM_{10} were paved (32%) and unpaved (29.7%) road dust, and construction and demolition emissions (23.5%). Automobiles, industrial processes, and livestock sources accounted for much of the rest.

Another important emission component in the Los Angeles Basin is sodium chloride from sea spray. While Table 3.2 shows that sodium and chloride have anthropogenic sources, the table does not include natural sources. Sea spray forms when

42

winds and waves force air bubbles to burst at the sea surface (Woodcock, 1953). The chloride to sodium ratio of these new particles is typically the same as that of sea water, which is about 1.8 (Duce and Hoffman, 1976; Hitchcock *et al.*, 1980). However, this ratio decreases to about 1.0 - 1.7 in marine aerosols because HCl is removed by dehydration or acidification (Eriksson, 1960; Duce, 1969; Martens *et al.*, 1973; Heisler *et al.*, 1973; Hitchcock *et al.*, 1980; Kritz and Rancher, 1980; Russell and Cass, 1984; Pilinis and Seinfeld, 1987). In fact, Hitchcock *et al.* (1980) observed that some marine aerosols that react with strong acids, such as nitric and sulfuric acid, lose up to 100% of their chloride. Kritz and Rancher (1980) estimated that steady-state sodium emissions from the ocean are about 1330 μg m^{-2} day^{-1}. The associated chloride emissions in the spray is about 1.8 times as large. However, this emissions rate assumed a constant boundary layer height of 1 km and no advection sources of sodium chloride. Thus, depending on meteorological conditions, this rate may be a factor of 10 to 20 too large.

Although most particle emissions emanate from Los Angeles County or from the ocean, the highest concentrations appear in Riverside and San Bernardino Counties (Figure 3.1). This occurs because the sea breeze blows particles towards the east and northeast and because secondary particulate matter accumulates onto primary emissions as the emissions travel.

3.1.3 Gas-to-Particle Conversion

While emissions inject significant aerosol mass into the atmosphere, that mass increases as a result of gas-to-particle conversion. The major gas-to-particle conversion processes in polluted air are condensational and dissolutional growth. Homogeneous nucleation is not a significant process since so many particles are available to compete for the available gas (Pilinis *et al.*, 1987), and the free energy required for heterogeneous nucleation is much less than that required for homogeneous nucleation. Growth, on the

43

other hand, readily occurs in two important cases: (1) when heterogeneous nucleation has occurred and the saturation vapor pressure is less than the partial pressure of the condensing gas and (2) when the equilibrium vapor pressure over a water-containing aerosol is less than the partial pressure of the gas.

Typically, Los Angeles aerosols contain a significant amount of water. Water will condense onto aerosols whenever its partial pressure exceeds its saturation vapor pressure. For large particles containing no solute, this occurs when the relative humidity exceeds 100%. However, the curvature of and the presence of electrolytes in particles affect the saturation vapor pressure. For example, small particles have a greater curvature than big particles, increasing the saturation vapor pressure over them (Kelvin effect). Also, electrolytes within particles attract liquid water molecules, decreasing the saturation vapor pressure over such particles.

Thus, even when the relative humidity is less than 100% and electrolytes are present, particles often contain water. Common inorganic electrolytes in Los Angeles aerosols are ammonium nitrate [NH_4NO_3], ammonium sulfate [$(NH_4)_2SO_4$], ammonium chloride [NH_4Cl], sodium nitrate [$NaNO_3$], sodium sulfate [Na_2SO_4], sodium chloride [$NaCl$], nitric acid [HNO_3], sulfuric acid [H_2SO_4], and hydrochloric acid [HCl]. Some of these species can exist as solids in equilibrium with the gas phase, without attracting water. For example, all the ammonium and sodium salts listed above have a deliquescence relative humidity (DRH) between 40 and 93% at 298 K (Pilinis and Seinfeld, 1988). However, the hydrogen salts (HNO_3, HCl, and H_2SO_4) attract water down to 0% relative humidity.

The DRH is defined as the humidity, above which, the species cannot exist as a solid, but below which, the species may or may not exist as a solid, depending on other conditions. Thus, for example, ammonium nitrate may exist as a solid, without attracting water, when the relative humidity is less than ammonium nitrate's DRH (62% at 298 K).

44

Sulfuric acid, on the other hand, attracts water and remains liquid regardless of the humidity. Even at 1% relative humidity, water will always associate with sulfuric acid.

Thus, below 100% humidity and above the lowest DRH of those electrolytes present, aerosols typically swell. In Los Angeles, several of these electrolytes originate from gas-phase sources, such as ammonia, nitric acid, and sulfur dioxide. For example, Russell and Cass (1986) estimated that livestock emitted about 84.8 tons per day (tpd) (51.6%), domestic sources emitted about 23.3 tpd (14.2%), soils emitted about 23.8 tpd (14.5%), and other sources emitted about 32.4 tpd (19.7%) of ammonia gas in August, 1982. Conversely, hydroxyl radical scavenging of nitrogen dioxide produces nitric acid gas. Also, power plants and other anthropogenic sources emit over 130 tons per day of $SO_2(g)$ and $SO_3(g)$ into the basin.

The gas-phase aerosol precursors listed above convert to the particulate phase through various mechanisms. For example, $SO_2(g)$ oxidizes to form $H_2SO_4(g)$ by

$$SO_2(g) \quad + \; OH(g) \qquad \text{--M->} \; HSO_3(g) \qquad\qquad (3.1)$$

$$HSO_3(g) \quad + \; O_2(g) \qquad \text{----->} \; SO_3(g) \; + \; HO_2(g) \quad (3.2)$$

$$SO_3(g) \quad + \; H_2O(g) \qquad \text{----->} \; H_2SO_4(g). \qquad\qquad (3.3)$$
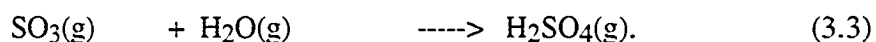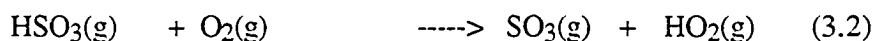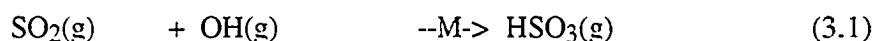
Since sulfuric acid has a low equilibrium vapor pressure, it easily condenses to the aerosol phase, attracting water as it condenses. Similarly, $HNO_3(g)$ dissolves in water and has a sufficiently low vapor pressure to deposit and attract water when water is scarce (although its equilibrium vapor pressure is higher than that of sulfuric acid).

Gas-phase ammonia, on the other hand, has a much higher equilibrium vapor pressure than does sulfuric acid. However, Table 2.2 shows that it has a fairly high Henry's constant, enabling it to dissolve readily if aerosols initially contain water. Alternatively, if aerosols are initially dry, then ammonia can react with nitric acid or

45

hydrochloric acid in one of three ways to form a solid. One possibility is if $NH_3(g)$ reacts with $HNO_3(g)$ to form $NH_4NO_3(g)$, which then deposits on a nucleated particle as $NH_4NO_3(s)$. A second possibility is if $NH_3(g)$ hits and sticks to a vacant crystal site on an existing particle. Then, $HNO_3(g)$ can react directly with the incorporated ammonia to form a solid. A third possibility is if both $NH_3(g)$ and $HNO_3(g)$ adsorb to a surface then react while adjacent to each other (Harrison and MacKenzie, 1990). While the correct mechanism has not been fully determined, the first is probably not dominant under atmospheric conditions (Wexler and Seinfeld, 1990).

Finally, in the case of sea spray, sodium chloride dissociates significantly, allowing the chloride to equilibrate with gas-phase hydrochloric acid. HCl has a high effective Henry's constant (Table 2.2); thus, in the absence of additional acids, most of it stays in the aqueous phase. However, if the gas-phase partial pressure of HCl is low or other acids are present, then aqueous-phase chloride forces its way to the gas-phase. For example, in the presence of nitric acid, HCl escapes to the gas phase by

$$HNO_3(l) \longleftrightarrow H^+ + NO_3^- \quad (3.4)$$

$$NaCl(s) \longleftrightarrow Na^+ + Cl^- \quad (3.5)$$

$$Cl^- + H^+ \longleftrightarrow HCl(l) \quad (3.6)$$

$$HCl(l) \longrightarrow HCl(g) \quad (3.7)$$
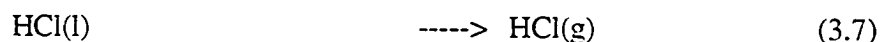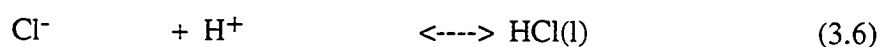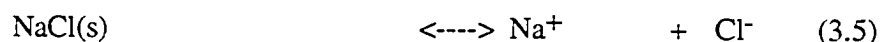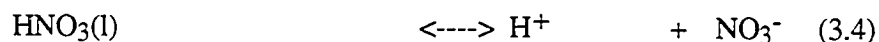
where (s) indicates a solid, (l) indicates a liquid, and (g) indicates a gas. Equation (3.7) is an evaporation process while the other three are fast equilibrium reactions. Meanwhile, sodium does not volatilize since its equilibrium vapor pressure is very low.

As an ocean air mass moves inland with the sea breeze during the day, additional organic and inorganic materials dissolve into or condense onto the sea spray particles. As shown above, when acids, such as sulfuric or nitric acid, enter the spray, they displace

46

the chloride, forcing the supersaturation of aqueous hydrochloric acid relative to the ambient partial pressure of HCl, causing HCl to volatilize (Eriksson, 1960; Duce, 1969; Martens *et al.*, 1973; Heisler *et al.*, 1973; Hitchcock *et al.*, 1980; Kritz and Rancher, 1980; Russell and Cass, 1984; Pilinis and Seinfeld, 1987). Subsequently, sodium solids, such as sodium sulfate or sodium nitrate, may form.

Once in aerosols, species take part in numerous chemical reactions. Some of these are so fast, they can be considered in equilibrium. For example, dissociation reactions, such as sulfuric acid dissociation to bisulfate and sulfate, or nitric acid dissociation to nitrate, are fast processes. Table A.7 lists several equilibrium reactions. Some of these, such as gas-aerosol reactions, are approximations only since gases generally are not in equilibrium with aerosols (Allen *et al.*, 1989; Harrison and MacKenzie, 1990; Wexler and Seinfeld, 1990, 1991, 1992). However, these reactions are useful for calculating equilibrium vapor pressures (Appendix E).

Alternatively, some aqueous-phase reactions proceed in one direction. One purpose of studying such reactions is to predict the rate of S(IV) oxidation to S(VI). Gas-phase oxidation of sulfuric acid, followed by sulfuric acid condensation, cannot account for the rapid buildup of aqueous sulfate in particles (*e.g.* Hering and Friedlander, 1982). However, the dissolution of $SO_2(g)$, followed by aqueous-phase oxidation, speeds the conversion of $SO_2(g)$ to aqueous sulfate.

While $SO_2(g)$ has a moderate Henry's constant, the rapid reaction of $SO_2(l)$ in liquid forces $SO_2(g)$ to dissolve faster. The primary oxidants of $SO_2(l)$ are $H_2O_2(l)$, $O_2(l)$ (catalyzed by Fe^{3+}, Mn^{2+}), $OH(l)$, $CH_2O(l)$, and, to a lesser extent, $O_3(l)$ (Hoffmann and Calvert, 1985; Jacob *et al.*, 1989; Pandis and Seinfeld, 1989).

Thus, emissions and secondary gas-to-particle formation are major causes of particle buildup in the Los Angeles Basin. Next, I discuss an effect of particle buildup.

47

3.2 Discussion of Visibility

A result of aerosol buildup is visibility degradation. While unnatural visibility degradation, itself, causes no adverse health effects, it usually indicates the presence of pollutants, which are often harmful. Furthermore, when pollutants degrade visibility, people often perceive that the quality of their environment is reduced. Here and in Section 8.1, characteristics of visibility reduction are discussed.

Several terms describe maximum visibility. First, the *meteorological range* is the distance from an ideal black object at which the object has a 0.02 liminal contrast ratio against a white background. The liminal or threshold contrast ratio is the lowest visually perceptible brightness contrast a person can see and usually varies from individual to individual. Koschmieder (1924) selected the value of 0.02 for the threshold contrast; however, researchers have concluded that it varies significantly. For example, Middleton (1952) tested 1000 people and found a threshold contrast range of between 0.01 and 0.20 with the mode of the sample between 0.02 and 0.03. Furthermore, Campbell and Maffel (1974) found a liminal contrast of 0.003 in laboratory studies of monocular vision. Nevertheless, 0.02 has become an accepted liminal contrast value for meteorological range measurements.

A slightly different measure of visibility, the *visual range*, is the actual distance at which a person can discern an ideal black object against the horizon sky. Finally, *prevailing visibility* is the greatest visual range a person can see around a 180° horizontal arc, but not necessarily in continuous sectors around the arc (Williamson, 1973).

The meteorological range, typically used for visibility calculations, is derived from the definition of the contrast ratio and from a form of the radiative transfer equation (*e.g.* Seinfeld, 1986). The contrast ratio at a particular wavelength is

48

$$C_\lambda(x) = \frac{I_{B,\lambda} - I_{0,\lambda}(x)}{I_{B,\lambda}}. \qquad (3.8)$$

where $I_{B,\lambda}$ and $I_{0,\lambda}(x)$ are the spectrally resolved background and object intensities (*e.g.* joules cm^{-2} s^{-1}), respectively, and x is the distance over which gases and particles attenuate the object intensity. While the background intensity is independent of distance, the object intensity increases from zero to the background intensity as the viewer moves away from the object. The change of the object intensity with distance is

$$\frac{dI_{0,\lambda}(x)}{dx} = \sigma' I_{B,\lambda} - \sigma_{ext,\lambda} I_{0,\lambda}(x), \qquad (3.9)$$

where $\sigma_{ext,\lambda}$ is the overall extinction coefficient (cm^{-1}) accounting for removal of light from the line of vision, and $\sigma' I_{B,\lambda}$ is a constant accounting for the scattering of background light back into the line of vision. The extinction coefficient is assumed to be independent of the distance from the source. A similar equation for the background intensity yields

$$\frac{dI_{B,\lambda}}{dx} = 0 = \sigma' I_{B,\lambda} - \sigma_{ext,\lambda} I_{B,\lambda}; \qquad (3.10)$$

thus, $\sigma' = \sigma_{ext,\lambda}$. Combining (3.8), (3.9), the result from (3.10), and the fact that the contrast ratio at distance $x = 0$ is 1 gives

$$\frac{dC_\lambda(x)}{dx} = -\sigma_{ext,\lambda} C_\lambda(x) \qquad (3.11)$$

and

49

$$C_\lambda(x) = \exp(-\sigma_{ext,\lambda} x)$$ (3.12)

Finally, when the contrast ratio is 0.02 for a particular wavelength of light, the resulting distance, x, becomes the meteorological range (also known as the *Koschmieder equation*),

$$x = \frac{3.912}{\sigma_{ext,\lambda}}.$$ (3.13)

Both gases and particles in the atmosphere reduce visibility by scattering or absorbing visible radiation. The extinction coefficient ($\sigma_{ext,\lambda}$) is the sum of extinction due to scattering by gases ($\sigma_{sg,\lambda}$), scattering by particles ($\sigma_{sp,\lambda}$), absorption by gases ($\sigma_{ag,\lambda}$), and absorption by particles ($\sigma_{ap,\lambda}$). In polluted tropospheric air, the only important gas-phase visible-light attenuation processes are Rayleigh scattering and absorption by nitrogen dioxide (Waggoner *et al.*, 1981). However, scattering by particles -- particularly sulfate, organic carbon, and nitrate -- causes between 60 and 95% of all visibility reduction. Also, absorption by soot particles causes between 5 and 40% of all reduction (Cass, 1979; Tang *et al.*, 1981; Waggoner *et al.*, 1981).

Larson *et al.* (1984) studied visibility in Los Angeles on two days in 1983: one day clear, and the second, polluted. They calculated gas and particle scattering and absorption coefficients, which were converted to meteorological ranges in Table 3.3.

Table 3.3. Meteorological ranges (x) due to scattering by gases (sg), absorption by gases (ag), scattering by particles (sp), absorption by particles (ap), and total extinction (ext) at a 0.55 μm wavelength on a clean and a polluted day in Los Angeles (extinction

50

coefficients from Larson *et al.*, 1984, reproduced in Seinfeld, 1986). Meteorological range due to total extinction is $x_{ext,\lambda} = 3.912 / [\sigma_{sg,\lambda} + \sigma_{ag,\lambda} + \sigma_{sp,\lambda} + \sigma_{ag,\lambda}]$.

Table 3.3

	Meteorological Range (km)				
	$x_{sg,\lambda}$	$x_{ag,\lambda}$	$x_{sp,\lambda}$	$x_{ap,\lambda}$	$x_{ext,\lambda}$
Clean Day (4 / 7 / 83)	352	326	151	421	67.1
Polluted Day (8 / 25 / 83)	366	130	9.59	49.7	7.42

Table 3.3 shows that particle scattering at 0.55 μm dominated light extinction on both the polluted and clear day. Even on a clear day in Los Angeles, the only impediment to visibility was particle scattering. Also, on the clear day, gas absorption by nitrogen dioxide had an effect comparable to that of Rayleigh scattering, while on the polluted day, its effect was only slightly more significant. Finally, absorption by soot had a significant effect on the polluted day.

Currently, no national standard exists for visibility degradation. However, California first set a standard in 1959 and modified it in 1969. The 1969 standard required the prevailing visibility (outside Lake Tahoe) to exceed 10 miles (16.09 km) when the relative humidity was less than 70%.

In addition, standards exist for visibility-reducing particles and gases. For example, a state and federal standard exists for PM_{10} concentrations (Section 3.1.1). Also, the state legal standard for NO_2 concentration is a one-hour average of 0.25 ppmv. In 1990 the SCAQMD monitored NO_2 at 24 sites. Four of the sites -- Pico Rivera, Los Angeles, Long Beach, and Lynwood -- exceeded the standard during the year

51

(SCAQMD, 1991). Typically, nitrogen dioxide concentrations range from 0.01 ppmv to 0.30 ppmv in the basin and are highest in winter and lower in summer.

However, because the definition of prevailing visibility did not give information about visibility reducing particles and because its determination was subjective, the CARB recently changed the state visibility standard and the methods of determining visibility reduction (CARB, 1989a,b). The new standard became effective in 1991.

The first changes were to require equipment to measure extinction by particles at 0.55 μm, the peak wavelength of the eye's sensitivity to radiation (Middleton, 1952), and to measure relative humidity. Such equipment includes the integrating nephelometer to calculate particle scattering extinction (σ_{sp}), an American Iron and Steel Institute (AISI) or equivalent tape sampler to measure coefficient of haze (*COH*), and a hygrometer to determine relative humidity. Particle absorption extinction can be estimated directly from a *COH* measurement by

$$\sigma_{ap} = 0.054 \ (COH')^{0.76}, \tag{3.14}$$

where $COH' = COH$ / (1000 lineal feet of air). Currently, the SCAQMD reports σ_{sp} and COH from three locations -- Azusa, San Bernardino, and Riverside.

Second, the CARB changed the visibility standard so that it is now based on a maximum allowable extinction coefficient for aerosols, derived from the *Koschmieder equation*, rather than on prevailing visibility. The maximum extinction at 0.55 μm is 0.231 km^{-1}, which is the extinction that gives a meteorological range of 10 miles (16.09 km) minus the extinction caused by Rayleigh scattering. This maximum assumes no NO_2 absorption at 0.55 μm. However, the extinction due to NO_2 ranges from 0.00245 - 0.0615 km^{-1} at this wavelength (*e.g.* Table 8.1). Thus, reported extinctions may give an incorrect meteorological range if NO_2 concentrations are significant.

52

Third, the CARB changed the averaging time of the visibility standard from *one observation* per day to one average of nine hourly observations between 9:00 A. M. and 5:00 P. M. Pacific Standard Time (PST). In sum, visibility is less than the state standard if the average particle extinction (absorption plus scattering) during a day exceeds 0.231 km^{-1} when the relative humidity is less than 70%.

In 1990, prior to the above changes, the SCAQMD monitored visibility at seven locations, mostly at airports near SCAQMD monitoring stations. Figure 3.2 is a map of the number of days in 1990 that visibility was below the state standard. While visibility at Ontario defied the standard during 250 days of the year, coastal visibility was better. Visibility degradation appears to follow the same physical path as ozone and particulate, indicating that particles degrade visibility and often take time to form.

Thus, emissions, gas-to-particle conversion, and transport are major factors leading to particulate buildup in the Los Angeles Basin. Further, emissions, photochemical reactions, and transport are major factors leading to gas buildup in the basin. Next, I discuss the development and use of a model designed to simulate the processes of gas and particle buildup.

53
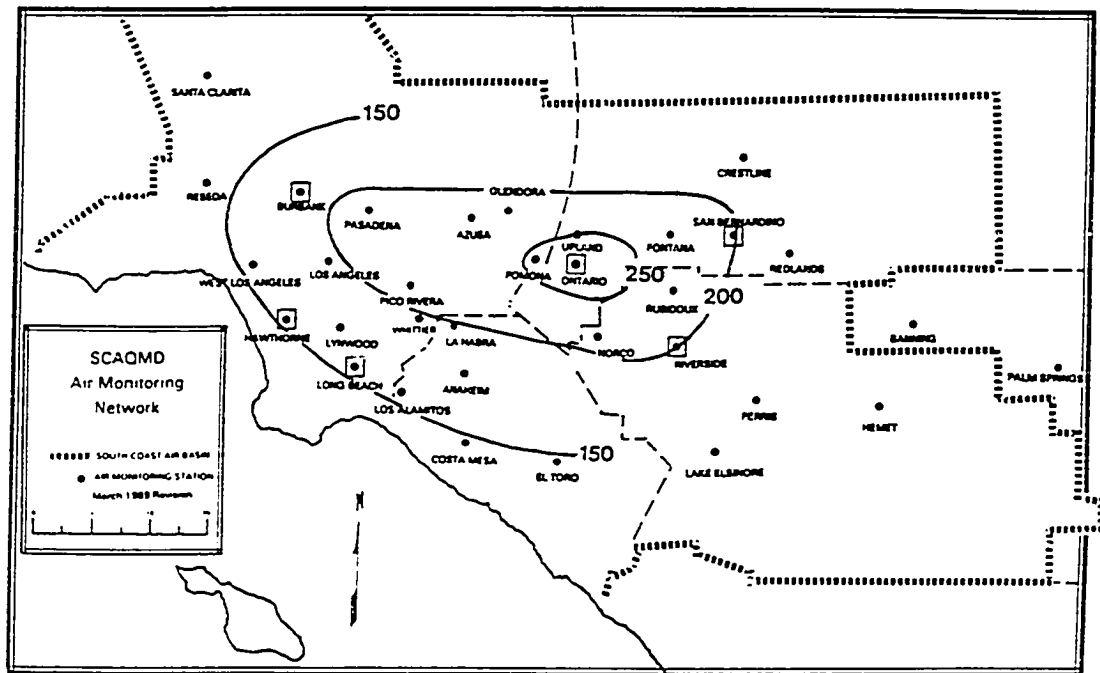
* Visibility less than 10 miles at relative humidity less than 70%.
[■] Measured closest to this location, but not at the air monitoring stations.

Fig. 3.2. Map showing the number of days in 1990 that the prevailing visibility at different places throughout the Los Angeles Basin was below the state standard. The standard requires that visibility exceeds 10 miles when the relative humidity is less than 70%. Map courtesy of SCAQMD (SCAQMD (1991).

54

Chapter 4

Theory of the Model

In this chapter, the continuity equation (Section 4.1), which is the basis of air quality modeling, is described. Further, the division of the continuity equation into several smaller equations and the use of coordinate scaling factors in the divided equations (Section 4.2) are discussed. Finally, this chapter summarizes the structural characteristics and sequence of calculations in the GATOR / MMTD system (Section 4.3).

4.1 The Continuity Equation

The rate of change of concentration, of each constituent in the atmosphere, can be described with the continuity equation, written as (*e.g.* Reynolds *et al.*, 1973, Seinfeld, 1986)

$$\frac{\partial c}{\partial t} + \nabla \cdot (\mathbf{v} c) = D \nabla^2 c + \sum_{i=1}^{m} R_i \,, \qquad (4.1)$$

55

where c is either the number concentration of a gas (No. cm^{-3}), the number concentration (No. cm^{-3}) of aerosols of a certain size, or the volume concentration (cm^3 cm^{-3}) of a particular aerosol component within aerosols of a given size. In addition,

$$\mathbf{v} = u\mathbf{i} + v\mathbf{j} + w\mathbf{k} \qquad (4.2)$$

is a precise wind velocity vector, where u, v, and w are the east-west, north-south, and vertical wind components (cm s^{-1}), respectively. In addition, D is the molecular diffusivity of a gas (cm^2 s^{-1}) and R_i is the time rate of change of concentration due to the ith process (*e.g.* chemistry, emissions, nucleation, etc.) affecting the gas or aerosol.

Expanding (4.1) and (4.2) gives

$$\frac{\partial c}{\partial t} + \frac{\partial uc}{\partial x} + \frac{\partial vc}{\partial y} + \frac{\partial wc}{\partial z} = D\left[\frac{\partial^2 c}{\partial x^2} + \frac{\partial^2 c}{\partial y^2} + \frac{\partial^2 c}{\partial z^2}\right] + \sum_{i=1}^{m} R_i . \qquad (4.3)$$

Because winds are turbulent, the precise wind component can be described with a deterministic and stochastic component (*e. g.* Reynolds *et al.*, 1973; Seinfeld, 1986),

$$\mathbf{v} = \overline{\mathbf{v}} + \mathbf{v}', \qquad (4.4),$$

where $\overline{\mathbf{v}}$ represents a mean wind vector and $\mathbf{v}'$ represents a perturbation component vector. The individual precise wind components in (4) can then be rewritten as

$$u = \overline{u} + u', \qquad v = \overline{v} + v', \quad \text{and} \quad w = \overline{w} + w', \qquad (4.5)$$

56

where $\bar{u}$, $\bar{v}$, and $\bar{w}$ are mean wind velocities and u', v', and w' are perturbed wind velocities. Since concentrations depend on wind velocity, the precise concentration should also have a mean and perturbed component. Thus,

$$c = \bar{c} + c', \tag{4.6}$$

where $\bar{c}$ is the mean component and c' is the perturbed component. Multiplying precise concentration by a precise wind component gives, for example,

$$uc = (\bar{u} + u')(\bar{c} + c') = \bar{u}\bar{c} + u'\bar{c} + \bar{u}c' + u'c'. \tag{4.7}$$

Further, the mean value of uc is

$$\overline{uc} = \overline{\overline{u}\overline{c}} + \overline{u'c'} = \bar{u}\bar{c} + \overline{u'c'}, \tag{4.8}$$

where each overbar indicates an average. In (4.8), $\overline{u'\bar{c}}$ and $\overline{\bar{u}c'}$ equal zero, thus they are not shown. If Equation (4.3) is averaged over an infinite number of turbulence cases, uc, vc, and wc can be replaced by their mean counterparts ($\overline{uc}$, $\overline{vc}$, and $\overline{wc}$), which can then be replaced by Equation (4.8), giving

$$\frac{\partial \bar{c}}{\partial t} + \frac{\partial \bar{u}\bar{c}}{\partial x} + \frac{\partial \bar{v}\bar{c}}{\partial y} + \frac{\partial \bar{w}\bar{c}}{\partial z} + \frac{\partial \overline{u'c'}}{\partial x} + \frac{\partial \overline{v'c'}}{\partial y} + \frac{\partial \overline{w'c'}}{\partial z}$$
$$= D\left[\frac{\partial^2 \bar{c}}{\partial x^2} + \frac{\partial^2 \bar{c}}{\partial y^2} + \frac{\partial^2 \bar{c}}{\partial z^2}\right] + \sum_{i=1}^{m} R_i. \tag{4.9}$$

.

57

A way to represent the perturbation components of (4.9) is by K-theory (Calder, 1949; Pasquill, 1962; Monin and Yaglom, 1971; Reynolds *et al.*, 1973). Under this theory, the perturbed components can be replaced by

$$\overline{u'c'} = -K_{xx}\frac{\partial \overline{c}}{\partial x}, \qquad \overline{v'c'} = -K_{yy}\frac{\partial \overline{c}}{\partial y}, \quad \text{and} \quad \overline{w'c'} = -K_{zz}\frac{\partial \overline{c}}{\partial z}, \qquad (4.10)$$

where K_{xx}, K_{yy}, and K_{zz} (cm^2 s^{-1}) are the diagonal terms of the eddy diffusivity tensor, **K**. Further, after assuming that molecular diffusion is much smaller than turbulent diffusion --

$$D\left[\frac{\partial^2 \overline{c}}{\partial x^2} + \frac{\partial^2 \overline{c}}{\partial y^2} + \frac{\partial^2 \overline{c}}{\partial z^2}\right] << \frac{\partial \overline{u'c'}}{\partial x} + \frac{\partial \overline{v'c'}}{\partial y} + \frac{\partial \overline{w'c'}}{\partial z}. \qquad (4.11)$$

-- then (4.9), (4.10), and (4.11) can be combined to give

$$\frac{\partial \overline{c}}{\partial t} + \frac{\partial \overline{u}\overline{c}}{\partial x} + \frac{\partial \overline{v}\overline{c}}{\partial y} + \frac{\partial \overline{w}\overline{c}}{\partial z} = \frac{\partial}{\partial x}\left(K_{xx}\frac{\partial \overline{c}}{\partial x}\right) + \frac{\partial}{\partial y}\left(K_{yy}\frac{\partial \overline{c}}{\partial y}\right)$$
$$+ \frac{\partial}{\partial z}\left(K_{zz}\frac{\partial \overline{c}}{\partial z}\right) + \sum_{i=1}^{m} R_i. \qquad (4.12)$$

which is the three-dimensional continuity equation for an atmospheric pollutant.

4.2 Time-Split Continuity Equation

An ideal atmospheric model would simultaneously solve Equation (4.12), together with the other primitive equations (Section 7.1), and the radiative transfer equation (Equation (8.9)), for all gas and aerosol constituents. Such a set of equations

58

links the atmospheric variables of temperature, pressure, humidity, wind speed, wind direction, and diffusion with other factors, such as radiative heating, changes in gas and aerosol concentration, and changes in aerosol composition. In theory, such a set of equations can be solved simultaneously. However, with current computer resources, they cannot be solved over a large grid domain and for hundreds to thousands of gases plus aerosol components. Instead, for practical use, the equations are broken into a series of smaller equations. Here, I discuss the division of Equation (4.12).

Usually, Equation (4.12) is broken into three or more one-dimensional equations (*e.g.* Toon *et al.*, 1988; Pepper *et al.*, 1979) for each species. However, before dividing (time-splitting) the continuity equation, Toon *et al.* (1988) generalized the equations for five horizontal coordinate systems and four vertical coordinate systems. To generalize, they introduced scaling factors for velocities, eddy diffusion coefficients, the grid coordinates, and densities. Tables 4.1 - 4.3 list values for the scaling factors and the modified parameters.

Table 4.1. Scaling factors for horizontal coordinates systems (Toon *et al.*, 1988)

Table 4.1

Coordinate System	Hm_1	Hm_2	Hm_3	ds_1	ds_2
Spherical	$\sin\gamma$	1	R	$d\lambda$	$d\gamma$
Mercator	$\cos\phi/\cos\phi_o$	Hm_1	1	dx	dy
Polar stereographic	$(1+\sin\phi)/(1+\sin\phi_o)$	Hm_1	1	dx	dy
Lambert conformal	$\left(\dfrac{1+\sin\phi}{1+\sin\phi_o}\right)^n \left(\dfrac{\cos\phi_o}{\cos\phi}\right)^{n-1}$	Hm_1	1	dx	dy
Rectangular	1	1	1	dx	dy

Definitions for Table 4.1
γ = colatitude

59

ϕ = latitude
ϕ_0 = latitude at which projection is true
λ = longitude
R = earth's radius (cm)
ds_1, ds_2 = horizontal coordinates used in Table 4.3

$$n = \ln\left\{\frac{\cos\phi_o}{\cos\phi_1}\right\} \Big/ \ln\left\{\frac{\tan(\pi/4)-(\phi_o/2)}{\tan(\pi/4)-(\phi_1/2)}\right\}$$

Table 4.2. Scaling factor for vertical coordinate system (Toon *et al.*, 1988)

Table 4.2

Coordinate system	Vm	ds_3
Altitude	1	dz
Pressure	$1/\rho g$	dp
Sigma	$P^*/\rho g$	$d\sigma$
Log Pressure	T/T_0	dZ

Definitions for Table 4.2

g = gravity
P^* = $P_{sfc} - P_{top}$; P_{sfc} = surface pressure; P_{top} = pressure at model top
σ = $(P - P_{top}) / P^*$
Z = $H\ln(P/P_{sfc})$; H = constant atmospheric scale height
ds_3 = vertical coordinate used in Table 4.3

Table 4.3. Model velocities, diffusion coefficients, grids, densities, and concentrations after scaling for coordinate system type (Toon *et al.*, 1988).

Table 4.3

Parameter	<----------------------------- scaling ----------------------------->		
velocities	$U = \bar{u}Hm_1^{-1}$	$V = \bar{v}Hm_2^{-1}$	$W = \dfrac{ds_3}{dt} + V_f Vm^{-1}$
diffusion coefficients	$K_1 = K_{xx}Hm_1^{-2}$	$K_2 = K_{yy}Hm_2^{-2}$	$K_3 = K_{zz}Vm^{-2}$
coordinates	$dX = Hm_3 ds_1$	$dY = Hm_3 ds_2$	$dZ = ds_3$
air density		$\rho^* = \rho Vm Hm_1 Hm_2$	

60

species
concentrations

$$C = \bar{c}\,VmHm_1Hm_2$$

Applying the scaled winds, diffusion coefficients, density, and concentrations from Table 4.3 to Equation (4.12), Toon *et al.* obtained

$$\frac{\partial C}{\partial t} + \frac{\partial UC}{\partial X} + \frac{\partial VC}{\partial Y} + \frac{\partial WC}{\partial Z} = \frac{\partial}{\partial X}\left(\rho^* K_1 \frac{\partial C/\rho^*}{\partial X}\right) + \frac{\partial}{\partial Y}\left(\rho^* K_2 \frac{\partial C/\rho^*}{\partial Y}\right)$$

$$+ \frac{\partial}{\partial Z}\left(\rho^* K_3 \frac{\partial C/\rho^*}{\partial Z}\right) + VmHm_1Hm_2 \sum_{i=1}^{m} R_i, \qquad (4.13)$$

which is the flux form of the scaled continuity equation for a trace gas or aerosol. This equation has the same form as (4.12) for rectangular coordinates when Vm, Hm_1, and Hm_2 equal one. The condensed form of (4.13) is

$$\frac{\partial C}{\partial t} + \nabla \cdot (\mathbf{V}C) = \nabla \cdot \left(\rho^* \mathbf{K}\nabla\left[C/\rho^*\right]\right) + VmHm_1Hm_2 \sum_{i=1}^{m} R_i, \qquad (4.14)$$

where $\mathbf{V}$ is the vector form of the scaled velocities. To time-split (4.13), Toon *et al.* separated it into a series of three one-dimensional equations -- one each for east-west, north-south, and vertical transport plus other processes. For this work, (4.13) was time-split into the same three equations, except additional equations were added for gas and aerosol chemical and microphysical processes and several terms were moved from the vertical one-dimensional equation of Toon *et al.* Currently, the first three one-dimensional continuity equations are

61

$$\frac{\partial C}{\partial t} + \frac{\partial UC}{\partial X} = \frac{\partial}{\partial X}\left(\rho^* K_1 \frac{\partial C/\rho^*}{\partial X}\right),$$ (4.15)

$$\frac{\partial C}{\partial t} + \frac{\partial VC}{\partial Y} = \frac{\partial}{\partial Y}\left(\rho^* K_2 \frac{\partial C/\rho^*}{\partial Y}\right),$$ (4.16)

and

$$\frac{\partial C}{\partial t} + \frac{\partial WC}{\partial Z} = \frac{\partial}{\partial Z}\left(\rho^* K_3 \frac{\partial C/\rho^*}{\partial Z}\right)$$
$$+ VmHm_1Hm_2\left[R_{emis} - C\left(1_{fall} + 1_{ddep} + 1_{rain}\right)\right],$$ (4.17)

where R_{emis} is the rate of emissions of either gases or aerosols (concentration s^{-1}), 1_{fall} is the implicit loss rate (s^{-1}) of aerosols due to sedimentation (Section 7.3.1), 1_{ddep} is the implicit loss rate of gases or aerosols due to dry deposition (Section 7.3.2), and 1_{rain} is the implicit loss rate of gases or aerosols due to rainout. During August 26 - 28th, 1987 in Los Angeles, the time and place under investigation, no rain occurred; thus, rainout was ignored for this work.

The above three equations describe the transport of all gases and aerosols between grid cells or between model cells and boundaries. All remaining processes occur within individual grid cells. Since such computations do not require information about adjacent spatial grid cells, no coordinate scaling is needed. However, non-scaled concentrations can be scaled to *model units*, simply by multiplying them by $VmHm_1Hm_2$ (Table 4.3).

All processes described in equations (4.15) - (4.17) apply to gases, aerosols, and aerosol components (except that gases have negligible fall velocity). However, physical and chemical processes affect gases differently than they affect aerosols. Below are three time-split, ordinary differential equations that describe changes in gas number

62

concentration, size-resolved aerosol number concentration, and size- and species-resolved aerosol volume concentration, respectively. These equations are

$$\frac{\partial \overline{c}_{G_n}}{\partial t} = R_{chem} - R_{nucg} - R_{dgrow} - R_{cgrow},$$ (4.18)

$$\frac{\partial \overline{c}_k}{\partial t} = R_{nucn} + R_{coagn},$$ (4.19)

and

$$\frac{\partial \overline{c}_{V_nk}}{\partial t} = R_{nucv} + R_{coagv} + R_{dgrow} + R_{cgrow} + R_{equil} + R_{aqchem},$$ (4.20)

where $\overline{c}_{G_n}$ identifies the number concentration (No molecules cm^{-3}) of the nth gaseous component, $\overline{c}_k$ identifies the number concentration (No. particles cm^{-3}) in the kth size bin of particles, and $\overline{c}_{V_nk}$ identifies the volume concentration of the nth component (cm^3 particles cm^{-3}) in the kth size bin of particles.

In equation (4.18), R_{chem} is the rate of change of gas concentration due to gas-phase chemistry, R_{nucg} is the loss rate of gas due to aerosol nucleation, R_{dgrow} is the net loss (or production) rate of gas due to dissolutional growth (or evaporation) of particles, and R_{cgrow} is the net loss (or production) rate of gas due to condensational growth (or evaporation) of particles. In (19) R_{nucn} is the number production rate of new particles due to aerosol nucleation and R_{coagn} is the change in bin-resolved number concentration of particles due to coagulation. In (20) R_{nucv} is the volume production rate of new particles due to nucleation, R_{coagv} is the volume rate of change of a given component and size due to coagulation, R_{dgrow} and R_{cgrow} are the rates of change in aerosol volume due to either dissolutional or condensational growth, R_{equil} is the rate of change of aerosol volume due

63

to chemical equilibrium processes, and R_{aqchem} is the rate of change of volume due to aqueous chemistry.

In later sections, each of the above physical processes is discussed. For example, Chapter 5 discusses changes of gas concentration due to chemistry, Section 6.2 discusses aerosol nucleation, Section 6.3 discusses coagulation, Sections 6.4 discusses condensational and dissolutional growth, and Section 6.5 discusses aqueous chemistry.

4.3 Structure of and Calling Sequence in GATOR / MMTD

The GATOR / MMTD system contains several subroutines and input data files. Here, I describe the order of calling fundamental processes in the model and some features of the computer code.

First, Figure 4.1 shows a simplified calling tree of the processes in the model. The first process called is radiative transfer. In fact, the model calls radiative transfer during model setup as well to obtain mean intensity values for initial photorates. It then calls radiative transfer a second time, shown here, at an advanced time interval. The purpose of the two calls is to obtain photodissociation rates for both the beginning and end of a time interval. SMVGEAR (gas and aqueous chemistry solver) interpolates between the photorates at the beginning and end of each time interval to obtain photorate values for each Gear time step, which is almost always smaller than a time interval.

The second call in the sequence is to the MMTD. Usually, the MMTD operates with a time step of six seconds. Thus, if the time interval of horizontal and vertical transport is 300 seconds, the MMTD runs through 50 time steps for each interval of transport. The MMTD uses heating rates from the radiative transfer code in GATOR to solve part of the temperature change (Section 8.2) ; however, all other calculations are currently independent of GATOR. The MMTD can also solve for heating rates on its own (Lu and Turco, 1994a).

64

```
                          V                                    Λ
              ┌─────────────────────────┐
              │   1. Radiative Transfer │                      Λ
              └─────────────────────────┘
                          V                                    Λ
              ┌─────────────────────────┐
              │  2. Meteorology (MMTD)  │                      Λ
              └─────────────────────────┘
                          V                                    Λ
    ┌──────────────────────────────────────────────────┐
    │ 3. Horizontal Transport; Emissions Rates; Fall Velocities; │  Λ
    │    Deposition Velocities; Vertical Transport       │
    └──────────────────────────────────────────────────┘
                          V                                    Λ
              ┌─────────────────────────┐
              │    4. Gas Chemistry     │                      Λ
              └─────────────────────────┘
                          V                                    Λ
         ┌────────────────────────────────────────┐
         │ 5. Homogeneous /Heterogeneous Nucleation │          Λ
         └────────────────────────────────────────┘
                          V                                    Λ
              ┌─────────────────────────┐
              │     6. Coagulation      │                      Λ
              └─────────────────────────┘
                          V                                    Λ
           ┌──────────────────────────────────┐
           │ 7. Equilibrium Vapor Pressures   │                Λ
           └──────────────────────────────────┘
                          V                                    Λ
        ┌────────────────────────────────────────┐
        │ 8. Condensational / Dissolutional Growth │            Λ
        └────────────────────────────────────────┘
                          V                                    Λ
        ┌────────────────────────────────────────┐
        │ 9. Chemical Equilibrium Within Particles │            Λ
        └────────────────────────────────────────┘
                          V                                    Λ
            ┌──────────────────────────────┐
            │    10. Aqueous Chemistry     │
            └──────────────────────────────┘
                          V                                    Λ
```

Fig. 4.1. Calculation sequence in the coupled GATOR / MMTD system. Each process is described in detail in Chapters 5 - 8 and Appendices B - F.

65

The third call is to the horizontal and vertical transport algorithms. Each time interval, GATOR alternates between calling horizontal or vertical transport first (Toon *et al.*, 1988). Before calling either transport scheme, MMTD output is transferred to GATOR arrays. Also, before calling vertical transport, the emission rates, fall velocities, and dry deposition velocities are calculated. The corresponding production and loss rates are placed in the vertical transport equations.

Fourth, the model calls the gas chemistry solver, SMVGEAR, which solves first-order ordinary differential equations over large grid domains. For each chemistry time interval (5 - 15 minutes) SMVGEAR integrates over many Gear time steps that vary in size. Currently, the time interval for gas chemistry may be smaller than, equal to, or larger than the time interval for horizontal or vertical transport. However, it is the same as the time interval for radiation since mean intensities for photorates are needed for the beginning and end of a chemistry time interval, as discussed above.

Next, the model simulates homogeneous nucleation, heterogeneous nucleation, coagulation, equilibrium vapor pressures, dissolutional growth, condensational growth, chemical equilibrium, and aqueous chemistry. All these processes use the same time interval as each other, which currently may be equal to or larger than the time interval for gas chemistry. After solving aqueous chemistry, GATOR returns to the radiative transfer code to begin calculations again.

The aerosol-process time interval in GATOR needs to be at least as long as the gas-chemistry interval because aqueous chemistry relies on mean intensities for aqueous photodissociation reactions. Since SMVGEAR solves aqueous chemistry and interpolates photorates between the beginning and end of a time interval, it needs photorate values at the beginning and end of the interval. Thus, the beginning of an aerosol-process interval is set to occur at the same time as the beginning of a gas chemistry interval. The end of an

66

aqueous chemistry interval, however, can occur at the same time as or later than the end of a gas interval.

Suppose, for example, the aerosol interval is twice as long as the gas interval. Then, aqueous chemistry photorates for the end of an interval are updated every two passes through the radiative transfer code. If the aerosol interval was shorter than the gas interval, then the radiative transfer code would need to be called more often. This is easy; however, it serves no purpose since gas chemistry solves much faster than do other aerosol processes. Therefore, gas chemistry should be called at least as many times as aerosol processes are called.

The processes (4) - (10) in Figure 4.1 require no communication between grid cells. Thus, they are easily vectorized around the grid-cell dimension (Section 5.1.3). GATOR contains additional features. For example, it accommodate any number of gas and aerosol species, any number of aerosol size bins, and any number of latitudinal, longitudinal, and vertical grid cells. The horizontal and vertical grids are expandable, collapsible, and transmutable so that the grid dimensions and location can be changed. In the model a user can input all gas species, gas chemical reactions, gas reaction rates, aerosol species, aqueous chemistry rates, and equilibrium constants into data sets. Thus, solving gas or aqueous chemistry for an additional species and / or reaction, requires just adding the species name, the reaction, and the rate to the appropriate data file.

Further, GATOR is controlled by a series of *switches* in an input data file. Thus, each process shown in Figure 4.1 can be turned on or off. These switches also control grid dimensions, coordinate system types, time intervals for different processes, types of output desired, and the time and date of the simulation. Finally, checkpoints throughout the code test whether dimensions have been exceeded.

Next, I discuss individual processes in the GATOR / MMTD air pollution modeling system.

Chapter 5

Gas-Phase Chemistry Solvers

This chapter and Appendix B focus on solutions to gas-phase chemical equations over large grid domains. The three solvers developed, in time-sequence, include a matrix inversion scheme for family chemistry, a multistep implicit-explicit (MIE) scheme, and a sparse-matrix, vectorized Gear code (SMVGEAR). In Section 5.1 and Appendix B, the theory behind Gear's method and the development of SMVGEAR are discussed. In Section 5.2 and Appendix B, the MIE method is discussed, and in Section 5.3, the matrix inversion scheme for family chemistry is detailed.

5.1 Development of SMVGEAR

5.1.1 Gear's Method

Gear's method (Gear, 1969, 1971) solves first-order ordinary differential equations (ODEs) that have initial value boundary conditions. Atmospheric models describe numerous physical processes with such equations. For example, gas and aqueous chemical rate equations are all first order ODEs. Similarly, condensational growth, evaporation, and coagulation can be described with such equations. Here, I

68

discuss the theory behind Gear's method and how SMVGEAR, the sparse-matrix, vectorized Gear code in GATOR, was developed.

Gear's scheme is a predictor-corrector method based on the backward differentiation formula (BDF) (*e.g.* Hindmarsh, 1983, 1974; Sherman and Hindmarsh, 1980; Byrne et al., 1977). The BDF can be written as

$$y_n = h\beta_0 \frac{dy_n}{dt} + \sum_{j=1}^{q} \alpha_j y_{n-j},$$

(5.1)

where

$$y_n = y(t_n) = \left[y_n^1 + y_n^2 + \ldots + y_n^N \right]$$

(5.2)

is an array of N real variables at time t_n. Also,

$$h = t_n - t_{n-1}$$

(5.3)

is the current time step, q is the current order of the method ($1 \le q \le 5$), α_j and β_0 are scalar multipliers ($\beta_0 > 0$) that depend on the current order, and

$$\frac{dy_n}{dt} = f_n = f(t_n, y_n) = \left[f_n^1 + f_n^2 + \ldots + f_n^N \right]$$

(5.4)

is an array of first derivatives for each value of y at time step n. The boundary conditions,

$$y(t_0) = y_0$$

(5.5)

define the initial values for the problem. Equation (5.1) can be rewritten as

$$y_n = h\beta_0 f(t_n, y_n) + a_n, \tag{5.6}$$

where

$$a_n = \sum_{j=1}^{q} \alpha_j y_{n-j}. \tag{5.7}$$

If

$$0 = a_n + h\beta_0 f(t_n, y_n) - y_n, \tag{5.8}$$

then y_n is the correct solution to the problem of $dy_n / dt_n = f_n$, given the boundary condition $y(t_0) = y_0$. In order to obtain this equality, Gear used a modified Newton iteration of the form

$$P_n\left[y_{n(m+1)} - y_{n(m)}\right] = a_n + h\beta_0 f(t_n, y_{n(m)}) - y_{n(m)}, \tag{5.9}$$

which can be rewritten as

$$P_n \Delta y_{n(m)} = B \tag{5.10}$$

by defining

$$B = a_n + h\beta_0 f(t_n, y_{n(m)}) - y_{n(m)} \tag{5.11}$$

and

$$\Delta y_{n(m)} = y_{n(m+1)} - y_{n(m)}. \tag{5.12}$$

In (5.9) - (5.12), m is the iteration number and

$$P_n \approx I - h\beta_0 J_n \tag{5.13}$$

70

is an approximation (predictor) matrix, in which I is the identity matrix and

$$J_n = J(t_n, y_n) = \left[\frac{\partial f_n^i}{\partial y_n^j} \right]_{i,j=1}^{N} \qquad (5.14)$$

is a Jacobian matrix of partial derivatives.

Gear's original code solves first-order ODEs in the following order: it (a) calculates first derivatives (f), (b) calculates initial values for the right side, B, (c) fills in the Jacobian (J) and predictor (P) matrices, (d) decomposes the predictor matrix, (e) backsubstitutes over B to obtain values of Δy, (f) adds Δy, multiplied by a method coefficient, to the value of y from the last iteration, (g) checks whether the corrector, Δy, has converged by checking whether the root-mean-square error of the corrections, weighted and normalized over all equations, is less than a local error tolerance, and (h) if the corrector has converged, it checks whether the root-mean-square error of the corrections, accumulated over all iterations for a time step, and weighted and normalized over all equations, is less than another error tolerance. If one of the error tolerances fails, then the code either re-evaluates the Jacobian, reduces the time step and re-evaluates the Jacobian, or reduces the order and time step and re-evaluates the Jacobian.

After a number of successful time steps dependent on the value of the current order, the code re-estimates the time step feasible at one order lower than, the same order as, and one order higher than the current order. It then chooses the next time step as the largest of the three estimates and chooses the order as that order allowing the largest step. Appendix B details additional characteristics of Gear's method.

71

5.1.2 General Characteristics of SMVGEAR

The advantage of a Gear-type code is that solutions are extremely accurate for reasonable values of the relative and absolute error tolerances. The disadvantage of early Gear codes was that they required numerous decompositions and backsubstitutions over matrices of partial derivatives. To reduce the speed disadvantage of Gear's method, I applied sparse-matrix and vectorization techniques to an original code of Gear's (Gear, 1971, pp. 158 - 166). Workers at Lawrence Livermore National Laboratory have applied banded- (*e. g.* Hindmarsh, 1975) and sparse- (*e. g.* Spellman and Hindmarsh, 1975; Sherman and Hindmarsh, 1980; Hindmarsh, 1983) matrix techniques to Gear's method to reduce computing time. LSODES, the Livermore Solver for Ordinary Differential Equations, is the most recent sparse-matrix Gear code emanating from Livermore (*ibid.*). While the speeds from LSODES and SMVGEAR are similar on non-vector machines, SMVGEAR is approximately 40 - 110 times faster than LSODES on a vectorized machine, such as the Cray 90 (Appendix B and subsequent tests). Further, results from other tests indicate that SMVGEAR is approximately 200 - 1000 times faster than Gear's original code.

Aside from containing sparse-matrix and vectorization features, SMVGEAR has additional attributes. First, it sets up different matrix arrays for day and night chemistry, which reduces the number of ODEs that need to be solved during nighttime. Second, it sets up different matrix arrays for ODE processes other than gas-phase chemistry (*e.g.* aqueous chemistry, aerosol condensational growth). Third, it contains automatic checks for normalized absolute gross error of ODE solutions. Thus, results from using a certain relative and absolute error tolerance can be compared to results from using much more rigorous tolerances or from using solutions from other solvers. Fourth, SMVGEAR contains an input data set for chemical equations that currently allows up to 12

72

fractionated and non-fractionated products per reaction. Thus, to change the chemical scenario, only the chemical equations in the data set need to be changed.

5.1.3 Vectorization in SMVGEAR

While about half the speedup of SMVGEAR, compared to Gear's original code, was from sparse-matrix techniques, the other half was from vectorization. Vectorization significantly speeds the calculations within inner DO...CONTINUE loops on vectorized machines such as those of the CRAY line. To vectorize SMVGEAR, I first divide the grid domain into blocks of grid cells then vectorize calculations around inner loops of length equal to the number of cells in a block. For example, if a domain (NTLOOP) of 10,000 cells contains 20 blocks (NBLOCKS), then each block consists of 500 cells (KTLOOP). For each block, SMVGEAR is called. Each loop in SMVGEAR is vectorized around the grid-block size (KTLOOP). Thus, the call sequence for SMVGEAR is

```
DO KBLK = 1, NBLOCKS
    CALL SMVGEAR
CONTINUE
```

and a typical loop in SMVGEAR has the form

```
DO JOUTER = 1, KOUTER
    DO KLOOP = 1, KTLOOP
    CONTINUE
CONTINUE
```

73

where the DO JOUTER... indicates an outer, non-vectorized secondary loop, and the DO KLOOP... loop is an inner, vectorized loop.

One reason to divide the domain into blocks is to reduce storage requirements. For example if KTLOOP = NTLOOP, then each inner loop in the example above would be 10,000 units long, and the dimensions of numerous arrays would equal 10,000. However, with KTLOOP = 500, space requirements in these arrays are 20 times smaller.

A second reason to divide the domain into blocks is to reduce the number of excess calculations. Since SMVGEAR solves the same number of equations each time step for each grid cell in a block (in order to vectorize), and that number is limited by the time that the cell with the stiffest equations takes to converge, then reducing the number of cells in a block reduces the overall number of excess calculations. For example, if a block contains two cells, and the stiffest cell requires 20 calculations while the other cell requires 10, the stiffest cell forces 40 calculations total. However, if two separate blocks contain one cell each, the stiffest cell does not affect the other cell, and the total number of calculations reduces to 30.

On a Cray YMP computer, a vectorized inner loop reaches 90% of its maximum speed when the inner vector length is about 512 elements (NAS, 1992) (The number is similar for a CRAY 90). Thus, to optimize performance, a balance needs to be struck between minimizing the number of grid cells in a block (to save space and to reduce excess calculations) and maximizing the number of cells in a block (to vectorize). Usually, a grid block length 500 cells or so gives speedy results, does not require too much array space, but allows nearly full vectorization.

For atmospheric chemistry problems, the stiffness of equations changes dramatically in each grid cell during the day due to changes in photolysis, emissions, transport, and other factors. Consequently, if no steps are taken to avoid the problem, grid cells with stiff equations will frequently be grouped together with grid cells that

74

contain non stiff equations. In the worst case, where every grid cell has at least one stiff equation, the speed of solution in each block is limited by the speed of solution in the stiffest cell, and the excess number of calculations is large.

To avoid this problem, all grid cells in the grid domain are reordered from least to most stiff, each time interval (where a time interval is a series of Gear time steps). Before SMVGEAR is called each interval (before the DO KBLK loop, above), the reordering takes place. To reorder, the least-stiff grid cells are placed together in some blocks and the stiffest cells are placed together in others. The stiffness of a cell is usually proportional to the first time step estimate, which is a function of initial chemical rate equation values. Reordering has hastened solutions over the grid domain by a factor of two or more compared to not reordering. Reordering is especially advantageous where sunrise or emissions occur because, at these locations, chemistry is usually stiffer than at other locations.

5.1.4 Sparse-Matrix Techniques Applied to SMVGEAR

To further speed up SMVGEAR, sparse-matrix techniques were implemented. The major techniques included (a) reordering the matrix of partial derivatives so that those with the fewest partial derivative terms reside at the top of the matrix and those with the most reside at the bottom and (b) eliminating all multiplies by zero during subsequent matrix decomposition and backsubstitution. Here, is an example of how the matrix of partial derivatives is set and reordered in SMVGEAR. First, suppose the following four chemical rate equations describe the transformation of five species (assume O_2 and M are unaffected by these equations):

$$(k_1) \quad NO \quad + O_3 \quad \longrightarrow NO_2 \quad + \ O \quad (5.15)$$

$$(k_2) \quad O \quad + O_2 \quad \text{-M->} \ O_3 \quad (5.16)$$

$$(J) \qquad NO_2 \qquad + h\nu \qquad \qquad ----> NO \qquad + O \qquad (5.17)$$

$$(k_3) \qquad NO_2 \qquad + O_3 \qquad \qquad ----> NO_3 \qquad + O_2, \qquad (5.18)$$

where k_1, k_2, and k_3 are kinetic rate coefficients and J is a photolysis rate. For each species -- NO, NO_2, O, O_3, and NO_3 -- the first-order ordinary differential equation are

$$\frac{d[NO]}{dt} = J[NO_2] - k_1[NO][O_3], \qquad (5.19)$$

$$\frac{d[NO_2]}{dt} = k_1[NO][O_3] - J[NO_2] - k_3[NO_2][O_3], \qquad (5.20)$$

$$\frac{d[O]}{dt} = J[NO_2] - k_2[O][O_2][M], \qquad (5.21)$$

$$\frac{d[O_3]}{dt} = k_2[O][O_2][M] - k_1[NO][O_3] - k_3[NO_2][O_3], \qquad (5.22)$$

and

$$\frac{d[NO_3]}{dt} = k_3[NO_2][O_3], \qquad (5.23)$$

and all the non-zero partial derivatives are

$$\frac{\partial^2[NO]}{\partial[NO]\partial t} = -k_1[O_3]. \qquad (5.24)$$

$$\frac{\partial^2[NO]}{\partial[NO_2]\partial t} = J. \qquad (5.25)$$

$$\frac{\partial^2[NO]}{\partial[O_3]\partial t} = -k_1[NO]. \qquad (5.26)$$

76

$$\frac{\partial^2[NO_2]}{\partial[NO]\partial t} = k_1[O_3],$$

(5.27)

$$\frac{\partial^2[NO_2]}{\partial[NO_2]\partial t} = -J - k_3[O_3],$$

(5.28)

$$\frac{\partial^2[NO_2]}{\partial[O_3]\partial t} = k_1[NO] - k_3[NO_2],$$

(5.29)

$$\frac{\partial^2[O]}{\partial[NO_2]\partial t} = J,$$

(5.30)

$$\frac{\partial^2[O]}{\partial[O]\partial t} = -k_2[O_2][M],$$

(5.31)

$$\frac{\partial^2[O_3]}{\partial[NO]\partial t} = -k_1[O_3],$$

(5.32)

$$\frac{\partial^2[O_3]}{\partial[NO_2]\partial t} = -k_3[O_3],$$

(5.33)

$$\frac{\partial^2[O_3]}{\partial[O]\partial t} = k_2[O_2][M],$$

(5.34)

$$\frac{\partial^2[O_3]}{\partial[O_3]\partial t} = -k_1[NO] - k_3[NO_2],$$

(5.35)

$$\frac{\partial^2[NO_3]}{\partial[NO_2]\partial t} = k_3[O_3],$$

(5.36)

and

$$\frac{\partial^2[NO_3]}{\partial[O_3]\partial t} = k_3[NO_2].$$

(5.37)

Further, from Equations (5.13) and (5.14), the matrix P_n takes the form

77

$$
\begin{array}{ccccc}
 & \text{NO} & \text{NO}_2 & \text{O} & \text{O}_3 & \text{NO}_3
\end{array}
$$

$$
\begin{array}{c}
\text{NO} \\ \\
\text{NO}_2 \\ \\
\text{O} \\ \\
\text{O}_3 \\ \\
\text{NO}_3
\end{array}
\left[
\begin{array}{ccccc}
1 - h\beta_0 \dfrac{\partial^2[\text{NO}]}{\partial[\text{NO}]\partial t} & -h\beta_0 \dfrac{\partial^2[\text{NO}]}{\partial[\text{NO}_2]\partial t} & -h\beta_0 \dfrac{\partial^2[\text{NO}]}{\partial[\text{O}]\partial t} & -h\beta_0 \dfrac{\partial^2[\text{NO}]}{\partial[\text{O}_3]\partial t} & -h\beta_0 \dfrac{\partial^2[\text{NO}]}{\partial[\text{NO}_3]\partial t} \\[2ex]
-h\beta_0 \dfrac{\partial^2[\text{NO}_2]}{\partial[\text{NO}]\partial t} & 1 - h\beta_0 \dfrac{\partial^2[\text{NO}_2]}{\partial[\text{NO}_2]\partial t} & -h\beta_0 \dfrac{\partial^2[\text{NO}_2]}{\partial[\text{O}]\partial t} & -h\beta_0 \dfrac{\partial^2[\text{NO}_2]}{\partial[\text{O}_3]\partial t} & -h\beta_0 \dfrac{\partial^2[\text{NO}_2]}{\partial[\text{NO}_3]\partial t} \\[2ex]
-h\beta_0 \dfrac{\partial^2[\text{O}]}{\partial[\text{NO}]\partial t} & -h\beta_0 \dfrac{\partial^2[\text{O}]}{\partial[\text{NO}_2]\partial t} & 1 - h\beta_0 \dfrac{\partial^2[\text{O}]}{\partial[\text{O}]\partial t} & -h\beta_0 \dfrac{\partial^2[\text{O}]}{\partial[\text{O}_3]\partial t} & -h\beta_0 \dfrac{\partial^2[\text{O}]}{\partial[\text{NO}_3]\partial t} \\[2ex]
-h\beta_0 \dfrac{\partial^2[\text{O}_3]}{\partial[\text{NO}]\partial t} & -h\beta_0 \dfrac{\partial^2[\text{O}_3]}{\partial[\text{NO}_2]\partial t} & -h\beta_0 \dfrac{\partial^2[\text{O}_3]}{\partial[\text{O}]\partial t} & 1 - h\beta_0 \dfrac{\partial^2[\text{O}_3]}{\partial[\text{O}_3]\partial t} & -h\beta_0 \dfrac{\partial^2[\text{O}_3]}{\partial[\text{NO}_3]\partial t} \\[2ex]
-h\beta_0 \dfrac{\partial^2[\text{NO}_3]}{\partial[\text{NO}]\partial t} & -h\beta_0 \dfrac{\partial^2[\text{NO}_3]}{\partial[\text{NO}_2]\partial t} & -h\beta_0 \dfrac{\partial^2[\text{NO}_3]}{\partial[\text{O}]\partial t} & -h\beta_0 \dfrac{\partial^2[\text{NO}_3]}{\partial[\text{O}_3]\partial t} & 1 - h\beta_0 \dfrac{\partial^2[\text{NO}_3]}{\partial[\text{NO}_3]\partial t}
\end{array}
\right].
$$

$$\tag{5.38}$$

After the partial derivative terms from (5.24) - (5.37) are placed in (5.38), (5.38) becomes

$$
\begin{array}{c}
\quad\; \text{NO} \qquad\qquad \text{NO}_2 \qquad\qquad \text{O} \qquad\qquad\quad \text{O}_3 \qquad\quad \text{NO}_3
\end{array}
$$

$$
\begin{array}{c}
\text{NO} \\[2em]
\text{NO}_2 \\[2em]
\text{O} \\[2em]
\text{O}_3 \\[2em]
\text{NO}_3
\end{array}
\left[
\begin{array}{ccccc}
1 - h\beta_0(-k_1[O_3]) & -h\beta_0(J) & 0 & -h\beta_0(-k_1[NO]) & 0 \\[1.5em]
-h\beta_0(k_1[O_3]) & \begin{array}{c}1-h\beta_0(-J \\ -k_3[O_3])\end{array} & 0 & \begin{array}{c}-h\beta_0(k_1[NO] \\ -k_3[NO_2])\end{array} & 0 \\[1.5em]
0 & -h\beta_0(J) & 1-h\beta_0(-k_2[O_2][M]) & 0 & 0 \\[1.5em]
-h\beta_0(-k_1[O_3]) & -h\beta_0(-k_3[O_3]) & -h\beta_0(k_2[O_2][M]) & \begin{array}{c}1-h\beta_0(-k_1[NO] \\ -k_3[NO_2])\end{array} & 0 \\[1.5em]
0 & -h\beta_0(k_3[O_3]) & 0 & -h\beta_0(k_3[NO_2]) & 1
\end{array}
\right]
$$

$$\tag{5.39}$$

From Gear's original code, this matrix array (P), multiplied by a corrector $(\Delta y_{n(m)})$ equals the rights side, B. For each decomposition of P, the code backsubstitutes over several B arrays. After each backsubstitution, $\Delta y_{n(m)}$ and B are both updated. At some point, the values from the decomposed matrix become *old*, causing either the local or global error to exceed its tolerance and requiring P to be updated.

While Gear's original scheme is elegant, it requires the decomposition and backsubstitution over a full matrix of partial derivatives. However, two sparse-matrix techniques reduce calculations enormously. The first is to eliminate all multiplies by zero during matrix decomposition and backsubstitution. However, a problem arises initially because, in order to maintain vectorization, zeros must be eliminated in the same matrix position for each grid cell.

This is initially a problem since most matrix decomposition / backsubstitution routines use partial pivoting (*e.g.* Press *et al.*, 1993), which is the process of interchanging rows for the purpose of putting a more desirable value in the matrix

79

diagonal. Since each interchange depends on the values of elements in the matrices, and the element values depend on the processes occurring in a given grid cell, the interchanges is almost always different for each cell. Thus, partial pivoting prevents vectorization around the grid-cell dimension.

Fortunately, partial pivoting is not required for Gear's method since, as Sherman and Hindmarsh (1980, p. 195) state, "...experience has shown that pivoting is only rarely required in certain applications, and, in any case, if the factorization process should fail, a change in the step-size h will usually improve matters because of the form of P." After eliminating partial pivoting, the same matrix operations can be performed for each grid cell, and zeros can be removed in the same matrix positions for each cell.

However, eliminating zeros without taking the second step of reordering the matrix of partial derivatives gives only a modest speedup. For example, in a set of equations with 92 species and 220 reactions, one pass through the first loop of matrix decomposition required 255,346 multiplications before any sparse-matrix techniques were implemented. When all multiplies by zero were eliminated (but the matrix was not reordered), the number of multiplications decreased to 138,963 (factor of 1.8 speedup). However, when the matrix was first reordered and all multiplies by zero were subsequently removed, the number of multiplications decreased to 1757 (factor of 145 speedup). Thus, the combination of reordering the matrix and removing zeros is the key to speeding up matrix calculations.

In Equation (5.39), the matrix is quite dense (many non-zeros). However, regardless of the matrix density, reordering and then eliminating zeros reduces calculations. In atmospheric chemistry problems, the sparsity of a matrix usually increases with more species. For example, in three cases tested (aqueous, stratospheric gas, and urban gas chemistry), the number of species was 37, 39, and 92, respectively. The corresponding matrix densities were 19.9%, 18.9%, and 8.2%, respectively

80

(Appendix B). Further, the number of operations in the resulting matrices increased fairly linearly with the number of species and equations (*ibid.*). Classical matrix decompositions, on the other hand, are a $(1/3)N^3$ process (Press *et al.*, 1993), where N is the order of the matrix (the number of species, in this case).

The method used to reorder the matrix of partial derivatives was to place rows with the largest number of partial derivative terms on the bottom of the matrix and rows with the fewest on the top. For example, reordering the matrix in Equation (5.39) gives

$$
\begin{array}{c|ccccc}
 & O & NO_3 & NO & NO_2 & O_3 \\
\hline
O & 1-h\beta_0(-k_2[O_2][M]) & 0 & 0 & -h\beta_0(J) & 0 \\
NO_3 & 0 & 1 & 0 & -h\beta_0(k_3[O_3]) & -h\beta_0(k_3[NO_2]) \\
NO & 0 & 0 & 1-h\beta_0(-k_1[O_3]) & -h\beta_0(J) & -h\beta_0(-k_1[NO]) \\
NO_2 & 0 & 0 & -h\beta_0(k_1[O_3]) & 1-h\beta_0(-J-k_3[O_3]) & -h\beta_0(k_1[NO]-k_3[NO_2]) \\
O_3 & -h\beta_0(k_2[O_2][M]) & 0 & -h\beta_0(-k_1[O_3]) & -h\beta_0(-k_3[O_3]) & 1-h\beta_0(-k_1[NO]-k_3[NO_2])
\end{array}
$$

(5.40)

Consequently, during decomposition and backsubstitution, the number of fill-ins is minimized. In the case of the 92-species matrix discussed above, where the initial matrix was 8.2% full, the final matrix was only 9.9% full. Without reordering, the final matrix would have been 73.9% full. Thus, reordering not only reduces computer time but also reduces storage space.

81

5.1.5 Summary of SMVGEAR

In sum, SMVGEAR enables the solution to first-order ordinary differential chemical equations over domains with many spatial grid cells. Further, it solves ODEs for other atmospheric processes, such as coagulation (Appendix C) and condensational growth (Appendix D). In addition, it has an ideal structure for use on parallel computers. Finally, as computer speeds increase, SMVGEAR can be used to solve numerous atmospheric processes simultaneously.

5.2 The Multistep Implicit-Explicit Scheme (MIE)

5.2.1 Description

Another scheme that solves stiff ordinary differential equations for atmospheric gas and aqueous chemical problems is the multi-step implicit-explicit (MIE) method. While MIE gives reasonably quick and accurate results, they are neither so fast nor so accurate as those from SMVGEAR. However, MIE is computationally simple and a reasonable alternative to SMVGEAR. Appendix B describe the mechanics of MIE. Here, additional accuracy and timing tests are shown.

In MIE, the concentration of each species is calculated with the explicit Euler method (first two terms of a Taylor expansion), but each rate of reaction is computed with concentrations estimated by iterating over an implicit formula. Implicit iteration has been used in a number of studies (*e.g.* Hunt, 1966; Shimazaki and Laird, 1970; Turco and Whitten, 1974; Hesstvedt *et al.*, 1978; Hertel *et al.*, 1993).

In MIE, all final concentrations are obtained at the end of a time interval by taking a series of fixed or variable time steps in the interval. In SMVGEAR, each time step is

82

variable and predicted with a formula that gauges the stiffness of the system. While such a prediction can be used in MIE, it currently is not. A characteristic of MIE is that it avoids small (*e.g.* 10^{-3}) startup time steps. However, if the system is too stiff for convergence to occur, the time step is reduced (Appendix B). Furthermore, MIE uses no matrices and requires only about 150 lines of code; thus, it is easily vectorized for use in a multi-dimensional model.

5.2.2 Comparisons to Gear Solutions

Here, comparisons of MIE solutions to accurate SMVGEAR solutions are shown. One set of tests involved a set of 92 species and 222 kinetic reactions and photodissociation processes. The time interval for MIE was 10,000 seconds, and the time steps were 10 and 100 seconds for two particular cases. The initial concentrations of most species were set to zero and those of others were set to values higher than found in the atmosphere. Large concentrations were used to stiffen the system of equations.

For the 10-second comparison, the average absolute-value species concentration difference between SMVGEAR and MIE was 0.07%. For the 100-second comparison, the difference was 0.34%. Figure 5.1 shows additional results from the same set of initial conditions. As the time step increased, the number of iterations during the interval decreased and the accuracy of MIE decreased. When the step exceeded 100 seconds, MIE often took more than the maximum number of iterations; thus, it reduced the time step and took extra iterations.
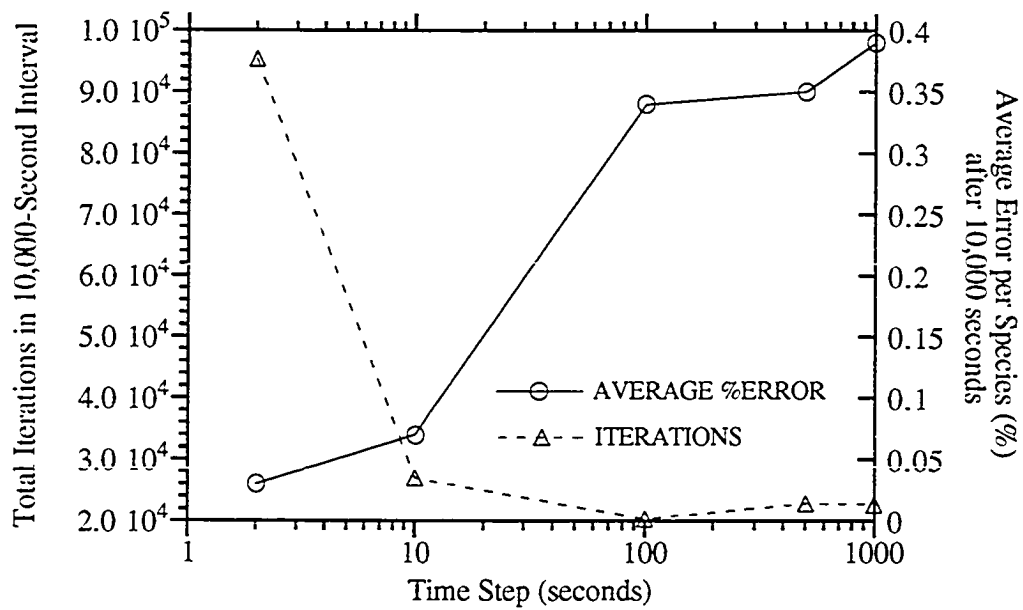
Fig. 5.1. Number of iterations and average absolute-value percent error of each species concentration calculated with the MIE compared to SMVGEAR, versus time step, during a 10,000-second interval. Five time steps are plotted.

Figure 5.2 shows the error per species after different time intervals and time steps. The error of MIE was larger after the first step but decreased each subsequent step. Thus, the time step should be shorter than the time interval. Also, the error after the first 10-second step was greater than that after the first 100- or 1000-second step because, during the latter cases only, the solver reduced the step-size. By reducing the step-size, MIE permitted a series of smaller steps in the 100- and 1000-second cases, and a series of steps reduces the final error.
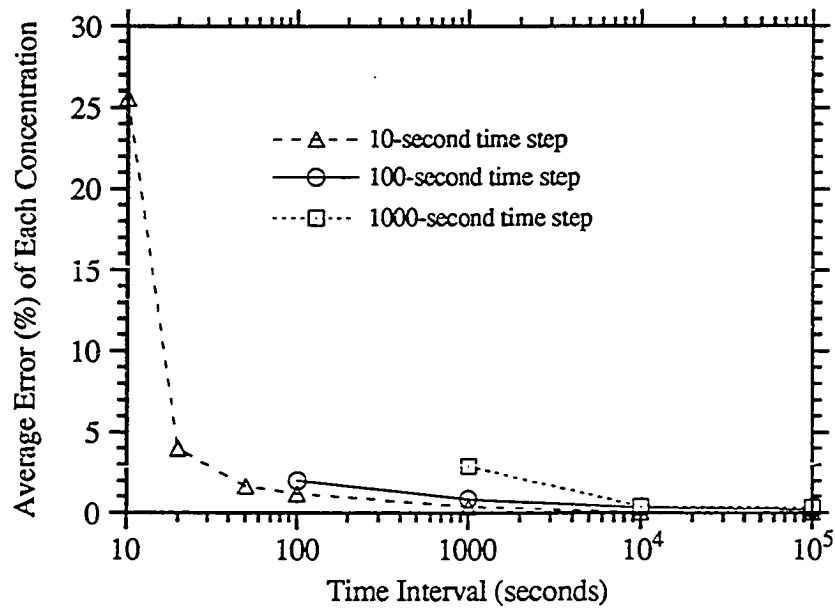
Fig. 5.2. Average absolute-value percent error of each species concentration calculated with MIE after a given time interval, for different time steps.

While the MIE code results in errors after the first in a series of time steps, it converges towards the correct solution in subsequent steps. Table 5.1 shows the rate equations for an example that supports this hypothesis. The initial concentrations of the four species, O_3, $O(3P)$, NO, and NO_2, were 0, 0, 10^{12} and 10^{10} molecules cm^{-3}, respectively. Figure 5.3 traces changes in MIE and SMVGEAR concentrations. The average species error decreased from 3.3% after the first 10-second step to 0.0% after 1000 seconds.

85

Table 5.1. Rate equations for example problem. T = 298 K.

Table 5.1

	EQUATION	RATE (s⁻¹ or cm³#⁻¹ s⁻¹)	REFERENCE

	EQUATION	RATE (s^{-1} or $cm^3 \#^{-1} s^{-1}$)	REFERENCE
$O(3P)$	$\xrightarrow{O_2,M} O_3$	$k_1 = 1.4 \times 10^3 \, e^{1175/T}$	Gery et al., 1989
$NO + O_3$	$\longrightarrow NO_2 + O_2$	$k_2 = 1.8 \times 10^{-12} \, e^{-1370/T}$	Gery et al., 1989
NO_2	$\longrightarrow NO + O(3P)$	$J_1 = 1.7 \times 10^{-2}$	assumed
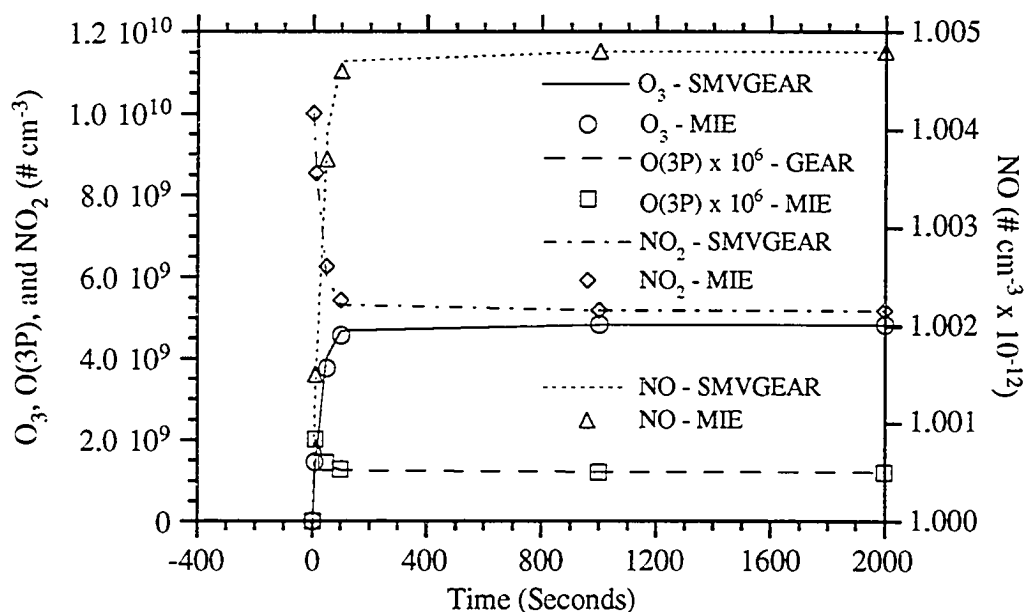
Fig. 5.3. O_3, $O(3P)$, NO, and NO_2 concentrations versus time: a comparison of MIE to SMVGEAR solutions. The time step was 10 seconds and the rate equations are listed in Table 5.1.

Next, the MIE code was tested against SMVGEAR, over a single time interval, using an aqueous reaction set that included 36 active species, 62 aqueous reactions and

86

two photolysis reactions. The pH was held at 4.83, the water content was held at 4.0 x 10^{-7} L-H_2O L^{-1}-air, and the temperature was held at 298 K. I also assumed a single drop of radius 10 μm, no continuous dissolution of gas into or out of the drop, and fairly random initial concentrations. Using a 10-second time step, MIE yielded an average concentration error of 0.09% after 10,000 seconds for this case. A 100-second time step caused a 0.42% error per species.

5.2.3 Determining Parameter Values

The MIE code requires the setting of three major parameters: the time step, LT, and Np (as described in Appendix B). To determine ideal parameter values for a given chemistry set, an accurate solution is needed for comparing MIE results against. While SMVGEAR gives an accurate solution, MIE can also give an accurate solution if its time step is reduced to 0.1 second or less and LT and Np are set to high values. After finding an accurate solution, the accuracy and speed of MIE are tested with varying values of LT and Np and with time steps longer than 0.1 second. After many comparisons, parameter values are selected that gave both fast and accurate solutions. Such tests were carried out for a multiple grid-cell model with both the air pollution and stratospheric chemistry set.

To prepare for the smog chemistry tests, two 24-hour simulations were run with SMVGEAR (S1 and S2), using the 92 species and 222 reactions described in Section 5.2.2. The initial conditions were the same as those described for cases SMOG1 and SMOG2 in Appendix B.

Next, several cases of simulations S1 and S2 (Table 5.2) were run with the MIE code, over one grid cell, on a single processor of a CRAY YMP. In each case, either a 10-, 30-, or 60-second time step and various values of LT and Np were used. In many cases, LT and Np were changed during only the last step of each 1200 second interval. $LT1$ always equaled the original value of LT, even during the last step. The differences

between MIE and SMVGEAR concentrations after the 24-hour simulations were then computed.

To time MIE over a large grid, cases of S1 and S2 were tested over 4000 grid cells for different lengths of time. In each case, the time to solve over 4000 cells was about 40 times faster per cell than the time to solve over one cell, regardless of the length of the run. Thus, if the time to solve over one box was 10 seconds, the time to solve over 4000 boxes was about 1000 seconds. Numerous grid cells increase efficiency because the code is vectorized around the grid-cell dimension.

Figures 5.4a and 5.4b and Table 5.2 summarize results from the simulations. They also identify several characteristics of MIE, listed as follows:

1) The time step, LT, and Np affected the efficiency of the solver. When the time step was large, MIE iterated less per time interval but more per time step. When LT was large, MIE iterated more to converge implicit concentrations of short-lived species. Finally, when Np was large, MIE iterated more, increasing solution accuracy.

2) When the code converged explicit concentrations during the last time step of an interval (Np during the last step = 250), the number of iterations was greater than and the accuracy was no better than when it calculated more concentrations implicitly during the last step (LT during the last step = 10^1 or 10^2).

3) When MIE calculated all final concentrations implicitly ($LT = 0$ -- connected points in Figures 5.4a and 5.4b) while taking 11 or 16 iterations per step ($Np = 11$ or 16), and a step of 10 or 30 seconds, the results were fairly accurate. The results were also reasonable when MIE took 21 iterations per step and a step of 60 seconds. However, explicit solutions ($LT \gg 0$) generally required fewer iterations for the same accuracy.

4) When the time step of MIE was increased, the minimum possible error increased. For a 10-second time step, the smallest error of S1 was 0.6% per species

88

(cases A and G) and that of S2 was 0.37% (B and C). For a 30-second step, the smallest error of S1 was 2.14% (P and T) and that of S2 was 1.11% (T). Finally, for a 60-second step, the smallest error of S1 was 4.42% (5) and that of S2 was 2.55% (5). Thus, smaller and smaller time steps increase the accuracy of solutions.

5) When MIE used a small enough time step, it rarely reduced the time step further. In no case of S1 did the code reduce the time step [column S1(a) of Table 5.2]. In the 30- and 60-second time step cases of S2, the code frequently reduced the step, increasing the solving time. For smog chemistry, a time step of 10 seconds or less usually permitted convergence and prevented a reduction in the time step.

6) The boxes in Figures 5.4a and 5.4b enclose cases where both accuracy and speed of the solution were minimized. For example, cases C-S1 and C-S2 resulted in an error of less than 1% per species and a speed of less than 75 minutes per day. Case R gave slightly less accurate solutions in faster time. The only difference between C and R was the time step. While values for time step, LT, and Np that result in accurate solutions during one simulation may not always result in accurate solutions during another, the probability of accuracy increases the smaller the time step and the larger LT and Np.

Table 5.2. Values of time step, LT, and Np for the cases identified in Figures 5.4a, 5.4b, and 5.6. Each letter in the CASE column corresponds to a point in at least one of the figures. S1 and S2 are air pollution simulations run with different initial conditions. ST1 and ST2 are stratospheric simulations run with different photorates. The only difference between each case of each simulation is the value of the time step, LT, and / or Np. Also shown are (column a) the total number of time steps taken by MIE over one day of simulations for S1 and S2 and over four days for ST1 and ST2, and (column b) the average number of iterations per time step in each case.

Table 5.2

CASE	STEP SIZE (SEC.) (b)	ORIGINAL LT	Np	LAST STEP LT	Np	S1 Np	S1 (a)	S2 (b)	S2 (a)	ST1 (b)	ST1 (a)	ST2 (b)	ST2 (a)
A	10	10^8	1	10^2	1	8640	10.0	8644	12.4				
B	10	10^7	1	10^2	1	8640	7.1	8640	9.4	34,560	3.5	34,560	3.7
C	10	10^6	1	10^2	1	8640	5.6	8640	7.3	34,560	3.1	34,560	3.1
D	10	10^5	1	10^2	1	8640	4.9	8640	8.3				
E	10	10^4	1	10^2	1	8640	3.5	8640	6.9				
F	10	10^3	1	10^2	1	8640	3.3	8640	5.3				
G	10	10^8	1	10^8	250	8640	11.3	8640	13.8				
H	10	10^7	1	10^7	250	8640	8.4	8640	10.6				
I	10	10^6	1	10^6	250	8640	6.9	8640	8.7				
J	10	10^5	1	10^5	250	8640	6.3	8640	6.9				
K	10	10^4	1	10^4	250	8640	4.9	8640	5.5				
L	10	10^3	1	10^3	250	8640	4.6	8640	3.9				
M	10	0	16	0	16	8640	16	8640	16				
N	10	0	11	0	11	8640	11	8640	11				
O	10	0	6	0	6	8640	6	8640	6				
P	30	10^8	1	10^2	1	2880	15.2	4288	25				
Q	30	10^7	1	10^2	1	2880	8.6	2944	11.1	11,520	4.5	11,520	4.2
R	30	10^6	1	10^2	1	2880	7.4	2956	10.7	11,520	3.7	11,520	3.5
S	30	10^5	1	10^2	1	2880	5.5	2960	9.6				
T	30	10^8	1	10^8	250	2880	19.0	4176	28.2				
U	30	10^7	1	10^7	250	2880	12.7	2956	15.0				
V	30	10^6	1	10^6	250	2880	11.4	2960	13.6				
W	30	10^5	1	10^5	250	2880	9.6	2960	13.6				
X	30	0	16	0	16	2880	16	2880	16				
Y	30	0	11	0	11	2880	11	2880	11				
Z	30	0	6	0	6	2880	6	2880	6	11,520	6	11,520	6
1	60	10^7	1	10^1	1	1440	12.1	2040	25.2				
2	60	10^6	1	10^1	1	1440	9.51	1912	22.4	5760	4.8	5760	4.6
3	60	10^5	1	10^1	1	1440	7.81	1716	18.9				
4	60	10^4	1	10^1	1	1440	7.15	1816	18.8				
5	60	10^7	1	10^7	250	1444	20.2	2060	31.8				
6	60	10^6	1	10^6	250	1440	18.1	1996	29.1				
7	60	10^5	1	10^5	250	1440	15.9	1736	25.7				
8	60	10^4	1	10^4	250	1440	13.6	1896	26.3				
9	60	0	26	0	26	1440	26	1440	26				
10	60	0	21	0	21	1440	21	1440	21				
11	60	0	16	0	16	1440	16	1440	16				
12	60	0	11	0	11	1440	11	1440	11				
12	60	10^5	250	10^5	250	5760	13.1	5760	12.9				

90
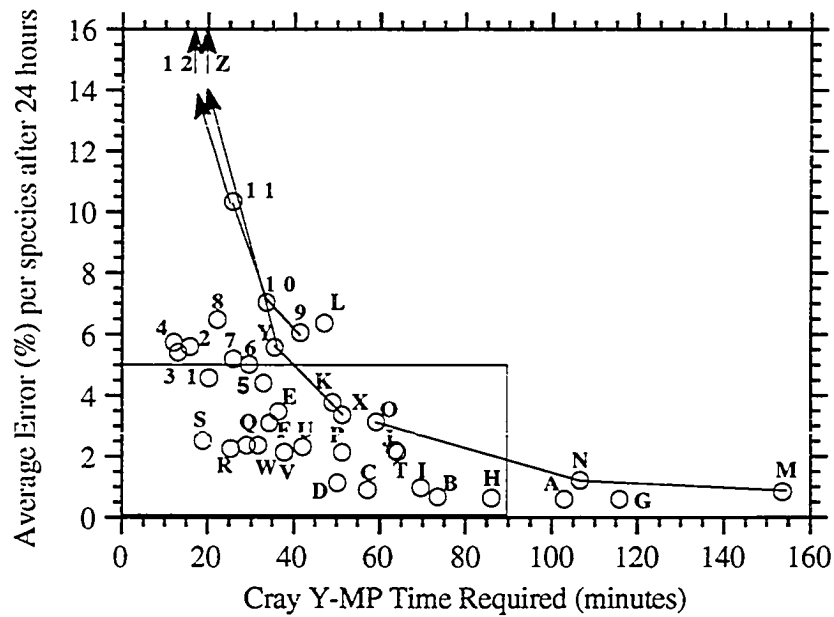
Fig. 5.4a. Cases of simulation S1.

Figs. 5.4a and 5.4b. Accumulated absolute-value percent error per species after 24 hours for several cases of simulations S1 and S2, versus CPU time to solve each case over a 4000-cell grid. Initial concentrations in all cases were the same. For each case, the time step, LT, and I or Np were varied in the MIE code. Each letter or number next to a data point corresponds to a case number in Table 5.2. The photorates were changed every one-half hour during the first 12 hours and were set to zero during the second 12 hours. The box in the bottom-left corner contains cases where the solving time was less than 90 minutes per day and the error was less than 5% per species after one day. The points connected by lines indicate cases where all final concentrations were calculated from Equation (13) of Appendix B, and no final concentrations were calculated explicitly.

91
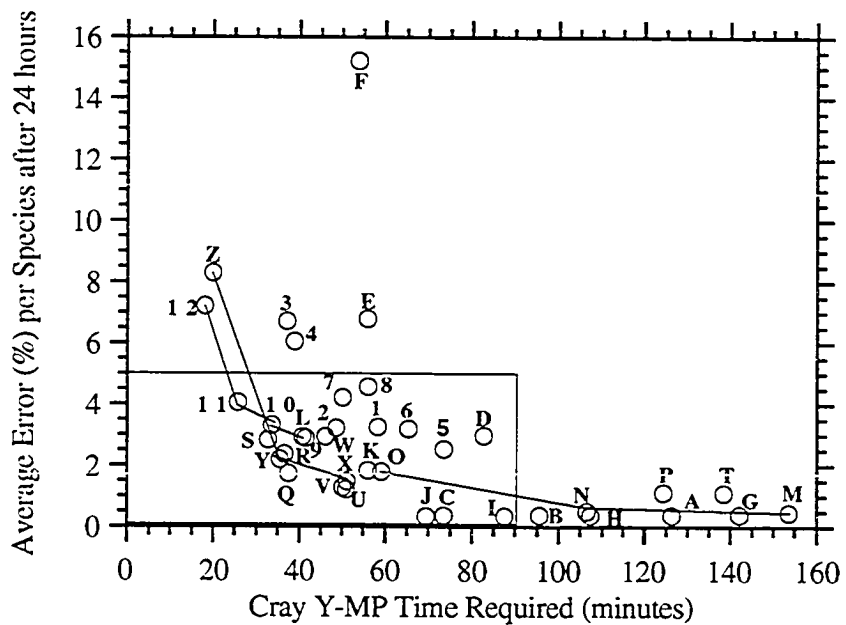
Fig. 5.4b. Cases of simulation S2.

Figures 5.5a and 5.5b show the diurnal change in concentration of seven of the 92 species simulated in case C-S1 of Table 5.2.

92
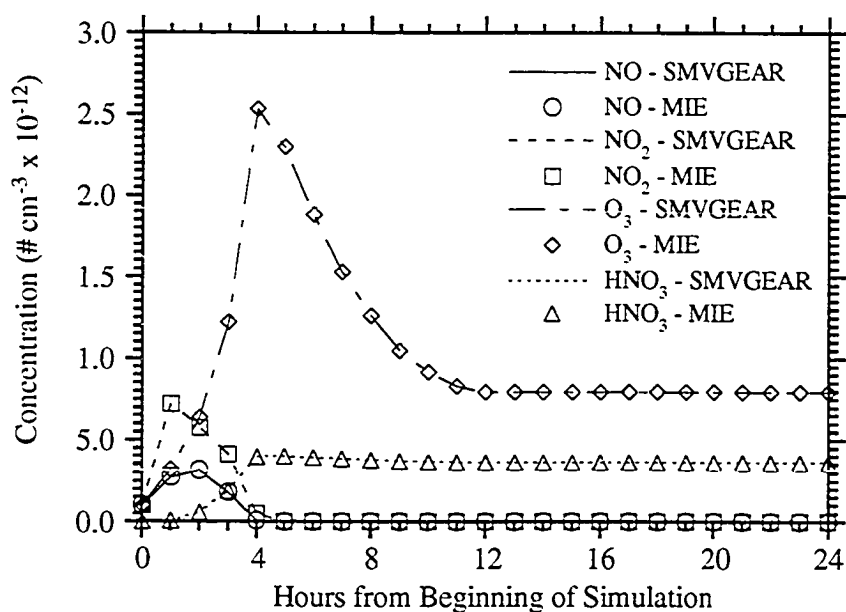
Fig. 5.5a. NO, NO$_2$, O$_3$, and HNO$_3$.

Figs. 5.5a and 5.5b. Twenty-four hour comparison of MIE vs. SMVGEAR concentrations of several species. The data are from air pollution simulation C-S1 of Table 5.2. The time step of the MIE code was 10 seconds. Photorates changed every one-half hour during the first 12 hours and were zero during the second 12 hours. MIE and SMVGEAR predictions are shown for each hour.

93
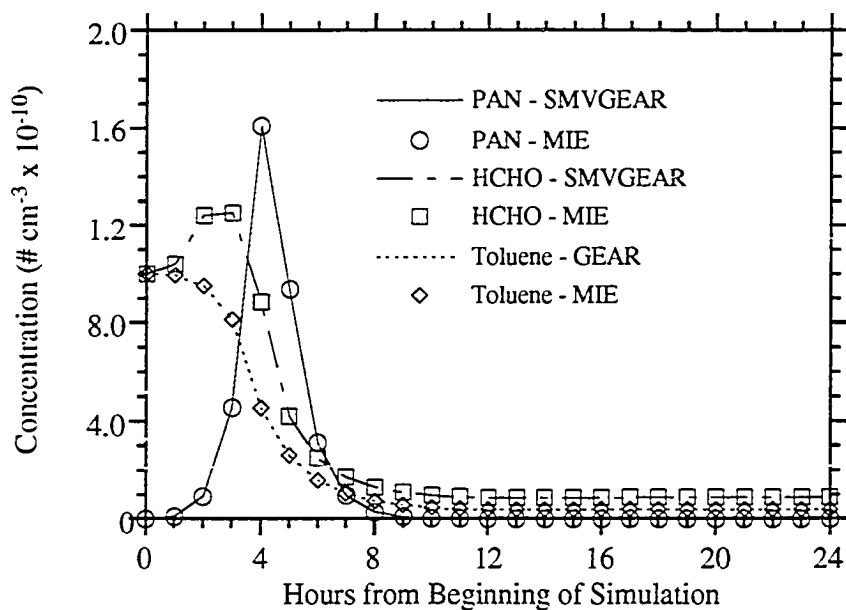
Fig. 5.5b. PAN, formaldehyde, and toluene.

In a second group of simulations, a set of 42 species, 84 chemical reactions, and 24 photodissociation processes were tested for a stratospheric chemistry case (S. Elliott and R. P. Turco, *pers. comm.*). An altitude of 20 km (pressure of 55.3 mb) and a temperature of 217 K were assumed. Two 4-day simulations (ST1 and ST2) were run with SMVGEAR. Photorates changed with a sine function 12 of every 24 hours.

After each MIE simulation was timed for a single grid cell, the time on a CRAY YMP was extrapolated to 4000 cells. Table 5.2 and Figure 5.6 summarize statistics from the simulations, and Figure 5.7 shows the change in concentration of four of the 42 species simulated in case B-ST2. In sum, with a 10-second time step, the time to solve was about three times greater but the accuracy was about six times greater than with a 30-second step. The number of iterations per step in each stratospheric case was approximately half that per step in each corresponding 24-hour air pollution case.

94

However, the number of species and equations in the stratospheric set was about half those in the air pollution set.
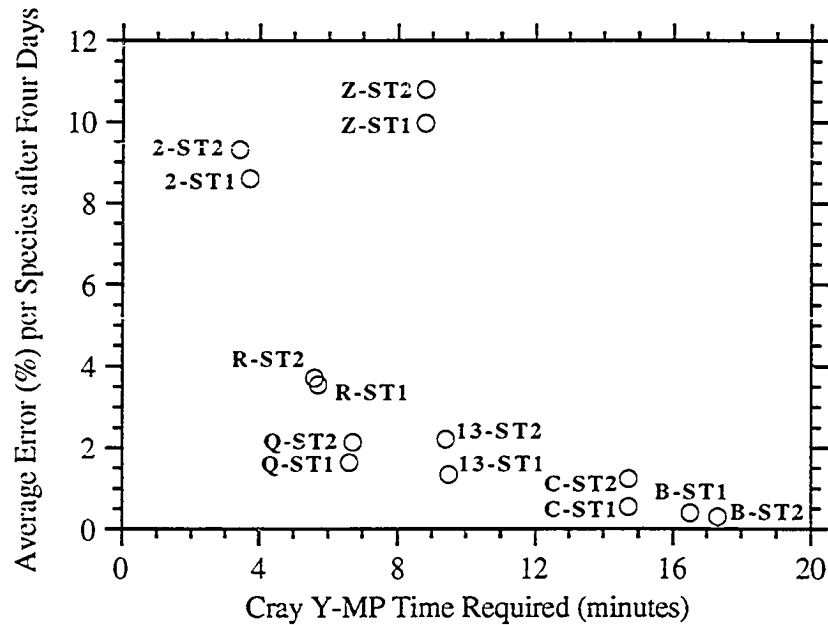
Fig. 5.6. Accumulated absolute-value percent error per species after four days for several cases of simulations ST1 and ST2, versus CPU time per day to solve each case over a 4000-cell grid. The initial concentrations in all cases were the same. For each case, the time step, LT, and / or Np in the MIE code were varied. Each identifier next to a data point corresponds to a case number in Table 5.2. Photorates were changed every half-hour during the first 12 hours and were set to zero during the second 12 hours of each day.

95
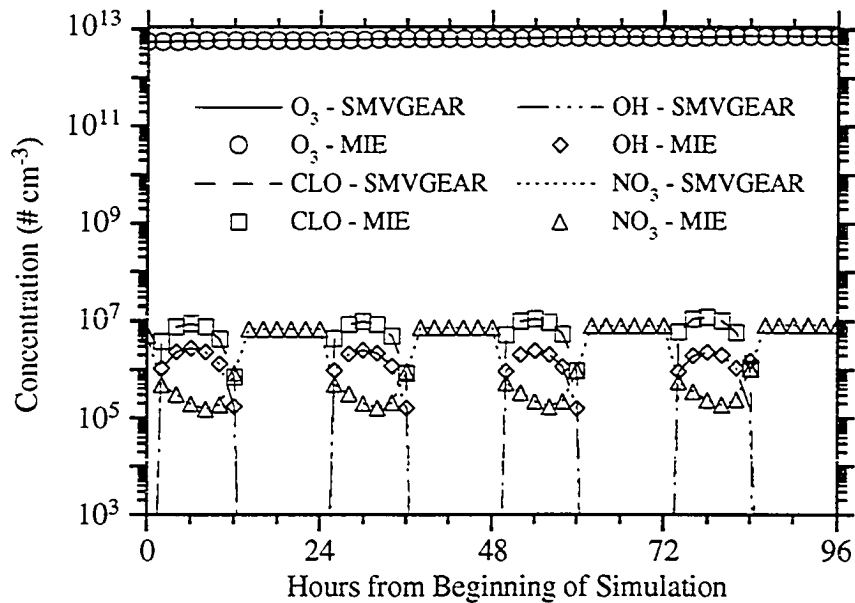
Fig. 5.7. Four day comparison of O3, CLO, OH, and NO3 concentrations calculated by MIE and SMVGEAR. The time step for MIE was 10 seconds. The data were from stratospheric simulation B-ST2 in Figure 5.6 and Table 5.2. Photorates changed every one-half hour during the first 12 hours and were zero during the second 12 hours of each day.

In the air pollution simulations, the conditions of cases C and R gave a combination of reasonably fast and accurate solutions. Figure 5.6 shows that, in the stratospheric cases, C and R also produced reasonable results. The figure further shows that when MIE calculated all final concentrations implicitly (cases Z-ST1 and Z-ST2), it required almost twice as many iterations yet resulted in solutions nearly one-third as accurate as when it calculated final concentrations explicitly (R-ST1 and R-ST2). Finally, columns ST1(a) and ST2(a) of Table 5.2 show that MIE never reduced the time step, probably because the conditions were less stiff than in the smog simulations.

96

5.2.4 Discussion of Convergence

MIE relies on convergence of iterated explicit to iterated implicit concentrations when rates are calculated with iterated implicit concentrations. It also relies on convergence of explicit to correct solutions after several time steps.

To demonstrate implicit and explicit convergence, an example generated from a smog chemistry simulation is shown. Figure 5.8 shows implicit and explicit concentrations of three species versus iteration number during a 10-second time step. Each implicit concentration converged by the 30th iteration. Explicit concentrations varied dramatically during the first 10 iterations, then converged to the implicit concentrations. While explicit NO_2 and O_3 converged by the 30th iteration, explicit O(3P) converged by only the 60th iteration. Explicit O(3P) converged slower than did implicit O(3P) because, while most of the 92 implicit concentrations in the system fully converged by the 30th iteration, some did not. Slight non-converged implicit solutions for some species can perturb explicit solutions for other, short-lived species.

In Figure 5.8 implicit O(3P) converged to 2.139×10^7 cm^{-3} by iteration 30 but explicit O(3P) converged by only iteration 50. Because implicit O(3P) converged faster, using its value as the final concentration at an early iteration, such as 20, could speed up the solver. However, at iteration 20, the implicit value was 2.135×10^7 cm^{-3} and the explicit value was 4.618×10^{10} cm^{-3}. While the implicit value was nearly correct, using it destroyed 4.616×10^{10} cm^{-3} of odd-oxygen since the explicit, not the implicit, value was mass-conserving. Because such losses can accumulate and cause errors after several time steps, explicit concentrations are used as final concentrations as frequently as possible.

97
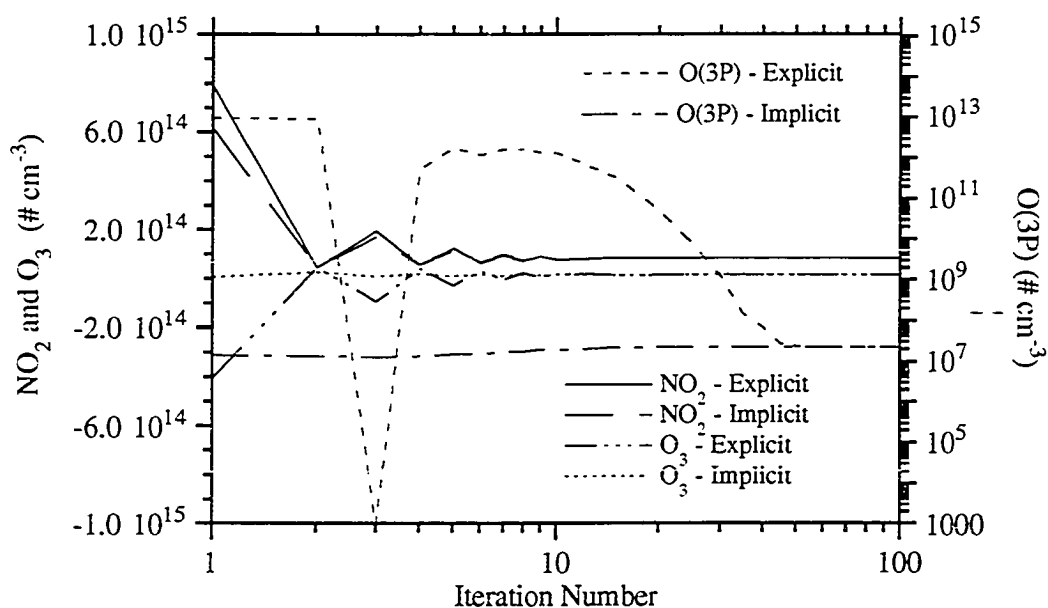
Fig. 5.8. Explicit and implicit concentrations from MIE of three species versus iteration number during a 10-second time step.

While explicit and implicit concentrations converge during a time step, neither converge to correct solutions during the first step of an interval unless the step is small or reaction rates are slow. This is because most chemistry adjustments occur during the first time step, and the ability of MIE to resolve rapid changes is limited by the step size. However, solutions converge towards correct values after a series of time steps because adjustments subsequently become less dramatic.

5.2.5 Summary of MIE

In sum, MIE solves ordinary differential equation for atmospheric chemical problems. It requires relatively little computer programming and can be applied to short and long timescale problems. Furthermore, three variables (the time step, LT, and Np)

control the accuracy and speed of the code. The model was applied to air pollution, stratospheric, and aqueous chemistry sets. In all cases, MIE solved fairly accurately when the time step was 10 seconds. Other chemistry sets, however, may require different time steps. One can choose ideal values for the time step, LT, and Np by following the procedure described in Section 5.2.3. An advantage of MIE is that it is easily vectorized on a supercomputer and it is efficient enough for many two- and three-dimensional modeling problems. However, as shown in Appendix B, it is not so fast or accurate as SMVGEAR.

5.3 A Matrix Inversion Scheme for Family Chemistry

5.3.1 Discussion of Family Chemistry Solutions

A third method to solve atmospheric chemical equations is the family method. Here, a matrix inversion technique to predict species concentrations in a family chemistry solver, is discussed.

Modelers have often used family chemistry methods to solve atmospheric chemistry problems (*e.g.* Crutzen, 1971; Turco and Whitten, 1974; Brasseur and Solomon, 1986; Austin, 1991; Elliott *et al.*, 1993). A family chemistry solution consists of grouping species that cycle quickly among each other in the same family and then projecting the family concentration forward a time step with the first two terms of a Taylor series (also known as an explicit [forward] Euler step). Grouping species together that cycle quickly cancels out the fast reaction rates. For example, suppose three species -- A, B, and C -- are in a family and one species -- D -- is outside the family. If the only reactions in the system are A --> B, B --> C, and C --> D, where k_a, k_b, and k_c are the

99

rates of the three reactions, respectively, then the first-order, ordinary differential equations for A, B, and C are

$$\frac{d[A]}{dt} = -k_a[A],$$ (5.41)

$$\frac{d[B]}{dt} = k_a[A] - k_b[B],$$ (5.42)

and

$$\frac{d[C]}{dt} = k_b[B] - k_c[C],$$ (5.43)

respectively. Because A, B, and C are in the same family, the family concentration equals [A] + [B] + [C], and the time rate of change of the family concentration equals

$$\frac{d[FAM]}{dt} = \frac{d[A]}{dt} + \frac{d[B]}{dt} + \frac{d[C]}{dt} = -k_c[C].$$ (5.44)

Thus, in (5.44), all rates involving the cycling species in the family cancel out, and the net loss term from the family remains. Consequently, after one explicit Euler time step, the new family concentration becomes

$$[FAM]^{t+1} = [FAM]^t + \frac{d[FAM]}{dt}\Delta t = [FAM]^t - k_c[C]\Delta t .$$ (5.45)

When setting up a family, fast leaks out of the family can be avoided by placing both quick-reacting reactants and their product(s) in the same family. After the future concentration of a family is found, the concentration of each species within a family

100

needs to be determined in order to calculate reaction rates for the next time step. One way to partition species is to set up the relationship,

$$[\text{FAM}]^{t+1} = [\text{A}]^{t+1} + [\text{B}]^{t+1} + [\text{C}]^{t+1} = [\text{A}]^{t+1}\left(1 + \frac{[\text{B}]^{t+1}}{[\text{A}]^{t+1}} + \frac{[\text{C}]^{t+1}}{[\text{A}]^{t+1}}\right), \quad (5.46)$$

and assume reactions (5.42) and (5.43) are in steady state, so that

$$\frac{[\text{C}]^{t+1}}{[\text{A}]^{t+1}} = \frac{k_a}{k_c} \qquad \text{and} \qquad \frac{[\text{B}]^{t+1}}{[\text{A}]^{t+1}} = \frac{k_a}{k_b}. \quad (5.47)$$

Consequently, the final concentration of A is

$$[\text{A}]^{t+1} = [\text{FAM}]^{t+1}\Big/\left(1 + \frac{k_a}{k_b} + \frac{k_a}{k_c}\right) \quad (5.48)$$

and those of B and C are

$$[\text{B}]^{t+1} = [\text{A}]^{t+1}\frac{k_a}{k_b} \qquad \text{and} \qquad [\text{C}]^{t+1} = [\text{A}]^{t+1}\frac{k_a}{k_c}. \quad (5.49)$$

However, to avoid assuming steady-state, each species can be partitioned with

$$[\text{A}]^{t+1} = \frac{[\text{FAM}]^{t+1}[\text{A}]^{est}}{[\text{A}]^{est} + [\text{B}]^{est} + [\text{C}]^{est}}, \quad (5.50)$$

(same for B and C) where

$$[\text{A}]^{est} = [\text{A}]^{t}e^{-1\Delta t} + \frac{P}{1}\left(1 - e^{-1\Delta t}\right) \quad (5.51)$$

101

(also same for B and C). In (5.51), P is the net production rate (No cm^{-3} s^{-1}) and l is the implicit chemical loss rate (s^{-1}) of the species. Partitioning is inherently an estimation process. However, while masses of individual atoms are usually not conserved during family chemistry calculations, masses of the entire family are.

5.3.2 Estimating Concentrations by Matrix Inversion

To calculate P, l, and the derivatives used to find family concentrations, reaction rates are multiplied by species concentrations. Over long time steps (*e.g.* one-half hour), these concentrations can change dramatically. Thus, a good estimate of a species concentration improves the reaction rate prediction. Often, concentration estimates from the middle of the time step are desired. A way to estimate such concentrations is with the scheme discussed here, a matrix-inversion concentration predictor. This scheme requires no iteration and serves only to estimate concentrations for use in family chemistry calculations.

For this scheme, any number of species can be identified as *matrix inversion* (MI) species. Concentrations of MI species are calculated and all other species concentrations are assumed constant during the matrix inversion. Suppose three species -- A, B, and C (matrix-inversion species) -- are in a particular family, and suppose species G, D, E, and F (non matrix-inversion species) are in other families. Further suppose estimated concentrations of A, B, and C at the middle of the time step are desired. Equations (5.52) - (5.59), below, list eight possible types of reactions involving MI and non-MI species. The equations are

| (k_1) | D | + E | ----> F | + G, | (5.52) |
| (k_2) | E | + G | ----> A | + F, | (5.53) |

(k_3)	**C**	+ F	---->	**B**	+ G,	(5.54)
(k_4)	**B**	+ G	---->	**B**	+ D + E,	(5.55)
(k_5)	**C**	+ G	---->	**C**	+ A + E,	(5.56)
(k_6)	**B**	+ A	---->	**C**	+ D,	(5.57)
(k_7)	**C**	+ B	---->	**B**	+ G + E,	(5.58)

and

(k_8)	**A**	+ A	---->	**C**	+ F,	(5.59)

where the bold indicates a matrix-inversion species, and the k's to the left are reaction rates. For each MI species, the first-order, ordinary differential equations arising from these reactions are

$$\frac{d[\mathbf{A}]}{dt} = k_2[\mathbf{E}][\mathbf{G}] + k_5[\mathbf{C}][\mathbf{G}] - k_6[\mathbf{B}][\mathbf{A}] - 2k_8[\mathbf{A}][\mathbf{A}], \tag{5.60}$$

$$\frac{d[\mathbf{B}]}{dt} = k_3[\mathbf{C}][\mathbf{F}] - k_6[\mathbf{B}][\mathbf{A}], \tag{5.61}$$

and

$$\frac{d[\mathbf{C}]}{dt} = k_8[\mathbf{A}][\mathbf{A}] + k_6[\mathbf{B}][\mathbf{A}] - k_3[\mathbf{C}][\mathbf{F}] - k_7[\mathbf{C}][\mathbf{B}]. \tag{5.62}$$

Next, by writing (5.60) - (5.62) in finite difference form, future concentrations of A, B, and C can be solved by inverting a matrix. The finite difference forms of the equations are

$$\frac{[\mathbf{A}]^{t+1} - [\mathbf{A}]^{t}}{\Delta t} = k_2[\mathbf{E}]^{t}[\mathbf{G}]^{t} + k_5[\mathbf{C}]^{t}[\mathbf{G}]^{t} - k_6[\mathbf{B}]^{t}[\mathbf{A}]^{t+1} - 2k_8[\mathbf{A}]^{t}[\mathbf{A}]^{t+1},$$

103

$$\frac{[\mathbf{B}]^{t+1} - [\mathbf{B}]^t}{\Delta t} = k_3[\mathbf{C}]^{t+1}[\mathbf{F}]^t - k_6[\mathbf{B}]^{t+1}[\mathbf{A}]^t, \tag{5.64}$$

and

$$\frac{[\mathbf{C}]^{t+1} - [\mathbf{C}]^t}{\Delta t} = k_8[\mathbf{A}]^t[\mathbf{A}]^{t+1} + \frac{1}{2}k_6\left([\mathbf{B}]^t[\mathbf{A}]^{t+1} + [\mathbf{B}]^{t+1}[\mathbf{A}]^t\right)$$

$$-k_3[\mathbf{C}]^{t+1}[\mathbf{F}]^t - k_7[\mathbf{C}]^{t+1}[\mathbf{B}]^t, \tag{5.65}$$

where loss terms of only species whose concentration change include the superscript

$(t+1)$. Rewriting (5.63) - (5.65) in matrix form gives

$$\begin{bmatrix} 1 \\ +k_6[\mathbf{B}]^t\Delta t & 0 & 0 \\ +2k_8[\mathbf{A}]^t\Delta t & & \\ 0 & 1 & -k_3[\mathbf{F}]^t\Delta t \\ & +k_6[\mathbf{A}]^t\Delta t & \\ -\frac{1}{2}k_6[\mathbf{B}]^t\Delta t & -\frac{1}{2}k_6[\mathbf{A}]^t\Delta t & 1 \\ -k_8[\mathbf{A}]^t\Delta t & & +k_3[\mathbf{F}]^t\Delta t \\ & & +k_7[\mathbf{B}]^t\Delta t \end{bmatrix} \begin{bmatrix} [\mathbf{A}]^{t+1} \\ [\mathbf{B}]^{t+1} \\ [\mathbf{C}]^{t+1} \end{bmatrix} = \begin{bmatrix} [\mathbf{A}]^t \\ +k_2[\mathbf{E}]^t[\mathbf{G}]^t\Delta t \\ +k_5[\mathbf{C}]^t[\mathbf{G}]^t\Delta t \\ [\mathbf{B}]^t \\ [\mathbf{C}]^t \end{bmatrix},$$

$$(5.66)$$

where the only unknowns are the future concentrations. Inverting (or decomposing and

backsubstituting over) the above matrix results in solutions for the estimated future

concentrations -- $[\mathbf{A}]^{t+1}$, $[\mathbf{B}]^{t+1}$, and $[\mathbf{C}]^{t+1}$ -- after time Δt.

5.3.3 Summary of Family Chemistry / Matrix Inversion Scheme

In sum, a family chemistry scheme is used to predict future concentrations of

families and then to partition the species within the family. The partitioned concentrations

are then used to calculate rates of reaction for the next advancement of the family concentration. Since time steps for family chemistry are often long, concentrations used for calculating reaction rates can be estimated at the middle of the time step. In order to estimate concentrations for selected species, a matrix inversion scheme was developed.

Chapter 6

Aerosol Processes

In this chapter and Appendices B - E, numerical methods used to simulate aerosol physical processes in GATOR are summarized. The primary processes are nucleation (Section 6.2), coagulation (6.3), condensational growth (6.4), dissolutional growth (6.4), chemical equilibrium (6.4 and 6.5), and aqueous chemistry (6.5). Aerosol deposition, sedimentation, and transport are discussed in Chapter 7. Further, Appendix C describes the numerical treatment of coagulation in more detail, Appendix D describes condensational growth and evaporation in more detail, Appendix E describes solutions to dissolutional growth, evaporation, and chemical equilibrium in more detail, and both Appendix B and Chapter 5 describe SMVGEAR, the aqueous chemistry solver.

6.1 Overview of the Aerosol Model

The aerosol model discussed here contains numerical solution mechanisms for several physical processes, described in Figure 1.3 and 4.1 and in Appendices B - E. Here, these processes are discussed.

In GATOR, aerosol microphysics and chemical processes are time-split from each other (Figure 4.1). Gas-aerosol physical and chemical processes in GATOR are solved in

106

the following order: (1) gas-phase chemistry, (2) homogeneous and heterogeneous nucleation, (3) coagulation, (4) equilibrium vapor pressures, (5) condensational, dissolutional growth, and evaporation, (6) chemical equilibrium within aerosols, and (7) aqueous chemistry.

In addition, GATOR permits any number of particle size bins whose volumes change independently of one another (Appendix D). Each size bin contains any number of particles, and the particles contain any number of solid, liquid, or ion components. Table A.5 lists the components currently simulated within particles of each aerosol size bin.

6.2 Nucleation Mechanisms

In GATOR, four types of nucleation rates are simulated: homogeneous homomolecular, homogeneous binary, heterogeneous homomolecular, and heterogeneous binary nucleation. Here, classical nucleation theory and the method of calculating nucleation rates in GATOR are briefly described.

Classical nucleation theory suggests that the Gibbs free energy change (Joules) for the nucleation of a material with radius r_p (cm) is (e.g. Seinfeld, 1986)

$$\Delta G = -\frac{4}{3}\pi r_p^3 \rho \frac{RT}{M} \ln S + 4\pi r_p^2 \sigma, \tag{6.1}$$

where ρ is the density (g cm^{-3}) of the nucleating drop, R is the gas constant (J mol^{-1} K^{-1}), T is temperature (K), M is the molecular weight of the species (g mole^{-1}), S is the saturation ratio (unitless), and σ is the surface tension (J cm^{-2}). When $S < 1$, ΔG increases with increasing radius. When $S > 1$, ΔG first rises then decreases with

107

increasing radius, peaking at the point where $d\Delta G / dr_p = 0$. Taking the derivative of Equation (6.1) with respect to radius gives

$$\frac{dG}{dr_p} = 0 = -4\pi r_c^2 \rho \frac{RT}{M} \ln S + 8\pi r_c \sigma. \qquad (6.2)$$

From this, the radius of maximum free energy (critical radius) is

$$r_c = \frac{2\sigma M}{\rho RT \ln S}, \qquad (6.3)$$

and the number of molecules in a nucleated cluster is

$$n_c = \frac{32\pi\sigma^3 M^2 A}{\rho^2 (RT \ln S)^3}. \qquad (6.4)$$

where A is Avogadro's number (No. molecules mole^{-1}). Further, combining (6.1) and (6.2) gives the change in free energy at the critical radius as

$$\Delta G_{hom}^* = \frac{4}{3}\pi r_c^2 \sigma. \qquad (6.5)$$

Consequently, the homogeneous nucleation rate (No. particles cm^{-3} s^{-1}) can be expressed as (Kiang and Stauffer, 1973; Hamil! et al., 1982; Zhao, 1993)

$$J_{hom} = 4\pi r_c^2 \beta_a N_b \exp\left(\frac{-\Delta G_{hom}^*}{k_B T}\right). \qquad (6.6)$$

108

where k_B is Boltzmann's constant (J K^{-1}, $k_B = R/A$) and

$$\beta_a = N_a \left(\frac{k_B T}{2\pi M_a} \right)^{1/2}, \qquad (6.7)$$

(No. molecules cm^{-2} s^{-1}). Further, N_a is the concentration (No. molecules cm^{-3}) of gas a, N_b is the concentration of gas b (gas b is the same as gas a for homomolecular but different for binary nucleation), and M_a is the molecular weight of gas a. For heterogeneous nucleation,

$$\Delta G_{het}^* = \Delta G_{hom}^* f(x,m), \qquad (6.8)$$

where $f(x,m)$ is a correction factor dependent on x, which is the ratio of the particle radius to the critical radius, and on m, which is the cosine of the contact angle. If $m = 0$, then all the nucleating gases will adsorb to the surface. If the contact angle is 180 degrees, no nucleating gases will adsorb to the surface. For empirical functions relating f to x and m, refer to Fletcher (1958), Zhao (1993), and Hamill *et al.* (1982).

Next, the rate of production of nucleated particles (No. particles cm^{-2} s^{-1}) is (*e.g.* Hamill *et al.*, 1982)

$$J_{het} = 4\pi r_c^2 \beta_a \beta_b \tau \exp\left(\frac{-\Delta G_{het}^*}{k_B T} \right). \qquad (6.9)$$

where

$$\beta_b = N_b \left(\frac{k_B T}{2\pi M_b} \right)^{1/2} \qquad (6.10)$$

109

(No. molecules cm^{-2} s^{-1}), M_b is the molecular weight of b, and

$$\tau = \tau_0 \exp\left(\frac{E}{RT}\right). \tag{6.11}$$

In (6.11), τ_0 is the characteristic time (sec) and E is the heat of adsorption (J mole^{-1}) given, in Hamill *et al.* (1982), as 2.4×10^{-16} sec and 4.52×10^4 J mole^{-1}, respectively, for water nucleating on carbon.

In the case of binary nucleation, the particle density, surface tension, and saturation ratio of the nucleating particle at the saddle point (point of maximum Gibbs free energy) depend on the weight fraction of the respective components in the particle at that point. To calculate the density, surface tension, and critical radius in such a case for the sulfuric acid - water system, the formulations discussed in Zhao (1993) was used.

In GATOR, homogeneous and heterogeneous nucleation is simulated after gas chemistry but before coagulation (Figure 4.1). An alternative order is to calculate homogeneous nucleation together with condensational growth, dissolutional growth, and evaporation. The advantage of the latter order is that it allows competition between growth and nucleation. The disadvantage is that it does not allow coagulation to affect the new particles until the subsequent time interval. Ideally, nucleation, coagulation, and growth would be solved simultaneously. While solving simultaneously is feasible for a small number of grid cells and a few species (*e. g.* Appendix D), it currently requires too much computer time for a large number of grid cells and many species. A reason is that the matrix of partial derivatives for the coagulation equations is dense, eliminating the benefits of sparse-matrix reductions accruing from the growth equations.

Although a mechanism for calculating homogeneous nucleation in GATOR is in place, homogeneous nucleation may be of little importance in Los Angeles air. For

110

example, in urban air, the only species that obtain sufficient free energy to homogeneously nucleate are sulfuric acid, nitric acid, and some secondary organics (Pilinis *et al.*, 1987, p. 947). However, sulfuric acid or nitric acid binary homogeneous nucleation with water is much more probable than homomolecular homogeneous nucleation, and sulfuric acid binary homogeneous nucleation occurs at 6-8 orders of magnitude lower concentration than does nitric acid binary nucleation (*ibid.*, p 947). In addition, since urban air parcels contain numerous existing aerosols, even binary homogeneous nucleation of sulfuric acid appears negligible (*ibid.*, p. 953).

Instead, heterogeneous nucleation is more probable than homogeneous nucleation because surface attractions (*e.g.* charges) lower the Gibbs free energy required for heterogeneous nucleation. Subsequently, once a cluster of like molecules nucleates onto a heterogeneous surface, condensational growth occurs rapidly.

6.3 Coagulation

Coagulation consists of the physical processes of collision and coalescence. Particles collide as a result of Brownian motion, differences in fall velocities, turbulent motions and intraparticle forces. If they stick upon collision, then the number of particles in the atmosphere decreases, the total volume in particles is conserved, but the average size of particles increase.

In GATOR, coagulation is solved after nucleation but before vapor pressure and growth calculations (Figure 4.1). With many particle types, size bins, and components, solving coagulation is difficult. However, the method discussed in Appendix C gives solutions among any number of particle types, size bins, and components Because Appendix C details solutions to and application of the coagulation equations, the information is not repeated here.

6.4 Condensational and Dissolutional Growth / Evaporation

In GATOR, growth is treated in a two-step process. The first step is to find the equilibrium vapor pressures of all condensing and dissolving gases, and the second step is to calculate growth to or evaporation from particles. Appendices D and E detail the treatment of condensational and dissolutional growth in GATOR.

The two types of growth discussed, condensational and dissolutional growth, differ with respect to how the equilibrium vapor pressure is calculated for each process. Otherwise, the two processes are the same. In both cases, gases transfer to particle surfaces by diffusion. If particle surfaces are wet and the condensing gas is soluble, then the condensing gas dissolves in the water. Otherwise, the condensing gas bounces off, sticks to, or chemically reacts with components on the surface. Some gases condense onto surfaces when the surfaces are dry and dissolve in the water when they are wet.

As discussed in Section 2.2.4, the primary dissolving species in the atmosphere are H_2SO_4, NH_3, HNO_3, HCl, H_2O_2, HO_2NO_2, HO_2, SO_2, OH, HO_2, CO_2, CH_2O, $HCOOH$, CH_3COOH, and CH_3COCHO. Of these, some, such as H_2SO_4, HNO_3, and H_2O_2, have low enough vapor pressures to condense onto dry surfaces (however, the acids will attract water when they condense). In addition, numerous high molecular weight organic oxidation products of toluene, xylene, alkylbenzenes, biogenic hydrocarbons, alkanes, and alkenes readily condense onto aerosols (Pilinis and Seinfeld, 1988; Pandis *et al.*, 1992), as does liquid water.

Since sulfuric acid condenses or dissolves with little or no barrier to growth, its equilibrium vapor pressure can be estimated directly from data, such as that of Gmitro and Vermeulen (1964), and it can grow by condensation. The vapor pressures of other inorganic and organic species that dissolve can be found by solving a set of equilibrium equations simultaneously between the gas-phase and multiple size bins of the aerosol

112

phase. To determine such vapor pressure, the method discussed in Appendix E is used. This method allows the simultaneous calculation of equilibrium equations, activity coefficients, and aerosol water content. Activity coefficients for mixed solutions are obtained by using Bromley's mixing method (Bromley, 1973), as discussed in Pilinis and Seinfeld (1987). This method requires data for binary activity coefficients. Temperature-dependent binary coefficients can be calculated using the formula of Harned and Owen (1958) and polynomial fittings described in Tabazadeh *et al.* (1994) and in Appendix E. Table A.7 lists a set of equilibrium equations solved for in each aerosol size bin in order to determine vapor pressures.

When the relative humidity exceeds 100%, the equilibrium vapor pressure of water can be calculated an empirical relation, such as that from Bolton (1980), given as

$$e_s(T) = 6.112 \exp\left(\frac{17.67T}{T + 243.5}\right), \qquad (6.12)$$

where e_s is in millibars and T is in degrees C. This expression is valid for the temperature range between -30 and +35 °C. When the humidity is less than 100%, the liquid water content of aerosols can be calculated using the equilibrium method discussed in Appendix E. This method assumes that the liquid water in each aerosol size bin is in equilibrium with water vapor, other gases, and other components with the aerosol bin.

After vapor pressures are determined, growth to and evaporation from aerosols are calculated using SMVGEAR. Appendix D describes this process. In sum, a series of ordinary differential growth / evaporation equations is set up between the gas phase and multiple size bins of the aerosol phase, for each species, and SMVGEAR solves the equations simultaneously.

113

6.5 Internal Chemical Equilibrium and Aqueous Chemistry

After calculating transfer between gases and all aerosol size bins, changes in the internal concentrations of particles in each bin are calculated. For equilibrium reactions, changes are simulated by solving sets of equilibrium equations simultaneously with binary activity coefficients and aerosol water content. For uni-directional reactions, changes are simulated by solving first-order, ordinary differential rate equations.

Appendix E describes the equilibrium solution mechanism. The mechanism is exactly the same as that used to solve for equilibrium vapor pressures. The only difference is in the actual equations solved. For example, while all equations in Table A.7 are solved simultaneously for each size bin during vapor pressure calculations, all except those that contain a gas-phase species are solved during aqueous equilibrium calculations. Solving for aqueous equilibrium is important since gas-aerosol transfer merely places certain species in the aerosol phase without dissociating them. For example, gas aerosol transfer puts sulfuric acid in the aerosol phase; however, equilibrium distributes the acid among itself, bisulfate, and sulfate. Similarly, many other species dissociate into ions, and equilibrium calculations permit this dissociation Further, the equilibrium equations permit the formation of solids.

After equilibrium is solved, SMVGEAR is used to solve aqueous chemistry ODEs. Appendix B discusses the application of SMVGEAR to aqueous chemistry problems and Table A.8 lists the chemical reactions solved for in each aerosol size bin.

In sum, GATOR simulates several significant aerosol physical and chemical processes. These include emission, nucleation, coagulation, condensational and dissolutional growth, equilibrium, aqueous chemistry, deposition, and transport. Next, transport processes are discussed.

114

Chapter 7

Transport Processes

In this chapter, the mechanisms of horizontal and vertical transport in GATOR and the coupled *m*esoscale *m*eteorological and *t*racer *d*ispersion (MMTD) model are discussed. Figure 4.1 shows that GATOR calls the MMTD before calling the horizontal and vertical transport schemes. Section 7.1, below, contains a brief discussion of the MMTD. Section 7.2 discussed horizontal advection and diffusion, Section 7.3 discusses sedimentation and dry deposition velocities, and Section 7.4 discusses vertical transport, including the addition of emissions and deposition terms to the equations.

7.1 Summary of the MMTD model

The MMTD model (Lu and Turco, 1993, 1994a,b) is a hydrostatic, finite difference prognostic meteorological model that uses sigma coordinates in the vertical and spherical coordinates in the horizontal. It predicts horizontal and vertical wind speeds and directions, vertical diffusion coefficients, convective mass transfer rates, temperature, pressure, humidity, changes in soil moisture, and cloud liquid water content. Further, the temperature profile that it predicts is used to calculate atmospheric stability and the boundary layer height. The MMTD has been used successfully to predict elevated layers of pollution, similar to those detected in lidar images by Wakimoto and McElroy (1986).

115

To predict the variables listed above, the MMTD solves the primitive equations, written as (Lu and Turco, 1994a)

$$\pi \frac{d\mathbf{V}}{dt} + f\mathbf{k} \times \pi\left(\mathbf{V} - \mathbf{V}_g\right) = -\pi\left(\nabla_\sigma \Phi + R\theta P \nabla_\sigma \ln p\right) + \pi\left(\mathbf{F}_v + \mathbf{D}_v\right), \qquad (7.1)$$

$$\pi \frac{d\theta}{dt} = \pi\left(\frac{Q}{C_p P} + F_\theta + D_\theta\right), \qquad (7.2)$$

$$\frac{\partial \pi}{\partial t} + \nabla_\sigma \cdot (\pi\mathbf{V}) + \frac{\partial \pi\dot{\sigma}}{\partial \sigma} = 0, \qquad (7.3)$$

$$\delta\Phi = -R\theta P \delta \ln p, \qquad (7.4)$$

$$\pi \frac{dq}{dt} = \pi\left(S_q + F_q + D_q\right), \qquad (7.5)$$

where Equation (7.1) is the momentum equation, (7.2) is the thermodynamic equation, (7.3) is the continuity equation, (7.4) is the hydrostatic equation, and (7.5) is the mass continuity equation for water vapor. Table 7.1 defines the parameters in these equations.

While the MMTD feeds winds, diffusion coefficients, convective mass transfer rates, pressure, temperature, and humidity to GATOR, GATOR calculates radiative heating rates and has the option of sending them back to the MMTD. The MMTD uses radiative heating rates to calculate part of diabatic heating rate (Q), which is used to calculate a part of the temperature change.

116

Table 7.1. Definition of parameters used in Equations (7.1) - (7.5).

Table 7.1

Variable	Definition
$\mathbf{V}$	= horizontal wind vector
θ	= potential temperature
q	= water vapor mixing ratio
Φ	= geopotential height
f	= coriolis parameter
$\mathbf{V_g}$	= geostrophic wind
Q	= diabatic heating rate
S_q	= water vapor source or sink term
$\mathbf{F_V}$	= turbulent friction force
F_θ	= vertical turbulent flux divergence of θ
F_q	= vertical turbulent flux divergence of q
$\mathbf{D_V}$	= horizontal subgrid eddy diffusion coefficient for $\mathbf{V}$
D_θ	= horizontal subgrid eddy diffusion coefficient for θ
D_q	= horizontal subgrid eddy diffusion coefficient for q
R	= gas constant for dry air
C_p	= specific heat at constant pressure
p	= air pressure in the model
p_{surf}	= surface air pressure
p_{top}	= constant pressure at the top of the model atmosphere
π	= difference between surface and top pressures = $p_{surf} - p_{top}$
σ	= vertical sigma coordinate = $\left(p - p_{top}\right)/\pi$
p_0	= reference pressure = 1000 mb
P	= $\left(p/p_0\right)^{R/C_p}$

117

The MMTD solves a slightly different set of equations than does GATOR. While GATOR divides the continuity equation (4.14) into three transport and several physical and chemical process equations, the MMTD solves all the primitive equations simultaneously and does not split the transport term into three equations. Ideally, all species in GATOR would be transported in the same manner as air, temperature, and water vapor are transported in the MMTD. However, such computations for a hundred or more gases and thousands of aerosol entities currently require too much computer time. Instead, the variables predicted by the MMTD are currently fed into GATOR's divided continuity equations.

7.2 Horizontal Transport

Figure 4.1 shows that the horizontal and vertical transport solvers in GATOR are called after the MMTD is called. Horizontal and vertical transport are solved by splitting the three-dimensional continuity equation (4.14) into two one-dimensional horizontal equations, (4.15) - (4.16) and a one-dimensional vertical equation (4.17). To solve the horizontal equations, the code developed by Toon *et al.* (1988) was used. This code is a Galerkin method with chapeau functions as finite elements (*e. g.* Pepper *et al.*, 1979).

In brief, the code solves a tridiagonal system of equations of the form

$$
\begin{bmatrix}
B_1 & D_1 & 0 & 0 & 0 \\
A_2 & B_2 & D_2 & 0 & 0 \\
0 & A_3 & B_3 & D_3 & 0 \\
0 & 0 & A_4 & B_4 & D_4 \\
0 & 0 & 0 & A_5 & B_5
\end{bmatrix}
\begin{bmatrix}
C_1^{t+1} \\
C_2^{t+1} \\
C_3^{t+1} \\
C_4^{t+1} \\
C_5^{t+1}
\end{bmatrix}
=
\begin{bmatrix}
F_1 & G_1 & 0 & 0 & 0 \\
E_2 & F_2 & G_2 & 0 & 0 \\
0 & E_3 & F_3 & G_3 & 0 \\
0 & 0 & E_4 & F_4 & G_4 \\
0 & 0 & 0 & E_5 & F_5
\end{bmatrix}
\begin{bmatrix}
C_1^{t} \\
C_2^{t} \\
C_3^{t} \\
C_4^{t} \\
C_5^{t}
\end{bmatrix},
\qquad (7.6)
$$

118

where A, B, D, E, F, and G are coefficients, described below, C is concentration, t is the initial time, $t+1$ is the final time, and the subscripts identify grid cell numbers. The example in (7.6) is for a one-dimensional grid of length N, where $N = 5$. Another way to write (7.6), where k is the grid-cell number along a one-dimensional array, is

$$A_k C_{k-1}^{t+1} + B_k C_k^{t+1} + D_k C_{k+1}^{t+1} = E_k C_{k-1}^t + F_k C_k^t + G_k C_{k+1}^t. \qquad (7.7)$$

The coefficients of (7.6) and (7.7), for any value $1 < k < N$, are (Toon *et al.*, 1988)

$$
\begin{aligned}
A_k &= (dX_k/\tau) - \mu\alpha_k & E_k &= (dX_k/\tau) + (1-\mu)\alpha_k \\
B_k &= (2/\tau)(dX_k + dX_{k+1}) + \mu\beta_k & F_k &= (2/\tau)(dX_k + dX_{k+1}) - (1-\mu)\beta_k \\
D_k &= (dX_{k+1}/\tau) + \mu\gamma_k & G_k &= (dX_{k+1}/\tau) - (1-\mu)\gamma_k,
\end{aligned}
\qquad (7.8)
$$

where τ is the time step, μ is the Crank-Nicolson parameter (chosen as 0.5) and

$$\alpha_k = (U_k + 2U_{k-1}) + \frac{3\left(\rho_k^* K_k + \rho_{k-1}^* K_{k-1}\right)}{\left(\rho_{k-1}^* dX_k\right)}, \qquad (7.9)$$

$$
\begin{aligned}
\beta_k &= (-U_{k-1} + U_{k+1}) \\
&+ \frac{3\left[\left(\rho_{k-1}^* K_{k-1} + \rho_k^* K_k\right)dX_{k+1} + \left(\rho_k^* K_k + \rho_{k+1}^* K_{k+1}\right)dX_k\right]}{\left(\rho_k^* dX_k dX_{k+1}\right)},
\end{aligned}
\qquad (7.10)
$$

and

$$\gamma_k = (U_k + 2U_{k+1}) - \frac{3\left(\rho_k^* K_k + \rho_{k+1}^* K_{k+1}\right)}{\left(\rho_{k+1}^* dX_{k+1}\right)} \qquad (7.11)$$

119

are coefficients for (7.8). All other parameters in (7.8) - (7.11) are defined in Table 4.3. When outflow off the grid occurs, the flux is either (Toon *et al.*, 1988)

$$Fl_{out1} = (U_1 + K_1/dX_2)(C_1^t + C_1^{t+1})$$ (7.12)

or

$$Fl_{outN} = (U_N + K_N/dX_N)(C_N^t + C_N^{t+1}),$$ (7.13)

or both, depending on whether outflow is occurring from the first grid-cell, the Nth cell, or both. If outflow occurs from the first cell, then the coefficients for Equation 7.7 that give the flux in 7.12 are

$$A_1 = 0 \qquad\qquad E_1 = 0$$
$$B_1 = (2dX_1/\tau) + \mu\beta_1 \qquad F_1 = (2dX_2/\tau) - (1-\mu)\beta_1$$
$$D_1 = (dX_2/\tau) + \mu\gamma_1 \qquad G_1 = (dX_2/\tau) - (1-\mu)\gamma_1 \qquad (7.14)$$

where

$$\beta_1 = -4U_1 + U_2 + \frac{(9\rho_1^* K_1 + 3\rho_2^* K_2)}{\rho_1^* dX_2}$$ (7.15)

and

$$\gamma_1 = U_1 + 2U_2 - \frac{3(\rho_1^* K_1 + \rho_2^* K_2)}{\rho_2^* dX_2}.$$ (7.16)

However, if outflow occurs from the Nth cell, then the coefficients for Equation 7.7 that give the flux in 7.13 are

$$A_N = (dX_N/\tau) - \mu\alpha_N \qquad E_N = (dX_N/\tau) + (1-\mu)\alpha_N$$

120

$$B_N = (2dX_N/\tau) + \mu\beta_N \qquad F_N = (2dX_N/\tau) - (1-\mu)\beta_N$$

$$D_N = 0 \qquad\qquad G_N = 0, \qquad\qquad (7.17)$$

where

$$\alpha_N = U_N + 2U_{N-1} + \frac{3\left(\rho_N^* K_N + \rho_{N-1}^* K_{N-1}\right)}{\rho_{N-1}^* dX_N} \qquad (7.18)$$

and

$$\beta_N = 4U_N - U_{N-1} + \frac{\left(9\rho_N^* K_N + 3\rho_{N-1}^* K_{N-1}\right)}{\rho_N^* dX_N}. \qquad (7.19)$$

In both (7.15) and (7.19), the expressions differ slightly from those of Toon *et al.* (1988) in order to account for the inflow and outflow of diffusive material.

Here, I discuss a new inflow boundary condition. Toon *et al.* (1988) describe a chapeau inflow flux, a no-flux inflow, and a constant concentration inflow. The boundary condition reported below allows a flux to be specified when inflow is occurring. For inflow into the first or N^{th} grid cell, a flux,

$$Fl_{in1} = (U_1 + K_1/dX_1)C_0^t \qquad (7.20)$$

or

$$Fl_{in1} = (U_N + K_1/dX_N)C_{N+1}^t, \qquad (7.21)$$

is specified, based on a concentration of the species in a virtual cell, which is a cell (either subscript 0 or $N+1$) just beyond the border grid cell. Section 9.3 discusses virtual grid-cell species concentrations. When boundary meteorological forcings are not available, the same wind speed and diffusion information for the border cell are used for the virtual

121

cell. Next, the flux is added as an explicit production term into the first or N^{th} position of the tridiagonal matrix:

$$B_1 C_1^{t+1} + D_1 C_2^{t+1} = F_1 C_1^t + G_1 \left(C_2^t + Fl_{in1} \tau / dX_1 \right) \qquad (7.22)$$

or

$$A_N C_{N-1}^{t+1} + B_N C_N^{t+1} = E_N C_{N-1}^t + F_N \left(C_N^t + Fl_{inN} \tau / dX_N \right). \qquad (7.23)$$

When an explicit flux is added, no other mass should enter the grid at the boundaries. Toon et al. (1988) discussed a no-flux boundary. It consists of subtracting a semi-implicit flux from a chapeau inflow (or outflow) term. In fact, the coefficients for the no-flux condition are the same as those for the chapeau outflow conditions (described in Equations (7.14) - (7.19)), except that, for the no-flux case,

$$\beta_1 = 2U_1 + U_2 + \frac{3 \left(\rho_1^* K_1 + \rho_2^* K_2 \right)}{\rho_1^* dX_2} \qquad (7.24)$$

and

$$\beta_N = -2U_N - U_{N-1} + \frac{3 \left(\rho_N^* K_N + \rho_{N-1}^* K_{N-1} \right)}{\rho_N^* dX_N} \qquad (7.25)$$

replace β_1 and β_N for the chapeau outflow case. Thus, the new specified explicit inflow flux consists of adding an explicit inflow term plus removing the inflow term from the chapeau inflow (same as chapeau outflow) boundary condition.

The primary advantages of the Galerkin technique are that it is fast and reasonably accurate. Because it is fast, it can transport thousands of gas and aerosol components across large grid domains in good time. Higher order methods, such as the accurate space derivative method (ASD) (Gazdag, 1973; Chock, 1991; Dabdub and Seinfeld, 1994) may

122

replace the Galerkin technique when computer speeds increase sufficiently. Until then, however, the Galerkin is a practical choice for solving advection for thousands of components.

7.3 Fall and Dry Deposition Velocities

7.3.1 Fall Velocities

GATOR calculates fall velocities of aerosols and dry deposition velocities of gases and aerosols. These velocities are subsequently used in the vertical transport calculation, described later.

To calculate vertical fall velocities, the technique discussed in Pruppacher and Klett (1978) and Toon et al. (1989) is used. This two-step method requires an estimation of the Reynolds number from a predicted fall velocity and a re-calculation of the fall velocity from the estimated Reynolds number. First, the estimated non-dimensional Reynolds number is

$$N_{Re}^{est} = \frac{2rV_f^{est}}{\nu},$$ (7.26)

where r is the radius of the falling particle, ν is the kinematic viscosity of air, and

$$V_f^{est} = \frac{2(\rho_p - \rho_a)gr^2 G}{9\eta f_1}$$ (7.27)

123

is the estimated fall velocity predicted. In (7.27), ρ_p is the density of the particle, ρ_a is the density of air, g is the acceleration of gravity, η is the dynamic viscosity of air, f_1 is a shape factor (= 1 for spheres), and

$$G = \left\{ 1 + f_1 f_2 Kn \left[A + B \exp\left(-CKn^{-1}\right) \right] \right\}$$ (7.28)

is a correction factor for particle resistance to motion. In (7.28), f_2 is a second shape factor (*ibid.*), Kn is the particle Knudsen number, and A, B, and C are experimental coefficients for G (*e.g.* Millikan, 1923; Kasten, 1968).

The final fall velocity, for all values of the estimated Reynolds number, is

$$V_f = \frac{N_{Re} \nu G}{2r},$$ (7.29)

where N_{Re} is the re-calculated Reynolds number. For estimated Reynolds numbers below 0.01, $N_{Re} = N_{Re}^{est}$. For $0.01 < N_{Re}^{est} < 300$, an empirical relation for the re-calculated Reynolds number is used. This relation is

$$N_{Re} = \exp(Y),$$ (7.30)

where

$$Y = B_0 + B_1 X + B_2 X^2 + \ldots$$ (7.31)

In (7.31), B_0, B_1.... are polynomial coefficients listed in Pruppacher in Klett (1978, p. 324), and

$$X = \ln\left(\frac{32r^3 \left(\rho_p - \rho_a\right)\rho_a g}{3\eta^2} \right).$$ (7.32)

124

Finally, in the case $N_{Re}^{est} \geq 300$, the drops are no longer spherical, and a different approximation must be made. In this case, the Reynolds number is recalculated as

$$N_{Re} = N_P^{1/6} \exp(Y),$$

(7.33)

where Y is the same polynomial as 7.31, but with different coefficients and with

$$X = \ln\left(\frac{16}{3} N_{Bo} N_P^{1/6}\right),$$

(7.34)

where

$$N_{bo} = \frac{r^2 (\rho_p - \rho_a) g}{\sigma},$$

(7.35)

and

$$N_P = \frac{\sigma^3 \rho_a^2}{\eta^4 (\rho_p - \rho_a) g}.$$

(7.36)

In (7.35) and (7.36), σ is the particle surface tension, N_{bo} is the *Bond* number, and N_P is the *physical property* number, as defined in Pruppacher and Klett (1978, p. 325).

In GATOR, fall velocities are calculated for each horizontal and vertical grid cell and each aerosol type and size. Section 7.4 shows how the fall velocities are converted to an implicit loss rate, l, which is used in the vertical transport equation.

7.3.2 Dry Deposition Velocities

Dry deposition occurs when gases or particles impact and stick to or react with surfaces near or on the ground. For example, gases or particles can deposit onto trees, buildings, grassy surfaces, ocean surfaces, car windows, or any other surface. Dry

125

deposition velocities are usually calculated as the inverse of the sum of a series of resistances. For example, the dry deposition velocity of a gas can be expressed as

$$\upsilon_{dg} = \left(r_a + r_b + r_s\right)^{-1},$$

(7.37)

where r_a is the resistance to turbulent transfer from the reference height (about 10 m deep) to the laminar sublayer just above the surface, r_b is the resistance to molecular diffusion through the laminar sublayer, which is about 0.1 to 0.01 cm deep, and r_s is the resistance to chemical or physical interaction between the surface and the gas once the gas has reached the surface (*e.g.* Seinfeld, 1986; Russell *et al.*, 1993).

The resistance to turbulent transfer depends on wind speed, surface roughness, and atmospheric stability. The resistance to molecular diffusion depends on the diffusion coefficient of the species, air viscosity, air conductivity, air temperature, and air density. Finally, the resistance to surface interactions depends on physical and chemical properties of the surface and of the depositing species.

For particles, the deposition velocity equation is similar to that for gases, except for two factors. First, particles are heavier than gases, so particle deposition velocities include a fall-speed term. Second, because of their weight, particles tend to stay on surfaces once they deposit; thus, the surface resistance term may be ignored. Consequently, the deposition velocity of a particle can be written as (*e.g.* Seinfeld, 1986)

$$\upsilon_{dp} = \left(r_a + r_b + r_a r_b V_f\right)^{-1} + V_f,$$

(7.38)

where V_f is the particle fall velocity, as defined in Section 7.3.1.

126

To calculate the three resistances -- r_a, r_b, and r_s -- algorithms from the California Institute of Technology (CIT) dry deposition model (McRae *et al.*, 1982; Russell *et al.*, 1993; D. Winner, *pers. comm.*) were used. First, McRae *et al.* (1982) calculated r_a as

$$r_a = \frac{\int_{z_0}^{z_r} \phi_p\left(\frac{z}{L}\right)\frac{dz}{z}}{ku^*} \qquad (7.39)$$

where k is von Karman's constant and

$$
\begin{aligned}
\int_{z_0}^{z_r} \phi_p\left(\frac{z}{L}\right)\frac{dz}{z} &= 0.74\ln\left(\frac{z_r}{z_0}\right) + \frac{4.7}{L}(z_r - z_0) && \text{for} \quad \frac{1}{L} < 0 \\[2mm]
&= 0.74\ln\left(\frac{z_r}{z_0}\right) && \text{for} \quad \frac{1}{L} = 0 \\[2mm]
&= 0.74\left\{\ln\left[\frac{\left(1-9\frac{z_r}{L}\right)^{1/2}-1}{\left(1-9\frac{z_r}{L}\right)^{1/2}+1}\right] - \ln\left[\frac{\left(1-9\frac{z_0}{L}\right)^{1/2}-1}{\left(1-9\frac{z_0}{L}\right)^{1/2}+1}\right]\right\} && \text{for} \quad \frac{1}{L} > 0
\end{aligned}
$$

$$(7.40)$$

is an empirical function dependent on atmospheric stability and surface roughness. Above, L is the Monin-Obukhov length, which is calculated with the MMTD, z_0 is the surface roughness height, and z_r is the reference height (usually 10m). If $1/L < 0$, then air near the surface is unstable. If $1/L = 0$, then air near the surface is neutral, and if $1/L > 0$, the air near the surface is stable. Further, in (7.39)

127

$$u^* = \frac{ku(z_r)}{\int_{z_0}^{z_r} \phi_m\left(\frac{z}{L}\right)\frac{dz}{z}}$$

(7.41)

is the friction wind speed, where $u(z_r)$ is the observed wind speed at the reference height and

$$\int_{z_0}^{z_r} \phi_m\left(\frac{z}{L}\right)\frac{dz}{z} = \ln\left(\frac{z_r}{z_0}\right) + \frac{4.7}{L}(z_r - z_0) \qquad \text{for} \quad \frac{1}{L} < 0$$

$$= \ln\left(\frac{z_r}{z_0}\right) \qquad \text{for} \quad \frac{1}{L} = 0$$

$$= \ln\left[\frac{\left(1-15\frac{z_r}{L}\right)^{1/4}-1}{\left(1-15\frac{z_r}{L}\right)^{1/4}+1}\right] - \ln\left[\frac{\left(1-15\frac{z_0}{L}\right)^{1/4}-1}{\left(1-15\frac{z_0}{L}\right)^{1/4}+1}\right] \quad \text{for} \quad \frac{1}{L} > 0.$$

$$+2\tan^{-1}\left(1-15\frac{z_r}{L}\right)^{1/4} - 2\tan^{-1}\left(1-15\frac{z_0}{L}\right)^{1/4}$$

(7.42)

Second, McRae *et al.* (1982) calculated the resistance to diffusion as

$$r_b = \frac{\ln(z_0/z_d)}{ku^*}.$$

(7.43)

where

$$\ln(z_0/z_d) = 2(Sc/Pr)^{2/3}.$$

(7.44)

In (7.43) and (7.44), z_d is the pollutant sink height, Sc is the gas or particle Schmidt Number, and Pr is the Prandtl number.

128

Finally, Russell *et al.* (1993) calculated surface resistance values for many gases. To do so, they identified resistance values as a function of landuse type and heating rates for two species, SO_2 and O_3, from Walcek *et al.* (1986), Sheih *et al.* (1986), and Chang *et al.* (1987). Subsequently, they scaled the resistances for other species to those of SO_2. Next, they combined detailed landuse data from the U. S. Geological Survey together with the surface resistance and other resistance information to calculate deposition velocities in each grid cell. Finally, they maintained the method described in McRae *et al.* (1982) to find the grid-cell average deposition velocity.

In sum, the methodology for calculating resistances and deposition velocities, discussed above, was implemented for both gases and aerosols. These deposition velocities are converted to an implicit loss rate, as described below, and added to the vertical transport code.

7.4 Vertical Transport

The vertical transport scheme solves the third one-dimensional continuity equation, (4.17). The mechanism emanates from Toon *et al.* (1988), who expanded on work by Turco *et al* (1979a,b) and Fiadeiro and Veronis (1977). The scheme solves the tridiagonal system of equations,

$$
\begin{bmatrix}
M_1 & N_1 & 0 & 0 & 0 \\
L_2 & M_2 & N_2 & 0 & 0 \\
0 & L_3 & M_3 & N_3 & 0 \\
0 & 0 & L_4 & M_4 & N_4 \\
0 & 0 & 0 & L_5 & M_5
\end{bmatrix}
\begin{bmatrix}
C_1^{t+1} \\
C_2^{t+1} \\
C_3^{t+1} \\
C_4^{t+1} \\
C_5^{t+1}
\end{bmatrix}
=
\begin{bmatrix}
P_1 & Q_1 & 0 & 0 & 0 \\
O_2 & P_2 & Q_2 & 0 & 0 \\
0 & O_3 & P_3 & Q_3 & 0 \\
0 & 0 & O_4 & P_4 & Q_4 \\
0 & 0 & 0 & O_5 & P_5
\end{bmatrix}
\begin{bmatrix}
C_1^t \\
C_2^t \\
C_3^t \\
C_4^t \\
C_5^t
\end{bmatrix}
+
\begin{bmatrix}
s_1 dZ_1 \\
s_2 dZ_2 \\
s_3 dZ_3 \\
s_4 dZ_4 \\
s_5 dZ_5
\end{bmatrix}, \quad (7.45)
$$

129

where L, M, N, O, P, and Q are coefficients, described below, C is concentration, t is the current time, $t+1$ is the advanced time, dZ is the vertical coordinate, defined in Table 4.3, and the subscripts identify grid-cell numbers. Equation (7.45) is an example of the matrix for a one-dimensional vertical grid of length N, where $N = 5$. Another way to write (7.45), where k is the grid-cell number along the one-dimensional array, is

$$L_j C_{j-1}^{t+1} + M_j C_j^{t+1} + N_j C_{j+1}^{t+1} = O_j C_{j-1}^t + P_j C_j^t + Q_j C_{j+1}^t + s_j dZ_j. \qquad (7.46)$$

The coefficients in (7.45) and (7.46), for $1 < j < N$, are

$$L_j = -\mu T_j \qquad\qquad O_j = (1 - \mu)T_j$$
$$M_j = \mu(T_{j+1} + S_j) + dZ_j(1_j + 1/\tau) \quad P_j = -(1 - \mu)(T_{j+1} + S_j) + dZ_j/\tau$$
$$N_j = -\mu S_{j+1} \qquad\qquad Q_j = (1 - \mu)S_{j+1}. \qquad (7.47)$$

where $\mu = 1$ (implicit) if $T_{j+1} + S_j > dZ_j / \tau$ and $\mu = 0$, otherwise. This constraint allows an implicit solution when the Courant criteria is violated and an explicit solution when it is not. In (7.47),

$$T_j = \frac{W_{j-1/2} + K_{j-1/2} \ln(\rho_{j-1}^* / \rho_j^*)/dZ_{bj}}{e^{2\theta_j} - 1} \qquad (7.48)$$

is the downward flux into level j from level j-1 and

$$S_j = T_j e^{2\theta_j} \qquad (7.49)$$

130

is the upward flux into level j-1 from level j. In (7.45) and (7.46), s_j is an explicit source term (*e.g.* emissions) into any layer j, and in (7.47), l_j is an implicit loss term that appears in the coefficient, M. This loss term, which has units of (s^{-1}) is the sum of vertical losses from each layer due to sedimentation, dry deposition, and rainout. In the case of deposition and sedimentation, it is calculated by dividing the deposition and fall velocities (cm s^{-1}) by the height (cm) of the current grid cell.

Also in (7.48) and (7.49),

$$dZ_{bj} = \left(d\, Z_j + dZ_{j-1}\right)\Big/2 \tag{7.50}$$

and

$$2\theta_j = \left(W_{j-1/2} dZ_{bj}\big/K_{j-1/2}\right) + \ln\!\left(\rho_{j-1}^* \big/ \rho_j^*\right). \tag{7.51}$$

To reduce numerical diffusion, Toon *et al.* (1988) introduced

$$W_{j-1/2}' = \lambda_j^{|\zeta|} W_{j-1/2}, \tag{7.52}$$

which replaces W in T and S, but not in θ. In (7.52),

$$\zeta = \coth(\theta) - 1/\theta \tag{7.53}$$

(Fiadeiro and Veronis, 1977) and

$$\lambda_j = \frac{dZ_{bj}\left(e^{-dZ_{cj}/H_j} - 1\right)}{dZ_{cj}\Psi_j}. \tag{7.54}$$

131

where

$$\Psi_j = \begin{cases} 1 - C_{j-1}/C_j & W_{j-1/2} < 0 \\ C_j/C_{j-1} - 1 & W_{j-1/2} > 0 \end{cases} \text{ for } \qquad (7.55)$$

$$dZ_{cj} = \tau W_{j-1/2}, \qquad (7.56)$$

and

$$H_j = dZ_{bj} \Big/ \ln\!\left(C_{j-1}/C_j\right). \qquad (7.57)$$

All parameters not defined here are defined in Table 4.3. Also, the subscript, j - 1/2 indicates a value at the edge of a layer, whereas the subscript j indicates a value at the center of a layer.

In sum, the vertical transport scheme is relatively non-diffusive, stable and fast. Coupled with the horizontal scheme, it simulates the continuity equation, (7.14). Next, I discuss radiative processes.

132

Chapter 8

Radiative Processes

In this chapter, radiative processes in GATOR are described. These include the equations for calculating extinction due to scattering by gases (Section 8.1), absorption by gases (8.2), scattering by aerosols (8.3), and absorption by aerosols (8.4), not only for visible, but also for ultraviolet and infrared wavelengths. In addition, mean intensities (8.5), heating rates (8.5), and photodissociation rates (8.6) are discussed.

8.1 Optical Properties

8.1.1 Gas Scattering

The only important gas-scattering process in the atmosphere is Rayleigh scattering, which is the scattering of radiation by gas molecules (primarily N_2 and O_2). Rayleigh scattering gives the sky a blue color. Further, it causes dark objects a few kilometers away to appear behind a blue haze of scattered light and bright objects greater than 30 km away to appear reddened (Waggoner *et al.*, 1981).

A Rayleigh scatterer is a species whose molecular radius (r) is much smaller than the light wavelength (λ) of interest. For most gases and wavelengths, this criterion,

133

$2\pi r/\lambda \ll 1$, holds. However, since oxygen and nitrogen are the most abundant gases in the atmosphere, they are the most effective Rayleigh scatterers.

Light extinction caused by Rayleigh scattering is inversely proportional to the fourth power of the light's wavelength. The extinction coefficient (cm^{-1}) due to Rayleigh scattering at sea level is

$$\sigma_{sg,\lambda,z} = \frac{32\pi(n_\lambda - 1)^2}{3\lambda^4 N_o^2} N(z),$$ (8.1)

where n_λ is the real part of the index of refraction of air at a given wavelength, which can be calculated empirically as
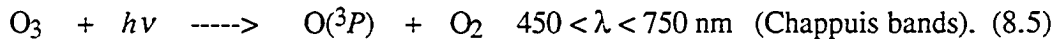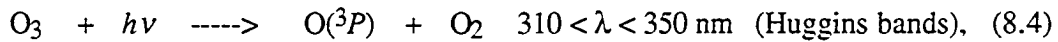
$$n_\lambda - 1 = 10^{-8}\left[6432.8 + \frac{2,949,810}{146 - \lambda^{-2}} + \frac{25,540}{41 - \lambda^{-2}}\right]$$ (8.2)

for standard temperature and pressure (e. g. Turco, 1990). In Equation (8.1), λ is in cm, N_o is the air concentration (No. cm^{-3}) under standard conditions (288 K, sea-level pressure), and $N(z)$ is the air concentration at the given altitude. Thus, at increasing altitude, Rayleigh scattering decreases proportionately to air density. For a 0.52 μm wavelength at sea level pressure and 288 K, Equation (8.1) gives an extinction coefficient of 1.38×10^{-7} cm^{-1}, resulting in a maximum meteorological range of 284 km. At 0.55 μm, the extinction coefficient decreases to 1.09×10^{-7} cm^{-1}, increasing the calculated visibility limit to 357 km. Waggoner et al. (1981) reported a total extinction at Bryce Canyon, Utah corresponding to a visual range of within a few percent of 400 km for a wavelength of 0.55 μm. Table 8.1 shows the meteorological range resulting from Rayleigh scattering at several visible wavelengths.

134

8.1.2 Gas Absorption

Gases absorb radiation in the ultraviolet, visible, and infrared portions of the spectrum. The primary gases that absorb ultraviolet radiation before it reaches the troposphere are N_2, O_2, O_3, CO_2, and H_2O. Below 150 km, the solar flux between 100 and 300 nm is attenuated primarily by molecular oxygen and ozone. Because of absorption by these and other gases, radiation reaching earth's surface is effectively eliminated at wavelengths below 280 nm.

However, for air pollution studies, the columnar abundance of ozone is important because ozone in the stratosphere absorbs at wavelengths above 280 nm as well as below. The ozone photoprocesses that occur at wavelengths above 280 nm are

$$O_3 + hv \longrightarrow O(^1D) + O_2 \quad \lambda < 310 \text{ nm} \qquad \text{(Hartley bands)}, \quad (8.3)$$

$$O_3 + hv \longrightarrow O(^3P) + O_2 \quad 310 < \lambda < 350 \text{ nm} \quad \text{(Huggins bands)}, \quad (8.4)$$

$$O_3 + hv \longrightarrow O(^3P) + O_2 \quad 450 < \lambda < 750 \text{ nm} \quad \text{(Chappuis bands)}. \quad (8.5)$$

The effect of these absorption processes depends significantly on the ozone column amount. While 90% of the column amount resides in the stratosphere, it can fluctuate 10 - 20% daily. Also, ozone column amounts change by season. For example, during winter and spring over mid-latitudes in the Northern Hemisphere, ozone concentrations tend to be higher than during summer and fall (WMO, 1988). In addition, columnar ozone concentrations are generally higher towards the poles than towards the equator. To estimate ozone column abundances above the GATOR domain, Total Ozone Mapping Spectrometer (TOMS) ozone data (NASA, 1990) are combined with estimated altitude-dependent mixing ratios (*e.g.* Brasseur and Solomon, 1986).

135

Next, while water vapor and carbon dioxide both absorb at wavelengths far below 280 nm, they also absorb significant infrared radiation. Water absorbs in bands that peak at 720, 820, 940, 1100, 1380, 1870, 2700, 3200, 6250 nm. Similarly, carbon dioxide absorbs at 1400, 1600, 2000, 2700, 4300, 4800, 5200, 15,000 nm and higher. Ozone, on the other hand, absorbs at only one major wavelength in the infrared, 9600 nm and one minor wavelength, 14,270 nm. Further, nitrous oxide absorbs at 4500, 7780, and 17,000 nm, methane absorbs at 3310, 3430, 6550, and 7650 nm, CH_3Cl absorbs at 7400 and 13,700 nm, CF_2Cl_2 absorbs at 8600 and 9130 nm, and $CFCl_3$ absorbs at 11,800 nm and 9200 nm (*e.g.* Liou, 1992). Currently the absorption bands of water vapor, carbon dioxide, and ozone are treated in GATOR.

However, none of the gases mentioned so far affect visibility. The only absorbing gas to erode visibility in polluted air is nitrogen dioxide, which appears either yellow, brown, or red because it absorbs blue light preferentially and green light to a lesser extent. Other photodissociating species listed at the bottom of Table (A.4) attenuate visibility only slightly, if at all.

The extinction coefficient (cm^{-1}), at each wavelength, due to absorption by all gases, is

$$\sigma_{ag,\lambda} = \sum_{i=1}^{N_{ag}} C_i b_{i\lambda}(T),$$ (8.6)

where N_{ag} is the total number of absorbing gases in the air, C_i is the concentration (No. cm^{-3}) of gas i, and $b_{i,\lambda}(T)$ is the absorption cross section (cm^2) of each gas at each wavelength and temperature. Table 8.1 shows extinctions and meteorological range as a function of absorption cross section and concentration of NO_2 ($N_{ag} = 1$).

Table 8.1. Extinction coefficients ($\sigma_{ag,\lambda}$) and meteorological ranges ($x_{ag,\lambda} = 3.912 /$ $\sigma_{ag,\lambda}$) due to nitrogen dioxide absorption at selected wavelength intervals (λ +/- 0.005 μm) and concentrations. b_λ is the integrated absorption cross-section of NO_2 in each interval (Schneider et al., 1987). Also shown is the meteorological range due to only Rayleigh scattering ($x_{sg,\lambda}$) at each wavelength. $T = 298$ K, $P_{air} = 1$ atm.

Table 8.1

$\lambda \times 10^{-4}$ (μm)	b_λ (10^{-19}cm²)	NO_2 concentration (ppmv)						$x_{sg,\lambda}$ (km)
		<----- 0.01 ---->		<------ 0.1 ------>		<----- 0.25 ---->		
		$\sigma_{ag,\lambda}$ (10^{-6} m^{-1})	$x_{ag,\lambda}$ (km)	$\sigma_{ag,\lambda}$ (10^{-6} m^{-1})	$x_{ag,\lambda}$ (km)	$\sigma_{ag,\lambda}$ (10^{-6} m^{-1})	$x_{ag,\lambda}$ (km)	
0.42	5.39	13.2	296	132	29.6	330	11.8	118
0.43	5.41	13.3	294	133	29.4	333	11.8	130
0.44	5.06	12.4	315	124	31.5	310	12.6	143
0.45	4.65	11.4	343	114	34.3	285	13.7	157
0.46	4.21	10.4	376	104	37.6	260	15.0	171
0.47	3.77	9.27	422	92.7	42.2	232	16.9	188
0.48	3.31	8.14	481	81.4	48.1	204	19.2	205
0.49	2.92	7.18	545	71.8	54.5	180	21.8	223
0.50	2.48	6.10	641	61.0	64.1	153	25.6	242
0.51	2.19	5.39	726	53.9	72.6	135	29.0	262
0.52	1.74	4.28	914	42.8	91.4	107	36.6	284
0.53	1.46	3.59	1090	35.9	109	89.8	43.6	307
0.54	1.10	2.71	1440	27.1	144	67.8	57.6	331
0.55	0.999	2.46	1590	24.6	159	61.5	63.6	357
0.56	0.699	1.72	2270	17.2	227	43.0	90.8	384
0.57	0.673	1.66	2360	16.6	236	41.5	94.4	413
0.58	0.414	1.02	3840	10.2	384	25.5	154	443
0.59	0.420	1.03	3800	10.3	380	25.8	152	475
0.60	0.292	0.72	5430	7.2	543	18.0	217	509
0.61	0.238	0.59	6630	5.9	663	14.8	265	544
0.62	0.243	0.60	6520	6.0	652	15.0	261	581
0.63	0.132	0.33	11,900	3.3	1190	8.3	476	621
0.64	0.139	0.34	11,500	3.4	1150	8.5	460	662
0.65	0.121	0.30	13,000	3.0	1300	7.5	520	705
0.66	0.059	0.15	26,100	1.5	2610	3.8	1040	750
0.67	0.073	0.18	21,700	1.8	2170	4.5	869	796
0.68	0.060	0.15	26,100	1.5	2610	3.8	1030	845
0.69	0.027	0.06	58,900	0.6	5890	1.5	2610	897
0.70	0.031	0.08	51,200	0.8	5120	2.0	1960	951
0.71	0.052	0.13	30,100	1.3	3010	3.3	1200	1008

137

Table 8.1 contains relevant information about visible light absorption by nitrogen dioxide. First, NO_2 absorbs more strongly at shorter (more blue) wavelengths. Second, at low concentrations (0.01 ppmv), its effect on visibility is less than that of Rayleigh scattering at all wavelengths. Finally, at typical polluted air concentrations (0.1 - 0.25 ppmv) it reduces visibility significantly for wavelengths less than 0.50 μm and moderately for wavelengths between 0.50 and 0.60 μm.

While NO_2 affects visibility, studies have shown that most of its effect is limited to times when its concentration peaks. For example, results from a project studying Denver's *brown cloud* showed that NO_2 accounted for about 6.6% of total extinction averaged over all sampling periods, and for about 37% of extinction during periods of maximum concentration. On average, scattering and absorption by particles appear to have caused most extinction (Groblicki *et al.*, 1981).

8.1.3 Particle Scattering

Of all extinction processes, particle scattering reduces visibility most. Particle scattering depends on aerosol size distributions and concentrations, indices of refraction, and scattering efficiencies. As discussed in Section 3.1.1, particle distributions are often trimodal (Whitby, 1978). Nucleation mode particles (below 0.1 μm diameter) originate from nucleation of emitted and ambient vapors. They grow primarily by coagulation, but also by condensation. Accumulation mode particles (between 0.1 and 2.0 μm) result from condensational growth, dissolutional growth, and coagulation of smaller particles and from direct emissions. Finally, coarse mode particles (above 2.0 μm) originate from wind blown dust, emissions, sea spray, volcanoes, and plant particles.

Size distributions are used to calculate particle extinction. The extinction due to scattering by spherical particles of uniform composition, at any wavelength, is

138

$$\sigma_{sp,\lambda} = \sum_{i=1}^{N_B} \pi r_i^2 n(r_i) Q_s \left(m_\lambda, \alpha_{i,\lambda} \right), \tag{8.7}$$

where r_i is the radius (cm) of the particle in a particular size bin i, N_B is the number of size bins, $n(r_i)$ is the number of particles (No. cm^{-3}) in bin i, and Q_s is the single particle light scattering efficiency. Q_s depends on m_λ --the complex (real plus imaginary) index of refraction of the material at a given wavelength -- and on $\alpha_{i,\lambda}$ -- the dimensionless size parameter ($2\pi r_i / \lambda$). The scattering extinction due to all particles types is a summation of (8.7) over all particle types. However, each particle type has a unique number distribution and index of refraction. If a particle of a given size is made of an internal mixture of components, its refractive index can be calculated by summing up the volume fraction of each component in the mixture multiplied by the component's refractive index (Kerker, 1969, Horvath, 1993; Wexler *et al.*, 1992).

Scattering efficiencies differ for different-sized particles and different light wavelengths. When a particle has a diameter much smaller than the wavelength of light ($r_i \ll \lambda$ or $\alpha_{i,\lambda} \ll 1$), it is in the *Rayleigh regime* and called a *Tyndall scatterer*. Such particles have a scattering efficiency of

$$Q_s \left(m_\lambda, \alpha_{i,\lambda} \right) = \frac{8}{3} \alpha_{i,\lambda}^4 \left| \frac{m_\lambda^2 - 1}{m_\lambda^2 + 2} \right|^2. \tag{8.8}$$

Since $\alpha_{i,\lambda}$ is small for such particles, the scattering efficiency is small. Thus, particles with diameter less than 0.1 μm are relatively inefficient scatterers.

When a particle has a diameter approximately equal to the wavelength of light (r_i ~λ or, more specifically, 0.1 $<\alpha_{i,\lambda}<$ 100) its scattering (and absorption) efficiencies can

139

be approximated with Mie's solution to Maxwell's equations (van de Hulst, 1957; Kerker, 1969). In GATOR, an algorithm (Toon and Ackerman, 1981; Dave, 1968) is used to obtain the efficiencies and single scattering albedos for stratified spherical particles (particles that have an inner core and outer shell).

Calculations from the code indicate that particles of size 0.2 - 1.0 μm scatter more efficiently than do particles outside this size range. Thus, the most efficient scatterers in the *Mie regime* are accumulation mode particles, which almost always determine the extent of particle extinction (Waggoner *et al.*, 1981). In the Los Angeles Basin, nitrate, sulfate, organic carbon, and elemental carbon make up most fine particle mass. Typically, 20 - 50% of this mass is sulfate. Thus, sulfate is correlated to particle scattering more closely than is any other species (*ibid.*). However, organic carbon and nitrate also contribute to particle scattering.

Finally, when a particle has a diameter much greater than the wavelength of light ($r_i \gg \lambda$ or $\alpha_{i,\lambda} \gg 1$) it is in the *geometrical regime*. Such particles not only reflect and refract but also diffract light significantly. As $\alpha_{i,\lambda}$ increases, the scattering efficiencies of these particles approach constant values in a sinusoidal fashion. However, large particles -- such as fog drops, cloud drops, dust, and sand -- obscure visibility not because they have high scattering efficiencies, but because they have large cross-sectional areas.

8.1.4 Particle Absorption

The absorption extinction of a particle of uniform composition,

$$\sigma_{ap,\lambda} = \sum_{i=1}^{N_B} \pi r_i^2 n(r_i) Q_a(m_\lambda, \alpha_{i,\lambda}),$$
(8.9)

140

is similar to the scattering extinction. In (8.9), Q_a is the single particle absorption efficiency. The major light absorber in polluted air is elemental carbon (soot), which has a peak absorption efficiency at 0.2 μm diameter (Ouimette and Flagan, 1982). While the absorption efficiency gradually decreases towards zero at larger sizes, it decreases to a constant, non zero value at lower sizes. Thus, while soot particles smaller than 0.1 μm scatter little light, they absorb significantly.

8.2 Mean Intensities and Heating Rates

The gas and aerosol extinction coefficients just discussed affect optical depth. Optical depth (τ -- unitless) equals total extinction (cm^{-1}) multiplied by the thickness of the layer of air (cm). In GATOR, extinction coefficients are used to calculate meteorological range, and optical depths are used to calculate mean intensities and heating rates. Mean intensities are subsequently used to calculate photodissociation rates, and heating rates are transferred to the MMTD to calculate part of the diabatic temperature change. To solve for mean intensities and heating rates, GATOR uses the solution to the radiative transfer equation given by Toon $et\ al.$ (1989b).

Toon $et\ al.$ wrote the radiative transfer equation in a plane parallel scattering atmosphere as

$$\mu \frac{\partial I_\lambda}{\partial \tau_\lambda}(\tau_\lambda, \mu, \phi) = I_\lambda(\tau_\lambda, \mu, \phi) - S_\lambda(\tau_\lambda, \mu, \phi)$$
$$-\frac{\omega_{0\lambda}}{4\pi} \int_0^{2\pi} \int_{-1}^1 P_\lambda(\mu, \mu', \phi, \phi') I_\lambda(\tau_\lambda, \mu', \phi') d\mu' d\phi', \qquad (8.10)$$

where λ is wavelength and $\mu = \cos\theta$. Here, θ is the zenith angle of scattering (the angle between the observed scattered intensity, I_λ, and the surface normal). Also in (8.10), μ' = $\cos\theta'$, where θ' is the zenith angle of incidence (the angle between the incident

141

direction of scattering and the surface normal). Further, ϕ is the azimuthal (or longitudinal) angle of scattering, ϕ' is the azimuthal angle of incidence, τ_λ is the optical depth from the top of the atmosphere to the point of interest, measured along the zenith angle (θ), $\omega_{0\lambda}$ is the single scattering albedo, and P_λ is the scattering phase function. The single scattering albedo is the ratio of the extinction due to scattering to the sum of the extinctions due to scattering and absorption. The phase function is the single-particle scattering law for radiation scattered from the incident direction defined by (μ',ϕ') into the direction defined by (μ,ϕ) (Meader and Weaver, 1980). In other words, it is the fraction of total energy scattered between the angle of incidence and the direction of scattering. For example, with Rayleigh scattering, the phase function equals 0.75(1 + $\cos^2\theta_T$), where θ_T is the angle between the directions of incidence and scattering.

Further, in (8.10), S_λ is the solar or infrared source function. For solar wavelengths,

$$S_\lambda = \frac{\omega_{0\lambda}}{4} F_{s\lambda} P_\lambda (\mu, -\mu_0, \phi, \phi_0) \exp(-\tau_\lambda/\mu_0),\qquad(8.11)$$

where $\pi F_{s\lambda}$ is the solar flux at the top of the atmosphere and $\mu_0 = \cos\theta$. Here, θ_0 is the zenith angle of the incident solar flux. The solar flux is a function of wavelength and varies with season. For example, the incident flux normal to earth's surface in January is approximately 6.7% greater than the incident flux in July since the earth-sun distances is further in July (about 1.53 x 10^{11}m) than it is in January (about 1.47 x 10^{11} m) (Robinson, 1966).

For infrared wavelengths,

$$S_\lambda = (1 - \omega_{0\lambda}) B_{T\lambda}.\qquad(8.12)$$

142

where $B_{T\lambda}$ is the temperature- and wavelength-dependent Planck function,

$$B_{T\lambda} = \int_0^\lambda \frac{2hc^2 d\lambda}{\lambda^5 \left[\exp(hc/k_B \lambda T) - 1\right]}. \qquad (8.13)$$

In (8.13), h is Planck's constant (6.626×10^{-34} J s), c is the speed of light (2.9979×10^8 m s^{-1}), k_B is Boltzmann's constant (1.38×10^{-23} J K^{-1}), T is temperature (K), and λ is wavelength in meters. When summed over all wavelengths, (8.13) gives the Stefan-Boltzmann law,

$$\pi B_T(\infty) = \sigma T^4, \qquad (8.14)$$

where σ is the Stefan-Boltzmann constant (5.669×10^{-8} W m^{-2} K^{-4}). Also, taking the maximum of the derivative of the integrand of (8.13) gives Wien's law, $\lambda_p = a / T$, where $a = 2898$ μm K. Wien's law relates the peak wavelength of emittance to temperature.

To calculate zenith angle, GATOR uses empirical equations from the Astronomical Almanac (Nautical Almanac Office, 1993). Further, for air pollution simulations, the shortest wavelength in the model is 282 nm, which is near the minimum received by the troposphere. For wavelengths between 282 and 800 nm, the spectrum is divided into 65 intervals of between 2.5 and 10 nm each (Jacobson et al., 1994e). For wavelengths of between 800 and 4300 nm, the spectrum is divided into 16 probability intervals and 61 finer wavelengths within these intervals. Finally, between 4300 and 75,000 nm the grid is divided into 18 probability intervals and 71 finer wavelengths within these intervals (Toon et al., 1989b). Thus, a heating rate calculation requires the

solution of the radiative transfer equation over all 203 intervals, and a mean intensity calculation for photorates requires the solution over the first 65 intervals.

To solve the radiative transfer equation for an inhomogeneous atmosphere, Toon *et al.* (1989b) organized two-stream equations that fit into a tridiagonal matrix of the form

$$
\begin{bmatrix}
B_1 & D_1 & 0 & 0 & 0 \\
A_2 & B_2 & D_2 & 0 & 0 \\
0 & A_3 & B_3 & D_3 & 0 \\
0 & 0 & A_4 & B_4 & D_4 \\
0 & 0 & 0 & A_5 & B_5
\end{bmatrix}
\begin{bmatrix}
Y_1 \\
Y_2 \\
Y_3 \\
Y_4 \\
Y_5
\end{bmatrix}
=
\begin{bmatrix}
E_1 \\
E_2 \\
E_3 \\
E_4 \\
E_5
\end{bmatrix},
\tag{8.15}
$$

where A, B, D, and E are coefficients (defined in Toon *et al*), the subscripts are layer numbers (five layers in this example), and Y is the array of solutions to the matrix. All wavelength subscripts are omitted for simplicity. Equation (8.15) also takes the form,

$$
A_l Y_{l-1} + B_l Y_l + D_l Y_{l+1} = E_l,
\tag{8.16}
$$

where l is the layer number. The matrix solutions, Y, are used to calculate net radiative fluxes and mean intensities at the bottom of each layer (n). The flux and intensity are given as

$$
F_n = Y_{1n}(e_{1n} - e_{3n}) + Y_{2n}(e_{2n} - e_{4n}) + C_n^+(\tau_n) - C_n^-(\tau_n) - direct
\tag{8.17}
$$

and

$$
4\pi J_n = \left[Y_{1n}(e_{1n} + e_{3n}) + Y_{2n}(e_{2n} + e_{4n}) + C_n^+(\tau_n) + C_n^-(\tau_n) \right]/\mu_1 + direct/\mu_0.
$$

144

$$(8.18)$$

where, for solar wavelengths,

$$direct = \mu_0 \pi F_s \exp\left[-(\tau_c + \tau_n)/\mu_0\right], \qquad (8.19)$$

and for infrared wavelengths, $direct = 0$. In (8.17) and (8.18),

$$C_n^+(\tau_n) = \frac{\omega_{0n}\pi F_s \exp\left[-(\tau_c + \tau_n)/\mu_0\right]\left[(\gamma_{1n} - \mu_0^{-1})\gamma_{3n} + \gamma_{4n}\gamma_{2n}\right]}{\chi_n^2 - \mu_0^{-2}} \qquad (8.20)$$

and

$$C_n^-(\tau_n) = \frac{\omega_{0n}\pi F_s \exp\left[-(\tau_c + \tau_n)/\mu_0\right]\left[(\gamma_{1n} + \mu_0^{-1})\gamma_{4n} + \gamma_{3n}\gamma_{2n}\right]}{\chi_n^2 - \mu_0^{-2}} \qquad (8.21)$$

for solar intervals and

$$C_n^+(\tau_n) = 2\pi\mu_1\left\{B_{T0n} + B_{T1n}\left[\tau_n + (\gamma_{1n} + \gamma_{2n})^{-1}\right]\right\} \qquad (8.22)$$

and

$$C_n^-(\tau_n) = 2\pi\mu_1\left\{B_{T0n} + B_{T1n}\left[\tau_n - (\gamma_{1n} + \gamma_{2n})^{-1}\right]\right\} \qquad (8.23)$$

for infrared intervals. In these equations,

$$B_{T1n} = \left[B_{Tbn} - B_{T0n}\right]/\tau_n \qquad (8.24)$$

is the slope of the Planck function evaluated at the bottom (B_{Tbn}) and top (B_{T0n}) of a layer, and $\gamma_{1n} \ldots \gamma_{4n}$ are coefficients that depend on whether the two-stream approximation is an Eddington, Quadrature, Hemispheric Mean, or another type (Meader

145

and Weaver, 1980; Toon *et al.*, 1989b). These coefficients are primarily a function of single scattering albedo and asymmetry factor. All parameters not defined above are defined in Toon *et al.* (1989b).

Further, for infrared calculations, Toon *et al.* (*ibid.*) improved the solution to the two stream technique by changing the source function. The improved source function scheme requires no tridiagonal matrix solutions and is energy conserving.

8.3 Photodissociation Rates

The purpose of calculating spectrally-resolved mean intensities in (8.18) is to use the values to determine photolysis rates for the reactions at the end of Table A.4. The photolysis rate (s^{-1}) of a species i in any grid cell is

$$j_i = \int_0^\infty I_\lambda(\tau_\lambda, \mu, \phi) b_{i\lambda}(T) \phi_{i\lambda}(\lambda, T) d\lambda,$$ (8.25)

where $I = 4\pi J$ (from 8.17) is the mean intensity (photons $cm^{-2} s^{-1}$) (the subscripts here are changed so that I reflects a wavelength dependence that is not shown in the equations of Section 8.2). Also in (8.25), b_i is the temperature- and wavelength-dependent absorption cross-section of each gas (cm^2 $molecule^{-1}$), and ϕ is the quantum yield (No. molecules $photon^{-1}$) of gas i at each temperature and wavelength. Summing up the integrand in (8.25) over all wavelength intervals gives the photolysis rate of the species in a given grid cell. In GATOR, most absorption cross section and quantum yield data were obtained from Atkinson *et al.* (1992), DeMore *et al.* (1990), their references, and Madronich and Chatfield (*pers. comm.*).

146

Chapter 9

Setup of Model Applications

To test the validity of the GATOR / MMTD system, I compared airshed simulation results to Southern California Air Quality Study (SCAQS) data for Wednesday, August 26 through Friday, August 28, 1987. Here, the setup of the GATOR / MMTD system for these simulations is described. Section 9.1 discusses model data, which include ambient data (9.1.1) for comparison, emissions data (9.1.2), and other data (9.1.3). Section 9.2 discusses the initializing of gas and aerosol concentrations and meteorological variables in the model. Section 9.3 discusses boundary conditions, and Section 9.4 discusses error checks that will be used in Chapter 10.

9.1 Model Data

9.1.1 Ambient Data for Comparisons

The primary reasons to simulate the period August 26 - 28, 1987 is that the number of available ambient measurements is large and a detailed California Air

147

Resources Board emissions inventory exists for that period. Lawson (1990) describes the data-gathering effort that occurred during the SCAQS.

One of the SCAQS data sets used here was the SCAQS modeling archive (King *et al.*, 1990), provided by the California Air Resources Board (B. Croes, *pers. comm.*). The archive contains surface mixing ratios of ambient ozone, carbon monoxide, nitrogen dioxide, nitric oxide, sulfur dioxide, non-methane hydrocarbons (NMHCs), and methane, measured at 56 monitoring sites during the period August 26 - 30, 1987. The archive also contains surface data for temperature, dew point, relative humidity, sea level pressure, wind speed, wind direction, visibility, cloud cover, ceiling height, sea surface temperature, precipitation, solar radiation, and standard deviation of wind direction. At least one variable was measured at each of 98 sites. Finally, the archive contains upper air data for pressure, temperature, dew point, relative humidity, wind speed, and wind direction, taken from 257 soundings measured at 15 locations.

In addition to comparing results to data in the SCAQS modeling archive, I compared results to other SCAQS data, listed in Table 9.1. Among these were SCAQS Sampler data, provided by the CARB (B. Croes, *pers. comm.*). The Sampler was developed by Fitz *et al.* (1989), and Eldering *et al.* (1994) describe the measurements taken from the Sampler during the SCAQS. Sampler data consist primarily of aerosol, aerosol precursor, and particle absorption coefficient measurements. The aerosol-phase species measured included elemental carbon, organic carbon, sodium, chloride, ammonium, nitrate, sulfate, and total aerosol mass. The gas-phase species measured included ammonia, nitric acid, and sulfur dioxide. Most aerosol components were divided into sub-2.5 μm and sub-10 μm size regimes.

Other data used for comparison were measurements of nitrous acid and formaldehyde (Winer *et al.*, 1989; Winer and Biermann, 1994), particle scattering coefficient (measured by U. Illinois, General Motors, and the SCAQMD -- see Eldering

148

et al., 1994), hydrogen peroxide data (Mackay *et al.*, 1988), and peroxyacetyl nitrate data (Williams and Grosjean, 1989).

The data described above were gathered at some or all of the SCAQS "A" and or "B" sites. The "A" sites were Claremont and Long Beach City College and the "B" sites consisted of the "A" sites plus Anaheim, Azusa, Burbank, Hawthorne, Los Angeles, Rubidoux, and San Nicolas Island.

Table 9.1. SCAQS ambient data (aside from SCAQS Modeling Archive Data) used to compare model results against. The column 'data collector' identifies the group(s) who measured the data. 'Variable' identifies the atmospheric gas or aerosol constituents measured. The (*) indicates that the aerosol data were resolved into two size regimes, smaller than 2.5 µm diameter and smaller than 10 µm diameter. 'Collection Technique' identifies the one or more techniques or instruments used to measure the data: SS = SCAQS Sampler; IC = Ion Chromatograph; AS = Absorption Spectrophotometer; TV = Thermal Volatilization; GR = Gravimeter; CM = Colorimeter; SP = Spectrometer; IN = Integrating Nephelometer; DO = Differential Optical Absorption Spectrometer; PA = DGA Pan Analyzer; GC = Gas Chromatograph; TD = Tunable Diode Laser Absorption Spectrometer. The *Dates* column identifies the dates between August 26 - 30, 1987 during which, data were measured. The sites are locations where data were measured: ANAH = Anaheim; AZUS = Azusa; BURK = Burbank; CELA = Los Angeles; CLAR = Claremont HAWT = Hawthorne; LBCC = Long Beach City College; RIVR = Riverside-Rubidoux; SNI = San Nicholas Island. Refer to Figure 1.7 for site locations.

149

Table 9.1

Data Collector	Variable	Collection Tool or Method	Dates in August, 1987	Sites
ENSR Consulting and Engineering	*Elemental C *Organic C	SS, TV SS, TV	8/27 - 8/29	ANAH; AZUS BURK; CELA CLAR; HAWT LBCC; RIVR SNI
C-E Environmental Inc.	Na^+ *Cl^- *NH_4^+ *NO_3^- *SO_4^{2-} *Aerosol Mass $HNO_3(g)$ $NH_3(g)$ $SO_2(g)$	SS, AS SS, IC SS, CM SS, IC SS, IC SS, GR SS, IC SS, CM SS, IC	8/27 - 8/29	ANAH; AZUS BURK; CELA CLAR; HAWT LBCC; RIVR SNI
Radiance Research	σ_{ap}	SS, SP	8/27 - 8/29	ANAH; AZUS BURK; CELA CLAR; HAWT LBCC; RIVR SNI
U. Illinois; General Motors Research Lab; SCAQMD	σ_{sp}	IN	8/26 - 8/30	CLAR; LBCC RIVR
U. C. Riverside	$NO_2(g)$ $HCHO(g)$ $HONO(g)$ $NO_3(g)$	DO DO DO DO	8/27 - 8/29	CLAR; LBCC
Daniel Grosjean and Associates, Inc.	$PAN(g)$	PA; GC	8/26 - 8/29	ANAH; AZUS; BURK; CELA; CLAR; LBCC; RIVR
Unisearch Associates, Inc.	$H_2O_2(g)$ $HCHO(g)$	TD	8/25 - 8/30	CLAR

150

9.1.2 Emissions Data

In addition to providing SCAQS ambient measurement data, the CARB has provided gridded emissions data for Wednesday, August 26 through Friday, August 28, 1987. (Allen and Wagner 1992). The emissions grid covers a region 325 km east-west by 180 km north south, with the southeast corner at 33° 8' 35" N latitude -119° 24' 44" E longitude. Table 3.2 summarized the speciated particulate emissions over the grid.

The gas data in the CARB inventory include hourly gridded emissions of NO_x, oxides of sulfur (SO_x), ROGs, and carbon monoxide. NO_x is partitioned into NO, NO_2, and HONO; SO_x is partitioned into SO_2 and SO_3; and ROGs are divided into both individual species and bond groups. The individual species include formaldehyde, methanol, ethene, and ethanol, and the bond groups include higher molecular weight aldehydes, paraffins (carbons bonded by a single bond), olefins (carbons bonded by a double bond), seven-carbon aromatics (represented by toluene), eight-carbon aromatics (represented by xylene), and terpenes (represented by isoprene). Table 9.2 summarizes the speciated emissions inventory for August 26 - 28, 1987.

While the CARB emissions inventory is detailed, some emissions may be underestimated. For example, based on a tunnel study by Ingalls *et al.* (1989), Harley *et al.* (1993a) concurred that emissions of carbon monoxide and reactive organic gases from on-road hot exhaust may be low by a factor of three. Table 9.2 shows an example of an emissions inventory, adjusted to account for the possible underestimation of hot exhaust emissions. In the emissions inventory provided by the CARB, a category exists for ROG hot exhaust; however, no category exists for CO hot exhaust. Thus, while ROG emissions from hot exhaust were multiplied by three in Table 9.2, total CO emissions were multiplied by 1.6 in order to capture the suggested underestimate in CO hot exhaust emissions. This factor gives a revised CO emissions rate slightly lower than the revised

151

rate reported by Harley *et al.* (1993a), who appear to have an emissions inventory that separates CO hot exhaust from other CO emissions.

Table 9.2. CARB emissions inventory for August 26 - 28, 1987 (Allen and Wagner, 1992) assuming (i) no adjustments and (ii) adjustment in ROG hot exhaust by a factor of 3 and total CO by a factor of 1.6. Units for CO, NO, NO_2, HONO, SO_2, and SO_3 are tons per day (tpd). Units for all ROGs are kmoles per day (kmpd). ROGs are speciated into carbon bond groups and individual components (*e.g.* Gery et al., 1989).

Table 9.2

species or bond group	<---original inventory---> 8/26	8/27	8/28	<---adjusted inventory---> 8/26	8/27	8/28
carbon monoxide (CO)	6057	5938	4659	9142	8951	8953
nitric oxide (NO)	758	754	658	758	754	658
nitrogen dioxide (NO_2)	130	129	113	130	129	113
nitrous acid (HONO)	7	6	6	7	6	6
total NO_x as NO_2 (tpd)	1300	1291	1127	1300	1291	1127
sulfur dioxide (SO_2)	109	108	102	109	108	102
sulfur trioxide (SO_3)	4	4	4	4	4	4
total SO_x as SO_2 (tpd)	112	111	105	112	111	105
paraffins (PAR)	62,300	65,371	65,586	85,740	85,639	85,854
olefins (OLE)	1524	1887	1918	3491	3437	3469
toluene (TOL)	1727	1722	1722	2456	2443	2443
xylene (XYL)	1105	1102	1102	1716	1706	1706
formaldehyde (HCHO)	674	662	663	1217	1197	1198
C_2+ aldehydes (ALD2)	668	961	983	1366	1352	1374
ethene (ETH)	2737	2664	2664	5263	5156	5156
methanol (MEOH)	171	171	171	171	171	171
ethanol (ETOH)	619	619	619	619	619	619
isoprene (ISOP)	406	792	868	406	792	868
total ROGs (kmpd)	71,931	75,951	76,296	102,445	102,512	102,858

152

The CARB emissions inventory separates stack from other gas emissions. Table 9.3 shows the relative rate of stack compared to non-stack emissions. In sum, about 1.2% of CO emissions, 7.2% of NO_x emissions, 12% of SO_x emissions, and 0.3% of ROG emissions originated from smokestacks. To calculate plume rise height for stack emissions, a subroutine by Ames *et al.* (1986) (S. Mitsutomi, *pers. comm.*) that uses formulae from Briggs (1975) was modified. Briggs gave plume rise height as a function of stack height, flowrate of emissions, exhaust temperature, wind speed, and the ambient temperature profile. The temperature profile and wind speeds for the plume rise height are calculated with the MMTD and stack height, exhaust temperature, and flowrate data are all included in the CARB emissions inventory.

Table 9.3. Comparison of non-stack to stack emissions for August 27, 1987, using the adjusted inventory described in Table 9.2. Units for CO, NO, NO_2, HONO, SO_2, and SO_3 are kg day^{-1}. Units for all ROGs are kmoles day^{-1}.

species or bond group	Table 9.3 non-stack	stack	total
carbon monoxide (CO)	8937.7	13.7	8951.4
nitric oxide (NO)	700.0	54.0	754.0
nitrogen dioxide (NO_2)	119.8	9.3	129.1
nitrous acid (HONO)	6.0	0.5	6.5
sulfur dioxide (SO_2)	96.2	12.7	108.9
sulfur trioxide (SO_3)	3.8	0.5	4.3
paraffins (PAR)	85,341	298	85,639
olefins (OLE)	3433	4	3437
toluene (TOL)	2435	8	2443
xylene (XYL)	1704	2	1706
formaldehyde (HCHO)	1186	11	1197
C_2+ aldehydes (ALD2)	1351	1	1352
ethene (ETH)	5154	2	5156
methanol (MEOH)	171	<1	171
ethanol (ETOH)	617	2	619
isoprene (ISOP)	792	0	792

153

In addition to obtaining the SCAQS emissions inventory, I received an ammonia gas emissions inventory (Russell and Cass, 1986; Gharib and Cass, 1984; Cass *et al.*, 1982) from the SCAQMD (J. Lestor, *pers. comm.*). This inventory estimates ammonia emissions during a day in August, 1982; however, it was used here for simulating pollution during the August, 1987 SCAQS period. The total ammonia emissions rate in this inventory is 164.3 tons per day, with 51.6% of the emissions originating from livestock sources, 14.2% originating from domestic sources, 14.5% originating from soil, and the rest originating from miscellaneous sources (Russell and Cass, 1986). Further, most emitted ammonia emanates from the east side of the basin, where livestock is abundant.

Next, for aerosol, the size-, temporally-, and spatially-distributed emissions data summarized in Table 3.2 were used. These emissions are divided into four size categories: < 1 µm diameter, 1 - 2.5 µm, 2.5 - 10 µm, and > 10 µm. Because GATOR uses more than four size bins, the CARB data were distributed onto the model size grid. For example, all CARB aerosol emissions smaller than 1 µm were distributed with a unimodal lognormal distribution. A second lognormal distribution was constructed with the three coarse CARB bins (> 1 µm). Consequently, CARB emissions were distributed with two lognormal modes over the model size distribution.

9.1.3 Additional Data

In addition to ambient and emissions data, other data were used to initialize and define parameters in GATOR. These included topographical data from the U. S. Geological Survey and landuse data from the USGS / California Institute of Technology (Russell *et al.*, 1993, D. Winner, *pers. comm.*). Further, surface roughness values for each landuse type (Russell *et al.*, 1993) and surface resistance values for SO_2 and O_3 (Walcck *et al.*, 1986; Sheih *et al.*, 1986; Chang *et al.*, 1987; Russell *et al.*, 1993) were

154

used. In addition, soil albedo, soil moisture, soil density, and soil heat capacity data from the SCAQMD (J. Lestor, *pers. comm.*) were used.

Further, chemical data were taken from numerous sources. For gas-phase chemistry, inorganic and organic reactions listed in Table A.4 were used These came primarily from Atkinson *et al.*, (1992), DeMore *et al.* (1990), Gery *et al.*, 1989, Paulson and Seinfeld (1992), and the references therein. Similarly, for aerosol chemistry, equilibrium constants originated from the sources listed in Table A.7 and aqueous chemical reaction rates originated from the sources in Table A.8.

Further, for particle indices of refraction, data were used from Bergstrom (1972) Hale and Query (1973), Roessler and Faxvog (1980), Ackerman and Toon (1981), Sloane, (1984), Wexler *et al.* (1992), and Lide (1993). Also temperature-dependent binary activity coefficient data for equilibrium simulations were calculated using activity coefficient data at 298K, heat of dilution data, and heat capacities data. The sources of these three types of data are listed in Tables 1 and 2 of Appendix E.

Next, because most gridded data -- including data for emissions, landuse, surface roughness length, soil wetness, soil density, soil specific heat, and albedo -- were designed for a Universal Transverse Mercator (UTM) grid projection, the data were interpolated to spherical (geographic) coordinates. Because UTM grid cells cross geographic cells at random locations, interpolating information from one coordinate system to the other is difficult. However, to interpolate, the area of a UTM cell lying in a geographic cell was physically integrated, as described next.

To integrate, each UTM grid cell (usually 5 x 5 km in area) was divided into 10,000 or more smaller cells (each 50 m x 50 m in area). Each smaller cell was assumed to contain the same data values as the larger UTM cell it was partitioned from. Next, the latitudes and longitudes of the four corners of each smaller cell were located using UTM to geographic conversion data and formulae (U. S. Dept. of the Army, 1958).

155

Subsequently, for each large UTM cell (U), the number of smaller UTM cells ($N_{U,G}$) in each geographic cell (G), was counted. Consequently, either the cumulative (S_G -- for emissions) or average (V_G -- for all other cases) datum value in each geographic cell was calculated from

$$S_G = \sum_{U=1}^{M_G} \left(\frac{N_{U,G} A_S D_U}{A_U} \right) \tag{9.1}$$

or

$$V_G = \frac{\sum_{U=1}^{M_G} \left(N_{U,G} A_S D_U \right)}{A_G}, \tag{9.2}$$

where M_G is the number of large UTM cells touching geographic cell G, A_S is the area of a small UTM cell, A_U is the area of a large UTM cell, A_G is the areas of a geographic cell, and D_U is the original datum value in a large UTM cell. The precision of this method increases with smaller and smaller mini-UTM cells.

9.2 Initializing Variables

Before the beginning of each simulation, all meteorological parameters, gas mixing ratios, aerosol concentrations, and model grids are initialized. GATOR and the MMTD are coupled together; but, to maintain flexibility, GATOR can nest horizontally and vertically within the dynamics model. In the horizontal, GATOR maintains the same grid spacing as the MMTD; however, the boundaries of GATOR may lie within or directly upon the boundaries of the MMTD. In the vertical GATOR can either match the MMTD layers or nest within them. Thus, the number of GATOR layers within each

156

MMTD layer may be greater than or equal to one. For the simulations discussed herein, both GATOR and the MMTD used spherical coordinates.

Figure 9.1 shows the horizontal model layout for these simulations. The southwest corner of the MMTD was 33.06° N latitude and 119.1° W longitude. The uniform grid-spacing was 0.05 degrees east-west (about 4.6 km) and 0.045 degrees north south (about 5.0 km), and the model dimension was 55 east-west grid cells by 38 north-south cells by 20 vertical sigma layers. Each edge of GATOR was placed two grid cells within each edge of the MMTD in order to reduce the effects of boundary wind values calculated by the MMTD. However, the horizontal grid spacing in GATOR and the MMTD were the same. Thus, GATOR consisted of 51 east-west cells by 34 north-south cells, with a southwest corner at 33.15 ° N latitude and 119.0° W longitude.

Further, while 20 vertical levels were used for the MMTD, 14 were used for GATOR in order to reduce computational time. These layers included the same bottom eight of the MMTD plus six more, each encompassing two MMTD layers. To obtain values for meteorological parameters in each of the six upper layers, the values from the two corresponding MMTD layers were averaged. The top in both models was set to 250 mb. The eight lowest layers (the same in both models) were all below about 850 mb (about 1.5 km). In sum, the MMTD solved equations in 41,800 grid cells while GATOR solved in 24,276 cells. All horizontal and vertical dimensions in each model are easily changed.

Next, meteorological parameters were initialized with interpolated SCAQS sounding data (King *et al.*, 1990). The data included information about pressure, temperature, dew point, wind speed, and wind direction at numerous altitudes. All simulations started at 4:30 a. m on either August 26th or 27th, 1987. Since no sounding occurred at either of these times, all soundings that occurred between 3:00 and 5:00 a. m. each day were interpolated. Three such soundings were taken on August 26th, and 13

157
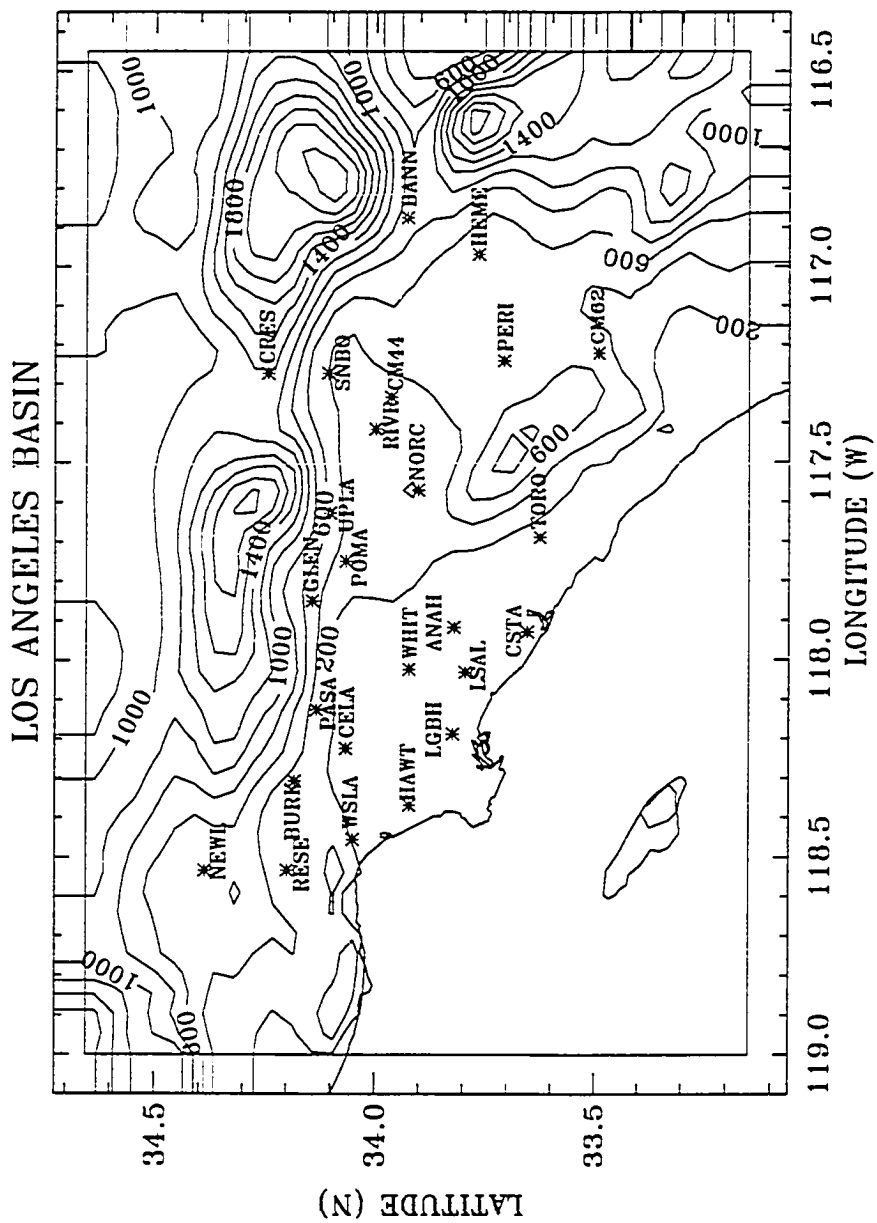
Fig. 9.1. Map of Los Angeles Basin showing the current MMTD and GATOR model domains. The GATOR domain lies within each MMTD boundary; however, the grid spacing is the same inside both models. Both domains are moveable. Plot developed by Ruiyan Lin.

158

were taken on August 27th. All winds were initialized with zero velocity to ensure mass conservation and to avoid startup waves near mountain regions. Finally, the sea-surface temperature was initialized at an average value of 17 °C.

Next, Table A.3 lists all gas-phase species in the model. To obtain initial mixing ratios of NO, NO_2, O_3, CH_4, CO, and non-methane hydrocarbons (NMHCs), I first horizontally interpolated their observed surface mixing ratios from SCAQS data and assumed the mixing ratios remained unchanged up through the morning inversion. Above this height and outside the interpolation domain of influence, the mixing ratios of these species were set to background values, as discussed below. For NMHCs, the interpolated mixing ratios were partitioned among about 10 major emitted hydrocarbons. For the mixing ratios of gases without surface information, some were set to background values and others were set to zero.

Initial clean background tropospheric gas mixing ratios were obtained from several sources. For nitric oxide, vertical profiles measured by Drummond *et al.* (1988) were used; for ozone, profiles measured by Marenco and Said (1989) were used; for carbon monoxide and methane, profiles were obtained from Marenco *et al.* (1989); for ethene, surface data from Singh *et al.* (1988) and upper air data from Bonsang *et al.* (1991) were used; for nitric acid, a profile suggested by Brasseur and Solomon (1986) was used; for water vapor, the SCAQS sounding data were interpolated, as discussed above, and for most other species and carbon bond groups, surface values suggested by USEPA (1991) were used.

Further, aerosol components were initialized with either zero, background, or interpolated concentrations in each size bin. During the SCAQS period of August 27 - 30, 1987, measurements of elemental carbon, organic carbon, sulfate, nitrate, ammonia, sodium, and chloride aerosol concentrations were taken at nine sites throughout the basin

159

(Table 9.1). One SCAQS site, San Nicholas Island (SNI), lies near relatively clean ocean air, south of Santa Barbara. To initialize background aerosol concentrations, I first distributed the aerosol mass from SNI (data for midnight - 5:00 am, August 27, 1987), among size bins in the nucleation, accumulation, and coarse particle modes, with a trimodal lognormal distribution. Data for most of the SCAQS Sampler aerosol species were gathered for two size regimes -- below 2.5 μm and below 10 μm diameter. For SNI, the difference between the sub-10 μm and sub 2.5 μm mode mass was distributed into the course mode. Further, sub-2.5 μm mass was partitioned between a nuclei and an accumulation mode using a marine surface particle nuclei to accumulation mode volume ratio (0.005:0.995) calculated from Whitby (1978). Since this ratio is similar to his ratio for clean continental nuclei mode particles (0.004:0.996), the marine ratio was used for both continental and marine background distributions.

After distributing mass among the modes, I gathered size distribution parameters to spread mode mass among model size bins. Each mode has a geometric mean number ($\overline{D}_N$) or mass ($\overline{D}_M$) diameter, geometric standard deviation (σ_g), and total number (N_T) or mass (M_T) associated with it. In some cases, average values of these parameters were obtained from observed data (*e.g.* Whitby (1978), Noll *et al.* (1990)). In other cases, $\overline{D}_M$ and σ_g were calculated from size-fractionated aerosol sample data (*e.g.* Kritz and Rancher (1980); Hering and Friedlander, 1982; Lyons *et al.*, 1993; Venkataraman and Friedlander, 1994b). For species without observed concentrations, default geometric mean mass diameters and standard deviations given by Whitby (1978), for the urban average case, were used. For a size-resolved aerosol number or mass distribution obtained from a field sample, the natural log of the geometric mean number and mass diameters are

160

$$\ln \overline{D}_N = \frac{1}{N_T} \sum_{i=1}^{\infty} (\Delta n_i \ln d_i) \qquad (9.3)$$

and

$$\ln \overline{D}_M = \frac{1}{M_T} \sum_{i=1}^{\infty} (\Delta m_i \ln d_i), \qquad (9.4)$$

where Δn_i and Δm_i are the number and mass, respectively of particles in size bin i, centered about diameter d_i. Further, the log of the geometric standard deviation is

$$\ln \sigma_g = \sqrt{\frac{1}{N_T} \sum_{i=1}^{\infty} \Delta n_i \ln^2 \left(d_i / \overline{D}_N\right)}$$

$$= \sqrt{\frac{1}{M_T} \sum_{i=1}^{\infty} \Delta m_i \ln^2 \left(d_i / \overline{D}_M\right)}. \qquad (9.5)$$

Thus, σ_g is the same for both number and mass distributions.

Using the lognormal parameters, I redistributed the mode mass of each species over the model size-bin structure. This size structure (Appendix D) allows any number of size bins that change in volume independently of one another. However, initially, they are arranged geometrically, from smallest to largest, and the volume of one size bin is a constant (V_{RAT}) multiplied by the volume of the previous size bin. Each size bin contains any number of particles; however, each particle in a bin has the same composition and size as each other particle in the bin.

The number and mass, respectively, of particles in each size bin of a lognormal mode are

161

$$\Delta N_i = \frac{N_T \Delta D_i}{D_i \sqrt{2\pi} \ln \sigma_g} \exp\left(-\frac{\ln^2\left(D_i/\overline{D}_N\right)}{2\ln^2 \sigma_g}\right) \tag{9.6}$$

and

$$\Delta M_i = \frac{M_T \Delta D_i}{D_i \sqrt{2\pi} \ln \sigma_g} \exp\left(-\frac{\ln^2\left(D_i/\overline{D}_V\right)}{2\ln^2 \sigma_g}\right), \tag{9.7}$$

where D_i is the average diameter of particles in the size bin and ΔD_i is the width of the bin, in diameter space. Integrating the mass over all particle sizes gives the total mass,

$$M_T = \int_0^\infty M(D)\,dD_i = \frac{1}{6}\pi\rho \int_0^\infty N(D)D^3\,dD$$
$$= \frac{1}{6}\pi\rho\overline{D}_N^3 \exp\left(\frac{9}{2}\ln^2 \sigma_g\right)N_T, \tag{9.8}$$

which is a function of total particle number and other parameters.

After distributing the mass among model size bins using a lognormal distribution for each mode, I distributed the values from SNI horizontally in each grid cell and scaled them vertically, with pressure. All components for which ambient data were unavailable were initialized with zero concentrations in each size bin.

Next, aerosol component data from the rest of the SCAQS Sampler stations were interpolated under the assumption that the radius of influence around each station was 10 km. Thus, the only grid cells interpolated were those within 10 km of one or more stations. Finally, the interpolated values were scaled, with pressure, to the top of the morning inversion. Thus, initial model aerosol concentrations within the basin and over the ocean closely resembled SCAQS Sampler data for the morning of August 27, 1987.

162

9.3 Boundary Conditions

The horizontal inflow boundary condition described in Section 7.2 requires time-dependent mixing ratios of gases and aerosols beyond the boundary. In the case of gases, mixing ratios of each gas were initialized in four distinct columns, each containing the same number of layers as GATOR. The columns represented conditions in the middle of the west, east, north, and south boundaries, respectively. Since boundary values vary significantly during the day due to chemistry, each cell in each column was sent through the chemistry solver each chemistry time interval during a simulation. Consequently, mixing ratios of gases at the boundaries followed diurnal patterns similar to those of free tropospheric gases. In the case of aerosols, all boundary concentrations were initialized with background values from SNI, scaled vertically with pressure.

Both the MMTD and GATOR currently assume that the wind conditions outside a boundary are the same as just inside the boundary. Future work will be to determine winds beyond the model domain. One way is to read synoptic-scale surface, 925 mb, 850 mb, 700 mb, and 500 mb pressure charts or interpolate upper-level wind measurements at UCLA, Pt. Mugu, Edwards Air Force Base, Vandenberg Air Force Base, and San Diego. The winds measured at these sites usually flow parallel to pressure-chart isobars at altitudes above the 850 mb level. Thus, the charts and data should give similar information at these altitudes. Below the 850 mb level, interpolating data from the stations would appear to be most accurate. An alternate approach to using observed winds outside the model domain is predicting them with a mesoscale model, such as the MM5.

At the model top (250 mb, or about 10.3 km), I assumed no gas escaped or entered. Since data at the surface were being compared over a short time period (one to three days), this assumption appears reasonable, especially since estimated fluxes at the

163

top are uncertain. However, GATOR can permit inflow and outflow from the top, and the top can be extended to any pressure level.

9.4 Error Checks

To determine model performance, several error checks were performed. These included checks for mean absolute normalized gross error, normalized bias, paired peak estimation accuracy, and temporally-paired peak estimation accuracy (Tesche *et al.*, 1988; DaMassa *et al.*, 1992). The normalized gross error, written as

$$NGE = \frac{1}{N_s} \sum_{i=1}^{N_s} \frac{\left| P_{x_i t} - O_{x_i t} \right|}{O_{x_i t}}, \qquad (9.3)$$

compares the absolute value of model to observed mixing ratio of a given species, summed and averaged over all observations. In (9.3), N_s is the number of observation sites, P is the predicted value, O is the observed value, x_i is the location of site i and t is the time. For *NGE*, all observations and predictions are paired in space and time. The normalized bias (*NB*) is the same as the gross error, except no absolute value is considered. Thus, the normalized bias is

$$NB = \frac{1}{N_s} \sum_{i=1}^{N_s} \frac{P_{x_i t} - O_{x_i t}}{O_{x_i t}}. \qquad (9.4)$$

Next, the paired peak accuracy identifies how well the model predicts the peak observed mixing ratio at the time and location of the peak. Thus,

164

$$PPA = \frac{P_{\hat{x}_i\hat{t}} - O_{\hat{x}_i\hat{t}}}{O_{\hat{x}_i\hat{t}}}, \qquad\qquad (9.5)$$

where the hats indicate values at the time and location of the peak observed value. Finally, the temporally-paired peak accuracy identifies how well the model predicts the peak observed mixing ratio at the same time of the peak, but at any other location. Thus,

$$TPPA = \frac{P_{x_i\hat{t}} - O_{x_i\hat{t}}}{O_{x_i\hat{t}}}. \qquad\qquad (9.6)$$

While actual station data were used to determine observed values, bilinear interpolation (*e.g.* Press *et al.*, 1993) of four surrounding grid cell centers was used to determine model variable values at the stations.

Thus, this chapter described the setup for gas and aerosol model simulations, including the description of data, initial conditions, boundary conditions, and error checks. Next, model results are discussed.

165

Chapter 10

Model Results

In this chapter, results from model simulations of pollution in the Los Angeles Basin during the SCAQS period of August 26 - 28, 1987 are shown. The results include comparisons of gas and aerosol distributions, aerosol compositions, and other parameters to data. Section 10.1 discusses results of simulations that excluded aerosol processes, Section 10.2 discusses results of simulations that included aerosol processes, and Sections 10.3 - 10.5 analyze results in more detail and discuss sources of model error.

10.1 Gas-Phase Simulations

In this section, model results are compared to observations for cases where no aerosol-phase processes were included in the model simulations. To obtain these results, I ran a three day simulation from 4:30 a. m., August 26 to 10:30 p. m., August 28 (Simulation A) and a two day simulation from 4:30 a. m., August 27 to 11:30 p. m., August 28, 1987 (Simulation B). Tables 10.1 - 10.3 show statistical results from Simulation A and Tables 10.4 - 10.5 show statistical results from Simulation B. The statistics shown, as well as statistics not shown, indicate a normalized gross error for ozone during daylight hours of between 20 - 35%, depending on the hour of the day.

166

These statistics were gathered assuming a suggested cutoff mixing ratio of 4 pphm (DaMassa et al., 1992). Without the cutoff, the gross error was typically only 0 - 3% higher during the day since most measured values were larger than the cutoff value.

Tables 10.1 - 10.5. GATOR / MMTD performance tests for different times of different days. Column (a) is the number of stations for which data (above a cutoff level) were available at the time of day, (b) is the mean absolute normalized gross error, (c) is the normalized bias, (d) is the name of the SCAQMD station where the observed peak parameter value at the time of day occurred, (e) is the model error at that time and location, (f) is the distance from the observed peak value where the model peak value occurred, and (g) is the difference in model versus observed peak value. The gross errors and biases for ozone, nitric oxide, and nitrogen dioxide were calculated using cutoff values of 4, 2, and 2 pphm, respectively (DaMassa et al., 1992). A cutoff was not used for any other parameter. A (*) indicates no cutoff was used for this particular parameter and time. A (---) indicates this value was not calculated.

Table 10.1: August 26, 16:30

Parameter	(a) No. of stations	(b) Gross error (%)	(c) Bias (%)	(d) Location of observed peak	(e) Model error at location of observed peak (%)	(f) Distance of model peak from observed peak (km)	(g) Difference between model and observed peaks (%)
O_3	36	28.9	-24.7	RDLD	-66.8	40.6	-41.9
NO	11*	46.9	-46.7	LBCC	-40.4	15.9	-25.7
NO_2	21	43.3	-41.1	AZUS	-50.4	17.2	-14.5
CO	21	56.4	-56.4	RIVM	-77.8	57.2	-57.8
CH_4	5	4.6	-1.2	CELA	-8.3	—	—
NMHCs	4	61.5	-19.0	RESE	-76.0	—	—
SO_2	3	52.8	-52.8	LBCC	-36.1	8.0	-26.6
Temp.	14	1.19	1.16	UPLA	-0.16	—	—
Rel. Hum.	8	18.4	15.8	HAWT	-9.1	—	—
Wind Spd.	33	51.0	30.2	HAWT	-51.5	—	—

167

Table 10.2: August 27, 10:30

Parameter	(a) No. of stations	(b) Gross error (%)	(c) Bias (%)	(d) Location of observed peak	(e) Model error at location of observed peak (%)	(f) Distance of model peak from observed peak (km)	(g) Difference between model and observed peaks (%)
O$_3$	28	23.9	-18.1	RDLD	-41.0	16.6	-31.1
NO	12	52.2	17.0	CELA	64.1	—	—
NO$_2$	22	59.4	-34.8	CELA	-50.2	17.5	-23.3
CO	21	55.5	-55.5	CELA	-70.6	17.5	-44.7
CH$_4$	4	14.3	-13.6	CELA	-22.6	—	—
NMHCs	3	90.4	13.9	CELA	-45.2	—	—
SO$_2$	11	62.3	-62.3	LBCC	-72.3	14.8	30.7
Temp.	14	0.79	-0.62	UPLA	-2.5	—	—
Rel. Hum.	8	13.5	6.3	HAWT	-20.2	—	—
Wind Spd.	33	134	112	HAWT	67.2	—	—

Table 10.3: August 27, 13:30

Parameter	(a) No. of stations	(b) Gross error (%)	(c) Bias (%)	(d) Location of observed peak	(e) Model error at location of observed peak (%)	(f) Distance of model peak from observed peak (km)	(g) Difference between model and observed peaks (%)
O$_3$	??	31.9	-16.8	GLEN	-55.0	96.7	-22.9
NO	1	43.5	-43.5	LYNN	-43.5	23.1	62.9
NO$_2$	21	57.8	-57.8	AZUS	-69.0	25.9	-46.9
CO	23	62.4	-62.4	BURK	-74.6	55.4	-60.1
CH$_4$	4	10.9	-10.9	CELA	-18.3	—	—
NMHCs	3	59.1	8.4	CELA	-15.4	—	—
SO$_2$	9	63.5	-49.0	LBCC	-28.6	4.5	-10.8
Temp.	14	1.0	-0.18	UPLA	-2.42	—	—
Rel. Hum.	8	28.5	23.1	HAWT	-5.8	—	—
Wind Spd.	33	87.6	79.3	SIMI	-36.4	—	—

168

Table 10.4: August 28, 12:30

Parameter	(a) No. of stations	(b) Gross error (%)	(c) Bias (%)	(d) Location of observed peak	(e) Model error at location of observed peak (%)	(f) Distance of model peak from observed peak (km)	(g) Difference between model and observed peaks (%)
O$_3$	33	28.7	-2.0	RESE	9.9	10.1	47.8
NO	1	14.1	14.1	LGBH	14.1	—	—
NO$_2$	19	39.7	-37.1	AZUS	-39.8	30.6	30.8
CO	24	52.5	-52.5	BURK	-67.3	28.3	-23.6
CH$_4$	4	12.2	-12.2	CELA	-23.5	—	—
NMHCs	3	57.1	9.9	CELA	-30.7	—	—
SO$_2$	12	52.8	-52.8	LGBH	-26.8	5.0	28.2
Temp.	14	1.8	-0.91	UPLA	-4.16	—	—
Rel. Hum.	8	92.2	91.7	HAWT	-1.7	—	—
Wind Spd.	33	58.5	0.59	BANN	-51.9	—	—

Table 10.5: August 28, 15:30

Parameter	(a) No. of stations	(b) Gross error (%)	(c) Bias (%)	(d) Location of observed peak	(e) Model error at location of observed peak (%)	(f) Distance of model peak from observed peak (km)	(g) Difference between model and observed peaks (%)
O$_3$	34	29.1	-4.4	GLEN	-59.0	65.0	-3.4
NO	—	—	—	—	—	—	—
NO$_2$	19	37.9	-25.9	POMA	-85.9	47.8	31.1
CO	22	51.8	-49.6	RIVM	-73.1	59.6	-26.1
CH$_4$	4	5.8	-2.8	CELA	-15.9	—	—
NMHCs	3	43.2	43.2	CELA	48.9	—	—
SO$_2$	10	53.2	-50.2	LGBH	-48.7	9.7	-13.2
Temp.	14	1.85	-0.42	UPLA	-3.61	—	—
Rel. Hum.	8	62.7	43.5	HAWT	-32.5	—	—
Wind Spd.	33	56.9	-0.8	BANN	-49.2	—	—

For these simulations, the normalized bias for ozone, averaged over all daylight hours, was -23.6%. In addition, time- and space-paired peak ozone accuracies ranged from 10 - 70% and time-paired accuracies ranged from 10 - 45%. Again, peak predictions of ozone were generally lower than peak observations.

169

Statistics for most other parameters in the tables indicate greater gross errors than those for ozone. The lone exception, methane, is a chemically unreactive species with a fairly uniform mixing ratio. Thus, neither transport, emissions, nor chemistry affect methane very much. Four species (or groups of species) in the table -- nitric oxide, carbon monoxide, sulfur dioxide, and non-methane hydrocarbons -- have significant emissions sources. Nitrogen dioxide is also emitted although its major source is through ambient chemical reaction of nitric oxide. Thus, errors in either time, location, or magnitude of emissions can reduce prediction accuracy of any of these species. Also, errors in wind and diffusion predictions can put gases in incorrect grid cells. Wind-speed errors often result from errors in temperature predictions, which appear to result primarily from errors in soil moisture data. Additional sources of error are discussed in Section 10.5.

In sum, for the three-day simulation discussed here, the model overpredicted nitric oxide (+39.8% normalized bias, averaged over all daylight hours) and hydrocarbons (+1.0%) but underpredicted nitrogen dioxide (-23.8.%), sulfur dioxide (-55.7%), methane (-8.1%), Kelvin temperature (-0.11%), and humidity (-8.9%). However, statistics for individual hours (*e. g.* 16:30 on August 26) show underpredictions of many variables. These underpredictions may have been caused by overpredictions of the boundary layer height during the day or underpredictions of emissions rates.

The mixing ratios of both NO_2 and O_3 were biased low in the mornings and afternoons. However, the mixing ratio of NO was usually biased high in the mornings but low in the afternoons. Thus, ozone mixing ratios in several locations failed to build up because nitrogen dioxide mixing ratios did not build up. NO_2 did not accumulate because either nitric oxide did not convert to nitrogen dioxide fast enough or too much nitrogen dioxide converted to nitric acid. If NO to NO_2 conversion was too slow, then

170

hydrocarbon - OH reaction rates may have been too slow. Conversely, if too much nitrogen dioxide converted to nitric acid, then the NO_2 - OH reaction may be too fast. In the aerosol simulation, shown later, nitric acid gas mixing ratio predictions were too high. However, aerosol nitrate concentrations were simultaneously too low, indicating that nitric acid mixing ratios may have been too high only because nitric acid did not enter into aerosols fast enough.

A third explanation for the low ozone and nitrogen dioxide is that the winds did not advect sufficient precursors to the eastern side of the basin. Since ozone concentrations on the west matched extremely well but those on the east were too low, the possibility exists that NO_x and hydrocarbon precursors diffused or reacted away to form end-products during their journey to the eastern side of the basin.

Figures 10.1 through 10.33 show time-series plots of parameter values at several locations throughout the basin. The parameters include temperature and mixing ratios of ozone, nitric oxide, nitrogen dioxide, carbon monoxide, sulfur dioxide, and non-methane hydrocarbons.

Figs. 10.1 - 10.33. (Following pages) Time-series comparisons of predicted to observed mixing ratios, temperatures, and humidity at different locations throughout the South Coast Air Basin. Figures 10.1 - 10.5 are results from Simulation (B), which was for August 27 - 28, 1987. The remaining figures (10.6 - 10.33) are from Simulation (A), which was for August 26 - 28, 1987. *Hour After First Midnight* means the hour after the midnight before the first day of simulation. For example, hour 28 for Simulation (B) is 4:00 a. m., August 28, 1987. The resolutions of CO and SO_2 observational data are 1 ppmv and 0.01 ppmv, respectively.

171

TIME-SERIES PLOTS

# OZONE
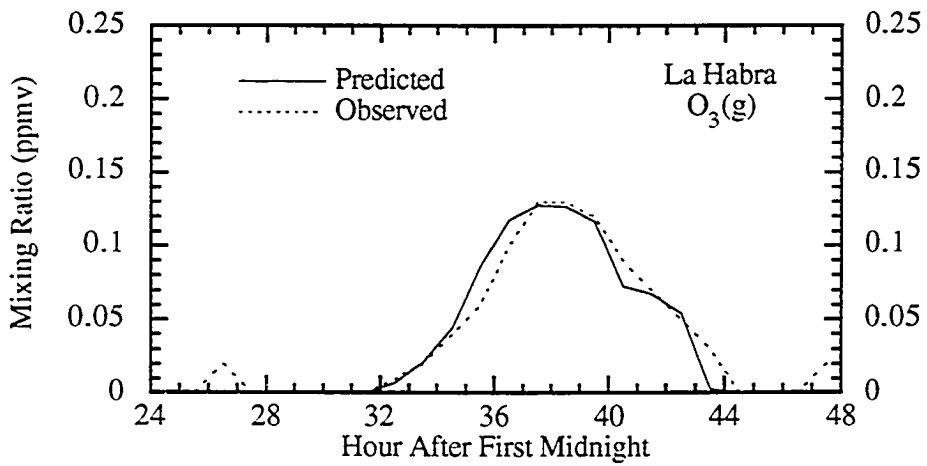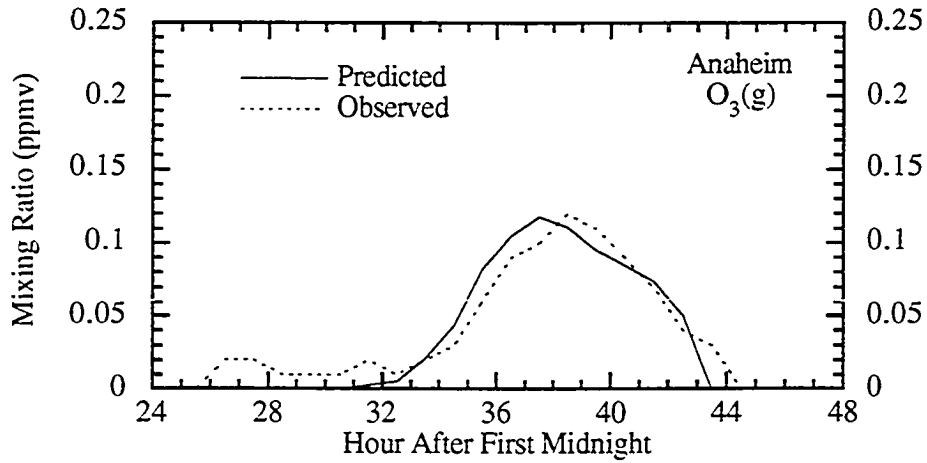
Figs. 10.1 - 10.2. Comparisons of predicted to observed ozone gas at Anaheim and La Habra for Simulation (B) (August 27 - 28, 1987).

172
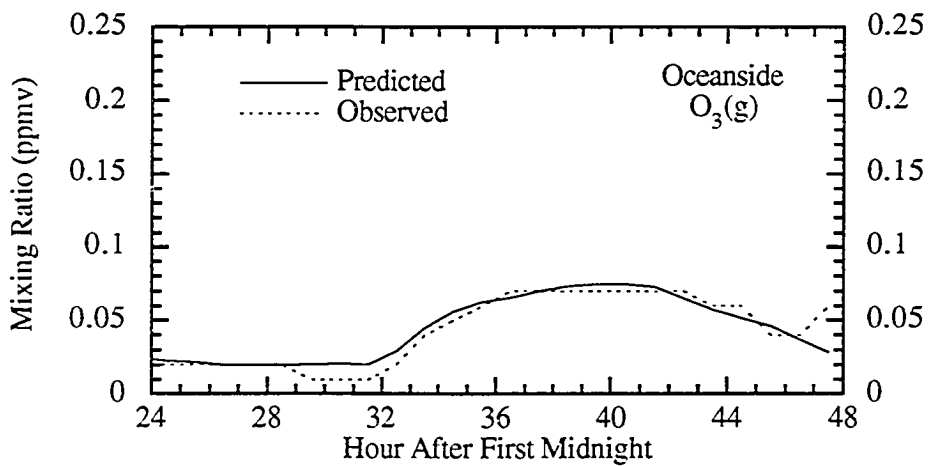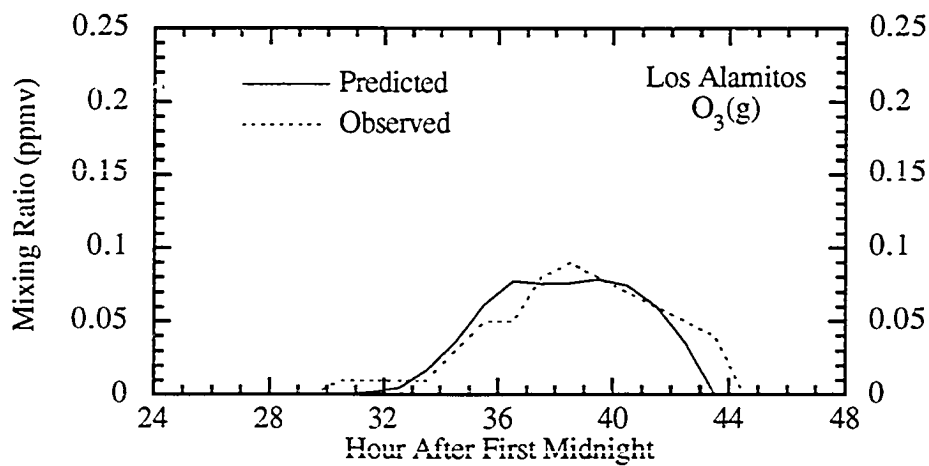
Figs. 10.3 - 10.4. Comparisons of predicted to observed ozone gas at Los Alamitos and Oceanside for Simulation (B) (August 27 - 28, 1987).

173
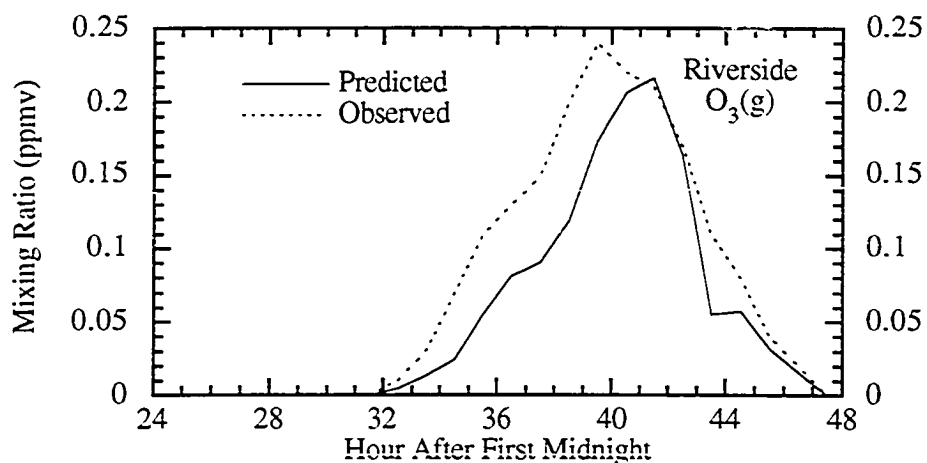
Fig. 10.5. Comparison of predicted to observed ozone gas at Riverside for Simulation (B) (August 27 - 28, 1987).
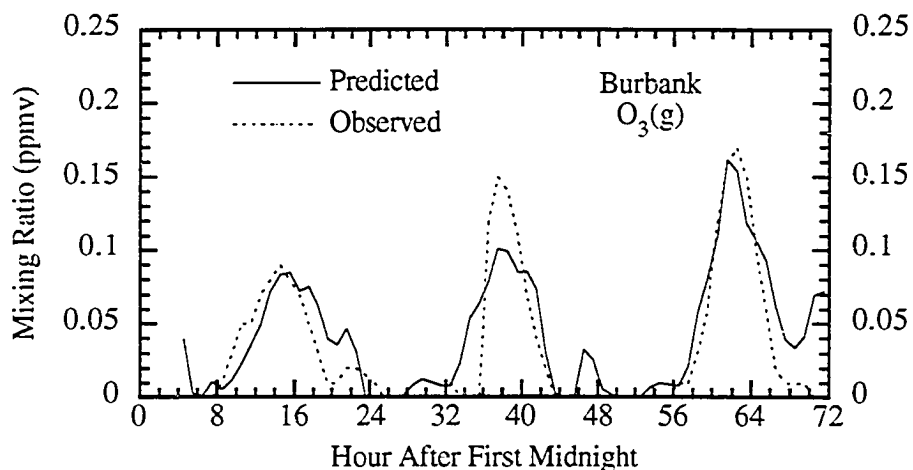
Fig. 10.6. Comparison of predicted to observed ozone gas at Burbank for Simulation (A) (August 26 - 28, 1987).

174
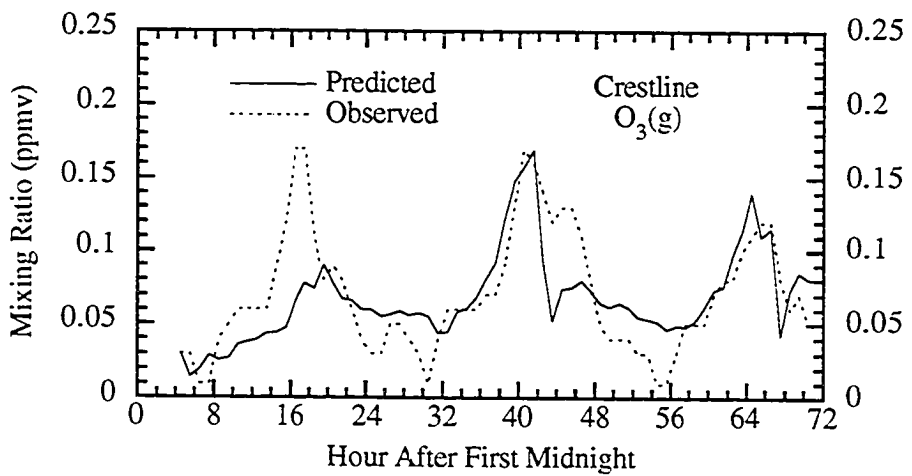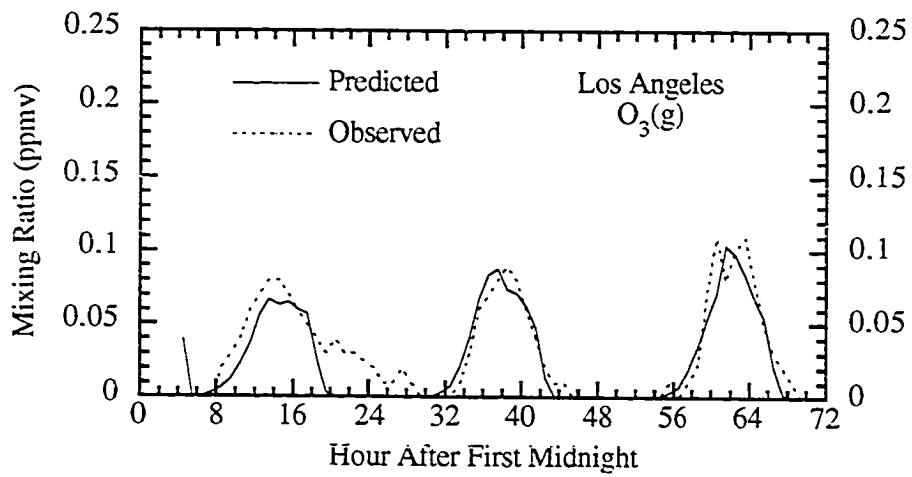
Figs. 10.7 - 10.8. Comparisons of predicted to observed ozone gas at Los Angeles and Crestline for Simulation (A) (August 26 - 28, 1987).

175
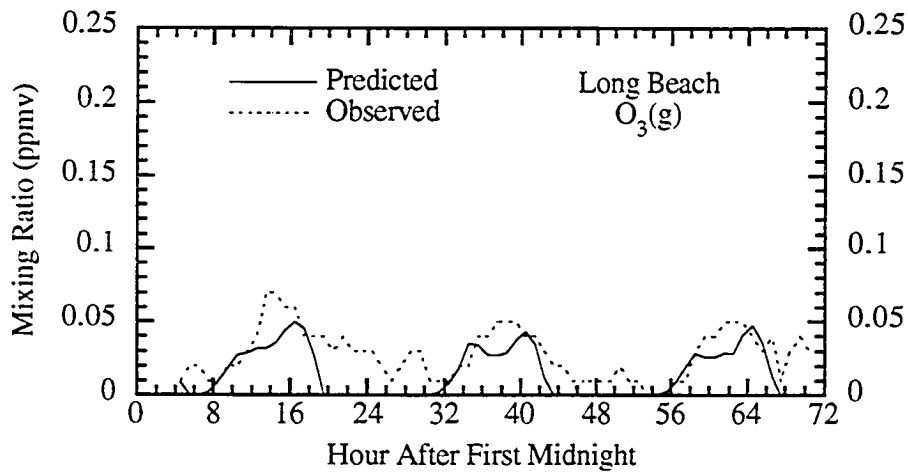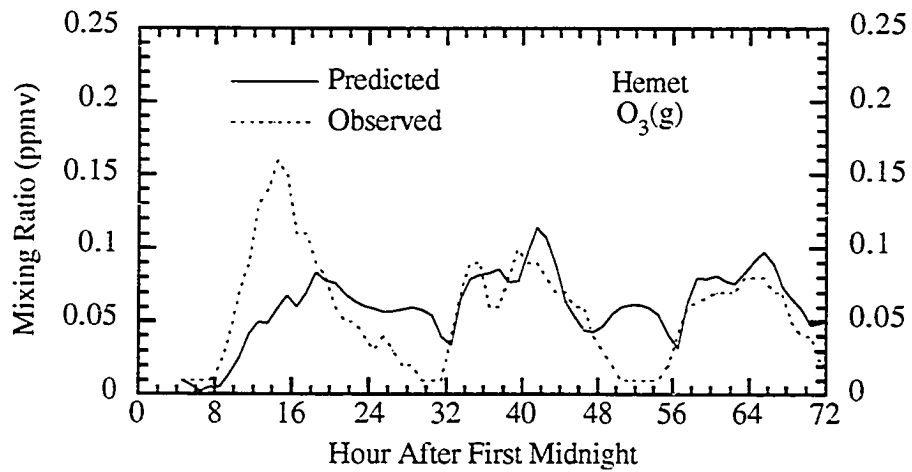
Figs. 10.9 - 10.10. Comparisons of predicted to observed ozone gas at Hemet and Long Beach for Simulation (A) (August 26 - 28, 1987).

176
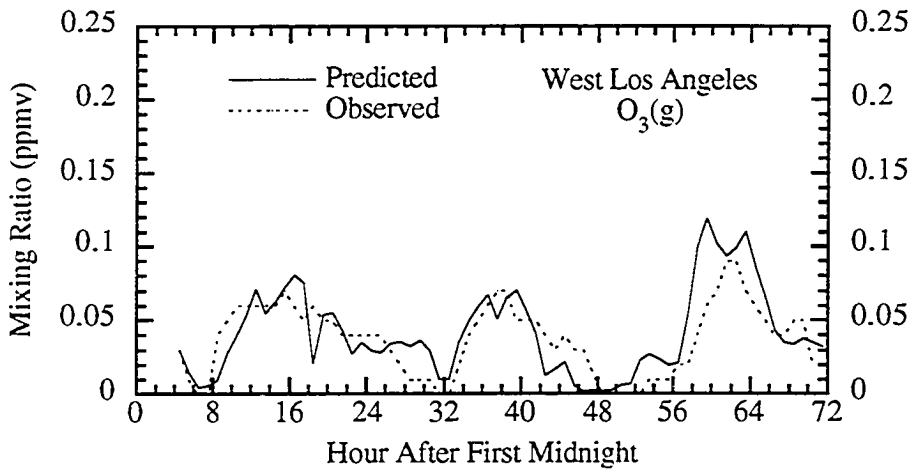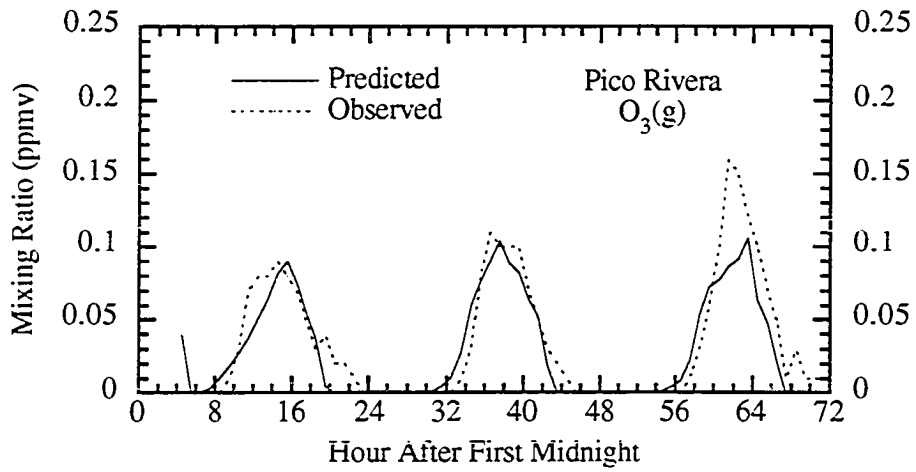
Figs. 10.11 - 10.12. Comparisons of predicted to observed ozone gas at Pico Rivera and West Los Angeles for Simulation (A) (August 26 - 28, 1987).

177
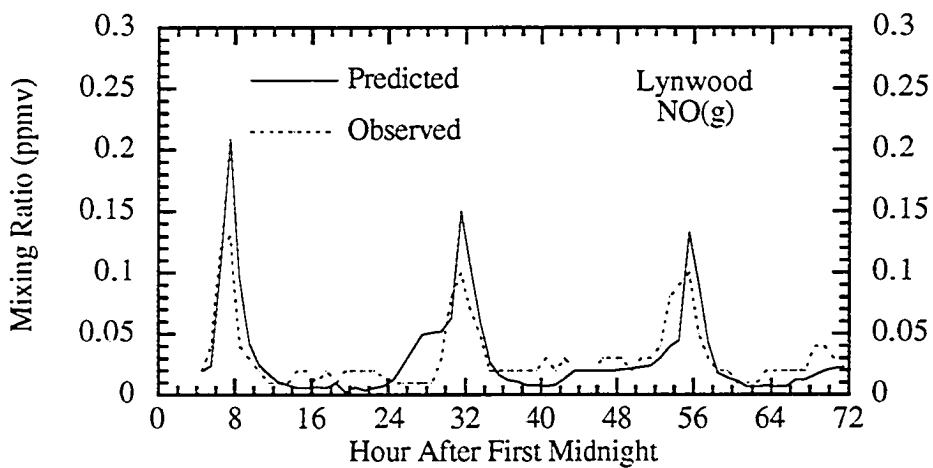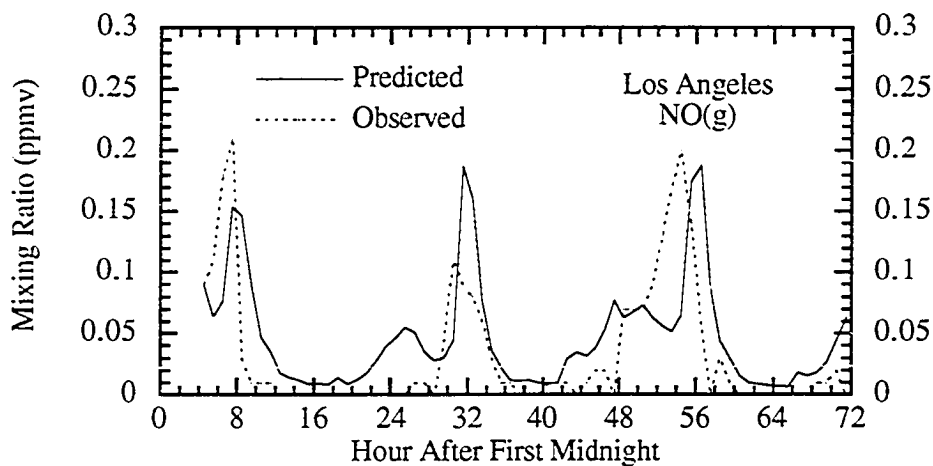
NITRIC OXIDE

Figs. 10.13 - 10.14. Comparisons of predicted to observed nitric oxide gas at Los Angeles and Lynwood for Simulation (A) (August 26 - 28, 1987).

178
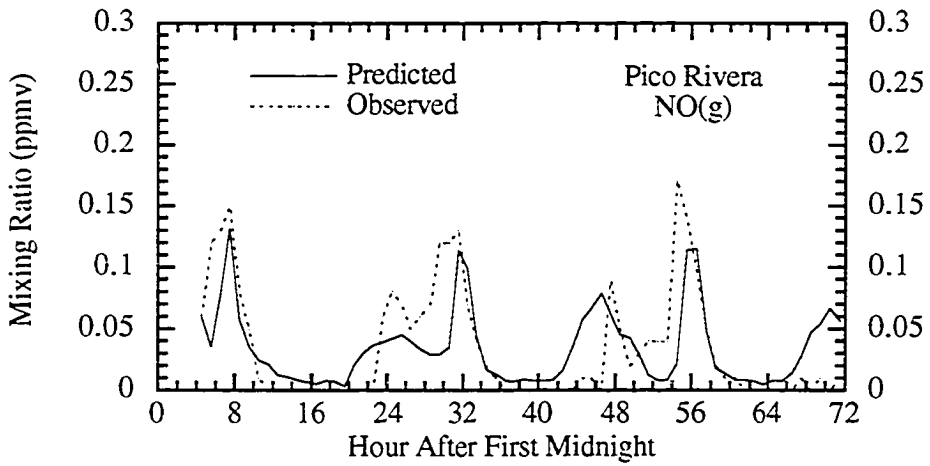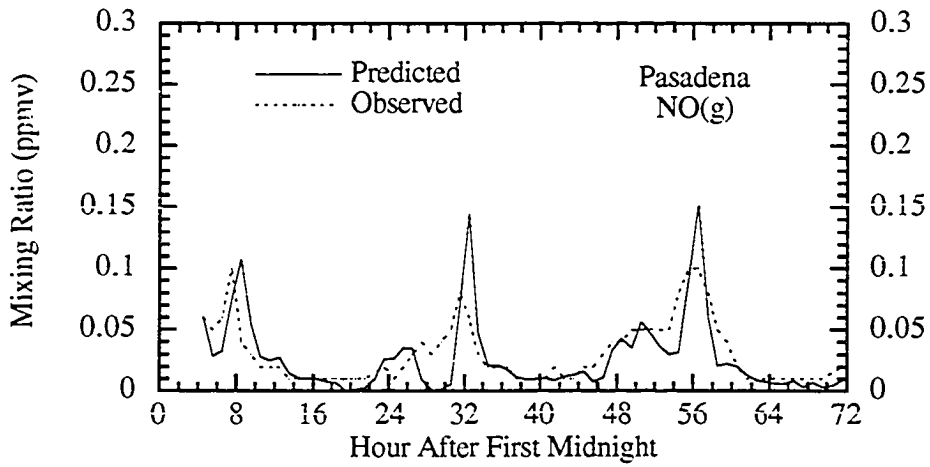
Figs. 10.15 - 10.16. Comparisons of predicted to observed nitric oxide gas at Pasadena and Pico Rivera for Simulation (A) (August 26 - 28, 1987).

179
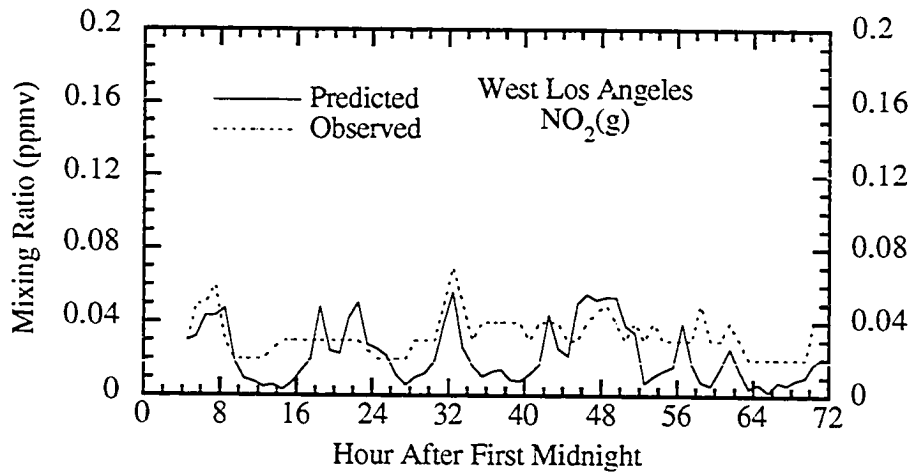
NITROGEN DIOXIDE

Fig. 10.17. Comparison of predicted to observed nitrogen dioxide gas at West Los Angeles for Simulation (A) (August 26 - 28, 1987).

METHANE
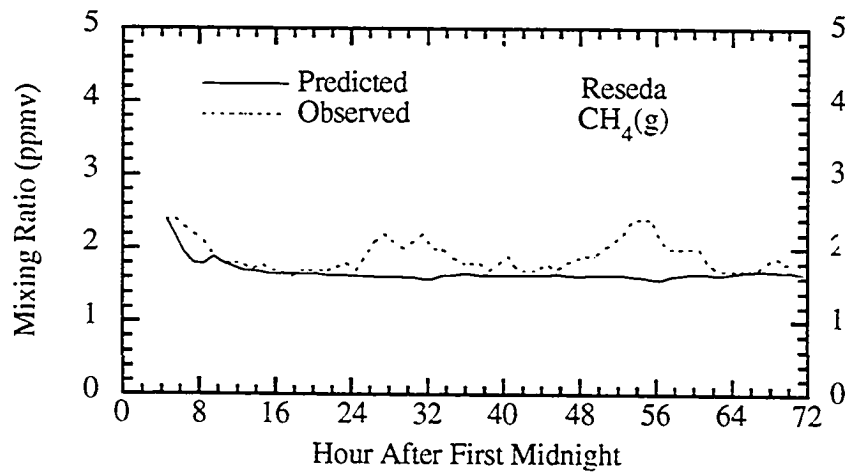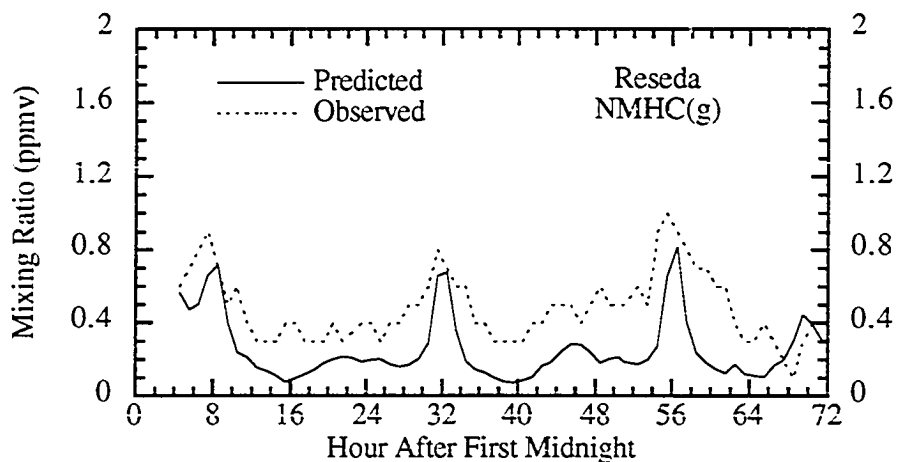

Fig. 10.18. Comparison of predicted to observed methane gas at Reseda for Simulation (A) (August 26 - 28, 1987).

180
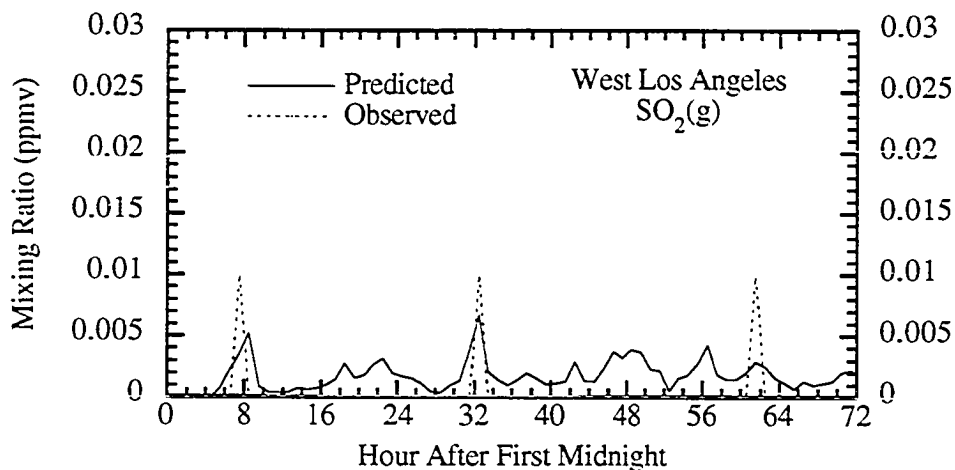
SULFUR DIOXIDE

Fig. 10.19. Comparison of predicted to observed sulfur dioxide gas at West Los Angeles for Simulation (A) (August 26 - 28, 1987).The resolution of SO_2 observational data is 0.01 ppmv.

NON-METHANE HYDROCARBONS
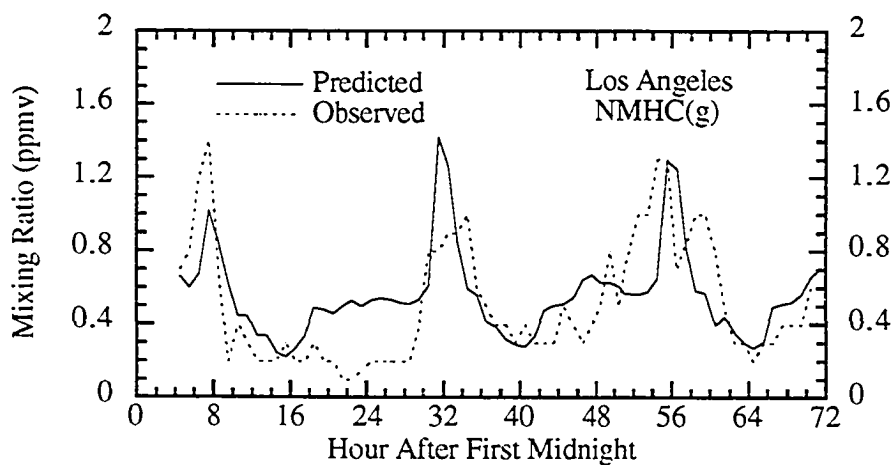
Fig. 10.20. Comparison of predicted to observed non-methane hydrocarbon gases at Los Angeles for Simulation (A) (August 26 - 28, 1987).

181

Fig. 10.21. Comparison of predicted to observed non-methane hydrocarbon gases at Reseda for Simulation (A) (August 26 - 28, 1987).
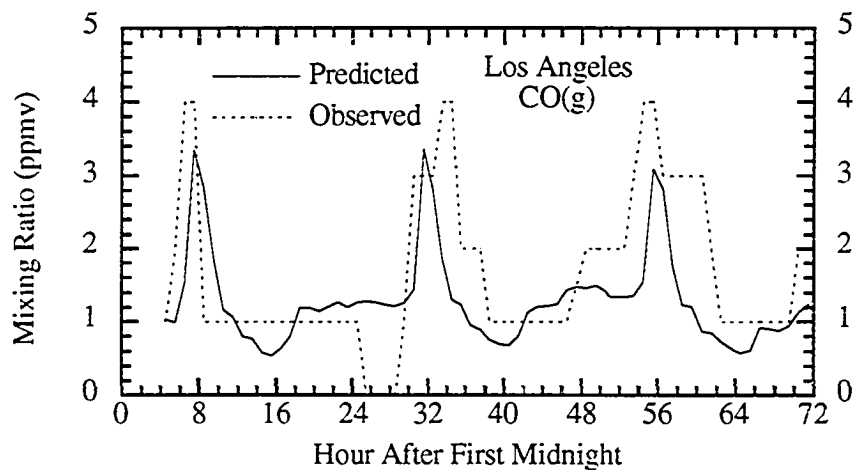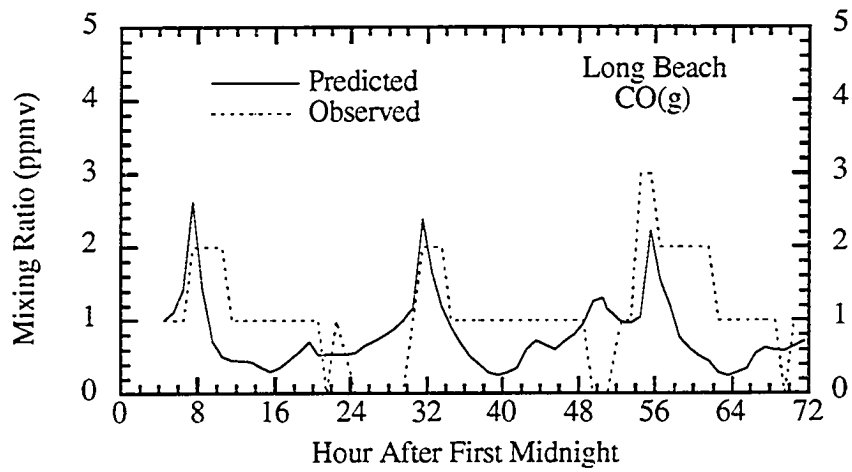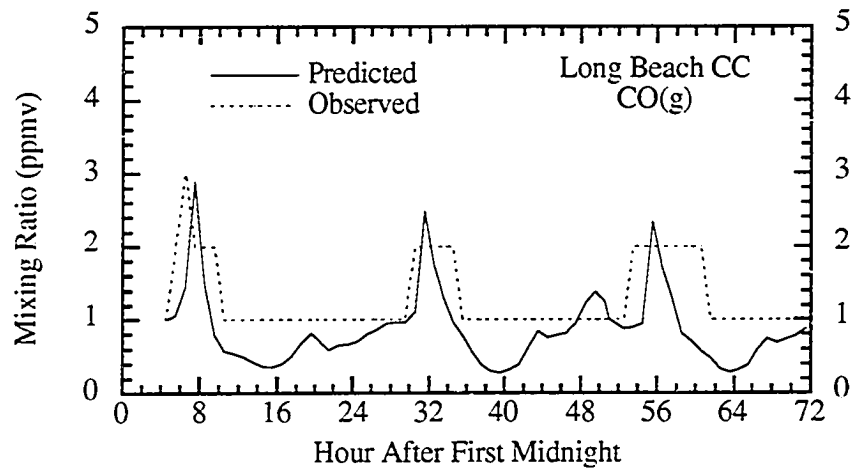
CARBON MONOXIDE

Fig. 10.22. Comparison of predicted to observed carbon monoxide gas at Los Angeles for Simulation (A) (August 26 - 28, 1987). The resolution of CO observational data is 1 ppmv.

182

Figs. 10.23 - 10.24. Comparisons of predicted to observed carbon monoxide gas at Long Beach City College and Long Beach for Simulation (A) (August 26 - 28, 1987). The resolution of CO observational data is 1 ppmv.
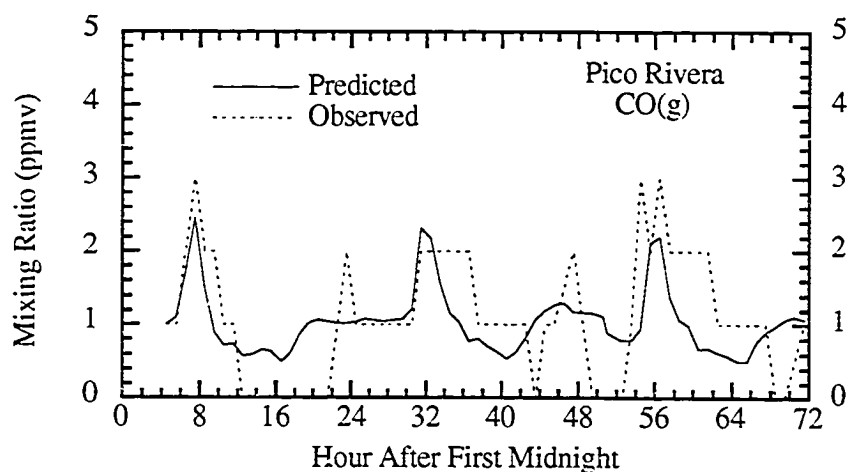
183

Fig. 10.25. Comparison of predicted to observed carbon monoxide gas at Pico Rivera for Simulation (A) (August 26 - 28, 1987). The resolution of CO observational data is 1 ppmv.
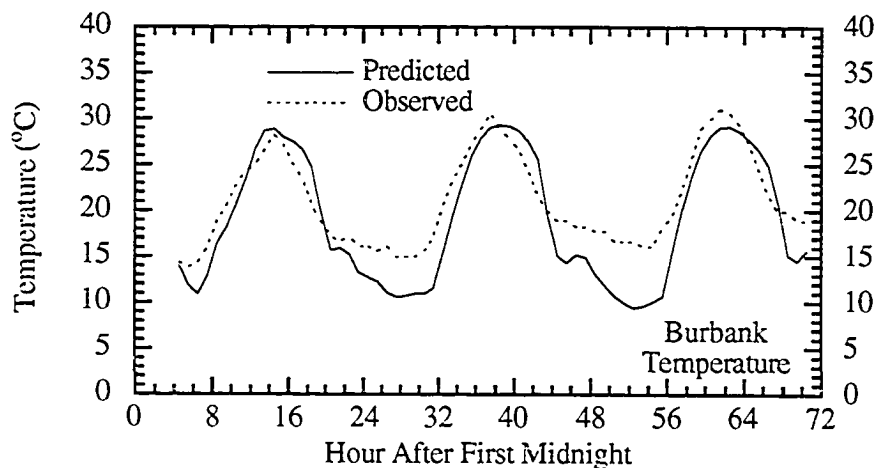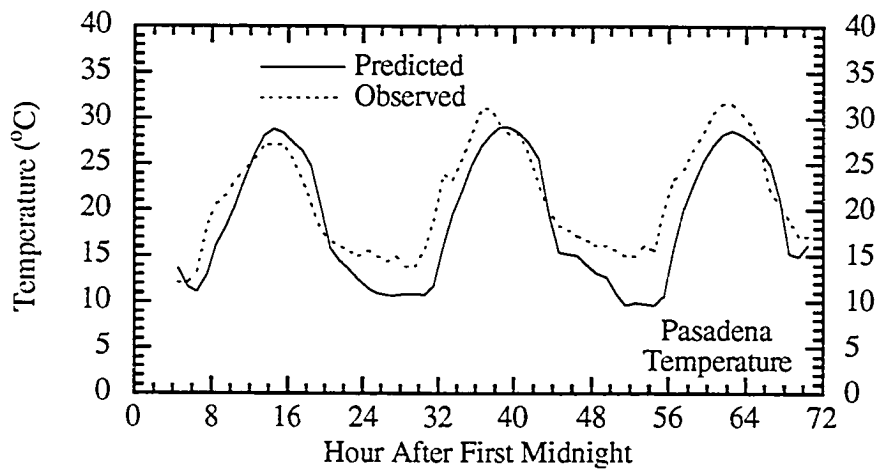
TEMPERATURE

Fig. 10.26. Comparison of predicted to observed temperature at Burbank for Simulation (A) (August 26 - 28, 1987) Temperature was calculated with the MMTD using radiation coupled from GATOR.

184

Figs. 10.27 - 10.28. Comparisons of predicted to observed temperature at Glendora and Pasadena for Simulation (A) (August 26 - 28, 1987) Temperature was calculated with the MMTD using radiation coupled from GATOR.
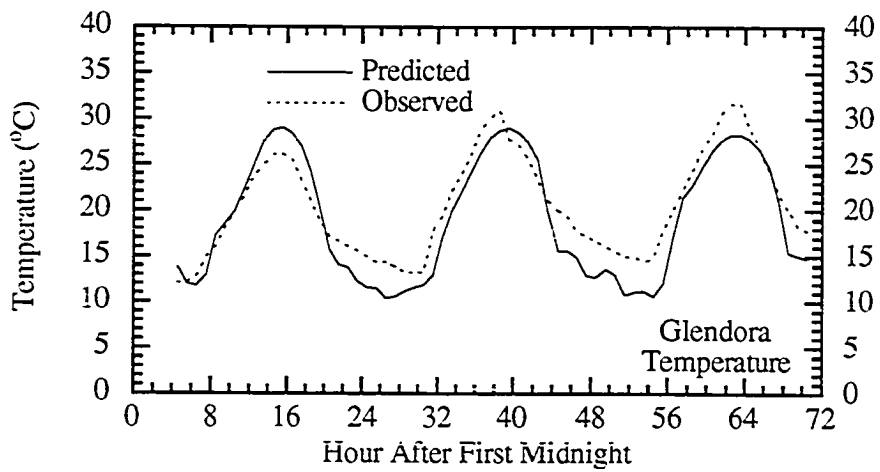
185
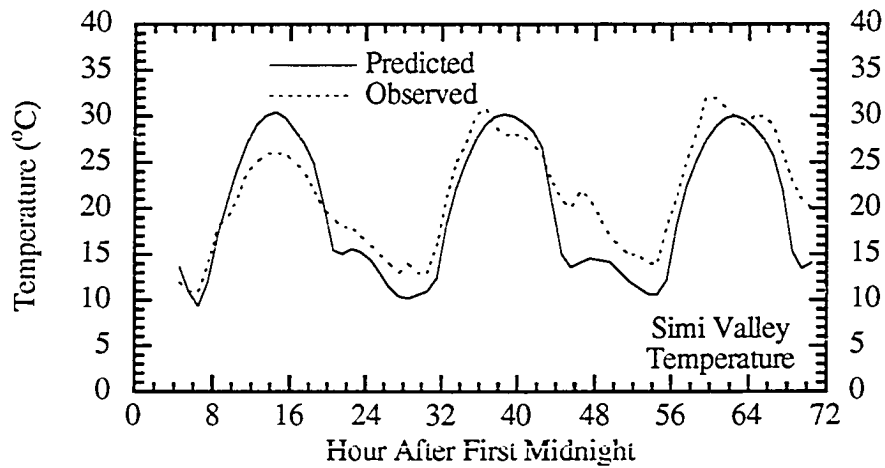
Fig. 10.29. Comparison of predicted to observed temperature at Simi Valley for Simulation (A) (August 26 - 28, 1987) Temperature was calculated with the MMTD using radiation coupled from GATOR.

RELATIVE HUMIDITY

Fig. 10.30. Comparison of predicted to observed relative humidity at Anaheim for Simulation (A) (August 26 - 28, 1987). Humidity was calculated with the MMTD.

186

Figs. 10.31 - 10.32. Comparisons of predicted to observed relative humidity at Los Angeles and Hawthorne for Simulation (A) (August 26 - 28, 1987). Humidity was calculated with the MMTD.
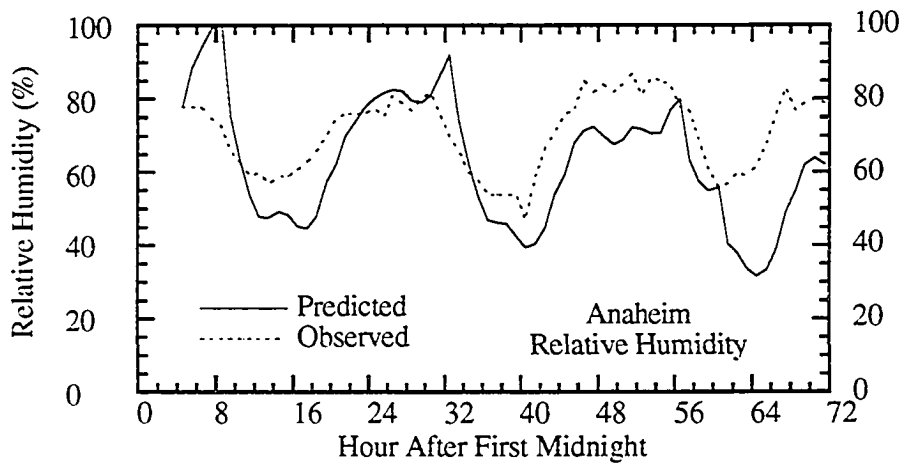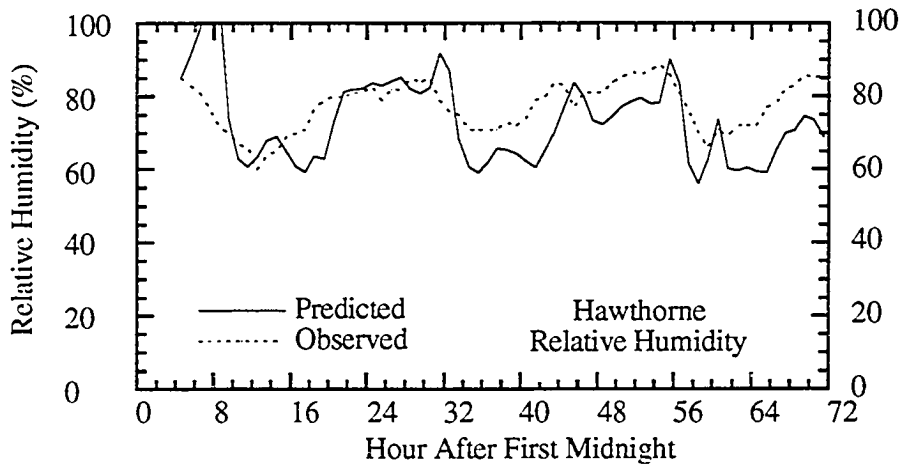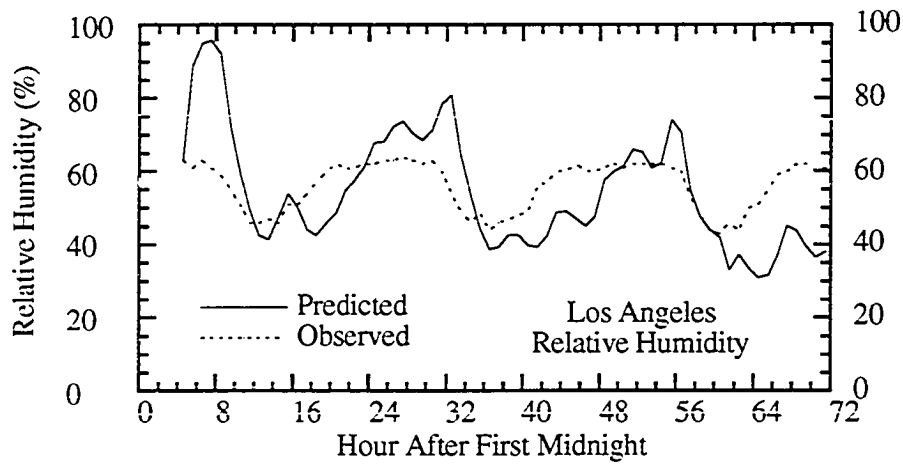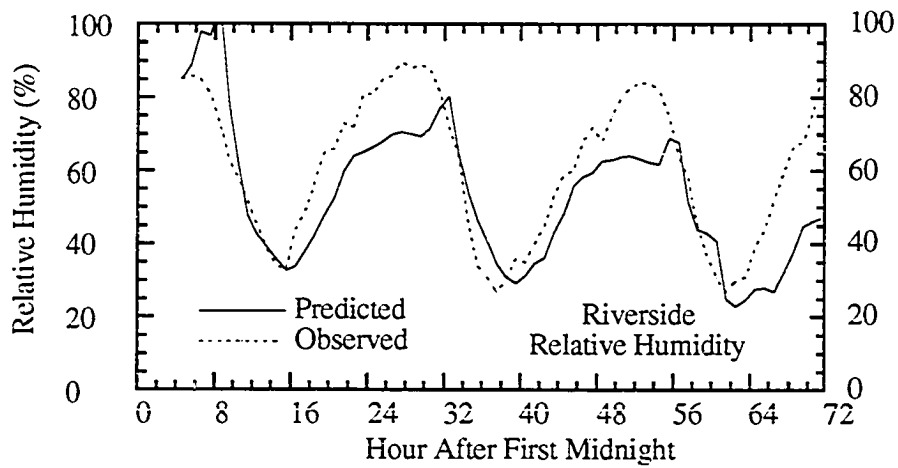
187

Fig. 10.33. Comparison of predicted to observed relative humidity at Riverside for Simulation (A) (August 26 - 28, 1987). Humidity was calculated with the MMTD.

188

In most cases, the ozone mixing ratio predictions (Figures 10.1 - 10.12) matched both the phase and amplitude of observations. The first five ozone figures show results from the second day (August 28) of Simulation B. In the case of Anaheim, the peak predicted mixing ratio was essentially identical to the observed value although the time of the peak was offset by one hour. In the case of La Habra, both the time and magnitude of the peak matched exactly. For Los Alamitos, the predicted peak was low by 0.01 ppmv, while for Oceanside, where the air is clean, the predicted peak matched the observed peak. In the case of Riverside, the peak occurred two hours late and was low by 0.02 ppmv. Since Riverside is towards the east end of the basin, underpredictions of wind speeds would explain the delay in the timing of the predicted peak there.

The last seven ozone figures compare results from all three days of Simulation A. Of the stations shown, Crestline lies in the San Bernardino Mountains and Hemet is in the far eastern end of the basin (Figure 1.7). Also, Burbank is in the San Fernando Valley and the rest of the stations lie near the coastal regions. While the predictions for the first day of simulation (August 26) were not good for Crestline and Hemet, those for the next two days were more accurate.

For nitric oxide, prediction accuracy depends significantly on the accuracy of the emissions inventory since NO is a major emitted pollutant. Accuracy of peak location also depends on wind speed and direction since incorrect speeds and directions will send emissions to the wrong grid cells or out of the correct grid cells too quickly. Figures 10.13 - 10.16 show time-series plots of NO at several monitoring sites. In the cases shown, the peak NO mixing ratio sometimes lagged behind the observed value.

In several cases for NO, a predicted peak occurred after sunset while no such measured peak occurred. This problem arose with CO, SO_2, and NMHCs as well. The reason for the false peaks is that, as the sun goes down, the surface temperature cools, increasing the stability of the bottom model layer. Consequently, diffusion in the model

189

decreases significantly between the bottom layer and the layer above it. For these simulations, the bottom layer was about 50 m thick. Since emissions decreased only slightly right after sunset while vertical mixing decreased significantly, primary pollutant mixing ratios increased in the bottom layer. In reality, the atmosphere over Los Angeles after sunset is often neutral, allowing air to rise more than predicted. Thus, to improve simulations, boundary layer physical processes need to be examined in more depth.

For nitrogen dioxide, a secondary pollutant, prediction accuracy depends significantly on the accuracy of hydrocarbon, nitric oxide, ozone, photorate, and meteorological predictions. Figure 10.17 shows a time-series plot of NO_2. While the plot indicates that predictions matched observations at hours 32 and 48, false peaks occurred at hours 19 and 22.

Next, Figure 10.18 shows that methane predictions matched observations well at Reseda. However, methane is quite unreactive and its distribution is relatively uniform; thus, its mixing ratio is easier to predict than that of other species.

Figure 10.19 shows a comparison of sulfur dioxide predictions to data. Observation data for SO_2 are rounded to the nearest 0.01 ppmv; thus discerning the accuracy of its predicted mixing ratios is difficult. However, the figure shows that the model picked up the occurrence of observed peaks.

Figures 10.20 - 10.21 show time-series plots of non-methane hydrocarbons. The model picked up the occurrence of the major peaks although the magnitude was often incorrect.

Next, carbon monoxide, like nitric oxide, is a primary pollutant. However, unlike NO, CO does not react significantly in the atmosphere. Figures 10.22 - 10.25 show time-series plots of CO. Unfortunately, observational data for CO were rounded to the nearest 1 ppmv; thus, the magnitude of peak under- or overpredictions cannot be discerned.

190

However, GATOR / MMTD predicted the occurrence of most observed peaks although the time of the peaks were usually off.

Next, Figures 10.26 - 10.29 show time-series plots of temperature. Ground radiative heat flux, latent heat flux, and turbulent heat flux all affect temperature calculations. While the MMTD model predicted the latter two heat fluxes, GATOR predicted the radiative flux for these simulations. Soil moisture affects latent heat flux and, therefore, temperature by up to 6 °C or more; thus, true soil moisture data and predictions are necessary to predict temperature accurately. The figures show reasonable agreement between predicted and observed temperature for most cases during both day and night. However, the model usually underestimated nighttime temperatures.

Finally, Figures 10.30 - 10.33 show predicted to observed values of relative humidity. Humidity is especially hard to predict since it depends on predictions of both water vapor mixing ratio and temperature. The figures show that the model picked up the diurnal cycle of humidity; however, in these simulations, humidity incorrectly decreased over time because of an error, discovered later, that affected soil moisture.

To run the two simulations discussed above, a Cray 90 computer was used. Over a grid domain of 41,800 MMTD model cells and 24,276 GATOR cells, total computational time was about 1.6 hours per day of simulation at an average speed of 330 megaflops. Chemistry required about 69%, the MMTD model required about 17%, radiative transfer required about 8%, horizontal and vertical transport required 5%, and setup and output routines required about 1% of the total time. Thus, chemistry was most computationally intensive. However, the dynamics and radiation modules also required significant computer time.

191

10.2 Simulations That Include Gases and Aerosols

In a second set of simulations, model results were compared to observations for the SCAQS day of August 27th, 1987 (Figures 10.34 - 10.85). The compared variables included concentrations of particle sulfate, nitrate, chloride, ammonium, sodium, elemental carbon, organic carbon, and total mass in sizes less than 2.5 μm and less than 10 μm diameter. In addition, calculations of solar radiation, scattering coefficient, $NH_3(g)$, $HNO_3(g)$, $HONO(g)$, $PAN(g)$, $HCHO(g)$, $NO(g)$, $NO_2(g)$, $O_3(g)$, $SO_2(g)$, $CO(g)$, temperature, humidity, and wind speed were compared to data.

For the results shown here, only one 15.5 hour simulation was attempted on the computer (4:30 a. m. - 10:00 p. m, August 27, 1987). The time required was 7.4 hours on a Cray 90. The grid setup, initial conditions, and boundary conditions were discussed in Chapter 9. For this simulation, 11 particle size bins were used. Particle volumes in a given size bin changed independently of volumes in other bins (Appendix D).

Figs. 10.34 - 10.85. (Subsequent pages) Time series comparisons of model results to data. Locations of the different stations were shown in Figures 1.7 and 9.1 Hour of day is the hour during the day of August 27, 1987. In the case of particulate matter, the observational data were given as an average over a four-hour interval. Thus, model predictions were averaged over the same interval.

192
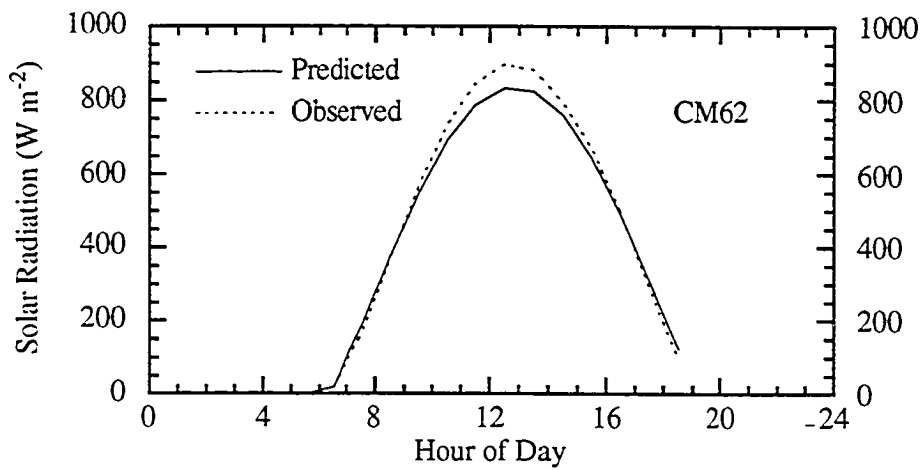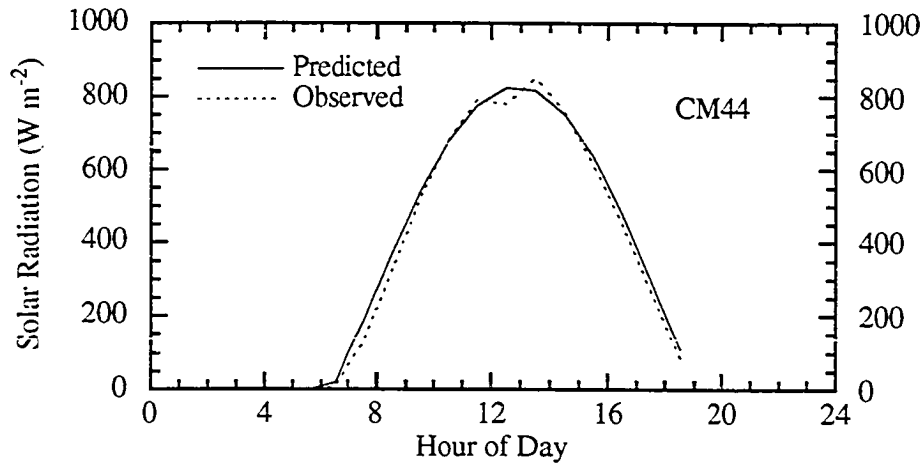
SOLAR RADIATION

Figs 10.34 - 10.35. Comparisons of predicted to observed solar (ultraviolet, visible, plus near infrared) radiation at two stations, each identified in Figure 9.1.

193

TOTAL PARTICULATE MASS
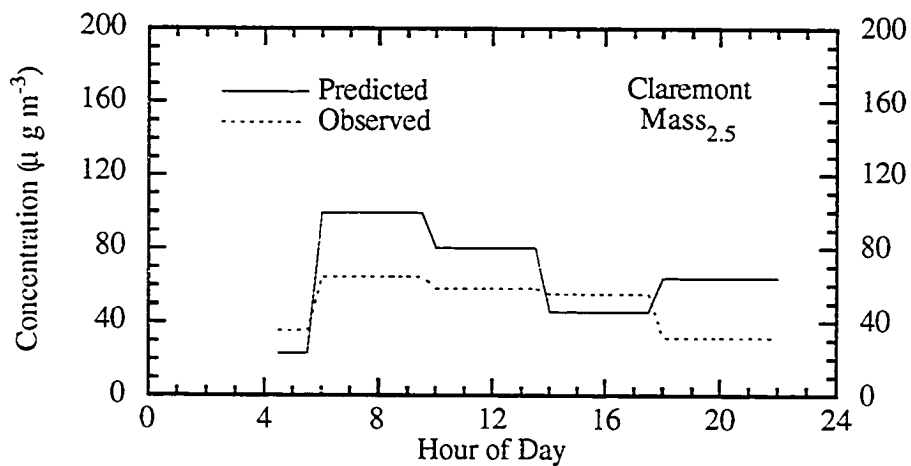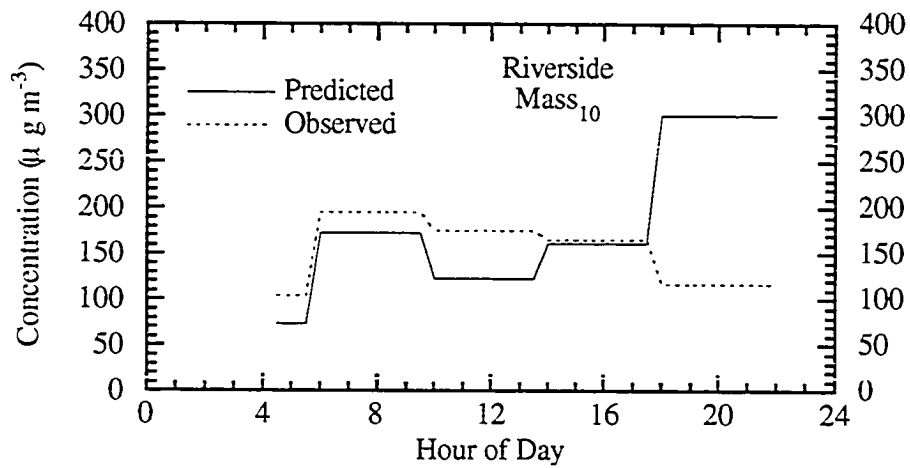
Figs 10.36 - 10.37. Comparisons of predicted to observed total particulate mass in sub-10 μm particles at Riverside and sub-2.5 μm particles at Claremont, respectively.

194

PARTICULATE ELEMENTAL CARBON
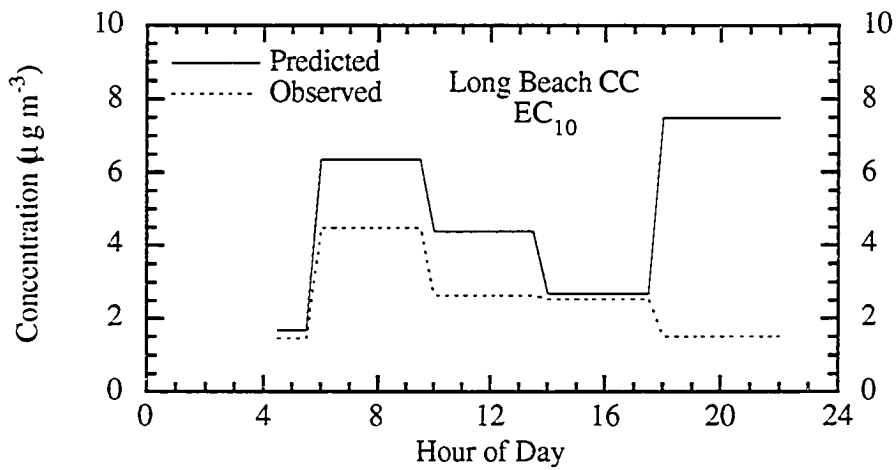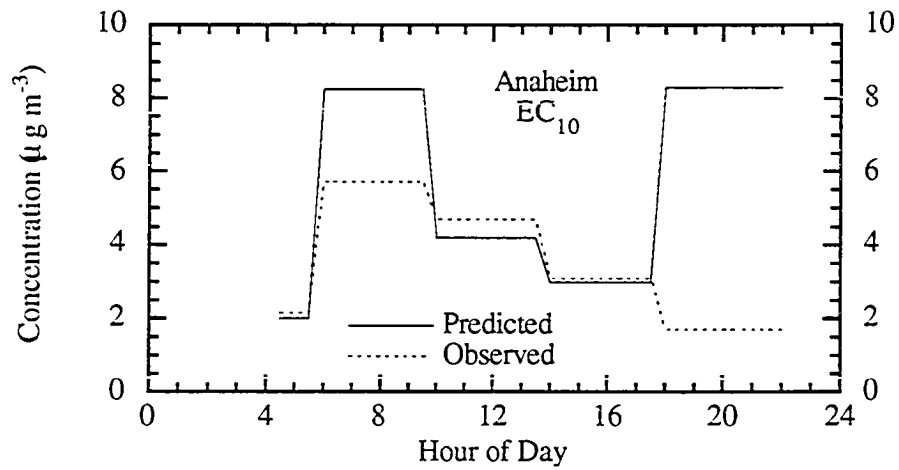
Figs. 10.38 - 10.39. Comparisons of predicted to observed elemental carbon in sub-10 μm particles at Anaheim and Long Beach City College.

195
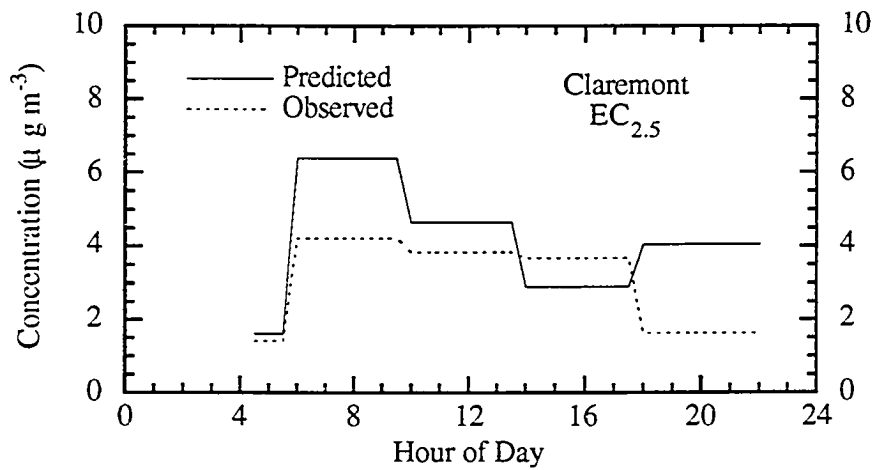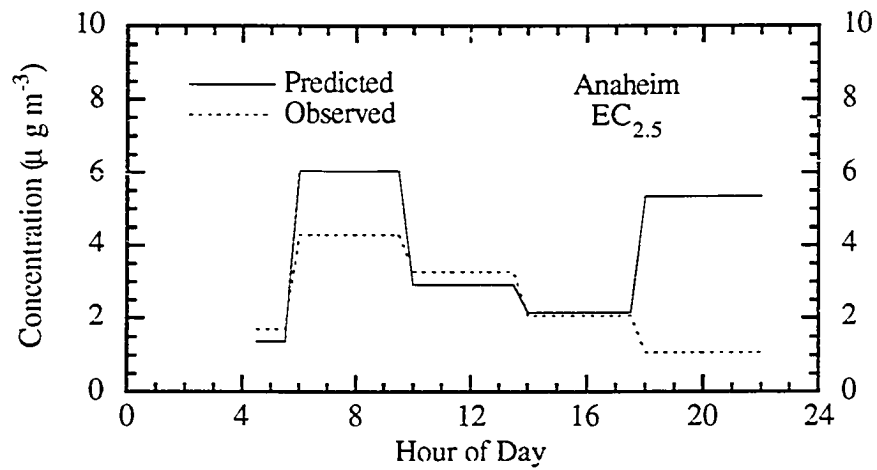
Figs. 10.40 - 10.41. Comparisons of predicted to observed elemental carbon in sub-2.5 μm particles at Anaheim and Claremont.

196

PARTICULATE ORGANIC CARBON
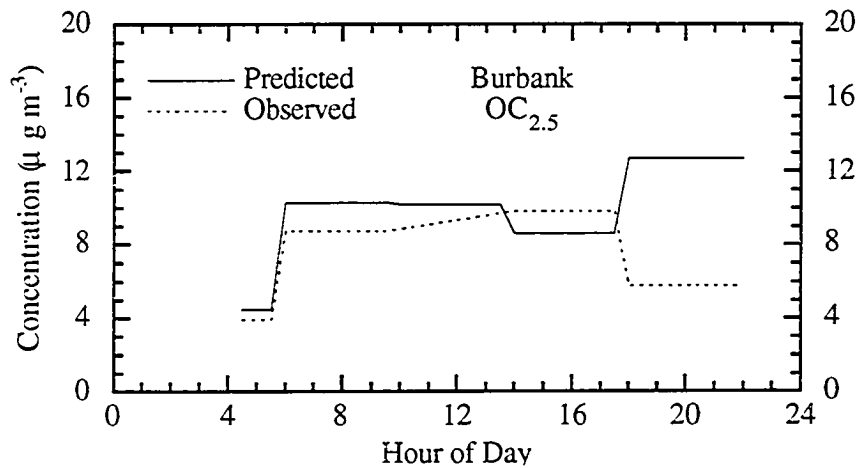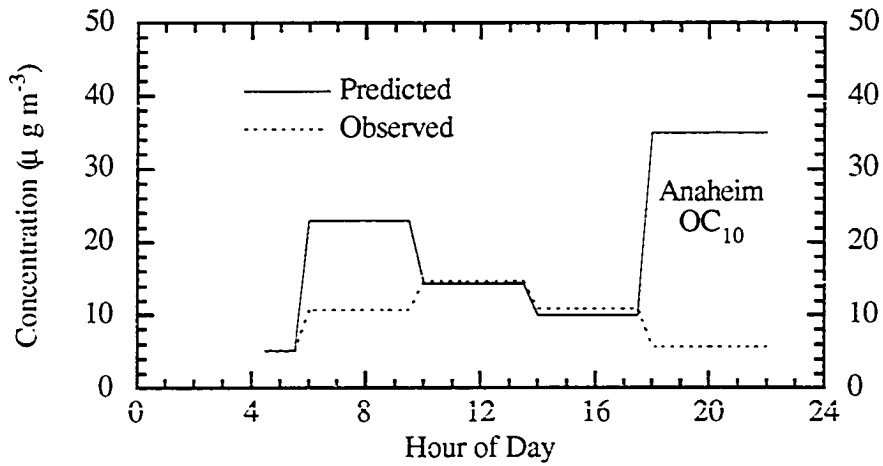
Figs. 10.42 - 10.43. Comparisons of predicted to observed organic carbon in sub-10 and sub-2.5 µm particles at Anaheim and Burbank, respectively. Between 10:00 and 14:00, no data were given for $OC_{2.5}$ at Burbank; thus, a line was drawn connecting the data points for these two times.
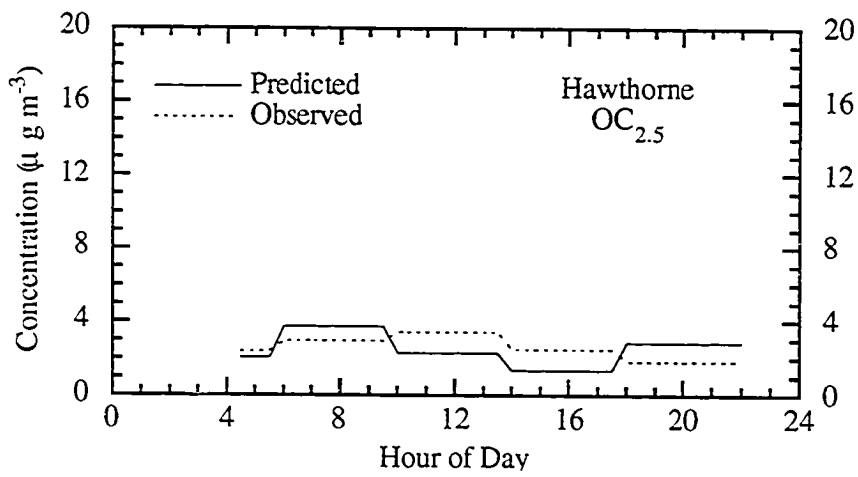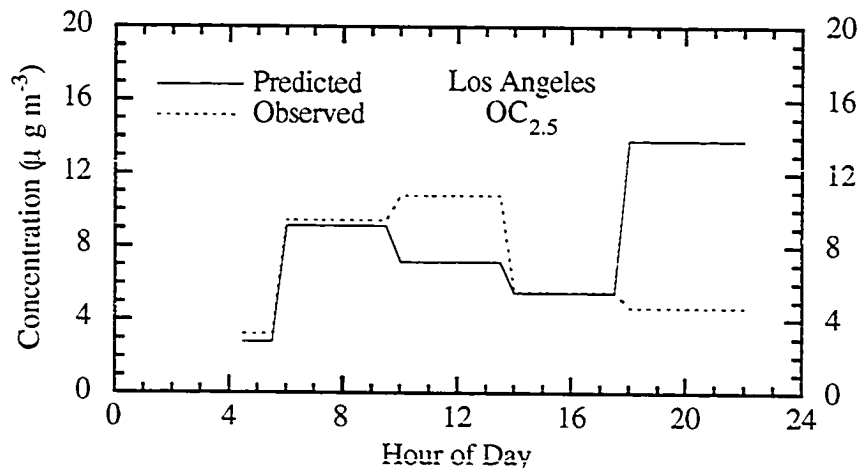
Figs. 10.44 - 10.45. Comparisons of predicted to observed organic carbon in sub-2.5 μm particles at Los Angeles and Hawthorne.

198
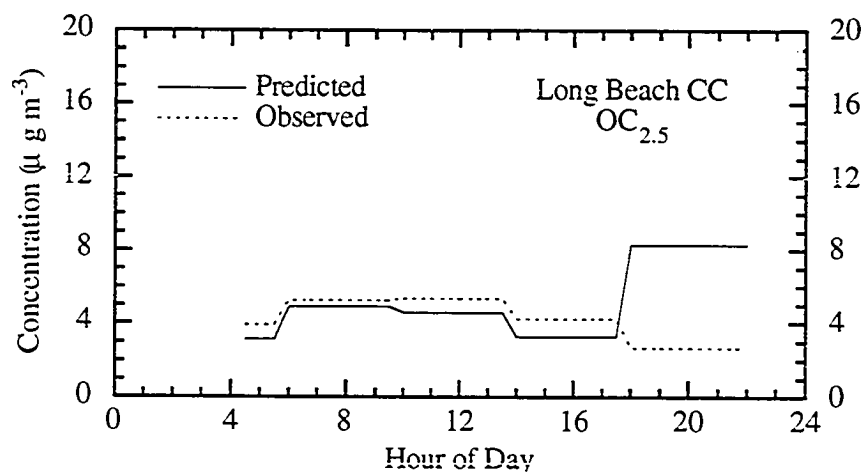
Fig. 10.46. Comparison of predicted to observed organic carbon in sub-2.5 μm particles at Long Beach CC.

PARTICULATE SODIUM
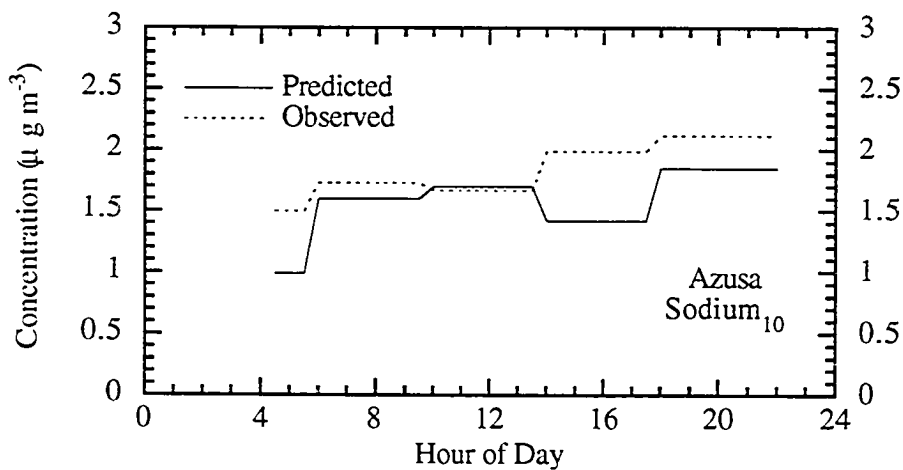
Fig. 10.47. Comparison of predicted to observed particulate sodium in sub-10 μm particles at Azusa.

199
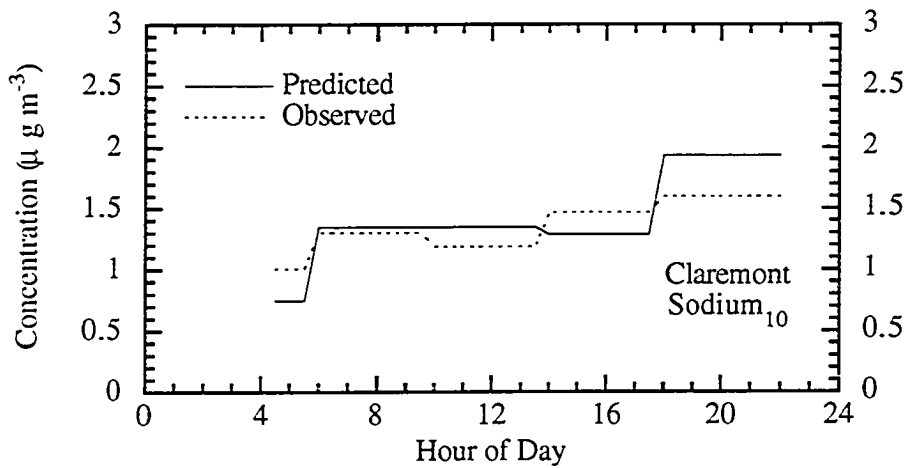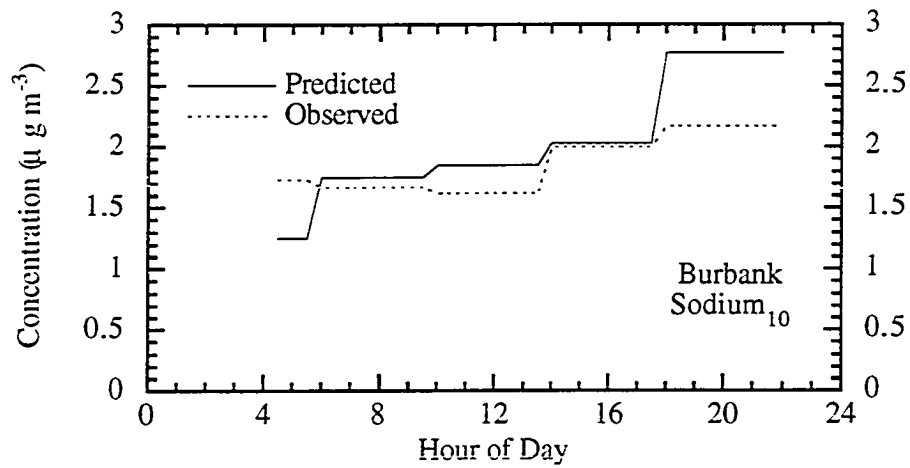
Figs. 10.48 - 10.49. Comparisons of predicted to observed particulate sodium in sub-10 μm particles at Burbank and Claremont.

200
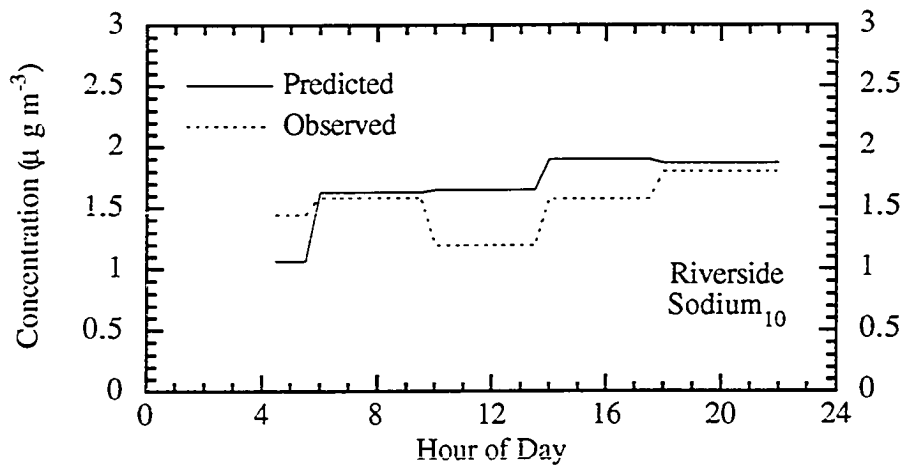
Fig. 10.50. Comparison of predicted to observed particulate sodium in sub-10 μm particles at Riverside.

PARTICULATE CHLORIDE
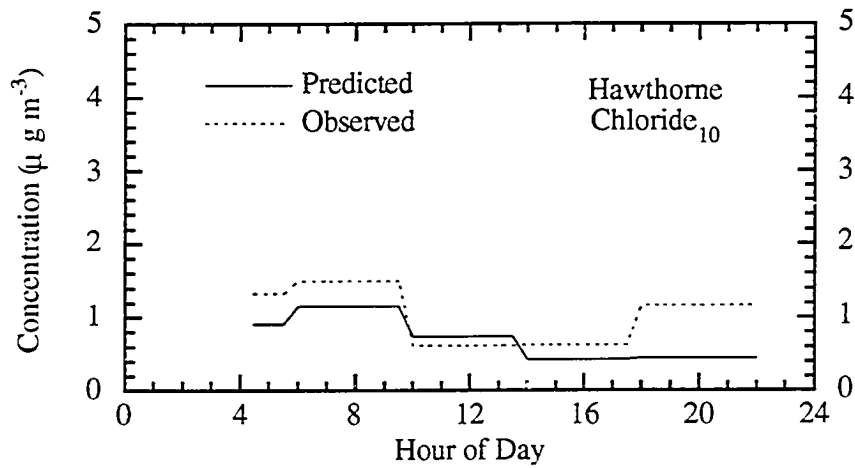
Fig. 10.51. Comparison of predicted to observed particulate chloride in sub-10 μm particles at Hawthorne.

201

PARTICULATE AMMONIUM
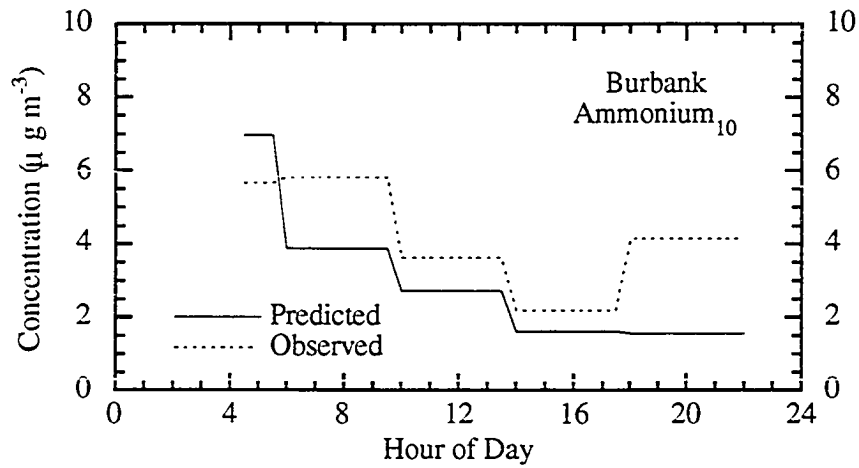
Fig. 10.52. Comparison of predicted to observed particulate ammonium in sub-10 μm particles at Burbank.

PARTICULATE NITRATE
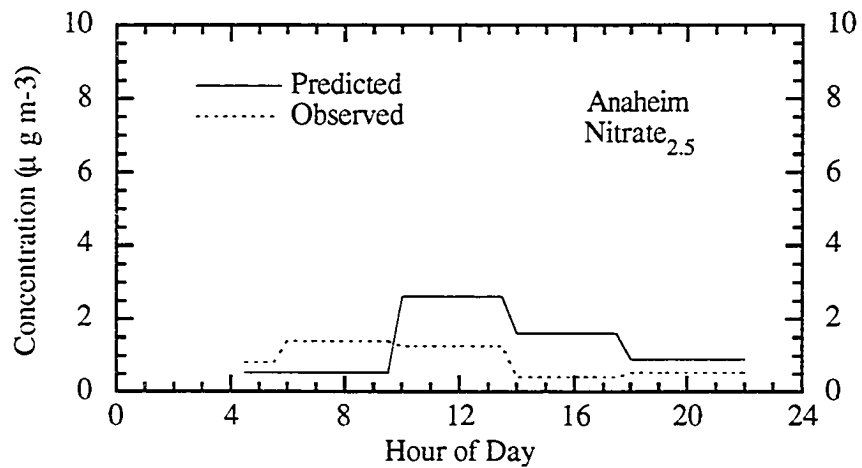
Fig. 10.53. Comparison of predicted to observed particulate nitrate in sub-2.5 μm particles at Anaheim.

202

PARTICULATE SULFATE
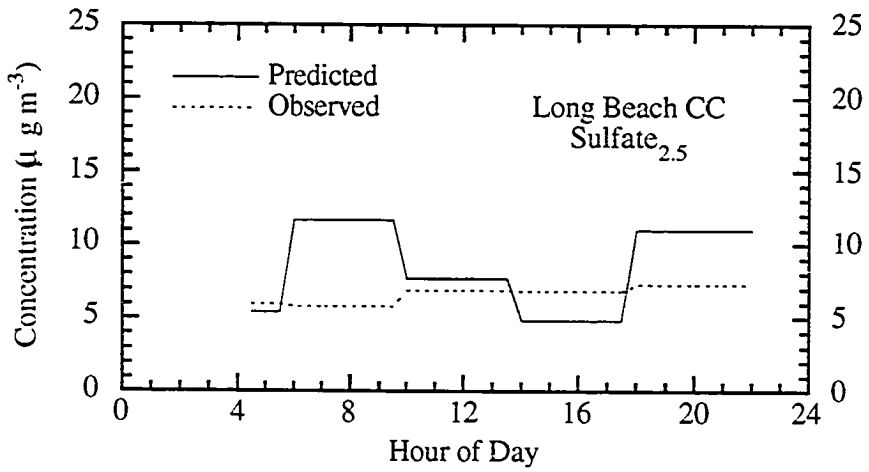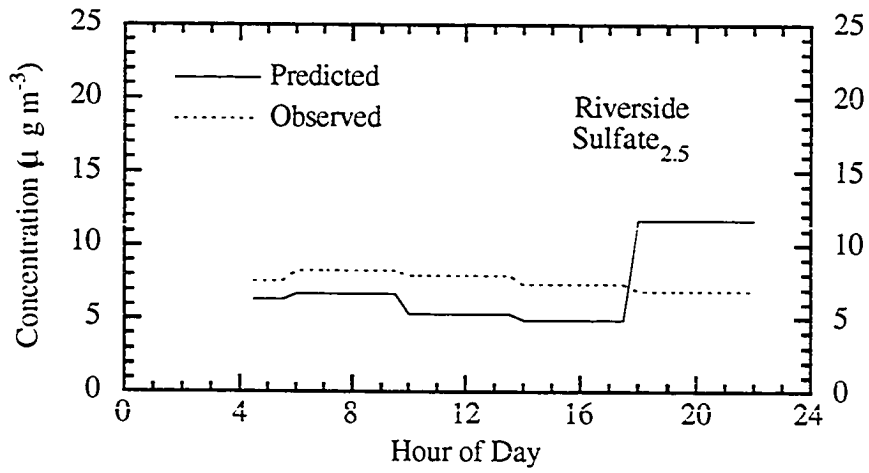
Figs. 10.54 - 10.55. Comparisons of predicted to observed particulate sulfate in sub-2.5 μm particles at Riverside and Long Beach City College.

203
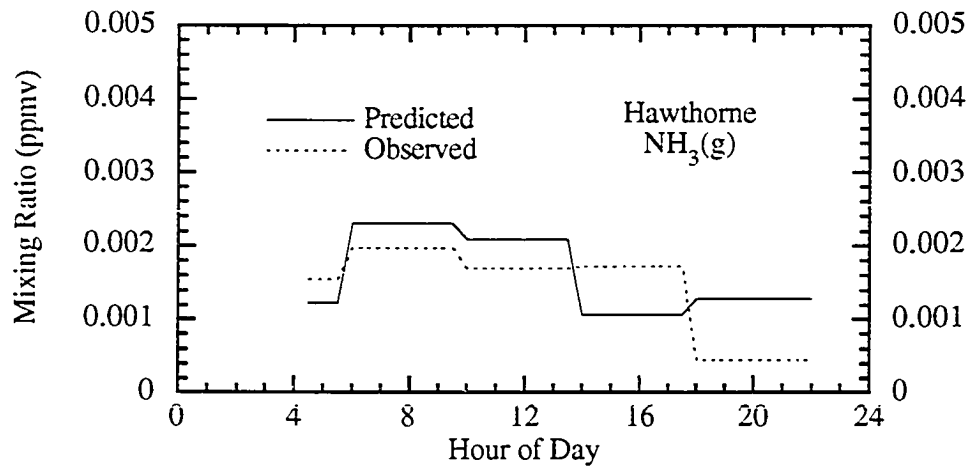
AMMONIA GAS

Fig. 10.56. Comparison of predicted to observed ammonia gas at Hawthorne.

NITRIC ACID GAS
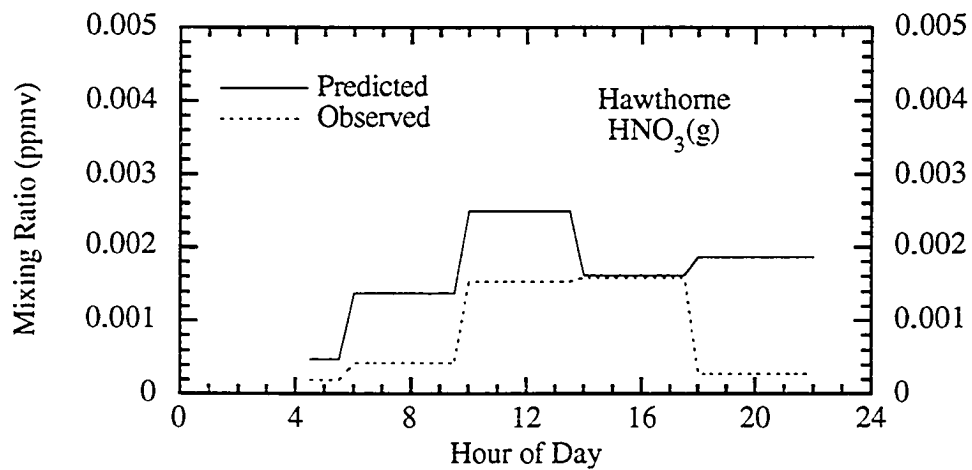
Fig. 10.57. Comparison of predicted to observed nitric acid gas at Hawthorne.

204
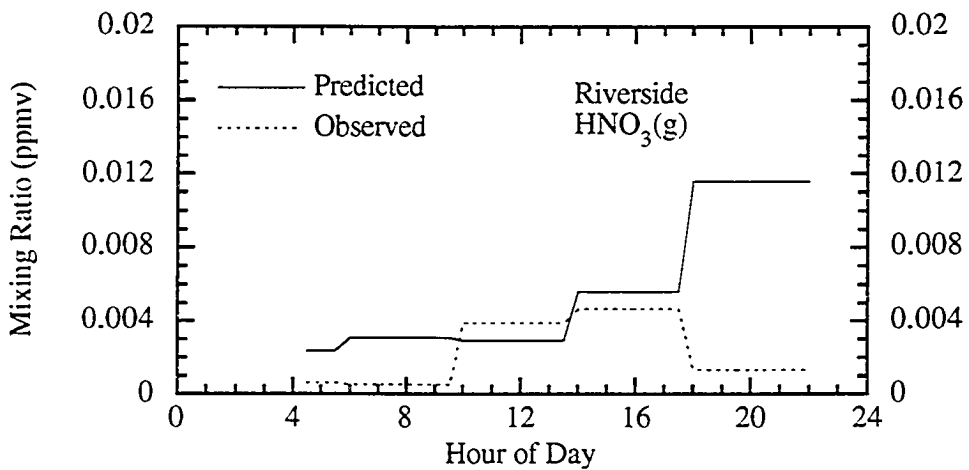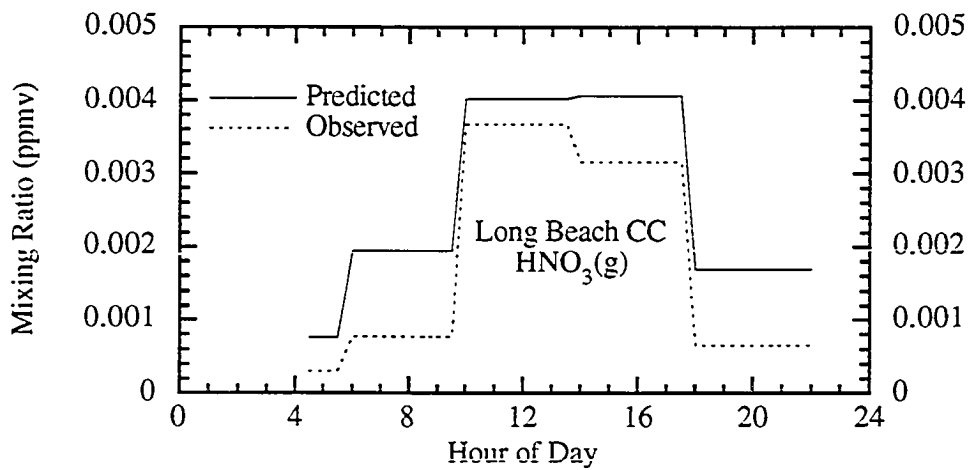
Figs. 10.58 - 10.59. Comparisons of predicted to observed ammonia gas at Long Beach City College and Riverside.

205
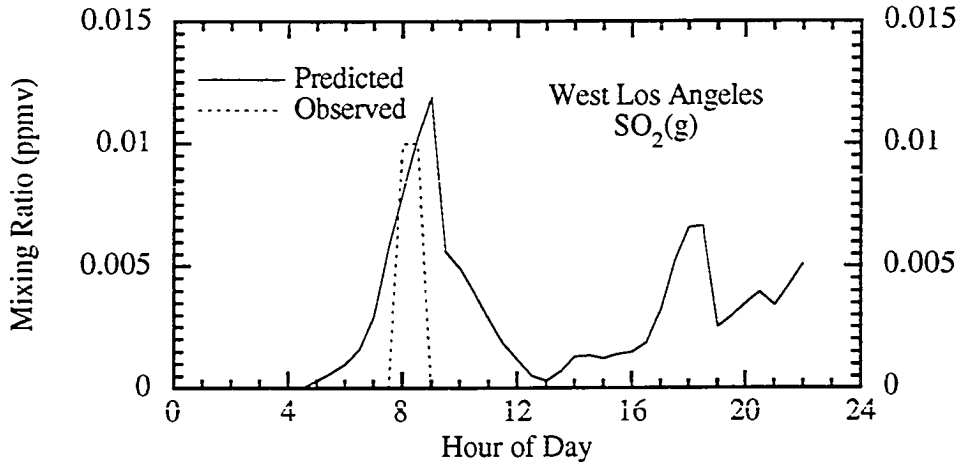
SULFUR DIOXIDE GAS

Fig. 10.60. Comparison of predicted to observed sulfur dioxide gas at West Los Angeles. The resolution of SO_2 observed data is 0.01 ppmv.

FORMALDEHYDE GAS
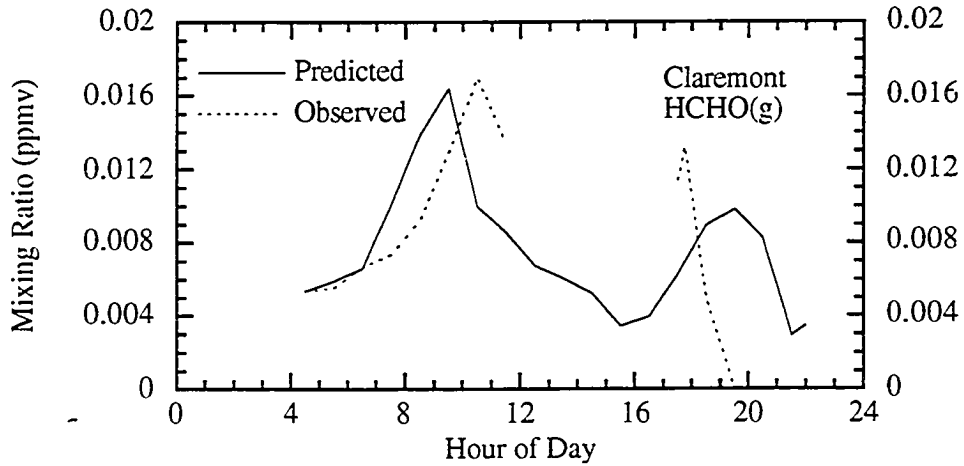
Fig. 10.61. Comparison of predicted to observed formaldehyde gas at Claremont. The space between the observed data indicates no data were measured for that time.

206
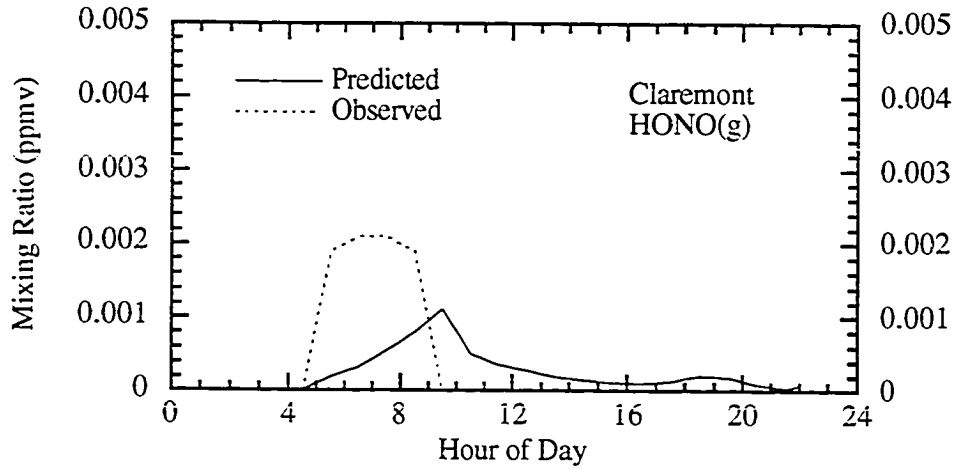
NITROUS ACID GAS

Fig. 10.62. Comparison of predicted to observed nitrous acid gas at Claremont.

NITRIC OXIDE GAS
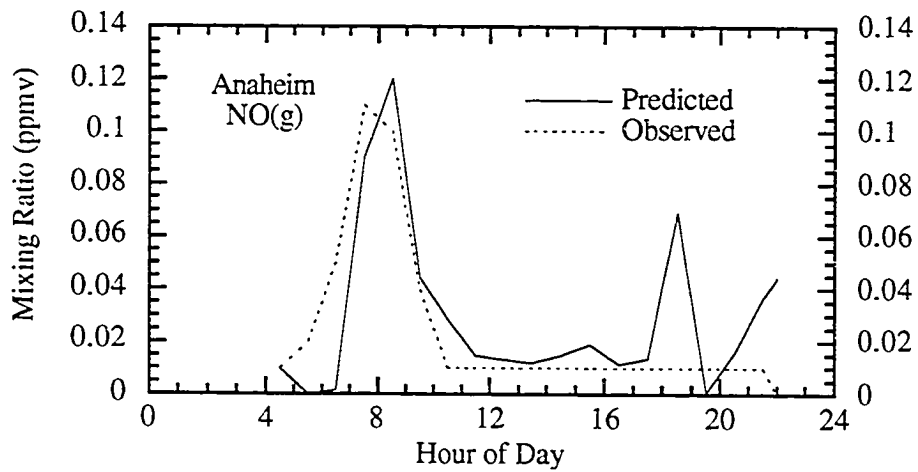
Fig. 10.63. Comparison of predicted to observed nitric oxide gas at Anaheim.

207
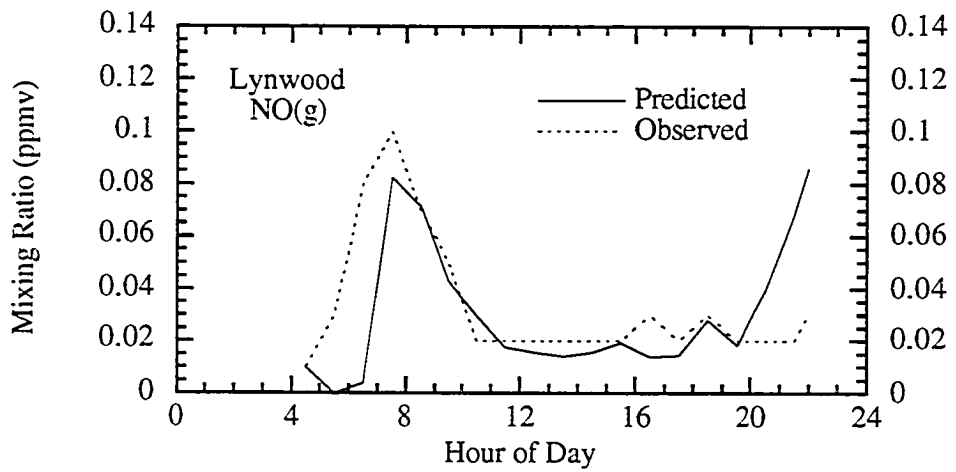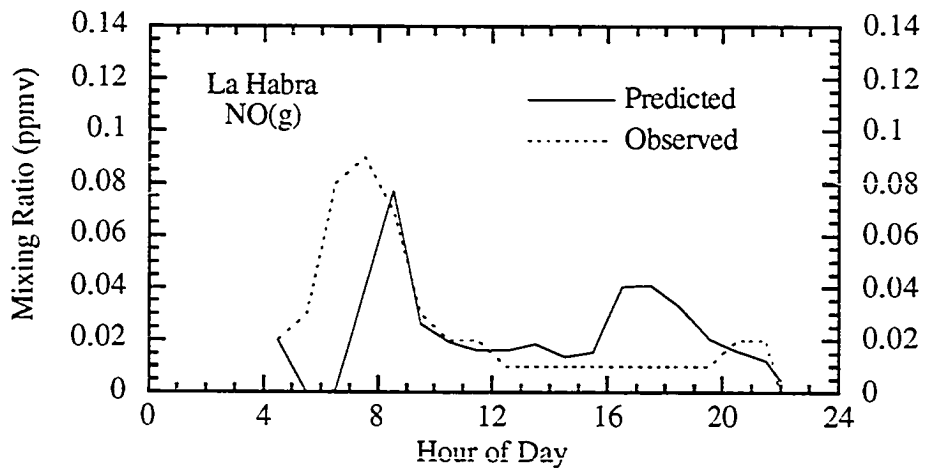
Figs. 10.64 - 10.65. Comparisons of predicted to observed nitric oxide gas at La Habra and Lynwood.

208
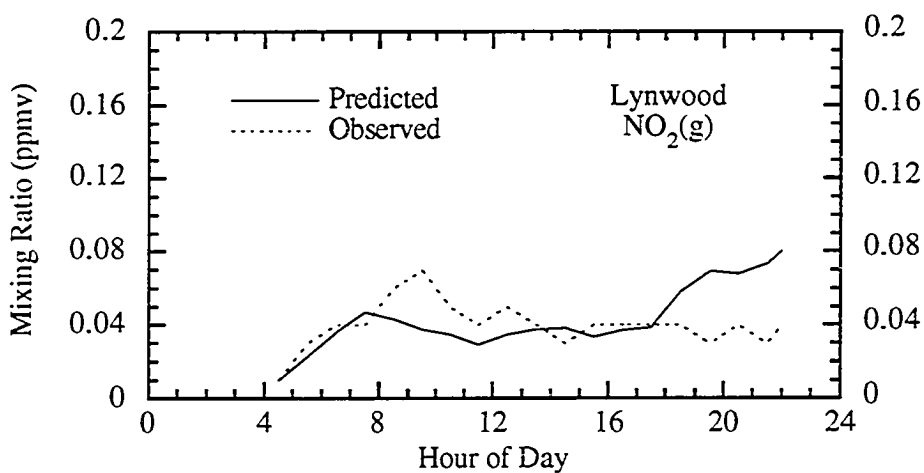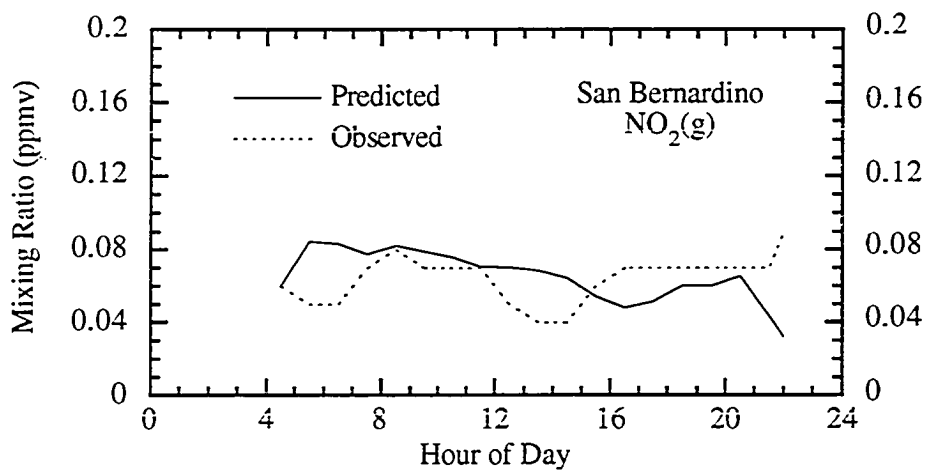
NITROGEN DIOXIDE

Figs. 10.66 - 10.67. Comparisons of predicted to observed nitrogen dioxide gas at San Bernardino and Lynwood.

209
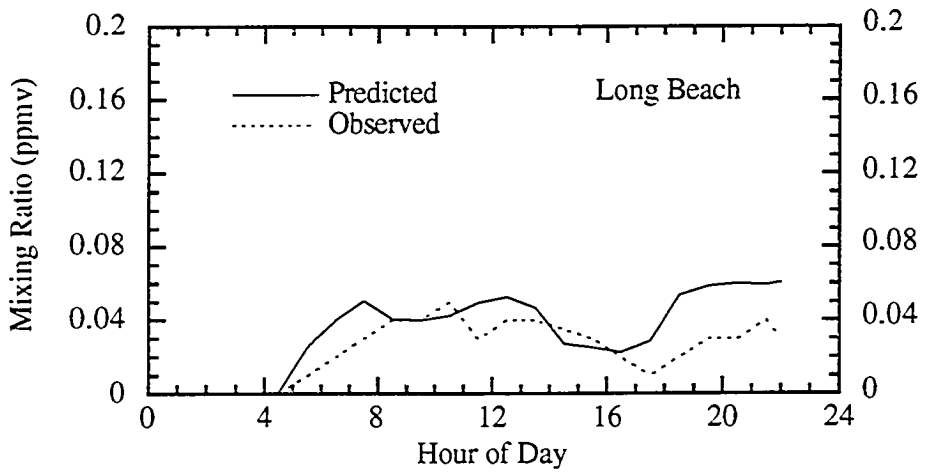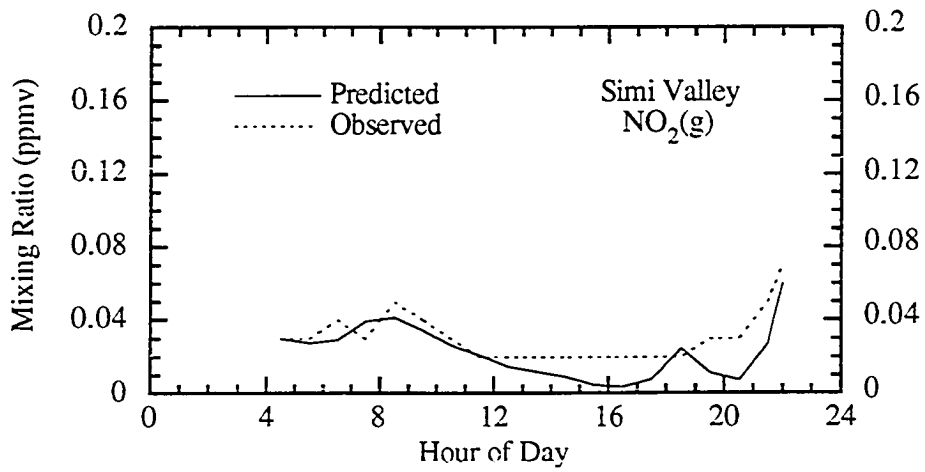
Figs. 10.68 - 10.69. Comparisons of predicted to observed nitrogen dioxide gas at Simi Valley and Long Beach.

210
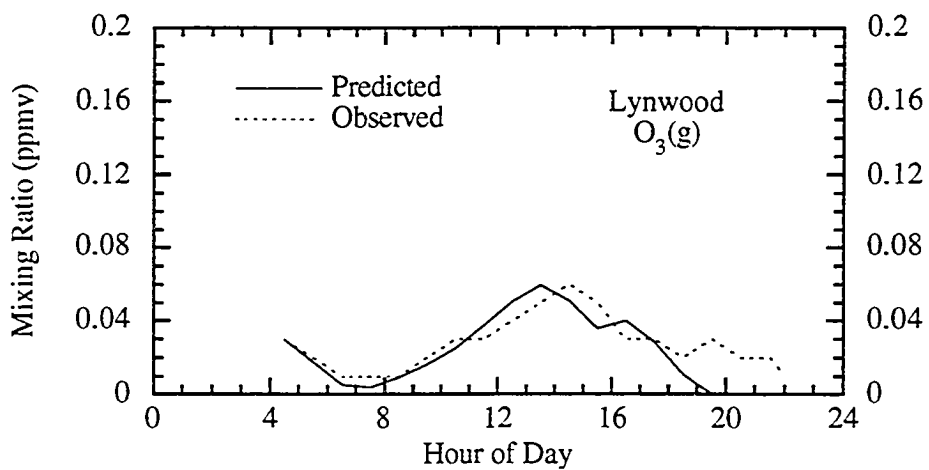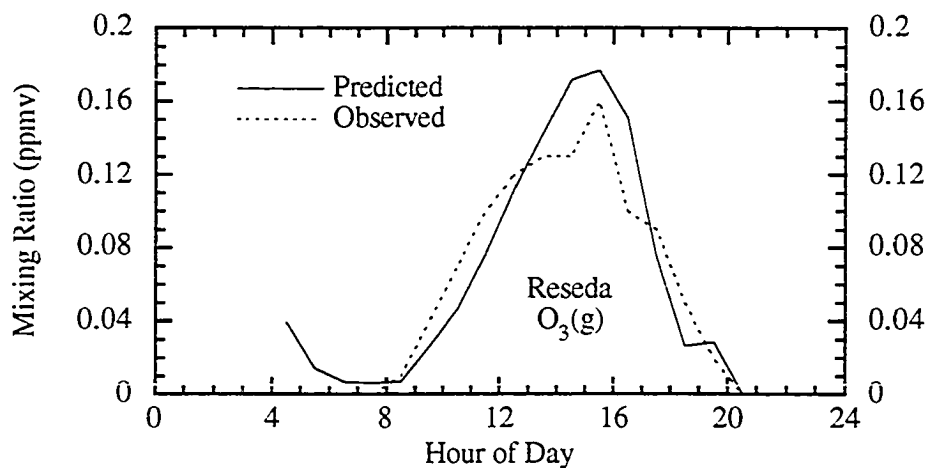
OZONE

Figs. 10.70 - 10.71. Comparisons of predicted to observed ozone gas at Reseda and Lynwood.

211
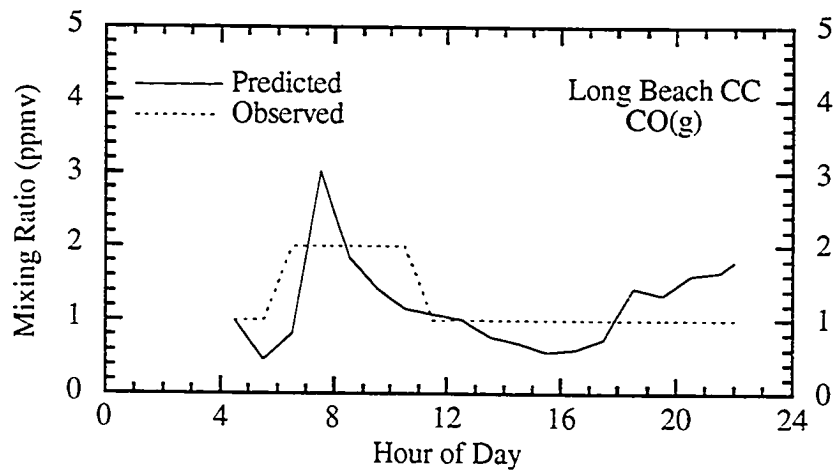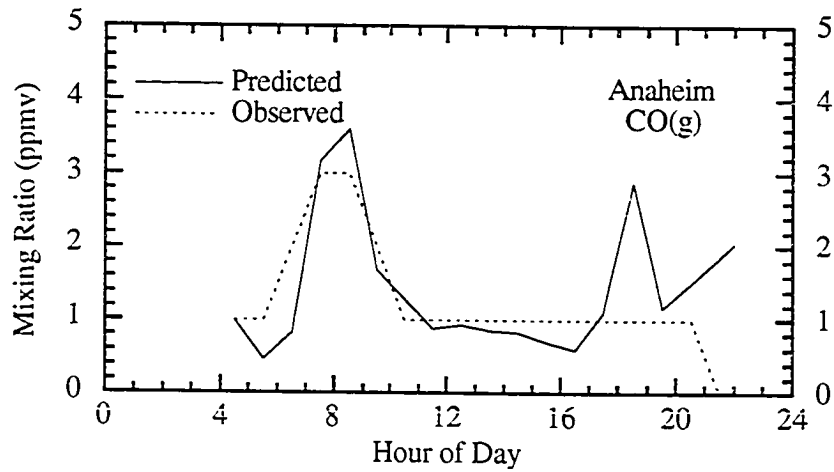
CARBON MONOXIDE

Figs. 10.72 - 10.73. Comparisons of predicted to observed carbon monoxide gas at Anaheim and Long Beach City College. The resolution of CO observed data is 1 ppmv.

212
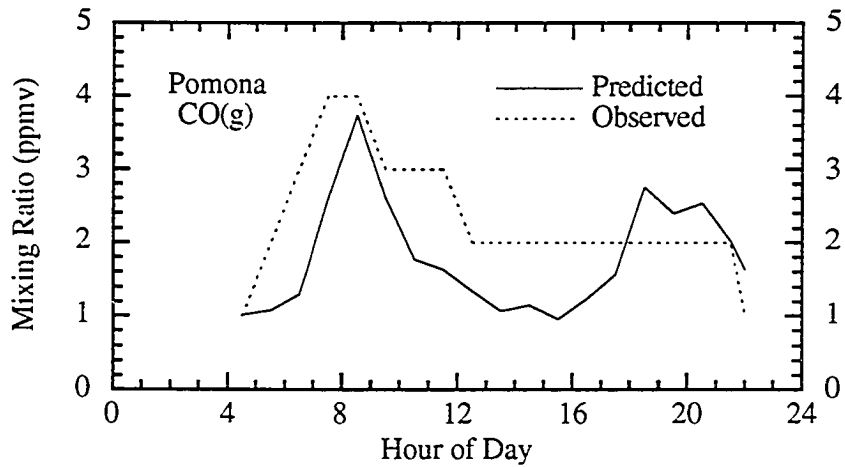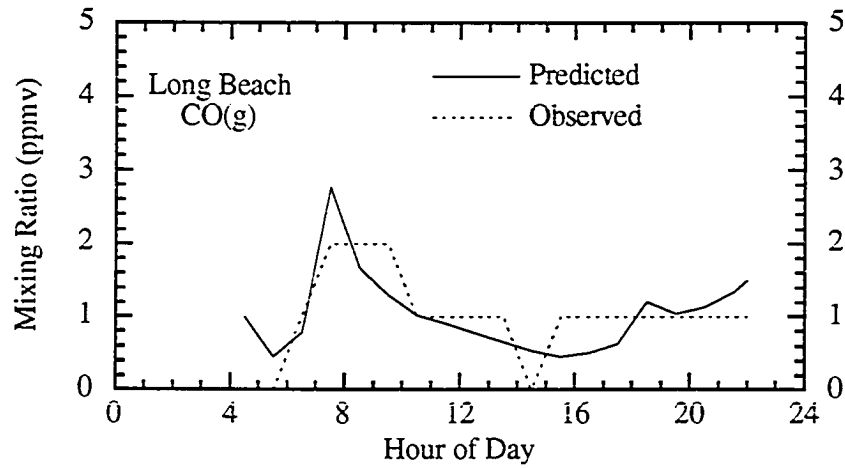
CARBON MONOXIDE

Figs. 10.74 - 10.75. Comparisons of predicted to observed carbon monoxide gas at Long Beach and Pomona. The resolution of CO observed data is 1 ppmv.

213
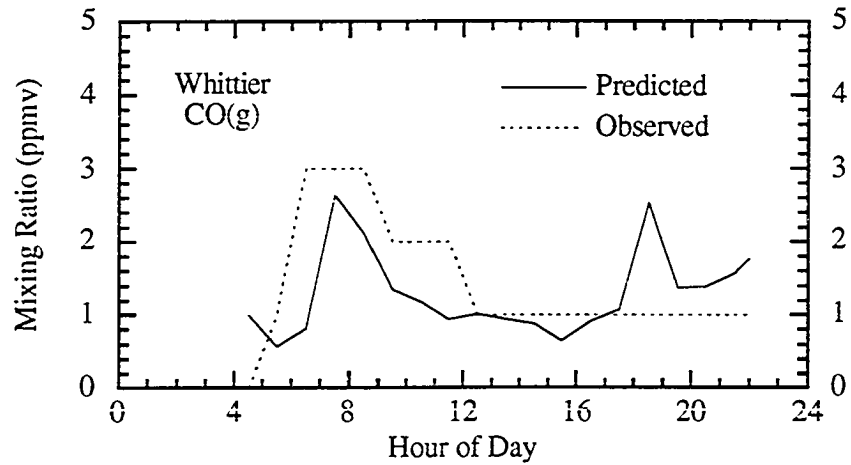
CARBON MONOXIDE

Fig. 10.76. Comparison of predicted to observed carbon monoxide gas at Whittier. The resolution of CO observed data is 1 ppmv.

TEMPERATURE
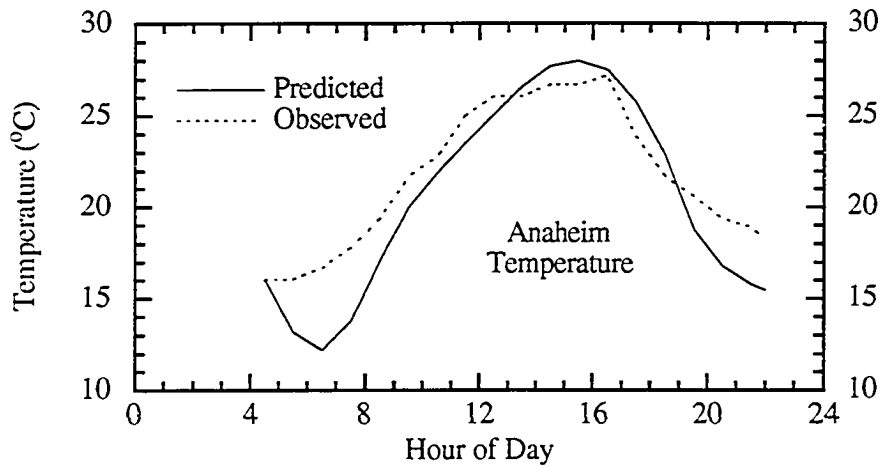
Fig. 10.77. Comparison of predicted to observed temperature at Anaheim (MMTD model results with radiation coupled from GATOR)

214
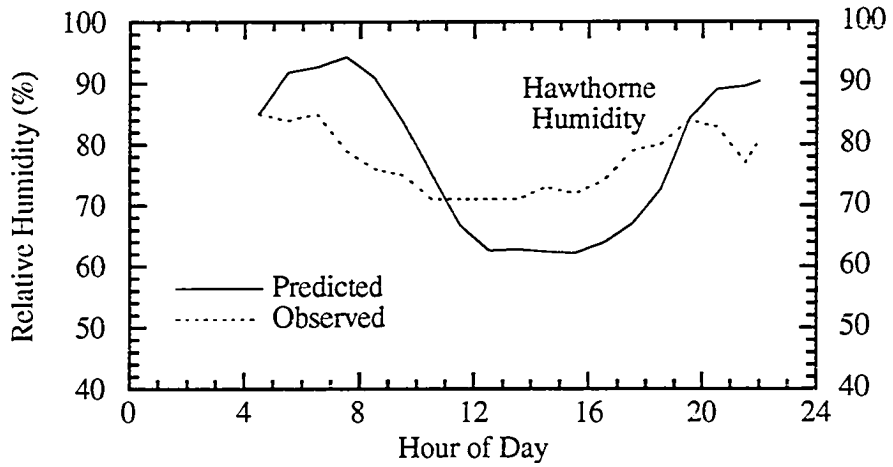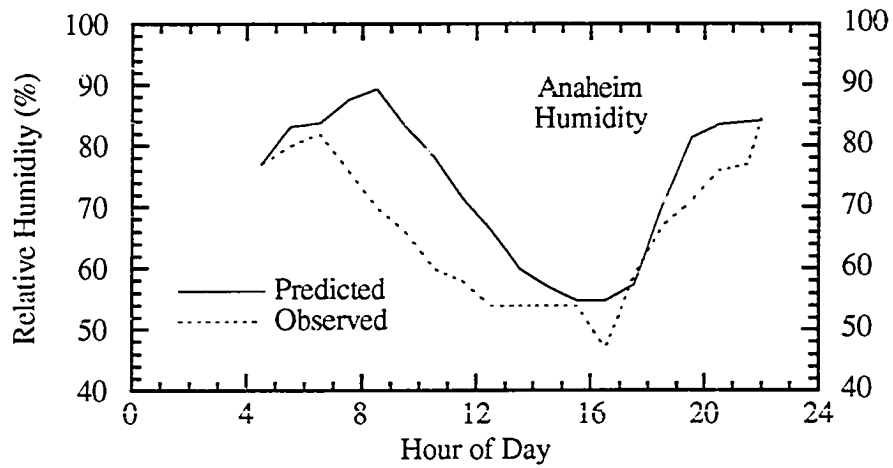
RELATIVE HUMIDITY

Fig. 10.78 - 10.79. Comparisons of predicted to observed relative humidity at Anaheim and Hawthorne (MMTD model results).

215
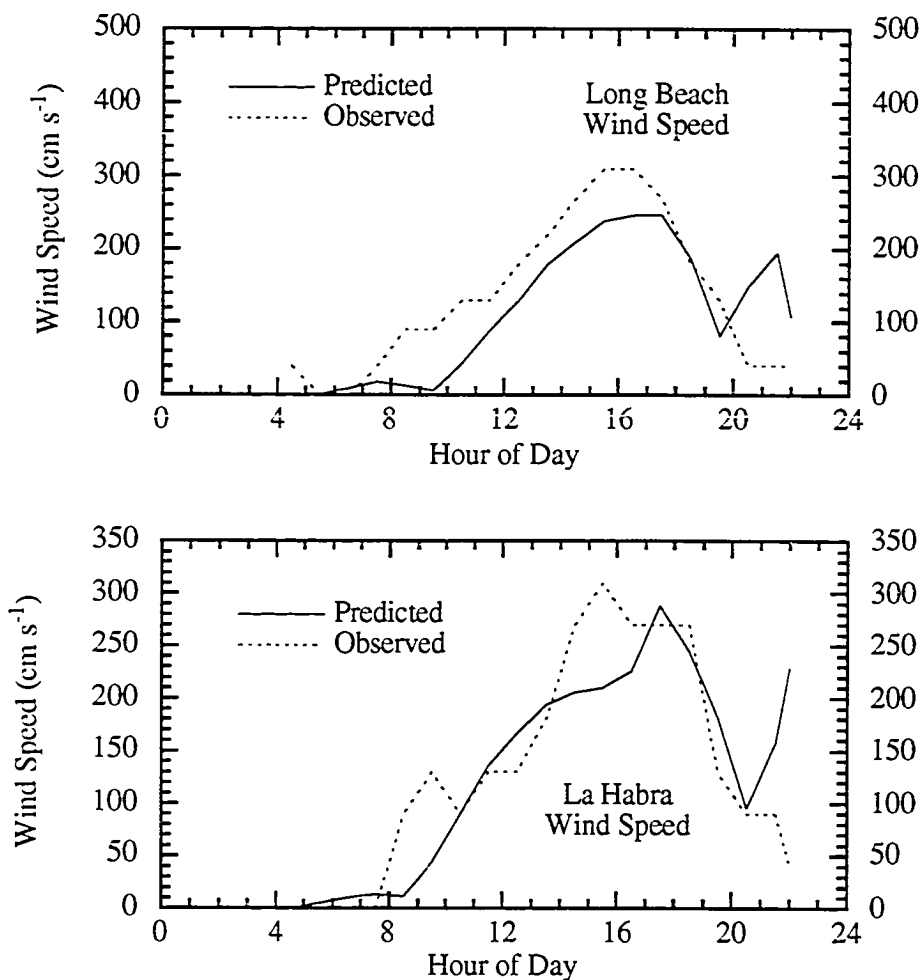
WIND SPEED

Figs. 10.80 - 10.81. Comparisons of predicted to observed wind speed at Long Beach and La Habra (MMTD model results)

216
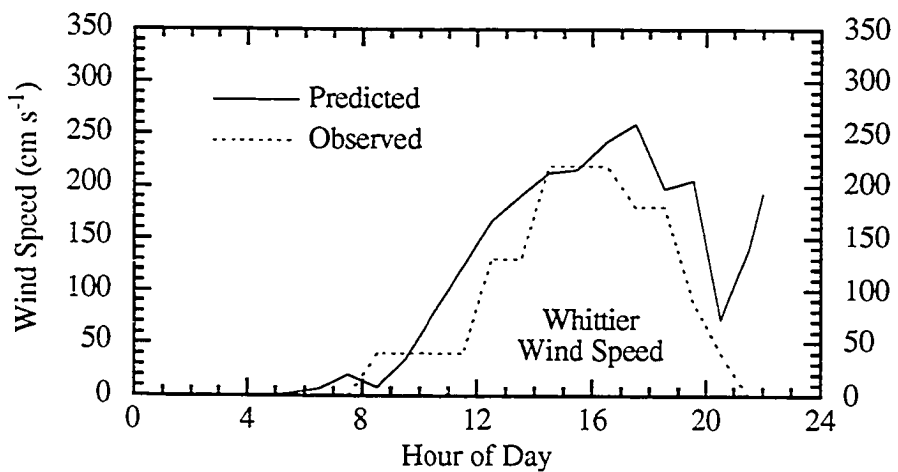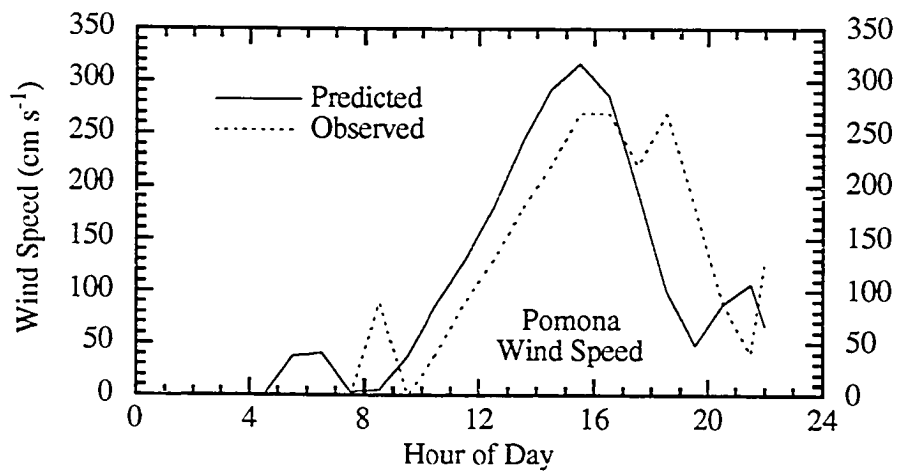
Figs. 10.82 - 10.83. Comparisons of predicted to observed wind speed at Pomona and Whittier (MMTD model results).

217
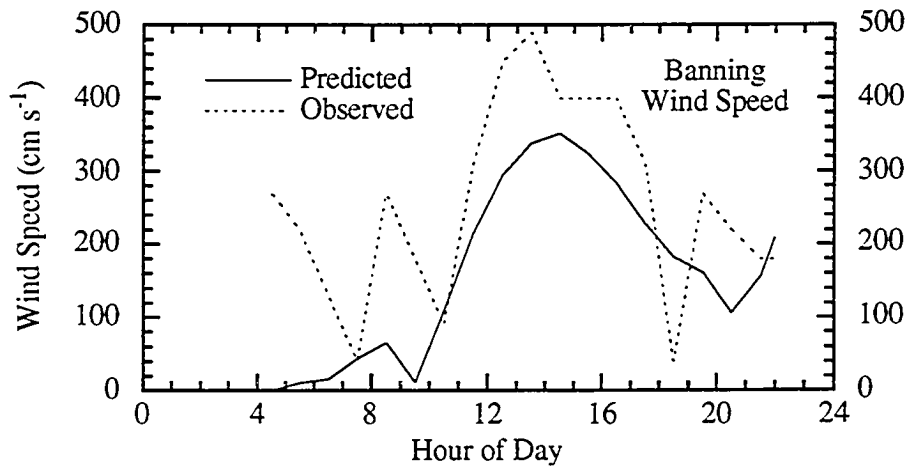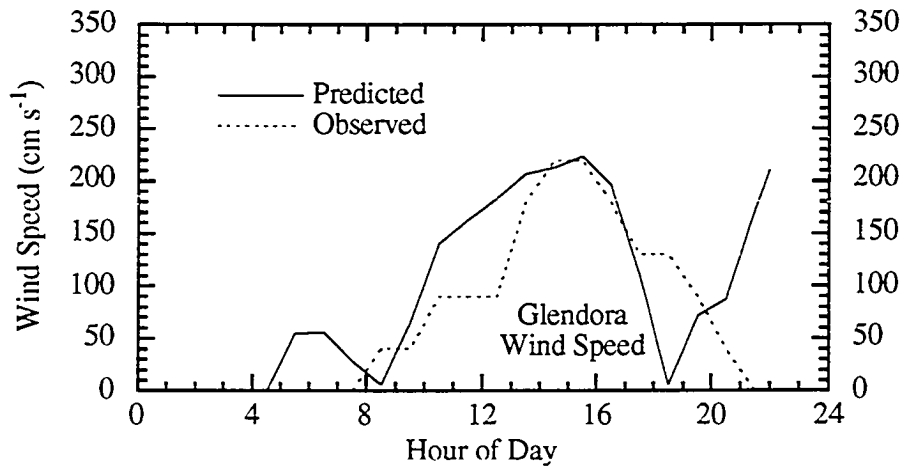
Figs. 10.84 - 10.85. Comparisons of predicted to observed wind speed at Glendora and Banning (MMTD model results).

218

Figures 10.34 - 10.85 identify some characteristics of the GATOR / MMTD modeling system. First, Figures 10.34 - 35 show that the radiation module predicted solar radiation well at CM44 (Riverside) and fairly well at CM62 (Temecula -- see Fig. 9.1). To calculate solar radiation in the model, surface heating rates for ultraviolet, visible, and near infrared wavelengths were summed. The blip in the observed curve for Riverside may have been caused by a small cloud that briefly passed by. Currently, the GATOR / MMTD system does not predict subgrid clouds. However, work will be done in the future to include the effects of such clouds.

Second, aerosol predictions were reasonable for some species, locations, and times but not so reasonable for others. For example, model concentrations of many species increased unrealistically after sunset (*e. g.* Fig. 10.36, 10.38 - 10.44, etc.). This occurred because the model predicted too stable of an atmosphere after sunset. In reality, the atmosphere over land in the basin is often neutral after dark, allowing pollutants to diffuse vertically. However, the model predicted stable surface layers, reducing diffusion and causing species concentrations to increase.

The figures for elemental and organic carbon (10.38 - 10.46) indicate other discrepencies between predictions and observations. These errors may have resulted from any one of a number of factors. First, the aerosol emissions inventory was not developed specifically for these particular SCAQS days; thus, mass emissions at each location are not necessarily accurate. Second, the given emissions were resolved into four size categories, and my assumptions about how to distribute the emissions within each size bin could be incorrect. Third, erroneous predictions of atmospheric stability at times other than after sunset may also cause concentrations to be too high or low. Fourth, for this simulation, only one organic species, nitro-cresol, was assumed to condense onto particles. This assumption could have caused underpredictions in fine-particle organic carbon concentrations.

219

Next, Figures 10.47 - 10.50 show comparisons of particulate sodium predictions to data. Sodium predictions matched the data fairly well, indicating that sodium emissions rates and initial concentrations may be within reason. After dark at some locations, the model predicted too much sodium and other species. For example, at Burbank, sodium (Fig. 10.48), organic carbon (Fig. 10.43), and ammonium (Fig. 10.52) concentrations were all too high. Again, this was caused by a prediction of too much atmospheric stability after dark.

Figure 10.51 shows that chloride concentrations were reasonably predicted at Hawthorne. However, results discussed later indicate that particulate chloride was overpredicted at most locations.

Figures 10.52 - 10.55 show comparisons of particulate ammonium, nitrate, and sulfate concentrations. In the case of ammonium at Burbank, predicted concentrations decreased at the same pace as measured concentrations; however, predictions were consistently higher than observations. In the case of nitrate at Anaheim, predicted concentrations were higher than measured concentrations; however, nitrate was generally underpredicted in aerosols at other locations. In the case of sulfate, predictions again leaped after dark. Further, at Long Beach City College, predicted sulfate was too high in the morning, possibly because of errors in emissions. Since $OC_{2.5}$ concentrations (Fig. 10.46) were not erroneous at this location in the morning, the high sulfate concentrations were probably not due to incorrect stability predictions.

Figures 10.56 - 10.76 show comparisons of gas mixing ratio predictions to data. All ammonia in the model originated as emissions. Since the ammonia emissions inventory (Section 9.1.2) was validated for a period in 1982; discrepancies between predictions and 1987 observations could be attributed partly to the age of the inventory.

Conversely, nitric acid gas is produced primarily by oxidation of nitrogen dioxide. In some locations, such as Long Beach City College (Fig. 10.58) and Riverside

220

(Fig. 10.59), its mixing ratio was predicted fairly accurately for daylight hours. At night and in the early morning, however, nitric acid predictions were not so good, partly because of errors in predicted atmospheric stability.

The sulfur dioxide comparison (Fig. 10.60) shows that the model almost predicted the primary SO_2 peak accurately. However, the false secondary peak that occurred after 18:00 resulted from the nighttime stability problem. Similarly, the model almost predicted the first formaldehyde peak (Fig. 10.61) and managed to predict the occurrence of a second peak. However, the time and magnitude of the second prediction were incorrect.

The model also predicted a small peak of nitrous acid (Fig. 10.62). However, measurements by Winer *et al.* (1989, 1994) indicated a much higher and an earlier observed mixing ratio of HONO at both Claremont and Long Beach City College. HONO is produced primarily from emissions, but also from the reactions (a) NO + NO_2 + $H_2O(l)$ --> 2HONO and (b) OH + NO -M-> HONO (reaction 24 in Table A.4). Reaction (a) may be a significant source of HONO; however, it occurs on particle surfaces and its reaction rate is difficult to determine (Kaiser and Wu, 1977). Because of the uncertainty in the rate, reaction (a) was not included in the simulation discussed here. Consequently, error in the predicted peak of HONO in Figure 10.62 may have resulted either because reaction (a) was omitted or because HONO emissions rates were low.

The major chemical loss process of nitrous acid is photodissociation (reaction 200 in Table A.4). The cross-sections and quantum yields used were those recommended by Atkinson *et al.* (1992). The corresponding summer photodissociation rate of HONO is approximately 1 - 3 x 10^{-3} s^{-1} (depending on time of day), giving HONO a photolysis lifetime of about 5 - 15 minutes. A second loss process is OH + HONO --> NO_2 + H_2O (reaction 25 in Table A.4). However, even with an OH concentration of 5 x 10^6 cm^{-3}, the lifetime of HONO from this reaction is about 11.4 hours. Thus, photolysis is the most

important daytime chemical loss mechanism of nitrous acid. Other loss mechanisms of HONO include deposition and transport; however, model results indicate that losses from chemistry were about 3 - 10 times more significant than losses from these other mechanisms.

Finally, Figure 10.62 shows a predicted HONO mixing ratio residual past morning but no observed residual. The emissions inventory includes a small but continuous source of HONO during the day; thus, even with a strong photodissociation loss rate, some predicted HONO is expected. However, the difference between predicted and observed HONO after morning may have resulted not only because the detection limit of observed HONO was 0.8 ppb, but also because HONO was emitted mostly from freeways and roads, away from the monitoring stations. During its journey to the monitoring stations, HONO may have photodissociated and dispersed; however, new HONO was constantly being emitted. In sum, since the model averaged mixing ratios over an entire grid cell, it averaged relatively high mixing ratios near the freeways together with lower mixing ratios away from the freeways, giving a residual prediction.

Next, nitric oxide, nitrogen dioxide, ozone, and carbon monoxide (Figures 10.63 - 10.76) results were similar to those for the gas-phase-only simulations. Future work will involve analyzing the effects of aerosols on gas concentrations in more detail.

Finally, the remaining figures show comparisons of temperature, humidity, and wind speed to data. Humidity predictions rely on both temperature and water vapor predictions; thus, errors in both will exacerbate errors in humidity. Wind speed comparisons shown in Figures 10.80 - 10.85 indicate that the MMTD predicted wind speeds reasonably. In Banning, where winds tend to be fairly high, the model did not pick up the correct peak speed; however, it nearly picked up the time of the peak speed.

Statistical output from the August 27 simulation show that the normalized gross error (*NGE*) at 2:30 p. m for elemental carbon particles smaller than 2.5 μm in diameter

($EC_{2.5}$) was 45.5% (8 stations). Similarly, the *NGE* was 44.2% for EC_{10}, 35.1% for $OC_{2.5}$ (organic carbon), 41.6% for OC_{10}, 58.5% for $MASS_{2.5}$ (total mass < 2.5 μm in diameter), and 71.8% for $MASS_{10}$. In addition, the *NGE* was 56.4% for $NH4_{2.5}$ (particulate ammonium), 50.1% for $NH4_{10}$, 70% for $NO3_{2.5}$ (particulate nitrate), 54.1% for $NO3_{10}$, 32.3% for NA_{10} (particulate sodium), over 100% for CL_{10} (particulate chloride), 40.7% for $SO4_{2.5}$ (particulate sulfate), and 47.3% for $SO4_{10}$.

As discussed, predicted chloride concentrations in coarse particles were too high while predicted nitrate concentrations in the same particles were too low. Since sodium concentrations were reasonable, the ocean emission rate of NaCl does not appear to have caused the chloride overpredictions. Instead, a possible explanation is that not enough chloride was forced out of particles into the gas phase by competing acids, such as nitric acid. For example, if more nitric acid had entered into coarse particles, more chloride would have been forced out (Section 3.1.3), improving both nitrate and chloride predictions.

Another explanation is that the particulate emissions inventory for chloride was not valid for August 27, 1987, causing chloride to build up excessively. If chloride emissions are too high then chloride in aerosols can prevent nitrate from entering the particles if the gas phase becomes supersaturated with hydrochloric acid. Thus, future work will include examining why the model predicted too little nitrate in the aqueous phase. The study will focus on testing the solubility of HCl and HNO_3 in relation to each other, on improving activity coefficient calculations in solutions with 70 or more components at high ionic strength, and on examining the anthropogenic chloride emissions inventory.

Because of errors in aerosol concentration predictions, aerosol scattering coefficient prediction errors were fairly high (*e. g. NGE* of 65.8% at 2:30 p. m). If

223

aerosol predictions improve, scattering coefficient prediction errors should decrease accordingly.

In addition, the *NGE* at 2:30 p. m. for solar radiation was 2.5%, for temperature was 1.49% (14 stations), for surface wind speed was 47.7% (33 stations), for ozone was 33% (35 stations), for NO gas was 46.1% (2 stations), for NO_2 was 37.8% (20 stations), for CO was 42% (21 stations), and for CH_4 was 10.8% (4 stations).

Thus, while the first test of aerosol processes provided some useful insight, it also revealed that significant work is needed to improve predictions. Such work will include studying particulate emissions more carefully, analyzing aqueous equilibria in more detail, improving treatment of the nighttime boundary layer, and including the condensation of additional organic gases.

10.3 Comparison to Photostationary State Assumption

Here, model predictions of ozone from several stations around the basin are compared to predictions by the photostationary state equation. This equation derives from the chemical reactions (a) $NO + O_3 \rightarrow NO_2 + O_2$ (reaction 2 of Table A.4) and (b) $NO_2 + h\nu \rightarrow NO + O$ (reaction 195 of Table A.4). Setting the first derivative of NO_2 from these equations to zero and solving for O_3 gives

$$[O_3] = J[NO_2]/k[NO] \qquad (10.1)$$

where J is the photolysis rate of reaction (a) and k is the rate of reaction (b). Reactions (a) and (b), along with (c) $O + O_2 + M \rightarrow O_3 + M$ (reaction 1 of Table A.4) react rapidly and are nearly in steady state in the absence of hydrocarbons. However, in the presence of hydrocarbons, reactions of the form (d) $NO + RO_2\cdot \rightarrow NO_2 + RO\cdot$ speed the conversion of NO to NO_2 (Seinfeld, 1989). Thus, adding (d) and other reactions to the

224

first derivative equation of NO_2 changes the photostationary state equation such that (10.1) may not represent the correct relationship of ozone to nitric oxide and nitrogen dioxide when hydrocarbons are present. Here, this hypothesis is tested. For given $NO_2:NO$ ratios in polluted air, the differences between ozone mixing ratios calculated from a full chemistry model to those calculated from Equation (10.1) are compared.

Table 10.6 Comparison of ozone predictions by the GATOR / MMTD model to predictions using the photostationary state assumption at 8:30 a. m. and 1:30 p. m. August 27, 1987. The photolysis rate of NO_2 and temperature at 8:30 a. m. were about 0.008 s^{-1} and 291 K, respectively. At 1:30 p. m., they were about 0.01 s^{-1} and 298 K (average), respectively. Equation 10.1 was used to calculate photostationary state ozone mixing ratios.

Table 10.6

Station	[NO](ppm) model	[NO2](ppm) model	[NO2]/[NO] model	[O3](ppm) model	[O3](ppm) photostat.	% diff [O3]
			8:30 a. m.			
ANAH	0.1757	0.0760	0.43	0.0058	0.0086	-32.6
COST	0.0607	0.0446	0.74	0.0119	0.0146	-18.5
HAWT	0.0654	0.0525	0.80	0.0104	0.0159	-34.6
LAHB	0.0764	0.0501	0.66	0.0092	0.0130	-29.2
LYNN	0.1209	0.0625	0.52	0.0073	0.0103	-29.1
PASA	0.1179	0.0740	0.63	0.0089	0.0125	-28.8
RESE	0.0704	0.0645	0.92	0.0125	0.0182	-31.3
SIMI	0.0232	0.0355	1.53	0.0204	0.0304	-32.9
			1:30 p. m.			
ANAH	0.0088	0.0374	4.25	0.0859	0.0960	-10.5
COST	0.0047	0.0131	2.79	0.0617	0.0630	-2.1
HAWT	0.0169	0.0394	2.33	0.0471	0.0526	-10.5
LAHB	0.0108	0.0461	4.26	0.0879	0.0963	-8.7
LYNN	0.0096	0.0372	3.88	0.0778	0.0875	-11.1
PASA	0.0321	0.0693	2.16	0.0491	0.0488	+0.6
RESE	0.0091	0.0495	5.44	0.1216	0.1228	-1.0
SIMI	0.0031	0.0148	4.77	0.0990	0.1077	-8.07

225

Table 10.6 shows test results of the above hypothesis. The two times tested were 8:30 a. m. and 1:30 p. m., August 26, 1987. The morning time corresponded to low $NO_2:NO$ ratios and the afternoon time corresponded to high $NO_2:NO$ ratios. The table shows that in the morning, the differences between model and photostationary predictions were greater than in the afternoon. Figures 10.20 and 10.21 show that hydrocarbon mixing ratios generally peaked near 8:00 a. m. each morning then declined. Thus, in the morning, hydrocarbons perturbed the photostationary state (Equation 10.1) while, in the afternoon, the system was closer to steady state and hydrocarbons played a smaller role.

10.4 Comparison of Emitted to Ambient NO:CO Ratios

Next, comparisons of emitted to ambient ratios of NO:CO are shown. Both NO and CO are emitted from automobiles in significant quantities. NO is also emitted from stacks (*e. g.* Table 9.3). Since carbon monoxide is a fairly *conserved* species (Main and Friedlander, 1990), and since NO is reactive and dry deposits more readily to surfaces, emitted NO:CO ratios should exceed ambient ratios.

To test this hypothesis, ambient NO:CO volume mixing ratios were calculated at three stations, Anaheim, Long Beach, and Pasadena. In addition, the volume ratio of emitted NO:CO was calculated each hour for the basin as a whole. Figure 10.86 shows that, while the emitted NO:CO ratios ranged from 0.07 to 0.18 during August 26, 1987, ambient NO:CO mixing ratios at each of three locations ranged from < 0.01 to 0.07. Thus, NO depleted relative to CO, supporting the hypothesis that CO is conserved relative to NO.

226

In Figure 10.86, the ambient NO:CO ratio peaked once at Anaheim and Pasadena, but it peaked twice at Long Beach City College. Even though the CO:NO ratio peaked a second time at LBCC, the mixing ratios of both CO and NO were much lower at that location in the afternoon than in the morning (*e. g.* Fig. 10.23). Further, ambient NO:CO ratios were higher at LBCC than at the other locations because NO was emitted from both stacks and autos near LBCC while it was emitted from just autos near the other locations. Since CO emissions from stacks are smaller than are NO emissions, ambient NO:CO ratios should increase near stacks.
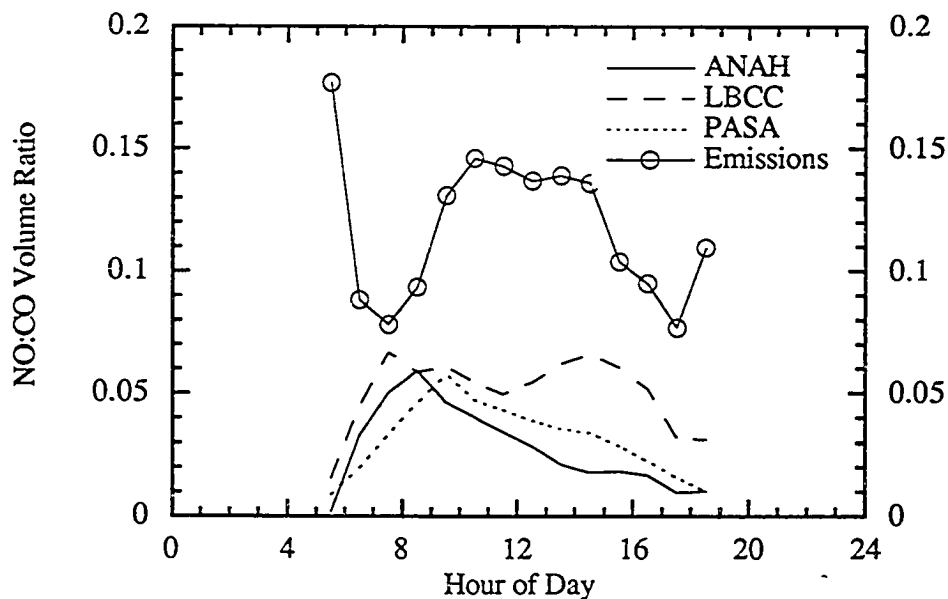
Fig. 10.86. Comparison of emitted to ambient NO:CO ratios for August 26, 1987. Emitted NO:CO is the ratio of the sum of the number of NO molecules to the sum of the number of CO molecules emitted over the entire basin each hour. Ambient NO:CO (ANAH, LBCC, and PASA) is calculated as [NO]/[CO] (No. No.$^{-1}$) at each location. ANAH is Anaheim, LBCC is Long Beach City College, and PASA is Pasadena. These results were obtained without adjusting the original CARB CO emissions inventory.

227

10.5 General Sources of Model Error

In a model that simulates numerous processes, errors can arise in many places. Here, I discuss possible sources of error in the GATOR / MMTD system. First, emissions rates may be incorrect. For example, ROG and CO emissions from hot exhaust emissions may be low by a factor of three or more. Also, aerosol emissions estimates are divided into only four size categories, with only one category accounting for sub-micron particles. Thus, errors can arise because the size resolution of emissions data is coarse.

Second, initial and boundary conditions may be a source of error. For example, initial species concentrations and meteorological variables are currently estimated or interpolated for each grid cell. Further, the concentrations of all species are estimated or calculated roughly at the boundaries each time interval. Such estimates may cause errors.

Third, gas-phase chemical equations, themselves, may be incorrect or unaccounted for, resulting in erroneous predictions. While inorganic reactions are considered fairly accurate, organic reactions differ slightly among smog chemistry mechanisms (Dodge 1989). Also, all organic reactions occurring in the atmosphere cannot be accounted for because the number of reactions is so large. Instead, condensed chemical mechanisms that simulate the explicit chemistry are relied upon. Errors probably arise by condensing explicit chemistry and assuming similar rates for species or carbon bonds that are lumped into groups. In addition, many organic reaction rates available in the literature do not include temperature and pressure dependencies, increasing uncertainties.

A fourth source of error may be the advection solver. Dabdub and Seinfeld (1994) showed that the Galerkin solver, a version of which was used for the simulations shown in Sections 10.1 and 10.2, may be more diffusive than the Accurate Space

228

Derivative (ASD) method. In a head-to-head comparison of advection in the Los Angeles Basin, the ASD method predicted sharper peaks on eastern side (*ibid.*). However, a drawback of the ASD method is that it is currently about thirty times slower than the Galerkin. Since GATOR advects up to thousands of gases and aerosol species, computational time currently prohibits a solver such as the ASD.

A fifth source of error may be in computing photolysis rates. The rates depend on the angle and intensity of the sun, attenuation of the incident light due to scattering and absorption, and on the absorption cross sections and quantum yields of the affected species. In GATOR, the sun's zenith angle is tracked at each grid cell and time by accounting for the mean anomaly, the obliquity of the ecliptic, the right ascension, and the longitude of the sun as weil as the earth-sun distance. Sunlight appears first in the southeast corner of the grid and disappears last from the southwest corner. Thus, the temporal angle of the sun is fairly accurate. Further, Figures (10.34) and (10.35) show that GATOR predicted solar radiation well in the absence of clouds. In addition, absorption cross-sections of many photodissociating species are known within 5-10% error (however, the cross-sections and quantum yields of several minor species are not well known).

Thus the biggest source of photolysis error would probably be the calculation of optical depth in the presence of clouds or fog. For example, the model might ignore many sub-grid scale clouds or plumes, which would normally decrease optical depth. Also, under some weather conditions, wind-blown particles, not accounted for in the emissions inventory, could enter the air, decreasing optical depth. While the model accounts for every absorbing and scattering gas and particle entering the model atmosphere, it can miscalculate the concentration of some gases and particles, reducing the accuracy of radiative transfer and, therefore, ozone and visibility calculations.

A sixth source of error could be local wind field calculations. While the MMTD appears to predict winds well over the basin as a whole, it's resolution prohibits it from predicting sub-grid scale winds. Since each SCAQMD observation station is a point location, and not spread over an entire grid cell, sub-grid meteorology and topography may affect observed concentrations at many stations. Further, if a certain monitoring station lies on or near terrain uncharacteristic of the terrain associated with its four surrounding grid centers, then observations from the site will consistently differ from model predictions since the model wind fields depend on the average terrain in each cell.

A seventh source of error could be soil moisture data. This data need to be correct for surface temperature calculations to be accurate. Soil moisture varies significantly during the day; however, the soil moisture data available appear to be an average over time.

With respect to visibility, additional errors can arise from the assumptions underlying the aerosol model. For example, all particles are assumed to be spherical. In reality, elemental carbon and other particles are far from spherical. Other errors can arise with respect to the processes of chemical equilibrium and aqueous chemistry, which are not fully understood. Furthermore, small errors in temperature or humidity will affect the rate of growth of particles and quickly affect visibility. Finally, errors in surface roughness and other deposition factors will affect the deposition rates of gases and particles.

In sum, numerous uncertainties exist in the GATOR / MMTD air pollution modeling system. In time, physical processes will be better understood, more data will be gathered, computational speed will increase, and the resolution of the model will increase. Thus, model results should improve significantly over the next few years.

230

Chapter 11

Conclusion

For this thesis, a *g*as, *a*erosol, *t*ransport, and *r*adiation model (GATOR) was developed for studying pollution in urban and regional areas. Further, R. Lu and I coupled GATOR to the *m*esoscale *m*eteorological and *t*racer *d*ispersion (MMTD) model of Lu and Turco (1993, 1994a,b). The integrated GATOR / MMTD air pollution modeling system (APMS) predicts time- and space-dependent gas and aerosol concentrations, aerosol size distributions and composition, meteorological variables, and radiative variables. For this work, the modeling system was applied to study pollution over the Los Angeles Basin.

To predict gas and aerosol concentrations and other atmospheric variables, GATOR simulates the following: gas processes of chemistry, emissions, gas-to-particle conversion, optical depth attenuation, and deposition; aerosol processes of size-resolved emissions, nucleation, coagulation, condensational growth, dissolutional growth, evaporation, chemical equilibrium, aqueous chemistry, optical depth attenuation, deposition, and sedimentation; transport processes of horizontal advection and diffusion and vertical diffusion of all gases and aerosols; and radiation processes of spatially-resolved ultraviolet, visible, and infrared radiative fluxes, which are used to calculate photodissociation and heating rates. Further, the coupled MMTD model predicts

231

spatially- and temporally-resolved wind speed, wind direction, temperature, humidity, and pressure, which are all used in GATOR. Similarly, the heating rates from GATOR feed back to the MMTD to take part in temperature calculations.

The individual numerical techniques in the GATOR / MMTD system have been reviewed extensively in recent studies. To test the performance of all processes acting together in an airshed model, simulations of Los Angeles pollution were run for the SCAQS period of August 26 - 28, 1987. In one simulation, aerosol processes were included, and in the others, they were not. The results for one- to three-day simulations indicate that the system predicted surface ozone mixing ratios within a normalized gross error of 20 - 35% for all daytime hours. Most other gas and aerosol components were predicted within normalized gross errors of between 10 - 65%.

Further, time-series plots indicate consistent agreement of both time and location of ozone, temperature, and solar radiation predictions versus observations. Agreement for other parameters, including nitric oxide, nitrogen dioxide, and carbon monoxide, are also reasonable, but more sporadic. In addition, preliminary simulations of aerosol processes indicate good agreement for some species but poor agreement for others.

From the results, I suspect that a combination of factors, including errors in input data and model assumptions, cause some of the prediction errors. Also, errors in calculated mixing ratios after sunset appear to result from predictions of atmospheric stability near the surface when the atmosphere is, in reality, neutrally stable. Future work includes rectifying known errors, improving treatment of subgrid scale processes, including the effects of large-scale meteorology, and improving treatment of aerosol, fog, and cloud microphysical and chemical processes.

The cases here were run on a Cray 90 computer, and the time for all computations that excluded the aerosol phase was about 1.6 hours per 24 hours of simulation when 41,800 grid cells were used for MMTD calculations and 24,276 cells were used for

232

GATOR calculations. The chemistry routines, used to solve 93 ordinary differential equations, took approximately 69% of all computer time.

The time to run the model with both gas and aerosol processes turned on and with 11 size bins and about 70 aerosol species in each bin for each grid cell, was 11.5 hours per day of simulation. This is about seven times slower than simulations without aerosols. Aqueous chemistry, chemical equilibrium, and condensational growth were the three processes that consumed most computer time when aerosols were included.

The goal of this research was to create a physical model that not only accounts for many processes leading to pollution but is also easy to use and to understand. Thus, I spent significant time commenting the code and optimizing it for speed. Most importantly, however, the model should predict pollutant concentrations reasonably, if not accurately. In the future, understanding of physical processes will improve, available data will increase, and computer resources will be more abundant. Thus, the groundwork has been laid for further improvement of this air pollution modeling system.

233

Appendix A

Tables

Table A.1. Summary of references for each of the numerical solvers and submodels currently within the GATOR / MMTD system.

Table A.1

Process	Reference(s)
Gas-phase processes	
Gas chemistry solver (SMVGEAR)	Jacobson and Turco, 1994a; Jacobson *et al.*, 1994e; this work
Gas surface emissions model	Jacobson *et al.*, 1994e
Gas stack emissions model	Ames *et al.*, 1986; Jacobson *et al.*, 1994e
Dry deposition model	McRae *et al.*, 1982; Russell *et al.*, 1993; this work
Aerosol-phase processes	
Nucleation model	Hamill *et al.*, 1982; Zhao, 1993; this work
Aerosol surface emissions model	Jacobson *et al.*, 1994e
Coagulation model	Jacobson *et al.*, 1994b; Toon *et al.*, 1988; Turco *et al.*, 1979a
Equilibrium vapor pressure solver (EQUISOLV)	Jacobson *et al,* 1994d
Condensational growth solver (SMVGEAR)	Jacobson and Turco, 1994c;
Dissolutional growth solver (SMVGEAR)	Jacobson *et al.*, 1994d
Chemical equilibrium solver (EQUISOLV)	Jacobson *et al.*, 1994d

234

Aqueous chemistry solver (SMVGEAR)	Jacobson *et al.*, 1994a; this work
Aerosol sedimentation model	Toon *et al.*, 1989a; Turco *et al.*, 1979a,b; this work
Aerosol dry deposition model	McRae *et al.*, 1982; Russell *et al.*, 1993; this work

<u>Meteorological Processes</u>

Meteorological model (MMTD)	Lu and Turco, 1994a,b
Boundary layer model (MMTD)	Lu and Turco, 1994a,b
Soil model (MMTD)	Lu and Turco, 1994a,b
Convective transport (MMTD)	Lu and Turco, 1994a,b
Horizontal transport	Toon *et al.*, 1988 this work
Horizontal boundary conditions	this work Toon *et al.*, 1988
Vertical transport	Toon *et al.*, 1988; Turco *et al.*, 1979a,b

<u>Radiative Processes</u>

Photodissociation model	Jacobson *et al.*, 1994e; this work; Turco, R. P. (pers. comm.).
Mie scattering code	Toon and Ackerman, 1981; Dave, 1968; this work
Visible optical depth	Jacobson *et al.*, 1994e; Toon *et al.*, 1989b
Infrared optical depth	Toon *et al.*, 1989b; this work
Two-stream radiative transfer	Toon *et al.*, 1988

<u>Coordinate systems, setup, output routines</u>

Horizontal / vertical coordinate systems	Toon *et al.*, 1988 this work
Setup routines	Jacobson *et al.*, 1994a-e; this work Toon *et al.*, 1988 Turco et al., 1979a,b
Output routines	Jacobson *et al.*, 1994a-e this work Toon *et al.*, 1988

<u>Data</u>

Topographical data	See Section 9.1.3

235

Emissions data	See Section 9.1.2
Soil moisture data	See Section 9.1.3
Soil density data	See Section 9.1.3
Soil heat capacity data	See Section 9.1.3
Landuse data	See Section 9.1.3
Surface albedo data	See Section 9.1.3
Gas-phase chemical reaction rates	See Table A.4
Aqueous-phase chemical reaction rates	See Table A.8
Henry's constants, equilibrium coefficients	See Table A.7
Temperature-dependent binary activity coef. data	See Section 9.1.3
Water activity data	See Section 9.1.3
Index of refraction data	See Section 9.1.3
UTM to geographic conversion data	See Section 9.1.3
Initial gas mixing ratio data	See Section 9.2
Initial aerosol concentration data	See Section 9.2
SCAQS surface gas observational data	See Section 9.1.1
SCAQS surface meteorological data	See Section 9.1.1
SCAQS upper air met. observational data	See Section 9.1.1
SCAQS surface aerosol, visibility data	See Table 9.1

Table A.2. Description of subroutines in GATOR and the coupled MMTD model. The last column indicates the author(s) of the actual computer subroutines or data file. Table A.1 defines the author(s) of and / or contributor(s) to work on the processes simulated. In some cases the individual who coded the algorithm relied on work of the author(s) listed in Table A.1. References are (A) Jacobson, M. Z., (B) Turco, R. P., (C) Lu, R., (D) Toon O. B., (E) Hamill, P., (F) Ackerman, T., (G) McRae *et al.*, 1982; Russell *et al.*, 1993, (H) Ackerman, A., (I) Westphal, D., (J) Zhao, J.-X., (K) Ames *et al.* (1986); (L) McKie, B., and (M) SCAQMD.

Table A.2

GATOR MODEL FORTRAN FILE	DESCRIPTION OF FILE	AUTHOR(S) / CONTRIB-UTOR(S)
add.f	solves two-stream tridiagonal matrix	D, A
aerset.f	reads aerosol species, characteristics	A
aqset.f	reads aqueous chemical reactions	A
backsub.f	solves SMVGEAR matrix backsubstitution	A
calcrate.f	calculates gas and aqueous chemical reaction rates	A
chemset.f (%)	reads gas chemical reactions	A, B

236

coagt.f	solves coagulation equations	A
decomp.f	solves SMVGEAR matrix decomposition	A
densig.f (!)	calculates sulfuric acid solution densities, surface tensions	E
dmiess.f (!)	calculates Mie scattering and absorption efficiencies	D, F, A
drydep.f (*)	calculates sedimentation, dry deposition velocities	A, G, D, B,I
equilset.f	reads equilibrium reactions and activity data	A
horsol.f (!)	solves horizontal transport tridiagonal matrix	D, A, C
hortran.f (!)	sets up horizontal transport tridiagonal matrix	D, A
initaer.f (*)	initializes aerosol concentrations	A
initatm.f (*)	initializes atmospheric variables, checks consistency of GATOR / MMTD model	A, C, D
initgas.f (*)	initializes gas concentrations	A
jsparse.f	initializes some arrays for chemistry solutions	A
ksparse.f	initializes sparse-matrix arrays for all processes	A
main.f (*)	main program -- organizes calling sequence	A
map.f (!)	displays numerical maps of output	I, A
mhbudget.f (*)	sums up mass entering and leaving grid for six possible horizontal boundary conditions	A, I
movebins.f	for stationary bins, moves particles to larger size	A
newflux1.f	calculates more accurate solution to infrared radiative transfer	D
nucleate.f	calculates nucleation rate of new particles	A, J
oppr.f (!)	finds optical depths of gases and aerosols	D, A
out.f (*)	sums gas and aerosol mass changes for individual and all processes, writes meteorological, gas, aerosol, and visibility output to 2-d maps	A, I
outdata.f	performs error checks, writes output to data files	A
pderiv.f	Sets partial derivatives for SMVGEAR	A
pdgrow.f	Sets partial derivatives for condensational growth	A
photdata.f (%)	reads cross section and quantum yield data	A, B
physproc.f	calls all gas and aerosol processes, reorders grid-cells for chemistry	A
plumris.f	calculates stack emission plume rise height	K, A
radout.f (*)	prints radiative transfer output	A
radtran.f (!)	calls radiative transfer routines	D, A
rainout.f (!)	sets simple rainout rate	D, A
readaqmd.f	reads emissions, observational, and other data	A
reader.f (*)	reads control switches, opens input and output files, checks parameter values	A, D
readmet.f	couples meteorological model output to GATOR	A, C
resetmet.f	resets atmospheric variables	A
setupaer.f (*)	sets up aerosol size distributions, coagulation fractions, some aerosol mapping arrays, and SMVGEAR growth arrays	A, B, D
setupgeo.f (!)	initializes horizontal coordinate systems, zenith angle calculations, mass balance arrays, clock	D, A
setuprad.f (!)	initializes radiative transfer calculations and data, optical depth above model top	D, A
smooth.f (!)	hole-filling algorithm for horizontal transport	L, A
smvgear.f	drives SMVGEAR	A

237

solvchem.f	solves chemistry using Multistep Implicit - Explicit (MIE) method	A
solveq.f	solves equilibrium equations, calculates vapor pressures for dissolving gases	A
solvgrow.f	sets up growth equations and calls SMVGEAR to solve them	A
subfgrow.f	calculates first derivative of growth equations	A
subfun.f	calculates first derivative of gas and aqueous chemical equations	A
tmshor.f (!)	initializes horizontal transport algorithms	D, A, C
transport.f	calls horizontal and vertical transport algorithms, sums vertical transport mass balances	D, A, B, C
twostr.f (!)	sets up radiative transfer calculations for add.f	D, A
vapor.f (!)	calculates vapor pressures for water vapor, sulfuric acid, and all other condensing gases	E, B, A, D
versol.f (!)	solves vertical transport tridiagonal matrix	D, B, A
vertran.f (!)	sets up vertical transport tridiagonal matrix	D, B, A, C
update.f	updates photorates and emissions rates during SMVGEAR calculations	A

DYNAMICS MODEL FORTRAN FILES	DESCRIPTION OF FILE	AUTHOR(S) / CONTRIB-UTOR(S)
dynmdl.f	main program -- organizes calling sequence	C
advect.f	calculates horizontal advection	C
advects.f	calculates horizontal advection for scalars	C
covdry.f	calculates dry convective adjustment when layers are absolutely unstable	C
diff.f	calculates diffusion terms	C
fcst.f	forecasts one time step	C
hydro.f	solves hydrostatic equation	C
initl.f	initializes parameters	C
lbdrs.f	lateral boundary relaxation scheme	C
cloudc.f	calculates turbulent cloud-scale condensation	C
pbl2o.f	second order planetary boundary layer routine	C
piuv.f	calculates pressure and vertical velocity	C
prhts.f	calculates right side of prognostic equation	C
printi.f	writes variable for re-reading later	C
printmet.f	averages and writes meteorological data	C
radflx.f	calculates radiation fluxes	C
smothk.f	smooth the field	C
soiltwml.f	calculates soil temperature and water content	C
tfconv.f	vertical diffusion by turbulent free convection	C

GATOR DATA FILE NAME	DESCRIPTION OF FILE	AUTHOR(S) / CONTRIB-UTOR(S)
aerosol.dat	aerosol species and characteristics data	A

238

aqueous.dat	aqueous chemical reaction and rate data	A
define.dat	defines variables, describes subroutines	A
emis.dat	surface emissions data	A
equil.dat	equilibrium reaction and constant data	A
geargas.dat	holds accurate solution to compare chemistry results to	A
m.dat (*)	file for data switches that control model	A, D
miess.dat	holds scattering and absorption efficiencies calculated previously	A
mixratio.dat	initial background gas distribution data	A
radtd.dat	temperature-dependent data for absorption cross-sections	A
readata.dat	default atmospheric variable data	A
refrac.dat	refractive index data	A
rerad.dat	absorption cross section, quantum yield, wavelength, and solar flux data	A, B
restart.dat	holding file for necessary GATOR variables so code can be stopped and restarted	A
roughuse.dat	interpolated UTM to geographic albedo, soil density, soil wetness, soil heat capacity, surface roughness, surface resistance, and other data	A, G, M
sflist.dat	ambient data to compare model results to	A
smog.dat	gas species, chemical reaction, and photoprocess reaction data	A
stack.dat	emissions data for stacks	A
station.dat	identifies stations and parameters used in sflist.dat	A

DYNAMICS MODEL DATA FILE NAME	DESCRIPTION OF FILE	AUTHOR(S) / CONTRIB-UTOR(S)
initl.dat	initial three-dimensional distribution of meteorological variables	C
reinit.dat	holds necessary meteorological variables when stopping and restarting model	C

Footnotes for Table A.2

(*) indicates the subroutine name is the same as that of a routine from the NASA Ames Tracer Transport code; however, 50 - 100% of the contents of the subroutine were added or changed for this work.

(%) indicates the subroutine name is the same as that of a routine developed by R. P. Turco (*pers. comm.*), but 50 - 80% of the contents of the subroutine were added or changed for this work.

(!) indicates the subroutine name is the same as that of a routine from the NASA model but 10 - 50% of the routine was added or changed in this work.

239

Table A.3. List of gas-phase species used in chemical kinetic (Table A.4) and equilibrium (Table A.7) reactions.

Table A.3

Chemical Formula	Chemical Name	Chemical Formula	Chemical Name
NO	nitric oxide	TOL	toluene
NO_2	nitrogen dioxide	BO_2	benzylperoxy radical
NO_3	nitrate radical	CRES	cresol and higher phenols
N_2O_5	dinitrogen pentoxide	TO_2	toluene-hydroxyl radical adduct
HONO	nitrous acid	BZA	benzaldehyde
HNO_3	nitric acid	BZO_2	peroxybenzoyl radical
HO_2NO_2	peroxynitric acid	PBZN	peroxybenzoyl nitrate
O(1D)	atomic oxygen (singlet)	PHO_2	phenylperoxy radical
O	atomic oxygen (triplet)	PHO	phenoxy radical
OH	hydroxyl radical	NPHN	nitrophenol
H_2O	water vapor	CRO_2	methylphenylperoxy radical
O_3	ozone	CRO	methylphenoxy radical
HO_2	hydroperoxy radical	NCRE	nitrocresol
H_2O_2	hydrogen peroxide	OPEN	high molecular weight aromatic oxidation ringring fragments
CO	carbon monoxide	ACID	aromatic ring fragment acid
CH_2O	formaldehyde	XYL	xylene
$CH_3C(O)OO$	peroxyacyl radical	XLO_2	methylbenzylperoxy radical
$CH_3C(O)OONO_2$	peroxyacyl nitrate	XINT	xylene-hydroxyl radical adduct
$CH_3C(O)OOH$	peroxyacetic acid	CH_3COCHO	methyl gloxyal
CH_3OOH	methyl hydroperoxide	MGPX	peroxide radical of methylgloxal
CH_3CHO	acetaldehyde and higher aldehydes	OPPX	peroxide radical of OPEN
CH_3O_2	methylperoxy radical	ISOP	isoprene
$HOCH_2OO$	hydroxymethylperoxy radical	ISOH	alkyl radicals from OH addition to isoprene
ROOH	organic peroxide	MACR	methacrolein
HCOOH	formix acid	MVK	methyl vinyl ketone
$CH_3O_2NO_2$	methylperoxy nitric acid	MV1	MVK OH-adduct
CH_3O	methoxy radical	MV2	MVK OH-adduct
CH_3ONO	methyl nitrite	MAC1	MACR OH-adduct
CH_3ONO_2	methyl nitrate	MAC2	MACR OH-adduct
CH_3OH	methanol	MPAN	methyl peroxyacyl nitrate
CH_3COCH_3	acetone	$CH_2CCH_3C(O)OO$	methyl peroxyacyl radical
$CH_3COCH_2O_2$	acetylmethylperoxy radical	ISNT	isoprene NO_3-adduct

240

PAR	paraffin carbon bond	ISNI1	organic nitrates resulting from OH addition to unsubstituted double bond
RO$_2$	promary organic peroxy radical	ISNI2	organic nitrates resulting from OH additon to substituted double bond and from OH reactions of primary products
RO$_2$R	secondary organic peroxy radical	ISNIR	alkyl peroxy radical from OH addition across the double bond of ISNI1 and ISNI2
NTR	organic nitrate	DISN	dinitrate of isoprene
ROR	secondary organic oxy radical	IPRX	organix peroxide from isoprene
KET	ketone carbonyl group	IALD1	group of hydroxy carbonyl alkenes from isoprene-OH reaction
AO$_2$	dimethyl 2nd organic peroxide radical	OOCHCCH$_3$CH$_2$	MVK + O$_3$ product
OLE	olefinic carbon bond	CH$_2$=CHCCH$_3$OO	MACR + O$_3$ product
H$_2$COO	criegee biradical	XOP	paraffin loss operator
CH$_3$HCOO	methyl criegee biradical	DOP	paraffin to peroxy radical operator
HOTA	excited formic acid	SO$_2$	sulfur dioxide
HTMA	excited acetic acid	SO$_3$	sulfur trioxide
PNO$_2$	nitrated organic peroxy radical	HSO$_3$	bisulfite
DNIT	C$_2$ dinitrate group	H$_2$SO$_4$	sulfuric acid
C$_2$H$_4$	ethene	NH$_3$	ammonia
CH$_3$CH$_2$OH	ethanol	HCl	hydrochloric acid
ETO$_2$	ethanol peroxide radical	CO$_2$	carbon dioxide
OZD	ozonide and further products	CH$_4$	methane
CH$_3$COOH	acetic acid	O$_2$	molecular oxygen

Table A.4. List of gas-phase chemical kinetic reactions, and reaction rates, and photoprocesses used for the air pollution studies. The authors referred to in the table are (A) Atkinson *et al.*, 1992; (B) Gery *et al.*, 1989, (C) DeMore *et al.*, 1990; (D) Paulson and Seinfeld, 1992; (E) Mozurkewich and Calvert, 1988 (F) Atkinson *et al.*, 1989; (G), Carter, 1990; (H) Toon *et al.*, 1987; (I) Stockwell, 1986; (J) Gery *et al.*, 1988; (K) Madronich and Chatfield, *pers. comm*; (L) assumed same as for acetone, (M) assumed same as for methyl ethyl ketone (which originated from K), and all references therein.

For photodissociating species, the two references are for absorption cross section and quantum yield, respectively. The species within the reaction arrows are not included in the rate, except as described in the footnotes for pressure-dependent reactions.

Table A.4

	Reaction	Rate $(s^{-1}, cm^3 s^{-1} \text{ or } cm^6 s^{-1})$	refs.
1.	$O + O_2 + M \rightarrow O_3 + M$	$5.63 \times 10^{-34} (300/T)^{2.8}$	A
2.	$NO + O_3 \rightarrow NO_2 + O_2$	$1.80 \times 10^{-12} e^{-1370/T}$	A
3.	$O + NO_2 \rightarrow NO + O_2$	$6.50 \times 10^{-12} e^{120/T}$	A
4.	$O + NO_2 - [N_2] \rightarrow NO_3$	$^P 9.00 \times 10^{-32} (300/T)^{2.0}$ 2.20×10^{-11} $F_c = 0.80$	A
5.	$O + NO - [N_2] \rightarrow NO_2$	$^P 1.00 \times 10^{-31} (300/T)^{1.6}$ $3.00 \times 10^{-11} (300/T)^{-0.3}$ $F_c = 0.85$	A
8.	$O_3 + NO_2 \rightarrow NO_3 + O_2$	$1.20 \times 10^{-13} e^{-2450/T}$	A
9.	$O(1D) + O_2 \rightarrow O + O_2$	$3.20 \times 10^{-11} e^{67/T}$	C
10.	$O(1D) + N_2 \rightarrow O + N_2$	$1.80 \times 10^{-11} e^{107/T}$	C
11.	$O(1D) + H_2O \rightarrow 2 H_2O$	2.20×10^{-10}	A
12.	$O_3 + OH \rightarrow HO_2 + O_2$	$1.90 \times 10^{-12} e^{-1000/T}$	A
13.	$O_3 + HO_2 \rightarrow OH + 2 O_2$	$1.40 \times 10^{-14} e^{-600/T}$	A
14.	$NO_3 + OH \rightarrow NO_2 + HO_2$	2.30×10^{-11}	A
15.	$NO_3 + O \rightarrow NO_2 + O_2$	1.70×10^{-11}	A
16.	$NO_3 + NO \rightarrow 2 NO_2$	$1.80 \times 10^{-11} e^{110/T}$	A
17.	$NO_3 + NO_2 \rightarrow NO + NO_2 + O_2$	$8.20 \times 10^{-14} e^{-1480/T}$	C
18.	$NO_3 + NO_2 - [N_2] \rightarrow N_2O_5$	$^P 2.70 \times 10^{-30} (300/T)^{3.4}$ $2.00 \times 10^{-12} (300/T)^{-0.2}$ $F_c = 0.33$	A
19	$N_2O_5 - [N_2] \rightarrow NO_3 + NO_2$	$^P 2.20 \times 10^{-3} (300/T)^{4.4} e^{-11080/T}$ $9.70 \times 10^{14} (300/T)^{-0.1} e^{-11080/T}$ $F_c = 0.33$	A
20.	$N_2O_5 + H_2O \rightarrow 2 HNO_3$	2.00×10^{-21}	A
21.	$N_2O_5 + H_2O(l) \rightarrow 2 HNO_3$	$^a 5.00 \times 10^{-1}$	E
22.	$NO_3 + HO_2 \rightarrow HNO_3 + O_2$	4.30×10^{-12}	A
23.	$NO + NO + O_2 \rightarrow 2 NO_2$	$3.30 \times 10^{-39} e^{530/T}$	A
24.	$OH + NO - [N_2] \rightarrow HONO$	$^P 7.40 \times 10^{-31} (300/T)^{2.4}$ 3.20×10^{-11} $F_c = 0.80$	A
25.	$OH + HONO \rightarrow NO_2 + H_2O$	$1.80 \times 10^{-11} e^{-390/T}$	A

242

26.	$OH + NO_2$ -[N_2]-> HNO_3	P 2.60×10^{-30} $(300/T)^{2.9}$ 6.00×10^{-11} $F_c = 0.43$	A
27.	$OH + HNO_3$ --> $NO_3 + H_2O$	b 7.20×10^{-15} $e^{785/T}$ 4.1×10^{-16} $e^{1440/T}$ 1.90×10^{-33} $e^{725/T}$	C
28.	$OH + HO_2$ --> $H_2O + O_2$	4.80×10^{-11} $e^{250/T}$	A
29.	$HO_2 + NO$ --> $OH + NO_2$	3.70×10^{-12} $e^{240/T}$	A
30.	$HO_2 + NO_2$ -[N_2]-> HO_2NO_2	P 1.80×10^{-31} $(300/T)^{3.2}$ 4.70×10^{-12} $F_c = 0.60$	A
31.	HO_2NO_2 -[N_2]-> $HO_2 + NO_2$	P 5.00×10^{-6} $e^{-10000/T}$ 2.6×10^{15} $e^{-10900/T}$ $F_c = 0.60$	A
32.	$OH + HO_2NO_2$ --> $NO_2 + H_2O + O_2$	1.50×10^{-12} $e^{360/T}$	A
33.	$HO_2 + HO_2$ --> $H_2O_2 + O_2$	2.20×10^{-13} $e^{600/T}$	A
34.	$HO_2 + HO_2 + M$ --> $H_2O_2 + O_2 + M$	1.70×10^{-33} $e^{1000/T}$	C
35.	$HO_2 + HO_2 + H_2O$ --> $H_2O_2 + O_2$	$2.03 \times 10{-34}$ $e2820/T$	I
36.	$OH + H_2O_2$ --> $HO_2 + H_2O$	2.90×10^{-12} $e^{-160/T}$	A
37.	$OH + CO$ --> $HO_2 + CO_2$	c1.50×10^{-13}	A
38.	$CH_2O + OH$ --> $HO_2 + CO + H_2O$	8.80×10^{-12} $e^{25/T}$	A
39.	$CH_2O + O$ -O_2-> $OH + HO_2 + CO$	3.40×10^{-11} $e^{-1550/T}$	C
40.	$CH_2O + NO_3$ -O_2-> $HNO_3 + HO_2 + CO$	5.80×10^{-16}	A
41.	$CH_2O + HO_2$ --> $HOCH_2OO$	9.70×10^{-15}	A
42.	$HOCH_2OO$ --> $HO_2 + CH_2O$	2.40×10^{12} $e^{-7000/T}$	A
43.	$HOCH_2OO + HO_2$ --> $ROOH$	5.60×10^{-15} $e^{2300/T}$	A
44.	$HOCH_2OO + NO$ -O_2-> $NO_2 + HO_2 + HCOOH$	7.00×10^{-12}	B
45.	$CH_3CHO + O$ -O_2-> $CH_3C(O)OO + OH$	1.80×10^{-11} $e^{-1100/T}$	C
46.	$CH_3CHO + OH$ -O_2-> $CH_3C(O)OO + H_2O$	5.60×10^{-12} $e^{310/T}$	A
47.	$CH_3CHO + NO_3$ -O_2-> $CH_3C(O)OO + HNO_3$	1.40×10^{-12} $e^{-1860/T}$	A
48.	$CH_3C(O)OO + NO$ -O_2-> $NO_2 + CH_3O_2 + CO_2$	2.00×10^{-11}	A
49.	$CH_3C(O)OO + NO_2$ -[N_2]-> $CH_3C(O)OONO_2$	P 2.70×10^{-28} $(300/T)^{7.1}$ 1.20×10^{-11} $(300/T)^{-0.9}$ $F_c = 0.30$	A
50.	$CH_3C(O)OONO_2$ -[N_2]-> $CH_3C(O)OO + NO_2$	P 4.90×10^{-3} $e^{-12100/T}$ 4.00×10^{16} $e^{-13600/T}$ $F_c = 0.30$	A
51.	$CH_3O_2 + NO_2$ -[N_2]-> $CH_3O_2NO_2$	P 2.50×10^{-30} $(300/T)^{5.5}$ 7.50×10^{-12} $F_c = 0.40$	A
52.	$CH_3O_2NO_2$ -[N_2]-> $CH_3O_2 + NO_2$	P 9.00×10^{-5} $e^{-9690/T}$ 1.10×10^{16} $e^{-10560/T}$ $F_c = 0.40$	A
53.	$CH_3O_2 + NO$ --> $CH_3O + NO_2$	4.20×10^{-12} $e^{180/T}$	A

243

54.	$CH_3O + NO$ -[N_2]-> CH_3ONO	P 1.60×10^{-29} $(300/T)^{3.5}$ 3.60×10^{-11} $(300/T)^{0.6}$ $F_c = 0.60$	A
55.	$CH_3O + NO$ -O_2-> $CH_2O + HO_2 + NO$	4.00×10^{-12} $(300/T)^{0.7}$	A
56.	$CH_3O + NO_2$ -[N_2]-> CH_3ONO_2	P 2.80×10^{-29} $(300/T)^{4.5}$ 2.00×10^{-11} $F_c = 0.44$	A
57.	$CH_3O + O_2$ --> $CH_2O + HO_2$	7.20×10^{-14} $e^{-1080/T}$	A
58.	$CH_3ONO_2 + OH$ --> $CH_2O + NO_2 + H_2O$	1.00×10^{-14} $e^{1060/T}$	A
59.	$CH_3ONO + OH$ --> $CH_2O + NO + H_2O$	2.00×10^{-13}	B
60.	$CH_3O_2 + CH_3O_2$ --> $2\ CH_3O + O_2$	6.30×10^{-14} $e^{220/T}$	F
61.	$CH_3O_2 + CH_3O_2$ --> $CH_2O + CH_3OH$	1.07×10^{-13} $e^{220/T}$	F
62.	$CH_3O_2 + CH_3C(O)OO$ --> $CH_3O_2 + CH_3O + CO_2$	3.00×10^{-12}	B
63.	$CH_3C(O)OO + CH_3C(O)OO$ --> $2\ CH_3O_2 + O_2$	2.80×10^{-12} $e^{530/T}$	A
64.	$CH_3O_2 + HO_2$ --> $CH_3OOH + O_2$	3.80×10^{-13} $e^{780/T}$	A
65.	$CH_3O_2 + HO_2$ --> $CH_3O + OH + O_2$	5.80×10^{-14} $e^{1300/T}$	B
66.	$CH_3OOH + OH$ --> $CH_3O_2 + H_2O$	1.90×10^{-12} $e^{190/T}$	A
67.	$CH_3C(O)OO + HO_2$ --> $CH_3O_2 + OH + CO_2$	3.00×10^{-13} $e^{1040/T}$	A
68.	$CH_3COCH_3 + OH$ -O_2-> $CH_3COCH_2O_2$	1.70×10^{-12} $e^{-600/T}$	A
69.	$CH_3COCH_2O_2 + NO$ -O_2-> $CH_3C(O)OO + CH_2O + NO_2$	8.10×10^{-12}	B
70.	$CH_4 + OH$ --> $CH_3O_2 + H_2O$	3.90×10^{-12} $e^{-1885/T}$	A
71.	$CH_3OH + OH$ --> $CH_2O + HO_2 + H_2O$	2.80×10^{-12} $e^{-380/T}$	A
72.	$CH_3OH + OH$ --> $CH_3O + H_2O$	5.00×10^{-13} $e^{-380/T}$	A
73.	$CH_3CH_2OH + OH$ --> $CH_3CHO + HO_2 + H_2O$	3.69×10^{-12} $e^{-70/T}$	A
74.	$PAR + OH$ -O_2-> $RO_2 + H_2O$	9.20×10^{-14}	B
75.	$PAR + OH$ --> $RO_2R + H_2O$	7.20×10^{-13}	B
76.	$RO_2 + NO$ -O_2-> $NO_2 + HO_2 + CH_3CHO + XOP$	7.70×10^{-12}	B
77.	$RO_2 + NO$ --> NTR	4.40×10^{-11} $e^{-1400/T}$	B
78.	$RO_2R + NO$ --> $NO_2 + ROR$	7.00×10^{-12}	B
79.	$RO_2R + NO$ --> NTR	1.20×10^{-10} $e^{-1400/T}$	B
80.	$ROR + NO_2$ --> NTR	1.50×10^{-11}	B
81.	ROR -O_2-> $KET + HO_2$	1.60×10^3	B
82.	ROR --> $KET + DOP$	2.10×10^{14} $e^{-8000/T}$	B
83.	ROR --> $CH_3CHO + DOP + XOP$	4.00×10^{14} $e^{-8000/T}$	B
84.	ROR --> $CH_3COCH_3 + DOP + 2\ XOP$	4.40×10^{14} $e^{-8000/T}$	B
85.	$XOP + PAR$ -->	6.80×10^{-12}	B
86.	$DOP + PAR$ -O_2-> RO_2	5.10×10^{-12}	B
87.	$DOP + PAR$ -O_2-> $AO_2 + 2\ XOP$	1.50×10^{-12}	B
88.	$DOP + PAR$ -O_2-> RO_2R	1.70×10^{-13}	B
89.	$DOP + KET$ -O_2-> $CH_3C(O)OO + XOP$	6.80×10^{-12}	B
90.	$AO_2 + NO$ -O_2-> $NO_2 + CH_3COCH_3 + HO_2$	8.10×10^{-12}	B
91.	$OLE + O$ --> $2\ PAR$	4.10×10^{-12} $e^{-324/T}$	B
92.	$OLE + O$ --> CH_3CHO	4.10×10^{-12} $e^{-324/T}$	B
93.	$OLE + O$ -$2O_2$-> $HO_2 + CO + RO_2$	1.20×10^{-12} $e^{-324/T}$	B
94.	$OLE + O$ -$2O_2$-> $RO_2 + XOP + CO + CH_2O + OH$	2.40×10^{-12} $e^{-324/T}$	B
95.	$OLE + OH$ -O_2-> $CH_3O_2 + CH_3CHO + XOP$	5.20×10^{-12} $e^{504/T}$	B

244

96.	$OLE + O_3 \rightarrow CH_3CHO + H_2COO + XOP$	$2.80 \times 10^{-15} e^{-2105/T}$	B
97.	$OLE + O_3 \rightarrow CH_2O + CH_3HCOO + XOP$	$2.80 \times 10^{-15} e^{-2105/T}$	B
98.	$OLE + O_3 \rightarrow CH_3CHO + HOTA + XOP$	$4.30 \times 10^{-15} e^{-2105/T}$	B
99.	$OLE + O_3 \rightarrow CH_2O + HTMA + XOP$	$4.30 \times 10^{-15} e^{-2105/T}$	B
100.	$OLE + NO_3 \xrightarrow{-O_2} PNO_2$	7.70×10^{-15}	B
101.	$PNO_2 + NO \rightarrow DNIT$	6.80×10^{-13}	B
102.	$PNO_2 + NO \rightarrow CH_2O + CH_3CHO + XOP + 2NO_2$	6.80×10^{-12}	B
103.	$C_2H_4 + O \xrightarrow{-2O_2} CH_3O_2 + HO_2 + CO$	$7.30 \times 10^{-12} e^{-792/T}$	B
104.	$C_2H_4 + O \xrightarrow{-O_2} CH_2O + HO_2 + CO + OH$	$3.10 \times 10^{-12} e^{-792/T}$	B
105.	$C_2H_4 + OH + \xrightarrow{-[N_2],O_2} ETO_2$	$P\ 7.00 \times 10^{-29} (300/T)^{3.1}$ 9.00×10^{-12} $F_c = 0.70$	A
106.	$ETO_2 + NO \xrightarrow{-O_2} NO_2 + 2 CH_2O + HO_2$	6.30×10^{-12}	B
107.	$ETO_2 + NO \xrightarrow{-O_2} NO_2 + CH_3CHO + HO_2$	1.80×10^{-12}	B
108.	$C_2H_4 + O_3 \rightarrow CH_2O + H_2COO$	$5.00 \times 10^{-15} e^{-2633/T}$	B
109.	$C_2H_4 + O_3 \rightarrow CH_2O + HOTA$	$7.50 \times 10^{-15} e^{-2633/T}$	B
110.	$HOTA \rightarrow CO_2 + H_2$	2.00×10^{-1}	B
111.	$HOTA \rightarrow CO + H_2O$	7.00×10^{-1}	B
112.	$HOTA \xrightarrow{-O_2} 2 HO_2 + CO_2$	1.00×10^{-1}	B
113.	$HTMA \rightarrow CH_4 + CO_2$	2.00×10^{-1}	B
114.	$HTMA \xrightarrow{-O_2} CH_3O_2 + CO + OH$	3.20×10^{-1}	B
115.	$HTMA \xrightarrow{-2O_2} CH_3O_2 + CO_2 + HO_2$	3.20×10^{-1}	B
116.	$HTMA \xrightarrow{-O_2} CH_2O + CO + 2 HO_2$	8.00×10^{-2}	B
117.	$HTMA \xrightarrow{-2O_2} CH_3O_2 + CO_2 + HO_2$	8.00×10^{-2}	B
118.	$H_2COO + NO \rightarrow NO_2 + CH_2O$	7.00×10^{-12}	B
119.	$H_2COO + H_2O \rightarrow HCOOH + H_2O$	4.00×10^{-16}	B
120.	$H_2COO + CH_2O \rightarrow OZD$	2.00×10^{-12}	B
121.	$H_2COO + CH_3CHO \rightarrow OZD$	2.00×10^{-12}	B
122.	$CH_3HCOO + NO \rightarrow NO_2 + CH_3CHO$	7.00×10^{-12}	B
123.	$CH_3HCOO + H_2O \rightarrow CH_3COOH + H_2O$	4.00×10^{-16}	B
124.	$CH_3HCOO + CH_2O \rightarrow OZD$	2.00×10^{-12}	B
125.	$CH_3HCOO + CH_3CHO \rightarrow OZD$	2.00×10^{-12}	B
126.	$OH + TOL \xrightarrow{-O_2} BO_2 + H_2O$	$1.70 \times 10^{-13} e^{322/T}$	B
127.	$OH + TOL \xrightarrow{-O_2} CRES + HO_2$	$7.60 \times 10^{-13} e^{322/T}$	B
128.	$OH + TOL \rightarrow TO_2$	$1.20 \times 10^{-12} e^{322/T}$	B
129.	$BO_2 + NO \xrightarrow{-O_2} NO_2 + BZA + HO_2$	8.10×10^{-12}	B
130.	$OH + BZA \xrightarrow{-O_2} BZO_2 + H_2O$	1.30×10^{-11}	B
131.	$BZO_2 + NO \xrightarrow{-O_2} NO_2 + PHO_2 + CO_2$	2.50×10^{-12}	B
132.	$BZO_2 + NO_2 - PBZN$	8.40×10^{-12}	G
133.	$PBZN \rightarrow BZO_2 + NO_2$	$1.60 \times 10^{15} e^{-13033/T}$	G
134.	$PHO_2 + NO \rightarrow NO_2 + PHO$	8.10×10^{-12}	B
135.	$PHO + NO_2 \rightarrow NPHN$	$1.30 \times 10^{-11} e^{300/T}$	G
136.	$OH + CRES \rightarrow CRO + H_2O$	1.60×10^{-11}	B
137.	$OH + CRES \xrightarrow{-O_2} CRO_2 + H_2O$	2.50×10^{-11}	B
138.	$NO_3 + CRES \rightarrow CRO + HNO_3$	2.20×10^{-11}	B
139.	$CRO + NO_2 \rightarrow NCRE$	1.40×10^{-11}	B
140.	$CRO_2 + NO \xrightarrow{-O_2} NO_2 + OPEN + HO_2$	4.00×10^{-12}	B

245

141.	$CRO_2 + NO\ -2O_2->\ NO_2 + ACID + HO_2$	4.00×10^{-12}	B
142.	$TO_2 + NO\ -->\ NO_2 + OPEN + HO_2$	7.30×10^{-12}	B
143.	$TO_2 + NO\ -->\ NTR$	8.10×10^{-13}	B
144.	$TO_2\ -O_2->\ HO_2 + CRES$	4.20	B
145.	$OH + XYL\ -O_2->\ CRES + PAR + HO_2$	$3.32 \times 10^{-12}\ e^{116/T}$	B
146.	$OH + XYL\ -O_2->\ XLO_2 + H_2O$	$1.70 \times 10^{-12}\ e^{116/T}$	B
147.	$OH + XYL\ -O_2->\ TO_2$	$5.00 \times 10^{-12}\ e^{116/T}$	B
148.	$OH + XYL\ -->\ XINT$	$6.60 \times 10^{-12}\ e^{116/T}$	B
149.	$XLO_2 + NO\ -O_2->\ NO_2 + HO_2 + BZA + PAR$	8.10×10^{-12}	B
150.	$XINT + NO\ -2O_2->\ NO_2 + HO_2 + 2\ CH_3COCHO +$ PAR	8.10×10^{-12}	B
151.	$OH + CH_3COCHO\ -O_2->\ MGPX + H_2O$	1.70×10^{-11}	B
152.	$MGPX + NO\ -O_2->\ NO_2 + CH_3C(O)OO + CO_2$	8.10×10^{-12}	B
153.	$OH + OPEN\ -O_2->\ OPPX + CH_3C(O)OO + HO_2 +$ CO	3.00×10^{-11}	B
154.	$OPPX + NO\ -O_2->\ NO_2 + CH_2O + HO_2 + CO$	8.10×10^{-12}	B
155.	$O_3 + OPEN\ -O_2->\ CH_3CHO + MGPX + CH_2O + CO$	$1.60 \times 10^{-18}\ e^{-500/T}$	B
156.	$O_3 + OPEN\ -->\ CH_2O + CO + OH + 2\ HO_2$	$4.30 \times 10^{-18}\ e^{-500/T}$	B
157.	$O_3 + OPEN\ -->\ CH_3COCHO$	$1.10 \times 10^{-17}\ e^{-500/T}$	B
158.	$O_3 + OPEN\ -O_2->\ CH_3C(O)OO + CH_2O + HO_2 +$ CO	$3.20 \times 10^{-17}\ e^{-500/T}$	B
159.	$O_3 + OPEN\ -->$	$5.40 \times 10^{-18}\ e^{-500/T}$	B
160.	$ISOP + OH\ -O_2->\ ISOH$	$2.55 \times 10^{-11}\ e^{410/T}$	D
161.	$ISOP + O_3\ -->\ 0.67\ MACR + 0.26\ MVK + 0.3\ O +$ $0.55\ OH + 0.07\ PAR + 0.07\ OLE + 0.07\ H_2COO$ $+ 0.8\ CH_2O + 0.06\ HO_2 + 0.15\ CO_2 + 0.05\ CO$	$1.23 \times 10^{-14}\ e^{-2013/T}$	D
162.	$ISOP + O\ -->\ 0.22\ MACR + 0.63\ MVK + 0.08\ ISOH$	3.30×10^{-11}	D
163.	$ISOP + NO_3\ -->\ ISNT$	7.80×10^{-13}	D
164.	$ISOH + NO\ -->\ 0.364\ MACR + 0.477\ MVK + 0.840$ $CH_2O + 0.08\ ISNI1 + 0.08\ ISNI2 + 0.886\ HO_2 +$ $0.840\ NO_2$	$1.22 \times 10^{-11}\ e^{-180/T}$	D
165.	$ISNT + NO\ -->\ 1.1\ NO_2 + 0.8\ HO_2 + 0.80\ ISNI1 +$ $0.1\ MACR + 0.15\ CH_2O + 0.05\ MVK + 0.05$ DISN	$1.39 \times 10^{-11}\ e^{-180/T}$	D
166.	$ISNI1 + OH\ -->\ ISNIR$	3.35×10^{-11}	D
167.	$ISNI2 + OH\ -->\ ISNIR$	1.88×10^{-11}	D
168.	$ISNIR + NO\ -->\ 0.05\ DISN + 0.05\ HO_2 + 1.9\ NO_2 +$ $0.95\ CH_3CHO + 0.95\ CH_3COCH_3$	$1.39 \times 10^{-11}\ e^{-180/T}$	D
169.	$ISNI1 + O_3\ -->\ 0.2\ O + 0.08\ OH + 0.5\ CH_2O + 0.5$ $IALD1 + 0.5\ ISNI2 + 0.5\ NO_2$	5.00×10^{-18}	D
170.	$ISOH + ISOH\ -->\ 0.6\ MACR + 0.6\ MVK + 1.2$ $CH_2O + 1.2\ HO_2$	2.00×10^{-13}	D
171.	$ISOH + HO_2\ -->\ IPRX$	$6.15 \times 10^{-11}\ e^{-900/T}$	D
172.	$IPRX + OH\ -->\ ISOH$	2.00×10^{-11}	D
173.	$IPRX + O_3\ -->\ 0.7\ CH_2O$	8.00×10^{-18}	D
174.	$MACR + O_3\ -->\ 0.8\ CH_3COCHO + 0.7\ CH_2O + 0.2$ $O + 0.09\ H_2COO + 0.2\ CO + 0.275\ HO_2 + 0.215$ $OH + 0.16\ CO_2 + 0.15\ CH_2=CHCCH_3OO$	$5.32 \times 10^{-15}\ e^{-2520/T}$	D

175.	MVK + O$_3$ --> 0.82 CH$_3$COCHO + 0.8 CH$_2$O + 0.2 O + 0.11 H$_2$COO + 0.05 CO + 0.06 HO$_2$ + 0.08 OH + 0.04 CH$_3$CHO + 0.07 OOCHCCH$_3$CH$_2$	$4.32 \times 10^{-15} e^{-2016/T}$	D
176.	MACR + OH --> 0.42 MAC1 + 0.08 MAC2 + 0.5 CH$_2$CCH$_3$CO$_3$	$1.86 \times 10^{-11} e^{175/T}$	D
177.	MVK + OH --> 0.28 MV1 + 0.72 MV2	$4.11 \times 10^{-12} e^{453/T}$	D
178.	MAC1 + NO --> 0.95 HO$_2$ + 0.95 CO + 0.95 CH$_3$COCH$_3$ + 0.95 NO$_2$ + 0.05 ISNI2	$1.39 \times 10^{-11} e^{-180/T}$	D
179.	MAC2 + NO --> 0.95 HO$_2$ + 0.95 CH$_2$O + 0.95 CH$_3$COCHO + 0.95 NO$_2$ + 0.05 ISNI2	$1.39 \times 10^{-11} e^{-180/T}$	D
180.	MV1 + NO --> 0.95 CH$_3$COCHO + 0.95 CH$_2$O + 0.05 ISNI2 + 0.95 NO$_2$ + 0.95 HO$_2$	$1.39 \times 10^{-11} e^{-180/T}$	D
181.	MV2 + NO --> 0.95 CH$_3$CHO + 0.95 CH$_3$C(O)OO + 0.05 ISNI2 + 0.95 NO$_2$	$1.39 \times 10^{-11} e^{-180/T}$	D
182.	MV1 + HO$_2$ --> ROOH	$6.15 \times 10^{-11} e^{-900/T}$	D
183.	MV2 + HO$_2$ --> ROOH	$6.15 \times 10^{-11} e^{-900/T}$	D
184.	MAC1 + HO$_2$ --> ROOH	$6.15 \times 10^{-11} e^{-900/T}$	D
185.	MAC2 + HO$_2$ --> ROOH	$6.15 \times 10^{-11} e^{-900/T}$	D
186.	CH$_2$CCH$_3$C(O)OO + NO$_2$ --> MPAN	8.40×10^{-12}	D
187.	MPAN --> CH$_2$CCH$_3$C(O)OO + NO$_2$	$1.58 \times 10^{16} e^{-13507/T}$	D
188.	CH$_2$CCH$_3$C(O)OO + NO --> C$_2$H$_4$ + CH$_3$O$_2$ + NO$_2$ + CO$_2$	1.40×10^{-11}	D
189.	SO$_2$ + O + N$_2$ --> SO$_3$ + N$_2$	$4.00 \times 10^{-32} e^{-1000/T}$	A
190.	SO$_2$ + HO$_2$ --> SO$_3$ + OH	1.00×10^{-18}	A
191.	SO$_2$ + OH -[N$_2$]-> HSO$_3$	P $4.00 \times 10^{-31} (300/T)^{3.3}$ 2.00×10^{-12} $F_c = 0.45$	A
192.	HSO$_3$ + OH --> SO$_3$ + H$_2$O	1.00×10^{-11}	H
193.	HSO$_3$ + O$_2$ --> SO$_3$ + HO$_2$	$1.30 \times 10^{-12} e^{-330/T}$	A
194.	SO$_3$ + H$_2$O --> H$_2$SO$_4$	6.00×10^{-15}	A
195.	NO$_2$ + hv --> NO + O	radiation dependent	C,C
196.	O$_3$ + hv --> O + O$_2$	310-350; 450-750 nm	C,C
197.	O$_3$ + hv --> O(1D) + O$_2$	<310 nm	C,C
198.	NO$_3$ + hv --> NO$_2$ + O	radiation dependent	A,A
199.	NO$_3$ + hv --> NO + O$_2$	radiation dependent	A,A
200.	HONO + hv --> OH + NO	radiation dependent	A,A
201.	H$_2$O$_2$ + hv --> 2 OH	radiation dependent	A,A
202.	N$_2$O$_5$ + hv --> NO$_2$ + NO$_3$	radiation dependent	C,C
203.	HNO$_3$ + hv --> OH + NO$_2$	radiation dependent	A,A
204.	HO$_2$NO$_2$ + hv --> HO$_2$ + NO$_2$	radiation dependent	A,A
205.	HO$_2$NO$_2$ + hv --> OH + NO$_3$	radiation dependent	A,A
206.	CH$_2$O + hv -2O$_2$-> 2 HO$_2$ + CO	radiation dependent	A,A
207.	CH$_2$O + hv --> CO + H$_2$	radiation dependent	A,A
208.	CH$_3$CHO + hv -O$_2$-> CH$_3$O$_2$ + HO$_2$ + CO	radiation dependent	A,A
209.	CH$_3$ONO + hv --> CH$_3$O + NO	radiation dependent	J,J
210.	CH$_3$COCH$_3$ + hv -2O$_2$-> CH$_3$O$_2$ + CH$_3$C(O)OO	radiation dependent	A,A
211.	KET + hv -2O$_2$-> CH$_3$C(O)OO + RO$_2$ + 2XOP	radiation dependent	L,L
212.	BZA + hv --> PHO$_2$ + CO + HO$_2$	radiation dependent	G,G

247

213.	$CH_3COCHO + h\nu -2O_2 \rightarrow CH_3C(O)OO + CO + HO_2$	radiation dependent	A,A
214.	$OPEN + h\nu -2O_2 \rightarrow CH_3C(O)OO + CO + HO_2$	radiation dependent	J,J
215.	$MVK + h\nu -2O_2 \rightarrow CH_3C(O)OO + C_2H_4 + HO_2$	radiation dependent	M,M
216.	$MACR + h\nu -2O_2 \rightarrow C_2H_4 + HO_2 + CO + CH_3O_2$	radiation dependent	K,K
217.	$CH_3O_2NO_2 + h\nu \rightarrow CH_3O_2 + NO_2$	radiation dependent	A,A
218.	$CH_3ONO_2 + h\nu \rightarrow CH_3O + NO_2$	radiation dependent	A,A

Footnotes to Table A.4

(P) Indicates a pressure-dependent reaction, for which the reaction rate is

$$K_g = \frac{k_{o,T}[M]}{1+X} F_c^{\left[1+(\log_{10} X)^2\right]^{-1}},$$

where

$$X = \frac{k_{o,T}[M]}{k_{\infty,T}}.$$

Above, $k_{o,T}$ is the temperature dependent three-body, low pressure limit rate (the first rate listed after the superscript, P), $k_{\infty,T}$ is the two-body, high pressure limit rate (the second rate shown after the superscript P), [M] is the concentration (No. cm^{-3}) of the third body (either N_2 or O_2) listed in the reaction arrow, and F_c is the broadening factor (e. g. Atkinson et al., 1992, P. 1145).

(a) Indicates a surface reaction rate $K_g = (1/4) V_{th} \gamma A$, where V_{th} is the thermal velocity of the gas (cm s^{-1}), γ is the sticking probability given by the number in the reaction rate position in Table A.4, and A is the surface area (cm^2) of liquid water aerosols (cm^2 cm^{-3}) in the atmosphere. $V_{th} = 8RT/\pi M)^{0.5}$, where R is the universal gas constant (8.314 J mol^{-1} K^{-1}), T is temperature (K), and M is the molecular weight of the reacting gas (g mol^{-1}).

(b) Indicates a non-elementary rate expression $K_g = k_1 + k_3[M] / (1 + k_3[M]/k_2)$, where k_1, k_2, and k_3 are the first, second, and third rates, respectively, listed after the superscript b, and [M] is the concentration (No. cm^{-3}) of air ($N_2 + O_2$).

(c) Indicates a non-elementary rate expression $K_g = k_1 (1 + 0.6 P_{atm})$, where k_1 is the rate listed after the superscript c and P_{atm} is the ambient air pressure, in atmospheres.

248

Table A.5. List of liquid, ion, and solid species used in the GATOR aerosol model.

Table A.5

Chemical Formula	Chemical Name	Chemical Formula	Chemical Name
$H_2O(l)$	water	O_2^-	peroxy ion
$H_2SO_4(l)$	sulfuric acid	HO_2^-	hydroperoxy ion
$SO_2(l)$	sulfur dioxide	NH_4^+	ammonium ion
$O_2(l)$	molecular oxygen	NO_3^-	nitrate ion
$O_3(l)$	ozone	NO_2^-	nitrogen dioxide ion
$OH(l)$	hydroxyl radical	HSO_4^-	bisulfate
$HO_2(l)$	hydroperoxy radical	SO_4^{2-}	sulfate
$H_2O_2(l)$	hydrogen peroxide	HSO_3^-	bisulfite
$NO(l)$	nitric oxide	SO_3^{2-}	sulfite
$NO_2(l)$	nitrogen dioxide	HSO_5^-	peroxymonosulfate
$NO_3(l)$	nitrate radical	SO_5^-	peroxysulfate radical
$HONO(l)$	nitrous acid	$HOCH_2SO_3^-$	hydromethanesulfonate
$HNO_3(l)$	nitric acid	$^-OCH_2SO_3^-$	oxymethanesulfonate ion
$HO_2NO_2(l)$	peroxynitric acid	Na^+	sodium ion
$NH_3(l)$	ammonia	Cl^-	chloride ion
$Cl(l)$	chlorine atom	Cl_2^-	dichloride ion
$HCl(l)$	hydrochloric acid	$ClOH^-$	chlorine hydroxide radical
$CO_2(l)$	carbon dioxide	HCO_3^-	bicarbonate ion
$C_2H_4(l)$	ethene	CO_3^{2-}	carbonate ion
$CH_3CHO(l)$	acetaldehyde	CO_3^-	carbonate radial ion
$CH_3COCH_3(l)$	acetone	$HCOO^-$	formate
$C_6H_5CH_3(l)$	toluene	CH_3COO^-	acetate
$C_6H_4(CH_3)_2(l)$	xylene	Fe^{3+}	iron (III) ion
$CH_3O_2(l)$	methylperoxy radical	Mn^{2+}	manganese (II) ion
$CH_3OH(l)$	methanol	Al^{3+}	Aluminum (II) ion
$CH_2O(l)$	formaldehyde	Si^{2+}	Silicon (II) ion
$H_2C(OH)_2(l)$	methylene glycol	$Na_2SO_4(s)$	sodium sulfate
$HCOOH(l)$	formic acid	$NaHSO_4(s)$	sodium bisulfate
$CH_3OOH(l)$	methyl hydroperoxide	$NaCl(s)$	sodium chloride
$CH_3COOH(l)$	acetic acid	$NaNO_3(s)$	sodium nitrate
$CH_3C(O)OOH(l)$	peroxyacetic acid	$(NH_4)_2SO_4(s)$	ammonium sulfate
$CH_3C(O)OONO_2(l)$	peroxyacetyl nitrate	$NH_4HSO_4(s)$	ammonium bisulfate
$CH_3COCHO(l)$	methylglyoxal	$NH_4Cl(s)$	ammonium chloride
$CH_3COCH_3O_2(l)$	hydrated methylglyoxal	$NH_4NO_3(s)$	ammonium nitrate
$NO_2CH_3C_6H_3OH(l)$	Nitrocresol	$(NH_4)_3H(SO_4)_2(s)$	tri ammonium bisulfate
H^+	hydrogen ion	$EC(s)$	Elemental carbon
OH^-	hydroxy ion	$OC(s)$	Organic Carbon

249

Tables A.6 and A.7. List of chemical equilibrium constant units (Table A.6) and equilibrium reactions and constants used (Table A.7) in EQUISOLV, the equilibrium model in GATOR. Most equations were gathered from Jacob (1986), Pilinis and Seinfeld (1987), Pandis and Seinfeld (1989), and Jacob *et al.* (1989). However, the actual references identified in Table A.7 are from (A) Smith and Martell, 1976; (B) Lind and Kok, 1986; (C) Kozac-Channing and Heltz, 1983; (D) Schwartz and White, 1981; (E) Schwartz, 1984; (F) Jacob, 1986; (G) Park and Lee, 1987; (H) Kim *et al.*, 1993; (I) Ledbury and Blair, 1925; (J) Latimer, 1952; (K) Snider and Dawson, 1985; (L) Weast, 1986; (M) Lee, 1984; (N) Betterton and Hoffmann, 1988; (O) Calvert, 1984; (P) Le Henaff, 1968; (Q) Wasa and Musha, 1970; (R) Jayson *et al.*, 1973; (S) Marsh and McElroy, 1985; (T) Perrin, 1982; (U) Martell and Smith, 1977; (V) Sorensen and Anderson, 1970. A (*) indicates the rates were combined from other rates that are in the table or not included in the table.

The equilibrium constant reads

$$K_{eq} = A e^{[B(T_o/T - 1) + C(1 + \ln(T_o/T) - T_o/T)]},$$

where A is the equilibrium constant at 298.15 K, T_o is the reference temperature (298.15 K), T is temperature (K), $B = -\Delta H / (R\, T_o)$ -- where R is the ideal gas constant (8.314 J mol^{-1} K^{-1}) and H is enthalpy (J mol^{-1}) -- and $C = -\Delta C_p / R$ -- where C_p is the heat capacity at constant pressure. Each of the following types of equilibrium equations has an equilibrium constant with the corresponding units shown. In both Tables A.6 and A.7, g indicates a gas, l indicates a liquid (aqueous), + or - indicates an ionic species, and s indicates a solid. In Table A.6, the species A, B, AB, etc. are fictitious.

250

Table A.6

	Reaction Type	Units
$A(g)$	$\Leftrightarrow A(l)$	mole kg^{-1} atm^{-1}
$AB(l)$	$\Leftrightarrow A^+ + B^-$	mole kg^{-1}
$AB(g)$	$\Leftrightarrow A^+ + B^-$	mole^2 kg^{-2} atm^{-1}
$A_2B(s)$	$\Leftrightarrow 2A^+ + B^{2-}$	mole^3 kg^{-3}
$AB(s)$	$\Leftrightarrow A^+ + B^-$	mole^2 kg^{-2}
$AB(s)$	$\Leftrightarrow A(g) + B(g)$	atm^2
$A(g) + B(g)$	$\Leftrightarrow A^+ + B^-$	mole^2 kg^{-2} atm^{-2}
$A_3B_2(s) + C^+$	$\Leftrightarrow 3A^+ + 2CB^-$	mole^4 kg^{-4}

Table A.7

	Reaction		A	B	C	reference
1.	$SO_2(g)$	$\Leftrightarrow SO_2(l)$	1.23×10^0	10.47		A
2.	$H_2O_2(g)$	$\Leftrightarrow H_2O_2(l)$	7.45×10^4	22.21		B
3.	$O_3(g)$	$\Leftrightarrow O_3(l)$	1.13×10^{-2}	7.72		C
4.	$NO(g)$	$\Leftrightarrow NO(l)$	1.90×10^{-3}	4.97		D
5.	$NO_2(g)$	$\Leftrightarrow NO_2(l)$	1.00×10^{-2}	8.38		E
6.	$NO_3(g)$	$\Leftrightarrow NO_3(l)$	2.10×10^5	29.19		F
7.	$OH(g)$	$\Leftrightarrow OH(l)$	2.50×10^1	17.72		F
8.	$HO_2(g)$	$\Leftrightarrow HO_2(l)$	2.00×10^3	22.28		F
9.	$HONO(g)$	$\Leftrightarrow HONO(l)$	4.90×10^1	16.04		D
10.	$HO_2NO_2(g)$	$\Leftrightarrow HO_2NO_2(l)$	2.00×10^4			G
11.	$HNO_3(g)$	$\Leftrightarrow HNO_3(l)$	2.10×10^5			E
12.	$NH_3(g)$	$\Leftrightarrow NH_3(l)$	5.76×10^1	13.79	-5.39	H
13.	$CH_2O(g)$	$\Leftrightarrow CH_2O(l)$	3.46	8.19		I
14.	$HCOOH(g)$	$\Leftrightarrow HCOOH(l)$	3.50×10^3	19.26		J
15.	$CO_2(g)$	$\Leftrightarrow CO_2(l)$	3.39×10^{-2}	8.12		A
16.	$CH_3OH(g)$	$\Leftrightarrow CH_3OH(l)$	2.20×10^2	16.44		K
17.	$CH_3O_2(g)$	$\Leftrightarrow CH_3O_2(l)$	6.00	18.79		F
18.	$CH_3OOH(g)$	$\Leftrightarrow CH_3OOH(l)$	2.27×10^2	18.82		B
19.	$CH_3COOH(g)$	$\Leftrightarrow CH_3COOH(l)$	8.80×10^3	21.62		L
20.	$CH_3C(O)OOH(g)$	$\Leftrightarrow CH_3C(O)OOH(l)$	4.73×10^2	20.70		B
21.	$CH_3C(O)OONO_2(g)$	$\Leftrightarrow CH_3C(O)OONO_2(l)$	2.90	19.83		M
22.	$CH_3COCHO(g)$	$\Leftrightarrow CH_3COCHO(l)$	3.70×10^3	25.33		N
23.	$CH_3CHO(g)$	$\Leftrightarrow CH_3CHO(l)$	1.50×10^1			O
24.	$CH_3COCH_3(g)$	$\Leftrightarrow CH_3COCH_3(l)$	3.00×10^1			O
25.	$TOL(g)$	$\Leftrightarrow C_6H_5CH_3(l)$	1.51×10^{-1}			O
26.	$XYL(g)$	$\Leftrightarrow C_6H_4(CH_3)_2(l)$	1.74×10^{-1}			O
27.	$CH_2O(l) + H_2O(l)$	$\Leftrightarrow H_2C(OH)_2(l)$	1.82×10^3	13.49		P
28.	$CH_3COCHO(l) + H_2O(l)$	$\Leftrightarrow CH_3COCH_3O_2(l)$	2.70×10^3			Q

251

No.	Reaction		Rate			Ref.
29.	SO_2 (l)+ H_2O(l)	$\Leftrightarrow$ HSO_3^- + H^+	1.23×10^{-2}	6.58		A
30.	CO_2(l) + H_2O(l)	$\Leftrightarrow$ HCO_3^- + H^+	4.46×10^{-7}	-3.35		A
31.	Cl(l) + H_2O(l)	$\Leftrightarrow$ $ClOH^-$ + H^+	6.20×10^{-8}			R
32.	NH_3(l) + H_2O(l)	$\Leftrightarrow$ NH_4^+ + OH^-	1.81×10^{-5}	-1.50	26.92	H
33.	HNO_3(l)	$\Leftrightarrow$ NO_3^- + H^+	1.96×10^{1}	29.17	16.83	*
34.	HCl(l)	$\Leftrightarrow$ Cl^- + H^+	1.72×10^{6}	23.15		S
35.	NH_3(l) + HNO_3(l)	$\Leftrightarrow$ NH_4^+ + NO_3^-	2.14×10^{10}	50.19	16.83	*
36.	H_2O(l)	$\Leftrightarrow$ H^+ + OH^-	1.01×10^{-14}	-22.52	26.92	H
37.	H_2SO_4(l)	$\Leftrightarrow$ HSO_4^- + H^+	1.00×10^{3}			T
38.	H_2O_2(l)	$\Leftrightarrow$ HO_2^- + H^+	2.20×10^{-12}	-12.52		A
39.	HO_2(l)	$\Leftrightarrow$ O_2^- + H^+	3.50×10^{-5}			T
40.	$HONO$(l)	$\Leftrightarrow$ NO_2^- + H^+	5.10×10^{-4}	-4.23		D
41.	$HCOOH$(l)	$\Leftrightarrow$ $HCOO^-$ + H^+	1.78×10^{-4}	-0.067		U
42.	$HOCH_2SO_3^-$	$\Leftrightarrow$ $^-OCH_2SO_3^-$ + H^+	2.00×10^{-12}			V
43.	CH_3COOH(l)	$\Leftrightarrow$ CH_3COO^- + H^+	1.70×10^{-5}	0.169		U
44.	$ClOH^-$	$\Leftrightarrow$ Cl^- + OH(l)	1.43			R
45.	Cl_2^-	$\Leftrightarrow$ Cl(l) + Cl^-	5.26×10^{-6}			R
46.	HSO_3^- + H^+	$\Leftrightarrow$ SO_3^{2-} + 2 H^+	6.61×10^{-8}	5.03		A
47.	HSO_4^- + H^+	$\Leftrightarrow$ SO_4^{2-} + 2 H^+	1.02×10^{-2}	8.85	25.14	H
48.	HCO_3^- + H^+	$\Leftrightarrow$ CO_3^{2-} + 2 H^+	4.68×10^{-11}	-5.91		A
49.	HNO_3(g)	$\Leftrightarrow$ NO_3^- + H^+	2.51×10^{6}	29.17	16.83	H
50.	HCl(g)	$\Leftrightarrow$ Cl^- + H^+	1.97×10^{6}	30.2	19.91	H
51.	NH_3(g) + HNO_3(g)	$\Leftrightarrow$ NH_4^+ + NO_3^-	2.59×10^{17}	63.98	11.44	*
52.	NH_3(g) + HCl(g)	$\Leftrightarrow$ NH_4^+ + Cl^-	2.03×10^{17}	65.01	14.52	*
53.	$(NH_4)_3H(SO_4)_2$(s) + H^+	$\Leftrightarrow$ 3 NH_4^+ + 2 HSO_4^-	2.93×10^{3}	-14.04	29.26	*
54.	NH_4HSO_4(s)	$\Leftrightarrow$ NH_4^+ + HSO_4^-	1.38×10^{4}	-2.87	15.83	H
55.	$(NH_4)_2SO_4$(s)	$\Leftrightarrow$ 2 NH_4^+ + SO_4^{2-}	1.82	-2.65	38.57	H
57.	NH_4Cl(s)	$\Leftrightarrow$ NH_4^+ + Cl^-	2.21×10^{1}	-6.03	16.92	*
58.	NH_4NO_3(s)	$\Leftrightarrow$ NH_4^+ + NO_3^-	1.49×10^{1}	-10.4	17.56	*
59.	$NaHSO_4$(s)	$\Leftrightarrow$ Na^+ + HSO_4^-	2.41×10^{4}	0.79	14.75	H
60.	Na_2SO_4(s)	$\Leftrightarrow$ 2 Na^+ + SO_4^{2-}	4.80×10^{-1}	0.98	39.57	H
61.	$NaCl$(s)	$\Leftrightarrow$ Na^+ +Cl^-	3.77×10^{1}	-1.56	16.9	H
62.	$NaNO_3$(s)	$\Leftrightarrow$ Na^+ + NO_3^-	1.20×10^{1}	-8.22	16.01	H

Table A.8. List of aqueous-phase chemical kinetic reactions, reaction rates, and photoprocesses used in the GATOR aqueous chemistry model. Most equations were gathered from Pandis and Seinfeld (1989), Jacob (1986), and Jacob *et al.* (1989). However, the actual references identified in Table A.7 are (A) Hoffmann and Calvert, 1985; (B) Conklin and Hoffmann, 1988; (C) Martin and Hill, 1987a; (Cc) Martin and

252

Hill, 1987b; (D) Huie and Neta, 1987; (E) Lind *et al.*, 1987; (F) Lee and Schwartz, 1983; (G) Boyce and Hoffmann, 1984; (H) Jacob, 1986; (I) Sehested *et al.*, 1968; (J) Christensen *et al.*, 1982; (K) Bielski, 1978; (L) Martin, 1984; (M) Weeks and Rabani, 1966; (N) Schmidt, 1972; (O) Behar *et al.*, 1970; (P) Ross and Neta, 1979; (Q) Hagesawa and Neta, 1978; (R) Graedel and Goldberg, 1983; (S) Treinin and Hayon, 1970; (T) Damschen and Martin, 1983; (U) Bothe and Schulte-Frohlinde, 1980; (V) Scholes and Willson, 1967; (W) Anbar and Neta, 1967; (X) Chen et al., 1973; (Y) Farhataziz and Ross, 1977; (Z) Lee, 1984; (AA) Wine et al., 1989; (BB) Graedel and Weschler, 1981. For photodissociating species, the reference for the cross-sectional data is listed.

The reaction rates (s^{-1}, $M^{-1} s^{-1}$, or $M^{-2} s^{-1}$) read

$$K_{aq} = Ae^{B(T_0/T - 1)},$$

where A is the reaction rate at 298.15 K, T_0 is the reference temperature (298.15 K), T is temperature (K), and $B = -\Delta H / (R T_0)$, where R is the ideal gas constant (8.314 J mol^{-1} K^{-1}) and H is enthalpy (J mol^{-1}). (1 cal = 4.184 J)

Table A.8

	Reaction	A	B	ref.
1.	$SO_2(l) + O_3(l) -H_2O(l)-> SO_4^{2-} + O_2(l) + 2 H^+$	2.40×10^4		A
2.	$HSO_3^- + O_3(l) --> SO_4^{2-} + O_2(l) + H^+$	3.70×10^5	-18.56	A
3.	$SO_3^{2-} + O_3(l) --> SO_4^{2-} + O_2(l)$	1.50×10^9	-17.72	A
4.	$HSO_3^- + H_2O_2(l) + H^+ --> SO_4^{2-} + 2 H^+ + H_2O(l)$	7.45×10^7	-15.96	A
5.	$SO_3^{2-} + Fe^{3+} -O_2(l), H_2O(l)-> SO_4^{2-} + H_2O_2(l) + Fe^{3+}$	9.50×10^7	-20.27	B,C
6.	$HSO_3^- + Mn^{2+} -O_2(l), H_2O(l)-> SO_4^{2-} + H_2O_2(l) + Mn^{2+} + H^+$	1.00×10^3	-30.06	Cc,A
7.	$HSO_3^- + OH(l) -O_2(l)-> SO_5^- + H_2O(l)$	4.20×10^9	-5.03	E
8.	$SO_3^{2-} + OH(l) -O_2-> SO_5^- + OH^-$	4.60×10^9	-5.03	E

253

#	Reaction			
9.	$HSO_3^- + CH_3OOH(l) + H^+ \rightarrow SO_4^{2-} + 2\,H^+ + CH_3OH(l)$	1.90×10^7	-12.75	A
10.	$HSO_3^- + CH_3C(O)OOH(l) \rightarrow SO_4^{2-} + H^+ + CH_3COOH(l)$	$^{x}3.60 \times 10^7$ 7.00×10^2	-13.42	E
11.	$HSO_3^- + HO_2(l) \rightarrow SO_4^{2-} + OH(l) + H^+$	4.35×10^5		A
12.	$SO_3^{2-} + HO_2(l) \rightarrow SO_4^{2-} + OH(l)$	5.65×10^5		A
13.	$HSO_3^- + O_2^- \rightarrow SO_4^{2-} + OH(l)$	4.35×10^4		A
14.	$SO_3^{2-} + O_2^- \text{-}H_2O(l) \rightarrow SO_4^{2-} + OH(l) + OH^-$	5.65×10^4		A
15.	$2\,NO_2(l) + HSO_3^- \text{-}H_2O(l) \rightarrow SO_4^{2-} + 3\,H^+ + 2\,NO_2^-$	2.00×10^6		F
16.	$HSO_3^- + CH_2O(l) \rightarrow HOCH_2SO_3^-$	7.90×10^2	-16.44	G
17.	$SO_3^{2-} + CH_2O(l) \text{-}H_2O(l) \rightarrow HOCH_2SO_3^- + OH^-$	2.48×10^7	-6.04	G
18.	$HOCH_2SO_3^- + OH(l) \text{-}O_2(l) \rightarrow SO_5^- + CH_2O + H_2O(l)$	1.40×10^9	-5.03	H
19.	$HSO_3^- + Cl_2^- \text{-}O_2(l) \rightarrow SO_5^- + 2\,Cl^- + H^+$	3.40×10^8	-5.03	D
20.	$SO_3^{2-} + Cl_2^- \text{-}O_2(l) \rightarrow SO_5^- + 2\,Cl^-$	1.60×10^8	-5.03	D
21.	$OH(l) + HO_2(l) \rightarrow H_2O(l) + O_2(l)$	7.00×10^9	-5.03	I
22.	$OH(l) + O_2^- \rightarrow OH^- + O_2(l)$	1.00×10^{10}	-5.03	I
23.	$OH(l) + H_2O_2(l) \rightarrow H_2O(l) + HO_2(l)$	2.70×10^7	-5.70	J
24.	$2\,HO_2(l) \rightarrow H_2O_2(l) + O_2(l)$	8.60×10^5	-7.94	K
25.	$HO_2(l) + O_2^- \text{-}H_2O(l) \rightarrow H_2O_2(l) + O_2(l) + OH^-$	1.00×10^8	-5.03	K
26.	$O_2^- + O_3(l) \text{-}H_2O(l) \rightarrow OH(l) + 2\,O_2(l) + OH^-$	1.50×10^9	-5.03	I
27.	$H_2O_2(l) + O_3(l) \rightarrow H_2O(l) + 2\,O_2(l)$	$^{y}7.80 \times 10^{-3}$		L
28.	$HCO_3^- + OH(l) \rightarrow H_2O(l) + CO_3^-$	1.50×10^7	-6.41	M
29.	$HCO_3^- + O_2^- \rightarrow HO_2^- + CO_3^-$	1.50×10^6		N
30.	$CO_3^- + O_2^- \text{-}H_2O(l) \rightarrow HCO_3^- + O_2(l) + OH^-$	4.00×10^8	-5.03	O
31.	$CO_3^- + H_2O_2(l) \rightarrow HO_2(l) + HCO_3^-$	8.00×10^5	-9.46	O
32.	$O_2^- + CL_2^- \rightarrow 2\,CL^- + O_2(l)$	1.00×10^9	-5.03	P
33.	$H_2O_2(l) + CL_2^- \rightarrow 2\,CL^- + HO_2(l) + H^+$	1.40×10^5	-11.31	Q
34.	$H_2O_2 + Cl(l) \rightarrow Cl^- + HO_2(l) + H^+$	4.50×10^7		R
35.	$NO_2^- + OH(l) \rightarrow NO_2(l) + OH^-$	1.00×10^{10}	-5.03	S
36.	$NO_2^- + O_3(l) \rightarrow NO_3^- + O_2(l)$	5.00×10^5	-23.32	T
37.	$NO_3(l) + O_2^- \rightarrow NO_3^- + O_2(l)$	1.00×10^9	-5.03	H
38.	$NO_3(l) + Cl^- \rightarrow NO_3^- + Cl(l)$	1.00×10^8	-5.03	P
39.	$H_2C(OH)_2(l) + OH(l) \text{-}O_2(l) \rightarrow HCOOH(l) + HO_2(l) + H_2O(l)$	2.00×10^9	-5.03	U
40.	$HCOOH(l) + OH(l) \text{-}O_2(l) \rightarrow CO_2(l) + HO_2(l) + H_2O(l)$	1.60×10^8	-5.03	V
41.	$HCOO^- + OH(l) \text{-}O_2(l) \rightarrow CO_2(l) + HO_2(l) + OH^-$	2.50×10^9	-5.03	W
42.	$HCOO^- + CO_3^- \text{-}H_2O(l),O_2(l) \rightarrow CO_2(l) + HCO_3^- + HO_2(l) + OH^-$	1.10×10^5	-11.41	X
43.	$HCOO^- + CL_2^- \text{-}O_2(l) \rightarrow CO_2(l) + HO_2(l) + 2\,Cl^-$	1.90×10^6	-8.72	Q
44.	$CH_3COOH(l) + OH(l) \text{-}O_2(l) \rightarrow HO_2(l) + CO(l) + CH_2O(l) + H_2O(l)$	2.00×10^7	-6.25	Y
45.	$CH_3COO^- + OH(l) \text{-}O_2(l) \rightarrow CO(l) + CH_2O(l) + H_2O(l) + O_2^-$	8.00×10^7	-5.07	Y
46.	$CH_3C(O)OONO_2(l) \rightarrow NO_3^- + products$	4.00×10^{-4}		Z

254

47.	$CH_3O_2(l) + HO_2(l) \rightarrow CH_3OOH(l) + O_2(l)$	4.30×10^5	-10.07	H
48.	$CH_3O_2(l) + O_2^- -H_2O(l) \rightarrow CH_3OOH(l) + O_2(l) + OH^-$	5.00×10^7	-5.37	H
49.	$CH_3OOH(l) + OH \rightarrow CH_3O_2(l) + H_2O(l)$	2.70×10^7	-5.70	H
50.	$CH_3OH(l) + OH(l) -O_2(l) \rightarrow CH_2O(l) + HO_2(l) + H_2O(l)$	4.50×10^8	-5.03	W
51.	$CH_3OOH(l) + OH(l) -O_2(l) \rightarrow CH_2O(l) + HO_2(l) + H_2O(l)$	1.90×10^7	-6.04	H
52.	$SO_5^- + HSO_3^- -O_2(l) \rightarrow HSO_5^- + SO_5^-$	3.00×10^5	-10.40	D
53.	$SO_5^- + SO_3^{2-} -H^+, O_2(l) \rightarrow HSO_5^- + SO_5^-$	1.30×10^7	-6.71	D
54.	$SO_5^- + O_2^- -H_2O(l) \rightarrow HSO_5^- + OH^- + O_2(l)$	1.00×10^8	-5.03	H
55.	$SO_5^- + HCOO^- -O_2(l) \rightarrow HSO_5^- + CO_2(l) + O_2^-$	1.40×10^4	-13.42	H
56.	$SO_5^- + SO_5^- \rightarrow 2 SO_4^- + O_2(l)$	6.00×10^8	-5.03	D
57.	$HSO_5^- + HSO_3^- + H+ \rightarrow 2 SO_4^{2-} + 3H^+$	7.10×10^6	-10.47	D
58.	$HSO_5^- + OH(l) \rightarrow SO_5^- + H_2O(l)$	1.70×10^7	-6.38	H
59.	$SO_4^- + HSO_3^- -O_2(l) \rightarrow SO_4^{2-} + H^+ + SO_5^-$	1.30×10^9	-5.03	H
60.	$SO_4^- + HO_2(l) \rightarrow SO_4^{2-} + H^+ + O_2(l)$	5.00×10^9	-5.03	H
61.	$SO_4^- + O_2^- \rightarrow SO_4^{2-} + O_2(l)$	5.00×10^9	-5.03	H
62.	$SO_4^- + H_2O_2(l) \rightarrow SO_4^{2-} + H^+ + HO_2(l)$	1.20×10^7	-6.71	P
63.	$SO_4^- + NO_2^- \rightarrow SO_4^{2-} + NO_2(l)$	9.80×10^8	-5.03	AA
64.	$SO_4^- + HCOO^- -O_2(l) \rightarrow SO_4^{2-} + CO_2(l) + HO_2(l)$	1.10×10^8	-5.03	AA
65.	$SO_4^- + Cl^- \rightarrow SO_4^{2-} + Cl(l)$	2.60×10^8	-5.03	AA
66.	$H_2O_2(l) + h\nu \rightarrow 2 OH(l)$	radiation dependent		BB
67.	$NO_3^- + h\nu -H_2O(l) \rightarrow NO_2(l) + OH(l) + OH^-$	radiation dependent		BB

Footnotes for Table A.8

x   Non-elementary rate expression $K = K_1[H^+] + K_2,$ where $K_1 = A_1 e^{B(298.15/T-1)}$ and $K_2 = A_2$.

y   Non-elementary rate expression, $K = K[O_3]^{-0.5}$

255

Appendix B

Paper -- SMVGEAR: A Sparse-Matrix Vectorized Gear Code for Atmospheric Models

256

SMVGEAR: A SPARSE-MATRIX, VECTORIZED GEAR CODE FOR ATMOSPHERIC MODELS*

Mark Z. Jacobson and Richard P. Turco

Department of Atmospheric Sciences, 405 Hilgard Ave, University of California, Los Angeles,
CA 90024-1565, U.S.A.

Abstract—We present a Gear-type code that efficiently solves ordinary differential equations in large grid-domains. To obtain the final code, we modified an original program of C.W. Gear, built and added a sparse-matrix package, and vectorized all loops about the grid-cell dimension. Furthermore, to obtain at least 90% vectorization potential while preventing equations in some regions of the grid from slowing the solution over the entire grid-domain, we divided the domain into blocks of grid-cells and vectorized around these blocks. The sparse-matrix solution reduced the average number of LU-decomposition calculations, compared to a full-matrix solution, by factors of between 20 (for a matrix of order 40) and 120 (for a matrix of order 90). It also reduced both back-substitution calculations and total array space by factors of between 5 and 12 for the above matrix sizes. Vectorization on a CRAY-90 computer increased the speed by another factor of about 120 over the code running in scalar form. We tested the speed and accuracy of the program for several chemical applications on a single processor of the CRAY-90 computer. The code averaged between 1 and 2 min of computer time per day of simulation to solve a smog-chemistry set of 92 species and 222 reactions over a 10,000-cell grid, with continuously changing photorates. It also took 3–4 min per day to solve a stratospheric-chemistry set of 39 species and 108 reactions over a 100,000-cell grid. In addition, we tested the speed of the code while it solved aqueous chemistry in 43 aerosol size bins, along with other physical processes and transport, over a large grid. Finally, we compared the speed and other statistics from SMVGEAR to those of an existing sparse matrix Gear code, LSODES, and to a new method that we call the Multistep Implicit-Explicit (MIE) method.

Key word index: Gear code, air pollution photochemistry, stratospheric photochemistry, aqueous chemistry, ordinary differential equations.

1. INTRODUCTION

Over the years, mathematicians and scientists have developed techniques to solve systems of stiff ordinary differential equations (ODEs). In chemical terms, a stiff system occurs when the lifetimes of some species are many orders of magnitude smaller than the lifetimes of other species. Because explicit ODE solvers require numerous short time-steps in order to maintain stability, most current techniques solve ODEs implicitly or semi-implicitly.

Among the high- and variable-order techniques to solve stiff ODEs include variations of Runge–Kutta, Richardson Extrapolation/Bulirsch–Stoer, and predictor–corrector methods (Press *et al.*, 1992; Gear, 1967, 1969, 1971; Stoer and Bulirsch, 1980). In particular, Gear's backward differentiation predictor–corrector scheme spawned a number of advanced Gear-type codes (e.g. Hindmarsh, 1972, 1974, 1975, 1976, 1977, 1980, 1983; Spellman and Hindmarsh, 1975; Morris and Hindmarsh, 1975; Byrne and Hindmarsh, 1976; Sherman and Hindmarsh, 1980; Brown and Hindmarsh, 1986).

Other techniques to solve stiff ODEs include the midpoint and trapezoidal methods (e.g. Gear, 1971; Press *et al.*, 1992), family methods (e.g. Crutzen, 1971; Turco and Whitten, 1974; Brasseur and Solomon, 1984; Austin, 1991; Elliott *et al.* 1993), parameterization methods (e.g. Jacob *et al.*, 1989), hybrid predictor–corrector methods (e.g. McRae *et al.*, 1982), iterative backward differentiation methods (e.g. Curtiss and Hirschfelder, 1952; Hunt, 1966; Shimazaki and Laird, 1970; Turco and Whitten, 1974; Rosenbaum, 1976), iterative hybrid schemes (Hesstvedt *et al.*, 1978) and many others.

To date, one limitation of most schemes has been their inability to solve equations *both* quickly and with a high order of accuracy in multiple grid-cell models. With the onset of faster vector machines and parallel processors, this limitation is eroding. However, even with a fast machine, accurate solutions in 10^4–10^5 grid-cells over simulation periods of months to years still requires considerable computer time. Here, we introduce SMVGEAR (Sparse-Matrix Vectorized Gear Code), which is designed to reach peak speed performance on vectorized machines when the number of grid-cells is large. On non-vector machines, SMVGEAR also has advantages.

The first building-block of SMVGEAR is an original code of Gear (1971, pp. 158–166). Gear's code

257

solves systems of ODEs using a time-step and order dependent on the stiffness of the equations. In summary, Gear's code solves the set of ODEs (e.g. Hindmarsh, 1983).

$$dy \, dt = f(t,y) \qquad (1)$$

where y is a vector of species concentrations, and t is time. To solve the equations, Gear sets up a prediction matrix

$$P \approx I - h\beta_0 J \qquad (2)$$

where I is the identity matrix, h the time-step, β_0 a scalar multiplier that depends on the order of the method, and

$$J = \partial f / \partial y \qquad (3)$$

is a Jacobian matrix of partial derivative for the system. With the prediction matrix, the code iteratively solves the equation

$$Px = B \qquad (4)$$

where x is a vector used to correct y and its derivatives, and B is a continuously changing vector found from evaluating equation (1) with corrected values of y. When the error from the correction vector x becomes less than a provided error, the corrector has converged, and the code then checks whether the sum of errors over all iterations for a time-step is less than another error tolerance. If the system of equations passes the second error check, the time-step is complete. Otherwise, the code either re-evaluates the Jacobian, reduces the time-step and re-evaluates the Jacobian, or reduces the order and time-step and re-evaluates the Jacobian.

After a number of successful time-steps dependent on the value of the current order, the code re-estimates the time-step feasible at one order lower than, the same order as, and one order higher than the current order. It then chooses the next time-step as the largest of the three estimates and chooses the order as that order allowing the largest step.

While Gear's original code is elegant, a shortcoming is its need to decompose a matrix many times and perform numerous back-substitutions for each decomposition. Both full matrix decomposition and back-substitution require a significant number of calculations. In response to this problem, researchers at Lawrence Livermore Laboratory and elsewhere began to look for ways to reduce the number of matrix calculations.

A characteristic of most ODE systems is that their initial matrices contain many zero values. To exploit the sparse structure of these matrices, Hindmarsh (1975) introduced the first of several versions of the Gear code that solves Jacobian matrices that have banded structures. In addition, Spellman and Hindmarsh (1975), Sherman and Hindmarsh (1980), and Hindmarsh (1983), introduced Gear codes that solve Jacobians that have arbitrary sparsity. These latter programs used subroutines from the Yale

Sparse Matrix Package (Sherman, 1975; Eisenstat et al., 1977a,b). More recently, the group at Livermore has studied matrix-free methods of integrating stiff ODEs (Brown and Hindmarsh 1986; Hindmarsh, 1986; Byrne, 1990).

The modified Gear-code and the accompanying sparse-matrix solver we present, SMVGEAR, have some similarities to, yet several differences from, some of the codes developed at Livermore. In this paper, we describe how we built SMVGEAR, compare SMVGEAR to LSODES, a 1987 sparse-matrix Gear code (see Hindmarsh, 1983, for the most recent update), and compare SMVGEAR to a new forward-backward Euler method, which we call the Multistep Implicit–Explicit (MIE) scheme.

2. BUILDING SMVGEAR

Starting with Gear's 1971 code, we made major modifications in two areas. We vectorized the code around the grid-cell dimension and built and implemented a vectorized sparse-matrix package. Other changes were minor in comparison.

2.1. Vectorization around the grid-cell dimension

Vectorization is a process by which many computers speed up calculations in an inner DO ... CONTINUE loop. Up to a point, the longer the inner vectorized loop, the faster the calculations in the loop, and the greater the number of megaflops (million floating point operations per second) the program achieves. On Cray computers, such as the CRAY Y-MP, a vectorized loop reaches 90% of its maximum speed when the inner vector length is about 512 elements (NAS, 1992). Vectorized loops are also sensitive to the types of operations performed within. For example, a loop will often not vectorize if a recursion occurs within it. Also, vectorized loops that contain certain operations or certain pointer arrays are often slower than vectorized loops written strategically with different operations or without the arrays.

At first glance, a Gear-type code appears to have two dimensions around which one can vectorize. One dimension is the number of species, and a less apparent dimension is the number of grid-cells. If one runs a Gear-type code in a single grid-cell, then the only practical vectorization dimension is the number of species. However, running a Gear-code in one grid-cell rarely presents a computational problem in the first place. Also, most atmospheric models contemplate calculations in multiple grid-cells.

Based on experience, we have found that an atmospheric model vectorized around the grid-cell dimension is much faster than one vectorized around the number of species when the model contains more than a few tens of grid-cells. A reason is that all classical matrix decomposition/back substitution codes require several varying-length inner loops. For example, matrix inner loops often march from length of one to

length of either the order or one-half the order of the matrix. Thus, if the model has many grid-cells, it will perform calculations in each cell with many inefficient inner loops.

However, if we vectorize the code around the grid-cell dimension, then the inner loop is efficient so long as the model contains at least a few tens of grid-cells. Theoretically, for a model with 50,000 grid-cells, every inner loop can have a length of 50,000. However, for pure chemistry models, this length is unnecessary and undesirable. For example, since the speed of a CRAY Y-MP computer reaches 90% of its maximum when the inner loop is 512 units, we save array space by dividing the *grid-domain* (entire grid) into *grid-blocks* of 500 or so cells.

Furthermore, by limiting the size of each grid-block, we reduce excess calculations. The reason is that, in order to vectorize around grid-cells, we perform the same operations in every cell; thus, the number of operations in a block is limited by the number of operations in the grid-cell containing the stiffest ODEs. Consequently, the smaller a grid-block, the fewer the number of cells forced to iterate at the same pace as the stiffest cell in the block.

To perform the same operations throughout a grid-block, we need to ensure that the time-step and the order of the integration method (different from the order of the matrix) are the same in each cell within the block. To obtain the same time-step and order, we first calculate the time-step required in each cell of a block for (a) the current order, (b) one order lower than the current order, and (c) one order higher than the current order. Next, for each of the three orders, we choose among the time-steps of all the cells in the block for the shortest. Finally, in the same manner as Gear, we choose among the three pairs of shortest steps and corresponding orders for the longest of these steps and for the order allowing the longest step. Thus, the time-step and order of all cells in a block will be identical and limited by the grid-cell with the stiffest equations.

If we include horizontal and vertical transport implicitly in the ODEs, then we still vectorize around grid-cells. However, in such cases, we need to solve all equations, simultaneously, over all grid-cells; thus, the grid-domain can have only one block.

The speed-up from vectorizing loops around the grid-cell dimension is large. For example, on the CRAY-90 computer, the speed of SMVGEAR in vectorized form is, on average, a factor of 120 greater than its speed in scalar form. Individual subroutines have exhibited speed-up factors of 220 or more. To the contrary, the same code vectorized around the species dimension can be up to forty times slower than the code vectorized around the grid dimension.

2.2. JSPARSE: a package for evaluating sparse Jacobian matrices

The second major adjustment we made to Gear's original code was to build into SMVGEAR an algo-

rithm (JSPARSE) that reduces the number of matrix calculations yet still vectorizes every matrix calculation around the grid-cell dimension. JSPARSE reduces the number of matrix calculations in several ways. First, it reorders species so that those with the fewest combined production and loss terms appear first in order and those with the most appear last. This ordering allows ODEs with the most terms to reside in the bottom rows of the matrix and ODEs with the fewest terms to reside in the top rows, maximizing the number of matrix multiplications that include a zero term (e.g. Zlatev, 1991, p. 111). Second, JSPARSE eliminates all calculations in which a zero, known in advance, multiplies another number. To determine, in advance, every occurrence of a zero multiplication, the code, at the beginning of the program, runs through a practice matrix decomposition/back-substitution, and sets new arrays eliminating all calculations in which a zero occurs.

Furthermore, since our atmospheric model contemplates running both gas- and aqueous-phase and day and night chemistry, we form different sparse-matrix arrays for each of four chemistry cases: (a) gas-phase day, (b) gas-phase night, (c) aqueous-phase day, and (d) aqueous-phase night. We designed the program to include any number of additional processes as well. Separating day from night chemistry reduces the number of matrix calculations since photo-dissociation equations do not operate at night.

To further reduce the number of matrix calculations, we removed partial pivoting from the decomposition process. The original reason to remove partial pivoting was to maintain the same sequence of calculations in each grid-cell. If we included partial pivoting, then the order of calculations in each grid-cell would differ, and we could not vectorize around the grid-cell dimension. Fortunately, the use of partial pivoting is unnecessary, as confirmed by Sherman and Hindmarsh (1980, p. 195). They state, "... experience has shown that pivoting is only rarely required in certain applications, and, in any case, if the factorization process should fail, a change in the step-size h will usually improve matters because of the form of P." Based on tests of SMVGEAR to date, removing the pivot has had little or no effect on stability or accuracy.

JSPARSE minimizes array space in several ways. First, it pre-determines how many matrix positions will fill in as a result of matrix decomposition and back-substitution. This value is the sparse-matrix array length for a given set of ODEs. For example, in a case of smog chemistry, with 92 species and 222 chemical reactions, the order of the original matrix was 92; thus its dimension was $92 \times 92 = 8464$. However, the initial matrix was sparse, with only 695 positions filled for day chemistry and 671 for night chemistry. As matrix calculations proceeded, JSPARSE filled-in about 150 more matrix positions in each case.

The number of fill-ins depends almost entirely on the ordering of the ODEs in the matrix. For example,

Table 1. Reduction in array space and number of matrix operations resulting from implementing sparse-matrix techniques. We show three cases — a smog-chemistry, a stratospheric-chemistry, and an aqueous-chemistry case. The first row shows the order of the matrix, the second and third rows show the number and percent of initial matrix positions filled, the fourth and fifth rows show the number and percent of final matrix positions filled, and the last four rows show the number of operations in each of four loops occurring during matrix decomposition, back-substitution. *Decomp.* 1 and 2 refer to the first and second loops occurring during each decomposition, while *Back-sub.* 1 and 2 refer to the first and second loops occurring during each back-substitution call. The first column in each chemistry case shows values without sparse-matrix reductions, and the second two columns in each case show values with the reductions, for each day and night chemistry.

	Gas-phase smog			Gas-phase stratosphere			Aqueous-phase		
	Initially	After sparse reductions Day	After sparse reductions Night	Initially	After sparse reductions Day	After sparse reductions Night	Initially	After sparse reductions Day	After sparse reductions Night
Order of matrix	92	92	92	39	39	39	37	37	37
No. init. matrix spots used	8464	695	671	1521	287	268	1369	273	270
% of initial spots used	100	8.2	7.9	100	18.9	17.6	100	19.9	19.7
No. final matrix spots used	8464	839	815	1521	334	305	1369	361	351
% of final spots used	100	9.9	9.6	100	22.0	20.0	100	26.4	25.6
No. operations Decomp. 1	255,346	1757	1642	19,019	729	595	16,206	951	881
No. operations Decomp. 2	4560	403	383	741	141	122	666	178	171
No. operations Back-sub. 1	4560	401	383	741	141	122	666	178	171
No. operations Back-sub. 2	4560	344	340	741	154	144	666	146	143

in the smog-chemistry case the ODEs originally had no specific ordering. Consequently, the final matrix contained 6255 non-zero terms for day and 6253 non-zero terms for night chemistry. By re-ordering the species (thus the ODEs) so that those with the most combined production and loss terms appeared last in the matrix, we reduced the final number of non-zero terms to 839/815.

The LU-decomposition/back-substitution process we use originated from Press *et al.* (1992). However, we removed partial pivoting (as discussed earlier) and made other adjustments. As a result, each decomposition process requires operations in two major loops (one much longer than the other), and each back-substitution requires operations in two major loops. For each of the four loops, we know in advance the number of operations that occur within; thus, setting up economical arrays to direct traffic within the loops is straightforward.

In summary, we set all sparse-matrix arrays at the beginning of the program, which allows the program to save time even if the matrix is dense. Because the arrays stay unchanged and no pivoting occurs, we easily vectorize the matrix decomposition/back-substitution process around the grid-cell dimension. Also, since JSPARSE minimizes the number of matrix positions that originate with a zero value but eventually fill-in with a non-zero value, it minimizes the total number of required matrix array positions. Table 1 shows how JSPARSE reduced the number of required array positions and the number of calculations within each of four matrix loops, for each a smog-, a stratospheric-, and an aqueous-chemistry system.

Table 1 shows that, even without vectorization, JSPARSE significantly reduced the time required in each of the four matrix loop operations. For example, JSPARSE reduced the number of operations in the first loop of the decomposition process by a factor of 145 in the larger, smog-chemistry case and factors of 26 and 17 for the smaller stratospheric- and aqueous-chemistry cases, respectively. Initially, about 8.2% of all matrix positions were filled in the smog-chemistry case compared to 18.8 and 19.9% for the other two cases. Naturally, the fewer initial spots filled, the greater the reduction in the number of matrix operations.

Finally, Table 1 shows that the ratio of calculations in the decomposition process compared to those in the back-substitution process was approximately 3:1 in all sparse-matrix cases. Since SMVGEAR typically calls the back-substitution process between 3 and 12 times for each call to the decomposition process, SMVGEAR usually performs comparatively more total calculations in the back-substitution process.

3. COMPARISON OF SMVGEAR TO LSODES AND MIE

To measure the efficiency of SMVGEAR, we compared it to another sparse-matrix Gear-code called LSODES (Livermore Solver for Ordinary Differential

260

SMVGEAR

Equations with Sparse Matrices), and to a code that we built prior to SMVGEAR, called MIE (Multistep Implicit–Explicit solver). LSODES, written jointly by A. C. Hindmarsh and A. H. Sherman, is part of ODEPACK (Hindmarsh, 1983), a collection of ODE solver software available through NETLIB, a public-domain software collection. LSODES originated as GEARS (Spellman and Hindmarsh, 1975; Sherman and Hindmarsh, 1980), and the version of LSODES we obtained was last updated in 1987.

3.1. *LSODES*

LSODES and SMVGEAR have several similarities. First, the driver routines of both codes are modifications of an original program of Gear (1971). Second, both codes set up sparse-matrix arrays at the beginning of the program. Third, both codes re-order the ODEs in the matrix to reduce fill-in and eliminate all calculations involving multiplication by zero. Fourth, neither code uses partial pivoting during the matrix computations.

On the other hand, the codes currently differ in several areas. First, while SMVGEAR vectorizes around the grid-cell dimension, LSODES vectorizes around the species and other dimensions. By restructuring all arrays, one could probably vectorize LSODES around grid-cells. Second, SMVGEAR sums up several terms at a time within matrix and other loops to further improve vectorization and reduce the number of overhead calculations.

Third, while one can adjust both codes for any ODE application, SMVGEAR includes changeable input data sets for atmospheric chemistry problems and routines that automatically determine first and partial derivatives. Thus, to change the chemical problem, one needs only to change the species and equations in the input data set. On the other hand, to run LSODES as provided, a user needs to write a routine for evaluating the first derivative. LSODES can internally calculate partial derivatives.

Fourth, SMVGEAR contains arrays that permit it to solve any number of ODE systems during the same model run. For example, it can solve gas-phase chemistry separately from aqueous-phase chemistry during the same run while minimizing array requirements. Furthermore, it contains different arrays for day and night chemistry. To run two or more processes in the same model with LSODES, one would have to either restructure all arrays or implement two or more full versions of LSODES in the model.

Fifth, SMVGEAR contains one common-block while LSODES includes COMMON statements in every subroutine. Thus, while the subroutines in LSODES are more modular, one can make changes in SMVGEAR more easily. Sixth, aside from the set-up routines, SMVGEAR has only five subroutines—(a) a driver routine that calculates time-steps, method orders, and final concentrations; (b) a routine that calculates partial derivatives; (c) a routine that performs matrix decomposition; (d) a routine that

performs back-substitutions; and (e) a routine that evaluates first derivatives. LSODES, on the other hand, calls about 13 subroutines during the solution-phase of the program.

For the most part, other differences are minor. We want to acknowledge, however, that we borrowed three ideas from LSODES. These include LSODES' method of (a) predicting the first time-step, (b) setting the error weight, and (c) determining convergence of the corrector iteration. For example, LSODES uses a relative and absolute error tolerance to determine convergence in a slightly different manner from Gear (1971), whose convergence test we previously used. LSODES calculates an error weight for each species i at time t, as

$$W_{E,i}^t = E_R C_i^t + E_A \qquad (5)$$

where C_i^t is the concentration of species i at time t, E_R is a relative error tolerance, and E_A an absolute error tolerance. LSODES then computes the root-mean-square norm over all species' errors divided by their error weights and uses the norm to determine convergence.

3.2. *MIE*

MIE, on the other hand, is not a Gear-type code. In this section, we describe the algorithm. In sum, to obtain results from MIE, we estimate species concentrations by iterating over a backward-Euler formula, and use the estimates in a forward-Euler to obtain final concentrations for a time-step. The step-size for the MIE method can vary, but currently it is not determined so elaborately as in Gear-type codes. Instead, we usually start with a fixed time-step, gradually increase the step, but reduce it if convergence becomes difficult. There is no reason why, however, we cannot predict a time-step for the MIE code. After a series of time-steps, we complete a time-interval, which has a pre-determined length. At the end of the interval, we go on to another process in the model and then return to MIE for another interval.

Here, we describe the iteration sequences of the MIE algorithm for a single time-step. In the following notation C is concentration, in units of molecules per cubic centimeter of air for gas-phase and moles per liter of water for aqueous-phase species. The superscripts t and $t+1$ indicate value at the beginning and end, respectively, of a time-step. The superscripts *est*, *MAX*, and *m*, respectively, indicate an estimated value, a maximum estimated value, and an iteration number. Finally, subscripts i and j identify species numbers. Thus, $C_i^{est,m}$ is the mth estimated concentration of species i, and $C_i^{est,1}$ is the first estimated concentration of i. One can solve for each species' final concentration, C_i^{t+1}, during a time-step in the following order:

(i) Set the first and the maximum estimated concentrations of each species to its initial concentration.

$$C_i^{est,1} = C_i^t \qquad (6)$$

$$C_i^{MAX,1} = C_i^t. \qquad (7)$$

261

(ii) Iterate over equations (8)–(17). The first step in the sequence is to calculate reaction rates with estimated concentrations. Each rate describes a uni-, bi-(equation (8)), or ter-molecular kinetic reaction, or a photodissociation process (equation (9)), such as

$$R_n^{est,m} = K_n C_i^{est,m} C_j^{est,m} \qquad (8)$$

and

$$R_n^{est,m} = J_n C_i^{est,m} \qquad (9)$$

where the subscript n is the reaction or photo process number and $R_n^{est,m}$ is the mth estimated overall rate of a reaction (e.g. No. cm^{-3} s^{-1} for gas-phase). Also, K_n is the kinetic reaction rate coefficient (e.g. s^{-1}, cm^3 No.$^{-1}$ s^{-1}, or cm^6 No.$^{-2}$ s^{-1} for gas-phase) and J_n is the coefficient of a photodissociation process (s^{-1}). If the rate coefficient is pressure-dependent, temperature-dependent, or empirical, then we calculate it at the beginning of a time-interval and change it only before the next interval.

(iii) Next, sum up the mth estimated explicit production rate, $P_i^{est,m}$, and explicit loss rate, $L_i^{est,m}$ (e.g. No. cm^{-3} s^{-1} for gas-phase), and calculate the implicit loss coefficient, $l_i^{est,m}$ (s^{-1}), of each species. Below, the subscript $n(p)$ is reaction rate n of the pth production term, and $n(l)$ is rate n of the lth loss term. The production and loss terms are

$$P_i^{est,m} = \sum_{p=1}^{No.\ prods} R_{n(p)}^{est,m} \qquad (10)$$

$$L_i^{est,m} = \sum_{l=1}^{No.\ losses} R_{n(l)}^{est,m} \qquad (11)$$

and

$$l_i^{est,m} = L_i^{est,m} / C_i^{est,m}. \qquad (12)$$

(iv) With the mth implicit loss and explicit production terms, calculate the $m+1$th estimated concentration of each species with a backward Euler formula (Curtiss and Hirschfelder, 1952). The backward Euler is implicit (Rosenbaum, 1976; Shampine and Gear, 1979) and can be written as

$$C_i^{est,m+1} = [C_i^t + P_i^{est,m} \Delta t] / [1 + l_i^{est,m} \Delta t] \qquad (13)$$

where Δt is the time-step, in seconds. Next, use the estimated concentrations to calculate production and loss terms during the subsequent iteration. Equation (13) always yields a positive concentration and contains no exponential terms, minimizing computer time.

In the special case where a species has no production, equation (13a) describes its final concentration. If we calculate estimates with equation (13b) instead of with equation (13) in such cases, the explicit concentration of the species will approach the solution from equation (13a). Equation (13b) gives a slightly more accurate solution than (13) when a species rapidly decays.

$$C_i^{t+1} = C_i^t e^{-l_i^{est,m} \Delta t} \qquad (13a)$$

$$C_i^{est,m+1} = C_i^t (1 - e^{-l_i^{est,m} \Delta t}) / l_i^{est,m} \Delta t. \qquad (13b)$$

(v) Calculate tentative final concentration of each species explicitly with the forward-Euler formula, written as

$$C_i^{t+1} = C_i^t + [P_i^{est,m} - L_i^{est,m}] \Delta t. \qquad (14)$$

(vi) Test whether the system has reasonably converged for the time-step. At some point during the iteration sequence, concentrations calculated from equation (14) should exceed zero and converge. The more iterations the code takes after all explicit concentrations exceed zero, the closer each concentration approaches the converged solution. We define N_P as a number of iterations we instruct the code to take, during which all values from equation (14) exceed zero. When all explicit concentrations exceed zero during a total of N_P iterations, the iteration sequence ends.

If $C_i^{t+1} \geq 0$ for every species i for N_P iterations, then stop iterating and set each final concentration to C_i^{t+1}. If $C_i^{t+1} < 0$ for at least one species, iterate more. (15)

At first, one might think the above convergence criteria is risky. However, to date, it has worked well. For a large set of equations, the criteria works when $N_P = 1$ because MIE usually takes 3–30 iterations before it dampens heavy oscillations and before every explicit concentration exceeds zero during a time-step. Thus, by the time all explicit values exceed zero, most, but not all, have converged.

Furthermore, when using the MIE code, we often take a series of time-steps during a time-interval. At the end of the interval, we go to another process in the model, and come back to MIE for its next interval. Because solutions to first-order rate equations tend to dampen over time, the implicit and, therefore, explicit solutions from equations (13) and (14), respectively, converge from time-step to time-step. Since we treat the implicit loss-coefficient (equation (12)) of second-order, self-reactions, as if they were first-order reactions, these equations also dampen. Thus, because errors tend to dampen each time-step and because we want an accurate solution only by the end of an interval, we need to fully converge concentrations only at the end of an interval.

For small sets of equations we set $N_P > 1$ during every time-step because all explicit solutions may exceed zero before MIE has dampened oscillations. By setting $N_P > 1$, we allow iterations after all explicit values exceed zero, improving the solution.

If convergence does not occur after a maximum number of iterations permitted (which we set to between 100 and 300), then we reduce the time-step. Typically, MIE iterates between three and 30 times per time-step.

(vii) The last iteration step is to "cap" the implicit estimate to prevent some from exploding to infinity upon iteration. A cap can also significantly decrease the number of iterations needed for convergence. The choice of a cap is not unique. Some include holding

262

the maximum estimate to the largest(est) of the initial concentration and (a) the first estimate, (b) any of the first four estimates, or (c) the value of the previous estimate before being limited by the cap. We use (c). The equations describing cap (c) are

$$C_i^{MAX,m+1} = MAX\{C_i^{rn,m+1}, C_i\}$$ (16)

and

$$C_i^{rn,m+1} = MIN\{C_i^{rn,m+1}, C_i^{MAX,m}\}.$$ (17)

(viii) In this scheme, iterated explicit concentrations from equation (14) and iterated implicit concentrations from equation (13) converge to the same value. However, if a species is short-lived ($l_i^{rn,m}\Delta t \gg 1$), its implicit concentration converges faster. Thus, a way to reduce computer time is to calculate final concentrations of short-lived species with equation (13) instead of (14). However, calculating too many final concentrations implicitly causes mass loss over time. A way to reduce mass loss is to solve only a few final concentrations implicitly. To do so, we define LT as a unitless number to compare $l_i^{rn,m}\Delta t$ against. If $l_i^{rn,m}\Delta t \geq LT$ for a species, then we set the species' final concentration to its last estimate from equation (13). Thus

if $l_i^{rn,m}\Delta t \geq LT$ then $C_i^{n+1} = C_i^{rn,last}$. (18)

We typically set LT and N_P at the start of a time-interval and re-set them for the last step of the interval. For example, at the start, we often set $N_P = 1$ and $LT = 10^0$. For the last step, we either reduce LT to 10^2, increase N_P to between 20 and 250, or both. Generally, to prevent accumulation of error over time, we want to force a sufficient number of iterations during each time-step. Setting $LT = 10^0$ or more for most steps usually forces sufficient iterations.

Finally, when $l_i^{rn,m}\Delta t \geq LT$, a species' explicit concentration does not need to exceed zero because we use its implicit concentration as the final value. Thus, to speed up the code we can replace (15) with (15m).

If $C_i^{n+1} \geq 0$ or $l_i^{rn,m}\Delta t \geq LT1$ for each species i for N_P iterations, then stop iterating and set final concentrations to C_i^{n+1} when $l_i^{rn,m}\Delta t < LT1$ or to $C_i^{rn,last}$ when $l_i^{rn,m}\Delta t \geq LT$. If $C_i^{n+1} < 0$ for at least one species, continue iterating. (15m)

Above, $LT1$ is any number greater than or equal to LT.

In summary, the MIE code solves ODEs by estimating species concentrations with an iterated backward-Euler formula and using the estimates to determine rates with a forward-Euler. While the forward-Euler predicts the final concentration of most species, the backward-Euler predicts the final concentration of the shortest-lived species. We have applied MIE to atmospheric chemistry problems only; however, there is no reason why MIE cannot solve ODEs for other processes.

3.3. Timing tests

We tested SMVGEAR against both LSODES and MIE for three cases: two smog chemistry and a stratospheric chemistry case. In the next section, we show additional timings of SMVGEAR solving both gas- and aqueous-chemistry in a full model.

The smog mechanism we tested was a combination of inorganic equations compiled from DeMore et al., 1990, organic equations from the Carbon-Bond IV expanded mechanism (Gery et al., 1988), sulfur equations from Toon et al. (1987), and additional reactions for a total of 92 gas-phase species or lumped bond groups, 200 chemical reactions, and 22 photodissociation processes. Of the 200 kinetic rates, we calculated several as three-body pressure-dependent reactions.

For the first smog simulation (SMOG11), we initialized 14 species with concentrations of 5.0×10^{11} cm^{-3}, and most other active species with zero concentration. However, we set the initial concentrations of major atmospheric constituents, such as oxygen, nitrogen, water, carbon monoxide, and methane, at realistic levels. For the second simulation (SMOG12), we increased the initial concentration of 14 species from 5×10^{11} to 5×10^{12} cm^{-3} to increase the stiffness of the system.

For the stratospheric test (STRAT), we used a set of 39 species, 84 chemical reactions, and 24 photodissociation processes compiled primarily by S. Elliott and R.P. Turco (personal communication). We assumed an altitude of 20 km (pressure of 55.3 mb), a constant temperature of 217 K, and fairly realistic initial concentrations.

For both the smog and stratospheric tests, we changed the photorates every time-step, no matter how small. To simplify the tests, we varied the photorates with a sine function during 12 of every 24 h and turned the photorates off every other 12 h. Thus, the only process occurring during the simulations shown in this section was chemistry with photorates continuously changing during each day.

Furthermore, we fixed the relative error tolerance of both SMVGEAR and LSODES to 10^{-3} and the absolute error tolerance of each species to 10^3. Both codes predicted their own time-steps. For the MIE code, we initialized the time-step at 10 s and allowed the step-size to increase by a factor of two every 30 steps. After every 1800-s interval, we re-set the time-step to 10 s. Also, for MIE, we set $LT = 10^6$ and $N_P = 1$ at the beginning of each interval and changed $LT = 10^2$ and $N_P = 20$ for the last time-step of each interval.

Before running speed comparisons among the codes, we determined error resulting from each code's parameter values. We calculated the average absolute-value concentration error over time as

$$ERROR = \frac{100\%}{N_I} \sum_{j=1}^{N_I} \left\{ \frac{1}{N_{s,j}} \sum_{i=1}^{N_{s,j}} ABS\left(\frac{C_{p,i}^{t(j)} - C_{e,i}^{t(j)}}{C_{e,i}^{t(j)}} \right) \right\}$$ (19)

263

Table 2. Average absolute-value percent error (as determined by equation (19)) in concentration for SMVGEAR and MIE resulting from the choice of parameter values and or error tolerances. In each case, SMOG11, SMOG12 and STRAT, we averaged errors over all 1800-s time-intervals during the given simulation period. The separate columns under SMVGEAR and MIE indicate the lowest concentrations we included in the error calculation

	Simulation period (d)	SMVGEAR		MIE	
		Include concs $> 10^1$ cm^{-3} (%)	Include concs $> 10^{-3}$ cm^{-3} (%)	Include concs $> 10^1$ cm^{-3} (%)	Include concs $> 10^{-3}$ cm^{-3} (%)
SMOG11	1	0.55	1.35	1.44	2.84
SMOG12	1	0.46	1.08	1.42	2.61
STRAT	9	0.25	0.51	1.20	1.42

where N_t is the number of time-intervals during a model run. $N_{s,j}$ is the number of species whose concentration are above a minimum value after the jth time interval. $C^{(t,j)}$ represents a concentration at time t, corresponding to the end of the jth interval, and the subscripts p, i and e, i refer to predicted and exact concentrations, respectively, of species i. In all cases, we used SMVGEAR with a stiff error tolerance to obtain "exact" solutions after each time-interval.

Table 2 shows the time- and species-averaged errors from MIE and SMVGEAR. For SMVGEAR, we tested the effect of assuming a relative error tolerance of 10^{-3} and an absolute tolerance of 10^3 instead of more stringent tolerances. For MIE, we tested the effect of using the values for the time-steps, LT and N_p, given above. Since we used LSODES with the same error tolerances as SMVGEAR, we assumed it gave errors similar to those of SMVGEAR. For these tests, we ran simulations of either one or nine days. For both SMVGEAR and MIE, we divided the simulation period into intervals of 1800 s in order to obtain the error at the end of these intervals. The results from Table 2 indicates that SMVGEAR gave lower errors than MIE in all cases.

Finally, we tested the three codes running in a one grid-cell model and tested SMVGEAR and MIE in a 500 grid-cell model. Because the chemistry in each grid-cell was the same and LSODES does not vectorize around grid-cells, LSODES takes the same time per grid-cell to solve in 10,000 or 100,000 cells as it does to solve in 1. Thus, to obtain LSODES results for many grid-cells, we multiplied its time to solve in one cell by the total number of cells in the domain. Similarly, because we limited the block-size of SMVGEAR and MIE to 500 cells in these examples, we extrapolated its time to solve in 500 cells to its time to solve in the entire domain.

For the two smog tests, we simulated chemistry for 3-day periods. For the stratospheric test, we simulated for a 30-day period. During these tests, only MIE divided the simulation period into intervals of 1800 s. The other two codes integrated continuously.

Table 3 shows results from the three simulations and characteristics of the different codes. First, in large grid-domains, SMVGEAR was about 60-times

faster than LSODES and 30–55-times faster than MIE. While some of SMVGEAR's speed-up compared to LSODES resulted from fewer matrix calculations, most resulted from vectorization. Because MIE vectorizes around grid-cells, it, too, runs faster over large domains than it does over small domains.

Second, in one grid-cell, LSODES was fastest because it vectorizes around the species dimension while both SMVGEAR and MIE vectorize around the grid-cell dimension. In fact, because SMVGEAR vectorizes around grid-cells, every inner loop is inefficient in a one grid-cell model. However, one can make SMVGEAR more efficient in one grid-cell simply by removing all the inner grid-cell loops.

Although SMVGEAR was slower in one grid-cell, it performed fewer matrix decomposition and back-substitution calculations, in all simulations, than did LSODES. Thus, the greater speed of LSODES in one grid-cell was attributable to its type of vectorization. In fact, row (e) of Table 3 shows that, if we remove the effects of vectorization, SMVGEAR performed slightly faster than LSODES. However, the number of matrix fill-ins in each case was similar for the two codes. Meanwhile, the MIE code was far slower than either of the other two codes in a one grid-cell model.

In sum, when we ran SMVGEAR over a grid-domain, and the only process was gas-phase chemistry with diurnally changing photorates, SMVGEAR was very fast on a vectorized machine compared to the other two codes tested. Furthermore, without vectorization, its time was slightly better than LSODES, one of the fastest available ODE solvers. From Table 3, we calculate that SMVGEAR required about 1.4 min of simulation time per day of smog-chemistry simulation over 10,000 grid-cells and 3.4 min per day of stratospheric-chemistry simulation over 100,000 cells. In the next section, we discuss the timing of SMVGEAR in a model containing other processes.

4. APPLICATION OF SMVGEAR

In this section, we report the speed of SMVGEAR in two other atmospheric applications. Because

264

Table 3. Statistics from two smog-chemistry and one stratospheric-chemistry comparisons on a CRAY-90 computer. The smog-chemistry tests, described in the text, were for 3 simulation days, and the stratospheric test was for 30 simulation days. For smog-chemistry, we tested the three solvers over both 10.000 grid-cells and 1 cell, while for the stratospheric case, we tested over 100.000 cells and 1 cell. Row (e) in each case normalizes the time of each code to a common speed of one megaflop since, with different numbers of grid-cells, each code vectorizes differently. For all three simulations, SMVGEAR and LSODES used the same error tolerances and a similar initial time-step

	SMVGEAR	LSODES	MIE
SMOG11 CHEMISTRY			
(a) CPU time to solve 3 days, 10,000 cells	3.9 min	4.08 h	2.16 h
(b) Megaflops for 3 days, 10,000 cells	342	10.9	341
(c) CPU time to solve 3 days, 1 cell	2.92 s	1.47 s	43.2 s
(d) Megaflops for 3 days, 1 cell	3.1	10.9	4.7
(e) CPU time 3 days, 1 cell, at 1 megaflop	9.1 s	16.0 s	203 s
(f) Vectorization speed-up — (d) × 10,000/(a)	124.8	1	55.6
(g) Number of time-steps taken, 1 cell	808	876	10,296
(h) Number of matrix decompositions, 1 cell	211	274	—
(i) Number of matrix back-substitutions, 1 cell	1394	1738	—
(j) Matrix size after fill-ins, 1 cell (day/night)	839/815	839	—
SMOG12 CHEMISTRY			
(a) CPU time to solve 3 days, 10,000 cells	4.24 min	4.58 h	3.86 h
(b) Megaflops for 3 days, 10,000 cells	342	10.97	340.5
(c) CPU time to solve 3 days, 1 cell	3.31 s	1.65 s	62.4 s
(d) Megaflops for 3 days, 1 cell	3.07	10.97	4.7
(e) CPU time 3 days, 1 cell, at 1 megaflop	10.2 s	18.1 s	293 s
(f) Vectorization speed-up — (d) × 10,000/(a)	130.1	1	44.9
(g) Number of time-steps taken, 1 cell	915	932	10,472
(h) Number of matrix decompositions, 1 cell	247	317	—
(i) Number of matrix back-substitutions, 1 cell	1531	1925	—
(j) Matrix size after fill-ins, 1 cell (day/night)	839/815	839	—
STRATOSPHERIC CHEMISTRY			
(a) CPU time to solve 30 days, 100,000 cells	1.7 h	115 h	51.1 h
(b) Megaflops for 30 days, 100,000 cells	346.7	9.83	342
(c) CPU time to solve 30 days, 1 cell	7.1 s	4.14 s	88.4 s
(d) Megaflops for 30 days, 1 cell	3.61	9.83	4.6
(e) CPU time 30 days, 1 cell, at 1 megaflop	25.6 s	40.7 s	293 s
(f) Vectorization speed-up — (d) × 100,000/(a)	116.0	1	48
(g) Number of time-steps taken, 1 cell	5188	4548	102,960
(h) Number of matrix decompositions, 1 cell	1743	2044	—
(i) Number of matrix back-substitutions, 1 cell	9008	9776	—
(j) Matrix size after fill-ins, 1 cell (day/night)	334/305	344	—

SMVGEAR solves ordinary differential equations, we can include advection, diffusion, emissions, deposition, aerosol growth and evaporation, and many other physical processes as terms in the equations. Furthermore, if we include advection and diffusion terms in the ODEs, we can still vectorize around grid-cells; but, we need to solve the equations in every grid-cell simultaneously. For a purely gas-phase atmospheric model, solving every process at the same time, using SMVGEAR, appears feasible, depending on the speed and memory abilities of the computer.

However, when we add multicomponent, size-resolved aerosols to the model, solving all processes simultaneously becomes a formidable task. For example, our air pollution model contains on the order of 70 aerosol species resolved into 40 or more size bins, and 92 gases. Thus, for a 10,000-cell domain we would need to solve almost three million ordinary differential equations simultaneously if we wanted SMVGEAR to take responsibility for the entire model. Furthermore, some aerosol processes, such as

multicomponent coagulation, require significant matrix fill-in.

Consequently, a more feasible approach to comprehensive atmospheric modeling is time-splitting different processes. A disadvantage of time-splitting is that, if we solve some processes with SMVGEAR, we need to re-start calculations in SMVGEAR every time-interval under conditions that often differ significantly from the conditions at the end of the previous interval. Because of the abrupt transition, SMVGEAR will often restart with a time-step and order smaller than those used at the end of the previous interval and the overall time spent in SMVGEAR will increase.

To test the speed of SMVGEAR in a time-split model, we ran a 24-h simulation in a 10,000 grid-cell domain (40 latitudinal cells × 50 longitudinal cells × 5 vertical layers), which we divided into blocks of 500 grid-cells. The model included gas-phase smog-chemistry, gridded emissions, horizontal advection, vertical diffusion, and dry deposition. The resolution of each horizontal grid-cell was about 4.5 × 5 km, and the

265

emissions data. provided by the California Air Resources Board. included emissions rates for 17 gases and lumped carbon-bond groups that differed in each surface grid-cell and for each hour. We added the emissions rates as terms into the ODEs of SMVGEAR. Because emissions rates during a given time-step are constant. we added the terms to the right-hand side of equation (4) but not to the Jacobian matrix. *J*.

Every SMVGEAR time-step. we interpolated the emissions rate in each grid-cell of each species between the rate for the current hour and that for either the hour ahead or behind. The reason we interpolated the emissions was to create a smooth profile. No matter how small the time-step, we performed this interpolation. The time taken to recalculate emissions every time-step was *de minimus* compared to the savings in iterations it permitted.

Next. we time-split the advection and remaining vertical transport terms. The advection code we used originated from Toon *et al.* (1988), and the vertical transport code originated from Turco *et al.* (1979a,b) and Toon *et al. (ibid.)*. During the 24-h simulation. we solved the horizontal and vertical transport using 300-s intervals. and we solved the 92 chemical ODEs (with continuously changing photorates and emissions) using 1800-s intervals. In other words. every 1800 s. we stopped the calculations in SMVGEAR. performed six transport steps. and returned to SMVGEAR for another interval.

For the 24-h simulation over 10.000 grid-cells. SMVGEAR took a total of 6.7 min at an average speed of 326 megaflops to perform the chemistry and emissions calculations. We stress that. during this simulation. species concentrations differed widely in each grid-cell. Table 4 displays the speed of the different SMVGEAR processes during this application. The table shows that SMVGEAR performed an average of 3.97 back-substitutions each time it decomposed a matrix. Because the ratio of decomposition to back-substitution operations is about 3:1 (Table 1). we would expect back-substitution to take more time. However. the back-substitution coding is about 1.8-times faster than the decomposition coding; thus. decomposition took more time.

Finally. if all processes in this simulation had achieved 420 megaflops (about the speed of the fastest

routine) SMVGEAR would have taken about 5.2 min. or 22%. less time than it actually took. Even better. if some SMVGEAR routines achieved over 600 megaflops. the speed of two other routines in the time-split model. the time to solve would decrease even more. Thus. a future job is to further increase the speed of individual processes in SMVGEAR.

In the second application. we used SMVGEAR to solve both gas- and aqueous-phase chemistry in the same model. Other processes we included during the run were horizontal advection. vertical diffusion. condensational and dissolutional growth. chemical equilibrium. and dry and wet deposition. Furthermore. we resolved the aerosols into 43 size bins. While each size bin contained 50 species for this simulation. 37 of the species were active in aqueous chemical reactions. and almost all of the 50 were included in either gas–aqueous transfer or aqueous–aqueous equilibrium reactions. We obtained most aqueous chemical equations from Pandis and Seinfeld (1989) and Jacob (1986).

Initially. the aerosols contained only solid matter and some water. We then increased the relative humidity to above 100% and allowed the 43 size bins to grow to various fog-size drops. Meanwhile. we initialized the gas-phase with concentrations similar to those in Pandis and Seinfeld (1989). and allowed SMVGEAR to solve gas-phase chemistry. Also. in time-split operations. we calculated the transfer of gases simultaneously to all size bins. calculated chemical equilibrium among aqueous species in each bin. and calculated the forward aqueous-phase chemistry in each bin. We used SMVGEAR to solve the aqueous chemistry and used codes we developed to compute the other processes. For this application. we solved all aerosol processes during 24 3600-s time-intervals. and calculated 12 transport intervals for every chemical and micro-physical interval.

While SMVGEAR performed the calculations in 500-cell grid. we extrapolated the results to 10.000 cells. For gas- and 43 size bins of aqueous-phase chemistry combined. the total time SMVGEAR needed for a 10.000-cell grid and a 24-h simulation period was 3.4 h. The gas-phase chemistry required less than 1.8% of the total time. The average speed of SMVGEAR on the CRAY-90 computer for this application was 348.6 megaflops. and the ratio of back-substitution to matrix decomposition calls was 5.7.

Table 4. Timing and speed of different processes in SMVGEAR during a 24-h simulation over 10,000 grid-cells. During the simulation SMVGEAR solved 92 ODEs that included chemical and emissions terms. Horizontal advection. vertical diffusion. and dry deposition were time-split and solved by other methods. Thus. the timings here are those for the chemical and emissions processes only

	Driver routine	Partial derivative evaluation	Matrix decomposition	Matrix back-substitution	First derivative evaluation	Total time/ average speed
Time speed	100 s	50.7 s	95.1 s	77.1 s	78.7 s	6.7 min
(megaflops)	427	205.7	226.7	414.8	308.5	326

266

The primary reason SMVGEAR took longer to solve aqueous reactions than gas-phase reactions is that aqueous reactions are much stiffer than gas reactions. A lesser reason is that we solved the aqueous chemistry in 43 size bins, compared to the equivalent of one size bin for the gas-phase.

An important difference between solving gas- or aqueous-phase chemistry with SMVGEAR is setting the absolute error tolerance. While we set similar relative error tolerances with gas and aqueous chemistry, the absolute tolerance depends on typical concentration values. Since we used units of No. cm^{-3} for the gas-phase and mol ℓ^{-1} for the aqueous-phase, the concentration values can differ by more than 30 orders of magnitude. Thus, while we usually set the absolute tolerance to 10^3 cm^{-3} for the gas-phase, we changed it to between 10^{-13} M and 10^{-15} M for the aqueous-phase. If a significant number of aqueous concentrations decay below the latter value, the aqueous error tolerance should be set to even smaller values.

5. CONCLUSION

We have presented a new sparse-matrix, vectorized Gear-type code (SMVGEAR). Because SMVGEAR vectorizes around grid-cells, one can use it on vector machines to solve multidimensional atmospheric problems. For problems in single grid-cells and for problems on non-vector machines, SMVGEAR performs similarly to LSODES, another sparse-matrix Gear-code. Based on CRAY-90 timing tests, SMVGEAR can solve chemistry in 10^2–10^5 grid-cells in good speed, and it is much faster than the MIE (Multistep Implicit–Explicit) method, which is the method we used previously.

To vectorize around the grid-cell dimension, SMVGEAR performs the same operations in each cell of each grid-block, where a grid-block is a chunk of cells within an overall grid-domain. Thus, the time-step and order of SMVGEAR in a grid-block are limited by the grid-cell with the stiffest ODEs. However, the speed-up from vectorizing over grid-blocks is far greater than the loss of speed from performing extra calculations in some cells of a block.

Furthermore, the grid-block concept is ideal for parallel computing. We can send each block to an individual processor, and if the processor is vectorized, computational time can decrease dramatically. For example, if a machine has 32 processors, 4 vector units per processor, and each vector unit achieves 32 megaflops at peak performance. Then, the maximum speed on this computer would be more than 4000 megaflops. Even if the practical speed of the CM-5 is 1000 megaflops, SMVGEAR would compute almost three-times faster than it currently computes on the CRAY-90.

Although SMVGEAR has been optimized, its speed can be improved. For example, some sections of the code do not achieve the same speed as other sections. By working on the loops of the less efficient sections, we can increase the program's speed. Furthermore, we can re-order the grid-cells, each time-step, by putting cells with the stiffest equations together in the same grid-block.

Currently, we use SMVGEAR to solve gas-phase and size bin-resolved aqueous-phase chemistry in an air pollution model that also computes the effects of many other processes. A challenge is to include more terms in the ODEs of SMVGEAR in order to reduce the discontinuities caused by time-splitting. As computer speed and memory increases, solving gas and aerosol processes together with transport in large grids will become more and more practical.

REFERENCES

Austin J. (1991) On the explicit versus family solution of the fully diurnal photochemical equations of the stratosphere. *J. geophys. Res.* **96**, 12,941–12,974.

Brown P. N. and Hindmarsh A. C. (1986) Matrix-free methods for stiff systems of ODEs. *SIAM J. numer. Anal.* **23**, 610–638.

Brasseur G. and Solomon S. (1984) *Aeronomy of the Middle Atmosphere*. D. Reidel, Dordrecht.

Byrne G. D. (1990) Pragmatic experiments with Krylov methods in the stiff ODE setting. Presented at the IMA Conference on Computational Ordinary Differential Equations, Imperial College of Science and Technology, London, 3–7 July, 1989.

Byrne G. D. and Hindmarsh A. C. (1976) EPISODEB: an experimental package for the integration of systems of ordinary differential equations with banded Jacobians. Lawrence Livermore Laboratory Report UCID-30132.

Byrne G. D., Hindmarsh A. C., Jackson K. R. and Brown H. G. (1977) A comparison of two ODE codes: GEAR and EPISODE. *Comput. chem. Engng* **1**, 133–147.

Crutzen P. J. (1971) Ozone production rates in an oxygen–hydrogen–nitrogen oxide atmosphere. *J. geophys. Res.* **76**, 7311–7327.

Curtiss C. F. and Hirschfelder J. O. (1952) Integration of stiff equations. *Proc. natn. Acad. Sci. U.S.A.* **38**, 235–243.

DeMore W. B., Sander S. P., Golden D. M., Molina M. J., Hampson R. F., Kurylo M. J., Howard C. J. and Ravishankara A. R. (1990) Chemical kinetics and photochemical data for use in stratospheric modeling. Evaluation number 9. Rep. 90-1. Jet Propul. Lab., Pasadena, California, U.S.A.

Eisenstat S. C., Gursky M. C., Schultz M. H. and Sherman A. H. (1977a) Yale Sparse Matrix Package: II. The symmetric codes. Research Report No. 112, Dept. of Computer Sciences, Yale University.

267

Eisenstat S. C., Gursky M. C., Schultz M. H. and Sherman A. H. (1977b) Yale Sparse Matrix Package: II. The non-symmetric codes. Research Report No. 114, Dept. of Computer Sciences, Yale University.

Elliott S., Turco R. P. and Jacobson M. Z. (1993) Tests on combined projection/forward differencing integration for stiff photochemical family systems at long time step. *Comput. Chem.* **17**, 91–102.

Gear C. W. (1967) The numerical integration of ordinary differential equations. *Math. Comp.* **21**, 146–156.

Gear C. W. (1969) The automatic integration of stiff ordinary differential equations. In *Information Processing 68*, (edited by Morrel A. J. H.), pp. 187–193. North Holland Publishing Company, Amsterdam.

Gear C. W. (1971) *Numerical Initial Value Problems in Ordinary Differential Equations*. Prentice-Hall, Englewood Cliffs, NJ.

Gery M. W., Whitten G. Z. and Killus J. P. (1988) Development and testing of the CBM-IV for urban and regional modeling. Rep. EPA-600/3-88-012, U. S. Environ. Prot. Agency, Research Triangle Park, N. C.

Hesstvedt E., Hov O. and Isaksen I. S. A. (1978) Quasi-steady-state approximations in air pollution modeling: Comparison of two numerical schemes for oxidant prediction. *Int. J. chem. Kinet.* **10**, 971–994.

Hindmarsh A. C. (1972) Linear multistep methods for ordinary differential equations: method formulations, stability, and the methods of Nordsieck and Gear. Lawrence Livermore Laboratory Report UCRL-51186, Rev. 1.

Hindmarsh A. C. (1974) GEAR: ordinary differential equation system solver. Lawrence Livermore Laboratory Report UCID-30001, Rev. 3.

Hindmarsh A. C. (1975) GEARB: solution of ordinary differential equations having banded Jacobians. Lawrence Livermore Laboratory Report UCID-30059, Rev. 1.

Hindmarsh A. C. (1976) Preliminary documentation of GEARIB: solution of implicit systems of ordinary differential equations with banded Jacobian. Lawrence Livermore Laboratory Report UCID-30130.

Hindmarsh A. C. (1977) GEARB: solution of ordinary differential equations having banded Jacobians. Lawrence Livermore Laboratory Report UCID-30059, Rev. 2.

Hindmarsh A. C. (1980) LSODE and LSODI, two new initial value ordinary differential equation solvers. *ACM Newsl.* **15**, 10–11.

Hindmarsh A. C. (1983) ODEPACK, a systematized collection of ODE solvers. In *Scientific Computing* (edited by Stepleman R. S. *et al.*), pp. 55–74. North-Holland, Amsterdam.

Hunt B. G. (1966) Photochemistry of ozone in a moist atmosphere. *J. geophys. Res.* **71**, 1385–1398.

Jacob D. J. (1986) Chemistry of OH in remote clouds and its role in the production of formic acid and peroxymonosulfonate. *J. geophys. Res.* **91**, 9807–9826.

Jacob D. J., Sillman S., Logan J. A. and Wofsy S. C. (1989) Least independent variables method for simulation of tropospheric ozone. *J. geophys. Res.* **94**, 8497–8509.

McRae G. J., Goodin W. R. and Seinfeld J. H. (1982). Nu-

merical solution of the atmospheric diffusion equation for chemically reacting flows. *J. comp. Phys.* **45**, 1–42.

Morris D. B. and Hindmarsh A. C. (1975) GEARV: a vectorized ordinary differential equations solver. Lawrence Livermore Laboratory Report UCID-30119.

NAS (1992) *NAS User Guide*. Vol. 2, version 6.0, section 4, p. 22. Moffett Field, California.

Pandis S. N. and Seinfeld J. H. (1989) Sensitivity analysis of a chemical mechanism for aqueous-phase atmospheric chemistry. *J. geophys. Res.* **94**, 1105–1126.

Press W. H., Teukolsky S. A., Vetterling W. T. and Flannery B. P. (1992) *Numerical Recipes in Fortran*. Cambridge University Press, New York.

Rosenbaum J. S. (1976) Conservation properties of numerical integration methods for systems of ordinary differential equations. *J. comp. Phys.* **20**, 259–267.

Shampine L. F. and Gear C. W. (1979) A user's view of solving stiff ordinary differential equations. *SIAM Rev.* **21**, 1–17.

Sherman A. H. (1975) Yale Sparse Matrix Package User's Guide. Lawrence Livermore Laboratory Report UCID-30114.

Sherman A. H. and Hindmarsh A. C. (1980) GEARS: a package for the solution of sparse, stiff ordinary differential equations. Lawrence Livermore Laboratory Report UCRL-84102.

Shimazaki T. and Laird A. R. (1970) A model calculation of the diurnal variation in minor neutral constituents in the mesosphere and lower thermosphere including transport effects. *J. geophys. Res.* **75**, 3221–3235.

Spellmann J. W. and Hindmarsh A. C. (1975) GEARS: solution of ordinary differential equations having a sparse Jacobian Matrix. Lawrence Livermore Laboratory Report UCID-3011.

Stoer J. and Bulirsch R. (1980) *Introduction of Numerical Analysis*. Springer, New York.

Toon O. B., Kasting J. F., Turco R. P. and Liu M. S. (1987) The sulfur cycle in the marine atmosphere. *J. geophys. Res.* **92**, 943–963.

Toon O. B., Turco R. P., Westphal D., Malone R. and Liu M. S. (1988) A multidimensional model for aerosols: description of computational analogs. *J. atmos. Sci.* **45**, 2123–2143.

Turco R. P. and Whitten R. C. (1974) A comparison of several computational techniques for solving some common aeronomic problems. *J. geophys. Res.* **79**, 3179–3185.

Turco R. P., Hamill P., Toon O. B., Whitten R. C. and Kiang C. S. (1979a) A one-dimensional model describing aerosol formation and evolution in the stratosphere. Part I: physical processes and mathematical analogs. *J. atmos. Sci.* **36**, 699–717.

Turco R. P., Hamill P., Toon O. B., Whitten R. C. and Kiang C. S. (1979b) The NASA-Ames Research Center Stratospheric Aerosol Model: I Physical processes and Computational Analogs. *NASA Tech. Publ. (TP)* 1362, iii–94.

Zlatev Z. (1991) *Computational Methods for General Sparse Matrices*. Kluwer, Dordrecht.

268

Appendix C

Paper -- Modeling Coagulation Among Particles of Different Composition and Size

.

MODELING COAGULATION AMONG PARTICLES OF
DIFFERENT COMPOSITION AND SIZE

Mark Z. Jacobson and Richard P. Turco

Department of Atmospheric Sciences, 405 Hilgard Ave. University of California, Los

Angeles, CA 90024-1565

and

Eric J. Jensen and Owen B. Toon

Space Science Division, NASA Ames Research Center, Moffett Field, CA 94035-1000

Abstract---We present a technique for simulating coagulation among any number of aerosol types, each with a different composition. The semi-implicit solution mechanism solves the coagulation equations over size ranges divided into any number of discrete bins. The scheme conserves particle volume, requires no iterations, and is numerically stable, regardless of the time-step. We compared the accuracy of the solution to both analytical and time-series numerical solutions. Practical use of the scheme demonstrates that it is computationally fast in a multiple grid-cell model.

Key word index: Aerosol microphysics, multicomponent aerosols, atmospheric modeling, semi-implicit solutions.

270

I. INTRODUCTION

Aerosol coagulation is important because it alters the composition and size distribution of particles primarily smaller than one micron in diameter, and these particles affect visibility, health, and physical processes in the atmosphere. For example, sulfate, nitrate, and organic carbon particles between 0.2 and 1.0 μm in diameter scatter light, and soot particles smaller than 1.0 μm absorb light efficiently (Waggoner et al., 1981; Ouimette and Flagan, 1982). Also, particles between 0.1 and 1.0 μm penetrate to the deepest parts of human lungs. Finally, small particles serve as cloud condensation nuclei and surfaces on which chemical reactions take place, and small aqueous particles absorb gases and serve as hosts for internal chemical reactions.

Simulating coagulation requires computing collision and coalescence rates and changes in particle size and composition over time. Atmospheric particles collide as a result of Brownian motion, differences in fall velocities, turbulent motions, and intraparticle forces. Generally, Brownian motion affects particles smaller than 1 μm in diameter, differential fall velocities and turbulent motions affect particles larger than 1 μm, and intraparticle forces affect particles independently of size (Fuchs, 1964).

Smoluchowski (1918) calculated an expression for the coagulation *kernel* associated with Brownian motion in the continuum regime, where the Knudsen number (Kn) is much less than unity. In the free molecular regime ($Kn > 10$), the Brownian coagulation kernel appears to follow the kinetic theory of binary collisions for gas molecules (Hidy and Brock, 1970; Hirschfelder et al., 1951). Fuchs (1964) developed an interpolation formula, described in Section III C, for the Brownian kernel in the transition regime ($0.1 < Kn < 10$). Fuchs' kernel matches the continuum value at low

271

Knudsen number and the free molecular value at high Knudsen number (see also Sitarski and Seinfeld, 1977).

To simulate changes in the size distribution of coagulating aerosols, modelers have developed a number of approaches that assume either a continuous size spectrum or discrete bins that vary in size (*e.g.* Lushnikov, 1975; Turco *et al.*, 1979a,b; Suck and Brock, 1979; Gelbard and Seinfeld, 1980; Tsang and Brock, 1982; Seigneur, 1982, Friedlander (1983), Warren and Seinfeld (1985), Toon *et al.*, 1988, Kim and Seinfeld, 1990; Strom *et al.*, 1992). While all of these models simulate changes in size of coagulating particles, few calculate changes in composition of such particles, and fewer calculate changes in size and composition among different types of particles, each with a different composition.

In one such case Turco *et al.* (1979a,b) derived a basic semi-implicit algorithm to describe aerosol droplets coagulating with condensation nuclei to form mixed aerosols. Their equations assumed a geometrically-related size distribution, with the volume ratio of adjacent size bins equal to two. Toon *et al.* expanded this semi-implicit technique to allow the fixed volume ratio between adjacent bins to exceed two. Here, we further develop the coagulation equations to allow the volume ratio of adjacent bins to approach unity. Furthermore, while we show results using a geometric size distribution, the method presented here solves over randomly-spaced size bins as well. Finally, the scheme simulates coagulation among any number of particle types, each containing any number of volume-fraction components.

272

II. TYPES AND SIZES OF AEROSOLS SIMULATED

The size-resolved model we present simulates coagulation over any number of *externally-mixed* (EM) particle types and a single *internally-mixed* (IM) type. EM types can contain any number of *volume fractions* (EMVFs). Examples of EM particles with one volume fraction are those containing only elemental carbon, organic carbon, or dust. An example of EM particles with two volume fractions are those containing sulfuric acid and water.

The internally-mixed particle type also can contain any number of volume fractions (IMVFs), but must contain at least the sum of the number of volume fractions in EM types. For example if we have one EM type with one volume fraction and another with two volume fractions, then we require at least three IMVFs because coagulation of the two EM types results in IM particles containing three components. The IM type, however, can contain any number of volume fractions beyond the minimum number. Examples of such additional components are condensed liquids, dissociated ions, aqueous chemistry by-products, emitted species, or background species. We can have more than one IM type; however, each IM type must contain all components in the system. For simplicity, we discuss modeling a single IM type in this paper.

The term, 'internally-mixed,' as used here, does not necessarily mean that the components are well-mixed in solution. It merely means that the components exist together in the same particle, possibly even in different phases (*e.g.* liquid and solid). Some of the components may be well-mixed in solution, but others may not be. The only difference between 'externally-mixed' and 'internally-mixed' particles, as defined here, is that the IM particles must contain at least the number of components in all the

273

EM particles, combined. Figure 1 shows an example of the particle types, and Table 1 shows the intended effect of different-type particles coagulating.

EM TYPE WITH
ONE COMPONENT

EM TYPE WITH
TWO COMPONENTS
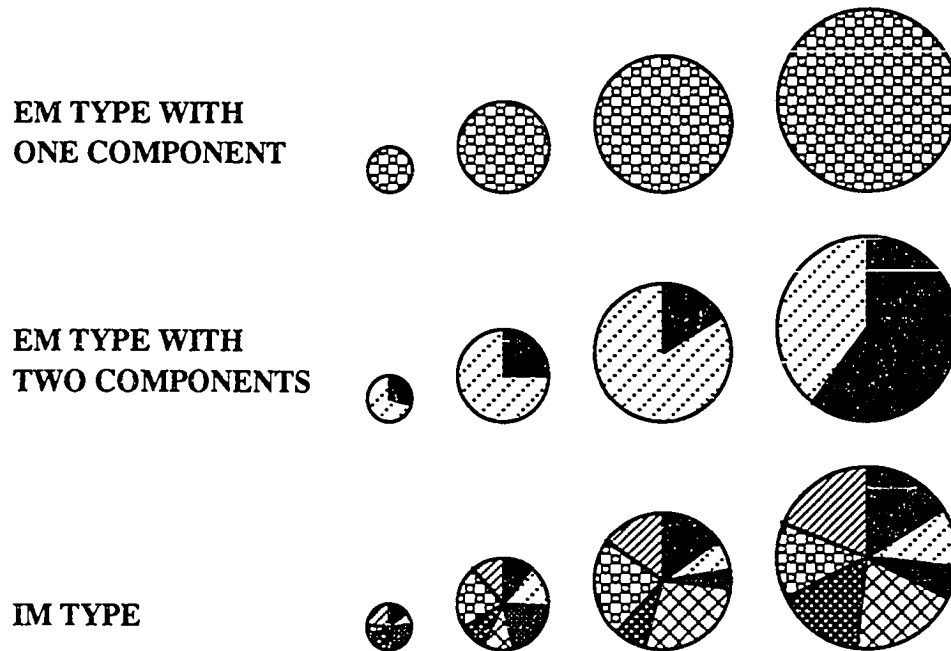
IM TYPE

Fig. 1. Simplified example of particle types in the model. Externally-mixed (EM) types can contain one or more volume fraction components and the single internally-mixed (IM) type contains at least the number of EM components but can also contain any number of additional components.

Table 1. The intended effects on number and volume concentrations when particles of one type coagulate with particles of either the same or another type. EM1 is one set of externally-mixed particles, EM2 is another set, IM is the internally-mixed type, EMVF1s and EMVF2s are volume fractions of EM1 and EM2, respectively, and IMVFs are volume fractions of the IM type. A (-) indicates a decrease in either number

274

or volume, a (+) indicates an increase, a (0) indicates no change, and a --- indicates that no effect is applicable. For example, when EM coagulate with IM particles, EM particles decrease and IM particles increase in number and volume, and volume fractions of EM particles transfer to IM particles.

Coagulating pairs	NUMBER			VOLUME					
	EM1	EM2	IM	EM1	EMVF1	EM2	EMVF2	IM	IMVF
EM1 w/ EM1	(-)	---	---	(0)	(0)	---	---	---	---
EM1 w/ EM2	(-)	(-)	(+)	(-)	(-)	(-)	(-)	(+)	(+)
EM1 w/ IM	(-)	---	(0)	(-)	(-)	---	---	(+)	(+)
IM w/ IM	---	---	(-)	---		---	---	(0)	(0)

Among the assumptions we make is that when an EM particle *hetero-coagulates* (*e.g.* an EM particle coagulates with any particle except an EM of the same type), then the resulting particle enters a multicomponent mixture (IM) representing all particle types. In reality, when two particles of different composition collide, they form a third particle of unique composition. However, while we can write the equations to solve for every combination of particles, modeling every combination is computationally impractical beyond a small number of particles and spatial grid-cells. For example, if we initially have 11 distinct particle types, then they will coagulate into 2047 mixtures (the sum of combinations of 11 taken 1, 2, ..., 11 at a time). If we distribute 72 volume fractions (typical of an air pollution model we currently run) among the 11 types, then each of the 2047 combinations will have between one and 72 components. In a model with 30 size bins and 10,000 grid-cells, we would track 12.3 billion pieces of

275

information each time-step if the average combined species had 20 components. The memory requirements for such a model are beyond most current computer capabilities.

However, by assuming that EM particles become IM particles when they hetero-coagulate, we reduce the number of resulting particle types in the above case from 2047 to 12. With 86 total elements (*e. g.* 10 EM types with one volume fraction each, one EM with two volume fraction, and one IM with 72 volume fractions) the model would track 25.8 million pieces of information over the 10,000-cell grid-domain, which is a factor of 500 savings in array space. Thus, while we can code all possible particle combinations, the computer memory requirements in a three-dimensional model are prohibitively large, and our assuming that different-type particles coagulate to a single IM type is more practical, although less ideal.

III. SOLUTIONS TO THE COAGULATION EQUATION

A. Semi-Implicit Solution for Particles of Uniform Composition

We first derive the semi-implicit solution to the coagulation equation for particles of uniform composition and later expand the derivation to particles of different composition. To derive the semi-implicit solution, we start with the integro-differential equation (Muller, 1928)

$$\frac{\partial C_v}{\partial t} = \frac{1}{2} \int_0^v \beta_{v-\bar{v},\bar{v}} C_{v-\bar{v}} C_{\bar{v}} \, \mathrm{d}\bar{v} - C_v \int_0^\infty \beta_{v,\bar{v}} C_{\bar{v}} \, \mathrm{d}\bar{v}, \tag{1}$$

where C is the time-dependent number concentration (# cm^{-3}) of particles of volume v, $v-\bar{v}$, or $\bar{v}$, and β is the coagulation kernel (cm^{-3} #$^{-1}$ s^{-1}) of two colliding particles. For

276

size bins consisting of monomers (*e. g.* the volume of bin k equals k x the volume of bin one), we rewrite Equation (1) as

$$\frac{\partial C_k}{\partial t} = \frac{1}{2} \sum_{j=1}^{k-1} \beta_{k-j,j} C_{k-j} C_j - C_k \sum_{j=1}^{\infty} \beta_{k,j} C_j, \qquad (2)$$

where we substituted the volume subscripts in (1) with the size-bin subscripts in (2).

The next step in the derivation of the semi-implicit solution is to write Equation (2) in fully-implicit finite difference form as

$$C_k^{t+1} = C_k^t + \frac{1}{2} \Delta t \sum_{j=1}^{k-1} P_{k,j} - \Delta t \sum_{j=1}^{\infty} L_{k,j}, \qquad (3)$$

where Δt is the time-step (s), superscripts t and $t+1$ indicate initial and final concentrations, respectively, while

$$P_{k,j} = \beta_{k-j,j} C_{k-j}^{t+1} C_j^{t+1}, \qquad (4)$$

and

$$L_{k,j} = \beta_{k,j} C_k^{t+1} C_j^{t+1} \qquad (5)$$

are production and loss rates (# cm^{-3} s^{-1}), respectively.

Third, to obtain the semi-implicit solution, we re-define the loss term from (5) in semi-implicit form as

$$L_{k,j} = \beta_{k,j} C_k^{t+1} C_j^t. \qquad (6)$$

277

Using (6) instead of (5) will allow a non-iterative solution to coagulation that approximates an exact solution. Equations (4) and (5) require that $P_{k,j} = L_{k-j,j}$ for each k and j. Applying this equality to (6) and plugging the result and (6) into (3), we obtain the semi-implicit coagulation solution for monomer particles of uniform composition as

$$C_k^{t+1} = \frac{C_k^t + \frac{1}{2}\Delta t \sum_{j=1}^{k-1} \beta_{k-j,j} C_{k-j}^{t+1} C_j^t}{1 + \Delta t \sum_{j=1}^{\infty} \beta_{k,j} C_j^t}, \qquad (7)$$

where k varies from one to infinity. While (7) correctly accounts for the reduction in particle number when two particles coagulate (reducing the number by one-half), it does not conserve volume [Equation (3) correctly accounts for both number and volume, but is fully implicit]. In order to conserve volume (which coagulation physically does) while giving up some accuracy in number, we reform (7) as

$$\upsilon_k C_k^{t+1} = \frac{\upsilon_k C_k^t + \Delta t \sum_{j=1}^{k-1} \beta_{k-j,j} \upsilon_{k-j} C_{k-j}^{t+1} C_j^t}{1 + \Delta t \sum_{j=1}^{\infty} \beta_{k,j} C_j^t}. \qquad (8)$$

Equation (8) satisfies the volume-conservation requirement, $\upsilon_{k-j} P_{k,j} = \upsilon_{k-j} L_{k-j,j}$, for each k and j.

While (8) solves the equation over a monomer size bin structure, we wish to solve it over different bin structures. For example, suppose we set up geometric bins, where the volume of one bin equals the volume of the previous bin multiplied by a constant factor. In this particular distribution, the volume of the smallest bin is $\upsilon_1 =$

278

$(4/3)\pi(r_1)^3$, where r_1 is the radius of the smallest bin. Furthermore $V_{RAT} = v_{i+1} / v_i$ is the volume ratio of two adjacent bins and N_B is the total number of size bins. For any value of V_{RAT} greater than one, the volume of bin i is

$$v_i = v_1 V_{RAT}^{i-1},$$ (9)

and the radius is

$$r_i = r_1 V_{RAT}^{(i-1)/3}.$$ (10)

Consequently, the number of bins that covers the particle size range from radius r_1 to r_i is

$$i = 1 + \ln\left[(r_i/r_1)^3\right]\Big/\ln[V_{RAT}].$$ (11)

Thus, for a radius range from 0.01 μm (10^{-6} cm) to 1 mm (10^{-1} cm), the model requires 87 ($= N_B$) bins when $V_{RAT} = 1.5$ and 26 bins when $V_{RAT} = 4$.

With this new bin structure, each time a model particle of size i collides and sticks to a model particle of size j, the resulting volume of the intermediate particle is

$$V_{i,j} = v_i + v_j.$$ (12)

The intermediate particle has volume between those of two model bins, k and $k + 1$. We partition the intermediate particle between the two bins by defining $f_{i,j,k}$, the volume fraction of intermediate particles of size $V_{i,j}$ that we partition to each model bin k. More precisely,

279

$$
f_{i,j,k} = \begin{cases}
\left(\dfrac{\upsilon_{k+1} - V_{i,j}}{\upsilon_{k+1} - \upsilon_k} \right) \dfrac{\upsilon_k}{V_{i,j}} & \upsilon_k \leq V_{i,j} < \upsilon_{k+1}; \quad k < N_B \\[2ex]
1 - f_{i,j,k-1} & \upsilon_{k-1} < V_{i,j} < \upsilon_k; \quad k > 1 \\[2ex]
1 & V_{i,j} \geq \upsilon_k; \quad\quad k = N_B \\[2ex]
0 & all \quad other \quad cases
\end{cases}
\tag{13}
$$

The fractions in (13) are independent of the size-bin structure. Thus, they work with monomer structures (where all values of f would be 1 or 0), geometric structures, or random structures. Applying the fractions in (13) to (8), we obtain the general formula for volume-conserving, semi-implicit coagulation for particles of uniform composition as

$$
\upsilon_k C_k^{t+1} = \frac{\upsilon_k C_k^t + \Delta t \sum_{j=1}^{k} \left\{ \sum_{i=1}^{k-1} f_{i,j,k} \beta_{i,j} \upsilon_i C_i^{t+1} C_j^t \right\}}{1 + \Delta t \sum_{j=1}^{N_B} \left(1 - f_{k,j,k} \right) \beta_{k,j} C_j^t}.
\tag{14}
$$

In (14) values for $f_{i,j,k}$ are frequently zero; thus, to speed the computer solution to (14), we eliminate every multiplication by a zero value of f. Also in (14) each C^{t+1} term on the right side of the equation is a final concentration calculated for a previous bin. No production occurs into the first bin, $k = 1$, since $k - 1 = 0$ in (14). Thus all C_i^{t+1} terms are known when calculating C_k^{t+1}.

The advantage of using a semi-implicit equation, such as (7), (8), or (14) instead of a fully-implicit equation, such as (2), is significant. For examples (7), (8), and (14) allow immediate, volume conserving solutions, using any time-step. A solution to (2), on the other hand, requires the use of an ordinary differential equation solver, which

280

performs iterations. The only disadvantage to (8) and (14) is that, as with most other schemes, particle number is not exactly accounted for. However, by increasing the resolution of the bin structure (*e.g.* by decreasing V_{RAT}), the error in number approaches zero (*e. g.* Section IV) while the solution remains non-iterative and volume conserving.

B. Semi-Implicit Solution for Particles of Different Type and Composition

The coagulation equations for particles of different type and composition are similar to those for particles of uniform composition. However, because the variety of particle types in the more complicated case can cause confusion, we present a simplified scenario and some definitions in the Appendix.

As discussed earlier, the particle types we use are externally-mixed (EM) and internally-mixed (IM). We first solve for the final concentration of all components in EM types by marching from bin $k = 1$ through bin $k = N_B$. EM types lose volume by coagulating either with other EM types or with the IM type. When such heterogeneous loss occurs, the IM type gains volume. When EM particles self-coagulate, their volume shifts to larger particles of the same type; thus, volume does not escape to the IM type. In sum, for each $N = 1, N_E$ EM type and each $U = 1, T_N$ component, where $Q = L_{N,U}$ is the component number (terms defined in Appendix), the final concentration in each bin is

$$\upsilon_k C_{Qk}^{t+1} = \frac{\upsilon_k C_{Qk}^{t} + \Delta t \sum_{j=1}^{k} \left(\sum_{i=1}^{k-1} f_{i,j,k} \beta_{Ni,Nj} \upsilon_i C_{Qi}^{t+1} C_{L_N,1j}^{t} \right)}{1 + \Delta t \sum_{j=1}^{N_B} \left[\left(1 - f_{k,j,k}\right) \beta_{Nk,Nj} C_{L_N,1j}^{t} + \sum_{\substack{M=1 \\ M \neq N}}^{N_T} \beta_{Nk,Mj} C_{L_M,1j}^{t} \right]}. \tag{15}$$

281

Thus, (15) accounts for homogeneous production and loss and heterogeneous coagulation loss of EM particles. No production occurs into the first bin of EM types. In (15) β is the coagulation kernel. However, the subscripts refer to particles of different-types. For example, $\beta_{Nk,Mj}$ indicates the rate that a particle of bin k, type N (an EM) coagulates with a particle of bin j, type M (either a different EM, or the IM).

After solving for concentrations of EM components, we solve for those of IM particles. IM particles gain volume when EM particles coagulate with them or when EM particles coagulate with EM particles of another type. IM particles never lose volume through coagulation; however, volume shifts to higher bins upon hetero- or self-coagulation. To solve for IM concentrations, we march from bin $k = 1$ through bin $k = N_B - 1$ (we do not allow IM particles to lose volume from the largest size bin but we allow heterogeneous production into the first bin of IM particles). For the single $N = N_T$ IM type and each $U = 1, T_N$ component of the IM type, where $Q = L_{N,U}$, the final concentration is

$$\upsilon_k C_{Qk}^{t+1} = \tag{16}$$

$$\frac{\upsilon_k C_{Qk}^t + \Delta t \sum_{M=1}^{N_T} \left\{ \sum_{j=1}^{k} C_{L_{M,1}j}^t \left[\sum_{i=1}^{k-1} f_{i,j,k} \beta_{Ni,Mj} \upsilon_i C_{Qi}^{t+1} + \sum_{\substack{I=1 \\ I \neq M \\ S_{Q,I}>0}}^{N_E} \sum_{i=1}^{k} f_{i,j,k} \beta_{Ii,Mj} \upsilon_i C_{S_{Q,I}i}^{t+1} \right] \right\}}{1 + \Delta t \sum_{\substack{M=1 \\ K \neq N_B}}^{N_T} \left\{ \sum_{j=1}^{N_B} \left(1 - f_{k,j,k}\right) \beta_{Nk,Mj} C_{L_{M,1}j}^t \right\}}$$

where the Appendix defines the subscript array $S_{Q,J}$. As in (14) and (15), Equation (16) contains many values of f that are zero. Each computation with such a value should be eliminated. For a single particle type of uniform composition, Equation (15) disappears ($N_E = 0$) and (16) simplifies to (14).

Thus, (15) and (16) define the generalized, volume-conserving semi-implicit coagulation equations for multicomponent, multitype aerosols. To conserve volume at the boundary, (16) assumes that particles cannot coagulate out of the largest size bin of IM particles. They can, however coagulate from the largest EM particles to become IM particles. The equations also assume that, upon hetero-coagulation, all volume goes to IM particles. To change this assumption so that when particles hetero-coagulate, they produce a new mixture, we need only to define the new particle types and shift the heterogeneous production term from Equation (16) to the equation for the new particle types. The new equation will also contain a homogeneous coagulation production term, a homogeneous loss term, and a heterogeneous loss term, all similar to those in (15).

C. Coagulation Kernel

For part of this work, we calculated the coagulation kernel by assuming only Brownian diffusion. However, empirical equations in Pruppacher and Klett (1978) describe additional coagulation rates, including those for convective diffusion enhancement, gravitation, turbulent shear, and turbulent inertial motion (see also Saffman and Turner [1956] for coagulation rates due to turbulent shear and inertial motion). To calculate the Brownian diffusion kernel ($\beta^B_{i,j}$ -- cm^3 $\#^{-1}$ s^{-1}) we used Fuchs' (1964) interpolation formula,

$$\beta_{i,j}^{B} = \frac{4\pi(r_i + r_j)(D_i + D_j)}{\dfrac{r_i + r_j}{r_i + r_j + (\delta_i^2 + \delta_j^2)^{1/2}} + \dfrac{4(D_i + D_j)}{(\bar{v}_{pi}^2 + \bar{v}_{pj}^2)^{1/2}(r_i + r_j)}}, \qquad (17)$$

where r_i and r_j are the radii (cm) of particles i and j, respectively. Also, D_i (or D_j) is the particle diffusion coefficient (cm^2 s^{-1}) defined as

$$D_i = \frac{k_B T}{6\pi r_i \eta}\left\{1 + Kn_i\left[A + B\exp\left(-CKn_i^{-1}\right)\right]\right\}, \qquad (18)$$

which simplifies to the Stokes-Einstein formula in the continuum regime ($Kn_i \ll 1$). In (18), $Kn_i = \lambda_g / r_i$ is the Knudsen number of particle i, k_B is Boltzmann's constant, T is the temperature (K), η is the dynamic viscosity of air, and A, B, and C are corrections for particle resistance to motion (see Millikan, 1923). We normally use the values $A = 1.249$, $B = 0.42$, and $C = 0.87$, suggested by Kasten (1968).

In addition, the mean free path (cm s^{-1}) of a gas molecule is

$$\lambda_g = \frac{2\eta}{\rho_g \bar{v}_g}, \qquad (19)$$

where ρ_g is the density of air, and $\bar{v}_g$ is the mean thermal velocity of an air molecule. The thermal velocity of an air molecule is similar to that of a particle of size i,

$$\bar{v}_g \quad \text{or} \quad \bar{v}_{pi} = \left(\frac{8k_B T}{\pi m_i}\right)^{1/2}, \qquad (20)$$

except that, for a particle of size i, m_i is the mass of the particle, and for an air molecule, m_i is the mass of the air molecule. Finally, Fuchs defined the mean distance from the center of a sphere reached by particles leaving the surface of the sphere and traveling a distance of particle mean free path λ_{pi} as

$$\delta_i = \frac{\left\{\left(2r_i + \lambda_{pi}\right)^3 - \left(4r_i^2 + \lambda_{pi}^2\right)^{3/2}\right\}}{6r_i\lambda_{pi}} - 2r_i, \tag{21}$$

where

$$\lambda_{pi} = \frac{8D_i}{\pi\bar{v}_{pi}}. \tag{22}$$

In the continuum regime Equation (17) simplifies to its numerator, while in the free molecular regime ($Kn_i \gg 10$) it simplifies to

$$\beta_{i,j}^B = \pi\left(r_i + r_j\right)^2 \left(\bar{v}_{pi}^2 + \bar{v}_{pj}^2\right)^{1/2}. \tag{23}$$

IV. TESTS OF THE ALGORITHM

To demonstrate the basic features of the coagulation solution scheme, we present tests against Smoluchowski's analytical solution, two numerical solutions, an analytical solution to a self-preserving distribution, and a published comparison. In the first test, we compared our semi-implicit coagulation solution to the analytical solution of Smoluchowski (1918 -- see also Hidy and Brock, 1970; Seinfeld, 1986). Smoluchowski's solution applies to an initial distribution where all particles are of uniform size (monodisperse) and composition, and where the coagulation kernel (β) is

285

constant for all interactions. The monodisperse distribution is the narrowest possible distribution. The size bin grid used for Smoluchowski's solution has a monomer structure (as discussed earlier), which is arranged so that the volume of the kth bin equals k multiplied by the volume of the first ($k = 1$) bin. Given an initial number concentration C^t in the first bin, Smoluchowski predicted that the concentration at any time $t + 1$ (or $t + \Delta t$) in bin k is

$$C_k^{t+1} = \frac{C^t \left(0.5\beta C^t \Delta t\right)^{k-1}}{\left(1 + 0.5\beta C^t \Delta t\right)^{k+1}}.$$

(24)

Using a constant $\beta = 8 k_B T / 3\eta$ and an initial number concentration of 10^6 cm^{-3}, we compared Smoluchowski's solution to our solution after a 12 hours simulation period (Figure 2). For the semi-implicit scheme, we calculated one case with $V_{RAT} = 1.2$ (39 bins per decade) another with $V_{RAT} = 1.5$ (18 bins per decade), and a third with $V_{RAT} = 2$ (11 bins per decade). Because the semi-implicit and analytical solutions extend over bin-widths of different sizes, we divided the number concentrations in Figure 2 by d log D_p to normalize them. Also, for the geometric size grid, when $V_{RAT} < 1.62$ and particles in the first bin coagulate with particles in the second bin, the resulting particles are larger than the third bin. Thus, a dip will occur in the concentration of the second bin. To remedy this, we made the volume of the second bin equal to two times the volume of the first bin ($V_{RAT} = 2$ for the second bin only), which is the same ratio as that between the first and second bin of the monomer structure. Since the semi-implicit solution is independent of the bin structure, the modification to the second bin when $V_{RAT} < 1.62$ requires no other changes.

286

Figure 2 also shows a solution to this monodisperse initial distribution generated by SMVGEAR, a Gear-type solver of ordinary differential equations (Jacobson and Turco, 1993). With SMVGEAR, we solved Equation (2) simultaneously for 1000 monomer size bins. Equation (2) applied to the given bin structure resulted in a non-sparse matrix of partial derivatives with order 1000. Since 1000 monomer bins covers only one decade in radius space and the matrix of partial derivatives has no sparsity, we conclude that solving the monomer structure with an integrator is inefficient for atmospheric models. However, as Figure 2 shows, SMVGEAR provided an exact solution to this problem.

By comparison, the semi-implicit method gave solutions that approached the analytical solution as V_{RAT} decreased. At $V_{RAT} = 1.2$, the semi-implicit solution almost matched the exact solution for the full range of sizes shown, while for larger values of V_{RAT} and large diameters, numerical diffusion increased. To obtain the semi-implicit solutions, we took a series of 600-second time-steps during the 12-hour simulation period. Using a larger (*e.g.* three hour) or smaller (*e.g.* 60 second) time-step hardly changed the results. For example, with $\Delta t = 3$ hours and $V_{RAT} = 1.2$, the semi-implicit solution resulted in less numerical diffusion than it did with $\Delta t = 600$ and $V_{RAT} = 1.5$. Thus, the time-step had a smaller effect on numerical diffusion than did the size bin resolution. Finally, the semi-implicit solution exactly conserved volume in all cases. As V_{RAT} decreased, bin resolution increased, and the total number concentration of particles approached the correct value. This held true for all the cases tested in Figures 2 - 4.
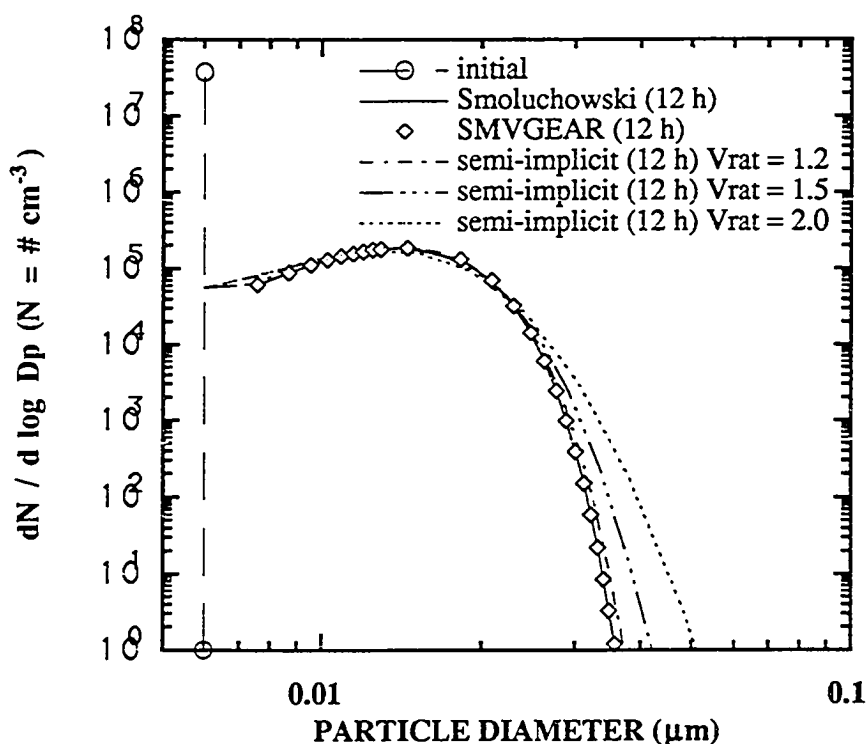
Fig. 2. Comparison of semi-implicit and integrated coagulation results to Smoluchowski's analytical solution. The coagulation period was 12 hours, the initial distribution was monodisperse, and the coagulation kernel was constant. For each of the three semi-implicit cases (V_{RAT} = 1.2, 1.5 and 2.0), the time-step was 600 seconds. We used SMVGEAR to solve 1000 equations and unknowns to produce an integrated solution to Equation (2) for 1000 monomer size-bins. The first bin for the Smoluchowski and SMVGEAR solutions were omitted from the graph since the lower bin diameter in both cases was zero, making dlogDp infinite.

In the second and third tests, we compared two time-series of semi-implicit solutions against those of integrated solutions. For these result, we started with initial

288

lognormal distributions, both with mean diameter 0.02 μm and number concentration of 10^6 cm^{-3}. In one case (Figure 3a) the initial geometric standard deviation was 1.4, and in the other (Figure 3b), the deviation was 1.15. We integrated Equation (2) with SMVGEAR, using 5500 monomer size bins for Figure 3a and 2000 bins for Figure 3b. In both cases, we solved the semi-implicit equations using V_{RAT} = 1.2, 1.5, and 2.0. However, Figures 3a and 3b show only the V_{RAT} = 1.2 time-series solutions. In both cases, the figures show that the semi-implicit solutions followed the integrated solutions almost exactly at each the 2-, 4-, and 6-hour marks. Again, we used a 600-second time-step for the semi-implicit solutions. A larger or smaller time-step hardly changed the results. However, increasing V_{RAT} increased numerical diffusion at higher diameters, although not so much as in Figure 2.

For the conditions of Figures 2, 3a, and 3b, the characteristic time for coagulation, $\tau = 2 / \beta C^t$, was less than one hour. Thus, the time intervals used (6 to 12 hours) were reasonably long enough to test for numerical diffusion.

289
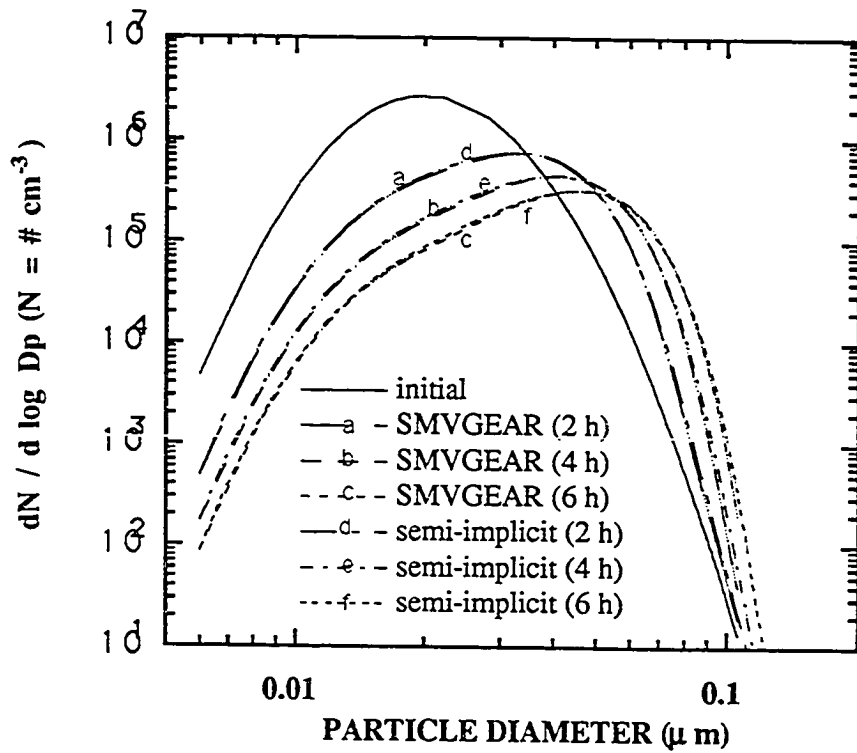
(Figure 3a)

Figs. 3a and 3b. Comparisons of semi-implicit to integrated coagulation results when the initial distributions were lognormal. The initial mean number diameter and concentration in both figures were 0.02 μm and 10^6 cm^{-3}, respectively. The initial geometric standard deviation was 1.4 in Figure 3a and 1.15 in Figure 3b. The coagulation kernel was constant and the same as in Example 1. The coagulation period was 6 hours, with results shown every two hours. For each of the semi-implicit cases, V_{RAT} was 1.2 and the time-step was 600 seconds. We used SMVGEAR to solve Equation (2) over 5500 monomer size bins (5500 equations and unknowns) for Figure 3a and 2000 bins for Figure 3b.

290
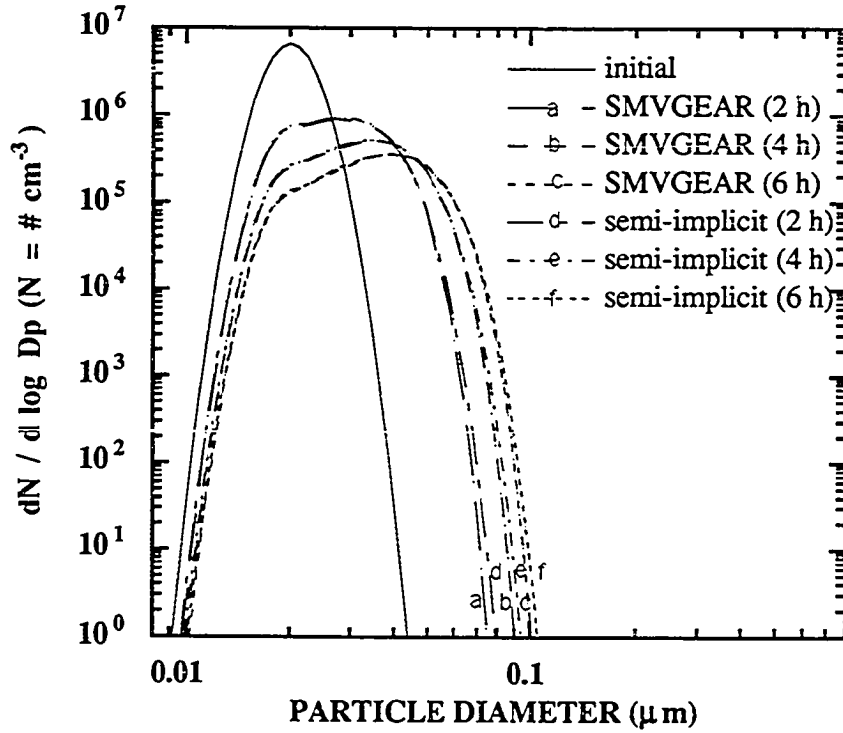
(Figure 3b)

In the fourth test, we compared the semi-implicit scheme to an analytical solution of a self-preserving distribution described in Seinfeld (1986). For this solution, the initial number density, C^t, of a uniform aerosol was spread exponentially about bin i $= p$, where υ_p is the volume of bin p. At any time t, coagulation changed the number concentration in size bin i to

$$C_i^{t+1} = \frac{C^t \, d\upsilon_i/\upsilon_p}{\left(1+0.5\beta C^t \Delta t\right)^2} \exp\left[-\frac{\upsilon_i/\upsilon_p}{\left(1+0.5\beta C^t \Delta t\right)}\right]. \tag{25}$$

For the geometric size grid,

291

$$dv_i = 2v_i \frac{V_{RAT} - 1}{V_{RAT} + 1}. \tag{26}$$

To compare solutions, we used the same initial number concentration and coagulation kernel as in the previous examples. Also, the peak volume diameter was 0.1 μm while the time-step and total coagulation period were 600 seconds and 12 hours, respectively. Figure 4 shows results when $V_{RAT} = 1.5$ and $V_{RAT} = 2$. The semi-implicit solution followed the analytical solution except at large sizes, where numerical diffusion caused some error. However, with decreasing V_{RAT}, numerical diffusion decreased while with a smaller or larger time-step (not shown), the results changed insignificantly.
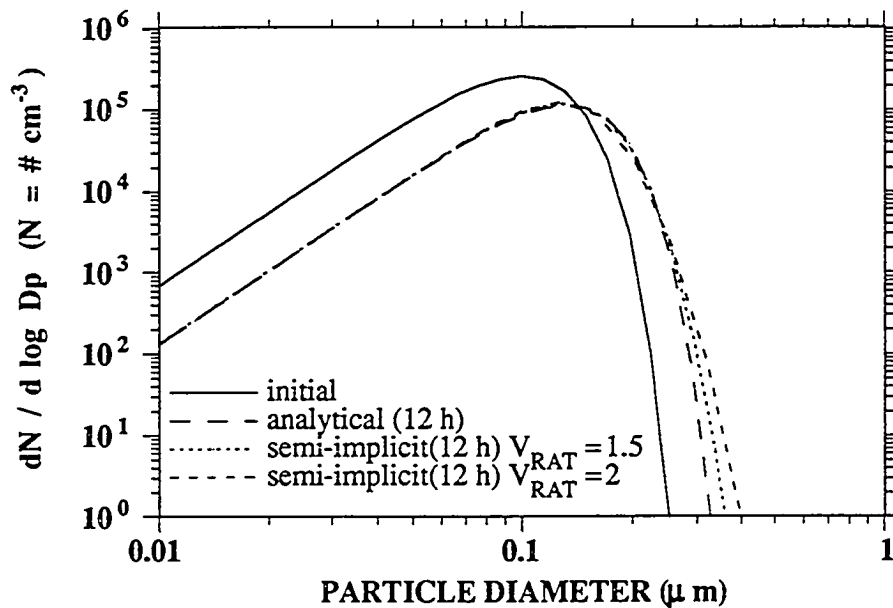
Fig. 4. Comparison of semi-implicit coagulation results to the analytical solution of Equation (25). The coagulation period was 12 hours, the initial distribution centered about a peak at 0.1 μm diameter, and the coagulation kernel was constant. The figure

292

shows semi-implicit solutions for V_{RAT} = 1.5 and V_{RAT} = 2. The time-step for the semi-implicit method was 600 seconds.

In the fifth test we compared the semi-implicit scheme to results from the continuous representation, J-space transformation model (COAGUL) of Suck and Brock (1979), as shown in Seigneur et al. (1986). The aerosol tested was uniform in composition and had an initial tri-modal distribution with mean volume diameters of 0.038, 0.32, and 5.7 μm, geometric standard deviations of 1.8, 2.16, and 2.21, and volumes of 0.63, 38.4, and 30.8 μm^3 cm^{-3}, respectively, in each mode (data from Whitby, 1978). The only coagulation rate term used was that for Brownian coagulation (Equation 29). Figure 5 shows results of the comparison after 12 hours of simulated coagulation. The semi-implicit model predicted the aerosol distribution similarly to that of COAGUL. Furthermore, semi-implicit coagulation conserved volume exactly, decreased the number density of particles, and moved particles to larger sizes. Because this was a model to model comparison, it is difficult to determine the extent of numerical diffusion.

293
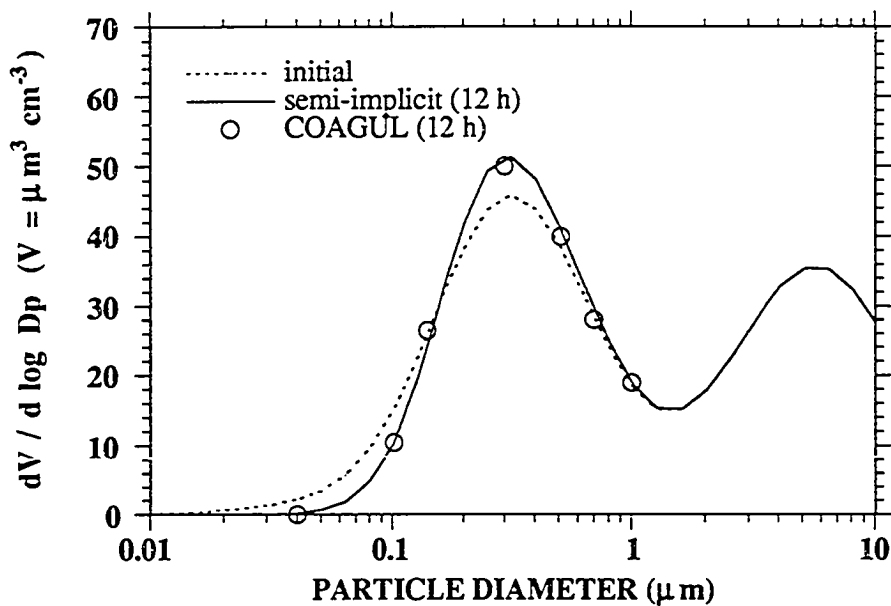
Fig. 5. Comparison of results from the semi-implicit scheme to those of COAGUL (Suck and Brock, 1979 -- results shown in Seigneur et al., 1986). The coagulation period was 12 hours, the initial distribution was tri-modal (Whitby, 1978), and the kernel was that for Brownian motion only. For the semi-implicit model, $\Delta t = 600$ seconds, $V_{RAT} = 2$, $r_1 = 0.005$ μm, and $N_B = 40$.

V. APPLICATION OF THE ALGORITHM

Here, we apply the semi-implicit model to a multicomponent set of aerosols and concentrations that could exist in an automobile tunnel. The purpose of the demonstration is to show the features, speed, and volume conservation of our mechanism and to suggest that pure particles quickly coagulate to become mixed

294

particles in a particle-rich environment. The only process included in this simulation was coagulation.

For the example, we used the species and conditions listed in Table 2. For modeling purposes, we separated elemental and organic carbon into separate EM types with one component each, constructed the organic carbon size distribution different from that of elemental carbon, and put no initial carbon in IM particles. Elemental carbon and other particles are not spherical in reality; however, we modeled them as such for simplicity. Because the semi-implicit model is independent of the size-bin structure, it can coagulate particles of odd shapes so long as the kernel is modified and average particle shapes are known.

Among the data we used were size-resolved elemental carbon data gathered from the Caldecott Tunnel (Venkataraman, 1992). We also assumed that the ratio of elemental to organic carbon particle concentrations in the tunnel was 1.4 (Hering *et al.*, 1984). Finally, we fit lognormal distributions to all carbon data.

Because vehicles emit little sulfur, we assumed sulfate entered the tunnel with other background material. For modeling purposes, we placed about 90% of initial sulfate in IM particles and 10% in EM particles. We assumed the sulfate distributions were tri-modal and used the *urban average* geometric mean volume diameter and standard deviation from Whitby, 1978 for the nuclei and accumulation modes. We also assumed a nuclei plus accumulation mode sulfate mass of 5.0 μg m^{-3} and distributed the mass among these two modes and the IM and EM types. For the coarse mode of sulfate, we used a size and mass distribution from Noll *et al.* (1990).

Finally, we distributed nitrate in the IM type using a tri-modal distribution. For the coarse mode, we used a size and mass distribution from Noll *et al.* (1990). For the other modes, we used the same distribution as for sulfate, but set a smaller mass

295

loading. Nitrate was the only species in the IM type which did not also appear in an EM type.

Table 2. Initial distribution of IM and EM aerosols. The distributions of each are the sum of their volume fraction distributions. D_{gv} is the geometric mean volume diameter and σ_g is the geometric standard deviation of each mode.

Particle	Nuclei Mode			Accumulation Mode			Coarse Mode		
	Mass (μg m^{-3})	D_{gv} (μm)	σ_g	Mass (μg m^{-3})	D_{gv} (μm)	σ_g	Mass (μg m^{-3})	D_{gv} (μm)	σ_g
1. EM1									
1a Elemental C	67	0.107	1.66	0	0	0	0	0	0
2. EM2									
2a Organic C	47.6	0.136	1.50	0	0	0	0	0	0
3. EM3									
3a. Sulfate	0.008	0.04	1.8	0.49	0.32	2.16	0.05	12.3	2.4
3b. Water	0.012	0.04	1.8	0.74	0.32	2.16	0.075	12.3	2.4
4. IM									
4a. Elemental C	0	0	0	0	0	0	0	0	0
4b. Organic C	0	0	0	0	0	0	0	0	0
4c. Sulfate	0.072	0.04	1.8	4.43	0.32	2.16	0.45	12.3	2.4
4d. Water	0.1	0.04	1.8	5.00	0.32	2.16	2.0	12.3	2.4
4e.Nitrate	0.003	0.04	1.8	2.0	0.32	2.16	2.5	8.1	2.4

Figure 6 shows the initial and final sum of the volume distributions of the four particle types we coagulated for this application. Coagulation of four types behaved similarly to self-coagulation of a single type containing the same initial distribution as the sum of the four separate distributions. The figure also shows that coagulation affected the size distribution of particles primarily less than one micron in diameter.
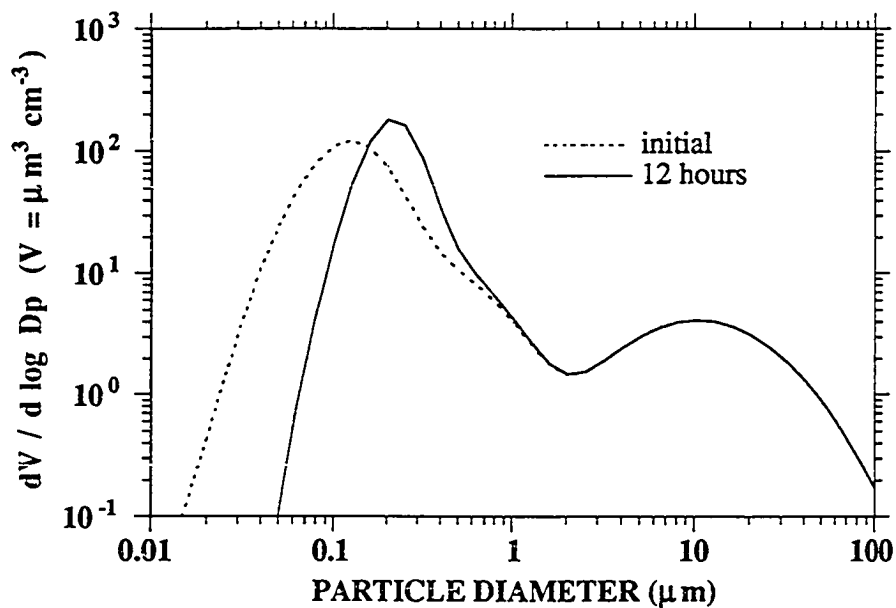
Fig. 6. Volume distribution of the sum of EM and IM particle distributions before and after 12 hours of coagulation. Coagulation moved the sum of the distribution of small particles towards larger sizes. Large particles tended to coagulate with much smaller particles, hardly affecting the total volume distribution of the large particles. While the sum of the coarse volume distributions changed little, the distribution of individual particle types changed dramatically (Figures 7-9).

By summing all volume in EM and IM particles before and after coagulation, we found that the semi-implicit mechanism exactly conserved volume. Furthermore, by summing the volume of each EM type and its IMVF counterpart, both before and after coagulation, we found that heterogeneous coagulation exactly conserved volume.

Figure 7 shows the individual changes in EM and IM particle size distributions. Many EM particles hetero-coagulated to become IM particles. Since most initial particles were small, most accumulation of IM particles occurred at sub-micron sizes.

297
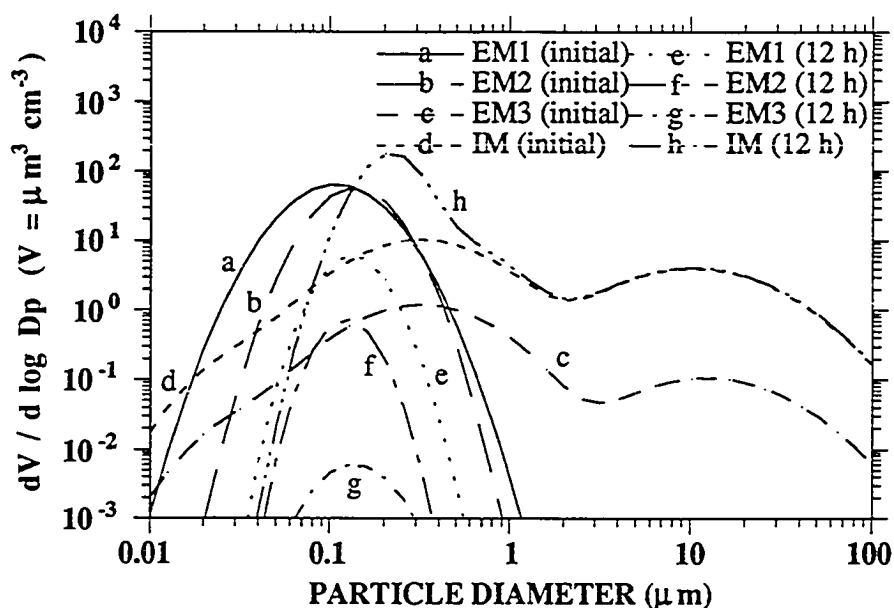
Fig. 7. Change in volume distributions due to 12 hours of coagulation. EM1 is elemental carbon, EM2 is organic carbon, EM3 is the sulfuric acid - water mixture, and IM is the internally-mixed type. Most volume shifted from EM to IM particles. Addition to the IM coarse mode is hardly noticeable since few large particles existed initially, and they usually coagulated with small particles.

Figures 8 and 9 show the initial and final distribution and composition, respectively, of the IM type. Initially, IM particles contained only sulfate, nitrate and water, in small amounts. Subsequently, significant amounts of carbon coagulated with and became part of IM particles, drowning out other sub-micron components.

298
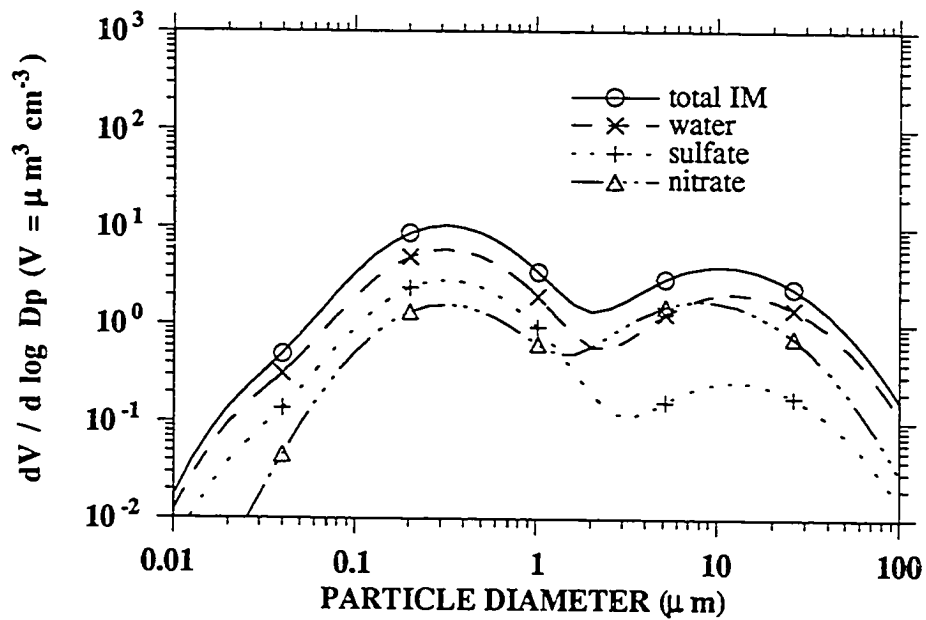
Fig. 8. Initial composition and size distribution of IM particles. IM particles initially consisted of water, sulfate, and nitrate, but no elemental or organic carbon. *Total IM* is the sum of the volumes of water, sulfate, and nitrate. Table 4 details the initial distributions.

299
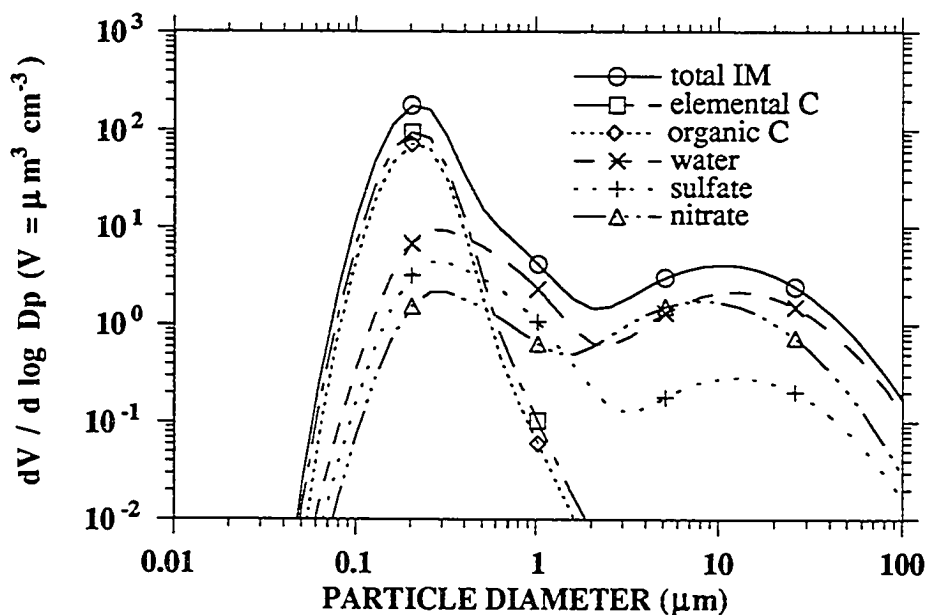
Fig. 9. Composition and size distribution of IM particles after 12 hours of coagulation. *Total IM* is the sum of the volumes of elemental and organic carbon, water, sulfate, and nitrate. Coagulation moved a significant amount of elemental and organic carbon from EM to IM particles.

To obtain the computer results for this application, we used seventy-two 600 second time-steps for a total of 12 hours. Also, we set $V_{RAT} = 2$, $r_1 = 0.005$ μm, $N_B = 41$, and $T = 298$ K. The 12-hour simulation over one spatial grid-cell took 1.25 seconds of CPU time on a CRAY Y-MP. Because we vectorized the coagulation code over the grid-cell dimension, increasing the number of grid-cells decreases the time to solve per grid-cell. For example, the same solution, over 16,000 grid-cells, took 571 seconds at a speed of 209 megaflops. Since we used 41 size bins, 11 distinct aerosol components, and 72 time-steps, the required time was 1.1×10^{-6} seconds per grid-cell per size bin per component per time-step.

300

In another coagulation example, not shown here, we ran a simulation with the same 600-second time-step and 12-hour interval, but with six components and 18 size bins. Over a 16,000-cell grid domain, the solution took 126.4 seconds at a speed of 205 megaflops. Thus the time required was 1.0×10^{-6} seconds per grid-cell per size bin per component per time-step, similar to the time in the example above.

VI. CONCLUSION

We have presented a model to compute coagulation among any number of particle types, each containing any number of components. The scheme is volume conserving and unconditionally stable, uses any time step, and solve over any size bin structure. With a geometric distribution as described in this paper, the scheme can solve for all cases where the volume ratio of adjacent bins (V_{RAT}) exceeds one. The solution mechanism discussed is an expansion of the semi-implicit numerical schemes of Turco *et al.* (1979a,b) and Toon et al. (1988). Because the code requires no iterations, it uses little computer time. With the model, we can study effects of coagulation on particle composition and size-distribution. For example, we can simulate coagulation of particles of the same size but of different composition.

The equations shown for multiple particle types assume that whenever a particle of one type coagulates with a particle of another type, the resulting particle enters a multicomponent mixture representing all particle types. In reality, hetero-coagulation results in unique types. We discussed a straightforward method of modifying the equations to account for all possible particle combinations. However, including all combinations drastically increases the number of aerosol constituents. Beyond a small

301

number of spatial grid-cells, aerosol components, and size bins, assuming unique particle types upon hetero-coagulation presses most computer memory limits.

In this paper, we compared results to two analytical solutions, two time-series numerical solutions, and a published solution. In all comparisons, the results matched very well with $V_{RAT} = 1.2$ and reasonably well with $V_{RAT} = 1.5$ to 2.0. With larger values of V_{RAT}, numerical diffusion increased at larger size bins. Finally, we demonstrated the use of the model in a slightly more complicated application. The results of the application suggest that single component particles quickly hetero-coagulate with particles of other types when the air is particle-rich. Along with coagulation, however, other processes -- such as growth, evaporation, nucleation, deposition, advection, chemical reaction, and emissions -- affect aerosol size and composition. Thus, calculating the effects of all processes, not just of coagulation, is important for simulating particle size and composition.

VII. REFERENCES

Friedlander S. K. (1983) Dynamics of aerosol formation by chemical reaction. *Ann. NY Acad. Sci.* **404**, 354 - 364.

Fuchs N. A. (1964) *The Mechanics of Aerosols.* (R. E. Daisley and M. Fuchs, Translation) Pergamon Press, New York.

Gelbard F. and Seinfeld J. H. (1980) Simulation of multicomponent aerosol dynamics. *J. Colloid Interface Sci.* **78**, 485-501.

Hidy G. M. and Brock J. R. (1970) *The Dynamics of Aerocolloidal Systems*, Chap. 9, Pergamon Press, Oxford.

Hirschfelder J., Curtiss J. and Bird R. (1951). *Molecular Theory of Gases and Liquids.* Wiley, N. Y..

Jacobson M. Z. and Turco R. P. (1993) SMVGEAR: A sparse-matrix, vectorized Gear code for Atmospheric models. *Atmospheric Environment, Part A*, in press.

Kasten F. (1968) Falling speed of aerosol particles. *J. Appl. Meteorol.* **7**, 944-947.

Kim Y. P. and Seinfeld J. H. (1990) Numerical solution of the multicomponent aerosol general dynamic equation. *Proc. 3rd Int. Aerosol Conf., Science, Industry, Health and Environment*, pp. 138-141. Pergamon Press, Oxford.

Lushnikov A. A. (1975) Evolution of coagulating systems. *J. Colloid Interface Sci.* **54**, 94-101.

Main H. H. and Friedlander S. K. (1990) Dry deposition of atmospheric aerosols by dual tracer method - I. Area source. *Atmospheric Environment* **24A**, 103-108.

Millikan R. A. (1923) The general law of fall of a small spherical body through a gas, and its bearing upon the nature of molecular reflection from surfaces. *Phys. Rev.* **22**, 1.

Muller H (1928) *Kolloidbeihefte* **27**, 223.

Noll K. E., Fang K. Y. P. and Khalili E. (1990) Characterization of atmospheric coarse particles in the Los Angeles Basin. *Aer. Sci. Technol.* **12**, 28 - 38.

Ouimette J. J. and Flagan R. C. (1982) The extinction coefficient of multicomponent aerosols. *Atmospheric Environment* **16**, 2405-2419.

Pruppacher H. R. and Klett J. D. (1978) *Microphysics of Clouds and Precipitation*. Reidel, The Netherlands.

Saffman P. G. and Turner J. S. (1956) On the collision of drops in turbulent clouds. *J. Fluid Mech.* **1**, 16-30.

Seigneur C. (1982) A model of sulfate aerosol dynamics in atmospheric plumes. *Atmospheric Environment* **16** 2207 - 2228.

Seigneur C., Hudischewskyj A. B., Seinfeld J. H., Whitby K. T., Whitby E. R., Brock J. R. and Barnes H. M. (1986) Simulation of aerosol dynamics: A comparative review of mathematical models. *Aerosol Sci. Tech.* **5**, 205-222.

Seinfeld J. H. (1986) *Atmospheric Chemistry and Physics of Air Pollution*. John Wiley, New York.

Sitarski M. and Seinfeld J. H. (1977). Brownian coagulation in the transition regime. *J. Colloid Interface Sci.* **61**, 261-271.

Smoluchowski M. V. (1918) Versuch einer mathematischen theorie der koagulationskinetik kolloider losungen. *Z. Phys. Chem.* **92**, 144.

Strom J., Okada K. and Heintzenber J. (1992) On the state of mixing of particles due to Brownian coagulation. *J. Aerosol Sci.* **23** 467-480.

Suck S. H. and Brock J. R. (1979) Evolution of atmospheric aerosol particle size distributions via Brownian coagulation: Numerical simulation. J. *Aerosol Sci.* **10**, 581-590.

Toon O. B., Turco R. P., Westphal D., Malone R. and Liu M. S. (1988) A Multidimensional model for aerosols: Description of computational analogs. *J. Atmos. Sci.* **45**, 2123-2143.

Tsang T. H. and Brock J. R. (1982) Aerosol coagulation in the plume from a cross-wind line source. *Atmospheric Environment* **16**, 2229-2235.

Turco R. P., Hamill P., Toon O. B., Whitten R. C. and Kiang C. S. (1979a) A one-dimensional model describing aerosol formation and evolution in the stratosphere. Part I: Physical processes and mathematical analogs. *J. Atmos. Sci.* **36**, 699-717.

Turco R. P., Hamill P., Toon O. B., Whitten R. C. and Kiang C. S. (1979b) The NASA-Ames Research Center Stratospheric Aerosol Model: I Physical Processes and Computational Analogs. *NASA Tech. Publ. (TP) 1362, iii-94.*

Venkataraman C. (1992) Polycyclic aromatic hydrocarbon and elemental carbon size distributions in Los Angeles aerosol: Source resolution and deposition velocities. Ph.D. Thesis, Dept. of Chemical Engineering, Univ. of California, Los Angeles.

Waggoner A. P., Weiss R. E., Ahlquist N. C., Covert D. S., Will S. and Charlson R. J. (1981) Optical characteristics of atmospheric aerosols. *Atmospheric Environment* **15**, 1891-1909.

Warren D. R. and Seinfeld J. H. (1985) Simulation of aerosol size distribution evolution in systems with simultaneous nucleation, condensation, and coagulation. *Aerosol Sci. Technol.* **4**, 31 - 43.

Whitby K. T. (1978) The physical characteristics of sulfur aerosols. *Atmospheric Environment* **12** 135-159.

VIII. APPENDIX

Table 3. Example set of aerosols used to describe coagulation among particles of different size and composition. EM = externally-mixed particles, EMVFs = volume fractions of EM particles, IM = internally-mixed particles, and IMVF = volume fraction of IM particles.

```
--------------------------------------------------------------------------------
```

AEROSOL #   DESCRIPTION OF TYPE

```
--------------------------------------------------------------------------------
```

AEROSOL #	DESCRIPTION OF TYPE
1	EM1 (MADE OF EMVF1a)
2	EMVF1a (ONLY VOLUME FRACTION OF EM1)
3	EM2 (MADE OF EMVF2a AND EMVF2b)
4	EMVF2a (FIRST VOLUME FRACTION OF EM2)
5	EMVF2b (SECOND VOLUME FRACTION OF EM2)
6	IM (MADE OF IMVFa-f)
7	IMVFa (CONTAINS SAME MATERIAL TYPE AS EMVF1a)
8	IMVFb (CONTAINS SAME MATERIAL TYPE AS EMVF2a)
9	IMVFc (CONTAINS SAME MATERIAL TYPE AS EMVF2b)
10	IMVFd (APPEARS ONLY IN IM)
11	IMVFe (APPEARS ONLY IN IM)
12	IMVFf (APPEARS ONLY IN IM)

PARAMETER DEFINITIONS AS APPLIED TO TABLE 3

N_B = Total number of aerosol size bins.

N_T = Total number of aerosol types (EM plus IM). Does not include volume fractions (N_T= 3 in Table 3).

N_E = Total number of EM types ($N_E = N_T$ - 1 = 2 in Table 3).

V_N = Total number of volume fractions of each N = 1, N_T aerosol type (V_1 = 1, V_2

= 2, V_3 = 6 in Table 3).

306

T_N = Total number of components of each $N = 1, N_T$ aerosol type. $T_N = 1 + V_N$. In

Table 3 $T_1 = 2, T_2 = 3$, and $T_3 = 7$.

$L_{N,U}$ = Aerosol number of each $U = 1, T_N$ component of each $N = 1, N_T$ aerosol type.

Table 4 lists example values resulting from Table 3.

$S_{Q,I}$ = Aerosol number mapping each $Q = L_{N,U}$ IM component to each EM

component that hetero-coagulates to form a portion of Q. Table 4 lists

example values resulting from Table 3.

$$C^t_{L_{N,1}j} = \sum_{m=1}^{V_N} C^t_{L_{N,m+1}j} \cdot \text{(Total number concentration of particles of type } N \text{, size } j\text{)}.$$

Since all concentrations, including those of volume components, are in units

of # cm^{-3}, the sum of the *number concentrations* of all volume fractions of

type N, size j equals the total number concentration of particles of that type

and size. Similarly, the total volume of a particle (cm^3 particle^{-1}) multiplied

by the number concentration of one of its volume fractions equals the volume

concentration (cm^3 cm^{-3}) of the volume fraction.

Table 4. Arrays of species numbers for the parameters $L_{N,U}$ and $S_{Q,M}$. N varies from 1

to N_T, U varies from 1 to T_N, and I varies from 1 to N_E. The values apply to Table 3.

	<-$N=1$->		<--- $N=2$ --->			<----------- $N=3$ ---------->						
U	1	2	1	2	3	1	2	3	4	5	6	7
$Q = L_{N,U}$	1	2	3	4	5	6	7	8	9	10	11	12
	<----------------------- $S_{Q,I}$ ---------------------->											
$I=1$	0	0	0	0	0	1	2	0	0	0	0	0
$I=2$	0	0	0	0	0	3	0	4	5	0	0	0

Appendix D

Paper -- Simulating Condensational Growth, Evaporation, and Coagulation of Aerosols Using a Combined Moving and Stationary Size Grid

SIMULATING CONDENSATIONAL GROWTH, EVAPORATION, AND COAGULATION OF AEROSOLS USING A COMBINED MOVING AND STATIONARY SIZE GRID

Mark Z. Jacobson and Richard .P. Turco
Department of Atmospheric Sciences, 405 Hilgard Ave. University of California, Los Angeles, CA 90024-1565

We present a numerical method of simulating the aerosol processes of coagulation, condensational growth, and evaporation over a hybrid size grid. In the hybrid grid, the volume of involatile core material is constant for each size bin, but the volume of volatile material fluctuates. Since particles in each bin grow and evaporates at their own pace, particles from one bin can obtain the same volume as those from another bin while maintaining different composition. Similarly, particles from different bins that grow to the same size can evaporate back to their respective original core sizes. Allowing independent growth of particles inhibits numerical diffusion since particles in each bin grow or evaporate to their actual sizes. When two particles coagulate, they form a new particle with core volume between the core volumes of particles in two other bins. We partition the new particle and its total volume between these two bins. Similarly, we adapt other processes, such as nucleation, emissions, and transport to the hybrid grid structure. The condensational growth equations developed conserve mass between the gas phase and size-distributed aerosol phase. Because the equations result in sparse matrices of partial derivatives, SMVGEAR, a sparse-matrix Gear-type integrator, solves them quickly. Furthermore, the semi-implicit coagulation equations used here conserve volume exactly, are absolutely stable, and require no iteration. Finally, we compared model solutions to both analytical and other integrated numerical

solutions. To obtain numerical solutions, we developed and integrated equations that simulate simultaneous coagulation and growth of multicomponent particles.

I. INTRODUCTION

Atmospheric models often simulate aerosol processes such as nucleation, coagulation, condensational and dissolutional growth, chemical equilibrium, aqueous chemistry, and transport. Currently, several numerical schemes are available to treat condensational growth and evaporation. Among these are discrete size bin (sectional) methods (*e. g.* Turco *et al.*, 1979a,b; Gelbard and Seinfeld, 1980; Seigneur, 1982; Warren and Seinfeld, 1985; Pilinis *et al.*, 1987a; Toon *et al.*, 1988; Rao and McMurry, 1989), finite element methods (Varoglu and Finn, 1980; Tsang and Brock, 1983, 1986; Tsang and Huang, 1990), modified upwind difference methods (*e. g.* Smolarkiewicz, 1983; Tsang and Korgaonkar, 1987; Kim and Seinfeld, 1990a), moments methods (*e. g.* Friedlander, 1983; Whitby, 1985; Lee, 1985; Brock et al., 1986; Brock and Oates, 1987), the cubic spline method (*e. g.* Middleton and Brock, 1976), and moving (or variable) bin methods (*e. g.* Mordy, 1959; Neiburger and Chien, 1960; Gelbard, 1990; Kim and Seinfeld, 1990b).

We define a stationary size bin as one where the volume of each particle in the bin is constant and the same as the volume of each other particle in the bin. When a particle grows (or evaporates), it transfers from its current bin to a bin containing larger (or smaller) particles. A moving bin, on the other hand, is one where the volume of each particle in the bin changes, and changes at the same rate as the volume of each other particle in the bin. Thus, when a particle grows (or evaporates), it stays in its current bin but increases (or decreases) in volume.

310

Every growth scheme has advantages and disadvantages associated with it. A disadvantage of many schemes is numerical diffusion, which lowers peak concentrations and spreads the distribution over a wider size interval. Numerical diffusion occurs in stationary bin models because, when mass moves to a larger or smaller bin, it often distributes itself uniformly throughout the bin. As a result, the distributed mass can quickly grow or evaporate to the next highest or lowest bin the very next time step. For a comparison of the levels of numerical diffusion in different growth models, refer to Tsang and Rao (1988).

Another problem is numerical dispersion, which appears as waves ahead of or behind the regions of high concentration. Typically, finite element methods without "upwinding" create dispersion, while those with "upwinding" eliminate dispersion but create diffusion (Tsang and Brock, 1983).

A third problem is the tracking of involatile material in multicomponent particles after growth. For example, when particles grow to a narrow distribution (*e. g.* in a fog) in a stationary bin model, the core material agglomerates into a few bins. Subsequently, when the particles evaporate, the aggregated materials cannot redistribute back to their original sizes unless additional information is stored.

A fourth obstacle is conserving mass of both gas and aerosols during growth. Often, growth models subtract off the amount of gas removed by aerosol growth. However, subtracting can result in negative gas concentrations, requiring subsequent adjustments. Thus, solving for the gas and aerosol concentrations together improves solutions to the growth equations.

For this paper, we used a moving size grid for growth and evaporation to overcome the problems stated above but maintained a stationary grid structure for other processes. We also derived and solved growth equations that conserve mass when it transfers from a gas to size-distributed aerosols. Among the first to use the moving bin

311

method, Mordy (1959) and Neiburger and Chien (1960) calculated condensational growth of cloud droplets. Recently, Gelbard (1990) also discussed a moving bin growth model that Kim and Seinfeld (1990b) expanded for multicomponent aerosols. Advantages of the moving bin method are that it avoids both numerical diffusion and dispersion (Gelbard, 1990; Kim and Seinfeld, 1990b).

For other processes, such as coagulation, emissions, and nucleation, we maintained the characteristics of a stationary grid. In the case of coagulation, we modified the equations described in Jacobson et al. (1994a) for the hybrid size grid. Jacobson et al. expanded upon the semi-implicit method of Turco et al. (1979a, b) and Toon et al. (1988) to permit coagulation over any size grid and among any number of particle types, each with a different size distribution and composition.

While several models have treated single-component coagulation and condensation together (e. g. Middleton and Brock, 1976; Gelbard and Seinfeld, 1978; Warren and Seinfeld, 1985; Tsang and Hippe, 1988; Wu and Flagan, 1988), fewer have treated multicomponent coagulation and condensation simultaneously (e. g. Bassett et al., 1981; Toon et al., 1988; Kim and Seinfeld, 1990a; among others). The model developed here combines moving bin growth with stationary bin coagulation for multicomponent and / or multitype aerosols.

The next section discusses growth, coagulation, and other processes using different size bin structures, and Section III describes the condensational growth equations we use. Finally, Section IV compares results to analytical and numerical solutions and Section V shows applications of the model.

312

II. COMPARISON OF SIZE BIN STRUCTURES

When simulating multicomponent aerosols, we can use one of several size bin structures. In this section, we compare advantages and disadvantages of just three -- a completely stationary grid, a hybrid stationary-moving grid, and a completely moving grid structure.

For all cases, we assume one multicomponent particle type and define the sum of the volumes of involatile material (*e. g.* elemental carbon, dust, and involatile organic carbon) in a particle as the *core volume* of the particle. Non-core material can either condense onto, equilibrate with, or react with core surfaces and can dissolve into water after water condenses. We define all secondary liquids, solids, and ions that accumulate onto cores as *volatiles*, and define the *total volume* of a particle as the volume of core plus volatile material in the particle.

In all three particle grid structures, we start with any number of distinct size bins covering any range of diameters. Also, each bin contains any number of particles, and the number of particles, summed over all bins, equals the total number of particles in the system at a given time. Particle number in each bin can increase through nucleation, emissions, and transport and can decrease through deposition, sedimentation, and transport. Also, particles can change in size through condensational growth, dissolutional growth, and evaporation. Finally, while coagulation reduces total particle number, it moves particles to large sizes. Below, we discuss the differences between the three grid structures and how we treat physical processes in each.

A. *Full Stationary Grid*

In a stationary grid structure, particles size bins are initialized in order of increasing total (core plus volatile) volume. For example, we can initialize size bins

with a geometric distribution, where the total volume of particles in one size bin equals the total volume of particles in the previous size bin multiplied by a constant (V_{RAT}). Thus, if we set $V_{RAT} = 2$, then each particle in size bin B has twice the total volume of each particle in size bin A and each particle in bin C has twice the volume of each particle in bin B, etc.

Further, in the full stationary structure, each particle in a given bin at a given time has the same total volume as each other particle in the bin, and that volume is the constant, characteristic volume of particles in the size bin. However, while each bin contains any number of particles, the number changes in time as a result of various physical processes. For example, suppose we initialize a bin structure with $V_{RAT} = 2$ and the volume of particles in the smallest bin (A) equal to 1 (generic units). Then, the volumes of particles in bins B, C, D, and E equal 2, 4, 8, and 16, respectively. Each bin contains any number of particles. Now, suppose one particle from bin B coagulates with one particle from bin C. The volume of the one resulting particle is 6, which is not represented exactly by either particle bin A, B, C, D, or E. Thus, to conserve particle number and volume, we partition half of the one new particle to bin C (volume of 4) and half to bin D (volume of 8). Consequently, coagulation reduces the number of particles in bin B by one, in bin C by one-half, and increases the number of particles in bin D by one-half. Further, coagulation conserves volume of the coagulated particles. However, each particle in bins A, B, C, D, and E still has its initial total volume (core plus volatile volume). Thus, the primary characteristic of a stationary grid is that particles in a given bin always have a constant, characteristic total volume; however, particles can move to larger or smaller bins.

Similarly, when growth (or evaporation) occurs over a stationary grid structure, individual particles move from one size bin to a larger (or smaller) size bin. For example, if a particle of total volume 2 (bin B) grows to volume 6, then one particle is

314

removed from bin B, one-half particle is added to bin C (volume 4), and one-half particle is added to bin D (volume 8). Thus, again, the characteristic total volume of each particle in each bin remains constant, but the number of particles in each bin changes.

Further, when emission or homogeneous nucleation occurs, certain bins gain additional particles; however, the volume of a particle in a given bin does not change. When transport occurs, particles move to nearby grid cells and replace particles that have the same total volume; thus, particles are removed from a given size bin in one spatial grid cell and added to the same size bin in an adjacent grid cell.

A second characteristic of a stationary grid relates to how components are mixed within the particles. While the total volume of a particle in a bin is constant, the core volume can range from zero to the total volume. Similarly, while the total volume of a particle in bin C is greater than the total volume of a particle in bin B by a factor of V_{RAT}, the core volume of a particle in bin C may be either greater than, equal to, or smaller than the core volume of a particle in bin B. Figure 1 illustrates how the total volumes of individual particles in three consecutive size bins (*e.g.* A, B, C) increase, but the core volumes are distributed without a pattern.

315
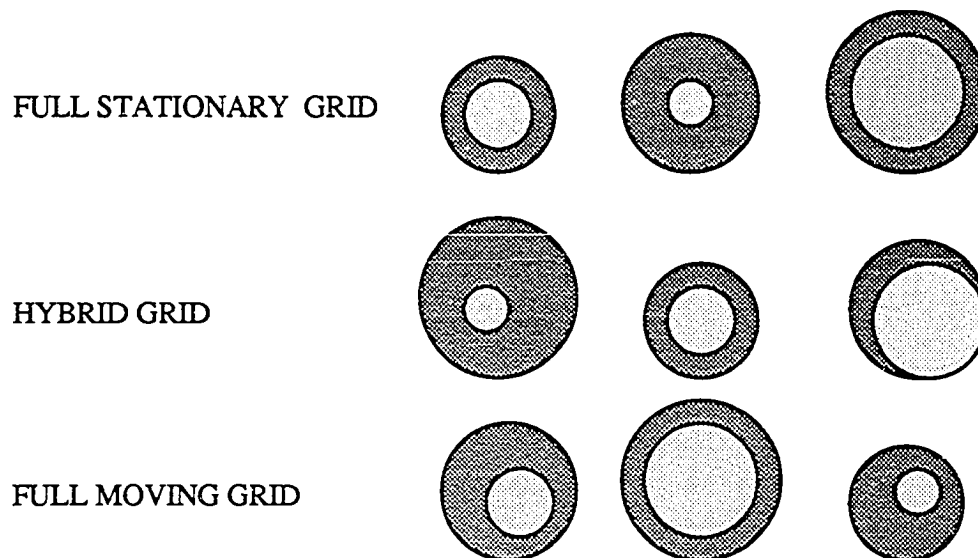
Fig. 1. Example of sizes and compositions of representative particles in three size grid structures. For each size structure, we show three particles, each representing a different size bin. Each particle shown has two components -- an involatile core and a volatile secondary component. In all structures, each size bin contains any number of particles, but all particles in a bin have the same composition and size. Thus, we represent each bin here by a single particle. In the case of the full stationary grid, the total volume (core plus volatile volume) of each particle in the first bin is smaller than the total volume of each particle in subsequent bins. However, the core volume of particles distributes randomly from one bin to the next. In the case of the hybrid grid, the core volume of each particle in the first bin is smaller than the core volume of each particle in subsequent bins. However, the total volume of particles distributes without pattern from one bin to the next. Last, in the case of the full moving grid, both core and total volumes of particles are initially ordered, but become distributed randomly from one bin to the next due to coagulation, growth, emissions, nucleation, transport, and other processes.

316

A stationary grid structure is most useful for simulating coagulation, nucleation, particle emission, and transport. However, it often leads to numerical diffusion during condensation and evaporation. For example, when growth occurred in the earlier example, half of a particle of volume 6 was placed in a bin with particles of volume 8, spreading the distribution artificially. Diffusion can also occur with coagulation; but, since coagulation rates are usually much slower than growth rates, diffusion is less significant with coagulation. Another problem with stationary bin growth is the loss of resolution when particles grow. For example, when aerosols activate into a fog in a stationary grid, core material from many small size bins moves into one or two large bins. By analogy, suppose all particles from bins B, C, and D grow to bin E. When particles move to bin E, volumes are averaged so that all particles in bin E have the same core and total volume. Upon evaporation, the core materials that agglomerated in bin E should evaporate back to the bins they came from. However, unless information is stored, the core materials do not "remember" whether they came from bin B, C, or D, and their redistribution becomes fairly arbitrary.

B. *Hybrid Grid*

A way to remedy the problems with condensational growth is to combine the stationary size bin structure with a moving bin structure in a hybrid model. In the hybrid bin structure, particle bins are initialized in order of increasing core (involatile) volume (Figure 1) as opposed to increasing total volume. For example, suppose we define V_{RATc} as the volume ratio of adjacent core bins. Thus, if $V_{RATc} = 2$ and the core volume of the smallest bin (A) equals 0.1 (generic units), then the core volumes of particles in bins B, C, D, and E equal 0.2, 0.4, 0.8, and 1.6, respectively. Each core bin -- A, B, C, D, and E -- contains any number of particles of the same average core size.

317

Also, each particle in a given bin contains the same amount of volatile material as each other particle in the bin; but, this amount is variable. In sum, while the total volume is fixed and the core volume is variable for each particle while it resides in a given stationary size bin, the core volume is fixed and the total volume is variable for each particle while it resides in a given hybrid size bin.

When growth occurs in a stationary grid structure, particles are transferred to bins where particles have larger or smaller total volume. However, in a hybrid structure, particles are not transferred; instead, their total volumes increase or decrease to their exact sizes, eliminating numerical diffusion. For example, suppose a particle in core bin B grows from total volume 0.2 (initial core volume) to total volume of 1.3 (core plus final volatile volume). Under the stationary structure, the resulting particle would be partitioned between two size bins -- one with particles of total volume smaller than and one with particles of total volume larger than 1.3. However, under the hybrid structure, particles keep their exact volume, and no particles are transferred to larger or smaller bins during growth. Thus, when the particle of total volume 1.3 evaporates, it evaporates back to its original core size of 0.2. Similarly, when a fog forms, particles in bins B, C, and D can all grow to approximately the same size, say volume 16. Upon evaporation, all particles in bins B, C, and D shrink to their original sizes of 0.2, 0.4, and 0.8. Thus, the hybrid grid eliminates two problems associated with the stationary structure -- numerical diffusion and loss of information upon evaporation.

When coagulation occurs in a stationary structure, two particles collide to form a new particle. The new particle and its total volume are partitioned between two bins -- one with particles of total volume smaller than and one with particles of total volume larger than the total volume of the new particle. When coagulation occurs in a hybrid structure, two particles also collide to form a third particle. However, in this case, we partition the new particle and its total volume between two different bins -- one with

318

particles of core volume smaller than and one with particles of core volume larger than the core volume of the new particle. Thus, the main difference between coagulating in the stationary and fixed structures is how we treat the resulting particle. In reality, this new particle has unique shape and size different from those of all other particles in the atmosphere. However, with limited computer resources, we need to fit the new particle into an imperfect model size structure.

When emission of involatile material occurs in the hybrid grid, we assume the new particles enter the bin containing particles with core volume the same as the core volume of the new particles. Thus, the composition of new particles is an average composition of new and existing particles of the same core size.

When emission or homogeneous nucleation of volatile material occurs, we assume the new particles enter the bin containing particles with core volume that is the same as the total volume of the new volatile particles. By definition, these volatile particles have zero core volume. Because we mix particles containing core material with those without core material in such cases, the average core volume in a size bin decreases below the characteristic (initial) core volume of the bin. However, it never increases above the characteristic core volume. To simulate coagulation under these conditions, we assume that, when two particles combine, they form a third particle of characteristic core volume that falls between the characteristic core volume of two adjacent particles.

When transport occurs in the hybrid grid, and no volatile emissions occur, we assume particles move and replace other particles with the same core volume. Thus, the final core volume in each size bin and grid cell after transport is always the same as the initial core volume. When volatile emissions or nucleation accompany transport, we assume particles move and replace other particles with the same initial core volume.

319

C. *Full Moving Grid*

Finally, in a completely moving bin model, particles in each bin can have any core and total volume, and both the core and total volumes of particles in the bin can change during the simulation (Figure 1). For example, we can initialize bins A, B, C, D, and E with any core and volatile volume. Each bin contains any number of particles, and each particle in a bin has the same size and composition as each other particle in the same bin. Over time, however, both core and volatile volumes of each bin can change.

To treat coagulation over the full moving grid, we first rearrange particle bins from smallest to largest total volume each time step. When two particles coagulate, we partition the new particle and its total volume between two size bins -- one with particles smaller than and one with particles larger than the volume of the new particle. Growth in a full moving grid occurs in the same manner as in a hybrid grid.

However, a full moving bin structure causes problems with respect to emissions, nucleation, and transport. For example, if most moving bins grow to become fog-sized drops, then few bins remain to put newly emitted particles into. In the hybrid bin case, the new particles are placed into bins that have the same core volumes as those of the emitted particles, and in the stationary bin case, the new particles are placed into bins that have the same total volumes as those of the emitted particles. Also, in the full moving bin case, when particles from all bins grow to the same total size, they have no bin to coagulate into. In a stationary grid, particles coagulate to bins with larger total volume and in a hybrid grid, particles coagulate to bins with larger core volume.

Finally, when transport occurs in a completely moving grid, there is no way to know which particles replace which other particles in adjacent grid cells. In the hybrid case, particles of a given core volume replace others with the same core volume, and in the stationary bin case, particles of a given total volume replace others with that volume.

320

In sum, we use the hybrid structure because, unlike the completely stationary structure, it allows growth without numerical diffusion and allows particles to evaporate back to their original core sizes. Furthermore, unlike the completely moving structure, it permits reasonable treatment of coagulation, nucleation, emissions, and transport of particles. Next we derive growth equations and describe a method to solve them.

III. METHOD OF SOLVING GROWTH EQUATIONS

In an ideal model, we would solve the rate equations for gas-phase processes simultaneously with those for gas-aerosol transfer, inter-aerosol processes, intra-aerosol processes, and spatial transfer. While such calculations are possible on a small scale with an integrator of stiff ordinary differential equations, they currently require too much computer time for large spatial domains and aerosol size grids. A more practical approach to solving aerosol processes is to time-split (solve independently) some groups of processes while solving other groups simultaneously. With this latter approach in mind, we time-split condensational growth from coagulation and other processes.

For the most part, growth equations usually ignore the reduction in gas-phase concentrations. Here, we present and solve equations that conserve mass between the gas and aerosol phase. For the model, we assume any number of aerosol types and any number of components and size bins within each type. In the equations, N_T is the number of particle types and N_B is the number of size bins, which is the same for all types. An example of a system with three aerosol types is one which contains an elemental carbon-water type, an organic carbon-water type, and an elemental carbon-organic carbon-water type. Jacobson et al. (1994a) give a more complete description of

321

aerosol types. In the example here, the core volume of each type consists of elemental carbon, organic carbon, and elemental plus organic carbon, respectively. The volatile material, water, can condense on all three types.

For multitype particles and a hybrid (or moving) size structure, we write the volume rate of growth or evaporation of a volatile component over a single particle as

$$\frac{d\upsilon_{VNi}}{dt} = \left(48\pi^2\right)^{1/3} A v_m D^{eff}_{VNi} \upsilon_{Ni}^{1/3}\left(G_V - P_V^o B_{VNi}\right),\qquad (1)$$

where υ_{VNi} is the volume (cm^3 particle^{-1}) of component V within a single particle of type N and bin i. The subscript N denotes the particle type (e. g. elemental carbon-water, organic carbon-water, or the mixture) and the subscript VN denotes each volatile component (e. g. water) of each particle type. For example each of the three particle types contains one volatile component. Thus, the Ns refer to particle types and VNs refers to individual volatile components that make up particle types.

Also in Equation (1), A is Avogadro's number (molecules mole^{-1}), v_m is the volume of a gas molecule (cm^3 molec^{-1}), G_V is the ambient concentration and P_V^o is the saturation vapor density (both in moles-gas cm^{-3}-air) of gas V condensing onto particle-type N. Furthermore,

$$D^{eff}_{VNi} = \frac{D_V' \eta_{dNi} F_{vNi}}{1 + \dfrac{D_V' \eta_{dNi} F_{vNi} L_{e,V}^2 M_V^2 G_V}{K' \eta_{tNi} F_{tNi} R T^2}}\qquad (2)$$

is a modified gas diffusion coefficient (cm^2 s^{-1}). Factors that affect the diffusion coefficient, D_V', are the geometry of vapor collision with small particles (e. g. Langmuir, 1944; Rooth, 1957; Mordy, 1959; Pruppacher and Klett, 1978, Toon et al.,

322

1989) and ventilation of heat and vapor during sedimentation of large particles containing liquid (*e. g.* Frossling, 1938; Keith and Arons, 1954; Beard and Pruppacher, 1971; Pruppacher and Klett, 1978; Toon *et al.*, 1989). In Equation (2), $L_{e,V}$ is the latent heat of evaporation (cm^2 s^{-2}) and M_V is the molecular weight of the condensing gas (g $mole^{-1}$). Also, R is the universal gas constant (erg $mole^{-1}$ K^{-1}), T is the temperature (K), K' is the thermal conductivity of air (erg cm^{-1} s^{-1} K^{-1}), and F_V and F_t are ventilation factors of condensing vapor and heat, respectively (unitless). Furthermore,

$$\eta_{dNi} = \left\{ 1 + \left[\frac{1.33 + 0.71 Kn_{dNi}^{-1}}{1 + Kn_{dNi}^{-1}} + \frac{4(1 - \alpha_{\alpha N})}{3\alpha_{\alpha N}} \right] Kn_{dNi} \right\}^{-1} \quad \text{and} \quad (3)$$

$$\eta_{tNi} = \left\{ 1 + \left[\frac{1.33 + 0.71 Kn_{tNi}^{-1}}{1 + Kn_{tNi}^{-1}} + \frac{4(1 - \alpha_{\tau N})}{3\alpha_{\tau N}} \right] Kn_{tNi} \right\}^{-1} \quad (4)$$

are corrections to diffusivity and thermal conductivity, respectively, due to collision geometry and sticking probability (Fuchs and Sutugin, 1971; Pruppacher and Klett, 1978; Toon *et al.*, 1989). In Equations (3) and (4) Kn_{dNi} and Kn_{tNi} are the Knudsen numbers of the condensing vapor and of air, respectively, α_{α} is the sticking coefficient of the condensing vapor, and a_{τ} is the thermal accommodation coefficient (Pruppacher and Klett, 1978 and Toon *et al.*, 1989).

Next, in Equation (1),

$$B_{VNi} = \left(1 + \frac{L_{e,V} M_V Q_{rad,Ni}}{4\pi r_{Ni} RT^2 K' \eta_{tNi} F_{tNi}} \right) \exp\left\{ \frac{2\sigma_V M_V}{r_{Ni} RT \rho_V} \right\} \quad (5)$$

323

is a series of adjustments to the saturation vapor pressure. Surface tension (Kelvin effect), ion content (solute effect), and radiative cooling (Barkstrom, 1978; Toon *et al.*, 1989) alter the saturation vapor pressure of a gas over a particle. For example, the Kelvin effect increases the saturation vapor pressure over small particles, the solute effect decreases it over small and medium-sized drops, and the radiative effect decreases it over large drops. Equation (5) accounts for the Kelvin effect and radiative cooling only. The solute effect can be treated either with simple parameters or with an extensive equilibrium model. In Equation (2) σ_V is the surface tension (dynes cm^{-1}) and ρ_V is the density (g cm^{-3}) of the condensed gas. Also, $Q_{rad,Ni}$ is the radiative heating rate (erg s^{-1} -- *ibid.*) and r_{Ni} is the current radius (cm) of size bin i of particle-type N.

Finally, in Equation (1)

$$\upsilon_{Ni} = \upsilon_{VNi} + \upsilon_{ONi} \tag{6}$$

is the volume of a single particle of type N, in bin i. The volume of the particle is the volume of the condensed gas in the particle plus the volume of all other material in the particle (υ_{ONi}). We rewrite the volume of the condensed species as $\upsilon_{VNi} = C_{VNi} / C_{Ni}$, where C_{VNi} is the aerosol volume concentration (cm^3-aerosol cm^{-3}-air) of component V in Ni particles, and C_{Ni}, is the number concentration (No. cm^{-3}-air) of Ni particles. Similarly, the volume of all other material in one particle is $\upsilon_{ONi} = Y_{ONi} / C_{Ni}$, where Y_{ONi} is the volume concentration (cm^3-aerosol cm-^{3}-air) of all other material in Ni particles. Combining (1) with the values in (6), we write the change in the volume concentration of condensed species VN in bin i as

$$\frac{dC_{VNi}}{dt} = C_{Ni}^{2/3} \left(48\pi^2\right)^{1/3} D_{VNi}^{eff} \left(Y_{ONi} + C_{VNi}\right)^{1/3} \frac{M_V}{\rho_V} \left(G_V - P_V^o B_{VNi}\right). \tag{7}$$

324

To conserve mass between the gas and aerosol phases, we express the rate of change of gas concentration as

$$\frac{dG_V}{dt} = -\frac{\rho_V}{M_V} \sum_{N=1}^{N_T} \left\{ \sum_{i=1}^{N_B} \frac{dC_{VNi}}{dt} \right\}. \tag{8}$$

Thus, the change in gas phase concentration is proportional to the negative of the sum, over all size bins and particle types, of the change in aerosol-phase concentrations.

To obtain gas and size-distributed volatile aerosol concentrations from Equations (7) and (8), we need to solve $N_T \times N_B + 1$ nonlinear, first-order ordinary differential equations. The equations are even more nonlinear if we express the radius in the Kelvin term as a function of condensed aerosol concentration.

An accurate way to solve the coupled equations is with an integrator of stiff ordinary differential equations. The integrator we used, SMVGEAR (Jacobson and Turco, 1994), speeds the solution to first order equations in a large grid domain because it takes advantage of the sparsity of the matrix of partial derivatives and vectorizes around the grid-cell dimension. Since the matrix of partial derivatives resulting from (7) and (8) requires zero fill in, SMVGEAR takes relatively little time to solve the coupled sets of these equations. When solving (7) and (8) with an integrator, we set maximum values of dC_{VNi} / dt and its corresponding partial derivative terms during evaporation to prevent negative values of C_{VNi}. The solution to (7) and (8) is an adjusted volume concentration of each size bin and an adjusted gas concentration. Thus, particles from different bins increase or decrease in size at their own pace, as we intended with the hybrid grid structure.

325

IV. COMPARISONS TO ANALYTICAL AND NUMERICAL SOLUTIONS

Here, we compare model results for condensational growth, coagulation, and a combination of the two, to results from both analytical and integrated numerical solutions. Jacobson *et al.* (1994a) compared the coagulation mechanism to several analytical and integrated numerical solutions; thus, we focus here primarily on testing growth alone and growth coupled to coagulation.

For the first test we compared model solutions of growth, coagulation, and a combination of both to an analytical solution given by Gelbard and Seinfeld (1978). The analytical solution assumes one particle type of uniform composition, with initial number concentration written as

$$C_i^t = \frac{C_{T,0}\, d\upsilon_i}{\upsilon_0} \exp\left(\frac{-\upsilon_i}{\upsilon_0}\right), \tag{9}$$

where $C_{T,0}$ is the total number of particles in the distribution, υ_i is the volume of particles in bin i, and υ_0 is mean initial volume of particles. The solution further assumes both a fixed growth rate and fixed coagulation kernel. The analytical (subscript a) number concentration resulting from this system is

$$C_{i,a}^{t+1} = \frac{4C_{T,0}\, d\upsilon_i}{\upsilon_0(\tau+2)^2} \exp\left(-\frac{2\upsilon_i}{\upsilon_0(\tau+2)}\exp(-\Lambda\tau) - \Lambda\tau\right), \tag{10}$$

where $\tau = C_{T,0}\,\beta_0\,t_f$ and $\Lambda = \sigma / (C_{T,0}\,b_0)$. In these last equations, β_0 is the coagulation kernel (cm^3 # s^{-1}), t_f is the time interval (s), and σ is a growth rate term (s^{-1}). Also, when plotting the analytical distribution over a stationary, geometric size bin structure,

we assumed $d\upsilon_i = 2\upsilon_i$ $(V_{RAT} - 1)$ / $(V_{RAT}+1)$, where $V_{RAT} = \upsilon_{i+1}$ / υ_i (as discussed earlier) is the volume ratio of adjacent size bins. Also, we used $\beta_0 = 8$ $k_B T$ / 3η, where k_B is Boltzmann's constant, T is temperature (K), and η is the dynamic viscosity of air, and assumed $C_{T,0} = 10^5$, $T = 298.15$ K, $t_f = 21{,}600$ s (6 hours), $V_{RAT} = 1.2$, and $\Lambda = 1$. For growth alone, $\beta_0 = 0$, and for coagulation alone, $\Lambda = 0$.

To obtain a model solution for comparison, we first initialized a distribution of uniformly composed, volatile particles, assuming $V_{RAT} = 1.2$. We then ran three cases: one with coagulation alone, one with coagulation combined with growth, and one with growth alone. In each case, we used thirty-six 600-second time steps. For coagulation combined with growth, we time-split (solved separately) the two processes.

To compute coagulation for this test, we modified the semi-implicit method discussed in Jacobson et al. (1994a). The lack of involatile material did not impede the calculations. For example, in the case of coagulation combined with growth, we assumed that when two particles coagulated, they formed a new particle with initial volume equal to the sum of the initial volumes of the two original particles. We then partitioned all volume of the new particle between two size bins that had initial volume smaller and larger, respectively, than the initial volume of the new particle.

Since the analytical solution required a fixed growth rate, we could not test Equations (7) and (8) for this particular comparison. We show results from these equations later. Instead, to solve for growth over the hybrid structure, we used

$$C_{vi,m}^{t+1} = C_{vi,m}^{t} + C_{i,m}^{t}\sigma\upsilon_i\Delta t, \tag{11}$$

where $C_{vi,m}^{t+1}$ is the model (subscript m) particle volume concentration (cm^3 cm^{-3}) in bin i after each Δt time step, and s is the growth term (calculated, in this instance, from the

expression for Λ, above). Also, $C_{i,m}^t$, for the first time step of the interval (t_f), is the initial number concentration from (9). The sum of $C_{i,m}^t$ over all size bins for the first time step equals C_{T_0}. When no coagulation occurs, both bin-resolved and total number concentrations remain unchanged during an entire interval. However, when coagulation occurs, the particle number in each bin changes. To simulate growth under these conditions, we used the value of $C_{i,m}^t$ in Equation (11) from the most recent coagulation calculation. Similarly, we used the value of $C_{vi,m}^t$ from the most recent coagulation and growth updates and the value of v_i from the most recent growth update. Coagulation does not change the volume of individual particles in a size bin but it does change the total volume of material in the bin.

Figure 2 compares analytical to model solutions for growth alone, coagulation alone, and coagulation combined with growth. It shows that the hybrid grid (which allows growth with moving bins) suppressed numerical diffusion during growth. Furthermore, for the value of V_{RAT} used (1.2), the coagulation equations suppressed diffusion. For larger values of V_{RAT} (lower bin resolution), numerical diffusion slightly increases during coagulation (Jacobson *et al.*, 1994a). Finally, Figure 2 shows that model results for growth combined with coagulation were similar to analytical results for all sizes.

328
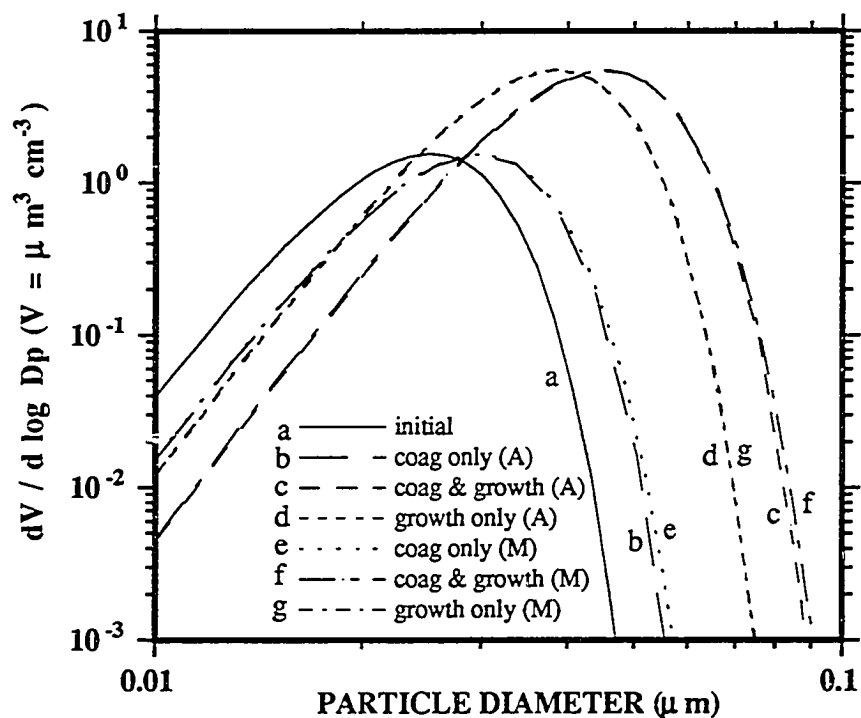
Fig. 2. Comparison of model results (M) to analytical solutions (A) for the processes of coagulation alone, coagulation combined with growth, and growth alone. The analytical solutions (Equation 10) are from Gelbard and Seinfeld (1978). The time interval for all solutions was six hours, and the time step used for the model solutions was 600 s. Also, $V_{RAT} = 1.2$ for the analytical solution and for the initial model size distribution (Equation 11). Remaining conditions are described in the text.

In the second test, we compared model results of coagulation combined with growth to fully-implicit integrated solutions calculated with SMVGEAR. For this example, we assumed that the size-distributed aerosol contained two components -- one

329

involatile and the other volatile. We assigned both components a hypothetical

molecular weight of 150 g mole^{-1} and an aerosol-phase density of 1.5 g cm^{-3}. Further,

we started with 10^6 particles cm^{-3} and distributed the particles and volume components

lognormally using a geometric mean number diameter of 0.02 μm and geometric

standard deviation of 1.4. Also, we assumed the gas-phase partial pressure of the

volatile material was 1.3 x 10^{-4} dynes cm^{-2} while its saturation vapor pressure was 7.5

x 10^{-6} dynes cm^{-2} (e. g. Experiment 23 A of Stern *et al.*, 1989). Finally, we assumed a

modified diffusion coefficient (D^{eff} - Equation [2]) of 0.1 cm^2 s^{-1}, a surface tension of

30 dynes cm^{-1}, a temperature of 298.15 K, and a radiative heating rate (Q_{rad}) equal to

zero.

To obtain the integrated numerical solution, we solved Equations (12) - (15),

written as

$$\frac{dC_k}{dt} = \frac{1}{2}\sum_{j=1}^{k}\left(\sum_{i=1}^{k}\frac{\upsilon_i+\upsilon_j}{\upsilon_k}f_{i,j,k}\beta_{i,j}C_iC_j\right) - C_k\sum_{j=1}^{N_B}\beta_{i,j}C_j, \qquad (12)$$

$$\frac{dC_{V_1k}}{dt} = \sum_{j=1}^{k}\left(\sum_{i=1}^{k}f_{i,j,k}\beta_{i,j}C_{V_1i}C_j\right) - C_{V_1k}\sum_{j=1}^{N_B}\beta_{i,j}C_j, \qquad (13)$$

$$\frac{dC_{V_2k}}{dt} = \sum_{j=1}^{k}\left(\sum_{i=1}^{k}f_{i,j,k}\beta_{i,j}C_{V_2i}C_j\right) - C_{V_2k}\sum_{j=1}^{N_B}\beta_{i,j}C_j + \left(\frac{dC_{V_2k}}{dt}\right)_{growth}, \text{ and } (14)$$

$$\frac{dG}{dt} = -\left(\frac{\rho_{V_2}}{M_{V_2}}\right)\sum_{i=1}^{N_B}\left(\frac{dC_{V_2k}}{dt}\right)_{growth}, \qquad (15)$$

330

simultaneously with SMVGEAR. Equation (12) describes the evolution of number concentration (No. cm^{-3}) of particles in each size bin, $k = 1$ to N_B, due to coagulation only. Equation (13) describes the evolution of volume concentration (cm^3 cm^{-3}) of involatile material (V_1), due to coagulation only. Equation (14) describes the change in volume concentration of volatile material (V_2) due to coagulation, condensational growth, and evaporation. Finally, (15) describes the change in concentration of the condensing gas (moles cm^{-3}) due to growth and evaporation. Equation (7) shows the growth derivative referred to in (14) and (15).

In the equations, $\beta_{i,j}$ is the rate at which particles of size i coagulate with particles of size j. Also, $f_{i,j,k}$ is the volume fraction of new particles $i + j$ that we partition into bin k. Many values for f are zero; thus, all calculations involving a zero-value for f were eliminated. Jacobson *et al.* (1994a) show the formulas for $\beta_{i,j}$ and the values for f.

While Jacobson *et al.* (*ibid.*) discuss the fully implicit coagulation equations for a monomer size distribution and the semi-implicit equations for a random size distribution, Equations (12), (13), and (14) describe the fully implicit equations for a random size distribution. An advantage of these new equations is that we can solve coagulation over an entire size distribution with fully-implicit equations but with far fewer size bins than the monomer distribution requires. However, the matrix of partial derivatives for coagulation is full; thus, we cannot take advantage of sparse-matrix computer speed increases like we can with other processes such as chemistry and condensational growth.

For the integrated numerical solutions, we solved Equations (12) - (15) over one-half hour time intervals, using variable time steps predicted by SMVGEAR. On the other hand, for model solutions, we time-split coagulation from condensational growth and took three 600-second time intervals for each. For coagulation, the time step

331

equaled the time interval of 600 s. For growth, the time step varied within SMVGEAR. For model solutions to coagulation, we used the semi-implicit method, discussed previously.

For model solutions to growth, we solved Equations (7) and (8) simultaneously with SMVGEAR. However, model solutions found with SMVGEAR were different from integrated solutions in one important respect. When time-splitting growth from coagulation, the only variables that we assumed changed during a time step of growth were the gas-phase concentration and aerosol volume of the condensing component. On the other hand, when solving growth and coagulation simultaneously with SMVGEAR, we assumed that the number of particles and the volume of involatile material in each bin changed along with those two parameters. Thus, the matrix of partial derivatives for the fully-integrated solution was much more complex than the matrix for the time-split integrated solution. The advantage of a time-split growth solution is large with respect to computer speed since the matrix of growth partial derivatives is sparse. On the other hand, since the matrix of coagulation partial derivatives in the fully-integrated case is already full, we cannot take advantage of sparse-matrix reductions when we add growth partial derivatives to it.

In sum, the fully-integrated solution is more accurate than the model solution because it solves Equations (12) - (15) exactly under the conditions provided. However, we desired to test how well a time-split solution that included a combination of semi-implicit and fully-implicit techniques compared to the fully-integrated result. Figures (3a) and (3b) show two of the comparisons. For Figure (3a), we ignored the Kelvin effect while for Figure (3b), we did not. The figures show that the model solutions for both whole-particle volume and volatile-component volume matched the integrated solutions at all sizes.

332

In the case of Figure (3a), the gas-phase partial pressure decreased to the saturation vapor pressure before the end of one-half hour; thus, growth ceased. In the case of Figure (3b), the partial pressure decreased to an effective saturation vapor pressure. Since the Kelvin effect modifies the saturation vapor pressure differently for different-sized particles, vapor continuously transferred between the gas and aerosol phases. However, after one-half hour, the saturation vapor pressure reached a point where particles above about 0.02 μm were growing from Kelvin-effect transfer and those below had evaporated down to their original cores. Finally, these model solutions required about fifteen times less computer time than did the fully integrated solutions.
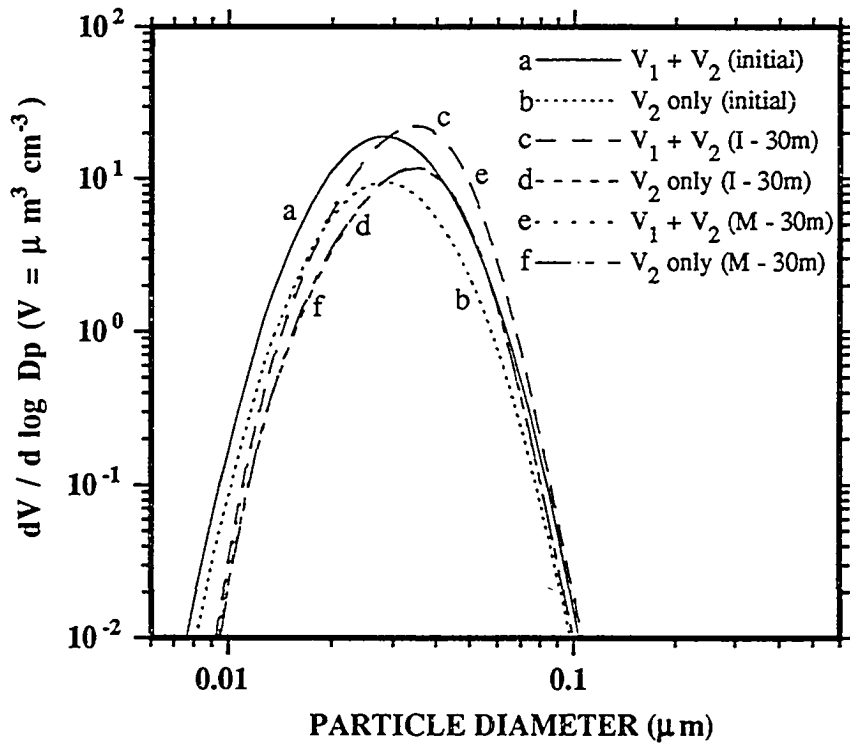
Fig. 3a
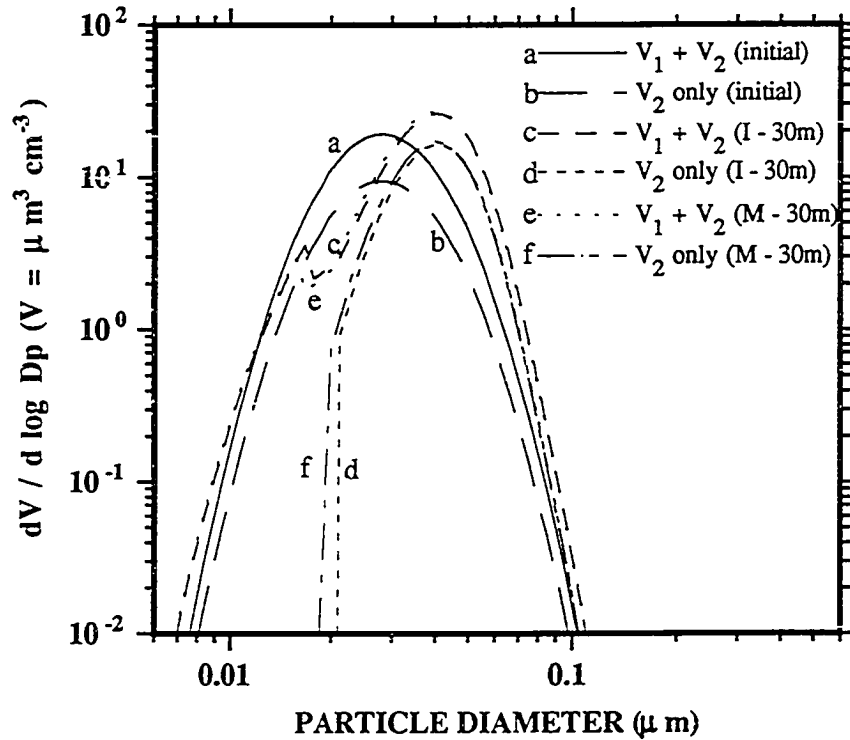
Fig. 3b.

Figs. 3a and 3b. Comparisons of model (M) to integrated (I) solutions for the processes of coagulation combined with growth. The particles simulated here contained two components -- an involatile core (V_1) and a volatile shell (V_2). Thus, $V_1 + V_2$ identifies the total particle. Equations (7) and (8) describe the growth equations used for both figures. However, the difference between Figures 3a and 3b are that 3a ignores the Kelvin effect while 3b includes it. To obtain the integrated solutions, we used SMVGEAR to solve Equations (12) - (15), simultaneously, over a continuous time interval. To obtain the model solution, we time-split the semi-implicit coagulation solution from the fully implicit growth solution. The time interval for both analytical

334

and model solutions was one-half hour while the time step for splitting model processes was 600 s. The text describes additional conditions for these simulations.

In the third set of tests, we compared model growth to an analytical solution shown in Seinfeld (1986). For this solution, particles are uniformly composed and initially distributed lognormally. The analytical number concentration (# cm^{-3}) in each bin i, resulting from the growth of the initial distribution, is

$$C_{i,a}^{t+1} = \frac{C_{To}}{\sqrt{2\pi} \ln \sigma_g} \frac{d_i \, \mathrm{d} d_i}{\left(d_i^2 - 2A_D t_f\right)} \exp\left[-\frac{\ln^2\left(\left(d_i^2 - 2A_D t_f\right)^{1/2} \Big/ d_{gno}\right)}{2 \ln^2 \sigma_g} \right], \quad (16)$$

where d_{gno} is the initial geometric mean number diameter (cm) of the distribution, σ_g is the geometric standard deviation, A_D is a constant growth term (cm^2 s^{-1}) dependent on the diffusion coefficient, saturation ratio, and saturation vapor pressure, d_i is the mean particle diameter (cm) of each discrete bin i, and

$$\mathrm{d} d_i = d_i 2^{1/3} \frac{V_{RAT}^{1/3} - 1}{\left(V_{RAT} + 1\right)^{1/3}} \quad (17)$$

is the width of discrete bin i for the initial bin structure.

In order to compare moving bin growth solutions to analytical solutions, we fixed the growth rate of each moving bin as

$$C_{vi,m}^{t+1} = C_{vi,m}^t + C_i^t \pi r_i A_D \Delta t, \quad (18)$$

which is similar to (11). As with (11), we grew each bin for several time steps during a time interval and updated the radius and number concentration before each model time step. Table 1 lists initial parameter values, time steps, and time intervals for three model comparisons to analytical solutions. It also shows the final aggregated particle volumes from the analytical and model solutions.

TABLE 1. Initial distributions and final volumes of three model comparisons to analytical solutions.

	$^a d_{gno}$	$^b \sigma_g$	$^c C_{To}$	$^d V_{To}$	$^e V_{Taf}$	$^f V_{Tmf}$	$^g V_{RAT}$	$^h \Delta t$	$^i t_f$
	μm	-	$\# \, cm^{-3}$	$\mu m^3 cm^{-3}$	$\mu m^3 cm^{-3}$	$\mu m^3 cm^{-3}$	-	s	s
Figure 4	0.2	1.4000	2.260×10^7	1.57×10^5	2.45×10^5	2.46×10^5	1.5	1000.	10,000
Figure 5	0.1	1.1447	8.796×10^6	5.00×10^3	7.06×10^4	7.05×10^4	1.2	0.01	5
Figure 6	0.6	1.3084	6.387×10^6	1.00×10^6	1.34×10^6	1.34×10^6	1.5	100.	10,000

(a)   Mean geometric number diameter of the initial lognormal distribution.
(b)   Geometric standard deviation of the distribution.
(c)   Initial aggregated number concentration.
(d)   Initial aggregated volume.
(e)   Final aggregated volume from the analytical solution.
(f)   Final aggregated volume from the model solution.
(g)   Volume ratio of adjacent size bins, used for initializing.
(h)   Model time step.
(i)   Total time interval for the simulation.

Figure 4 shows the first comparison of analytical to model growth. The initial distribution parameters and the growth rate were from Seinfeld (1986), p. 421. The figure shows that the moving bin solution slightly underpredicted the lower radius bound of the final number concentration.

336
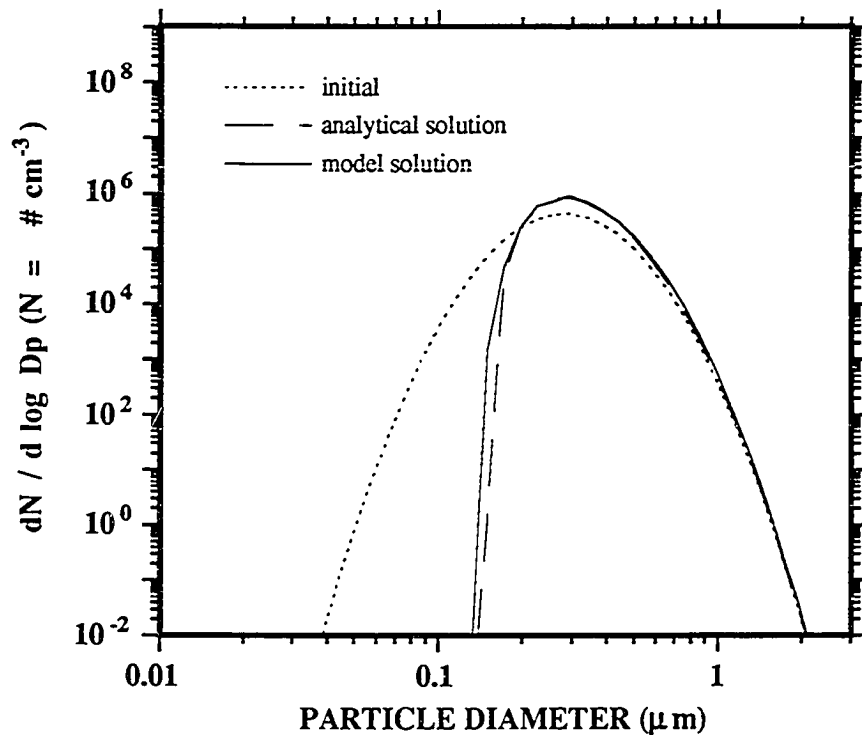
Fig. 4. Model versus analytical growth solutions. Table 1 lists the initial conditions, some parameter values, and final volume for this simulation. The constant growth term used was $A_d = 1.06 \times 10^{-14}$ cm² s⁻¹. To obtain the moving bin solution, we used Equation (18), and to obtain the analytical solution, we used Equation (16).

Figure 5a shows analytical versus model growth and Figure 5b shows model coagulation alone and model coagulation combined with growth. First, the initial distribution and growth rate for these simulations were similar to those presented in Figure 1 of Tsang and Rao (1988). Because the growth rate was fast, we reduced the model time step significantly and increased the number of bins per decade in the initial distribution to 39 (by decreasing V_{RAT} to 1.2). Figure 5a shows that, after five seconds,

337

the moving bin solution paralleled the analytical solution. However, it slightly underpredicted the lower radial end of the analytical distribution.

Figure 5b, shows coagulation alone and coagulation combined with growth. We did not compare these model solutions to analytical solutions. However, elsewhere in this paper and in Jacobson *et al.* (1994a), coagulation alone was compared to analytical solutions. The results here indicate that, under the conditions presented, both growth and coagulation pushed particles toward larger sizes, However, while coagulation widened the size distribution, growth narrowed it. Growth combined with coagulation also narrowed the distribution but pushed the leading edge of the distribution further than did growth alone.
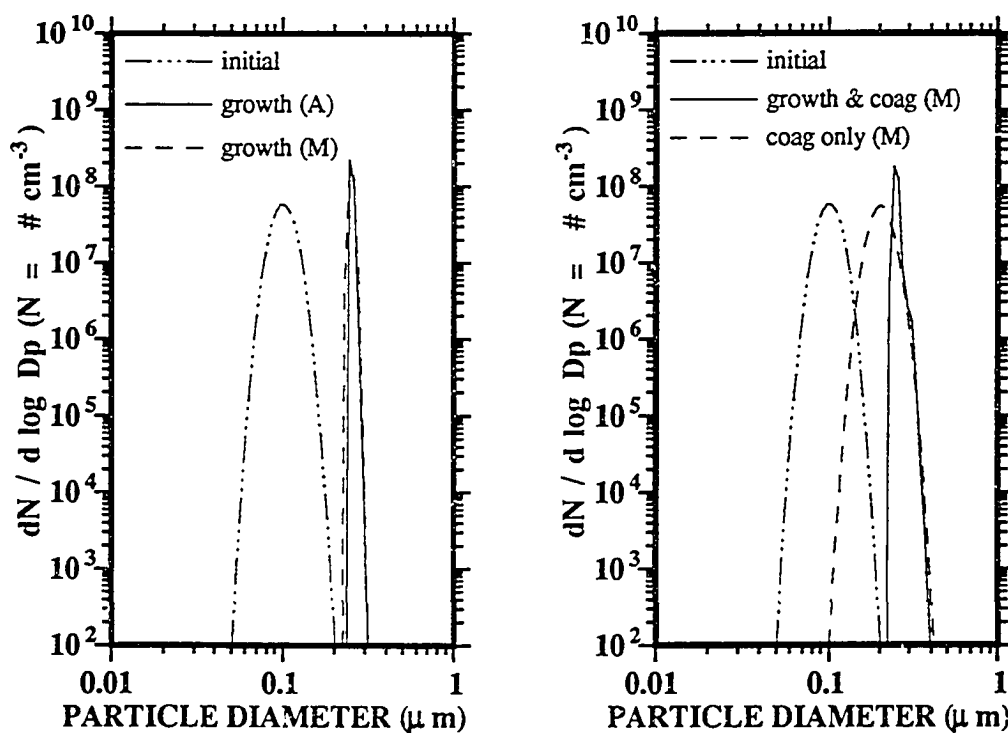
Figs. 5a and 5b. Figure 5a shows a comparison of a model (M) to an analytical (A) growth solution. Figure 5b shows model simulations of coagulation only and

338

coagulation combined with condensational growth. Table 1 lists the initial conditions, some parameter values, and final volumes for the comparison of analytical to moving bin growth. The constant growth term used here was $A_d = 1.0 \times 10^{-10}$ cm^2 s^{-1}. To obtain the moving bin solution, we solved Equation (18), and to obtain the analytical solution, we solved Equation (16).

Figure 6 shows plots of simulations similar to those in Figure 5, except the initial conditions and growth rate in the new plots are like those used in Figure 2 of Tsang and Rao (1988). The growth rate in this example is much slower than that in the previous example. Again, the moving bin results paralleled those of the analytical solution. Only at the lower radial end of the distribution did the moving bin solution slightly underpredict the analytical distribution. For this example, we initialized the distribution with 18 size bins per decade ($V_{RAT} = 1.5$) and used a model time step of 100 seconds.

Results shown in this figure indicate that coagulation was more significant than growth under the conditions provided. The fact that coagulation alone and coagulation combined with growth gave solutions similar to each other supports this position. Also, because the initial number concentration was high, we expected coagulation to be important. Finally, because the growth rate was relatively slow (compared to in the previous example) we expected growth to be less important than in the previous example.

339
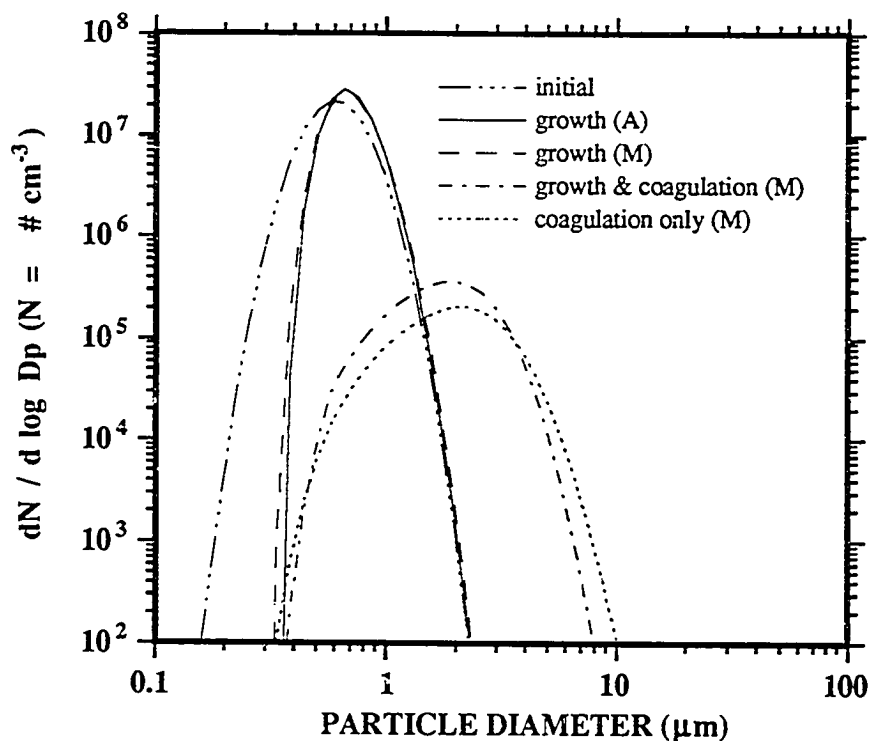
Fig. 6. This graph shows (a) an initial lognormal aerosol distribution, (b) a comparison of a model (M) to an analytical (A) growth solution, (c) a model simulation of coagulation only, and (d) a model simulation of coagulation combined with condensational growth. Table 1 lists the initial conditions, some parameter values, and final volumes for the these simulations. The constant growth term used here was $A_d =$ 1.0 x 10^{-13} cm^2 s^{-1}. To obtain the moving bin solution, we solved Equation (18), and to obtain the analytical solution, we solved Equation (16).

340

V. APPLICATIONS

Here, we demonstrate advantages of using a hybrid grid to simulate growth. Figure 7 shows growth and evaporation of particles containing two components. The initial lognormal distribution of particles consisted of only elemental carbon. We allowed m-xylene to condense onto the particles and assumed the same constant pressure difference as in Experiment 23A of Stern et al. (1989). After 6000 seconds, we removed all gas and allowed the particles to evaporate. To simulate each time step of evaporation, we solved Equations (7) and (8) simultaneously. When evaporation occurred, the gas-phase concentration quickly increased to its saturation vapor pressure. To allow evaporation to continue after saturation, we removed all gas at the end of each 100-second time step. Eventually, all condensed aerosol evaporated. Growth occurred much faster than evaporation because we allowed an endless supply of gas to condense over a low vapor pressure. When evaporation occurred, the partial pressure quickly increased to the saturation pressure, inhibiting evaporation. To allow evaporation to continue, we removed gas at the end of a time step.

The purpose of this exercise was not to demonstrate a real situation, but to show the ability of multicomponent particles to grow and then to evaporate back to their original cores. Achieving the original cores is difficult with fixed-bin growth methods, but is straightforward with a moving bin method.

341
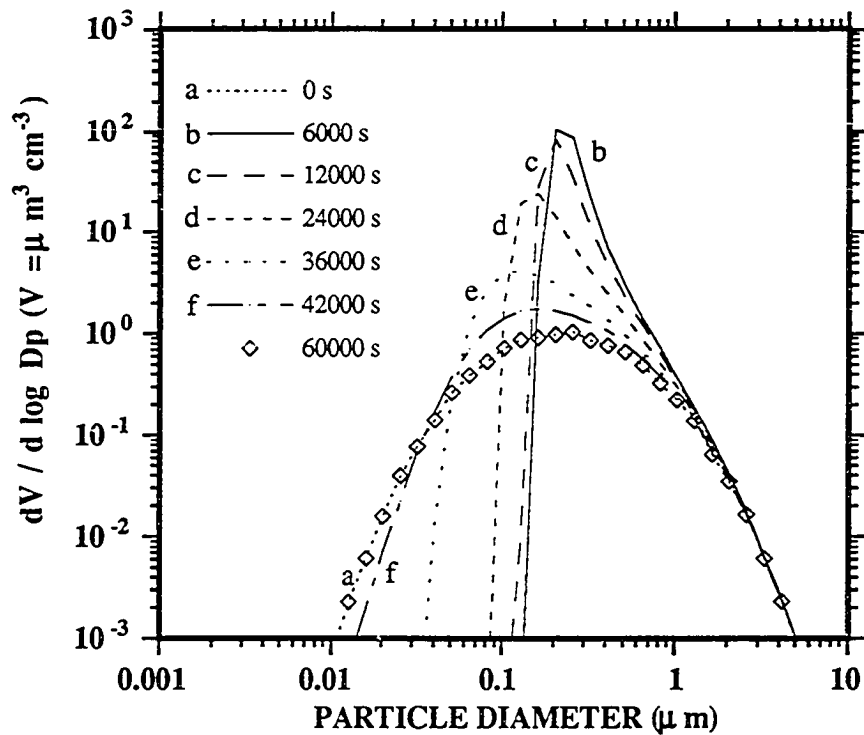
Fig. 7. Model simulation of condensational growth followed by evaporation. The initial aerosol consisted of a lognormal distribution of elemental carbon only, with d_{gno} = 0.129 µm and σ_g = 2.00. Subsequently, *m*-xylene grew for 6000 s. At 6000 s, we set the gas-phase partial pressure to zero and allowed evaporation to occur. To speed evaporation, we removed all existing gas every 100 seconds. This figure shows that particles simulated with moving bins evaporated back to their original cores.

Figure 8 stresses a point similar to that made in Figure 7. However, in the new case, we show results from 12 cycles of growth and evaporation of a fog. In this simulation, we started with a trimodal lognormal distribution of elemental carbon. By alternating the temperature every 600 seconds, we changed the relative humidity,

342

allowing a fog to repeatedly grow and evaporate. For each growth, the fog achieved the same distribution as for the previous growth, and for each evaporation, the fog shrunk to its initial core distribution. Achieving the initial core distribution with a stationary bin method is more difficult than with a hybrid or moving bin method. Figure 8 also shows that the Kelvin effect prevented some particles from growing to fog-size drops. To obtain the results for this figure, we solved Equations (7) and (8) with SMVGEAR over a hybrid size grid.
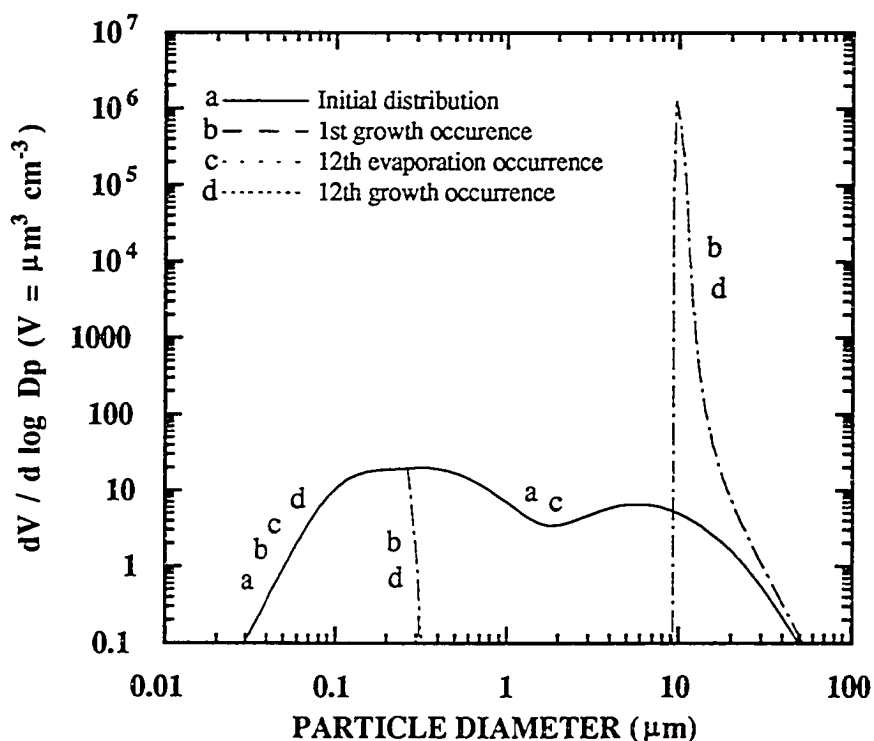
Fig. 8. Model results of 12 cycles of growth and evaporation. The initial distribution of elemental carbon was trimodal and the initial temperature and relative humidity were 290 K and 85.9%, respectively. After 600 seconds the temperature decreased to 287.5 K, causing the relative humidity to increase to 100.5% and water to condense rapidly

onto the core material to form a fog. The figure shows the volume distribution of the total particle (elemental carbon plus water). Because the saturation vapor pressure of particles below about 0.3 μm exceeded the actual vapor pressure multiplied by the Kelvin effect, these particles did not grow. After another 600 seconds we increased the temperature again to 290 K, causing the relative humidity to fall back to 85.9% and particles to evaporate to their original core sizes. We repeated this growth-evaporation cycle a total of 12 times. The figure demonstrates that allowing particles with the same core sizes to grow and evaporate independently of particles with different core sizes preserves the initial core distribution and permits continuous duplication of fog growth.

Next, Figure 9 shows a four-hour model comparison of fog growth alone to fog growth coupled with coagulation. The initial distribution was the same as in Figure 8, the initial humidity was about 100.5%, and the temperature was constant at 287.5 K. In both cases, each of the 24 time-intervals was 10 minutes. We solved coagulation with the semi-implicit method, using time steps equal to the time interval (no iteration required). The coagulation kernel included the effects of Brownian motion, convective diffusion enhancement, gravitation, turbulent shear, and turbulent inertial motion (Fuchs, 1964; Pruppacher and Klett, 1978; Saffman and Turner, 1956). Also, in both cases, we solved growth with SMVGEAR, which uses variable time steps.

The figure shows that coagulation slightly broadened the cloud-drop portion of the distribution and moved unnucleated cores to slightly larger sizes. While Brownian coagulation affected particles primarily less than 1 μm in diameter, differential fall velocities and turbulent motions were responsible for most coagulation in particles larger than 1 μm. Finally, while most growth occurred within the first few minutes of the simulation, coagulation continued to affect all modes of the distribution during the entire simulation period.
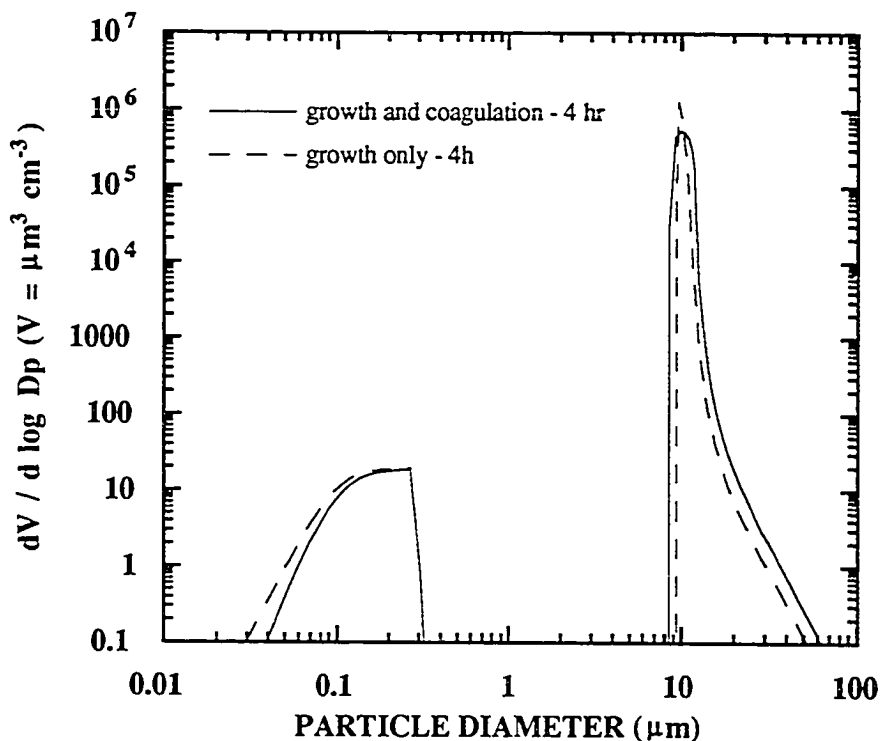
Fig. 9. A four-hour model comparison of fog growth alone compared to fog growth coupled with coagulation. The initial distribution was the same as that in Figure 8, the initial humidity was about 100.5%, and the temperature stayed constant at 287.5 K throughout the simulation. The figure shows the volume distribution of the total particle (carbon plus water) at the end of the simulation. The text describes remaining conditions.

The last figures (10a and 10b) show condensational growth of sulfuric acid and water and the corresponding conservation of the gas phase during growth. The initial distribution of elemental carbon was the same as in Figure (8). Also, the initial gas

345

concentration of sulfuric acid was 10^{11} cm^{-3}, the ambient temperature was 287.5 K, and the relative humidity was 81%. At this temperature and humidity, the saturation number density of sulfuric acid over a flat surface is about 10^1 cm^{-3}. The difference in ambient versus saturation densities forced gas-phase sulfuric acid to condense.

When sulfuric acid condenses, water condenses simultaneously. As the acid dissociates into ions, each ion attracts liquid water molecules. A convenient technique to estimate the amount of water that condenses to satisfy the change in ion content of the aerosol is the ZSR methods (Zdanovskii, 1948; Stokes and Robinson, 1966; Cohen et al., 1987; Pilinis and Seinfeld, 1987b). We used the ZSR method combined with an equilibrium model (Jacobson et al., 1994b) to calculate both the amount of water that condensed with sulfuric acid and the distribution of HSO_4^-, SO_4^{2-}, and H^+ ions that resulted from the condensation of acid.

In sum, the processes included to obtain Figures (10a) and (10b) were condensational growth (gas and aerosol phase solved simultaneously with SMVGEAR) and chemical equilibrium (including calculation of aerosol water content). Figure 10a shows the growth of the aerosol distribution. The final distribution contained about 45.3 μg m^{-3} of liquid water, compared to 10.7 μg m^{-3} of HSO_4^-, 5.4 μg m^{-3} of SO_4^{2-}, and 0.1 μg m^{-3} of H_2SO_4(aq). Thus, about 74% of the increase in aerosol mass was due to water condensation although sulfuric acid was the initial condensing species.

Figure (10a) also shows that the resulting aerosol distribution peaked near 0.65 μm diameter. While this distribution did not account for gas-phase chemistry, emissions, deposition, transport, and other processes, the resulting diameter fell within the accumulation mode. Hering and Friedlander (1982) measured ambient sulfur distributions and found an average mass median diameter of about 0.54 μm when the maximum humidity ranged from 69 - 100%.

346

Finally, Figure (10b) shows the reduction in gas-phase sulfuric acid during the period of condensation. The figure shows that condensation actually ceased after about 45 minutes of simulation.
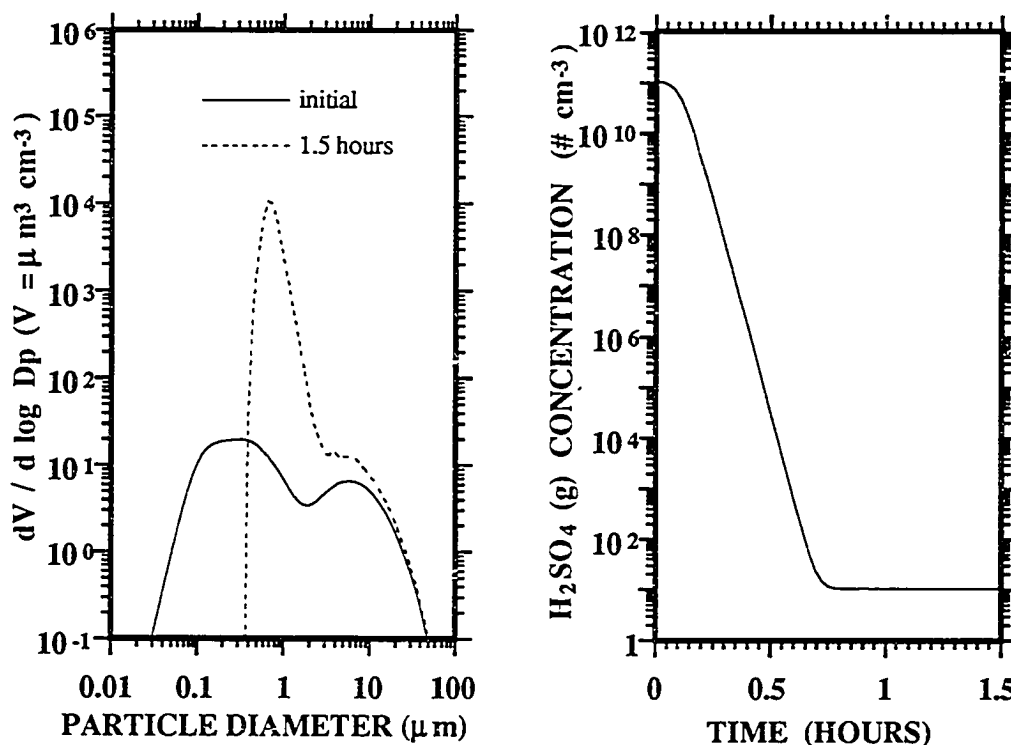
Figs. 10a and 10b. Model simulation of condensational growth of sulfuric acid and water onto a trimodal, lognormal elemental carbon initial distribution. Fig. (10a) shows the growth of the particle and (10b) shows the corresponding depletion in gas-phase sulfuric acid to its saturation number density. As sulfuric acid condensed, it attracted water. In fact, about 74% of the mass added to the distribution was liquid water. Within the sulfuric acid - water mixture, hydrogen ions, sulfate and bisulfate ions existed in equilibrium.

347

VI. CONCLUSIONS

We discussed an aerosol model that uses a hybrid size grid that has characteristics of both a stationary and moving grid. For the most part, the core volume of particles in each size bin remains fixed while the volatile volume of particles fluctuates. Allowing particles of one core volume to grow and evaporate independently of particles of other core volumes eliminates numerical diffusion. Furthermore, it permits grown particles to condense back to their exact core sizes and particles of the same size to have different composition.

For this model, we set up and solved growth equations that conserve mass between the gas and size-resolved aerosol phases. To calculate the solution to the growth equations, we used SMVGEAR, a sparse-matrix vectorized Gear-type code. SMVGEAR exploits the sparsity of the matrix of partial derivatives to solve the growth equations. Furthermore, it vectorizes around the grid-cell dimension, allowing relatively rapid solutions to first-order ordinary differential equations in large grid domains.

Next, we modified the coagulation code of Jacobson *et al.* (1994a) to permit coagulation over the hybrid grid structure. The modified code allows us to partition each coagulated particle and its total volume between particles of two size bins -- one with particles of smaller core volume and the other with particles of larger core volume than that of the coagulated particle.

To test growth and coagulation over the hybrid grid structure, we compared results to analytical and integrated numerical solutions. For the integrated solutions, we devised fully implicit coagulation and growth equations and solved them with SMVGEAR. When computer speeds increase further, fully integrated solutions will become more feasible over large grid domains. However, for now, the time-split model

348

scheme presented here predicts solutions similar to those of the integrated solutions while taking much less computer time.

REFERENCES

Barkstrom, B. R. (1978). *J. Atmos. Sci.* 35: 665 - 673.

Bassett, M., Gelbard, F., and Seinfeld, J. H. (1981). *Atmos. Environ.* 15: 2395.

Beard, K. V., and Pruppacher, H. R. (1971). *J. Atmos. Sci.* 28: 1455 - 1464.

Brock, J. R., Zehavi, D., and Kuhn, P. (1986). *J. Aerosol Sci.* 17: 11 - 22.

Brock, J. R., and Oates, J. (1987). *J. Aerosol Sci.* 18: 59 - 64.

Cohen, M. D., Flagan, R. C., and Seinfeld, J. H. (1987). *J. Phys. Chem* 91: 4575 - 4582.

Friedlander, S. K. (1983). *Ann. NY Acad. Sci.* 404: 354 - 364.

Frossling, N. (1938). *Beitr. Geophys.* 52: 170.

Fuchs, N. A. (1964) *The Mechanics of Aerosols.* (R. E. Daisley and M. Fuchs, Translation) Pergamon Press, New York.

Fuchs, N. A., and Sutugin, A. G. (1971). Highly dispersed aerosols, in *Topics in Current Aerosol Research* (G. M. Hidy and J. R. Brock, ed.). Pergamon Press, New York, Vol. 2, pp. 1 - 60.

349

Gelbard, F., and Seinfeld, J. H. (1978). *J. Comp. Phys.* 28: 357.

Gelbard, F., and Seinfeld, J. H. (1980). *J. Colloid Interface Sci.* 78: 485 - 501.

Gelbard, F. (1990). *Aerosol Sci. Technol.* 12: 399 - 412.

Hering, S. V., and Friedlander, S. K. (1982). *Atmos. Environ.* 16: 2647 - 2656.

Jacobson, M. Z., and Turco, R. P. (1994). *Atmospheric Environment* 28A: 273 - 284.

Jacobson, M. Z., Turco, R. P., Jensen, E. J., and Toon, O. B. (1994a). *Atmos. Environ. Part A.*, in press.

Jacobson, M. Z., Turco, R. P., and Tabazadeh, A. (1994b). *J. Geophys. Res.*, in review

Keith, C. H., and Arons, A. B. (1954). *J. of Met.* 11: 173 - 184.

Kim, Y. P., and Seinfeld, J. H. (1990a). In *Proc. 3rd Int. Aerosol Conf., Science, Industry, Health and Environment*, Pergamon Press, Oxford, pp. 138 - 141..

Kim, Y. P., and Seinfeld, J. H. (1990b). *J. Colloid Interface Sci.* 135: 185 - 199.

Langmuir, I. (1944). *Super cooled droplets in rising of cold saturated air.* General Electric Company, Schenectady, N. Y. 150 pp..

Lee, K. W. (1985). *J. Colloid and Interface Sci.* 108: 199 - 206.

Middleton P., and Brock, J. R. (1976). *J. Colloid Interface Sci.* 54: 249 - 264.

Mordy, W. (1959). *Tellus* 11: 16 - 44.

Neiburger, M., and Chien, C. W. (1960). In *Physics of Precipitation, Proceedings of the Cloud Physics Conference, Woods Hole, Massachusetts, June 3 - 5, 1959.* AGU, pp. 191 - 210.

Pilinis, C., Seinfeld, J. H. and Seigneur, C. (1987a). *Atmos. Environ.* 21: 943 - 955.

Pilinis, C., and Seinfeld, J. H. (1987b). *Atmos. Environ.* 21: 2453 - 2466.

Pruppacher H. R., and Klett, J. D. (1978). *Microphysics of Clouds and Precipitation.* Reidel, The Netherlands.

Rao, N. P., and McMurry, P. H. (1989). *Aerosol Sci. Technol.* 11: 120 - 133.

Rooth, C. (1957). *Tellus* 9: 372 - 377.

Saffman, P. G., and Turner, J. S. (1956). *J. Fluid Mech.* 1, 16 - 30.

Seigneur, C. (1982). *Atmos. Environ.* 16: 2207 - 2228.

Seinfeld, J. H. (1986). *Atmospheric Chemistry and Physics of Air Pollution.* John Wiley, New York.

Smolarkiewicz, P. K. (1983). *Mon. Weather Rev.* 111: 479 - 486.

Stern, J. E., Flagan, R. C., and Seinfeld, J. H. (1989). *Aerosol Sci. Technol.* 10: 515 - 534.

Stokes, R. H., and Robinson, R. A. (1966). *J. Phys. Chem.* 70: 2126 - 2130.

Toon, O. B., Turco, R. P., Westphal, D., Malone, R., and Liu, M. S. (1988). *J. Atmos. Sci.* 45: 2123 - 2143.

Toon, O. B., Turco, R. P., Jordan, J., Goodman, J., and Ferry, G. (1989). *J. Geophys. Res.* 94: 11,359 - 11,380.

Tsang, T. H., and Brock, J. R. (1983). *Aerosol Sci. Technol.* 2: 311 - 320.

Tsang, T. H., and Brock, J. R. (1986). *Aerosol Sci. Technol.* 5: 385 - 388.

Tsang, T. H., and Hippe, J. M. (1988). *Aerosol Sci. Technol.* 8: 265 - 278.

Tsang, T. H., and Huang, L. K. (1990). *Aerosol Sci. Technol.* 12: 578 - 597.

Tsang, T. H., and Korgaonkar, N. (1987). *Aerosol Sci. Technol.* 7: 317 - 328.

Tsang, T. H., and Rao, A. (1988). *Aerosol Sci. Technol.* 9: 271 - 277.

Turco, R. P., Hamill, P., Toon, O. B., Whitten, R. C., and Kiang, C. S. (1979a). *J. Atmos. Sci.* 36: 699 - 717.

Turco, R. P., Hamill, P., Toon, O. B., Whitten, R. C., and Kiang, C. S. (1979b). *NASA Tech. Publ. (TP) 1362, iii-94.*

Varoglu, E., and Finn, W. D. L. (1980). *J. Comp. Phys.* 34: 371 - 389.

Warren, D. R., and Seinfeld, J. H. (1985). *Aerosol Sci. Technol.* 4: 31 - 43.

351

Whitby, E. R. (1985). *The Model Aerosol Dynamics Model. Part I*. Report to the U. S. Environmental Protection Agency, Dept. of Mechanical Engineering, University of Minnesota, Minneapolis.

Wu, J. J., and Flagan, R. C. (1988). *J. Colloid Interface Sci.* 123: 339.

Zdanovskii, A. B. (1948). *Zhur. Fiz. Khim.* 22:1475 - 1485.

Appendix E

Paper -- Simulating Equilibrium Within Aerosols and non-Equilibrium Between Gases and Aerosols

353

Simulating Equilibrium Within Aerosols and non-Equilibrium Between Gases and Aerosols

Mark Z. Jacobson*, Richard P. Turco, and Azadeh Tabazadeh

Department of Atmospheric Sciences, University of California, Los Angeles, CA

90024-1565

We discuss both a model (EQUISOLV) that simulates chemical equilibrium processes and a method to couple the equilibrium calculations to non-equilibrium growth and evaporation. EQUISOLV solves any number of equations for gas, liquid, ionic, and solid equilibrium concentrations over large spatial grids and particle size grids. It also simultaneously computes ion activity coefficients and aerosol water content. The model uses Bromley's method to calculate activity coefficients for mixed electrolytes. Bromley's method requires binary activity coefficient information. To compute temperature-dependent binary activity data, we constructed polynomials using binary data at 298 K, apparent molal enthalpy data, and apparent molal heat capacity data. The equilibrium solver is mole and charge conserving, requires iteration, but always converges. For this work, we coupled EQUISOLV to SMVGEAR, a sparse-matrix, vectorized Gear code, to simulate aerosol growth and chemistry. When the two models are coupled, EQUISOLV first determines equilibrium vapor concentrations of gases, SMVGEAR then computes gas-aerosol transfer, EQUISOLV next determines intra-aerosol equilibrium, and SMVGEAR finally calculate the effect of aqueous chemical reactions. In addition, all processes are solved among any number of aerosol

354

size bins. The calculation of both equilibrium vapor concentrations and gas-aerosol transfer involve the simultaneous solution among all size bins. EQUISOLV has been used to study aerosols in tropospheric and stratospheric air.

To obtain a copy of EQUISOLV, please send a request by either e-mail to jacobson@yosemite.atmos.ucla.edu or regular mail to the authors at the address above.

1. INTRODUCTION

Aerosols and fogs affect pollution in many regions of the atmosphere. For example, near the surface, particles impede visibility, serve as hosts for acid-producing chemical reactions, and impair human health. In the stratosphere, aerosol constituents catalyze chemical reactions that can produce ozone-depleting gases. Current studies of particle chemistry and microphysics are usually experimental, observational, or theoretical. Theoretical studies, such as the one undertaken here, are particularly difficult because data are often scarce and computer speed and memory is often limited. Furthermore, a full theoretical study of atmospheric particles requires treating numerous processes, such as meteorology, emissions, deposition, radiation, nucleation, chemistry, growth, and more.

In this work we discuss some of the building blocks for the treatment of atmospheric aerosols in a three-dimensional Eulerian grid model. The primary processes that affect aerosol concentration and composition include emissions, nucleation, coagulation, condensational growth, dissolutional growth, aqueous equilibrium, aqueous chemistry, deposition, and transport. In other work (*e.g.* Jacobson *et al.*, 1994a-e), most of these processes have been discussed in detail. Here, we

355

describe primarily the coupling of chemical equilibrium calculations with gas-aerosol transfer.

A process is in equilibrium when the time required for it to reach a steady state is much less than the time interval of interest. For example, in liquid water, dissociation of an acid often occurs so fast that, for modeling purposes, it is instantaneous. Acid-base dissociation reactions occur in oceans, aerosols, fogs, clouds, and rain.

With respect to atmospheric aerosols, in 1979 Stelson *et al.* proposed an equilibrium relation between gas-phase ammonia and nitric acid and solid-phase ammonium nitrate. Similarly, Scott and Cattell (1979) theorized an equilibrium between gas-phase ammonia, and solid ammonium-sulfate compounds. Subsequently, many studies examined gas-solid as well as gas-liquid, liquid-ion, and liquid-solid atmospheric equilibrium (*e. g.* Stelson and Seinfeld, 1982a, b, c; Seigneur, 1982; Seigneur *et al.*, 1984; Russell *et al.*, 1983, 1988; Saxena *et al.*, 1981, 1983, 1986; Bassett and Seinfeld, 1983, 1984; Hildemann *et al.*, 1984; Russell and Cass, 1986; Pilinis *et al.*, 1987; Pilinis and Seinfeld, 1987, 1988; Wexler and Seinfeld, 1990, 1991, 1992; Kim *et al.*, 1993a,b; Saxena *et al.*, 1993).

In 1989 Allen *et al.* suggested that, under some conditions, the assumption of equilibrium between the gas and aerosol phase may not always be valid. Subsequently, Harrison and MacKenzie (1990) and Wexler and Seinfeld (1990, 1991, and 1992) supported this hypothesis. Furthermore, Wexler and Seinfeld (1991, 1992) developed a model to simulate both transport of gas to and equilibrium treatment within aerosols.

Here, we discuss a new model in which the gas phase is not in equilibrium with the aerosol phase. Instead, we assume that, over a time interval, the ambient concentration of each gas approaches an equilibrium vapor concentration (EVC) (moles-gas cm^{-3}-air). To obtain the EVC, equilibrium equations are solved between the gas and multiple size bins of the aerosol phase with a chemical equilibrium solver named EQUISOLV.

The EVCs are then used in growth equations to calculate the transfer between the gas and all size bins of the aerosol phase, simultaneously. Once mass has been transferred to or from aerosols, EQUISOLV is used a second time to determine internal equilibrium concentrations. Finally, aqueous chemistry forward reactions within aerosols are computed. To solve the first order, ordinary differential equations for growth and aqueous chemistry, SMVGEAR, a sparse-matrix, vectorized Gear-type code (Jacobson and Turco, 1994a,c) is used.

EQUISOLV solves equilibrium equations, mixed-solution activity coefficients, and the water equation, simultaneously. Two types of methods have previously been used to solve these equations together. These include Newton-Raphson methods (Pilinis and Seinfeld, 1987; Kim et al., 1993a,b) and methods that minimizes free energy (Bassett and Seinfeld, 1983, 1984; Wexler and Seinfeld, 1990-2). EQUISOLV and these other methods require iteration and are mass and charge conserving. The primary advantages of EQUISOLV are its simplicity and its ability to converge thousands of equilibrium equations simultaneously without fear of a negative concentration or non-convergence. Further, it requires no first guesses and is easily vectorized (e.g. it achieves 355 megaflops on a C-90).

In sum, this paper discusses both a solver of chemical equilibrium equations and a methodology of joining equilibrium solutions with non-equilibrium gas-aerosol transfer. It also presents several newly-derived temperature-dependent activity coefficient polynomials for tropospheric aerosols. Recently, Tabazadeh et al. (1994a) developed a method to derive binary activity coefficients for cold stratospheric temperatures. They applied EQUISOLV along with their low-temperature activity coefficients to study stratospheric aerosol composition. Similarly, Tabazadeh et al. (1994b) and Drdla et al. (1994) used EQUISOLV with the cold-temperature activity coefficients to study the formation of polar stratospheric clouds. Finally, EQUISOLV

357

has been applied to study equilibrium in the oceans. With appropriate activity coefficient data, it can also be used to study equilibrium within the earth's crust.

2. SOLVING GAS-AEROSOL TRANSFER

To date, many models have assumed that the equilibrium vapor pressure (or concentration) of soluble species can be determined using either a direct or an effective Henry's constant (*e. g.* Schwartz and Freiberg, 1981; Schwartz, 1984; Chameides, 1984; Jacob, 1986; Pandis and Seinfeld, 1989; Bott and Carmichael, 1993). Another model has assumed that partial pressures of gases equal equilibrium vapor pressures, which are calculated by solving gas-aerosol and aerosol-aerosol equilibrium equations, electrolyte activity coefficients, and aerosol water content (*e.g.* Pilinis and Seinfeld, 1987). A more recent model has calculated vapor pressures by solving detailed equilibrium within aerosols (excluding gas-aerosol equilibrium) and dividing equilibrium molalities in solution by the Henry's constants (Wexler and Seinfeld, 1990-2). These vapor pressures were then used in gas-aerosol transfer calculations.

However, no model, to date, has first used equilibrium equations / activity coefficients / water content to calculate vapor pressures, then used these vapor pressures to calculate gas-aerosol transfer, then recalculated detailed equilibrium within aerosols. This approach allows partial pressures to converge to equilibrium vapor pressures that are determined by accounting for interactions and competition between the gas phase and aerosols of all composition and size. Since vapor pressures depend on how much of a gas is dissolved in solution at equilibrium, and this depends on how much vapor was available in the gas phase prior to equilibrium, which depends on how much gas has dissolved in all particles, then accounting for competition among particles improves the prediction of EVCs.

358

While we calculate EVCs for most species by solving equilibrium equations, we solve them empirically for sulfuric acid and water above 100% humidity. For example, sulfuric acid has a very low EVC and its Henry's constant is not well known. Thus, we calculate its EVC with a relation derived by Gmitro and Vermeulen (1964). Also, the EVC of water vapor above 100% relative humidity is calculated with an empirical relation given by Bolton (1980). However, below 100% humidity, water vapor is assumed to be in equilibrium with the aerosol.

Whether the EVC is calculated empirically or from equilibrium, it can be input directly into growth equations. To calculate gas-aerosol transfer, we solve such equations between the gas phase and all size bins of the aerosol phase, simultaneously. The growth equations are written as (Jacobson and Turco, 1994c)

$$\frac{\mathrm{d}C_{VNi}}{\mathrm{d}t} = C_{Ni}^{2/3}\left(48\pi^2\right)^{1/3} D_{VNi}^{e\!f\!f}\left(Y_{ONi} + C_{VNi}\right)^{1/3}\frac{M_V}{\rho_V}\left(G_V - P_V^o B_{VNi}\right) \quad (1)$$

and

$$\frac{\mathrm{d}G_V}{\mathrm{d}t} = -\frac{\rho_V}{M_V}\sum_{N=1}^{N_T}\left\{\sum_{i=1}^{N_B}\frac{\mathrm{d}C_{VNi}}{\mathrm{d}t}\right\}, \quad (2)$$

where C_{VNi} is the aerosol volume concentration (cm^3-aerosol cm^{-3}-air) of component V in Ni particles, Y_{ONi} is the volume concentration (cm^3-aerosol cm^{-3}-air) of all material except for C_{VNi}, in Ni particles C_{Ni}, is the number concentration (No. cm^{-3}-air) of Ni particles, G_V is the ambient concentration (moles cm^{-3}-air) of gas V condensing onto particle-type N, P_V^o is the equilibrium vapor concentration (moles cm^{-3}-air) of gas V, M_V is the molecular weight (g mole^{-1}) of the gas, ρ_V is the density (g cm^{-3}) of the condensed gas, B_{VNi} is a series of adjustments to the saturation vapor pressure (e.g. Kelvin effect, solute effect, and radiative cooling effect), and $D_{VNi}^{e\!f\!f}$ is a

gas diffusion coefficient (cm^2 s^{-1}), modified by the geometry of vapor collision with small particles and ventilation of heat and vapor during sedimentation. Above, the subscript N denotes a particle type, VN denotes each volatile component of an N-type particle, and i denotes each size bin of an N-type particle (Jacobson et al., 1994b). A simple set of three particle types could include a sulfuric acid-water type, an organic carbon-water type, and a sulfuric acid - water - organic carbon mixture. Each type has its own set of size bins. For the remainder of this paper, however, we assume one mixed particle type (N = 1) that contains any number of volume components within any number of size bins.

To solve Equations (1) and (2) numerically between the gas phase and all size bins of the aerosol phase for each component, V, SMVGEAR was used. The advantage of SMVGEAR is that the matrix of partial derivatives resulting from (1) and (2) requires no fill in during matrix decomposition and backsubstitution. SMVGEAR takes advantage of the sparsity and solves the equations rapidly.

By using Equations (1) and (2), we assume that particle size bins change in volume independently of one another (Jacobson and Turco, 1994c). Thus, when material is added to a particle size bin, the volumes of all particles in the bin increase to their actual sizes (moving bin method). In a stationary-bin method, particle number is decreased in smaller bins and increased in larger bins when growth occurs. The advantage of a moving bin method is that it eliminates numerical diffusion during growth (ibid.).

3. SOLVING CHEMICAL EQUILIBRIUM

To solve the growth equations above, equilibrium vapor concentrations are needed as input. Also, after growth equations are solved, the mass transferred to

360

aerosols needs to be distributed among dissociated ions. For example, gas-aerosol transfer moves sulfuric acid from the gas to the aerosol phase; however, in solution, sulfuric acid needs to be dissociated among sulfate, bisulfate, and aqueous sulfuric acid.

In order to calculate equilibrium vapor concentrations and internal aqueous equilibrium, we use EQUISOLV, discussed here. EQUISOLV solves any number of liquid-ion, ion-ion, ion-solid, gas-solid, gas-liquid, and gas-ion equilibrium equations simultaneously between the gas phase and multiple size bins of the aerosol phase. At the same time it calculates activity coefficients and aerosol water content. When using EQUISOLV to calculate EVCs, we include gas-solid, gas-liquid, and gas-ion equations together with all other equation types listed above. However, when using EQUISOLV to calculate internal aqueous equilibrium, we exclude all gas-aerosol equations.

To solve a system of equilibrium equations, we developed a scheme that takes advantage of Villars' method (1959). Villars' method requires solving one equilibrium equation at a time by iteration. To solve a system of equations, all equations are iterated many times. For example, suppose we have a single aerosol size bin and fifteen equations representing the equilibrium chemistry within that bin (excluding the gas phase). To begin solving for equilibrium concentrations, the first equation is iterated. When the first equation converges, the updated and other initial concentrations are used as inputs into the second equation. This continues until the fifteenth equation has converged. At this point, concentrations from the first equation are no longer in equilibrium. Thus, the sequence is repeated, from the first through fifteenth equation, over and over, until concentration no longer change upon more iteration.

Equations between multiple aerosol size bins and the gas phase are solved in a similar manner. For example, suppose we have fifty size bins, fifteen equations per bin, and three gas species that equilibrate with aqueous-phase species in each bin. Starting with the first bin, each equation is iterated until convergence occurs for that equation. If

361

the equilibrium equation includes a gas, the gas concentration will change as the equation converges. After the equations in the first bin are iterated and converged, the equations in the second bin are iterated. The updated gas concentrations from the first bin affect the equilibrium distribution in the second size bin and, conversely, the equilibrium distribution in the second bin affects the gas phase. After the last size bin is iterated, the sequence of iterations is repeated in reverse order, from the fiftieth to the first bin. The marches back and forth among the size bins continue until gas and aerosol concentrations do not change from iteration to iteration.

After solving equilibrium equations, the gas phase will be in equilibrium with all liquids, ions, and solids in each size bin and all liquids, ions, and solids in each bin will be in equilibrium with each other and the gas phases. Further, the appropriate amount of water will have condensed onto or evaporated from each particle (for humidities less than 100%). For above 100% humidity, the water content must be determined separately by solving the condensational growth equations, discussed earlier.

To account for the Kelvin effect when particles are small, the equilibrium constant of each gas-aerosol equilibrium reaction is adjusted by appropriate Kelvin-effect terms. Since particle volumes fluctuate continuously during calculations due to water and solute growth or evaporation, the Kelvin terms, which include a radius dependence, are adjusted each iteration of each size bin.

A feature of the solution method discussed here is that it is mass and charge conserving at all times so long as the equilibrium equations are written in a mass- and charge-conserving manner. For example, the equation, $HNO_3(g) + NH_3(g) = NO_3^- + NH_4^+$, conserves mass and charge. With such equations, the computation can stop after any iteration with a mass-conserved system.

362

A second feature of the method is that it requires no intelligent first guess. The only constraints are that the system must start in charge balance and the sum of moles of each atom must equal the total number of desired moles of the atom in the system. For example, if the total nitrate in the system is known to be 20 μg m^{-3}, then the nitrate can be distributed initially, in any proportion, among $HNO_3(g)$, $HNO_3(aq)$, NO_3^-, $NH_4NO_3(s)$, etc. Similarly, the charge balance constraint allows initial charges to be distributed among all aqueous species, except the sum of charges over all species must equal zero. The simplest way to initialize charge is to set all aqueous ion molalities to zero. However, components can be initialized subject to the constraints in numerous ways that can be automatized in the computer program.

A third feature of the method is that it is absolutely stable. Concentrations can never decrease below zero and individual equilibrium equation always converge. This feature gives EQUISOLV an immediate advantage over a Newton-Raphson (NR) technique since NR iterations can converge to negative roots if initial guesses are not precise enough. In a model with 20,000 grid cells and numerous aerosol size bins, the probability increases that NR interations fail to converge. We compared solving the equilibrium equations, the water equation, and mixed activity coefficients simultaneously with a NR technique to solving with EQUISOLV, over a grid of 10,000 cells. With a few equilibrium equations, the NR technique required pre-generated tables of first guesses for different conditions masses of total sulfate, nitrate, etc., in the system, but EQUISOLV required none. When both solutions converged, they always converged to the same answers. However, the NR technique failed to converge in many grid cells while EQUISOLV never failed to converge. When more and more equilibrium equations were added, the NR failed increasingly until it became impractical to use.

363

3.1. *The Basic Mechanism.*

Here, the iteration sequence for one equilibrium equation is discussed. For this description, we dropped all subscripts identifying particle type and size bin. The general structure of such an equation is

$$v_D D \; + \; v_E E \; + ... \; <=> \; v_A A \; + \; v_B B \; + ... \; Keq, \qquad (3)$$

where the v's are the number of moles of each gas, liquid, ion, or solid reactant or product, D, E, A, and B are the chemical symbols of the reactants and products, and K_{eq} is the equilibrium constant, which is a function primarily of temperature.

The relationship among the equilibrium constant, the stoichiometric coefficients, and the reactant and product activities in (3) is

$$\frac{\{A\}^{v_a}\{B\}^{v_b}...}{\{D\}^{v_d}\{E\}^{v_e}...} = K_{eq}, \qquad (4)$$

where $\{A\}$ denotes the activity of species A. For a gas, the activity is the partial pressure of the gas; for solids, the activity is unity; for liquid water, the activity is the relative humidity; and for ions, the activity is the species' molality multiplied by its activity coefficient.

In the model all concentrations for gases, liquids (including water), ions, and solids are set in units of moles of species per cubic centimeter of air. Thus, to convert liquid or ion mole concentrations to units of molality, we write

$$m_a = \frac{1000 c_a}{M_w c_w}, \qquad (5)$$

364

where, m_a and c_a are the molality (moles kg^{-1}-solution) and mole concentration (moles cm^{-3}-air), respectively, of aqueous species a, c_w is the mole concentration of water, and M_w is the molecular weight of water (g mole^{-1}). Similarly, to convert gas mole concentrations to pressure units, we write

$$p_d = 1000 G_d R_u T, \tag{6}$$

where p_d is the partial pressure (atm) of gas d, G_d is the mole concentration of d (moles cm^{-3}-air), R_u is the universal gas constant (L atm mole^{-1} K^{-1}), and T is temperature (K).

To demonstrate the solution to one equilibrium equation, an example where two gases equilibrate with two ions is shown. The sample equation has the form of (3), with two gases on the left side of the equation. The first step is to calculate Q_D and Q_N, the smallest ratio of mole concentration to moles among species appearing in the denominator and numerator, respectively, of Equation (4). Thus,

$$Q_D = \text{MIN}\left\{\frac{G_d^1}{v_d}, \frac{G_e^1}{v_e}\right\} \tag{7}$$

and

$$Q_N = \text{MIN}\left\{\frac{c_a^1}{v_a}, \frac{c_b^1}{v_b}\right\}, \tag{8}$$

where the superscript "1" refers to initial concentrations. If the equilibrium equation contains solids, each solid's concentration is included in (7) or (8). By putting species of all physical states in the same units, confusion is avoided in these and subsequent

365

calculations. Next, in a manner similar to Villars, we initialize two parameters, $Z^l = 0.5$ $(Q_D + Q_N)$ and $\Delta x^l = Q_D - Z^l$, and re-estimate mole concentrations as

$$c_a^{l+1} = c_a^l + v_a \Delta x^l \qquad c_b^{l+1} = c_b^l + v_b \Delta x^l \qquad (9)$$

and

$$G_d^{l+1} = G_d^l - v_d \Delta x^l \qquad G_e^{l+1} = G_e^l - v_e \Delta x^l, \qquad (10)$$

respectively. Since iterations begin with Equation (9), iteration numbers are referred to by superscripts l and $l+1$. If the equation contain solids, then the change of each solid's concentration is calculated similarly to in (9) or (10) (solid, liquid, and ion mole concentrations are all identified with a c). Equations (9) and (10) indicate that, during each iteration, mass and charge are transferred either from reactants to products or vice-versa. This transfer continues until $\Delta x = 0$. Thus, the scheme conserves mass and charge each iteration.

Next, we compare the updated ratio of activities to the equilibrium constant, K_{eq}. The ratio is

$$F = \left(\frac{\left\{ m_a^{l+1} \gamma_a^{l+1} \right\}^{v_a} \left\{ m_b^{l+1} \gamma_b^{l+1} \right\}^{v_b}}{\left\{ p_d^{l+1} \right\}^{v_d} \left\{ p_e^{l+1} \right\}^{v_e}} \right) \bigg/ K_{eq}. \qquad (11)$$

To perform this calculation, mole concentrations are converted to either molality or atmospheres with Equations (5) and (6). In the case of solids, the activities are unity; thus, none will appear in (11). Further, activity coefficients (γ) and the water content (c_w) are updated before each iteration sequence.

In the final steps of the iteration, we reset $Z^{l+1} = 0.5 \, Z^l$ and check whether convergence has occurred. The convergence criteria is

$$F = \begin{cases} >1 & \Delta x^{l+1} = -Z^{l+1} \\ <1 & \Delta x^{l+1} = +Z^{l+1} \\ =1 & \text{CONVERGENCE} \end{cases} \qquad (12)$$

Each non-convergence, we update Δx, advance the iteration number, and return to Equation (9). Eventually, all molalities converge to a positive number.

3.2. Temperature-Dependent Ion Activity Coefficients.

Activity coefficients correct for the non-ideal behavior of electrolytes as the ionic strength of a solution increases. To calculate activity coefficients in a multicomponent solution, we use Bromley's model (1973), described by Pilinis and Seinfeld (1987) and Kim et al. (1993a). Bromley's method solves for activity coefficients in a multicomponent mixture using binary electrolyte activity coefficients. It simplifies to the Kusik and Meissner model (1978) when the Debye-Huckel term is ignored. The only temperature-dependent parameter in Bromley's model, aside from the binary activity coefficients, is the Debye-Huckel parameter (scaled, in Bromley (1973), by $3 / \ln 10$). To account for the temperature dependence of the Debye-Huckel term, we used the empirical formula given by Clegg and Whitfield (1991).

We obtained binary activity coefficient data at 298 K from a variety of sources, listed in Table A.1. Among the sources are measurements from Hamer and Wu (1972) and recent parameters from Pitzer (1991). Figure 1 compares binary coefficients for three species obtained from these two sources. The measured data is often accurate to high molality while the Pitzer parameters are valid up to about six molal. Since the

367

aerosols of interest are usually concentrated, we generally use the measured values. In all cases, the activity coefficient were fitted to polynomials of the form

$$\ln \gamma_{T_0} = B_0 + B_1 m^{1/2} + B_2 m + B_3 m^{3/2} + \ldots, \tag{13}$$

where γ_{T_0} is the activity coefficient (unitless) at 298 K, m is the molality of an electrolyte alone in solution but giving the same ionic strength as the mixture under investigation, and $B_0, B_1,\ldots$ are fitting coefficients for the polynomial.

We write the temperature dependence of the solute activity coefficients (Harned and Owen, 1958; Stelson *et al.*, 1984; Bassett and Seinfeld, 1983; Clegg and Brimblecombe, 1990; Tabazadeh *et al.*, 1994) as

$$\ln \gamma_T = \ln \gamma_{T_0} + \frac{T_L}{\nu R T_0}\left[\phi_L + m\frac{\partial \phi_L}{\partial m}\right] + \frac{T_C}{\nu R}\left[\phi_{C_P} + m\frac{\partial \phi_{C_P}}{\partial m} - \phi_{C_P}^0\right], \tag{14}$$

where γ_T is the activity coefficient at temperature T, T_0 is the reference temperature (298 K), ν is the number of moles of ions making up the electrolyte, R is the gas constant (J mole^{-1} K^{-1}), ϕ_L is the relative apparent molal enthalpy (J mole^{-1}) of the species at molality m, ϕ_{C_P} is the apparent molal heat capacity (J mole^{-1} K^{-1}) at molality m, and $\phi^0_{C_P}$ is the apparent molal heat capacity at infinite dilution. Furthermore, $T_L = (T_0 / T) - 1$ and $T_C = 1 + \ln (T_0 / T) - (T_0 / T)$ are temperature-dependent parameters.
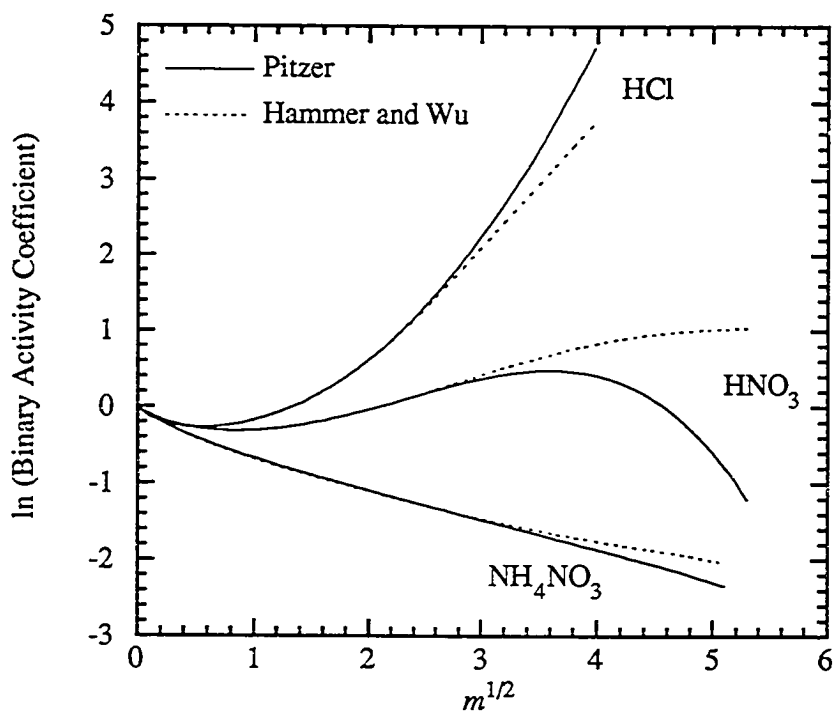
Fig. 1. Comparison of binary activity coefficient data measured by Hamer and Wu (1972) to those computed using Pitzer's method (Pitzer, 1991).

The relative apparent molal enthalpy equals the negative of the heat of dilution, ΔH_D. Table A.1 lists our sources of data for heat of dilution and apparent molal heat capacity. Using this data, we constructed polynomials of the form

$$\phi_L = U_1 m^{1/2} + U_2 m + U_3 m^{3/2} + \dots \tag{15}$$

and

$$\phi_{C_P} = \phi_{C_P}^{o} + V_1 m^{1/2} + V_2 m + V_3 m^{3/2} + \dots \tag{16}$$

369

Equation (15) does not include a U_0 term since $\phi_L = \phi_H - \phi^o_H$ (apparent molal enthalpy minus molal enthalpy at infinite dilution -- infinite dilution occurs when $m = 0$).

Combining (14), (15), and (16), we rewrite the temperature-dependent, binary activity coefficients in direct polynomial form as

$$\ln \gamma_T = F_0 + F_1 m^{1/2} + F_2 m + F_3 m^{3/2} + F_4 m^2 ..., \tag{17}$$

where $F_0 = B_0$ and

$$F_j = B_j + G_j T_L + H_j T_C \tag{18}$$

for each additional term, beginning with $j = 1$. In (18), $G_j = 0.5(j+2)U_j/(\nu RT_0)$, while $H_j = 0.5(j+2)V_j/(\nu R)$. Thus, given sufficient data, we can write all temperature- and molality-dependent binary activity coefficients in terms of Equations (17) and (18). Table A.1 lists B's, G's and H's for 10 electrolytes and the range of validity for data. Since polynomial fits tend to wander off in random directions when the molality increases much beyond the limit of the given data, we use the polynomial value from the last valid molality when modeling activities.

Obtaining the temperature-dependent binary activity coefficients of bisulfate and sulfate is more difficult. When sulfuric acid dissolves in water, the resulting mixture contains both sulfate and bisulfate ions. Pitzer *et al.*'s model (1977) describes how to obtain the molalities and activity coefficients of the two ions in such a mixture as a function of temperature. However, we need to find the activity coefficients of bisulfate and sulfate assuming they are alone in the mixture. Kusik and Meissner's model (1978), as discussed in Stelson *et al.* (1984), can mathematically isolate the

370

binary activity coefficients given the coefficients in a mixture, such as those calculated by the model of Pitzer *et al.*

Thus, to find temperature-dependent binary activity coefficients of bisulfate and sulfate, we solved Equations (6), (8), (9), (10), (11a), (11b), (12), and (13) of Pitzer *et al.* together with Equations (72) and (73) of Stelson *et al.* with a Newton-Raphson iteration. After computing for several temperatures and molalities, we wrote the temperature coefficients in the form,

$$F_j = W_{0,j} + W_{1,j}T + W_{2,j}T^2 + W_{3,j}T^3, \qquad (19)$$

where the resulting F's fit into Equation (17). Table A.2 contains values for the W parameters, for which j varies from 0 to 5, and Figure 2 depicts how the binary coefficients of sulfate and bisulfate vary with molality and temperature.

The reason we write all activity coefficients in the form of simple polynomials is to speed the solution of equilibrium equations over a large modeling domain. During a model time interval, the temperature is usually known. Thus, (18) and / or (19) can be calculated once for each species at the beginning of each time interval. Subsequently, during the iteration of the equilibrium equations, only Equation (17) is solved to find binary activity coefficients. These binary activities are then used in Bromley's mixed model to calculate activity coefficients for the electrolyte in the mixture, and the mixed activities are finally used in Equation (11).

371
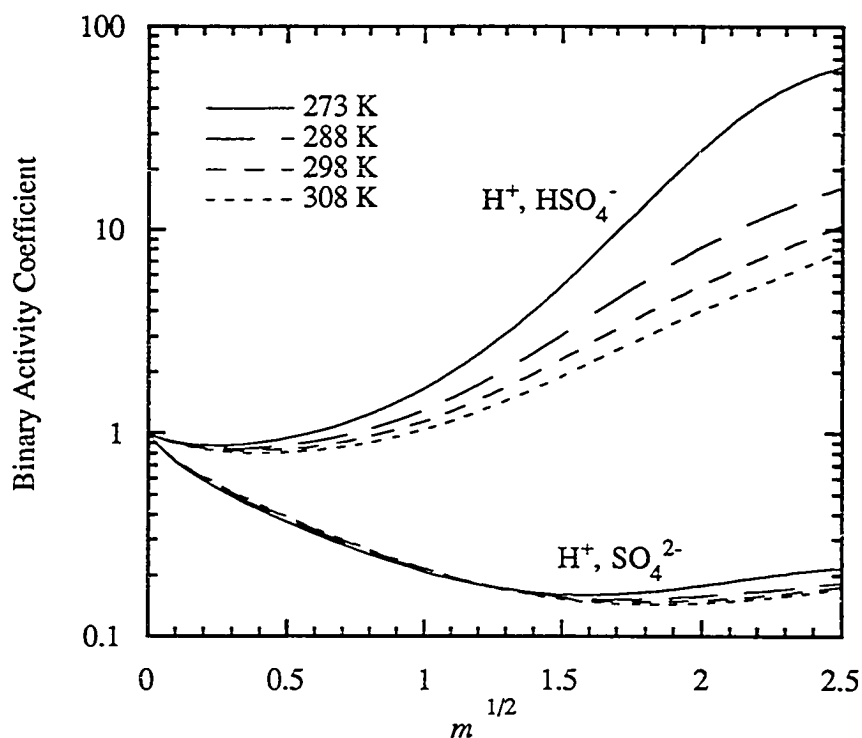
Fig. 2. Binary activity coefficients of sulfate and bisulfate as a function of molality and temperature, calculated from Equations (17) and (19).

3.3. The Water Equation.

When the model relative humidity (r. h.) exceeds 100%, the actual vapor pressure of water exceeds the equilibrium vapor pressure, and water condenses rapidly. When modeling such cases, we calculate the water content of aerosols using condensational growth equations before solving equilibrium equations. When the r. h. is below 100%, solute lowers the equilibrium vapor pressure of water over aerosols and permits condensation. In these cases, water molecules latch onto ions. In fact, the water content of aerosols is a strong function of ion content.

372

To calculate the amount of water that condenses when the r. h. falls below 100%, we assume water is in equilibrium with the aerosol phase. Since the empirical equations for water content are a function of electrolyte concentration, water concentrations in Equation (5) can be updated as soon as electrolyte concentrations from (9) or (10) change. Alternatively, the water content can be updated more sporadically. In either case, the water equation converges with the equilibrium equations.

The empirical scheme used to calculate water content is the ZSR method (Zdanovskii, 1948; Robinson and Stokes, 1964). The authors Cohen et al. (1987b), Pilinis and Seinfeld (1987; 1989), Wexler and Seinfeld (1991, 1992), and Kim et al. (1993a,b) have all used the ZSR method to predict aerosol water content. With the ZSR method, the mole concentration of water in a solution of mixed salts is calculated as

$$c_w = \sum_{i=1}^{N_h} \frac{1000 c_{h,i}}{m_{i,0}(\mathrm{r.h.}) M_w},$$ (20)

where $c_{h,i}$ is the hypothetical mole concentration (moles cm^{-3}-air) of electrolyte i in a multicomponent mixture, N_h is the number of the these hypothetical electrolytes, and $m_{i,0}(\mathrm{r. h.})$ is the molality of i when alone in solution at the same relative humidity as the mixture.

Pilinis and Seinfeld give polynomials expressions of water activity (equal to relative humidity) as a function of molality ($m_{i,0}$) for several binary electrolytes at 298 K. Much of this data was derived from Cohen et al. (1987a,b), Bassett and Seinfeld (1983), and Pitzer and Mayorga (1973). We recomputed the polynomials in the form

$$m^{1/2} = Y_0 + Y_1 a_w + Y_2 a_w^2 + Y_3 a_w^3 + ...,$$ (21)

373

where a_w is the water activity (relative humidity expressed as a fraction), the Y's are parameters listed in Table A.3, and m is the molality of the binary electrolyte alone in solution at the given relative humidity. Equation (21) permits the use of binary molalities directly in Equation (20), further speeding computer time.

Unlike temperature dependence of binary solute activity coefficients, the temperature dependence of binary water activity coefficients under ambient surface conditions is smaller. To show this, we write the temperature dependence of the activity as (Harned and Owen, 1958)

$$\ln a_{w,T} = \ln a_{w,T_0} - \frac{M_w m^2}{1000R} \left[\frac{T_L}{T_0} \frac{\partial \phi_L}{\partial m} + T_C \frac{\partial \phi_{C_P}}{\partial m} \right]. \tag{22}$$

If the water activity at the reference temperature are expressed as

$$\ln a_{w,T_0} = A_0 + A_1 m^{1/2} + A_2 m + A_3 m^{3/2} + ..., \tag{23}$$

then (22), (15), (16), and (23) can be combined to form

$$\ln a_{w,T} = A_0 + A_1 m^{1/2} + A_2 m + E_3 m^{3/2} + E_4 m^2 ..., \tag{24}$$

where

$$E_j = A_j - \frac{0.5(j-2)M_w}{1000R} \left[\frac{T_L}{T_0} U_{j-2} + T_C V_{j-2} \right] \tag{25}$$

for each j greater than two. From (24), we see that temperature affects the water-activity polynomial beginning only in the fourth term. In (17) temperature affected the solute

374

activity beginning with the second term of the polynomial. At high molalities (above 10 m) and at ambient surface temperatures (273 - 310 K), temperature only slightly affects water activity. For example, at 16 m, HCl gives a binary water activity of 0.09 at $T = 273$ K and an activity of about 0.11 at 310 K. At lower molalities, temperature has even less of an effect.

However, here, we include temperature-dependent parameters for three species, HCl, HNO$_3$, and NH$_4$NO$_3$. Table A.4 in the Appendix shows the parameters, which fit the equation

$$Y_j = X_{0,j} + X_{1,j}T + X_{2,j}T^2 + X_{3,j}T^3. \qquad (26)$$

Equation (26) subsequently plugs into (21). Thus, to calculate binary molalites as a function of relative humidity, we can either use Equation (21) directly with the Y's in Table A.3 or compute the Y's with (26) as a function of temperature with the data in Table A.4. In both cases, the Y's and the binary molalities are determined at the beginning of a model time interval and do not need to be iterated in the equilibrium solver.

3.4. Treatment of Solids.

EQUISOLV treats the formation of secondary, inorganic solids. A secondary solid cannot precipitate in a particle when the ambient relative humidity is greater than the deliquescent relative humidity (DRH) of the solid. Further, when the relative humidity is below the DRH, the solid may or may not form, depending on other equilibrium constraints. Finally, the DRH of the solid in equilibrium with a multicomponent mixture is lower than the DRH of the solid alone (Wexler and Seinfeld, 1991, Tang and Munkelwitz, 1993). However, lacking detailed deliquescence information, we can only

375

assume that a solid might form if the relative humidity is below the DRH of the solid in a multicomponent solution.

In EQUISOLV, temperature-dependent DRH data for NaCl, $NaNO_3$, NH_4Cl, NH_4NO_3, and $(NH_4)_2SO_4$ are used from Wexler and Seinfeld (1991). In addition, DRHs at 298 K for $NaHSO_4$, $NaNO_3$, $(NH_4)_2SO_4$, and $(NH_4)_3H(SO_4)_2$ were obtained from Pilinis and Seinfeld (1987).

Inorganic solids, such as NH_4NO_3 or NH_4Cl, form differently under moist, compared to dry, conditions. If aerosols are initially aqueous, then ammonia, nitrate, and chlorine can dissolve in the water, and if the relative humidity falls below the DRH of one or both possible solids, one or both may precipitate. However, if the aerosols are initially dry, the solid-forming process is more complicated. For example, gases NH_3 and HA may form $NH_4A(g)$, which can deposit on a nucleated particle in the form $NH_4A(s)$. Alternatively, one gas can hit and stick to a vacant crystal site on an existing particle, and the complimentary gas can react with the incorporated species to form a solid. Finally, both gases may absorb to the surface and react while adjacent to each other on surface sites (Harrison and MacKenzie, 1990). While the correct mechanism has not been fully determined, mechanism (1) is probably not dominant under atmospheric conditions (Wexler and Seinfeld, 1990).

In EQUISOLV, solids, liquids, and ions are solved for simultaneously during both EVC and intra-aerosol concentration calculations. First, EVCs of each gases are determined by solving solid, liquid, ion, and gas equilibrium equations together between the gas phase and all aerosol size bins. These EVCs are then used in growth equations (1) and (2), which are solved to determine the diffusion-limited transfer of gas to or from particles size bins. This step results in ambient gas concentrations somewhere between initial concentrations and equilibrium vapor concentrations. After mass is transferred, another equilibrium calculation, that does not involve the gas phase,

376

is performed within each aerosol size bin. This computation forces the formation of either solids, liquids, or ions and an appropriate amount of water in each aerosol bin. If no other process occurs in the model, aerosol compositions over time should approach equilibrium compositions. However, when aqueous chemistry and other processes, such as transport, coagulation, and gas chemistry are included, equilibrium vapor pressures change each time interval.

3.5. *Speeding up EQUISOLV*

As shown in Section 4.2, iterating equilibrium equations in a model with many grid cells, especially while solving for activities and the water content of an aerosol, is a slow process. To reduce computer time, Pilinis and Seinfeld (1987) solved sets of equations for specific cases of relative humidity and ammonia plus sodium to sulfate ratios. Here, we solve all equations relevant to an atmospheric situation, at all times, but take other measures to reduce computer time. By solving all equations at all times, the possibility of errors arising from fixing specific equations for specific situations is reduced. The only case where an equation is eliminated occurs when the relative humidity exceeds the DRH of a solid. In that case, the solid cannot exist; thus, we do not equilibrate any equation containing it.

The first method taken to speed solutions on some computers is to vectorize the computer code around the grid-cell dimension. Dividing the *grid domain* (all grid cells) into *grid blocks* (groups of grid cells) and vectorizing around the cells in each block speeds up the code tremendously (Jacobson and Turco, 1994a). In order to vectorize in such a manner, the calculation sequence must be the same in each grid cell. This is accomplished by iterating all equations in a block until the stiffest cell converges. While the extra iterations in the already-converged grid cells may be unnecessary, the speedup from vectorization outweighs the loss in speed due to excess computations.

377

A second method is to update ion activity and water content sporadically, as opposed to before every iteration of an equilibrium equation. For example, suppose that one equation requires 20 iterations to converge. Instead of updating activities and water content before each of the twenty iterations, we can update them once before the first iteration and take more marches through the size bins. The time for extra marches is smaller than the time saved from using sporadic computations.

If the water content is updated before the first iteration of each equation, then a third measure can be taken to speed the solver, which is to solve equations of the form A(g) <=> B(aq), without iteration. Such equations are typical of Henry's-law type equations, and the direct equilibrium solution is $c_B{}^{eq} = (G_A{}^i + c_B{}^i) K_{eq} / (1 + K_{eq})$ and $G_A{}^{eq} = c_B{}^{eq} / K_{eq}$, where G and c are both in moles cm^{-3}-air and the superscript i denotes the initial concentration. More complex equilibrium equations can be solved without iteration; however, even with 14 digits of computer accuracy, roundoff error makes some solutions very inaccurate. Excessive roundoff errors usually occur within the quadratic equation that arise for many of these solutions. Since the error often occurs within the square-root term, common techniques to avoid roundoff error do not help. Even the simple Henry's-law type equation, above, is subject to some roundoff errors. Fortunately, the iterative solution in EQUISOLV is not subject to the same degree of roundoff error since Equations (7) and (8) limit the value subtracted from or added to an initial concentration.

4. SIMULATION RESULTS

4.1. *Results from Equilibrium and Equilibrium Coupled to Growth*

To show the properties of EQUISOLV, we first demonstrate its ability to converge a large set of equations. Figure 3 shows the concentrations of three gases and total liquid water converging in a system containing 21 gases, 30 aerosol size bins, 46 aerosol species in each size bin, and 47 equilibrium equations solved within each size bin (total of 1401 components and 1410 equilibrium equations converged). Table A.5 lists the aqueous-phase species in each size bin. Since the simulation was run for a 90% relative humidity, and the DRH of 8 out of 9 solids in the Table A.5 is below 90%, only 46 of the 54 species in the table were used. Table A.6b shows the equilibrium equations solved for. Of the 55 equations in the table, only 47 were used for each size bin since the remaining 8 corresponded to solids which could not form. All 21 gases were initialized with mass concentrations (*e.g.* 10 μg m^{-3} NH$_3$, 30 μg m^{-3} HNO$_3$, etc.), but only sulfate (10 μg m^{-3}) and sodium chloride (10 μg m^{-3}) were initialized in the aerosol phase, and they were distributed with trimodal lognormal distributions. Most sulfate was placed in the accumulation mode and most sodium chloride was placed in the coarse particle mode.

Further, each Henry's constant equilibrium equation was solved for without iteration using the method described in Section 3.5 and all other equations were solved for using the iterative method discussed in Section 3.1. For 12 electrolyte combinations, mixed activity and water activity coefficients were solved for simultaneously with the equilibrium equations. For this simulation, the normalize gross error of all gas concentrations reached 10^{-4} after about 500 rotations around the size bins.

379
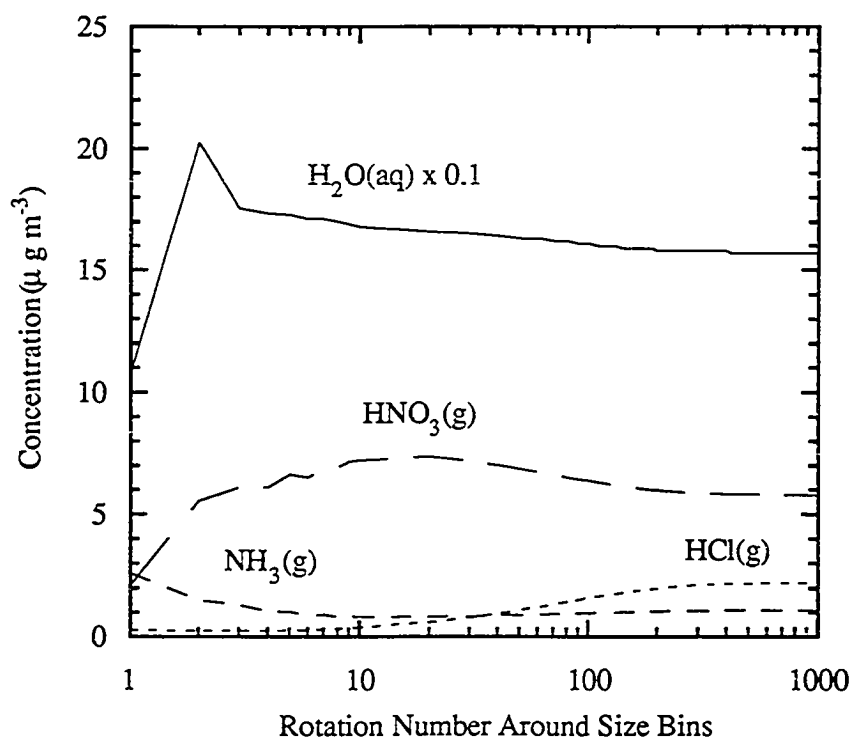
Fig. 3. Convergence of three gases and liquid water during a test where equilibrium was solved between 21 gases and 46 aerosol species in each of 30 aerosol size bins. The total number of equilibrium equations converged was 1410. Conditions are described in the text. Convergence occurred after about 250 rotations around all equations and size bins. Each equation, itself, was either iterated or solved in a one-step calculation.

Next, we compared results to those from Pilinis and Seinfeld (P&S -- 1987). Figures 4 - 6 show cases where the initial conditions, equilibrium equations, equilibrium constants, and activity data were the same as in Figures 1, 2, and 5, respectively, of their paper. Figure 4, here, shows an equilibrium scenario for one aerosol size bin, where the relative humidity was 90%, and Figure 5 shows the same

380

scenario where the humidity was 40%. The results followed those of P&S. Figure 6 shows how the aerosol water content changed with humidity. Although the results for this figure are similar to those from P&S, slight differences occurred possibly because we solved the same equilibrium equations for all humidities, sulfur, sodium, and nitrate contents and P&S solved specific equations were solved for specific humidities and ammonia plus sodium to sulfate ratios.
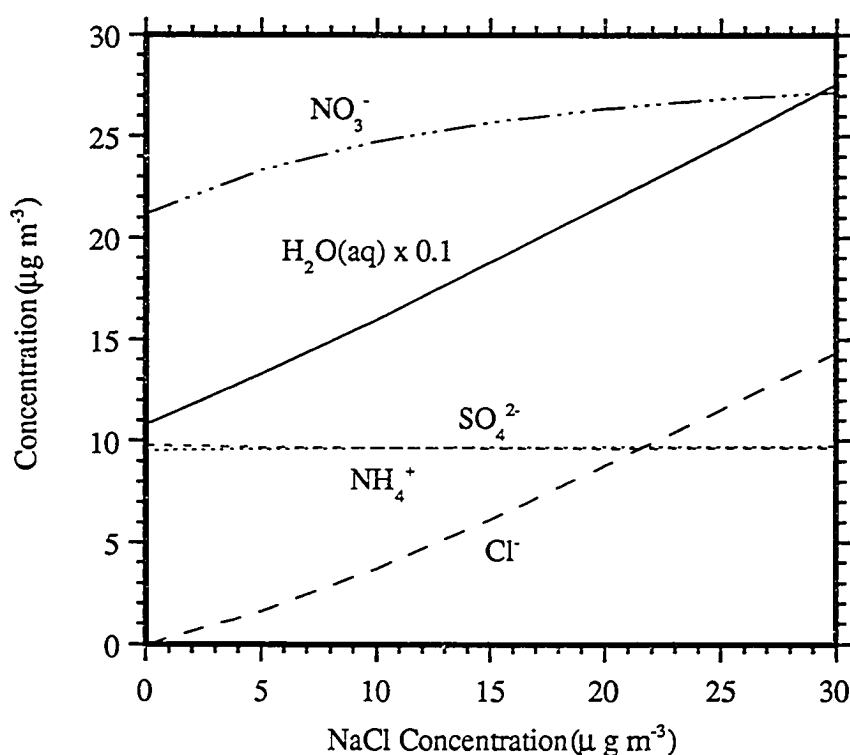
Fig. 4. Aerosol composition versus NaCl concentration when the relative humidity was 90%. Other initial conditions were $H_2SO_4(aq)$ = 10 mg m^{-3}, HCl(g) = 0 mg m^{-3}, NH_3(g) = 10 mg m^{-3}, HNO_3(g) = 30 mg m^{-3}, and T = 298 K. Compare to Pilinis and Seinfeld (1987), Figure 1.

381
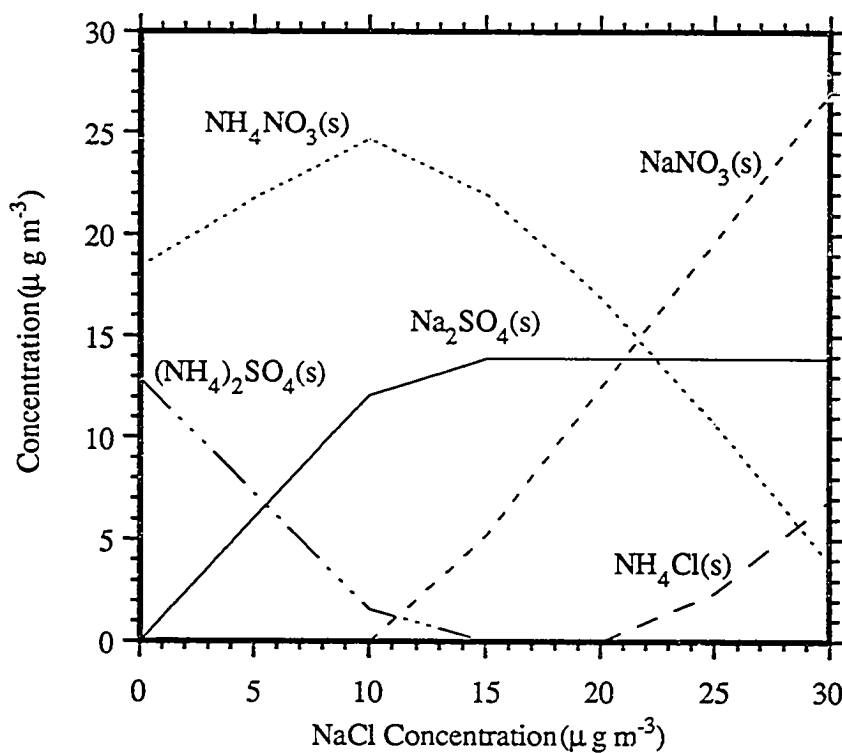
Fig. 5. Aerosol composition versus NaCl concentration when the relative humidity was 40%. Other initial conditions were $H_2SO_4(aq) = 10$ mg m^{-3}, $HCl(g) = 0$ mg m^{-3}, $NH_3(g)$ = 10 mg m^{-3}, $HNO_3(g) = 30$ mg m^{-3}, and T = 298 K. Compare to Pilinis and Seinfeld (1987), Figure 2.

382
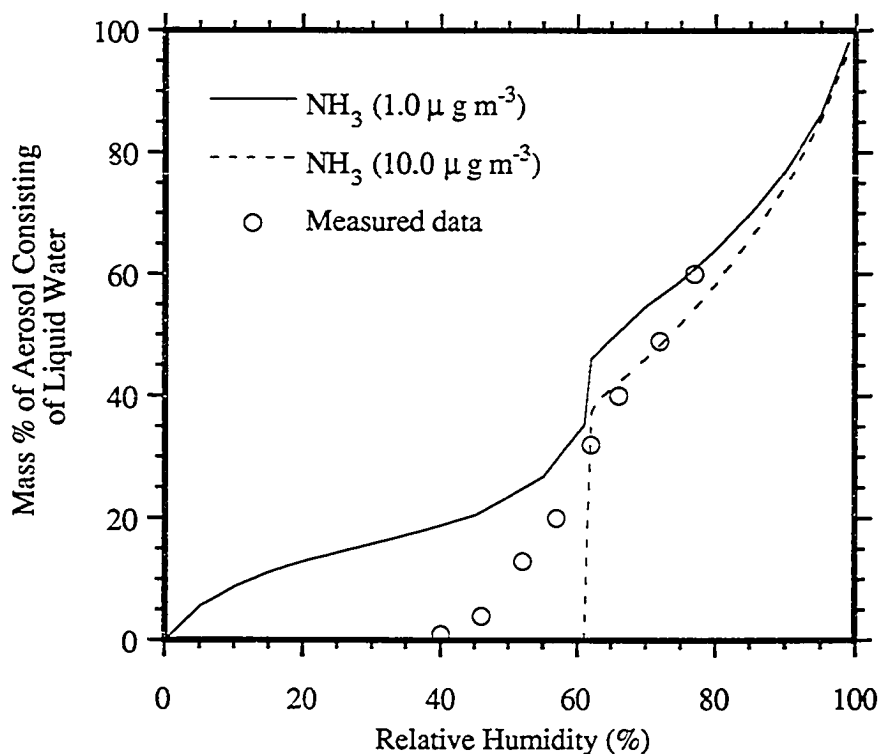
Fig. 6. Calculated water mass fraction versus relative humidity when $NH_3(g) = 1$ or 10 mg m^{-3}. Other initial conditions were $H_2SO_4(aq) = 10$ mg m^{-3}, $HCl(g) = 0$ mg m^{-3}, $HNO_3(g) = 20$ mg m^{-3}, and $T = 298$ K. Compare to Pilinis and Seinfeld (1987), Figure 5.

Figure 7 shows a model simulation of the change in aerosol composition as a function of relative humidity. As humidity decreased from 100%, water, chloride, nitrate, and ammonium decreased steadily. At about 62% humidity, which is near the deliquescence humidity of ammonium nitrate, both ammonium nitrate and ammonium sulfate precipitated. Ammonium sulfate did not precipitate at a higher relative humidity although its DRH is about 80% because supersaturation did not occur until the aerosol

383

became drier. Above the DRH, a solid may not precipitate; below the DRH, a solid may or may not precipitate, depending upon other equilibrium constraints (Pilinis and Seinfeld, 1987). Ammonium sulfate can remain in the aqueous phase until the relative humidity decreases below 30% (Tang, 1980).
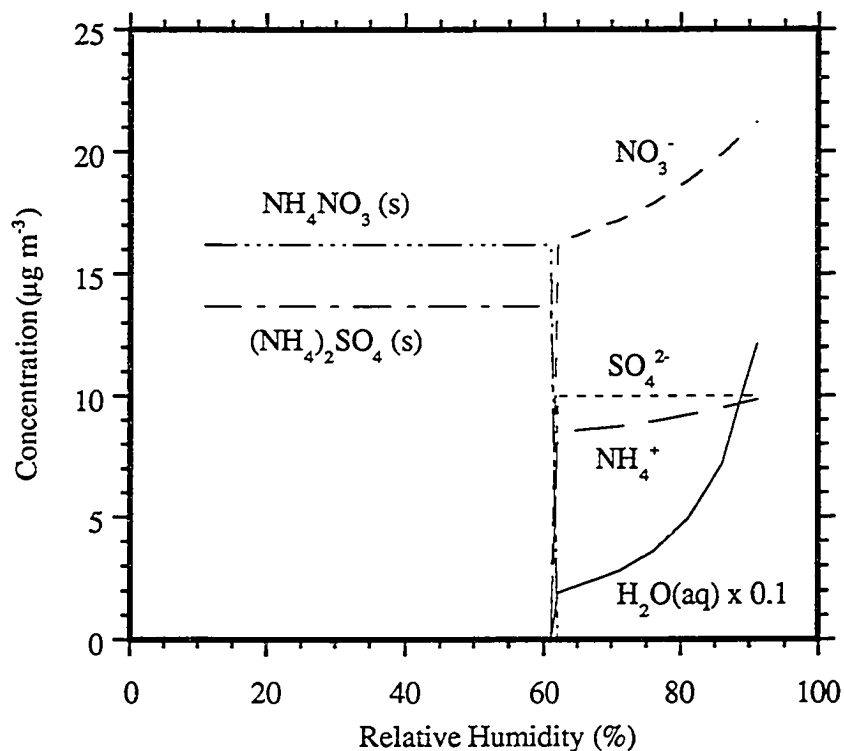
Fig. 7. Aerosol composition versus relative humidity. Initial conditions were $H_2SO_4(aq)$ = 10 mg m^{-3}, HCl(g) = 0 mg m^{-3}, NH$_3$(g) = 10 mg m^{-3}, HNO$_3$(g) = 30 mg m^{-3}, and T = 298 K.

Figure 8 shows several comparison between predicted and measured activity coefficients in a mixed solution. The measurements, taken by Conceicao *et al.* (1983),

384

were for sodium sulfate and sodium chloride. To obtain model results, we calculated the activity coefficients of the mixed electrolytes by simultaneously solving equilibrium equations together with binary activity coefficients, the water equation, and Bromley's mixing equation.
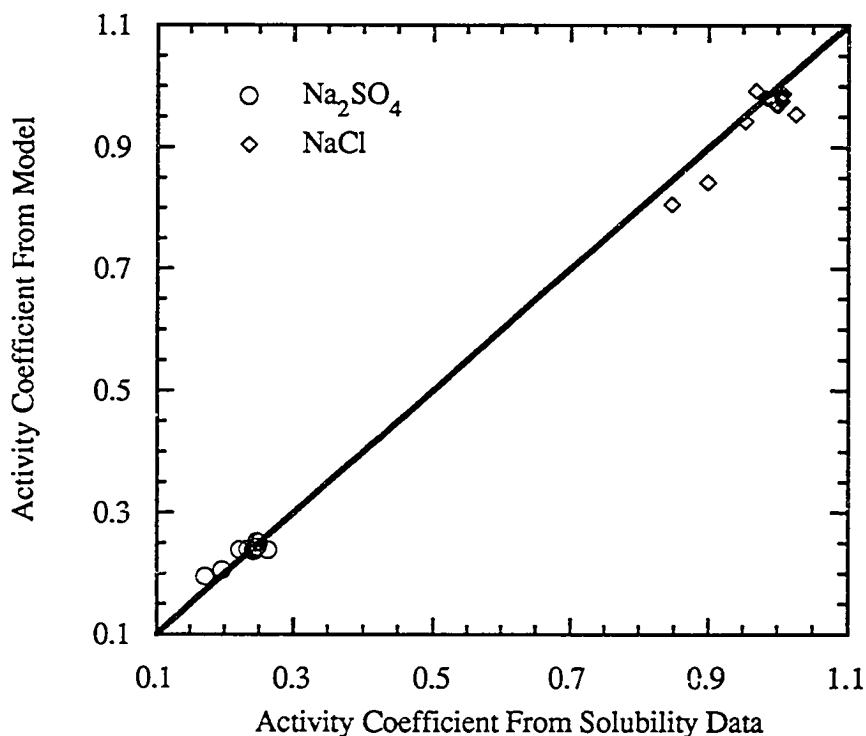
Fig. 8. Comparison between activity coefficients of sodium sulfate and sodium chloride calculated with EQUISOLV with those measured from solubility data (Conceicao *et al.*, 1983).

The remaining figures show model simulations of equilibrium coupled with condensational growth. Figures 9 and 10 show a case where the initial size distribution

385

was monodisperse and Figures 11 and 12 show a case where the initial aerosol masses were distributed over 43 distinct size bins. In both cases, the initial conditions were $H_2SO_4(aq) = 10$ mg m^{-3}, NaCl(aq) $= 10$ mg m^{-3}, HCl(g) $= 0$ mg m^{-3}, NH$_3$(g) $= 10$ mg m^{-3}, HNO$_3$(g) $= 30$ mg m^{-3}, r. h. $= 90\%$, and T $= 298$ K. For the first case, we assumed the monodisperse particles were large enough so that the Kelvin effect could be ignored. However, for the second case, the Kelvin effect was included since the size distribution was spread over small as well as large bins. Also, in the second case, we distributed all initial aerosol mass among three lognormal modes: a nucleation, accumulation, and coarse particle mode. The aerosols initially consisted of water, dissolved sulfuric acid, and dissolved sodium chloride. Most sodium chloride was distributed in the coarse mode while most sulfuric acid was distributed in the accumulation mode.

In both cases, concentrations were computed in the following manner: each 5-minute time interval, we (1) solved equilibrium between gases and all aerosol bins to determine vapor pressures of gases, (2) calculated growth and evaporation with SMVGEAR using the vapor pressure information just calculated, and (3) recalculated equilibrium within each aerosol bin, excluding the gas phase. To compute vapor pressures, Equations 10, 11, 31, 32, 41, 43, 44, 45, and 53 of Table A.6b were solved between the gas and each size bin of the aerosol phase. To compute intra-aerosol concentrations, equations 30, 31, 32, 41, and 53 of the table were solved for each size bin.

Figure 9 shows that, for the monodisperse distribution of about 5×10^3 particles and excluding the Kelvin effect, gas ambient concentrations converged to equilibrium values. Figure 10 shows a time-series plot of the corresponding aqueous concentrations, which also converged to equilibrium values.
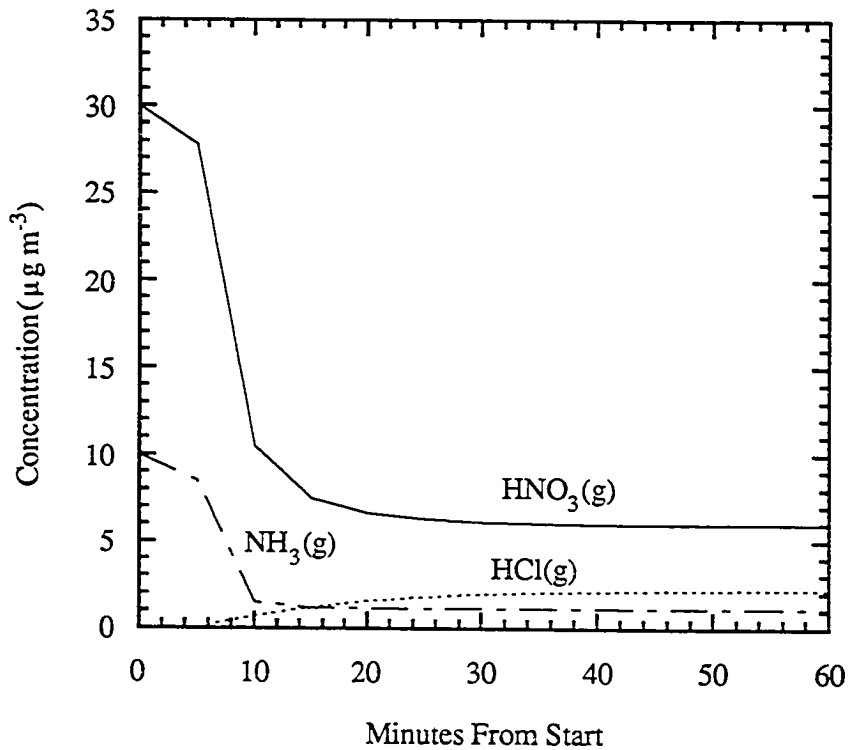
Fig. 9. Time series plot of gas concentrations during gas-aerosol transfer and equilibrium calculations. Initial conditions were H_2SO_4(aq) = 10 mg m^{-3}, NaCl(aq) = 10 mg m^{-3}, HCl(g) = 0 mg m^{-3}, NH_3(g) = 10 mg m^{-3}, HNO_3(g) = 30 mg m^{-3}, r. h. = 90%, and T = 298 K. The initial aerosol size distribution was monodisperse, the Kelvin effect was ignored, and the time interval between equilibrium calculations was five minutes. The text describes the method of calculation. Gas concentrations in the figure approach their respective equilibrium concentrations.

387
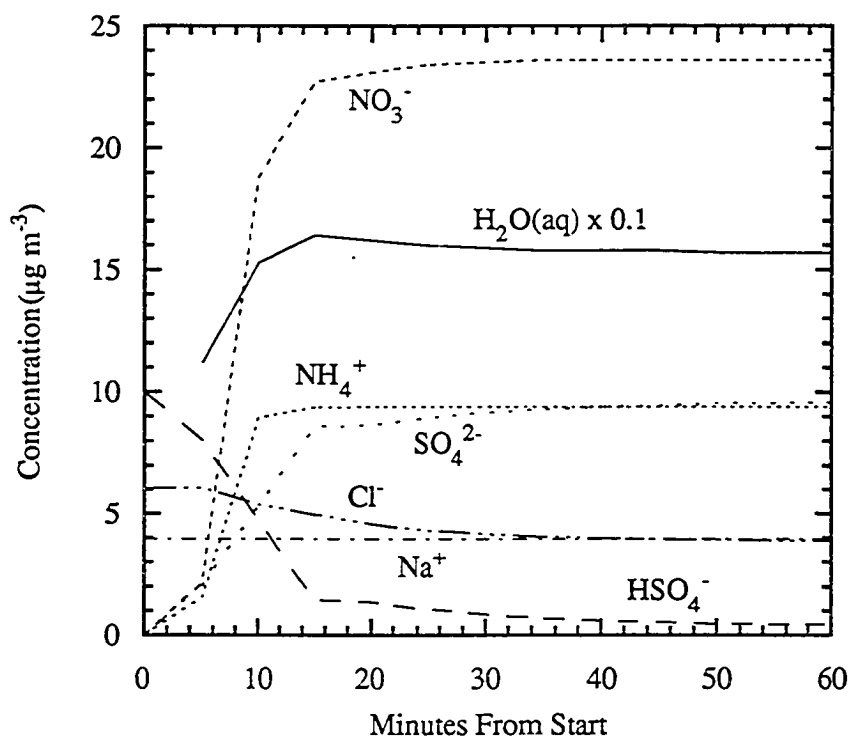
Fig. 10. Time series plot of aerosol composition for the case described in Figure 9 and the text. The concentration of each component in the figure approaches its equilibrium concentration.

Figures 11 and 12 show model results when we solved equilibrium and growth over 43 size bins simultaneously. The total number of particles in the system was about 4 x 10^4. Figure 11 shows that ambient gas concentrations approached Kelvin effect-adjusted equilibrium values. Figure 12 shows the corresponding aerosol-phase concentrations from this simulation, summed over all size bins. Cumulative aerosol concentrations also approached their equilibrium values.

388
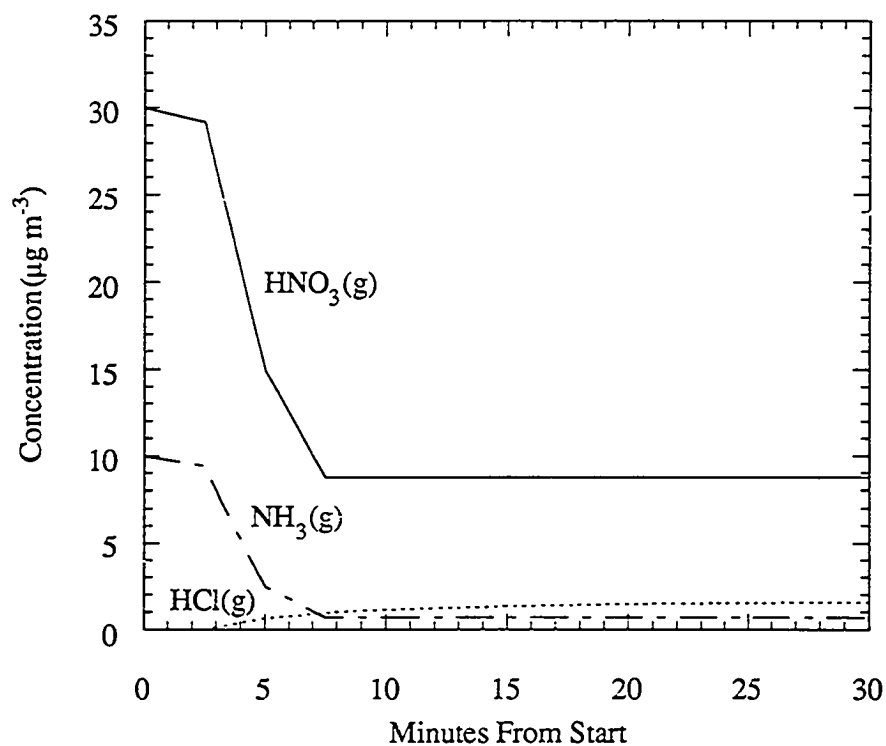
Fig. 11. Time series plot of gas concentrations during gas-aerosol transfer and equilibrium calculations. Initial conditions were $H_2SO_4(aq) = 10$ mg m^{-3}, $NaCl(aq) = 10$ mg m^{-3}, $HCl(g) = 0$ mg m^{-3}, $NH_3(g) = 10$ mg m^{-3}, $HNO_3(g) = 30$ mg m^{-3}, r. h. = 90%, and T = 298 K. The initial aerosol size distribution was distributed among 43 bins, the Kelvin effect was included, and the time interval between equilibrium calculations was 2.5 minutes. The text describes the method of calculation. Gas concentrations in the figure approach their respective equilibrium values.

389
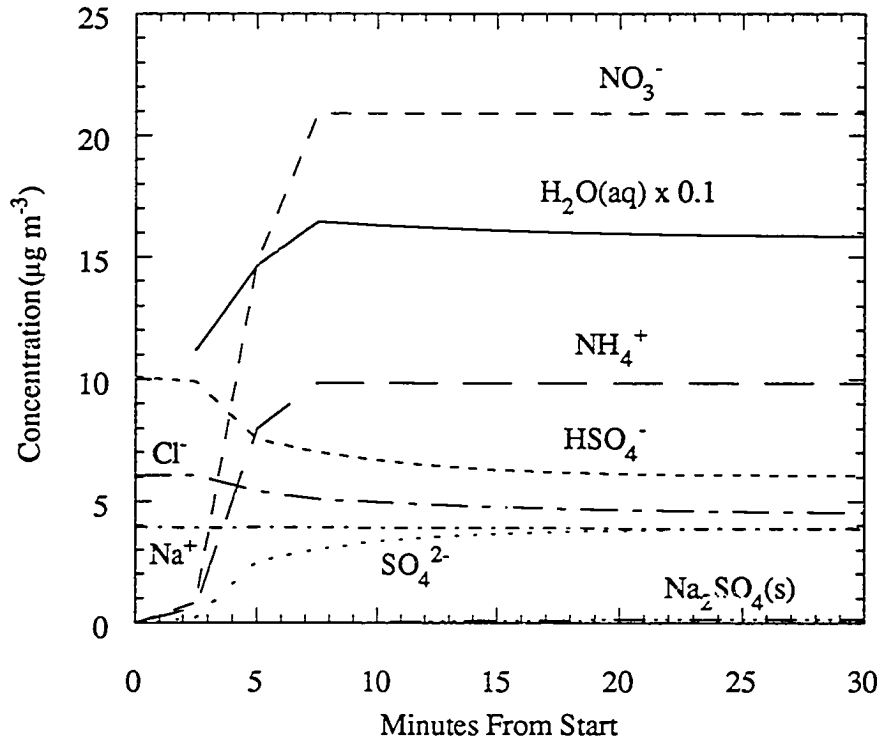
Fig. 12. Time series plot of aerosol composition, summed over all size bins, for the case described in Figure 11 and the text. The aerosol concentration of each component in the figure, summed over all bins, approaches its equilibrium concentration.

4.2 Timing Tests

The time to solve equilibrium equations varies significantly, depending on the number of equations, time intervals, size bins, and error tolerance. To give an indication of the speed of EQUISOLV, we compared it to a timing test shown in Kim *et al.* (1993b) and computed an absolute timing on a Cray-90.

Table 7 of Kim *et al.* (1993b) shows timings of simulations for four cases. Here, we compare their case 4, which originated from the conditions of Figure 3 of Pilinis and

390

Seinfeld (1987). The time for their equilibrium model, SCAPE, to solve the equations for the conditions given in Pilinis and Seinfeld (using activities from Bromley's method), for one size bin and one time step, and with a convergence criteria of 10^{-3} for gases and water, was 42 seconds on a SUN SPARC station SLC. For the same conditions and case, the time EQUISOLV took to obtain a normalized gross error in gas concentrations of 10^{-4} on a SUN SPARC station 1+ was 0.62 seconds. On a C-90, the time to solve the same simulation was 0.00196 seconds. In the case of EQUISOLV, we actually solved the same equations over 1000 grid cells and divided the total time by 1000 to obtain the time to solve in one grid cell.

Completely converging all equilibrium equations in a three-dimensional model with multiple aerosol size bins is often impractical with today's computer resources. For example, suppose we have 43 aerosol size bins, 20,000 grid cells, and wish to compute equilibrium vapor pressures every 15 minutes during one day of simulation. Then, EQUISOLV requires a minimum of 45 hours on a C-90 and 592 days on a SUN SPARC station 1+, and SCAPE requires a minimum of 110 years on a SUN SPARC station SLC to solve the above problem. Thus, the only practical way to run an equilibrium model in a large grid domain with many size bins is to increase the allowable error. Fortunately, for EQUISOLV, mass will be conserved and concentrations will be positive, regardless of the error tolerance.

While equilibrium calculations take a long time, growth calculations take much less because the growth equation solver, SMVGEAR, takes advantage of sparse matrices of partial derivatives. For example, solving growth of three species between the gas and 43 bins of the aerosol phase for one 15-minute time interval and 500 grid cells took 1.4 seconds on a C-90. This translates to about 1.5 hours per day of simulation for 20,000 grid cells.

391

5. CONCLUSIONS

We discussed a model that simulates growth and chemical equilibrium processes. The code converges any number of gas, liquid, ion, or solid equilibrium equations. Further, it conserves mass between the gas and multiple size bins of the aerosol phase and simultaneously solves for aerosol water content and ion activity coefficients. To solve for activity coefficients, the mixing model of Bromley, which requires binary activity data, was used. Temperature-dependent expressions for binary coefficients were developed using data from the literature. We also discussed methods of speeding the solution to the equilibrium equations in a multidimensional spatial model.

A practical application of the equilibrium model is simulating gas-aerosol transfer in a three-step process. The first step is to compute equilibrium vapor concentrations, the second is to solve condensational growth equations while using the equilibrium values, and the third is to apply the equilibrium model again to determine intra-aerosol distributions. Model simulations indicate that gases are not immediately in equilibrium with aerosols. However, simulations of growth coupled with equilibrium indicate that the partial pressures of gases approach equilibrium vapor pressures within a short time period when other physical processes are excluded from consideration.

Finally, EQUISOLV can be used to study tropospheric aerosols, stratospheric aerosols, ocean composition, and composition in the earth's crust. For each of these applications, appropriate activity coefficient data are required. While a significant amount of data for relative apparent molal enthalpy, apparent molal heat capacity, and binary activity coefficients at 298 K are available, more is needed to study solutions at high ionic strength.

392

REFERENCES

Allen, A. G., Harrison, R. M., and Erisman, J., Field measurements of the dissociation of ammonium nitrate and ammonium chloride aerosols, *Atmospheric Environment*, *17*, 1591 - 1599, 1989.

Bassett, M. E., and Seinfeld, J. H., Atmospheric equilibrium model of sulfate and nitrate aerosol, *Atmospheric Environment*, *17*, 2237 - 2252, 1983.

Bassett, M. E., and Seinfeld, J. H., Atmospheric equilibrium model of sulfate and nitrate aerosol-II. Particle size analysis, *Atmospheric Environment*, *18*, 1163 - 1170, 1984.

Betterton E. A. and Hoffmann M. R., Henry's law constants of some environmentally important aldehydes. *Environ. Sci. Technol.*, *22*, 1415 - 1418, 1988.

Bolton, D., The computation of equivalent potential temperature, *Mon. Wea. Rev.*, *108*, 1046 - 1053, 1980.

Bott, A., and Carmichael, G. R., Multiphase chemistry in a microphysical radiation fog model -- A numerical study, *Atmospheric Environment*, *27A*, 503 - 522, 1993.

Bromley, L. A., Thermodynamic properties of strong electrolytes in aqueous solutions, *AIChE J.*, *19*, 313 - 320, 1973.

Chameides, W. L., The photochemistry of a remote marine stratiform cloud, *J. Geophys. Res.*, *89*, 4739 - 4755, 1984.

393

Clegg, S. L., and Brimblecombe, P., Equilibrium partial pressures and mean activity and osmotic coefficients of 0 - 100% nitric acid as a function of temperature, *J. Phys. Chem.*, *94*, 5369 - 5380, 1990.

Clegg, S. L. and Whitfield, M., Activity coefficients in natural waters. In *Activity Coefficients in Electrolyte Solutions, 2nd Edition* (edited by Pitzer K. S.), CRC Press, Boca Raton, FL, 1991.

Cohen, M. D., Flagan, R. C., and Seinfeld, J. H., Studies of concentrated electrolyte solutions using the electrodynamic balance. 1. Water activities for single-electrolyte solutions, *J. Phys. Chem.*, *91*, 4563 - 4574, 1987a.

Cohen, M. D., Flagan, R. C., and Seinfeld, J. H., Studies of concentrated electrolyte solutions using the electrodynamic balance. 2. Water activities for mixed-electrolyte solutions, *J. Phys. Chem.*, *91*, 4575 - 4582, 1987b.

Conceicao, M., de Lima, P., and Pitzer, K., Thermodynamics of saturated electrolyte mixtures of NaCl with Na_2SO_4 and with $MgCl_2$, *J. Solution Chem.*, *12*, 187 - 199, 1983.

Drdla, K., Tabazadeh, A., Turco, R. P., Jacobson, M. Z., Dye, J. E., Twohy, C., Baumgardner, D., Fahey, D. W., Kelly, K. K., Chan, R. P., and Loewenstein, M., Analysis of the physical state of one Arctic polar stratospheric cloud based on observations, *Geophys. Res. Lett.*, in review, 1994.

Filippov, V. K., Charykova, M. V., and Trofimov, Y. M., Thermodynamics of the system $NH_4H_2PO_4$-$(NH_4)_2SO_4$-H_2O at 25°C, *J. Appl. Chem. U. S. S. R.*, *58*, 1807, 1985.

Goldberg, R. N., Evaluated activity and osmotic coefficients for aqueous solutions: Thirty-six uni-Bivalent electrolytes, *J. Phys. Chem. Ref. Data.*, *10*, 671 - 764, 1981.

394

Gmitro, J. I., and Vermeulen T., Vapor-liquid equilibrium for aqueous sulfuric acid, *AIChE J.*, *10*, 740 - 746, 1964.

Grosjean, D., The stability of particulate nitrate in the Los Angeles Atmosphere, *Sci. Total Envir.*, *25*, 263 - 275, 1982.

Hamer, W. J., and Wu, Y.-C., Osmotic coefficients and mean activity coefficients of uni-univalent electrolytes in water at 25°C, *J. Phys. Chem. Ref. Data*, *1*, 1047 - 1099, 1972.

Harned, H. S., and Owen, B. B., *The Physical Chemistry of Electrolyte* Solutions. Chap. 8, Reinhold, New York, NY, 1958.

Harrison, R. M., and MacKenzie, A. R., A numerical simulation of kinetic constraints upon achievement of the ammonium nitrate dissociation equilibrium in the troposphere, *Atmospheric Environment*, *24A*, 91 - 102, 1990.

Harvie, C. E., Moller, N., and Weare, J. H., The prediction of mineral solubilities in natural waters: The $Na-K-Mg-Ca-H-Cl-SO_4-OH-HCO_3-CO_3-CO_2-H_2O$ system to high ionic strengths at 25°C, *Geochimica et Cosmochimica Acta*, *48*, 723 - 751, 1984.

Hildemann, L. M., Russell, A. G., and Cass, G. R., Ammonia and nitric acid concentrations in equilibrium with atmospheric aerosols: experiment vs. theory, *Atmospheric Environment*, *18*, 1737 - 1750, 1984.

Holmes, H. F., and Mesmer, R. E., Thermodynamics of aqueous solutions of the alkali metal sulfates, *J. Solution Chem.*, *15*, 495 - 518, 1986.

Jacob, D., Chemistry of OH in remote clouds and its role in the production of formic acid and peroxymonosulfate, *J. Geophys. Res.*, *91*, 9807 - 9826, 1986.

Jacob D. J., Gottlieb E. W. and Prather M. J., Chemistry of a polluted cloudy boundary layer. *J. Geophys. Res.*, *94*, 12,975 - 13,002, 1989.

Jacobson, M. Z., and Turco, R. P., SMVGEAR: A sparse-matrix, vectorized Gear code for atmospheric models, *Atmos. Environ.*, *28A*, 273 - 284, 1994a.

Jacobson, M. Z., Turco, R. P., Jensen, E. J., and Toon, O. B., Modeling coagulation among particles of different composition and size, *Atmos. Environ., Part A*, in press, 1994b.

Jacobson, M. Z., and Turco, R. P., Simulating condensational growth, evaporation, and coagulation of aerosols using a combined moving and stationary size grid, *Aerosol Sci. Technol,* in review, 1994c.

Jacobson, M. Z., Turco, R. P., Lu, R., and Toon, O. B., GATOR: A gas, aerosol, transport, and radiation modeling system for studying urban and regional air pollution. *Atmos. Environ., Part A*, in review, 1994d.

Jacobson, M. Z., Developing, coupling, and applying a gas, aerosol, transport, and radiation modeling system for studying urban and regional air pollution. Ph. D. Thesis, Univ. of California, Los Angeles, 1994e.

Jayson G. G., Parsons B. J. and Swallow A. J., Some simple, highly reactive, inorganic chlorine derivatives in aqueous-solution. *Trans. Faraday Soc.*, 69, 1597 - 1607, 1973.

Kim, Y. P., Seinfeld, J. H., and Saxena, P., Atmospheric gas - aerosol equilibrium I. Thermodynamic model, *Aerosol Sci. Technol.*, *19*, 157 - 181, 1993a.

Kim, Y. P., Seinfeld, J. H., and Saxena, P., Atmospheric gas - aerosol equilibrium II. Analysis of common approximations and activity coefficient calculation methods, *Aerosol Sci. Technol.*, *19*, 182 - 198, 1993b.

Kozac-Channing L. F. and Heltz G. R., Solubility of ozone in aqueous solutions of 0 - 0.6 M ionic strength at 5 - 30ºC. *Environ. Sci. Technol.*, *17*, 145 - 149, 1983.

Kusik, C. L., and Meissner, H. P., Electrolyte activity coefficients in inorganic processing, *AIChE Symp. Ser.*, *173*, 14 - 20, 1978.

Latimer W. M., *The Oxidation States of the Elements and Their Potentials in Aqueous Solutions*, pp. 70 - 89. Prentice-Hall, New York, 1952.

Ledbury W. and Blair E. W., The partial formaldehyde vapour pressure of aqueous solutions of formaldehyde, II. *J. Chem. Soc.*, *127*, 2832 - 2839, 1925.

Lee Y. -N., Atmospheric aqueous-phase reactions of nitrogen species, Gas-Liquid Chemistry of Natural Waters, vol. 1, *BNL 51757*, pp. 20/1-20/10, Brookhaven Natl. Lab., 1984.

Le Henaff P., Methodes d'etude et proprietes des hydrates, hemiacetals et hemiacetals derives des aldehydes et des cetones. *Bull. Soc. Chim. France*, 4687 - 4700, 1968.

Lind J. A. and Kok G. L., Henry's law determinations for aqueous solutions of hydrogen peroxide, methylhydroperoxide, and peroxyacetic acid. *J. Geophys. Res.*, *91*, 7889 - 7895, 1986.

Marsh A. R. W. and McElroy W. J., The dissociation constant and Henry's law constant of HCl in aqueous solution. *Atmos. Environ.*, *19*, 1075 - 1080, 1985.

Martell A. E. and Smith R. M., *Critical stability constants, vol. 3, Other Organic Ligands*, Plenum, New York, 1977.

Pandis, S. N., and Seinfeld, J. H., Sensitivity analysis of a chemical mechanism for aqueous-phase atmospheric chemistry, *J. Geophys. Res.*, *94*, 1105 - 1126, 1989.

Park J. -Y and Lee Y. -N, Aqueous solubility and hydrolysis kinetics of peroxynitric acid, paper presented at 193rd Meeting, Am. Chem. Soc., Denver, Colo., April 5-10, 1987.

Parker, V. B., *Thermal properties of aqueous uni-univalent electrolytes*. National Standard Reference Data Series --NBS 2, U. S. Government Printing Office, Washington, DC, 1965.

397

Perrin D. D., *Ionization Constants of Inorganic Acids and Bases in Aqueous Solution*, 2nd ed., Pergamon, New York, 1982.

Perron, G., Roux, A., and Desnoyers, J. E., Heat capacities and volumes of NaCl, $MgCl_2$, $CaCl_2$, and $NiCl_2$ up to 6 molal in water, *Can J. Chem.*, *59*, 3049 - 3054., 1981

Pilinis, C., Seinfeld, J. H., and Seigneur, C., Mathematical modeling of the dynamics of multicomponent atmospheric aerosols, *Atmospheric Environment*, *21*, 943 - 955, 1987.

Pilinis, C., and Seinfeld, J. H., Continued development of a general equilibrium model for inorganic multicomponent atmospheric aerosols, *Atmospheric Environment*, *21*, 2453 - 2466, 1987.

Pilinis, C., and Seinfeld, J. H., Development and Evaluation of an Eulerian Photochemical Gas-Aerosol Model, *Atmospheric Environment*, *22*, 1985 - 2001, 1988.

Pilinis, C., Seinfeld, J. H., and Grosjean, D. J., Water content of atmospheric aerosols, *Atmospheric Environment*, *23*, 1601 - 1606, 1989.

Pitzer, K. S., and Mayorga, G., Thermodynamics of electrolytes II. Activity and osmotic coefficients for strong electrolytes with one or both ions univalent, *J. Phys. Chem.*, *77*, 2300 - 2308, 1973.

Pitzer, K. S., Roy R. R., and Silvester, L. F., Thermodynamics of electrolytes 7. Sulfuric Acid, *J. Am. Chem. Soc.*, *99*, 4930 - 4936, 1977.

Pitzer, K. S., Ion interaction approach: Theory and data correlation. In *Activity Coefficients in Electrolyte Solutions, 2nd Edition* (edited by Pitzer K. S.), CRC Press, Boca Raton, FL, 1991.

Robinson, R. A., and Stokes, R. H., *Electrolyte Solutions*, Second Edn. Buttersworth, London, 1964.

Roux, A., Musbally, G. M., Perron, G., Desnoyers, J. E., Singh, P. P., Woolley, E. M., and Hepler, L. G., Apparent molal heat capacities and volumes of aqueous electrolytes at 25°C: NaClO$_3$, NaClO$_4$, NaNO$_3$, NaBrO$_3$, NaIO$_3$, KClO$_3$, KBrO$_3$, KIO$_3$, NH$_4$NO$_3$, NH$_4$Cl, and NH$_4$ClO$_4$, *Can. J. Chem.*, *56*, 24 - 28, 1978.

Russell, A. G., McRae, G. J., and Cass, G. R., Mathematical modeling of the formation and transport of ammonium nitrate aerosol, *Atmospheric Environment*, *17*, 949 - 964, 1983.

Russell, A. G., and Cass, G. R., Verification of a mathematical model for aerosol nitrate and nitric acid formation and its use for control measure evaluation, *Atmospheric Environment*, *20*, 2011 - 2025, 1986.

Russell, A., McCue, K., and Cass, G., Mathematical modeling of the formation of nitrogen-containing air pollutants.-1. Evaluation of an Eulerian photochemical model, *Envir. Sci. Technol.*, *22*, 263 - 271, 1988.

Saxena, P., and Peterson, T. W., Thermodynamics of multicomponent electrolytic aerosols, *J. Colloid Interface Sci.*, *79*, 496 - 510, 1981.

Saxena, P., Seigneur, C., and Peterson, T. W., Modeling of multiphase atmospheric aerosols, *Atmospheric Environment*, *17*, 1315 - 1329, 1983.

Saxena, P., Hudischewskyj, A. B., Seigneur C., and Seinfeld, J. H., A comparative study of equilibrium approaches to the chemical characterization of secondary aerosols, *Atmospheric Environment*, *20*, 1471 - 1483, 1986.

Saxena, P., Mueller, P. K., Kim, Y. P., Seinfeld, J. H., and Koutrakis, P., Coupling thermodynamic theory with measurements to characterize acidity of atmospheric particles, *Aerosol Sci. Technol.*, *19*, 279 - 293, 1993.

Schwartz S. E. and White W. H., Solubility equilibria of the nitrogen oxides and oxyacids in aqueous solution. *Adv. Environ. Sci. Eng.*, *4*, 1 - 45, 1981.

399

Schwartz, S. E., and Freiberg, J. E., Mass-transport limitation to the rate of reaction of gases in liquid droplets: application to oxidation of SO_2 in aqueous solutions, *Atmospheric Environment, 15,* 1129 - 1144, 1981.

Schwartz S. E., Gas- and aqueous-phase chemistry of HO_2 in liquid water clouds, *J. Geophys. Res., 89,* 11,589 - 11,598, 1984.

Scott, W. D., and Cattell, F. C. R., Vapor pressure of ammonium sulfates, *Atmospheric Environment, 13,* 307 - 317, 1979.

Seigneur, C., A model of sulfate aerosol dynamics in atmospheric plumes, *Atmospheric Environment, 16,* 270 - 294, 1982.

Seigneur, C., and Saxena, P., A study of atmospheric acid formation in different environments, *Atmospheric Environment, 18,* 2109 - 2124, 1984.

Smith R. M. and Martell A. E., *Critical Stability Constants, vol. 4: Inorganic Complexes.* Plenum, New York, 1976.

Snider J. R. and Dawson G. A., Tropospheric light alcohols, carbonyls, and acetonitrile: Concentrations in the southwestern United States and Henry's law data. *J. Geophys. Res., 90,* 3797 - 3805, 1985.

Sorensen P. E. and Andersen V. S., The formaldehyde-hydrogen sulphite system in alkaline aqueous solution: Kinetics, mechanism, and equilibria. *Acta Chem. Scand., 24,* 1301 - 1306, 1970.

Stelson, A. W., Friedlander, S. K., and Seinfeld, J. H., A note on the equilibrium relationship between ammonia and nitric acid and particulate ammonium nitrate, *Atmospheric Environment, 13,* 369 - 371, 1979.

Stelson, A. W., and Seinfeld, J. H., Relative humidity and temperature dependence of the ammonium nitrate dissociation constant, *Atmospheric Environment, 16,* 983 - 992, 1982a.

Stelson, A. W., and Seinfeld, J. H., Relative humidity and pH dependence of the vapor pressure of ammonium nitrate-nitric acid solutions at 25° C, *Atmospheric Environment*, *16*, 993 - 1000, 1982b.

Stelson, A. W., and Seinfeld, J. H., Thermodynamic prediction of the water activity, NH_4NO_3 dissociation constant, density and refractive index for the NH_4NO_3-$(NH_4)_2SO_4$-H_2O system at 25°C, *Atmospheric Environment*, *16*, 2507 - 2514, 1982c.

Stelson, A. W., Bassett, M. E., and Seinfeld, J. H., Thermodynamic equilibrium properties of aqueous solutions of nitrate, sulfate and ammonium, In *Chemistry of Particles, Fogs and Rain* (edited by Durham J. L.). Ann Arbor Publication, Ann Arbor, MI, 1984.

Sukhatme, S. P., and Saikhedkar, N., Heat capacities of glycerol-water mixtures and aqueous solutions of ammonium sulfate ammonium nitrate and strontium nitrate, *Ind. J. Technol.*, *7*, 1 - 4, 1969.

Tabazadeh, A., Turco, R. P., and Jacobson, M. Z., A model for studying the composition and chemical effects of stratospheric aerosols, *J. Geophys. Res.*, in press, 1994.

Tabazadeh, A., Turco, R. P., and Jacobson, M. Z., A study of Type I Polar Stratospheric Cloud formation, *Geophys. Res. Let.*, in review, 1994.

Tang, I. N., Deliquescence properties and particle size change of hygroscopic aerosols in generation of aerosols. In *Generation of Aerosols and Facilities for Exposure Experiments* (Edited by Willeke, K.) pp. 153 - 167, Ann Arbor Science, Ann Arbor, MI, 1980.

Tang, I. N., and Munkelwitz, H. R., Composition and temperature dependence of the deliquescence properties of hygroscopic aerosols, *Atmospheric Environment*, *27A*, 467 - 473, 1993.

Vanderzee, C. E., Waugh, D. H., and Haas, N. C., Enthalpies of dilution and relative apparent molar enthalpies of aqueous ammonium nitrate. The case of a weakly hydrolysed (dissociated) salt, *J Chem. Thermodynam.*, *12*, 21 - 25, 1980.

Villars, D. S., A method of successive approximations for computing combustion equilibria on a high speed digital computer, *J. Phys. Chem.*, *63*, 521 - 525, 1958.

Wagman, D. D., Evans, W. H., Parker, V. B., Schumm, R. H., Halow, I., Bailey, S. M., Churney, K. L., and Nuttall R. L., The NBS tables of chemical thermodynamic properties: selected values for inorganic and C_1 and C_2 organic substances in SI units, *J. Phys. Chem. Ref. Data*, *11*, *Suppl. 2*, 1982.

Wasa T. and Musha S., Polarographic behavior of glyoxal and its related compounds. *Univ. Osaka Prefect. Ser.*, *19*, 169 - 180, 1970.

Wexler, A. S., and Seinfeld, J. H., The distribution of ammonium salts among a size and composition dispersed aerosol, *Atmospheric Environment*, *24A*, 1231 - 1246, 1990.

Wexler, A. S., and Seinfeld, J. H., Second-generation inorganic aerosol model, *Atmospheric Environment*, *25A*, 2731 - 2748, 1991.

Wexler, A. S., and Seinfeld, J. H., Analysis of aerosol ammonium nitrate: Departures from equilibrium during SCAQS, *Atmospheric Environment*, *26A*, 579 - 591, 1992.

Wu, Y.-C., and Hamer, W. J., Revised values of the osmotic coefficients and mean activity coefficients of sodium nitrate in water at 25°C, *J. Phys. Chem. Ref. Data*, *9*, 513 - 518, 1980.

Zdanovskii, A. B., New methods of calculating solubilities of electrolytes in multicomponent systems, *Zhur. Fiz. Khim*, *22*, 1475 - 1485, 1948.

402

APPENDIX

Table A.1. Parameters for calculating the activity coefficients of binary electrolytes. The parameters fit into Equation (18), which is subsequently used in Equation (17). The B parameters [which also fit into Equation (13)] give the activity coefficient at 298 K, the G parameters (described in the text) give the heat of dilution term, and the H parameters give the heat capacity term. The references identify where data was obtained for our calculations, and the molalites are the maximum values for either the activity coefficient data at 298 K, the heat of dilution data, or the heat capacity data.

	j	Hamer and Wu (1972) 16 m B_j	Parker (1965) 55.5 m G_j	Parker (1965) 15.9 m H_j
HCl	0	-1.998104×10^{-2}	0	0
	1	-7.959068×10^{-1}	5.532198×10^{-1}	2.108728×10^{0}
	2	6.580198×10^{-1}	-2.571126×10^{-1}	8.542292×10^{-1}
	3	-7.409941×10^{-2}	2.790048×10^{-1}	-6.237459×10^{-1}
	4	1.345075×10^{-2}	-4.691631×10^{-2}	1.935911×10^{-1}
	5	-2.248651×10^{-3}	2.382485×10^{-3}	-2.037543×10^{-2}

	j	Hamer and Wu (1972) 28 m B_j	Parker (1965) 55.5 m G_j	Parker (1965) 55.5 m H_j
HNO$_3$	0	-2.388378×10^{-2}	0	0
	1	-7.777787×10^{-1}	5.785894×10^{-1}	-4.785171×10^{-1}
	2	5.950086×10^{-1}	-9.860271×10^{-1}	6.521896×10^{0}
	3	-1.284278×10^{-1}	6.043012×10^{-1}	-2.605544×10^{0}
	4	1.291734×10^{-2}	-1.123169×10^{-1}	3.739984×10^{-1}
	5	-6.257155×10^{-4}	6.688134×10^{-3}	-1.832646×10^{-2}

	j	Hamer and Wu (1972) 6.1 m B_j	Parker (1965) 6.1 m G_j	Perron et al. (1981) 6.0 m H_j
NaCl	0	-6.089937×10^{-3}	0	0
	1	-1.015184×10^{0}	5.808744×10^{-1}	2.261834×10^{0}
	2	9.345503×10^{-1}	-1.163239×10^{0}	3.622494×10^{0}
	3	-4.615793×10^{-1}	5.136893×10^{-1}	-1.608598×10^{0}
	4	1.431557×10^{-1}	-1.029523×10^{-1}	2.092972×10^{-1}
	5	-1.700298×10^{-2}	1.401488×10^{-2}	0

	Wu and Hamer (1980) 10.8 m	Parker (1965) 9.2 m	Parker (1965) 2.2 m
NaNO$_3$			

403

j	B_j	G_j	H_j
0	-6.638145×10^{-3}	0	0
1	-1.024329×10^{0}	5.678220×10^{-1}	7.232987×10^{-1}
2	6.877457×10^{-1}	-2.136826×10^{0}	1.918907×10^{1}
3	-3.336161×10^{-1}	1.145031×10^{0}	-2.382164×10^{1}
4	8.387414×10^{-2}	-2.585350×10^{-1}	1.367081×10^{1}
5	-8.154844×10^{-3}	2.390815×10^{-2}	-3.064556×10^{0}

NaHSO$_4$ Harvie et al. (1984) 6.0 m | Used same as for NaCl 6.1 m | Used same as for NaCl 6.0 m

j	B_j	G_j	H_j
0	-8.890979×10^{-3}	0	0
1	-9.559487×10^{-1}	5.808744×10^{-1}	2.261834×10^{0}
2	8.758970×10^{-1}	-1.163239×10^{0}	3.622494×10^{0}
3	-4.607380×10^{-1}	5.136893×10^{-1}	-1.608598×10^{0}
4	1.309144×10^{-1}	-1.029523×10^{-1}	2.092972×10^{-1}
5	-1.398546×10^{-2}	1.401488×10^{-2}	0

Na$_2$SO$_4$ Goldberg (1981) 4.4 m | Wagman et al. (1982) 3.1 m | Holmes & Mesmer (1986) 2.0 m

j	B_j	G_j	H_j
0	-2.323071×10^{-2}	0	0
1	-3.321509×10^{0}	1.698182×10^{0}	9.410224×10^{0}
2	3.388793×10^{0}	-5.160108×10^{0}	2.213823×10^{1}
3	-2.402946×10^{0}	2.132810×10^{0}	-3.481895×10^{1}
4	8.926764×10^{-1}	8.840108×10^{-1}	2.348397×10^{1}
5	-1.225933×10^{-1}	-5.143058×10^{-1}	-6.471345×10^{0}

NH$_4$Cl Hamer and Wu (1972) 7.4 m | Wagman et al. (1982) 7.0 m | Parker (1965) 7.4 m

j	B_j	G_j	H_j
0	-5.022484×10^{-3}	0	0
1	-1.037873×10^{0}	4.890513×10^{-1}	1.959107×10^{0}
2	8.517483×10^{-1}	-7.013315×10^{-1}	9.894682×10^{-1}
3	-4.225323×10^{-1}	4.682151×10^{-1}	-1.024499×10^{-1}
4	1.214996×10^{-1}	-1.702461×10^{-1}	-2.354376×10^{-1}
5	-1.471525×10^{-2}	2.502643×10^{-2}	6.600384×10^{-2}

NH$_4$NO$_3$ Hamer and Wu (1972) 25.9 m | Vanderzee et al. (1980) 25.0 m | Roux et al. (1978) 22.4 m

j	B_j	G_j	H_j
0	-1.044572×10^{-2}	0	0
1	-1.004940×10^{0}	4.362921×10^{-1}	2.611682×10^{0}
2	4.674064×10^{-1}	-1.455444×10^{0}	3.158677×10^{0}
3	-1.750495×10^{-1}	6.282104×10^{-1}	-2.005748×10^{0}
4	3.253844×10^{-2}	-1.123507×10^{-1}	4.113737×10^{-1}
5	-2.276789×10^{-3}	7.438990×10^{-3}	-2.820677×10^{-2}

NH$_4$HSO$_4$ Bassett & Seinfeld (1983) | Used same as for NH$_4$Cl | Used same as for NH$_4$Cl

404

j	6.0 m B_j	7.0 m G_j	7.4 m H_j
0	-2.708121×10^{-3}	0	0
1	-1.095646×10^{0}	4.890513×10^{-1}	1.959107×10^{0}
2	1.042878×10^{0}	-7.013315×10^{-1}	9.894682×10^{-1}
3	-6.289405×10^{-1}	4.682151×10^{-1}	-1.024499×10^{-1}
4	2.079631×10^{-1}	-1.702461×10^{-1}	-2.354376×10^{-1}
5	-2.776957×10^{-2}	2.502643×10^{-2}	6.600384×10^{-2}

$(NH_4)_2SO_4$ — Filippov *et al.* (1985); Wagman *et al.* (1982) — Sukhatme and Saikhedkar (1969)

j	5.8 m B_j	5.5 m G_j	H_j
0	-2.163694×10^{-2}	2.297972×10^{-1}	0
1	-3.377941×10^{0}	4.255129×10^{-1}	1.609902×10^{-3}
2	3.118007×10^{0}	-2.220594×10^{0}	4.437758×10^{0}
3	-1.920544×10^{0}	2.607601×10^{0}	6.101756×10^{-3}
4	6.372975×10^{-1}	-1.243384×10^{0}	4.021805×10^{-1}
5	-8.277292×10^{-2}	2.102563×10^{-1}	4.375833×10^{-4}

Table A.2. Parameters for calculating the activity coefficients of solutions containing only hydrogen and either bisulfate or sulfate ions. The parameters fit into Equation (19), which is subsequently used in (17). We calculated the W's by solving equations in Pitzer *et al.* (1977) and Stelson *et al.* (1984), simultaneously, as described in the text. The fits are valid up to 6.0 m

	j	$W_{0,j}$	$W_{1,j}$	$W_{2,j}$	$W_{3,j}$
H^+/HSO_4^-	0	-1.225455×10^{2}	1.230707×10^{0}	-4.119776×10^{-3}	4.595935×10^{-6}
	1	1.996164×10^{3}	-1.997451×10^{1}	6.660462×10^{-2}	-7.403799×10^{-5}
	2	-4.102617×10^{3}	4.080428×10^{1}	-1.352508×10^{-1}	1.494309×10^{-4}
	3	2.665534×10^{3}	-2.610425×10^{1}	8.525047×10^{-2}	-9.282615×10^{-5}
	4	-5.421704×10^{2}	5.121146×10^{0}	-1.611159×10^{-2}	1.687197×10^{-5}
	5	1.886410×10^{1}	-1.415977×10^{-1}	3.214582×10^{-4}	-1.950665×10^{-7}
$2H^+/SO_4^{2-}$	0	-2.316892×10^{1}	2.357379×10^{-1}	-8.020047×10^{-4}	9.096087×10^{-7}
	1	3.559700×10^{2}	-3.656462×10^{0}	1.243911×10^{-2}	-1.409604×10^{-5}
	2	-6.199375×10^{2}	6.260075×10^{0}	-2.108119×10^{-2}	2.369106×10^{-5}
	3	3.107313×10^{2}	-3.073566×10^{0}	1.018136×10^{-2}	-1.128845×10^{-5}
	4	-2.457443×10^{1}	2.147608×10^{-1}	-6.330187×10^{-4}	6.306867×10^{-7}
	5	-6.413438×10^{0}	6.935867×10^{-2}	-2.461235×10^{-4}	2.877242×10^{-7}

405

Table A.3. Parameters for calculating molalities of binary electrolytes as a function of relative humidity. The Y coefficients fit into Equation (21). The table also lists the lowest relative humidity (r. h.) and corresponding highest molality (m) each fit is valid for. The reverse fit (humidity as a function of molality) was given by Pilinis and Seinfeld (1987), while the original data came from Cohen *et al.* (1987a,b), Bassett and Seinfeld (1983), and Pitzer and Mayorga (1973).

Species Lo r. h. / Hi m	HCl 0% r. h.; 18.5 m	HNO₃ 0% r. h.; 22.6 m	H+/HSO₄⁻ 0% r. h.; 29.1 m	2H⁺ / SO₄²⁻ 0% r. h.; 29.1 m
Y_0	4.382962×10^0	4.852977×10^0	5.611895×10^0	5.611895×10^0
Y_1	-5.357632×10^0	-6.621314×10^0	-1.387446×10^1	-1.387446×10^1
Y_2	3.098542×10^1	3.390133×10^1	1.750682×10^1	1.750682×10^1
Y_3	-2.000641×10^2	-1.985191×10^2	7.138146×10^1	7.139146×10^1
Y_4	6.504476×10^2	6.281150×10^2	-3.109173×10^2	-3.109173×10^2
Y_5	-1.081413×10^3	-1.038494×10^3	4.662288×10^2	4.662288×10^2
Y_6	8.842283×10^2	8.498917×10^2	-3.128612×10^2	-3.128612×10^2
Y_7	-2.829861×10^2	-2.729090×10^2	7.767097×10^1	7.767097×10^1

Species Lo r. h. / Hi m	NaCl 43% r. h.; 13.6 m	NaNO₃ 46% r. h.; 40 m	NaHSO₄ 0% r. h.; 20.5 m	Na₂SO₄ 51% r. h.; 12.8 m
Y_0	-1.918004×10^2	4.976285×10^3	4.662777×10^0	-3.295311×10^3
Y_1	2.001540×10^3	-4.971878×10^4	-1.128472×10^1	3.188349×10^4
Y_2	-8.557205×10^3	2.099707×10^5	7.049464×10^1	-1.305168×10^5
Y_3	1.987670×10^4	-4.855791×10^5	-2.788050×10^2	2.935608×10^5
Y_4	-2.717192×10^4	6.648387×10^5	6.103105×10^2	-3.920423×10^5
Y_5	2.187103×10^4	-5.396606×10^5	-7.409417×10^2	3.109519×10^5
Y_6	-9.591577×10^3	2.407868×10^5	4.614577×10^2	-1.356439×10^5
Y_7	1.763672×10^3	-4.561394×10^4	-1.150735×10^2	2.510249×10^4

Species Lo r. h. / Hi m	NH₄Cl 47% r. h.; 23.2 m	NH₄NO₃ 62% r. h.; 28 m	NH₄HSO₄ 0% r. h.; 31.2 m	(NH₄)₂HSO₄ 47% r. h.; 17.9 m
Y_0	5.499544×10^2	1.235157×10^4	5.515580×10^0	4.363511×10^2
Y_1	-6.162768×10^3	-1.097966×10^5	3.588744×10^0	-4.947645×10^3
Y_2	2.954960×10^4	4.173924×10^5	-6.363443×10^1	2.399693×10^4
Y_3	-7.757513×10^4	-8.792165×10^5	3.687630×10^2	-6.364664×10^4
Y_4	1.202065×10^5	1.108433×10^6	-1.023972×10^3	9.952891×10^4
Y_5	-1.099605×10^5	-8.364973×10^5	1.394436×10^3	-9.179112×10^4
Y_6	5.502138×10^4	3.499527×10^5	-9.168213×10^2	4.626748×10^4

406

Y_7 -1.162895×10^4 -6.261910×10^4 2.328726×10^2 -9.844195×10^3

Table A.4. Parameters for calculating temperature-dependent binary molalities as a function of relative humidity. The X's fit into Equation (26), which subsequently fits into Equation (21). The functions are valid from 273 - 310 K, from 0 - 100% relative humidity for HCl and HNO_3, and from about 62 to 100% humidity for NH_4NO_3.

	j	$X_{0,j}$	$X_{1,j}$	$X_{2,j}$	$X_{3,j}$
HCl	0	4.317512×10^0	9.018501×10^{-5}	-4.567419×10^7	-
	1	-2.333926×10^1	1.152893×10^{-1}	-1.272329×10^{-4}	-
	2	1.365286×10^2	-9.868246×10^{-1}	1.331139×10^{-3}	-
	3	-3.626892×10^2	3.264258×10^0	-4.736964×10^{-3}	-
	4	4.469631×10^2	-5.167199×10^0	7.788239×10^{-3}	-
	5	-2.376030×10^2	3.913351×10^0	-6.042720×10^{-3}	-
	6	3.598574×10^1	-1.139077×10^0	1.788247×10^{-3}	-
HNO_3	0	4.764789×10^0	1.877614×10^{-4}	-7.141204×10^{-7}	-
	1	-2.453410×10^1	1.186790×10^{-1}	-1.367524×10^{-4}	-
	2	1.227688×10^2	-8.836610×10^{-1}	1.167858×10^{-3}	-
	3	-2.454977×10^2	2.461343×10^0	-3.395230×10^{-3}	-
	4	1.619147×10^2	-3.260771×10^0	4.602386×10^{-3}	-
	5	5.740429×10^1	1.973276×10^0	-2.831021×10^{-3}	-
	6	-7.557552×10^1	-4.168263×10^{-1}	6.071508×10^{-4}	-
NH_4NO_3	0	-2.864930×10^6	2.917190×10^4	-9.908866×10^1	1.122209×10^{-1}
	1	2.144525×10^7	-2.183035×10^5	7.414076×10^2	-8.395919×10^{-1}
	2	-6.654196×10^7	6.771936×10^5	-2.299614×10^3	2.603965×10^0
	3	1.095612×10^8	-1.114726×10^6	3.784981×10^3	-4.285680×10^0
	4	-1.009605×10^8	1.026985×10^6	-3.486746×10^3	3.947832×10^0
	5	4.937135×10^7	-5.021046×10^5	1.704586×10^3	-1.929949×10^0
	6	-1.001036×10^7	1.017845×10^5	-3.455270×10^2	3.912036×10^{-1}

Table A.5. Liquid, ion, and solid species used in the equations of Table A.6b.

Chemical Formula	Chemical Name	Chemical Formula	Chemical Name
$H_2O(aq)$	water	OH^-	hydroxy ion
$H_2SO_4(aq)$	sulfuric acid	O_2^-	peroxy ion
$SO_2(aq)$	sulfur dioxide	HO_2^-	hydroperoxy ion

407

$O_3(aq)$	ozone	NH_4^+	ammonium ion
$OH(aq)$	hydroxyl radical	NO_3^-	nitrate ion
$HO_2(aq)$	hydroperoxy radical	NO_2^-	nitrogen dioxide ion
$H_2O_2(aq)$	hydrogen peroxide	HSO_4^-	bisulfate
$NO_2(aq)$	nitrogen dioxide	SO_4^{2-}	sulfate
$NO_3(aq)$	nitrate radical	HSO_3^-	bisulfite
$HONO(aq)$	nitrous acid	SO_3^{2-}	sulfite
$HNO_3(aq)$	nitric acid	Na^+	sodium ion
$HO_2NO_2(aq)$	peroxynitric acid	Cl^-	chloride ion
$NH_3(aq)$	ammonia	Cl_2^-	dichloride ion
$Cl(aq)$	chlorine atom	$ClOH^-$	chlorine hydroxide radical
$HCl(aq)$	hydrochloric acid	HCO_3^-	bicarbonate ion
$CO_2(aq)$	carbon dioxide	CO_3^{2-}	carbonate ion
$CH_3O_2(aq)$	methylperoxy radical	$HCOO^-$	formate
$CH_3OH(aq)$	methanol	CH_3COO^-	acetate
$CH_2O(aq)$	formaldehyde	$Na_2SO_4(s)$	sodium sulfate
$H_2C(OH)_2(aq)$	methylene glycol	$NaHSO_4(s)$	sodium bisulfate
$HCOOH(aq)$	formic acid	$NaCl(s)$	sodium chloride
$CH_3OOH(aq)$	methyl hydroperoxide	$NaNO_3(s)$	sodium nitrate
$CH_3COOH(aq)$	acetic acid	$(NH_4)_2SO_4(s)$	ammonium sulfate
$CH_3C(O)OOH(aq)$	peroxyacetic acid	$NH_4HSO_4(s)$	ammonium bisulfate
$CH_3C(O)OONO_2(aq)$	peroxyacetyl nitrate	$NH_4Cl(s)$	ammonium chloride
$CH_3COCHO(aq)$	methylglyoxal	$NH_4NO_3(s)$	ammonium nitrate
H^+	hydrogen ion	$(NH_4)_3H(SO_4)_2(s)$	tri ammonium bisulfate

Tables A.6a and A.6b. List of equilibrium constant units (Table A.6a) and equilibrium reactions and constants (Table A.6b) used for the simulation presented in Figure 3. The equations were gathered from Jacob (1986), Pilinis and Seinfeld (1987), Pandis and Seinfeld (1989), and Jacob et al. (1989). Specific references are (A) Smith and Martel', 1976; (B) Lind and Kok, 1986; (C) Kozac-Channing and Heltz, 1983; (D) Schwartz and White, 1981; (E) Schwartz, 1984; (F) Jacob, 1986; (G) Park and Lee, 1987; (H) Kim et al., 1993a; (I) Ledbury and Blair, 1925; (J) Latimer, 1952; (K) Snider and Dawson, 1985; (L) Jacob et al., 1989, 1986; (M) Lee, 1984; (N) Betterton and Hoffmann, 1988; (P) Le Henaff, 1968; (Q) Wasa and Musha, 1970; (R) Jayson et al., 1973; (S) Marsh and McElroy, 1985; (T) Perrin, 1982; (U) Martell and Smith, 1977; (V) Sorensen and

408

Anderson, 1970. A (*) indicates the rates were combined from other rates that are in the table or not included in the table.

The equilibrium constant reads

$$K_{eq} = Ae^{[B(T_o/T - 1) + C(1 + \ln(T_o/T) - T_o/T)]},$$

where A is the equilibrium constant at 298.15 K, T_o is the reference temperature (298.15 K), T is temperature (K), B = $-\Delta H / (R\, T_o)$ -- where R is the ideal gas constant (8.314 J mol^{-1} K^{-1}) and H is enthalpy (J mol^{-1}) -- and C = $-\Delta C_p / R$ -- where C_p is the heat capacity at constant pressure. Each of equilibrium equations has an equilibrium constant with the corresponding units shown in Table A.6a. In both Tables A.6a and b, g or no state symbol indicates a gas, aq indicates a liquid, + or -, indicates an ionic species, and s indicates a solid. In Table A.6a, the species A, B, AB, etc. are fictitious.

Table A.6a

	Reaction Type	Units
A(g)	<=> A(aq)	mole kg^{-1} atm^{-1}
AB(aq)	<=> A$^+$ + B$^-$	mole kg^{-1}
AB(g)	<=> A$^+$ + B$^-$	mole^2 kg^{-2} atm^{-1}
A$_2$B(s)	<=> 2A$^+$ + B^{2-}	mole^3 kg^{-3}
AB(s)	<=> A$^+$ + B$^-$	mole^2 kg^{-2}
AB(s)	<=> A(g) + B(g)	atm^2
A(g) + B(g)	<=> A$^+$ + B$^-$	mole^2 kg^{-2} atm^{-2}
A$_3$B$_2$(s) + C(aq)	<=> 3A$^+$ + 2CB$^-$	mole^4 kg^{-4}

Table A.6b

	Reaction		A	B	C	reference
1.	SO$_2$(g)	<=> SO$_2$(aq)	1.23 x 10^0	10.47		A
2.	H$_2$O$_2$(g)	<=> H$_2$O$_2$(aq)	7.45 x 10^4	22.21		B

409

#	Reactant	Reaction	K			Ref
3.	$O_3(g)$	$\Leftrightarrow O_3(aq)$	1.13×10^{-2}	7.72		C
4.	$NO_2(g)$	$\Leftrightarrow NO_2(aq)$	1.00×10^{-2}	8.38		E
5.	$NO_3(g)$	$\Leftrightarrow NO_3(aq)$	2.10×10^5	29.19		F
6.	$OH(g)$	$\Leftrightarrow OH(aq)$	2.50×10^1	17.72		F
7.	$HO_2(g)$	$\Leftrightarrow HO_2(aq)$	2.00×10^3	22.28		F
8.	$HONO(g)$	$\Leftrightarrow HONO(aq)$	4.90×10^1	16.04		D
9.	$HO_2NO_2(g)$	$\Leftrightarrow HO_2NO_2(aq)$	2.00×10^4			G
10.	$HNO_3(g)$	$\Leftrightarrow HNO_3(aq)$	2.10×10^5			E
11.	$NH_3(g)$	$\Leftrightarrow NH_3(aq)$	5.76×10^1	13.79	-5.39	H
12.	$CH_2O(g)$	$\Leftrightarrow CH_2O(aq)$	3.46	8.19		I
13.	$HCOOH(g)$	$\Leftrightarrow HCOOH(aq)$	3.50×10^3	19.26		J
14.	$CO_2(g)$	$\Leftrightarrow CO_2(aq)$	3.39×10^{-2}	8.12		A
15.	$CH_3OH(g)$	$\Leftrightarrow CH_3OH(aq)$	2.20×10^2	16.44		K
16.	$CH_3O_2(g)$	$\Leftrightarrow CH_3O_2(aq)$	6.00	18.79		F
17.	$CH_3OOH(g)$	$\Leftrightarrow CH_3OOH(aq)$	2.27×10^2	18.82		B
18.	$CH_3COOH(g)$	$\Leftrightarrow CH_3COOH(aq)$	8.80×10^3	21.62		L
19.	$CH_3C(O)OOH(g)$	$\Leftrightarrow CH_3C(O)OOH(aq)$	4.73×10^2	20.70		B
20.	$CH_3C(O)OONO_2(g)$	$\Leftrightarrow CH_3C(O)OONO_2(aq)$	2.90	19.83		M
21.	$CH_3COCHO(g)$	$\Leftrightarrow CH_3COCHO(aq)$	3.70×10^3	25.33		N
22.	$CH_2O(aq) + H_2O(aq)$	$\Leftrightarrow H_2C(OH)_2(aq)$	1.82×10^3	13.49		P
23.	$CH_3COCHO(aq)+H_2O(aq)$	$\Leftrightarrow CH_3COCH_3O_2(aq)$	2.70×10^3			Q
24.	$SO_2(aq)+ H_2O(aq)$	$\Leftrightarrow HSO_3^- + H^+$	1.23×10^{-2}	6.58		A
25.	$CO_2(aq) + H_2O(aq)$	$\Leftrightarrow HCO_3^- + H^+$	4.46×10^{-7}	-3.35		A
26.	$Cl(aq) + H_2O(aq)$	$\Leftrightarrow ClOH^- + H^+$	6.20×10^{-8}			R
27.	$NH_3(aq) + H_2O(aq)$	$\Leftrightarrow NH_4^+ + OH^-$	1.81×10^{-5}	-1.50	26.92	H
28.	$HNO_3(aq)$	$\Leftrightarrow NO_3^- + H^+$	1.96×10^1	29.17	16.83	*
29.	$HCl(aq)$	$\Leftrightarrow Cl^- + H^+$	1.72×10^6	23.15		S
30.	$NH_3(aq) + HNO_3(aq)$	$\Leftrightarrow NH_4^+ + NO_3^-$	2.14×10^{10}	50.19	16.83	*
31.	$H_2O(aq)$	$\Leftrightarrow H^+ + OH^-$	1.01×10^{-14}	-22.52	26.92	H
32.	$H_2SO_4(aq)$	$\Leftrightarrow HSO_4^- + H^+$	1.00×10^3			T
33.	$H_2O_2(aq)$	$\Leftrightarrow HO_2^- + H^+$	2.20×10^{-12}	-12.52		A
34.	$HO_2(aq)$	$\Leftrightarrow O_2^- + H^+$	3.50×10^{-5}			T
35.	$HONO(aq)$	$\Leftrightarrow NO_2^- + H^+$	5.10×10^{-4}	-4.23		D
36.	$HCOOH(aq)$	$\Leftrightarrow HCOO^- + H^+$	1.78×10^{-4}	-0.067		U
37.	$CH_3COOH(aq)$	$\Leftrightarrow CH_3COO^- + H^+$	1.70×10^{-5}	0.169		U
38.	$ClOH^-$	$\Leftrightarrow Cl^- + OH(aq)$	1.43			R
39.	Cl_2^-	$\Leftrightarrow Cl(aq) + Cl^-$	5.26×10^{-6}			R
40.	$HSO_3^- + H^+$	$\Leftrightarrow SO_3^{2-} + 2 H^+$	6.61×10^{-8}	5.03		A
41.	$HSO_4^- + H^+$	$\Leftrightarrow SO_4^{2-} + 2 H^+$	1.02×10^{-2}	8.85	25.14	H
42.	$HCO_3^- + H^+$	$\Leftrightarrow CO_3^{2-} + 2 H^+$	4.68×10^{-11}	-5.91		A
43.	$HNO_3(g)$	$\Leftrightarrow NO_3^- + H^+$	2.51×10^6	29.17	16.83	H
44.	$HCl (g)$	$\Leftrightarrow Cl^- + H^+$	1.97×10^6	30.2	19.91	H
45.	$NH_3(g) + HNO_3(g)$	$\Leftrightarrow NH_4^+ + NO_3^-$	2.59×10^{17}	63.98	11.44	*
46.	$NH_3(g) + HCl(g)$	$\Leftrightarrow NH_4^+ + Cl^-$	2.03×10^{17}	65.01	14.52	*
47.	$(NH_4)_3H(SO_4)_2(s) + H^+$	$\Leftrightarrow 3 NH_4^+ + 2 HSO_4^-$	2.93×10^3	-14.04	29.26	*

48.	$NH_4HSO_4(s)$	$\Leftrightarrow NH_4^+ + HSO_4^-$	1.38×10^4	-2.87	15.83	H
49.	$(NH_4)_2SO_4(s)$	$\Leftrightarrow 2\,NH_4^+ + SO_4^{2-}$	1.82	-2.65	38.57	H
50.	$NH_4Cl(s)$	$\Leftrightarrow NH_4^+ + Cl^-$	2.21×10^1	-6.03	16.92	*
51.	$NH_4NO_3(s)$	$\Leftrightarrow NH_4^+ + NO_3^-$	1.49×10^1	-10.4	17.56	*
52.	$NaHSO_4(s)$	$\Leftrightarrow Na^+ + HSO_4^-$	2.41×10^4	0.79	14.75	H
53.	$Na_2SO_4(s)$	$\Leftrightarrow 2\,Na^+ + SO_4^{2-}$	4.80×10^{-1}	0.98	39.57	H
54.	$NaCl(s)$	$\Leftrightarrow Na^+ + Cl^-$	3.77×10^1	-1.56	16.9	H
55.	$NaNO_3(s)$	$\Leftrightarrow Na^+ + NO_3^-$	1.20×10^1	-8.22	16.01	H

411

References

Ackerman T. P. and Toon O. B. (1981) Absorption of visible radiation in atmosphere containing mixtures of absorbing and nonabsorbing particles. *Appl. Optics* **20**, 3661 - 3667.

Ahrens C. D. (1991) *Meteorology Today . An Introduction to Weather, Climate, and the Environment.* West Publishing Company, St. Paul, MN.

Allen A. G., Harrison R. M. and Erisman J. (1989) Field measurements of the dissociation of ammonium nitrate and ammonium chloride aerosols. *Atmos. Environ.* **17**, 1591 - 1599.

Allen P. D. and Wagner K. K (1992) 1987 SCAQS emissions inventory, magnetic tape numbers ARA806 and ARA807. Technical Support Division, California Air Resources Board, Sacramento, Calif.

Ames J., Whitney D. C. and Allen P. D. (1986) Subroutine to calculate plume rise from Briggs formulae (1977 - 1986).

Anbar M. and Neta P. (1967) A compilation of specific bimolecular rate constants for the reactions of hydrated electrons, hydrogen atoms, and hydroxyl radicals with inorganic and organic compounds in aqueous solution. *Int. J. Appl. Radiat. Isot.* **18**, 493 - 523.

Atkinson R., Baulch D. L., Cox R. A., Hampson Jr. R. F., Kerr J. A. and Troe J. (1992) Evaluated kinetic and photochemical data for atmospheric chemistry. Supplement IV. *J. Phys. Chem. Ref. Data* 21, 1125 - 1571.

Austin J. (1991) On the explicit versus family solution of the fully diurnal photochemical equations of the stratosphere. *J. Geophys. Res.* 96, 12,941 - 12,974.

Behar D., Czapski G. and Duchovny I. (1970) Carbonate radical in flash photolysis and pulse radiolysis of aqueous carbonate solutions. *J. Phys. Chem.* 74, 2206 - 2210.

Bergstrom R. W. Jr. (1972) Predictions of the spectral absorption and extinction coefficients of an urban air pollution aerosol model. *Atmos. Environ.* 6, 247 - 258.

Betterton E. A. and Hoffmann M. R. (1988) Henry's law constants of some environmentally important aldehydes. *Environ. Sci. Technol.* 22, 1415 - 1418.

Bielski B. H. J. (1978) Reevaluation of the spectral and kinetic properties of HO_2 and O_2^- free radicals. *Photochem. Photobiol.* 28, 645 - 649.

Bolton D. (1980) The computation of equivalent potential temperature. *Mon. Wea. Rev.* 108, 1046 - 1053.

Bonsang B., Martin D., Lambert G., Kanakidou M., Le Roulley J. C. and Sennequier G (1991) Vertical distribution of non methane hydrocarbons in the remote marine boundary layer. *J. Geophys. Res.* 96, 7313 - 7324.

Bothe E. and Schulte-Frohlinde D. (1980) Reaction of dihydroxymethyl radical with molecular oxygen in aqueous solution. *Z. Naturforsch. B, Anorg. Chem. Org. Chem.* 35, 1035 - 1039.

Boyce S. D. and Hoffmann M. R. (1984) Kinetics and mechanism of the formation of hydroxymethanesulfonic acid at low pH. *J. Phys. Chem.* 88, 4740 - 4746.

413

Brasseur G. and Solomon S. (1986) *Aeronomy of the Middle Atmosphere*. D. Reidel, Dordrecht, Holland.

Briggs G. A. (1975) Plume rise predictions. In *Lectures on Air Pollution and Environmental Impact Analysis*, D. A. Haugen, ed., American Meteorological Society, Boston, Mass., 59 - 111.

Bromley L. A. (1973) Thermodynamic properties of strong electrolytes in aqueous solutions. *AIChEJ* 19, 313 - 320.

Byrne G. D., Hindmarsh A. C., Jackson K. R. and Brown H. G. (1977) A comparison of two ODE codes: GEAR and EPISODE. *Comput. chem. Engng* 1, 133 - 147.

Calder K. L. (1949) Eddy diffusion and evaporation in flow over aerodynamically smooth and rough surfaces: a treatment based on laboratory laws of turbulent flow with special reference to conditions in the lower atmosphere. *Q. J. Mech. appl. Math.* 2, 153.

Calvert J. G., Ed. (1984) *SO_2, NO, and NO_2 Oxidation Mechanisms*. Butterworth, Boston, Mass.

California Air Resources Board (1989a) Instrumental measurement of visibility reducing particles. Staff Report. CARB, Sacramento, Calif.

California Air Resources Board (1989b) Instrumental measurement of visibility reducing particles. Technical Support Document. CARB, Sacramento, Calif..

Campbell F. W. and Maffel L. (1974) Contrast and spatial frequency. *Sci. Am.*, 231, 106.

Carter W. P. (1990) A detailed mechanism for the gas-phase atmospheric reactions of organic compounds. *Atmos. Environ.* 24A, 481 - 518.

Cass G. R. (1979) On the relationship between sulfate air quality and visibility with examples in Los Angeles. *Atmospheric Environment*, 13, 1069 - 1084.

Cass G. R., Gharib S., Peterson M. and Tilden J. W. (1982) The origin of ammonia emissions to the atmosphere in an urban area. Open File Report 82-6, Environmental Quality Laboratory, California Institute of Technology, Pasadena, CA.

Cassmassi J. (1992) Supplemental notes for UCLA class, Atmospheric Sciences 2: Air Pollution.

Chang J. S., Brost R. A., Isaksen S. A., Madronich S., Middleton P., Stockwell R. and Walcek C. J. (1987) A three-dimensional Eulerian acid deposition model: Physical concepts and formulation. *J. Geophys. Res.* **92**, 14,681 - 14,700.

Chen S., Cope V. W. and Hoffman M. Z. (1973) Behavior of CO_3^- radicals generated in the flash photolysis of carbonatoamines complexes of cobalt(III) in aqueous solution. *J. Phys. Chem.* **77**, 1111 - 1116.

Chock D. P. (1991) A comparison of numerical methods for solving the advection equation -- III. *Atmos. Environ.* **25A**, 853 - 871.

Christensen H., Sehested K. and Corfitzen H. (1982) Reactions of hydroxyl radicals with hydrogen peroxide at ambient and elevated temperatures. *J. Phys. Chem.* **86**, 1588 - 1590.

Conklin M. H. and Hoffmann M. R. (1988) Metal ion - S(IV) chemistry III. Thermodynamics and kinetics of transient iron(III)-sulfur(IV) complexes. *Environ. Sci. Technol.* **22**, 891 - 898. 1988.

Crutzen P. J. (1971) Ozone production rates in an oxygen-hydrogen-nitrogen oxide atmosphere. *J. Geophys. Res.* **76**, 7311 - 7327.

Dabdub D. and Seinfeld J. H. (1994) Numerical advective schemes used in air quality models -- sequential and parallel implementation. *Atmos. Environ.*, in press.

DaMassa J., Allen P., McGuire T., McNerny D., Ranzieri A, and Wagner K. (1992) Technical Guidance Document: Photochemical Modeling. California Environmental Protection Agency / Air Resources Board.

Damschen D. E. and Martin L. R. (1983) Aqueous aerosol oxidation of nitrous acid by O_2, O_3, and H_2O_2. *Atmos. Environ.* **17**, 2005 - 2011.

Dave J. V. (1968) Subroutines for computing the parameters of the electromagnetic radiation scattered by a sphere. *Report 320-3236*, IBM Scientific Center, Palo Alto, Calif.

DeMarrais G. A., Holzworth G. C. and Hosler C. R. (1965) Meteorological summaries pertinent to atmospheric transport and dispersion over Southern California. *U. S. Dept. of Commerce Tech. Paper 54*, Washington, D. C..

DeMore W. B., Sanders S. P., Golden D. M., Molina M. J., Hampson R. F., Kurylo M. J., Howard C. J. and Ravishankara A. R. (1990) Chemical kinetics and photochemical data for use in stratospheric modeling. Evaluation number 9. *Rep 90-1*. Jet Propul. Lab., Pasadena, Calif.

Dodge M. C. (1989) A comparison of three photochemical oxidant mechanisms. *J. Geophys Res.*, **94**, 5121 - 5136.

Drummond J. W., Ehhalt D. H. and Volz A. (1988) Measurements of nitric oxide between 0-12 km altitude and 67°N to 60°S latitude obtained during STRATOZ III. *J. Geophys. Res.* **93**, 15,831 - 15,849.

Duce R. A. (1969) On the source of gaseous chlorine in the marine atmosphere. *J. Geophys. Res.* **70**, 1775 - 1779.

Duce R. A. and Hoffman E. J. (1976) Chemical fractionation at the air / sea interface. *Annu. Rev. Earth. Planet. Sci.* **4**, 187.

Eldering A., Cass G. R. and Moon K. C. (1994) An air monitoring network using continuous size distribution monitors: Connecting pollutant properties to visibility via Mie scattering calculations. *Atmos. Environ.*, in press.

Elliott S., Turco R. P. and Jacobson M. Z. (1993) Tests on combined projection / forward differencing integration for stiff photochemical family systems at long time step. Submitted to *Computers Chem.* **17**, 91 - 102.

Eriksson E. (1960) The yearly circulation of chloride and sulfur in nature; meteorological, geochemical and pedological implications. Part II. *Tellus* **12**, 63 - 109.

Farhataziz and Ross A. B. (1977) Selected specific rates of transients from water in aqueous solutions, III., Hydroxyl radical and perhydroxyl radical and their radical ions. *Rep. NSRDBS-NBS 59*, U. S. Dept. of Commerce, Washington, D. C.

Fiadeiro M. E. and Veronis G. (1977) On weighted-mean schemes for the finite-difference approximation to the advection-diffusion equation. *Tellus* **29**, 512 - 522.

Finlayson-Pitts B. J. and Pitts J. N. (1986) *Atmospheric Chemistry: Fundamentals and Experimental Techniques*. John Wiley & Sons, New York.

Fitz D., Chan M., Cass G., Lawson D. and Ashbaugh L. (1989) A multi-component size-classifying aerosol and gas sampler for ambient air monitoring. Air and Waste Management Association paper 89-140.1.

Fletcher N. H. (1958) Size effect in heterogeneous nucleation. *J. Chem. Phys.* **29**, 572 - 576.

Friedlander S. K. (1977) *Smoke, Dust, and Haze. Fundamentals of Aerosol Behavior*. Wiley & Sons, New York.

417

Gazdag J. (1973) Numerical convective schemes based on accurate computation of space derivatives. *J. Comp. Phys.* **13**, 100 - 113.

Gear C. W. (1969) The automatic integration of stiff ordinary differential equations. In *Information Processing* **68**, (edited by Morrel A. J. H.), pp. 187 - 193. North Holland Publishing Company, Amsterdam.

Gear C. W. (1971) *Numerical Initial Value Problems in Ordinary Differential Equations.* Prentice Hall, Englewood Cliffs, N. J.

Gery M. W., Whitten G. Z. and Killus J. P. (1988) Development and testing of the CBM-IV for urban and regional modeling. Rep. EPA-600/3-88-012, U. S. Environ. Prot. Agency, Research Triangle Park, N. C.

Gery M. W., Whitten G. Z., Killus J. P. and Dodge M. C. (1989) A photochemical kinetics mechanism for urban and regional scale computer modeling. *J. Geophys. Res.* **94**, 12,925 - 12, 956.

Gharib S. and Cass G. R. (1984) Ammonia emissions in the South Coast Air Basin 1982. Open File Report 84-2, Environmental Qualiy Laboratory, California Institute of Technology, Pasadena, CA.

Gmitro J. I. and Vermeulen T. (1964) Vapor-liquid equilibrium for aqueous sulfuric acid. *AIChE J.* **10**, 740 - 746.

Graedel T. E. and Goldberg K. I. (1983) Kinetic studies of raindrop chemistry, 1, Inorganic and organic processes. *J. Geophys. Res.* **88**, 10,865 - 10,882.

Graedel T. E. and Weschler C. J. (1981) Chemistry within aqueous atmospheric aerosols and raindrops. *Rev. Geophys.* **19**, 505 - 539.

Groblicki P. J., Wolff G. T. and Countess R. J. (1981) Visibility-reducing species in the Denver "brown Cloud"--I. Relationships between extinction and chemical composition. *Atmos. Environ.* **15**, 2473 - 2484.

418

Hagesawa K. and Neta P. (1978) Rate constants and mechanisms of reaction for Cl_2^- radicals. *J. Phys. Chem.* **82**, 854 - 857.

Hale G. M. and Querry M. R. (1973) Optical constants of water in the 200-nm to 200-μm wavelength region. *Appl. Optics* **12**, 555 - 563.

Hamill P., Turco R. P., Kiang C. S., Toon O. B. and Whitten R. C. (1982) An analysis of various nucleation mechanisms for sulfate particles in the stratosphere. *J. Aer. Sci.* **13**, 561 - 585.

Harley R. A., Russell A. G., McRae G. J., Cass G. R. and Seinfeld J. H. (1993a) Photochemical modeling of the Southern California Air Quality Study. *Environ. Sci. Technol.* **27**, 378 - 388.

Harley R. A., Russell A. G. and Cass G. R. (1993b) Mathematical modeling of the concentrations of volatile organic compounds: Model performance using a lumped chemical mechanism. *Environ. Sci. Technol.* **27**, 1638 - 1649.

Harned H. S. and Owen B. B. (1958) *The Physical Chemistry of Electrolyte Solutions.* Chap. 8, Reinhold, New York, NY.

Harrison R. M. and MacKenzie A. R. (1990) A numerical simulation of kinetic constraints upon achievement of the ammonium nitrate dissociation equilibrium in the troposphere. *Atmos. Environ.* **24A**, 91 - 102.

Heisler S. L., Friedlander S. K and Husar R. B. (1973) The relationship of smog aerosol size and chemical element distribution to source characteristics. *Atmos. Environ.* **7**, 633 - 649.

Hering S. V. and Friedlander S. K. (1982) Origins of aerosol sulfur size distributions in the Los Angeles Basin. *Atmos. Environ.* **16**, 2647 - 2656.

419

Hertel O., Berkowicz R., Christensen J. and Hov. O. (1993) Test of two numerical schemes for use in atmospheric transport-chemistry models. *Atmos. Environ.* **27A**, 2591 - 2611.

Hesstvedt E., Hov O. and Isaksen I. S. A. (1978) Quasi-steady-state approximations in air pollution modeling: Comparison of two numerical schemes for oxidant prediction. *Int. J. Chem. Kin..* **10**, 971 - 994.

Hindmarsh A. C. (1974) GEAR: ordinary differential equation system solver. Lawrence Livermore Laboratory Report UCID-30001, Rev. 3.

Hindmarsh A. C. (1975) GEARB: solution of ordinary differential equations having banded Jacobians. Lawr. Liv. Lab. Report UCID-30059, Rev. 1.

Hindmarsh A. C. (1980) GEARS: A package for the solution of sparse, stiff ordinary differential equations. Lawrence Livermore Laboratory report UCRL-84102.

Hindmarsh A. C. (1983) ODEPACK, a systematized collection of ODE solvers. In Scientific Computing (edited by Stepleman R. S. *et al.*), pp. 55-74. North-Holland, Amsterdam.

Hitchcock D. R., Spiller L. L. and Wilson W. E. (1980) Sulfuric acid aerosols and HCl release in coastal atmospheres: evidence of rapid formation of sulfuric acid particulates. *Atmos. Environ.* **14**, 165 - 182.

Hoffmann M. R. and Calvert J. G. (1985) Chemical transformation modules for Eulerian acid deposition models, vol. 2, The aqueous-phase chemistry. *EPA/600/3-85/017*, U. S. Environ. Prot. Agency, Research Triangle Park, N. C.

Horvath H. (1993) Atmospheric light absorption -- a review. *Atmos. Environ.* **27A**, 293 - 317.

Huie R. E. and Neta P. (1987) Rate constants for some oxidations of S(IV) by radicals in aqueous solutions. *Atmos. Environ.* **21**, 1743 - 1747.

420

Hunt B. G. (1966) Photochemistry of ozone in a moist atmosphere. *J. Geophys. Res.* **71**, 1385 - 1398.

Ingalls M. N., Smith L. R. and Kirksey R. E. (1989) Measurement of on-road vehicle emission factors in the California South Coast Air Basin. Volume I: regulated emissions. *Report to the Coordinating Research Council under Project SCAQS-1*. Southwest Research Institute, San Antonio, TX.

Jacob D. J. (1986) Chemistry of OH in remote clouds and its role in the production of formic acid and peroxymonosulfonate. *J. Geophys. Res.* **91**, 9807 - 9826.

Jacob D. J., Gottlieb E. W. and Prather M. J. (1989) Chemistry of a polluted cloudy boundary layer. *J. Geophys. Res.* **94**, 12,975 - 13,002.

Jacobson M. Z. and Turco R. P. (1994a) SMVGEAR: A sparse-matrix, vectorized Gear code for atmospheric models. *Atmos. Environ.* **28A**, 273 - 284.

Jacobson M. Z., Turco R. P., Jensen E. J. and Toon O. B. (1994b) Modeling coagulation among particles of different composition and size. *Atmos. Environ.* **28A**, 1327 - 1338.

Jacobson M. Z. and Turco R. P. (1994c) Simulating condensational growth, evaporation, and coagulation of aerosols using a combined moving and stationary size grid. *Aerosol Sci. Technol.*, in press.

Jacobson M. Z., Turco R. P. and Tabazadeh A. (1994d) Simulating equilibrium within aerosols and non-equilibrium between gases and aerosols. *J. Geophys. Res.*, in review.

Jacobson M. Z., Turco R. P., Lu R. and Toon O. B. (1994e) GATOR: A gas, aerosol, transport, and radiation modeling system for studying urban and regional air pollution. *Atmos. Environ.*, in final review.

421

Jayson G. G., Parsons B. J. and Swallow A. J. (1973) Some simple, highly reactive, inorganic chlorine derivatives in aqueous-solution. *Trans. Faraday Soc.* **69**, 1597 - 1607.

Jensen E. J. and Toon O. B. (1992) The potential effect of volcanic aerosols on cirrus cloud microphysics. *Geophys. Res. Lett.* **19**, 1759 - 1762.

Kaiser E. W. and Wu C. H. (1977) A kinetic study of the gas phase formation and decompostion reactions of nitrous acid. *J. Phys. Chem.* **81**, 1701 - 1706.

Kao C-Y J., Glatzmaier G. A., Malone R. C. and Turco R. P. (1990) Global three-dimensional simulations of ozone depletion under post-war conditions. *J. Geophys. Res.* **95**, 22,495 - 22,512.

Kasten F. (1968) Falling speed of aerosol particles. *J. Appl. Meteorol.* **7**, 944 - 947.

Kerker M. (1969) *The Scattering of Light and Other Electromagnetic Radiation.* Academic Press, New York.

Kiang C. S and Stauffer D. (1973) *Faraday Symp. Chem. Soc.* **7**, 26.

Kim Y. P., Seinfeld J. H. and Saxena P. (1993) Atmospheric gas-aerosol equilibrium I. Thermodynamic model. *Aerosol Sci. Technol.* **19**, 157 - 181.

King D., Wheeler N. and Wagner K. (1990) Southern California Air Quality Study Modeling Data Archive. California Air Resources Board Technical Support Division, Sacramento, Calif.

Koschmieder H. (1924) Theorie der horizontalen Sichtweite. *Beitr. Phys. freien Atm.* **12**, 33-53; 171 - 181.

Kozac-Channing L. F. and Heltz G. R. (1983) Solubility of ozone in aqueous solutions of 0 - 0.6 M ionic strength at 5 - 30°C. *Environ. Sci. Technol.* **17**, 145 - 149.

Kritz M. A. and Rancher J. (1980) Circulation of Na, Cl, and Br in the tropical marine atmosphere. *J. Geophys. Res.* **85**, 1633 - 1639.

Larson S., Cass G., Hussey K., and Luce F. (1984) Visibility model verification by image processing techniques. Final Report to State of California Air Resources Board under Agreement A2-077-32.

Latimer W. M. (1952) *The Oxidation States of the Elements and Their Potentials in Aqueous Solutions*, pp. 70 - 89. Prentice-Hall, New York.

Lawson D. R. (1990) The Southern California air quality study. *J. Air Waste Manage. Assoc.* **40**, 156 - 165.

Ledbury W. and Blair E. W. (1925) The partial formaldehyde vapour pressure of aqueous solutions of formaldehyde, II. *J. Chem. Soc.* **127**, 2832 - 2839.

Le Henaff P. (1968) Methodes d'etude et proprietes des hydrates, hemiacetals et hemiacetals derives des aldehydes et des cetones. *Bull. Soc. Chim. France*, 4687 - 4700.

Lee Y. -N. and Schwartz S. E. (1983) Kinetics of oxidation of aqueous sulfur(IV) by nitrogen dioxide. In *Precipitation Scavenging, Dry Deposition, and Resuspension*, vol. I, edited by H. R. Pruppacher, R. G. Semonin, and W. G. N. Slinn. Elsevier Science, New York.

Lee Y. -N. (1984) Atmospheric aqueous-phase reactions of nitrogen species, Gas-Liquid Chemistry of Natural Waters, vol. 1, *BNL 51757*, pp. 20/1-20/10, Brookhaven Natl. Lab., 1984.

Lide D. R., Ed.-in-chief (1993) *CRC Handbook of Chemistry and Physics*. CRC Press, Inc., Boca Raton, Fla..

Lind J. A. and Kok G. L. (1986) Henry's law determinations for aqueous solutions of hydrogen peroxide, methylhydroperoxide, and peroxyacetic acid. *J. Geophys. Res.* **91**, 7889 - 7895.

423

Lind J. A., Kok G. L. and Lazrus A. L. (1987) Aqueous phase oxidation of sulfur(IV) by hydrogen peroxide, methylhydroperoxide, and peroxyacetic acid. *J. Geophys. Res.* **92**, 4171 - 4177.

Liou K. N. (1992) *Radiation and Cloud Processes in the Atmosphere. Theory, Observation, and Modeling.* Oxford University Press, New York.

Lu R. and Turco R. P. (1993) Numerical investigation of the formation of elevated pollution layers over the Los Angeles Air Basin. *Air Pollution 93 Conference Proceedings*, Computational Mechanics Publications, p. 165 - 172 .

Lu R. and Turco R. P. (1994a) Air pollutant transport in a coastal environment Part I: Two-dimensional simulations of sea-breeze and mountain effects. *J. Atmos. Sci.*, in press.

Lu R. and Turco R. P. (1994b) Air pollutant transport in a coastal environment Part II: three dimensional simulations over the Los Angeles Basin. *Atmos Environ.*, in review.

Lurmann F. W., Carter W. P. L. and Coyner L. A. (1987) A surrogate species chemical reaction mechanism for urban-scale air quality simulation models. *Rep. EPA/600/3-87/014*, U. S. Environ. Prot. Agency, Research Triangle Park, N. C..

Lyons J. M., Venkataraman C., Main H. H. and Friedlander S. K. (1993) Size distribution of trace metals in the Los Angeles atmosphere. *Atmos. Environ.* **27B**, 237 - 249.

Mackay G. I., Karecki D. R. and Schiff H. I. (1988) The SCAQS: tunable diode laser absorption spectrometer measurements of H_2O_2 and H_2CO at the Claremont and Long Beach "A" sites. Unisearch Associates, Concord, Ontario, Canada. Report to the California Air Resources Board under Contract A732-973.

424

Main H. H. and Friedlander S. K. (1990) Dry deposition of atmospheric aerosols by dual tracer method -- I. Area source. *Atmos. Environ.* **24A**, 103 - 108.

Malone R. C., Auer L. H., Glatzmaier G. A., Wood M. C. and Toon O. B. (1986) Nuclear winter: Three-dimensional simulations including interactive transport, scavenging and solar heating of smoke. *J. Geophys. Res.* **91**, 1039 - 1054.

Marenco A., Macaigne M. and Prieur S. (1989) Meridional and vertical CO and CH4 distributions in the background troposphere (70°N-60°S; 0-12 km altitude) from scientific aircraft measurements during the STRATOZ III experiment (June 1984). *Atmos. Environ.* **23**, 185 - 200.

Marenco A. and Said F. (1989) Meridional and vertical ozone distribution in the background troposphere (70°N-60°S; 0-12 km altitude) from scientific aircraft measurements during the STRATOZ III experiment (June 1984). *Atmos. Environ.* **23**, 201 - 214.

Marsh A. R. W. and McElroy W. J. (1985) The dissociation constant and Henry's law constant of HCl in aqueous solution. *Atmos. Environ.* **19**, 1075 - 1080.

Martell A. E. and Smith R. M. (1977) *Critical stability constants, vol. 3, Other Organic Ligands*, Plenum, New York.

Martens C. S., Wesolowski J. J., Hariss R. C. and Kaifer R. (1973) Chlorine loss from Puerto Rican and San Francisco Bay Area Marine Aerosols. *J. Geophys. Res.* **78**, 8778 -8792.

Martin L. R. (1984) Kinetic studies of sulfite oxidation in aqueous solution. In *SO2, NO, and NO2 Oxidation Mechanisms: Atmospheric Considerations*, edited by J. G. Calvert, pp. 63 - 100, Butterworth, Stoneham, Mass.

Martin and Hill (1987a) The iron-catalyzed oxidation of sulfur: Reconciliation of the literature rates. *Atmos. Environ.* **21**, 1487 - 1490.

425

Martin and Hill (1987b) The effect of ionic strength on the manganese catalyzed oxidation of sulfur(IV). *Atmos. Environ.* **21**, 2267 - 2270.

McRae G. J. (1981) Mathematical modeling of photochemical air pollution. Ph. D. Thesis, California Institute of Technology, Pasadena CA.

McRae G. J., Goodin W. R. and Seinfeld J. H. (1982) Development of a second-generation mathematical model for urban air pollution -- I. Model formulation. *Atmos. Environ.* **16**, 679 - 696.

McRae G. J. and Russell A. G. (1984) Dry Deposition of Nitrogen-Containing Species, in *Deposition Both Wet and Dry*, B. B. Hicks, Ed., Chapter 9, pp. 153 - 193, Acid Precipitation Series, J. I. Teasley, Series Ed., Butterworth, Boston.

Meader W. E. and Weaver W. R. (1980) Two-stream approximations to radiative transfer in planetary atmospheres: A unified description of existing methods and new improvement. *J. Atmos. Sci.* **37**, 630 - 643.

Middleton W. E. K. (1952) *Vision Through the Atmosphere*. U. Toronto Press, Toronto, Canada.

Millikan R. A. (1923) The general law of fall of a small spherical body through a gas, and its bearing upon the nature of molecular reflection from surfaces. *Phys. Rev.* **22**, 1.

Monin A. S. and Yaglom A. M. (1971) *Statistical Fluid Mechanics*. MIT Press, Cambridge, Mass.

Mozurkewich M. and Calvert J. G. (1988) Reaction probability of N_2O_5 on aqueous aerosols. *J. Geophys. Res.* **93**, 15,889 - 15,896.

Mylonas D. T., Allen D. T., Ehrman S. H. and Pratsinis S. E. (1991) The sources and size distributions of organonitrates in Los Angeles aerosol. *Atmos. Environ.* **25A**, 2855 - 2861.

Nautical Almanac Office and Her Majesty's Nautical Almanac Office (1993) Astronomical Almanac. U. S. Government Printing Office, Washington D. C..

NAS (1992) NAS User Guide. Vol. 2, version 6.0, section 4, p. 22. Moffett Field, California.

NASA (1990) TOMS gridded ozone data (1978 - 1988). NASA Upper Atmosphere Research Program, Goddard Ozone Processing Team.

Noll K. E., Fang K. Y. P. and Khalili E. (1990) Characterization of atmospheric coarse particles in the Los Angeles Basin. *Aerosol Sci. Technol.* **12**, 28 - 38.

Ouimette J. J. and Flagan R. C. (1982) The extinction coefficient of multicomponent aerosols. *Atmos. Environ.* **16**, 2405 - 2419.

Pandis S. N. and Seinfeld J. H. (1989) Sensitivity analysis of a chemical mechanism for aqueous-phase atmospheric chemistry. *J. Geophys. Res..* **94**, 1105 - 1126.

Pandis S. N., Harley R. A., Cass G. R. and Seinfeld J. H. (1992) Secondary organic aerosol formation and transport. *Atmos. Environ.* **26A**, 2269 - 2282.

Park J. -Y and Lee Y. -N (1987) Aqueous solubility and hydrolysis kinetics of peroxynitric acid, paper presented at 193rd Meeting, Am. Chem. Soc., Denver, Colo., April 5-10, 1987.

Pasquill F. (1962) *Atmospheric Diffusion.* Van Nostrand, London.

Paulson S. E. and Seinfeld J. H. (1992) Development and evaluation of a photooxidation mechanism for isoprene. *J. Geophys. Res.* **97**, 20,703 - 20,715.

Pepper D. W., Kern C. D. and Long P. E. Jr. (1979) Modeling the dispersion of atmospheric pollution using cubic splines and chapeau functions. *Atmos. Environ.* **13**, 223 - 237.

Perrin D. D. (1982) *Ionization Constants of Inorganic Acids and Bases in Aqueous Solution,* 2nd ed., Pergamon, New York.

Pilinis C., Seinfeld J. H. and Seigneur C. (1987) Mathematical modeling of the dynamics of multicomponent atmospheric aerosols. *Atmos. Environ.* **21**, 943 - 955.

Pilinis C. and Seinfeld J. H. (1987) Continued development of a general equilibrium model for inorganic multicomponent atmospheric aerosols. *Atmos. Environ.* **21**, 2453-2466.

Pilinis C. and Seinfeld J. H. (1988) Development and Evaluation of an Eulerian Photochemical Gas-Aerosol Model. *Atmos. Environ.* **22**, 1985 - 2001.

Press W. H., Flannery B. P., Teukolsky, S. A. and Vetterling W. T. (1993) *Numerical Recipes: The Art of Scientific Computing.* Cambridge University Press, Cambridge.

Pruppacher H. R. and Klett J. D. (1978) *Microphysics of Clouds and Precipitation.* D. Reidel, Hingham, Mass..

Reynolds S. D., Roth P. M. and Seinfeld J. H. (1973) Mathematical modeling of photochemical air pollution -- I: Formulation of the model. *Atmos. Environ.* **7**, 1033 - 1061.

Reynolds S. D., Liu M. K., Hecht T. A., Roth P. M. and Seinfeld J. H. (1974) Mathematical modeling of photochemical air pollution -- III: Evaluation of the model. *Atmos. Environ.* **8**, 563 - 596.

Robinson N., ed. (1966) *Solar Radiation.* Elsevier Publishing Co., Amsterdam.

Roessler D. M. and Faxvog F. R. (1980) Optical properties of agglomerated acetylene smoke particles and 0.5145 μm and 10.6 μm wavelengths. *J. Opt. Soc. Am.* **70**, 230 - 235.

Ross A. B. and Neta P. (1979) Rate constants for reactions of inorganic radicals in aqueous solutions. *NSRDS-NBS 65.* Natl. Bur. of Stand., U. S. Dep. of Commer., Washington, D. C.

428

Roth P. M., Reynolds S. D., Roberts P. J. W. and Seinfeld J. H. (1971) Development of a simulation model for estimating ground-level concentrations of photochemical pollutants. Systems Applications Inc., San Rafael, Calif, (SAI 71/21).

Roth P. M., Roberts, P. J. W., Liu M. K., Reynolds S. D. and Seinfeld J. H. (1974) Mathematical modeling of photochemical air pollution -- II: A model and inventory of pollutant emissions. *Atmos. Environ.* **8**, 97 - 130.

Russell A. G. and Cass G. R. (1984) Acquisition of regional air quality model validation data for nitrate, sulfate, ammonium ion and their precursors. *Atmos. Environ.* **18**, 1815 - 1827.

Russell A. G. and Cass G. R. (1986) Verification of a mathematical model for aerosol nitrate and nitric acid formation and its use for control measure evaluation. *Atmos. Environ.* **20**, 2011 - 2025.

Russell A. G., McCue K. F., and Cass G. R. (1988a) Mathematical modeling of the formation of nitrogen-containing air pollutants. 1. Evaluation of an Eulerian photochemical model. *Environ. Sci. Technol.* **22**, 263 - 271.

Russell A. G., McCue K. F., and Cass G. R. (1988b) Mathematical modeling of the formation of nitrogen-containing air pollutants. 2. Evaluation of the effect of emission controls. *Environ. Sci. Technol.* **22**, 1336 - 1347.

Russell A. G., Winner D A., Harley R. A., McCue K. F. and Cass G. R. (1993) Mathematical modeling and control of the dry deposition flux of nitrogen-containing air pollutants. *Environ. Sci. Technol.* **27**, 2772 - 2782.

Scheffe R. D. and Morris R. E. (1993) A review of the development and application of the Urban Airshed Model. *Atmos. Environ.* **27B**, 23 - 39.

Schmidt K. H. (1972) Electrical conductivity techniques for studying the kinetics of radiation-induced chemical reactions in aqueous solutions. *Int. J. Radiat. Phys. Chem.* **4**, 439 - 468.

Schneider W., Moortgat G. K., Tyndall G. S. and Burrows J. P. (1987) Absorption cross-sections of NO2 in the UV and visible region (200 - 700 nm) at 298 K). *J. Photochem. Photobiol, A: Chemistry* **40**, 195 - 217.

Schuetzle D., Cronn D., Crittenden A. L. and Charlson R. J. (1975) Molecular composition of secondary aerosol and its possible origin. *Environ. Sci. Technol.* **9**, 838 - 845.

Schwartz S. E. and White W. H. (1981) Solubility equilibria of the nitrogen oxides and oxyacids in aqueous solution. *Adv. Environ. Sci. Eng.* **4**, 1 - 45.

Schwartz S. E. (1984) Gas- and aqueous-phase chemistry of HO_2 in liquid water clouds, *J. Geophys. Res.* **89**, 11,589 - 11,598.

Scholes G. and Willson R. L. (1967) γ-radiolysis of aqueous thymine solutions. Determination of relative reaction rates of OH radicals. *Trans. Faraday Soc.* **63**, 2982 - 2993.

Sehmel G. A. (1980) Particle and gas dry deposition: a review. *Atmos. Environ.* **14**, 983 - 1011.

Seinfeld J. H. (1986) *Atmospheric Chemistry and Physics of Air Pollution.* John Wiley & Sons, New York.

Seinfeld J. H. (1989) Urban air pollution: State of the Science. *Science* **243**, 745 - 752.

Sehested K., Rasmussen O. L. and Fricke H. (1968) Rate constants of OH with HO_2, O_2^-, and $H_2O_2^+$ from hydrogen peroxide formation in pulse-irradiated oxygenated water. *J. Phys. Chem.* **72**, 626 - 631.

430

Sheih C. M., Wesely M. L. and Walcek C. J. (1986) A dry deposition module for regional acid deposition. *EPA/600/3-86/037*. U. S. Government Printing Office, Washington, D. C.

Sherman A. H. and Hindmarsh A. C. (1980) GEARS: a package for the solution of sparse, stiff ordinary differential equations. Lawrence Livermore Laboratory Report UCRL-84102.

Shimazaki T. and Laird A. R. (1970) A model calculation of the diurnal variation in minor neutral constituents in the mesosphere and lower thermosphere including transport effects. *J. Geophys. Res.* **75**, 3221 - 3235.

Singh H. B., Viezee W. and Salas L. J. (1988) Measurements of selected C_2-C_5 hydrocarbons in the troposphere: Latitudinal, vertical, and temporal variations. *J. Geophys. Res.* **93**, 15,861 - 15,878.

Sloane C. S. (1984) Optical properties of aerosols of mixed composition. *Atmos. Environ.* **18**, 871 - 878.

Smith R. M. and Martell A. E. (1976) *Critical Stability Constants, vol. 4: Inorganic Complexes*. Plenum, New York.

Snider J. R. and Dawson G. A. (1985) Tropospheric light alcohols, carbonyls, and acetonitrile: Concentrations in the southwestern United States and Henry's law data. *J. Geophys. Res.* **90**, 3797 - 3805.

Sorensen P. E. and Andersen V. S. (1970) The formaldehyde-hydrogen sulphite system in alkaline aqueous solution: Kinetics, mechanism, and equilibria. *Acta Chem. Scand.* **24**, 1301 - 1306.

South Coast Air Quality Management District (SCAQMD) and Southern California Association of Governments (SCAG) (1991) 1991 Air Quality Management Plan: South Coast Air Basin.

431

Spellmann J. W. and Hindmarsh A. C. (1975) GEARS: solution of ordinary differential equations having a sparse Jacobian Matrix. Lawrence Livermore Laboratory Report UCID-3011.

Stockwell W. R. (1986) A homogeneous gas-phase mechanism for use in a regional acid deposition model. *Atmos. Environ.* **20**, 1615 - 1632.

Tabazadeh A., Turco R. P. and Jacobson M. Z. (1994) A model for studying the composition and chemical effects of stratospheric aerosols. *J. Geophys. Res.*, in press.

Tang I. N., Wong W. T. and Munkelwitz H. R. (1981) The relative importance of atmospheric sulfates and nitrates in visibility reduction. *Atmos. Environ.* **15**, 2463 - 2471.

Tesche T. W. (1988) Accuracy of ozone air quality models. *J. Environmental Engineering* **114:4**, 739 - 752.

Toon O. B. and Ackerman T. P. (1981) Algorithms for the calculation of scattering by stratified spheres. *Applied Optics* **20**, 3657 - 3660.

Toon O. B., Kasting J. F., Turco R. P. and Liu M. S. (1987) The sulfur cycle in the marine atmosphere. *J. Geophys. Res.* **92**, 943 - 963.

Toon O. B., Turco R. P., Westphal D., Malone R. and Liu M. S. (1988) A Multidimensional model for aerosols: Description of computational analogs. *J. Atmos. Sci.* **45**, 2123 - 2143.

Toon O. B., Turco R. P., Jordan J., Goodman J. and Ferry G. (1989a) Physical processes in polar stratospheric ice clouds. *J. Geophys Res.* **94**, 11,359 - 11,380.

Toon O. B., McKay C. P. and Ackerman T. P. (1989b) Rapid calculation of radiative heating rates and photodissociation rates in inhomogeneous multiple scattering atmospheres. *J. Geophys. Res.* **94**, 16,287 - 16.301.

Treinin A. and Hayon E. (1970) Absorption spectra and reaction kinetics of NO_2, N_2O_3, and N_2O_4 in aqueous solutions. *J. Am. Chem. Soc.* **92**, 5821 - 5828.

Turco R. P. and Whitten R. C. (1974) A comparison of several computational techniques for solving some common aeronomic problems. *J. Geophys. Res.* **79**, 3179 - 3185.

Turco R. P., and Whitten R. C. (1977) The NASA Ames research center one and two dimensional stratospheric models part 1: the one dimensional model. *NASA Tech. Publ. (TP) 1002.*

Turco R. P., Hamill P., Toon O. B., Whitten R. C. and Kiang C. S. (1979a) A one-dimensional model describing aerosol formation and evolution in the stratosphere. Part I: Physical processes and mathematical analogs. *J. Atmos. Sci.* **36**, 699 - 717.

Turco R. P., Hamill P., Toon O. B., Whitten R. C. and Kiang C. S. (1979b) The NASA-Ames Research Center Stratospheric Aerosol Model: I Physical Processes and Computational Analogs. *NASA Tech. Publ. (TP) 1362, iii-94.*

Turco R. P., Toon O. B., Whitten R. C., Keesee R. G. and Hamill P. (1982) Importance of heterogeneous processes to tropospheric chemistry: Studies with a one-dimensional model. *Heterog. Atmos. Chem., Geophys. Monograph Series,* **26** 231 - 240.

Turco R. P. (1990) *Atmospheric Radiation: Atmospheric Sciences 203C, Spring 1990.* Course Notes.

Turco R. P. (1994) *Air Pollution: Local, Regional, and Global Issues.* Dept. of Atmospheric Sciences, Univ. of California, Los Angeles.

U. S. Department of the Army (1958) Universal Transverse Mercator grid. Tables for transformation of coordinates from grid to geographic; Clarke 1866 Spheroid. U. S. Government Printing Office, Washington, D. C..

433

U. S. Environmental Protection Agency (USEPA) (1978) Air quality criteria for ozone and other photochemical oxidants. *Report No. EPA-600/8-78-004.*

U. S. Environmental Protection Agency (USEPA) (1991) Guideline for regulatory application of the Urban Airshed Model. U. S. EPA Office of Air Quality Planning and Standards, Technical Support Division, Research Triangle Park, North Carolina.

van de Hulst H. C. (1957) *Light Scattering by Small Particles.* John Wiley, New York.

Venkataraman C., Lyons J. M. and Friedlander S. K. (1994a) Size distributions of polycyclic aromatic hydrocarbons and elemental carbon. 1. Sampling, measurement methods, and source characterization. *Environ. Sci. Technol.* **28**, 555 - 562.

Venkataraman C. and Friedlander S. K. (1994b) Size distributions of polycyclic aromatic hydrocarbons and elemental carbon. 2. Ambient measurements and effects of atmospheric processes. *Environ. Sci. Technol.* **28**, 563 - 572.

Waggoner A. P., Weiss R. E., Ahlquist N. C., Covert D. S., Will S. and Charlson R. J. (1981) Optical characteristics of atmospheric aerosols. *Atmos. Environ.* **15**, 1891 - 1909.

Wakimoto R. M. (1987) The Catalina Eddy and its effects on pollution over Southern California. *Mon. Wea. Rev.* **115**, 837 - 855.

Wakimoto R. M. and McElroy J. L. (1986) Lidar observations of elevated pollution layers over Los Angeles. *J. Climate Appl. Meteor.* **25**, 1583 - 1599.

Walcek C. J., Brost R. A., Chang J. S. and Wesely M. L. (1986) SO_2, sulfate, and HNO_3 deposition velocities computed using regional landuse and meteorological data. *Atmos. Environ.* **20**, 949 - 964.

Wasa T. and Musha S. (1970) Polarographic behavior of glyoxal and its related compounds. *Univ. Osaka Prefect. Ser.* **19**, 169 - 180.

Weast R. C., Ed. (1986) *Handbook of Chemistry and Physics*. CRC Press, Inc., Cleveland, OH.

Weeks J. L. and Rabani J. (1966) The pulse radiolysis of dearated aqueous carbonate solutions. *J. Phys. Chem.* **70**, 2100 - 2106.

Westphal D. L., Toon O. B. and Carlson T. N. (1988) A case study of transport and mobilization of Saharan dust storms. *J. Atmos. Sci.* **45**, 2144 - 2160.

Westphal D. L. and Toon O. B. (1991) Simulations of microphysical, radiative, and dynamical processes in a continental-scale forest fire smoke plume. *J. Geophys. Res.* **96**, 22,379 - 22,400.

Wexler A. S. and Seinfeld J. H. (1990) The distribution of ammonium salts among a size and composition dispersed aerosol. *Atmos. Environ.* **24A**, 1231 - 1246.

Wexler A. S. and Seinfeld J. H. (1991) Second-generation inorganic aerosol model. *Atmos. Environ.* **25A**, 2731 - 2748.

Wexler A. S. and Seinfeld J. H. (1992) Analysis of aerosol ammonium nitrate: Departures from equilibrium during SCAQS. *Atmos. Environ.* **26A**, 579 - 591.

Wexler A. S., Eldering A., Pandis S. N., Cass G. R., Seinfeld J. H., Moon K. C. and Hering S. (1992) Modeling aerosol processes and visibility based on the SCAQS data. Final Report to the California Air Resources Board under Contract No. A932-054, California Environmental Protection Agency.

Whitby K. T. (1978) The physical characteristics of sulfur aerosols. *Atmos. Environ.* **12**, 135 - 159.

William E. L. II and Grosjean D. (1989) SCAQS: peroxyacetyl nitrate (PAN) measurements. Daniel Grosjean and Associates, Inc., Ventura, CA. Report to the California Air Resources Board under contract A6-099-32.

Williamson S. J. (1973) *Fundamentals of Air Pollution*. Addison Wesley, Reading, Mass..

435

Wine P. H., Tang Y., Thom, R. P., Wells J. R. and Davis D. D. (1989) Kinetics of aqueous-phase reactions of the SO_4^- radical with potential importance in cloud chemistry. *J. Geophys. Res.* **94**, 1085 - 1094.

Winer A. M., Atkinson R. and Pitts J. N. Jr. (1984) Gaseous nitrate radical: Possible nighttime atmospheric sink for biogenic organic compounds. *Science* **224**, 156.

Winer A. M., Biermann H. W., Dinoff T., Parker L. and Poe M. P. (1989) Measurements of nitrous acid, nitrate radicals, formaldehyde and nitrogen dioxide for the SCAQS by differential Optical Absorbtion Spectroscopy. Statewide Air Pollution Research Center, University of California, Riverside, CA. Report to the California Air Resources Board under Contract A6-146-32.

Winer A. M. and Biermann H. W. (1994) Long pathlength differential optical absorption spectroscopy (DOAS) measurements of gaseous HONO, NO_2 and HCHO in the California south coast air basin. *Res. Chem. Intermed.* **20**, 423-445.

Woodcock A. H. (1953) Salt nuclei in marine air as a function of altitude and wind force. *J. Meteorol.* **10**, 362.

World Meteorological Organization (WMO) (1988) Report of the international ozone trends panel - 1988. Vol. II. *Global Ozone Research and Monitoring Project -- Report 18.*

Zhao J.-X. (1993) Numerical studies of the stratospheric aerosol layer under background and perturbed conditions. Ph. D. Thesis, Dept. of Atmospheric Sciences, Univ. of California, Los Angeles, CA.